Novel Chemical Probes for the Identification of Physiological Intracellular ADP-ribosylation Targets of PARPs

A Thesis Presented for the Degree of Doctor of Philosophy

by

Simeon Dimitrov Draganov

Department of Chemistry

Imperial College London

June 2022

Declaration of Originality

I, Simeon Dimitrov Draganov, declare that this thesis and the work presented herein are my own original research. Any ideas or information derived from the work of other people, or are the result of collaboration, have been attributed appropriately, fully acknowledged and referenced.

X

SIMEON DIMITROV DRAGANOV
Author

Declaration of Copyright

The copyright of this thesis rests with the author. Unless otherwise indicated, its contents are licensed under a Creative Commons Attribution-Non Commercial 4.0 International License (CC BY-NC).

Under this licence, you may copy and redistribute the material in any medium or format. You may also create and distribute modified versions of the work. This is on the condition that: you credit the author and do not use it, or any derivative works, for a commercial purpose.

When reusing or sharing this work, ensure you make the licence terms clear to others by naming the licence and linking to the licence text. Where a work has been adapted, you should indicate that the work has been changed and describe those changes.

Please seek permission from the copyright holder for uses of this work that are not included in this licence or permitted under UK Copyright Law.

Abstract

Protein post-translational modifications (PTMs) are important for regulating protein function. One such modification, known as ADP-ribosylation, has been shown to be involved in the regulation of various biological processes, and to play a crucial role in the development of pathological conditions and diseased phenotypes, such as cancer. However, the lack of appropriate tools for identifying the protein targets this PTM is found on, in a cellular context and *in vivo*, limits the identification of novel, biologically relevant therapeutic targets.

This thesis focuses on the development, synthesis and biological validation of novel chemical probes for the identification of intracellular physiological ADP-ribosylation targets. Specifically, cell-permeable clickable NAD^+ precursor probes were designed and synthesised. Their utilisation in the cellular NAD^+ biosynthesis pathway, for intracellular metabolic conversion into the corresponding NAD^+ analogues, was investigated through a combination of metabolomics and proteomics methods in several cell lines. Metabolomics analysis revealed that the precursor probes 6Yn-Ad (**25**) and 6Yn-Pro (**47**) were successfully converted intracellularly into the corresponding 6Yn-NAD^+ (**3**) analogue in multiple cell lines. Subsequent analysis by proteomics demonstrated the utilisation of 6Yn-Pro (**47**) for labelling and enrichment of ADP-ribosylated proteins through its metabolic conversion into 6Yn-NAD^+ (**3**), which resulted in the identification of automodified PARP1 and of multiple known ADP-ribosylated proteins in HEK293T cells.

This work therefore provides novel chemical probes for identification of intracellular ADP-ribosylation targets. Ultimately, their use will provide fundamental insights into the role of ADP-ribosylation in biological processes and its contribution to the development of diseased states.

Acknowledgements

First, I would like to thank my supervisors, Prof. Ed Tate, Prof. Dorian Haskard and (my former supervisor) Dr Pete DiMaggio, for providing me with the opportunity to work on an MRes and PhD project under their supervision. Ed, you have been such an amazing supervisor throughout all these years. I wholeheartedly believe, and there is no doubt in my mind, that you are the best mentor I could have ever asked for. You have always been very supportive and understanding. I could only say I wish there were more people like you in academia, who are just as great as individuals as they are talented as scientists. I have always felt very lucky to be in your group and I could never thank you enough for having me in your group and lab since Pete left Imperial, shortly after the beginning of my PhD. Dorian, it has been an absolute privilege to have you as a supervisor. Thank you for being always supportive and for having the patience to endure all those super relevant and interesting organic synthesis schemes. I could not express enough how grateful I am for having you support my British citizenship application back in 2020. I have been able to proudly call myself a British citizen for the past two years thanks to you. You have inspired me to learn more about biology and I am genuinely going to miss our biweekly journal clubs. Pete, I would be lying if I said that it did not make me sad that you left Imperial shortly after my MRes year. If you ever read this, you should know that I always appreciated your guidance and support, and that everyone in your lab and your former students always thought very highly of you.

I have had the pleasure of collaborating with Prof. Hector Keun's group at Imperial College. Particularly, I would like to thank PhD student Michael Gruet for his contribution to this work. Michael, this project would have been so much more difficult without your ideas and dedication. Our discussions have been invaluable to me, and it has always been a pleasure to talk to you.

It has been a privilege to be a part of the Tate group over the past four years. A big thank you to all Tate group members for making the lab and office such a friendly and nice environment to be working in. I have looked forward to coming to lab every single day, and it has been thanks to you. The Tate group is a very special place. Elena, Ravi, Maria Maneiro, Roxani, Cyrille, Sarah, Leran – I am glad to call you my friends, you have all been amazing and have always lifted me up when I was down. I would like to thank Dan Conole and Jack for their help and guidance with proteomics, and for always being happy to answer my questions. Thank you also to Dan Lucy and Masha for your help with molecular cloning, I could not have done it

without your input. Thank you to Edward, Ravi and Jennie for always going the extra mile to make sure the lab was running smoothly and to listen to the concerns of all group members. I would like to express my eternal appreciation to Elena, Ravi, Jack and Dorian for their time spent on proofreading the different chapters in this thesis – thank you all so much for your comments and suggestions.

Finally, I would like to thank my parents. You have supported me unconditionally throughout the years and have always encouraged me to do better and achieve more. None of my achievements would have been possible if it were not for you.

List of Figures

Figure 1.1. Mechanism of protein ADP-ribosylation 28
Figure 1.2. Mechanism of DNA damage repair 30
Figure 1.3. Summary of PARP inhibitors approved for use in the clinic (olaparib, talazoparib, rucaparib, niraparib) or in clinical/preclinical studies (PJ34, veliparib). 34
Figure 1.4. Principle behind the 'bump-hole' approach for PARP target profiling 48
Figure 1.5. Mechanism of diazirine-protein photocrosslinking (photoaffinity labelling) 50
Figure 1.6. Example bifunctional (YnT) and trifunctional (AzTB) click chemistry capture reagents. 53
Figure 1.7. Applications of NAD^+ analogues for the study and analysis of ADP-ribosylation 55
Figure 1.8. Principle of LC-MS/MS analysis for identification of modified sites 59
Figure 1.9. Methods for detection of ADP-ribosylation sites by LC-MS/MS analysis 60
Figure 1.10. Mechanism of fragmentation by HCD 63
Figure 1.11. Mechanism of fragmentation by ETD 65
Figure 1.12. Structure of aminooxy probe (**19**). 68
Figure 1.13. Illustration of compartmentalisation of intracellular ATP, β-NMN and NAD^+ biosynthesis 69
Figure 1.14. Mechanism of intracellular conversion of ProTide prodrug adenosine into AMP. 71
Figure 1.15. Structures of β-NMN and NAD^+ precursors involved in NAD^+ biosynthesis. 72
Figure 2.1. Interaction maps of NAD^+ (**A**) and ATP (**B**) 77
Figure 2.2. Schematic representation of the NAD^+ biosynthesis pathway 79
Figure 2.3. Structures of the five metabolite analogue series investigated for utilisation in NAD^+ biosynthesis 81
Figure 2.4. Co-crystal structure of adenosine kinase 84
Figure 2.5. Docking of 6Yn-Ad (**25**) with AdK 85
Figure 2.6. Docking of 2Yn-Ad (**26**) with AdK 85
Figure 2.7. Docking of 8But-Yn-Ad (**27**) with AdK 86
Figure 2.8. Docking of 8Yn-Ad (**29**) with AdK 87
Figure 2.9. Docking of 6Az-Ad (**28**) with AdK 87
Figure 2.10. Co-crystal structure of adenylate kinase 1 91
Figure 2.11. Docking of 6Yn-AMP (**30**) with AK1 92
Figure 2.12. Docking of 2Yn-AMP (**31**) with AK1 93
Figure 2.13. Docking of 8But-Yn-AMP (**32**) with AK1 94
Figure 2.14. Docking of 8Yn-AMP (**34**) with AK1 95
Figure 2.15. Docking of 6Az-AMP (**33**) with AK1 96
Figure 2.16. Co-crystal structure of bovine F1-ATPase 99
Figure 2.17. Docking of 6Yn-ADP (**35**) with F1-ATPase 100
Figure 2.18. Docking of 2Yn-ADP (**36**) with F1-ATPase 101
Figure 2.19. Docking of 8But-Yn-ADP (**37**) with F1-ATPase 102
Figure 2.20. Docking of 6Az-ADP (**38**) with F1-ATPase 103

Figure 2.21. Docking of 8Yn-ADP (**39**) with F1-ATPase 104
Figure 2.22. Co-crystal structure of NMNAT1 107
Figure 2.23. Docking of 6Yn-ATP (**40**) with NMNAT1 108
Figure 2.24. Docking of 8But-Yn-ATP (**42**) with NMNAT1 109
Figure 2.25. Docking of 8Yn-ATP (**44**) with NMNAT1 110
Figure 2.26. Docking of 2Yn-ATP (**41**) with NMNAT1 111
Figure 2.27. Docking of 2Yn-ATP (**41**) with V186G NMNAT1 112
Figure 2.28. Docking of 6Az-ATP (**43**) with NMNAT1 113
Figure 2.29. Co-crystal structure of PARP1 116
Figure 2.30. Docking of 2Yn-NAD^+ (**9**) with PARP1 117
Figure 2.31. Docking of 8Yn-NAD^+ (**46**) with PARP1 118
Figure 2.32. Docking of 6Yn-NAD^+ (**3**) with PARP1 119
Figure 2.33. Side view of the binding modes of NAD^+ (white) and docked 6Yn-NAD^+ (**3**) (yellow) in the NAD^+ binding site 120
Figure 2.34. Docking of 8But-Yn-NAD^+ (**14**) with PARP1 121
Figure 2.35. Docking of 6Az-NAD^+ (**45**) with PARP1 122
Figure 2.36. Docking of 8But-Yn-NAD^+ (**14**) with L877A PARP1 124
Figure 2.37. Binding modes of docked NAD^+ in the NAD^+ binding site of WT PARP1 (**A**) and 8But-Yn-NAD^+ (**14**) in the NAD^+ binding site of L877A PARP1 mutant (**B**) 125
Figure 2.38. Structures of proposed ProTide prodrugs of adenosine analogues 129
Figure 3.1. Summary of adenosine analogues attempted for synthesis 136
Figure 3.2. Summary of successfully synthesised ProTide analogue probes. 142
Figure 3.3. Structures of bulky bases tested for AMP analogue synthesis. 145
Figure 3.4. Summary of 6Yn- and ^{15}N- phosphorylated metabolites attempted for synthesis 154
Figure 4.1. NAD^+ biosynthesis pathway starting from adenosine or adenosine ProTide prodrug 160
Figure 4.2. In-gel fluorescence images showing protein labelling in live-cell samples after treatment with 6Yn-Ad (N^6pA, (**25**)), 2Yn-Ad (**26**) or Yn-C14 (positive control) 162
Figure 4.3. Overview of the sample processing workflows employed for analysis by IGF and proteomics in Westcott et al.[164] (top), and in this work (bottom). 163
Figure 4.4. In-gel fluorescence images showing protein labelling in live-cell MDA-MB-231 samples treated with 6Yn-Ad (**25**), 6Yn-Pro (**47**), co-treated with 6Yn-Ad (**25**) and 2Yn-Ad (**26**), or Yn-C14 (positive control) 165
Figure 4.5. In-gel fluorescence images showing protein labelling in denatured MDA-MB-231 lysates (**A**) and live-cell MDA-MB-231 samples (**B**) 167
Figure 4.6. In-gel fluorescence and western blot images showing protein labelling in live-cell MDA-MB-231 samples treated with 6Yn-Ad (**25**) and 2Yn-Ad (**26**) 169
Figure 4.7. Screening of overall MARylation/PARylation protein levels in MDA-MB-231 cells 171
Figure 4.8. Utilisation of 6Yn-Pro (**47**) for protein AMPylation 172
Figure 4.9. Screening of protein expression levels in MDA-MB-231, HEK293T, T47D and COV318 cells 175

Figure 4.10. Screening of NMNAT1 expression levels in MDA-MB-231, HEK293T, T47D, COV318 and MDA-MB-435 cells....176
Figure 4.11. In-gel fluorescence images showing protein labelling in live-cell MDA-MB-231, MDA-MB-435, HEK293T and T47D samples....177
Figure 4.12. In-gel fluorescence (top panels) and western blot (bottom panels) images showing protein labelling in live-cell HEK293T and T47D samples....179
Figure 4.13. In-gel fluorescence images showing RNA loading (**A**) and RNA labelling (**B**) in HEK293T-probe treated samples....181
Figure 4.14. In-gel fluorescence (top panel) and western blot (bottom panel) images showing protein labelling in live-cell HEK293T samples....183
Figure 4.15. Western blot (**A**) and in-gel fluorescence (**B**) images showing protein labelling in live-cell HEK293T samples after probe treatment and NMNAT1 overexpression....185
Figure 4.16. In vitro assay with recombinant NMNAT1 and (6Yn-)ATP....187
Figure 4.17. Workflows followed in metabolomics experiments....192
Figure 4.18. Intracellular metabolic production of 6Yn-AMP (**30**) in probe-treated COV318 cells....194
Figure 4.19. Time course experiment for COV318 cells treated with 6Yn-Ad (**25**)....196
Figure 4.20. Metabolite profiling in HEK293T cells following NMNAT1 overexpression and treatment with 6Yn-Ad (**25**)....199
Figure 4.21. Effect of supplementation of NAD^+ precursors on intracellular NAD^+ levels....201
Figure 4.22. Effect of supplementation of NAD^+ precursors on intracellular 6Yn-metabolites levels....203
Figure 4.23. Effect of H_2O_2 treatment on intracellular 6Yn-metabolites levels in the presence/absence of NRH (**24**) supplementation....205
Figure 4.24. Overview of the proteomics workflow followed for protein identification....210
Figure 4.25. Overview of TMT-labelling for peptide quantification....211
Figure 4.26. Profile plots showing protein labelling profiles in HEK293T cells....212
Figure 4.27. Protein labelling profiles of 6Yn-Pro-treated HEK293T cells....217
Figure 4.28. Screening of MARylation/PARylation protein levels by western blotting before and after treatment with the PARG inhibitor PDD00017273....219
Figure 4.29. Protein labelling profiles of 6Yn-Pro-treated HEK293T cells following NMNAT1 overexpression....220
Figure 4.30. Protein labelling profiles of 6Yn-Pro-treated HEK293T cells following NMNAT1 overexpression and sequential protein pull-down steps....223
Figure 4.31. Protein labelling profile of 6Yn-Pro-treated HEK293T cells following NMNAT1 overexpression (reanalysis)....226
Figure 4.32. Comparison of protein labelling profiles of 6Yn-Pro-treated HEK293T cells following NMNAT1 overexpression, with (**A**) and without (**B**) H_2O_2 treatment prior to cell lysis....227
Figure 4.33. Comparison of protein labelling profiles of 6Yn-Pro-treated HEK293T cells following NMNAT1 overexpression, with (**A**) and without (**B**) H_2O_2 treatment prior to cell lysis (S-plots)....227

Figure 4.34. Summary statistics for the mean enrichment (Log_2 Fold change) for the data set of 21 known ADP-ribosylated proteins (highlighted in green) from **Figure 4.32** and **Figure 4.33**.....229
Figure 6.1. Pharmacophore placement (highlighted in green) on adenine moiety on (**A**) adenosine, AMP, ADP and ATP ligands, and (**B**) on adenine and nicotinamide moieties on NAD^+ ligands.....291
Figure A.1. Domain structures of PARPs.....317
Figure A.2. Structures of all click chemistry capture reagents employed in this work.....318
Figure A.3. Analytical LC-MS traces for 6Yn-Pro (**47**) synthesis reactions.....319
Figure A.4. Analytical LC-MS trace for 6Yn-AMP (**30**) synthesis reaction.....320
Figure A.5. Analytical LC-MS trace for 6Yn-AMP morpholidate (**87**) after precipitation in MeCN.....320
Figure A.6. RNA expression levels of (**A**) SLC12A8 and (**B**) PARP1 in different cell lines 321
Figure A.7. Plasmid map for CMV NMNAT1 plasmid 323
Figure A.8. Plasmid map for CMV N-FLAG-NMNAT1 plasmid 324
Figure A.9. Plasmid map for CMV 3x N-FLAG-PARP1 plasmid.....325
Figure A.10. Cytotoxicity data (IncuCyte assays) for MDA-MB-231 cells following treatment with 6Yn-Ad (**25**) or 2Yn-Ad (**26**) 332

List of Tables

Table 1.1. Summary of PARP ADP-ribosylation activity and their corresponding catalytic motifs 29
Table 1.2. Overview of NAD^+ analogues developed and used in literature studies 39
Table 1.3. Summary of click reactions commonly used for click probe capture and bioconjugation applications 52
Table 2.1. Summary of adenylate kinases from different species 88
Table 2.2. Active site sequence alignment comparison for all PARPs relative to the PARP1 residue region 873 – 881 125
Table 3.1. Summary of the isolated % yield obtained for each synthesised ProTide probe. 140
Table 4.1. Summary of absorbance gradients (see **Figure 4.16B**) 188
Table 4.2. Summary of PARP1 enrichment in 6Yn-Pro-treated samples compared to DMSO (AzB) control (see **Figure 4.26**). 213
Table 4.3. Summary of the total number of proteins enriched (Log_2 Fold change >0) in 6Yn-Pro-treated samples compared to DMSO (AzB) control (see **Figure 4.26**) 214
Table 4.4. Summary of HSPA5 enrichment in 2Yn-Ad-treated samples compared to DMSO (AzB) control (see **Figure 4.26**). 215
Table 6.1. Volumes of appropriate media/buffer used for cell seeding, cell assays, cell washing and cell lysis. 257
Table 6.2. Recipes for the preparation of SDS-PAGE gels of different gradients. 259
Table 6.3. Types of antibodies and reagents used for western blotting applications 261
Table 6.4. Summary of the reagents and the corresponding amounts used in PCR amplification reactions. 263
Table 6.5. Summary of the thermocycling conditions used for PCR amplification reactions. 264
Table 6.6. Forward primer and reverse primer sequences for retroviral NMNAT1 and CMV FLAG plasmids 265
Table 6.7. Forward primer and reverse primer sequences for retroviral NMNAT1 and CMV plasmids 266
Table 6.8. Measured concentrations of NMNAT1 fragments, non-ligated CMV plasmid and non-ligated CMV FLAG plasmid after PCR amplification 268
Table 6.9. Summary of the reagents and the corresponding amounts used in Gibson Assembly 268
Table 6.10. Summary of the reagents and the corresponding amounts used for plasmid mutagenesis by PCR amplification. 270
Table 6.11. Summary of the thermocycling conditions used for plasmid mutagenesis PCR amplification reactions. 270
Table 6.12. Forward primer and reverse primer sequences for retroviral NMNAT1 and CMV FLAG plasmids 270
Table 6.13. Forward primer and reverse primer sequences possessing the relevant point mutation 3-base long sequence 271

Table 6.14. Volumes/amounts of reagents used for transfection of HEK293T cells in the appropriate volume of seeding media.. 272
Table 6.15. Summary of the reagents and the corresponding amounts used for recombinant NMNAT1 in vitro assays. 273
Table 6.16. List of stock compounds and amounts used in cell culture experiments. 274
Table 6.17. Summary of experimental set-up and reagents used in IncuCyte cell viability assays. 276
Table 6.18. Summary of the reagents and the corresponding amounts used in cell culture RNA labelling experiments....277
Table 6.19. H_2O_2 concentrations and volumes used in H_2O_2 titration cell culture experiments. 279
Table 6.20. Summary of the elution gradients, reagents and the corresponding amounts used in 4-layer fractionation experiments. 281
Table 6.21. Summary of the elution gradients, reagents and the corresponding amounts used in 8-layer fractionation experiments. 282
Table 6.22. List of all monitored metabolites in LC-MS/MS metabolomics experiments ...286
Table A.1. Metabolomics samples treated with isotopically labelled ^{15}N-Pro 326
Table A.2. Proteins in **Figures 4.31A** and **4.31C** (**6Yn-Pro+NM1 vs DMSO+NM1**) that were also identified in **Figures 4.31B** and **4.31D** (**6Yn-Pro+NM1+O vs DMSO+NM1**). .327
Table A.3. Proteins in **Figures 4.31B** and **4.31D** (**6Yn-Pro+NM1+O vs DMSO+NM1**) that were also identified in **Figures 4.31A** and **4.31C** (**6Yn-Pro+NM1 vs DMSO+NM1**).....328
Table A.4. Proteins in **Figures 4.31B** and **4.31D** (**6Yn-Pro+NM1+O vs DMSO+NM1**) that were **not** identified in **Figures 4.31A** and **4.31C** (**6Yn-Pro+NM1 vs DMSO+NM1**).....329
Table A.5. Proteins in **Figures 4.32A** and **4.33A** (**6Yn-Pro+NM1 vs DMSO+NM1, +H_2O_2**) that were also identified in **Figures 4.32B** and **4.33B** (**6Yn-Pro+NM1 vs DMSO+NM1 (PD1), no H_2O_2**) 329
Table A.6. Proteins in **Figures 4.32B** and **4.33B** (**6Yn-Pro+NM1 vs DMSO+NM1 (PD1), no H_2O_2**) that were also identified in **Figures 4.32A** and **4.33A** (**6Yn-Pro+NM1 vs DMSO+NM1, +H_2O_2**) 330
Table A.7. Proteins in **Figures 4.32A** and **4.33A** (**6Yn-Pro+NM1 vs DMSO+NM1, +H_2O_2**) that were **not** identified in **Figures 4.32B** and **4.33B** (**6Yn-Pro+NM1 vs DMSO+NM1 (PD1), no H_2O_2**) 331
Table A.8. Proteins in **Figures 4.32B** and **4.33B** (**6Yn-Pro+NM1 vs DMSO+NM1 (PD1), no H_2O_2**) that were **not** identified in **Figures 4.32A** and **4.33A** (**6Yn-Pro+NM1 vs DMSO+NM1, +H_2O_2**) 331

List of Schemes

Scheme 3.1. Synthetic route for 6Yn-Ad (**25**).....130
Scheme 3.2. Synthetic route for 6Az-Ad (**28**).....131
Scheme 3.3. Synthetic route for 2Yn-Ad (**26**).....132
Scheme 3.4. Synthetic route for 8Yn-Ad (**29**).....133
Scheme 3.5. Synthetic route for 8-iodoadenosine (**59**).....133
Scheme 3.6. Synthetic route for 8But-Yn-Ad (**27**).....134
Scheme 3.7. Synthetic route for ^{15}N-Ad (**63**).....135
Scheme 3.8. Synthesis of 6Yn-Pro (**47**) via 2' and 3' diol protection.....137
Scheme 3.9. Proposed two-step one-pot synthetic route for the synthesis of 6Yn-Pro (**47**). All other ProTide analogues (**48**-**51**, **64**) were synthesised in the exact same manner from their corresponding adenosine analogue starting material (**25**-**28**, **63**).....139
Scheme 3.10. Synthesis of 6Yn-AMP (**30**) via direct 5' OH phosphorylation.....144
Scheme 3.11. Proposed three-step synthesis of 6Yn-AMP (**30**) via 2' and 3' diol protection.....146
Scheme 3.12. Synthetic route for 6Yn-ATP (**40**) and ^{15}N-ATP (**73**).....147
Scheme 3.13. Proposed two-step synthesis of 6Yn-NAD$^+$ (**3**) *via* activation of b-NMN.NEt$_3$ (**82**) with CDI (**83**).....149
Scheme 3.14. Proposed synthetic route for 6Yn-NAD$^+$ (**3**) via coupling to DPS (**85**) and generation of 6Yn-AMP morpholidate (**87**).....150
Scheme 3.15. Proposed synthetic route for 6Yn-NAD$^+$ (**3**) via activation of b-NMN.NEt$_3$ (**82**) with diphenyl phosphoryl chloride (**88**).....151
Scheme 3.16. Synthetic route for NR (**23**).....155
Scheme 3.17. Synthesis of NRH (**24**) via reduction of NR (**23**).....155
Scheme 3.18. Two-step synthesis of NRH (**24**).....156

Table of Contents

Chapter 1 Introduction 27
1.1 Introduction 27
1.1.1 Overview of ADP-ribosylation and PARPs 27
1.1.2 Biological Functions of PARPs and Role of ADP-ribosylation in Disease 29
1.1.2.1 PARylating PARPs 29
1.1.2.2 MARylating PARPs 32
1.1.2.3 PARP Inhibitors in the Clinic 33
1.2 Chemical and Biological Tools for Studying Protein ADP-ribosylation 34
1.2.1 Phosphopeptide/protein Enrichment by TiO_2/Fe-NTA Affinity Chromatography 35
1.2.2 Boronate Affinity Column Chromatography 35
1.2.3 Anti-MAR/PAR Antibodies for Immunofluorescence, Immunoprecipitation and Western Blotting of ADP-ribosylated Proteins 36
1.2.4 MAR/PAR Binding Reagents for Immunofluorescence, Immunoprecipitation and Western Blotting of ADP-ribosylated Proteins 37
1.2.5 Tagging of ADP-ribosylation with NAD^+ Analogues 38
1.2.5.1 Biotinylated and Clickable NAD^+ Analogues for Studying ADP-ribosylation 45
1.2.5.2 Clickable 'Bumped' NAD^+ Analogues for PARP Target Profiling 47
1.2.5.3 Photoclickable NAD^+ Analogues for Identification of NAD^+ Readers 49
1.2.5.4 Fluorescent NAD^+ Analogues for Labelling Nucleic Acids 51
1.3 Capturing of ADP-ribosylation *via* Click Chemistry 52
1.3.1 Overview of Click Chemistry Reactions and Ligation Handles 52
1.3.2 Copper-catalysed Azide-alkyne Cycloaddition 56
1.3.3 Strain-promoted Azide-alkyne Cycloaddition 56
1.3.4 Inverse Electron Demand Diels-Alder Cycloaddition 57
1.3.5 Staudinger Ligation 57
1.4 Identification of ADP-ribosylation Sites by Tandem-mass Spectrometry 58
1.4.1 Principle Behind Tandem-mass Spectrometry 58
1.4.2 Methods for Introducing a Characteristic Mass Shift *via* Reduction of the Size of PAR Chains 59

1.4.2.1 Conversion of PARylation to MARylation by PARG 60
1.4.2.2 Hydrolysis of ADP-ribosylation Chains by Hydroxylamine Treatment 61
1.4.2.3 Reduction of ADP-ribosylation Chains by Hydrofluoric Acid Treatment 61
1.4.2.4 Hydrolysis of ADP-ribosylation Chains by Phosphodiesterases 62
1.4.3 Tandem-mass Spectrometry Peptide Fragmentation Approaches for Identification of MARylation Sites 62
1.4.3.1 Fragmentation by Higher-energy Collision-dissociation 62
1.4.3.2 Fragmentation by Electron-transfer Dissociation 64
1.4.3.3 Fragmentation by Electron-transfer/Higher-energy Collision-dissociation 66
1.4.3.4 Fragmentation by Activated-ion Electron-transfer Dissociation 66
1.5 Studying intracellular ADP-ribosylation 67
1.5.1 Aminooxy Probe for Capturing ADP-ribosylation on D and E Residues 67
1.5.2 NAD^+ Biosynthesis Pathway 68
1.5.3 ProTide Adenosine Prodrugs 70
1.5.4 Boosting NAD^+ Levels Through NAD^+ Precursor Supplementation 72
1.6 Thesis Aims and Objectives 73
Chapter 2 *In Silico* Probe Design 75
2.1 Introduction to Molecular Docking 75
2.1.1 Overview 75
2.1.2 Homology modelling 75
2.1.3 Mutational Analysis 76
2.1.4 Ligand Pharmacophore Constraints 77
2.1.5 Limitations of Molecular Docking 78
2.1.5.1 General Limitations 78
2.1.5.2 Limitations of Homology Modelling 78
2.1.5.3 Limitations on the Use of Pharmacophore Constraints 78
2.2 Modelling of Protein-Ligand Interactions in the NAD^+ Biosynthesis Pathway 79
2.2.1 Rationale for Molecular Docking and Choice of Ligands 79
2.2.2 Adenosine Kinase and Adenosine Analogues 82
2.2.3 Adenylate Kinases and AMP Analogues 88
2.2.4 ATP Synthase and ADP Analogues 97
2.2.5 NMNAT1 and ATP Analogues 105
2.3 Modelling of Protein-Ligand Interactions of PARPs and NAD^+ Analogues 114

2.3.1 PARP1 and NAD^+ Analogues 114
2.3.2 Target Profiling of PARPs *via* the 'Bump-Hole' Approach 123
2.4 Summary and Conclusions 127
Chapter 3 Synthesis of NAD^+ Precursors, Probes and Metabolites 130
3.1 Synthesis of Adenosine Analogues 130
3.1.1 Synthesis of 6Yn-Ad 130
3.1.2 Synthesis of 6Az-Ad 130
3.1.3 Synthesis of 2Yn-Ad 131
3.1.4 Attempted Synthesis of 8Yn-Ad 132
3.1.5 Synthesis of 8But-Yn-Ad 134
3.1.6 Synthesis of ^{15}N-Ad 134
3.1.7 Summary of Adenosine Analogues Synthesised 135
3.2 Synthesis of ProTide Probes 136
3.2.1 Synthesis of ProTides *via* Protection of 2' and 3' OH Groups 136
3.2.2 Synthesis of ProTides *via* Direct 5' Activation 138
3.2.3 Summary of ProTide Probes Synthesised 141
3.3 Synthesis of 6Yn- and ^{15}N-Metabolites 142
3.3.1 Synthesis of 6Yn-AMP and ^{15}N-AMP 143
3.3.1.1 Direct Phosphorylation at 5' OH 143
3.3.1.2 Purification via Reverse-phase and Anion Exchange Chromatography 145
3.3.1.3 Protection of 2' and 3' OH Groups Followed by 5' Phosphorylation 145
3.3.2 Synthesis of 6Yn-ATP and ^{15}N-ATP Metabolites 146
3.3.2.1 Synthesis via Direct 5' Activation and Pyrophosphate Coupling 146
3.3.2.2 Purification via Reverse-phase and Anion Exchange Chromatography 148
3.3.3 Synthesis of 6Yn-NAD^+ and ^{15}N-NAD^+ 148
3.3.3.1 Synthesis of 6Yn-NAD^+ 148
3.3.3.2 Purification of 6Yn-NAD^+ 152
3.3.3.3 Attempted Synthesis of ^{15}N-NAD^+ 153
3.3.4 Summary of 6Yn- and ^{15}N-Metabolites Synthesised 153
3.4 Synthesis of the NAD^+ Precursors NR and NRH 154
3.4.1 Synthesis of NR 154
3.4.2 Synthesis of NRH 155
3.5 Conclusions 156

Chapter 4 Biological Validation of Clickable NAD^+ Precursor Probes 157
4.1 Importance of Studying ADP-ribosylation Intracellularly 157
4.1.1 Identification of Physiological ADP-ribosylation Targets 157
4.1.2 Monitoring Live Cell Dynamics of Physiological ADP-ribosylation 158
4.1.3 Profiling of Intracellular PARP Targets 158
4.2 Evaluation of Previous Studies with 6Yn-Ad, 2Yn-Ad and 6Yn-Pro 159
4.2.1 Protein Labelling Following 6Yn-Ad Treatment 159
4.2.2 Protein Labelling Following 2Yn-Ad Treatment 168
4.2.3 Protein Labelling Following 6Yn-Pro Treatment 171
4.2.4 Conclusions on Previously Published Work 172
4.3 Screening of Cell Lines and Probe Validation by In-gel Fluorescence and Western Blotting 174
4.3.1 Screening of Protein Expression Profiles *via* Western Blotting 174
4.3.2 Probe Validation *via* In-gel Fluorescence and Western Blotting 177
4.3.3 Incorporation of Probes into RNA 180
4.3.4 Utilisation of 6Yn-Pro for AMPylation 182
4.3.5 Effect of NMNAT1 Overexpression on Protein Labelling and ADP-ribosylation Levels 184
4.3.6 NMNAT1 *In Vitro* Assay with ATP and 6Yn-ATP 186
4.3.7 Conclusions from Initial Validation Experiments 189
4.4 Validation of 6Yn-Pro and 6Yn-Ad by Metabolomics 192
4.4.1 Importance of Metabolomics in Studying NAD^+ Biosynthesis 192
4.4.2 Utilisation of 6Yn-Pro for Intracellular 6Yn-AMP Production 194
4.4.3 Utilisation of 6Yn-Ad in 6Yn-NAD^+ Biosynthesis 195
4.4.4 Effect of NMNAT1 Overexpression on 6Yn-NAD^+ Biosynthesis 198
4.4.5 Effect of NR/NRH/β-NMN Supplementation on NAD^+ Biosynthesis 200
4.4.6 Effect of NR/NRH/β-NMN Supplementation on 6Yn-NAD^+ Biosynthesis 202
4.4.7 Effect of H_2O_2 on 6Yn-NAD^+ Biosynthesis 204
4.4.8 Conclusions from Metabolomics Experiments and Future Work 207
4.5 Validation of ProTide Probes by Proteomics 209
4.5.1 Importance of Chemical Proteomics in Studying ADP-ribosylation 209
4.5.2 Protein Quantification Using TMT-labelling 210
4.5.3 Initial Screening of Probes by Proteomics 212
4.5.4 Further Validation of 6Yn-Pro by Proteomics 215

4.5.5 Effect of NMNAT1 Overexpression on Protein Identification by Proteomics 219
4.5.6 Effect of Sequential Pull-downs on Protein Enrichment 222
4.5.7 Suitability of Olaparib for Monitoring ADP-ribosylome 224
4.5.8 Effect of H_2O_2 Treatment on Protein Identification by Proteomics 226
4.5.9 Conclusions from Proteomics Experiments 230
Chapter 5 Conclusions and Future Perspectives 233
Chapter 6 Experimental, Materials and Methods 236
6.1 Chemical Synthesis 236
6.1.1 General Synthetic Methods 236
6.1.2 Analytical Techniques 236
6.1.3 Purification Techniques 236
6.1.4 Synthesis of Adenosine Analogues 237
6.1.4.1 N-(prop-2-yn-1-yl)-9H-purin-6-amine (6Yn-adenine, 93) 237
6.1.4.2 (2R,3S,4R,5R)-2-(hydroxymethyl)-5-(6-(prop-2-yn-1-ylamino)-9H-purin-9-yl)tetrahydrofuran-3,4-diol (6Yn-Ad, 25) 238
6.1.4.3 2-azidoethan-1-amine (54) 238
6.1.4.4 (2R,3R,4S,5R)-2-(6-((2-azidoethyl)amino)-9H-purin-9-yl)-5-(hydroxymethyl) tetrahydrofuran-3,4-diol (6Az-Ad, 28) 239
6.1.4.5 (2R,3R,4S,5R)-2-(6-amino-2-((trimethylsilyl)ethynyl)-9H-purin-9-yl)-5-(hydroxy methyl)tetrahydrofuran-3,4-diol (56) 239
6.1.4.6 (2R,3R,4S,5R)-2-(6-amino-2-ethynyl-9H-purin-9-yl)-5-(hydroxymethyl)tetra hydrofuran-3,4-diol (2Yn-Ad, 26) 240
6.1.4.7 (2R,3R,4S,5R)-2-(6-amino-8-bromo-9H-purin-9-yl)-5-(hydroxymethyl)tetra hydrofuran-3,4-diol (57) 241
6.1.4.8 But-3-yn-1-yl carbamimidothioate (62) 241
6.1.4.9 (2R,3R,4S,5R)-2-(6-amino-8-(but-3-yn-1-ylthio)-9H-purin-9-yl)-5-(hydroxy methyl)tetrahydrofuran-3,4-diol (8But-Yn-Ad, 27) 242
6.1.4.10 (2R,3R,4S,5R)-2-(6-(amino-15N)-9H-purin-9-yl)-5-(hydroxymethyl)tetrahydro furan-3,4-diol (^{15}N-Ad, 63) 242
6.1.5 Synthesis of ProTide Analogues 243
6.1.5.1 Benzyl ((((2R,3S,4R,5R)-3,4-dihydroxy-5-(6-(prop-2-yn-1-ylamino)-9H-purin-9-yl)tetrahydrofuran-2-yl)methoxy)(phenoxy)phosphoryl)-L-alaninate (6Yn-Pro, 47) 244

6.1.5.2 Benzyl ((((2R,3S,4R,5R)-5-(6-((2-azidoethyl)amino)-9H-purin-9-yl)-3,4-dihydro xytetrahydrofuran-2-yl)methoxy)(phenoxy)phosphoryl)-L-alaninate (6Az-Pro, 50).....245

6.1.5.3 Benzyl ((((2R,3S,4R,5R)-5-(6-amino-2-ethynyl-9H-purin-9-yl)-3,4-dihydroxy tetrahydrofuran-2-yl)methoxy)(phenoxy)phosphoryl)-L-alaninate (2Yn-Pro, 48).....246

6.1.5.4 Benzyl ((((2R,3S,4R,5R)-5-(6-amino-8-(but-3-yn-1-ylthio)-9H-purin-9-yl)-3,4-dihydroxytetrahydrofuran-2-yl)methoxy)(phenoxy)phosphoryl)-L-alaninate (8But-Yn-Pro, 49).....247

6.1.5.5 Benzyl ((((2R,3S,4R,5R)-5-(6-(amino-15N)-9H-purin-9-yl)-3,4-dihydroxytetra hydrofuran-2-yl)methoxy)(phenoxy)phosphoryl)-L-alaninate (^{15}N-Pro-Ad, 64).....248

6.1.6 Synthesis of AMP, ATP and NAD$^+$ Analogues.....248

6.1.6.1 ((2R,3S,4R,5R)-5-(6-(amino-15N)-9H-purin-9-yl)-3,4-dihydroxytetrahydrofuran-2-yl)methyl dihydrogen phosphate (^{15}N-AMP, 72).248

6.1.6.2 ((2R,3S,4R,5R)-3,4-dihydroxy-5-(6-(prop-2-yn-1-ylamino)-9H-purin-9-yl)tetra hydrofuran-2-yl)methyl dihydrogen phosphate (6Yn-AMP, 30).....249

6.1.6.3 ((2R,3S,4R,5R)-5-(6-(amino-15N)-9H-purin-9-yl)-3,4-dihydroxytetrahydrofuran-2-yl)methyl tetrahydrogen triphosphate (^{15}N-ATP, 73).....250

6.1.6.4 ((2R,3S,4R,5R)-3,4-dihydroxy-5-(6-(prop-2-yn-1-ylamino)-9H-purin-9-yl)tetra hydrofuran-2-yl)methyl tetrahydrogen triphosphate (6Yn-ATP, 40)....251

6.1.6.5 3-carbamoyl-1-((2R,3R,4S,5R)-5-(((((((((2R,3S,4R,5R)-3,4-dihydroxy-5-(6-(prop-2-yn-1-ylamino)-9H-purin-9-yl)tetrahydrofuran-2-yl)methoxy)(hydroxy)phosphoryl) oxy)(hydroxy)phosphoryl)oxy)methyl)-3,4-dihydroxytetrahydrofuran-2-yl)pyridin-1-ium (6Yn-NAD, 3).....252

6.1.7 Synthesis of NR and NRH.....253

6.1.7.1 3-carbamoyl-1-((2R,3R,4R,5R)-3,4-diacetoxy-5-(acetoxymethyl)tetrahydrofuran-2-yl)pyridin-1-ium (93).....253

6.1.7.2 3-carbamoyl-1-((2R,3R,4S,5R)-3,4-dihydroxy-5-(hydroxymethyl)tetrahydro furan-2-yl)pyridin-1-ium (NR, 23).....254

6.1.7.3 (2R,3R,4R,5R)-2-(acetoxymethyl)-5-(3-carbamoylpyridin-1(4H)-yl)tetrahydro furan-3,4-diyl diacetate (94).....254

6.1.7.4 1-((2R,3R,4S,5R)-3,4-dihydroxy-5-(hydroxymethyl)tetrahydrofuran-2-yl)-1,4-dihydropyridine-3-carboxamide (NRH, 24).....255

6.2 Biological Methods.....256

6.2.1 Tissue Culture.....256

6.2.2 Biochemical Techniques.....258

6.2.2.1 Click Reaction (CuAAC) 258
6.2.2.2 Gel Electrophoresis and In-Gel Fluorescence 258
6.2.2.3 Western Blotting 260
6.2.2.4 Protein Pull-down (Protein Enrichment) 261
6.2.3 Molecular Cloning 262
6.2.3.1 General Methods 262
6.2.3.2 Bacterial Selection, Plasmid Production and Harvesting 263
6.2.3.3 Polymerase Chain Reaction (PCR) Amplification and Primer Design 263
6.2.3.3.1 Primer Sequences and Thermocycling Conditions for Generating CMV N-FLAG-NMNAT1 Plasmid 265
6.2.3.3.2 Primer Sequences and Thermocycling Conditions for Generating CMV NMNAT1 Plasmid 266
6.2.3.4 DNA Gel Electrophoresis 266
6.2.3.5 PCR Product Purification, Gibson Assembly and Plasmid Transformation 267
6.2.3.5.1 PCR Product Purification Protocol 267
6.2.3.5.2 Gibson Assembly Protocol 268
6.2.3.5.3 Plasmid Transformation Protocol 269
6.2.3.6 FLAG-NMNAT1 and 3x-FLAG-PARP1 Plasmid Mutagenesis 269
6.2.3.7 NMNAT1 Overexpression via Transfection of HEK239T Cells 272
6.2.4 Recombinant NMNAT1 *in vitro* Assay 273
6.2.5 Metabolic Incorporation of Adenosine/ProTide Analogues in Cell Lines 274
6.2.5.1 General Methods 274
6.2.5.2 Cytotoxicity Assay in MDA-MB-231 Cells 275
6.2.5.3 RNA Sample Processing – Extraction, Click Reaction and Analysis by RNA Gel Electrophoresis 276
6.2.5.4 Induction of MARylation/PARylation via Hydrogen Peroxide Titration 278
6.3 Proteomics Analysis 279
6.3.1 Sample Preparation for Proteomics Analysis 279
6.3.1.1 General Methods 279
6.3.1.2 Sample Processing (Click, Pull-down, Reduction and Alkylation, Trypsin Digestion) 279
6.3.1.3 Six(6)-plex/ten(10)-plex Tandem Mass Tag (TMT)-labelling 280
6.3.1.4 4-/8-Layer Fractionation 281
6.3.1.5 Desalting 282

6.3.1.6 Sample Dissolution, Filtering and Submission for Analysis 283
6.3.2 LC-MS/MS Proteomics Analysis of TMT-labelled Samples 283
6.3.3 Data Processing and Analysis in MaxQuant/Perseus/PEAKS 284
6.3.3.1 Data Processing in MaxQuant 284
6.3.3.2 Data Analysis in Perseus 284
6.3.3.3 Data Processing and Analysis in PEAKS 285
6.4 Metabolomics Analysis 285
6.4.1 Sample Preparation for Metabolite Extraction 285
6.4.1.1 General Methods 285
6.4.1.2 Sample Processing 285
6.4.2 Targeted Metabolomics LC-MS/MS Method Development 286
6.4.2.1 Parameter Optimisation for MS^2 286
6.4.2.2 Liquid Chromatography Optimisation 288
6.4.3 LC-MS/MS Metabolomics Analysis 288
6.4.4 Data Analysis in Analyst 289
6.5 Molecular Docking 289
6.5.1 General Procedures and Software Information 289
6.5.2 3D Structure Preparation for Ligands 289
6.5.3 Protein-ligand Docking 290
6.5.3.1 General Methods 290
6.5.3.2 Pharmacophores and Constraints 290
6.5.4 Mutational Analysis 291
6.5.5 Homology Modelling of PARPs 291
Bibliography 292
Appendix A 317

Abbreviations

A5PA	Diadenosine pentaphosphate
ABA	3-aminobenzamide
Ac	Acyl
Ad	Adenosine
ADH	Alcohol dehydrogenase
AdK	Adenosine kinase
ADK1	Adenylate kinase (yeast)
ADP	Adenosine diphosphate
ADPr	ADP-ribosylated; ADP-ribosylation; ADP-ribose
AI-ETD	Activated-ion electron-transfer dissociation
AIF	Apoptosis-inducing factor
AK	Adenylate kinase
AKe	Adenylate kinase (*E. coli*)
AMBIC	Ammonium bicarbonate
AMP	Adenosine monophosphate
APE1	Apurinic/apyrimidinic endonuclease 1
APTX	Aprataxin
ARH3	ADP-ribosylhydrolase 3
ATP	Adenosine triphosphate
AUC	Area under the curve
AXC	Anion exchange chromatography
AzB	Azide-biotin
AzRB	Azide-arginine-biotin
AzT	Azide-TAMRA
AzTB	Azide-TAMRA-biotin
BAD	Benzamide adenine dinucleotide
bp	Base pairs
BRCA(1/2)	Breast cancer type (1/2) susceptibility protein
BSA	Bovine serum albumin
CAA	2-chloroacetamide
CD38	ADP-ribosyl cyclase/ cyclic ADP-ribose hydrolase 1
CDI	Carbonyldiimidazole
CE	Collision energy
CID	Collision-induced dissociation
CMV	Cytomegalovirus
CRISPR/Cas9	CRISPR-associated endonuclease caspase 9

CSE1L	Chromosome segregation 1-like protein
CTSB	Cathepsin B
CTSC	Cathepsin C
CTSL	Cathepsin L
CuAAC	Copper-catalysed azide-alkyne cycloaddition
CV	Column volume
Cy(n)	Cyanine
d	Doublet
DAC	Diels-Alder cycloaddition
DCM	Dichloromethane
DDR	DNA damage response
DEAE	Diethylaminoethanol
DHX9	ATP-dependent RNA helicase A
DIPEA	Diisopropylethylamine
DME	Dimethyl ether
DMEM	Dulbecco's Modified Eagle's Medium
DMF	Dimethylformamide
DMSO	Dimethylsulfoxide
DNA	Deoxyribonucleic acid
DP	Declustering potential
DPS	2,2'-dipyridyldisulfide
EDTA	Ethylenediaminetetraacetic acid
EF2	Elongation factor 2
EM	Electron microscopy
ENT	Equilibrative nucleoside transporter
Eq.	Equivalents
$ESI^{(-/+)}$	Electron spray ionisation (negative/positive mode)
Et	Ethyl
ETD	Electron-transfer dissociation
EThcD	Electron-transfer/higher-energy collision dissociation
FA	Formic acid
FBS	Fetal bovine serum
FDR	False discovery rate
NTA	Nitriloacetate
FICD	FIC domain containing protein (protein adenylyltransferase FICD)
GAPDH	Glyceraldehyde-3-phosphate dehydrogenase
GFP	Green fluorescent protein
GSTO1	Glutathione S-transferase omega-1
HCD	Higher-energy collision-dissociation
HEK	Human embryonic kidney

HeLa	Henrietta Lacks
HEPES	4-(2-hydroxyethyl)-1-piperazineethanesulfonic acid
HILIC	Hydrophilic interaction chromatography
HIST1H1C	Histone 1, H1c
HMGB1	High mobility group protein B1
HPF1	Histone PARylation Factor 1
HPLC	High-performance liquid chromatography
HRMS	High-resolution mass spectrometry
HRP	Horseradish peroxidase
HSPA5	Heat shock 70-kDa protein 5
ID	Identification
IGF	In-gel fluorescence
IR	Infrared
J	Coupling constant
KD	Knockdown
K_d	Dissociation constant
KO	Knockout
LB	Lysogeny broth
LC-MS	Liquid chromatography-mass spectrometry
LC-MS/MS	Liquid chromatography/tandem-mass spectrometry
Lig3	DNA ligase 3
△m	Mass shift
m	Multiplet
M	Molecular ion
m/z	Mass to charge ratio
MAR	Mono-ADP-ribose
MARylation	Mono-ADP-ribosylation
MDH1	Malate dehydrogenase, mitochondrial
Me	Methyl
MIF	Migration inhibitory factor
MMS	Methyl methanesulfonate
MOE	Molecular Operating Environment
MOPS	3-(N-morpholino)propanesulfonic acid
MS	Mass spectrometry
MS/MS	Tandem mass spectrometry
MS^1	First mass spectrometer
MS^2	Second mass spectrometer
mTOR2	Mammalian target of rapamycin complex 2
MWL	Molecular weight ladder
MYL6	Myosin light polypeptide 6
N^6pA	6Yn-Ad

NAD^+	Nicotinamide adenine dinucleotide
NADH	Reduced nicotinamide adenine dinucleotide
NAM	Nicotinamide
NAMPT	Nicotinamide phosphoribosyltransferase
NF-kB	Nuclear factor kappa-light-chain-enhancer of activated B cells
NM1	NMNAT1; Nicotinamide mononucleotide adenylyltransferase 1
NMNAT(1/2/3)	Nicotinamide mononucleotide adenylyltransferase (1/2/3)
NMR	Nuclear magnetic resonance
NR	Nicotinamide riboside
NRH	Reduced nicotinamide riboside
NRK1	Nicotinamide riboside kinase 1
NUDT16	Nudix hydrolase 16
O; Ola	Olaparib
OE	Overexpression
PAGE	Polyacrylamide gel electrophoresis
PAR	Poly-ADP-ribose
PARG	Poly(ADP-ribose) glycohydrolase
PARGi	PARG inhibitor
PARP	Poly(ADP-ribose) polymerase
PARylation	Poly-ADP-ribosylation
PBM	PAR-binding motif
PBS	Phosphate-buffered saline
PCA	Principal component analysis
PCR	Polymerase chain reaction
PD(1/2)	Pull-down step (1/2)
PDB	Protein data bank
PDIA3	Protein disulfide-isomerase family A member 3
PDIA6	Protein disulfide-isomerase family A member 6
PNKP	Polynucleotide kinase-phosphatase
Polβ	DNA polymerase beta
PPME1	Protein phosphatase methylesterase 1
PTM	Post-translational modification
PVDF	Polyvinylidene fluoride
q	Quartet
r.t.	Room temperature
RBMX	RNA-binding motif protein X
R_f	Retention factor
RIPA	Radioimmunoprecipitation assay
RNA	Ribonucleic acid

RNF146	Ring finger protein 146
RP	Reverse-phase
RPE1	Retinal pigment epithelial
RPMI	Roswell Park Memorial Institute
rRNA	Ribosomal ribonucleic acid
RSP23	40S ribosomal protein S23
R_t	Retention time
s	Singlet
SAR	Structure-activity relationship
SDB-XC	Polystyrene-divinylbenzene copolymer
SDS	Sodium dodecyl sulfate
SLC12A8	Solute carrier family 12 member 8
SPAAC	Strain-promoted azide-alkyne cycloaddition
SSB	Single-strand break
SVP	Snake venom protein
t	Triplet
Ta	Annealing temperature
TAE	Tris-acetate-EDTA
TAMRA	Carboxytetramethylrhodamine
TBS	1X tris-buffered saline
TBS-T	1X tris-buffered saline + 0.1% (v/v) Tween-20
TBTA	Tris((1-benzyl-4-triazolyl)methyl)amine
*t*Bu	tert-Butyl
TCEP	Tris(2-carboxyethyl)phosphine
TDP1	Tyrosyl-DNA phosphodiesterase 1
TDP2	Tyrosyl-DNA phosphodiesterase 2
TEAB	Triethylammonium bicarbonate
TEB	Tobacco Etch Virus
TFA	Trifluoroacetic acid
TGFβ	Transforming growth factor beta
THF	Tetrahydrofuran
TIC	Total ion chromatogram
TLC	Thin-layer chromatography
TMS	Trimethylsilyl
TMT	Tandem mass tag
UPLC	Ultra-performance liquid chromatography
UV	Ultraviolet
v/v	Volume/volume concentration
VIM	Vimentin
w/v	Weight/volume concentration
WB	Western blotting

WT	Wild-type
XRCC1	X-ray repair cross-complementing protein 1
Yn-C14	Myristic acid alkyne
YnT	Alkyne-TAMRA
β-NMN	Beta-nicotinamide mononucleotide
β-NMNH	Reduced beta-nicotinamide mononucleotide
δ_C	Carbon-13 NMR chemical shift
δ_H	Proton NMR chemical shift
λ_{abs}	Absorbance wavelength
λ_{em}	Emission wavelength

Chapter 1 Introduction

1.1 Introduction

1.1.1 Overview of ADP-ribosylation and PARPs

ADP-ribosylation is a type of reversible post-translational modification (PTM) catalysed by a family of seventeen enzymes, known as poly(ADP-ribose) polymerases (PARPs).[1-3] PARPs utilise the cellular cofactor nicotinamide adenine dinucleotide (NAD^+) for addition of a single (mono-ADP-ribosylation, MARylation) or multiple (poly-ADP-ribosylation, PARylation), up to 200, ADP-ribose units to their targets (**Figure 1.1**).[4] Although best known as a protein PTM, recent studies have demonstrated that PARPs can also catalyse ADP-ribosylation on nucleic acids, including DNA and RNA.[5-8] Due to its high heterogeneity and the build-up of negative charge on a protein upon its modification, substrates possessing this PTM typically acquire different properties and functions from their non-modified state, leading to a large diversity in biological functions.[3]

PARPs are categorised in accordance with their ADP-ribosylation activity (**Table 1.1**). A MARylating PARP is only able to catalyse MARylation of substrate proteins, and PARylating PARPs can only catalyse the formation of poly-ADP-ribose (PAR) chains. A common feature between PARylating PARPs (1, 2, 5a and 5b) is the presence of a catalytic triad in their active site, the motif H-Y-E, necessary for their PARylation activity.[9,10] Due to the presence of the H-Y-E motif in PARP3 and PARP4, these proteins were initially suspected to catalyse PARylation. However, it was later shown that both proteins catalyse MARylation.[3] In contrast to PARylating PARPs, MARylating ones (6 – 12 and 14 – 16) possess a greater variety of catalytic triads, with five motifs identified in total (**Table 1.1**).[9,10] PARP13, on the other hand, possesses a Y-Y-V motif that has been shown to be catalytically inactive.[9,10]

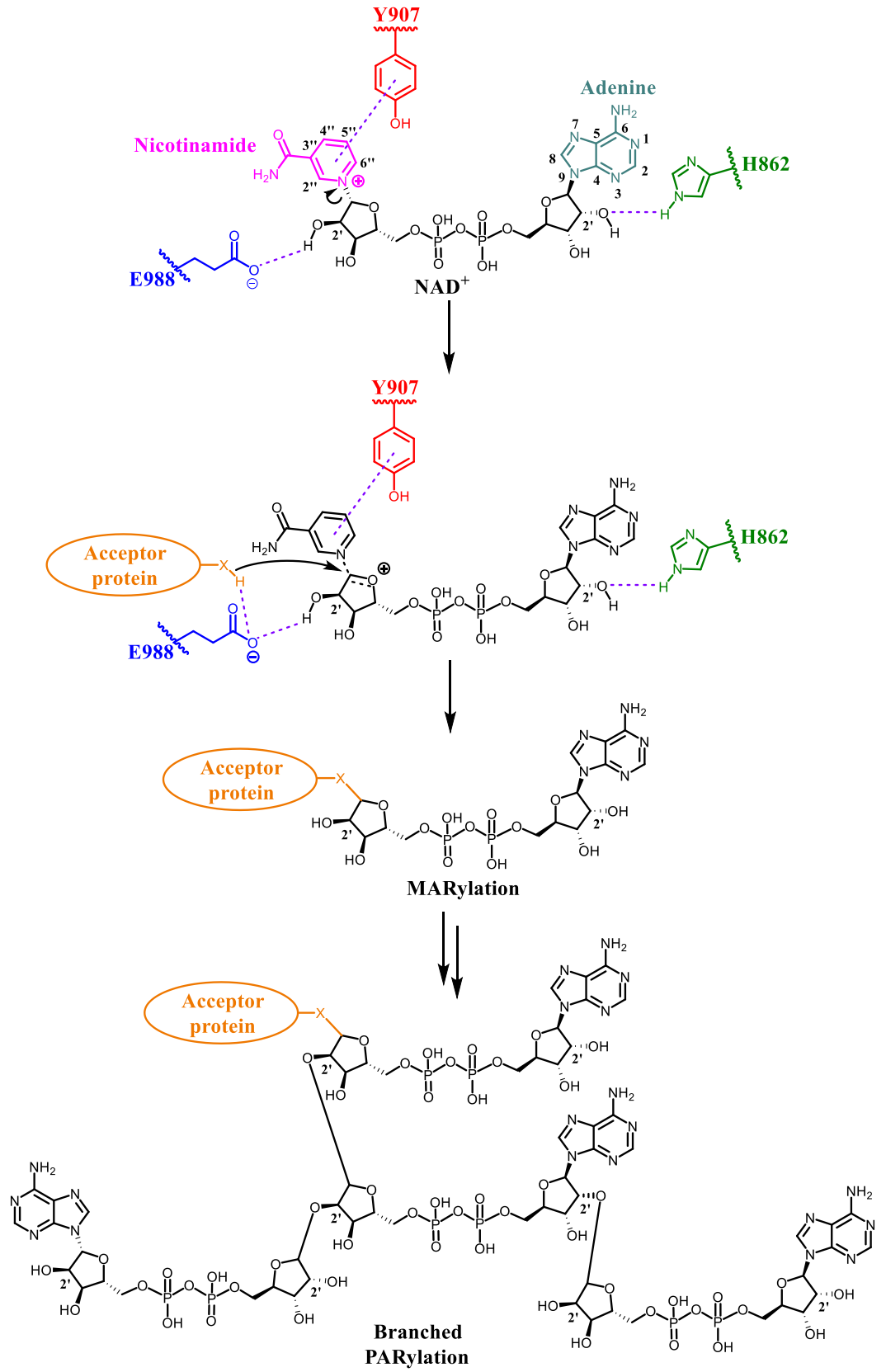


Figure 1.1. Mechanism of protein ADP-ribosylation.[2,11-14] Protein substrate initially undergoes the addition of a single ADP-ribose unit (MARylation), which may be followed by further addition of ADP-ribose units to produce linear or branched chains (PARylation). Elongation/branching occurs at 2'-OH sites. Nicotinamide (pink), adenine

(grey) and PARP catalytic residues (red, blue, green) are highlighted. Purple dotted lines represent interactions between NAD^+ and catalytic residues.

Table 1.1. Summary of PARP ADP-ribosylation activity and their corresponding catalytic motifs.

ADP-ribosylation activity	Catalytic triad	PARP proteins
MARylation	H-Y-E	3 and 4
	H-Y-I	6, 7, 8, 10, 11 and 12
	H-Y-L	14 and 15
	H-Y-Y	16
PARylation	H-Y-E	1, 2, 5a and 5b
None (inactive)	Y-Y-V	13
	Q-Y-T	9

1.1.2 Biological Functions of PARPs and Role of ADP-ribosylation in Disease

1.1.2.1 PARylating PARPs

PARP1

The functions of PARylating PARPs have been well-established over the years and are significantly better understood than those of MARylating PARPs. PARP1, by far the most studied PARP protein, has been shown to consume as much as 90% of all cellular NAD^+ for ADP-ribosylation and to play a pivotal role in the DNA damage response (DDR) for DNA repair (**Figure 1.2**).[15-20] Its activation is highly upregulated in the presence of DNA damage induced by oxidative or genotoxic stress by undergoing self-ADP-ribosylation, a process known as automodification.[15-20] In the presence of a single-strand DNA break, PARP1 binds to the site of damage *via* its three zinc finger domains (**Appendix Figure A.1**). Histone PARylation factor 1 (HPF1), a vital component of the DDR and a PARP1/histone interactor, similarly associates at the site of damage by binding to the PARP1 catalytic domain (binding is independent of PARP1 PARylation activity/automodification, and HPF1 only interacts with histones in the presence of PARP1), ultimately resulting in the formation of a PARP1-HPF1-histone DNA-protein complex.[21,22] In the DDR, the DNA-bound activated PARP1 initially undergoes self-PARylation by automodification. The PARP1-bound HPF1 results in remodelling of the PARP1 active site, which leads to limiting of PARP1 self-PARylation and instead shifts PARP1 ADP-ribosylation activity from aspartate/glutamate residues towards

histone PARylation at serine residues.[21,22] The PARP1/histone PARylation scaffolds subsequently recruit DNA repair proteins (XRCC1, APTX, Polβ, PNKP, APE1, Lig3, TDP1, TDP2, see **Figure 1.2**), all of which are also known to undergo PARylation, at the site of DNA damage. The DNA repair proteins contain PAR-interacting (PAR reader) domains, which facilitate their recruitment towards the PARP1/histone PARylation scaffolds at the site of damage. The resulting formation of the DNA-protein repair complex ultimately leads to the repair of the single-strand break (SSB) DNA site,[2,23] and once DNA repair is complete, PAR chains on histones are hydrolysed by PARG and the DNA-protein complex is dissociated.

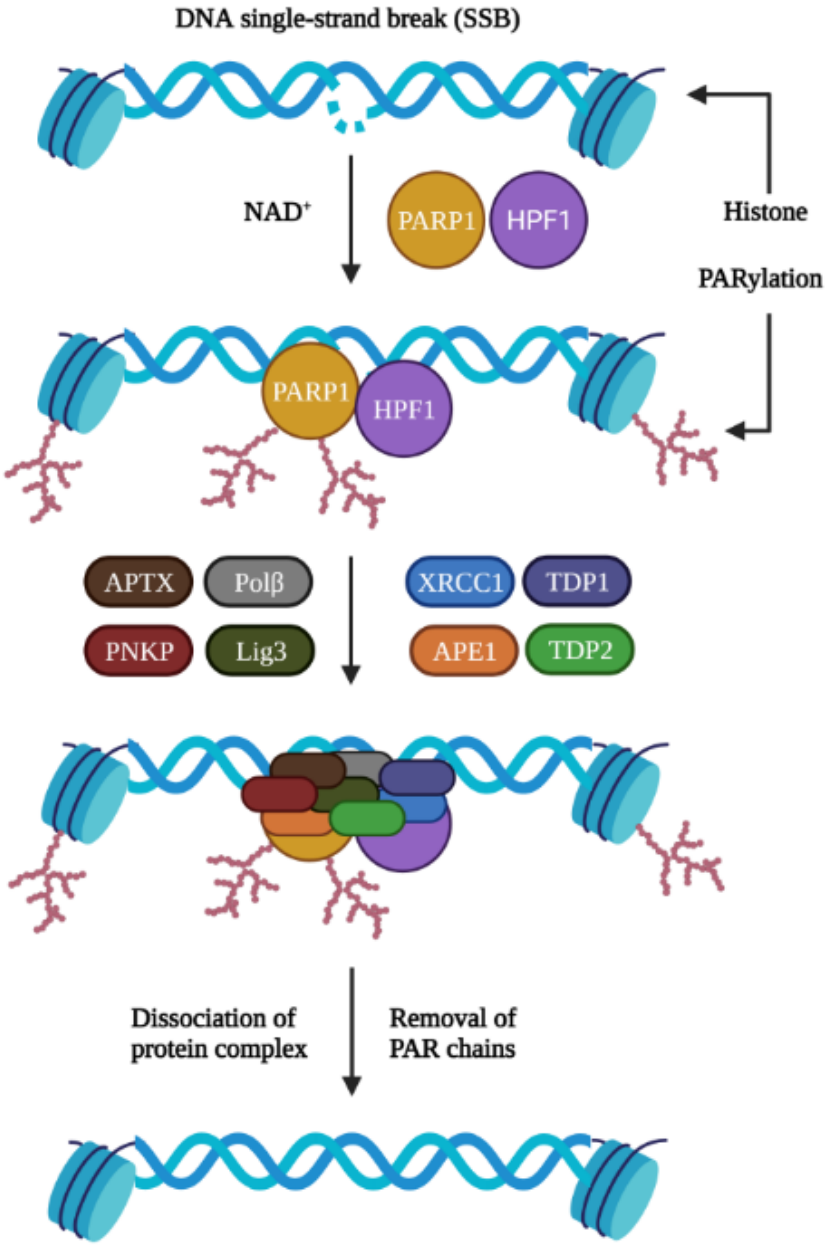


Figure 1.2. Mechanism of DNA damage repair. PARP1 detects SSB, binding to the site of DNA damage along with HPF1. PARP1 binding to the site of damage leads to its activation and automodification. HPF1 remodels the

PARP1 active site, limiting PARP1 automodification and shifting PARylation activity of PARP1 towards serine residues on histones. The PARP1/histone PAR chains recruit DNA repair proteins to the site of damage, resulting in the formation of a DNA-protein repair complex. Following repair of SSB, PAR chains are hydrolysed by PARG and the protein complex dissociates.

In addition to its role in the DDR, PARP1 has been shown to play a primary role in a type of programmed cell death known as parthanatos.[24-26] This arises from over-activation of PARP1 in the DDR, leading to generation of a high number of free large PAR polymers due to PAR chain hydrolysis by poly(ADP-ribose) glycohydrolase (PARG), which then migrate from the nucleus into the cytosol. The resulting build-up of free PAR polymers in the cytosol causes release of apoptosis-inducing factor (AIF) from the mitochondrial membrane into the cytosol.[24,25] Subsequently, AIF associates with migration inhibitory factor (MIF) and the newly formed complex is translocated back into the nucleus, where the complex associates with DNA leading to its degradation and cell death.[25]

Despite its essential functions in the DDR and maintaining genome integrity, PARP1 overexpression has been observed in multiple types of cancer including breast, ovarian, lung and endometrial cancers.[27,28] A 2010 research study demonstrated that PARP1 is upregulated in over 30% of infiltrating ductal carcinoma breast samples and that PARP1 expression levels are at least 2-fold higher in 70% of primary breast carcinomas compared to correspondingly healthy tissue.[27] Given the involvement of PARP1 in tumourigenesis,[27-29] inhibition of PARP1 had been proposed as a viable approach towards development of novel cancer treatments, which ultimately resulted in the discovery of PARP inhibitors and their use in the clinic (see **Section 1.1.2.3**).

PARP2

Alongside PARP1, PARP2 has also been shown to play an important role in the DDR and to catalyse the majority of non-PARP1 cellular ADP-ribosylation.[30,31] In addition to its involvement in the DDR, its importance in maintaining telomere integrity has been demonstrated as well as its role in chromatin remodelling, cell cycle regulation and DNA replication.[32-34] It has also been established that PARP2 partially compensates for loss of PARP1 activity *in vivo*, and, despite sensitisation to genotoxic stress as a result, PARP2 activity compensates enough such that PARP1 knockout (KO) mice are still viable.[35-37] Similarly, PARP2 KO mice are also viable, although, loss of PARP2 activity has been associated with testicular hypoplasia and hypofertility.[32] Further experiments have shown that knockout of both

PARP1 and PARP2 in mice results in early embryonic lethality, demonstrating that although PARP1 and PARP2 partially compensate for loss of activity of each other, other PARPs cannot compensate for complete loss of function of both PARP1 and PARP2.[35-37] PARP2 has also been shown to play an important role in proliferative signalling through regulation of the tumour suppressor transforming growth factor β (TGFβ),[38] thus suggesting that its dysregulation is likely to have major biological consequences, including the development of diseased phenotypes, and could therefore represent a putative therapeutic target.

PARP5a and PARP5b

PARP5a and PARP5b (also known as tankyrase-1 and tankyrase-2, respectively), similarly to PARPs 1 and 2, are PARylating PARPs, and have been shown to play a role in a variety of cellular processes, including the regulation of protein stability through proteasomal degradation, telomere elongation and Wnt signalling.[39-41] Given their diverse functions, dysregulation of both PARPs 5a and 5b has been associated with numerous diseased states, such as the development of obesity, sclerosis and multiple types of cancer.[42-48] In particular, high expression levels of either or both tankyrases have been observed in colon, ovarian, brain and breast cancer.[44,46-48] Thus, recognising PARP5a and PARP5b as therapeutic targets could lead to the development of novel treatments for those diseases.

1.1.2.2 MARylating PARPs

Although the role of PARylating PARPs in different cellular processes has been fairly well established, the biological functions of MARylating PARPs are less well understood and fewer MARylation targets are known in comparison to PARylation targets. Nevertheless, most MARylating PARPs have been implicated in at least one biological function or associated with a diseased state. PARP3, similarly to PARPs 1 and 2, has a well-established role in the DDR.[49,50] On the other hand, PARPs 9, 11, 12, 13, 14 and 15 have been shown to play an important role in antiviral responses and host-virus conflicts.[1,51-56] PARP10 has been shown to be involved in gene transcription *via* regulation of the NF-kB signalling pathway,[57] whereas PARP16 has been implicated in the unfolded protein response,[58] and PARP6 is involved in neurogenesis and neuronal development[59]. PARPs have also been implicated in RNA binding and RNA metabolism, with PARPs 7, 10, 12, 13 and 14 known to bind to RNA through RNA binding CCCH zinc finger domains (PARPs 7, 12 and 13; **Appendix Figure A.1**), or through RNA recognitions motifs (PARPs 10 and 14; **Appendix Figure A.1**).[60,61]

Dysregulation of MARylating PARPs, however, has been linked to development of numerous cancers. High expression levels of PARP14 have been shown to promote proliferation of human pancreatic cancer cells and hepatocellular carcinoma through activation of the nuclear factor kappa B (NF-kB) signalling pathway and the Warburg effect, respectively, whereas knockdown (KD) of PARP14 significantly repressed proliferation.[62,63] PARP10 overexpression has been similarly observed in numerous cancer types, including breast, prostate, pancreas and ovarian.[64] Its knockout by CRISPR/Cas9 genetic editing has been shown to result in decreased proliferation and tumourigenesis of HeLa cells, whereas its overexpression was directly linked to tumour formation in retinal pigment epithelial (RPE1) cells.[64] In a similar manner, it has been demonstrated that PARP3 catalytic activity promotes tumourigenicity of breast cancer type 1 susceptibility protein (BRCA1)-deficient breast cancer cell lines *via* promotion of the Rictor/mTORC2 signalling pathway, and its inhibition led to reduced survival and reduced proliferation of the cancer cells.[65]

1.1.2.3 PARP Inhibitors in the Clinic

The significance of ADP-ribosylation and PARPs in biology and their established roles and relevance in many diseased states, particularly in cancer, has ultimately led to the development of PARP inhibitors (**Figure 1.3**) and their utilisation in the clinic for treatment of certain diseases. Clinical PARP inhibitors are employed for the treatment of cancers possessing mutations in the tumour suppressor breast cancer type 1 and 2 (BRCA1 and BRCA2) genes, which are associated with BRCA loss of activity and tumourigenesis. Olaparib, a potent PARP1 and PARP2 inhibitor, has been used in the clinic since 2014 for the treatment of BRCA-mutated ovarian cancer and has subsequently been approved for the treatment of fallopian tube, peritoneal and metastatic breast cancers.[66,67] The approval of niraparib and rucaparib followed for the treatment of ovarian, fallopian tube and peritoneal cancers, and talazoparib has been used for the treatment of BRCA-mutated advanced breast cancer.[68] Although not yet approved for use in the clinic, clinical studies evaluating the efficacy of veliparib for the treatment of breast and ovarian cancer are under way, and a preclinical study in human pancreatic cancer xenografts with PJ34 has demonstrated its potential for eradication of pancreatic cancer cells.[69,70]

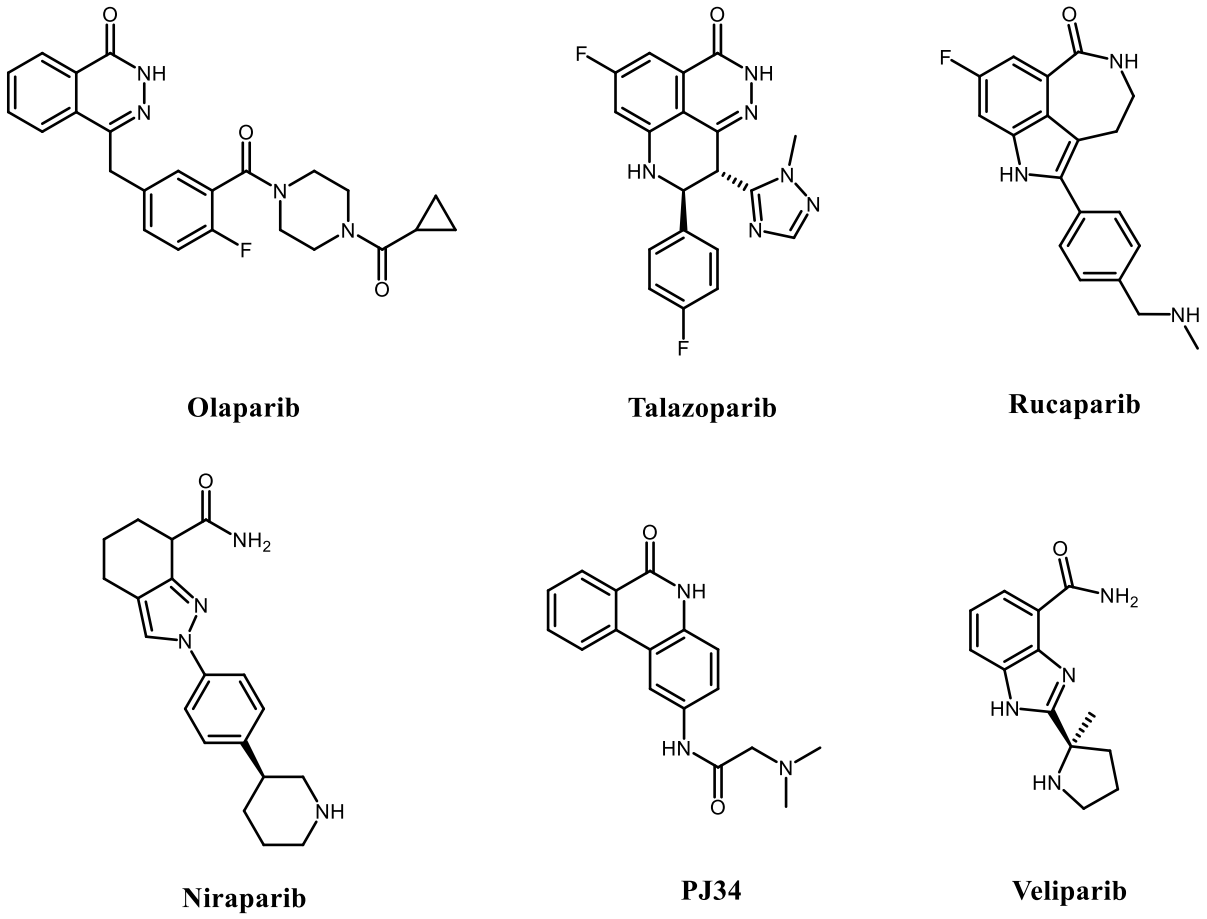


Figure 1.3. Summary of PARP inhibitors approved for use in the clinic (olaparib, talazoparib, rucaparib, niraparib) or in clinical/preclinical studies (PJ34, veliparib).

Due to similarity of PARP active sites, current inhibitors in the clinic exhibit pan-inhibitory activity towards multiple PARPs, although the potency of inhibition varies across the different members of the family. It has been of much interest to develop PARP-specific inhibitors, which has led to discovery of specific inhibitors towards PARP3, PARP5a, PARP5b, PARP10, PARP11 and PARP14.[71-76] However, none of the specific inhibitors developed for those PARPs have been approved for use in the clinic at this stage.

1.2 Chemical and Biological Tools for Studying Protein ADP-ribosylation

The ability to reliably detect and identify ADP-ribosylated proteins in an unbiased fashion is pivotal to better understanding and dissecting the biological functions of ADP-ribosylation. The development of a systematic approach towards identification of the protein substrates that possess this PTM is therefore highly desirable. However, this has been difficult to achieve due to the structural complexity of the modification as well as its lability. Different chemical and biochemical tools have been developed over the years and their suitability investigated for

studying ADP-ribosylation. It is therefore important to address the advantages and limitations of each method, and a discussion of the various methods is outlined in the next sections (**Sections 1.2.1 – 1.2.5**).

1.2.1 Phosphopeptide/protein Enrichment by TiO_2/Fe-NTA Affinity Chromatography

Given the presence of phosphate groups in ADP-ribose units, enrichment of ADP-ribosylated proteins has been previously attempted through phosphoenrichment kits developed for selective pull-down of phosphorylated proteins and peptides.[77] These typically utilise a metal chelate based resin, such as iron-nitrilotriacetate (Fe-NTA), or TiO_2-based resins, which have high affinity for the negatively charged phosphorylated groups.[78,79] The applicability of metal-based resin phosphoenrichment methods, however, is limited since they have no selectivity towards ADP-ribosylated proteins over other phospho-containing species. As a result, those phosphorylated species would represent a significant background signal during liquid chromatography-mass spectrometry (LC-MS) analysis, the main analytical technique employed for identification of ADP-ribosylated proteins (proteomics). Furthermore, the efficiency of enrichment is generally poor and typically estimated to be at a maximum of 3 – 4%,[79] which, in combination with the low abundance of ADP-ribosylation relative to other PTMs, would translate to a need for large sample amounts to ensure reliable detection of protein-derived ADP-ribosylated peptides. Therefore, phosphoenrichment kits are largely deemed unsuitable for proteome-wide enrichment of ADP-ribosylated proteins and peptides, and for their subsequent identification by proteomics methods.

1.2.2 Boronate Affinity Column Chromatography

An alternative method for pull-down of ADP-ribosylated proteins that has been more widely used is boronate affinity chromatography in combination with elution by hydroxylamine (NH_2OH).[80] Zhang *et al.* attempted to profile the global ADP-ribosylome on E and D residues by employing this approach, which led to the identification of 1048 ADP-ribosylation sites on a total of 340 proteins. The methodology has also been applied for the enrichment of PARylated proteins from osteoblasts and vascular smooth muscle cells, in a study performed by (Müller *et al.*,[81] where a potential link between ADP-ribosylation arising from DDR and its role in calcification of arteries through biomineralisation was investigated.

Boronate affinity chromatography, however, relies on the interaction of a boronate group with 1,2-cis-diol groups on molecules/proteins, which makes it a non-specific method for enrichment of ADP-ribosylated proteins. Essentially, any entity possessing 1,2-cis-diol

functionality, including small molecules, nucleic acids, glycoproteins and proteins containing a nucleoside-based PTM (AMPylation,[82] phosphorylation,[83] ADP-ribosylation) will be enriched by this approach. As a result, substantial downstream processing is required to deplete as many 'contaminants' as possible. Furthermore, it is suspected that boronate affinity chromatography may have a bias towards enrichment of PARylated proteins relative to MARylated ones due to the presence of multiple ADP-ribose units in PAR chains.[4] In addition, the combination of boronate enrichment coupled with NH_2OH elution (see **Section 1.4.2.2**) only allows for identification of acidic residues E and D, therefore introducing bias in site identification thus limiting its use for studying ADP-ribosylation.[80]

1.2.3 Anti-MAR/PAR Antibodies for Immunofluorescence, Immunoprecipitation and Western Blotting of ADP-ribosylated Proteins

Given the need for a more specific method for enrichment of ADP-ribosylated proteins, antibodies developed for recognition of ADP-ribose units were employed for use in immunoprecipitation experiments.[84-86] The first antibody to recognise PAR chains was the mouse 10H antibody, developed by Kawamitsu *et al*.[84] Its utilisation for proteome-wide identification of ADP-ribosylated proteins was investigated by Gagné *et al.*,[85] where 10H was conjugated to magnetic beads and employed for the specific pull-down of PARylated proteins *via* immunoprecipitation. In combination with mass spectrometry, the approach led to the identification of ~330 PARylated proteins.[85]

Drawbacks associated with the use of 10H antibody place significant limitations on its use for the study of ADP-ribosylation. Among the main drawbacks is the inability of 10H to recognise MARylation, making it unsuitable for the study of MARylated proteins.[84] Furthermore, the antibody was found to have low affinity for PARylated proteins of 10 ribose units or less thus making it unsuitable for studying proteins possessing shorter PAR chains.[84]

The introduction of a specific monoclonal rabbit antibody by Cell Signalling Technology that was shown by Lu *et al.*[87] to recognise both MARylation and PARylation overcame the limitations associated with the use of antibody 10H. It was successfully used for identification and validation of ADP-ribosylation targets of PARP7 (a MARylating PARP) as well as in immunofluorescence staining experiments for investigating the selectivity of different PARP inhibitors, and for monitoring ADP-ribosylation following PARPs overexpression.[87] Subsequently, MAR-specific antibodies were developed against serine MARylation as well as generic MARylation and MAR/PAR recognising antibodies.[88] In Bonfiglio *et al.*, serine-

specific and generic anti-MAR antibodies were used in immunoprecipitation experiments with H_2O_2-treated HeLa cells for the enrichment of ADP-ribosylation targets associated with the HPF1/PARP1 complex (i.e., ADP-ribosylation targets involved in the DDR). This led to the identification of 272 MARylation sites on 151 known targets by tandem mass spectrometry (LC-MS/MS) analysis.[88] Through a combination of western blotting (WB) and immunofluorescence, Bonfiglio *et al.* further demonstrated the surprising prevalence of MARylation over PARylation on serine PARP1 and histone H3 residues in H_2O_2-treated HeLa cells. Bonfiglio *et al.*'s findings also showed that PARP1 generated PARylation at those sites was rapidly degraded by PARG into MARylation in wild-type (WT) cells, as illustrated by the substantial decrease in detected MARylation upon PARG knockdown, and hence the observed prevalence of MARylation.[88]

1.2.4 MAR/PAR Binding Reagents for Immunofluorescence, Immunoprecipitation and Western Blotting of ADP-ribosylated Proteins

Prior to the development of anti-MAR and anti-pan-ADP-ribose antibodies, ADP-ribose binding reagents based on MARylation/PARylation recognition (macro)domains that bind MAR and/or PAR chains were developed.[89,90] Functionalisation of the domains by Gibson *et al.*[90] was achieved *via* their fusion to a rabbit Fc domain, which allowed for their use in western blotting, immunoprecipitation and affinity pull-down experiments involving ADP-ribosylated proteins.

Forst *et al.*[89] demonstrated the ability of human PARP14 macrodomains 2 and 3 to bind MARylated PARP10 as well as its MARylated substrates *via* recognition of the MAR unit. In contrast, the macrodomain on human macroH2A1.1 was found to bind PAR chains and interact with automodified PARP1 but not with automodified PARP10, leading to the hypothesis that this histone macrodomain only recognised PAR chains but not MAR. Another type of domain, the WWE domain of human RNF146, an E3 ubiquitin ligase involved in regulating axin degradation, was shown to recognise PAR chains and bind PARylated proteins, and subsequently ubiquitinate them.[91,92]

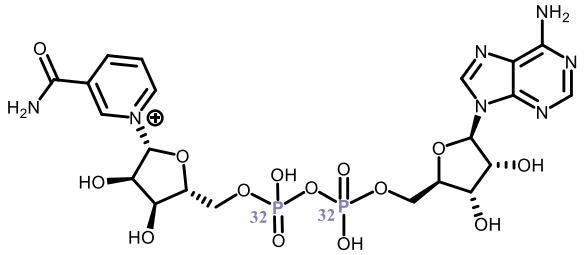
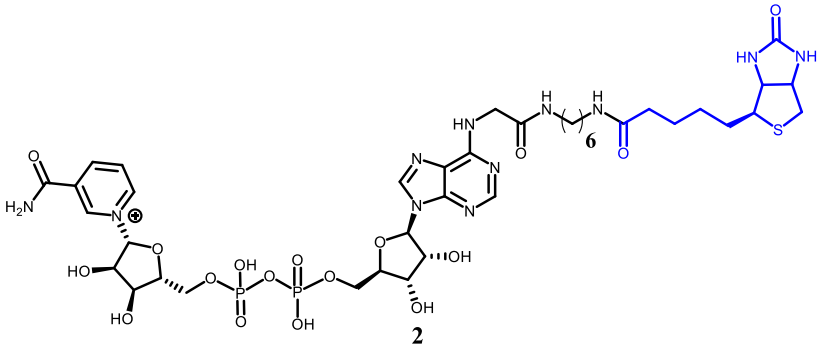
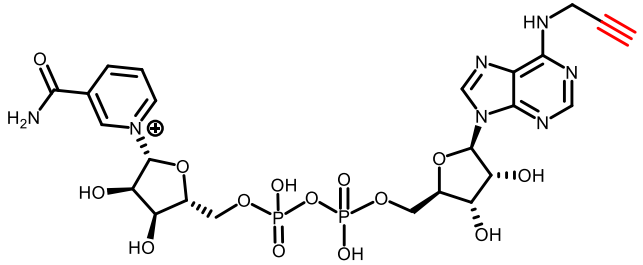
In addition to ADP-ribosylation recognition domains from human proteins, a macrodomain of the ADP-glycohydrolase Af1521 from *Archaeglobus fulgidus* was shown to exhibit high affinity, in the nanomolar range, for PAR chain binding.[93,94] Af1521 macrodomain-based affinity resins were subsequently developed and employed in numerous studies for unbiased proteome-wide enrichment of MARylated and PARylated proteins and peptides *via* affinity

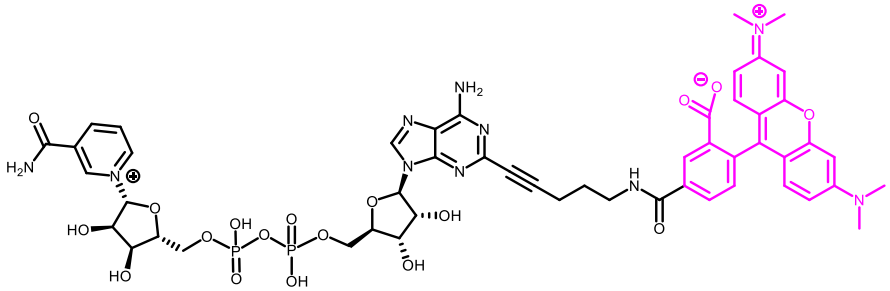
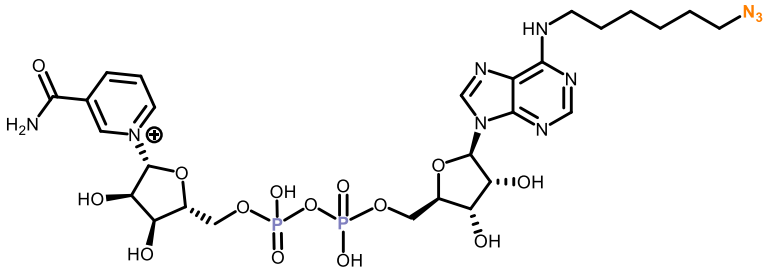
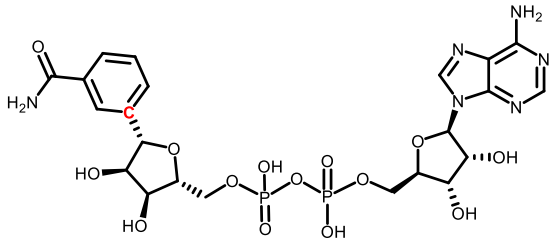
purification.[95-100] Their use has proven popular in combination with MS-based proteomics analysis for site identification and localisation of ADP-ribosylation.[95-100] More recently, Hendriks *et al.* employed Af1521 for peptide-level enrichment and demonstrated through proteomics analysis that MARylation appears to be the dominant form of cellular ADP-ribosylation.[100] Similarly, Buch-Larsen *et al.* utilised the Af1521 macrodomain enrichment strategy in combination with LC-MS/MS analysis for the identification of over 5000 ADP-ribosylation sites from HeLa lysates,[99] thus demonstrating the applicability of Af1521 for proteome-wide scale study of ADP-ribosylation.

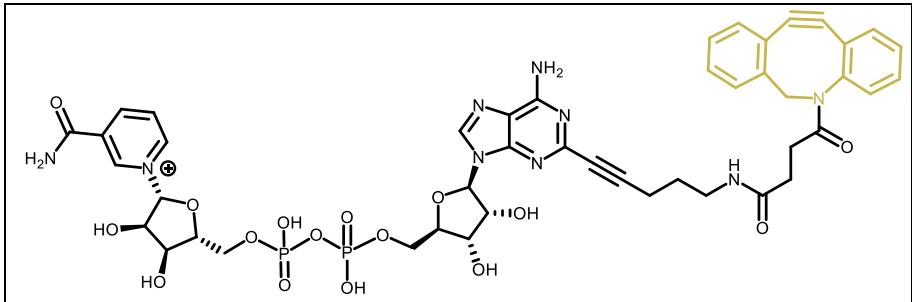
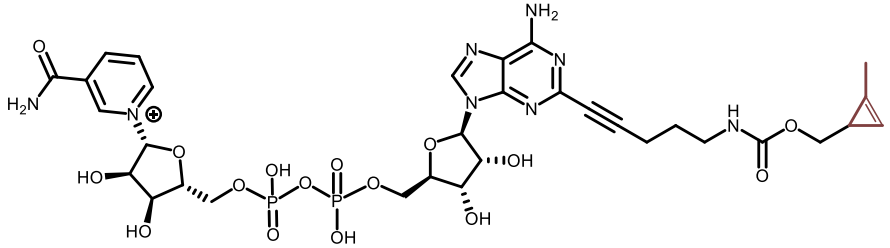
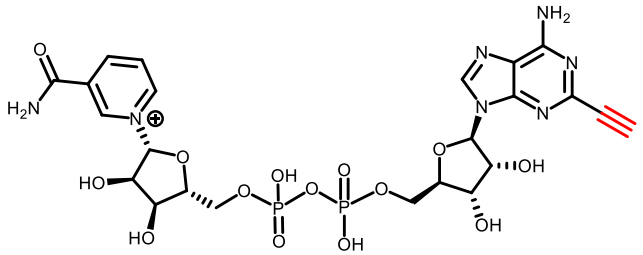
1.2.5 Tagging of ADP-ribosylation with NAD^+ Analogues

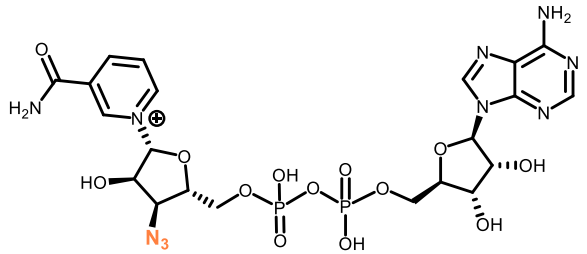
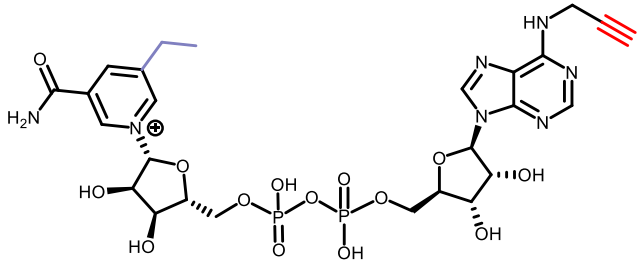
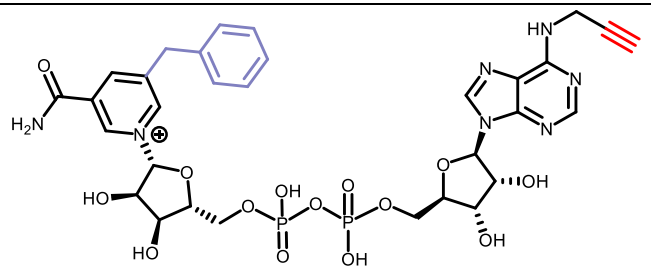
A relatively novel approach employed for the study of ADP-ribosylation dynamics and identification of ADP-ribosylated proteins is the use of tagged NAD^+ analogues (**Table 1.2**), particularly those incorporating clickable groups. A radiolabelled ^{32}P-NAD^+ analogue (**1**) has been used for decades for in-gel visualisation, by autoradiography, of labelled ADP-ribosylated proteins, free PAR chains and ADP-ribosylation labelling on the nucleic acids DNA and RNA.[5,6,101-103] However, the lack of an affinity handle on ^{32}P-NAD^+ does not allow for selective pull-down of ADP-ribosylated substrates and the analogue also cannot be used for fluorescence imaging/microscopy in cells. The development of functionalised NAD^+ analogues that can be used for multiple applications has therefore been a topic of much research. An overview of NAD^+ analogues synthesised in the literature, along with a summary of their applications, is provided in **Table 1.2**.

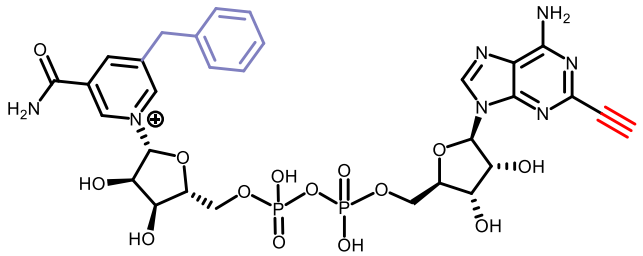
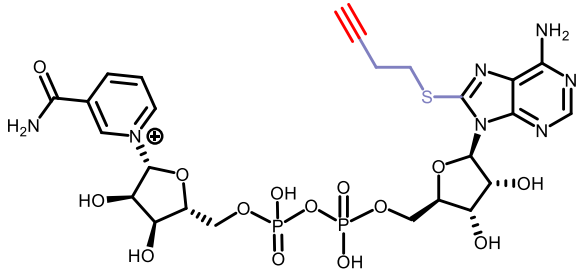
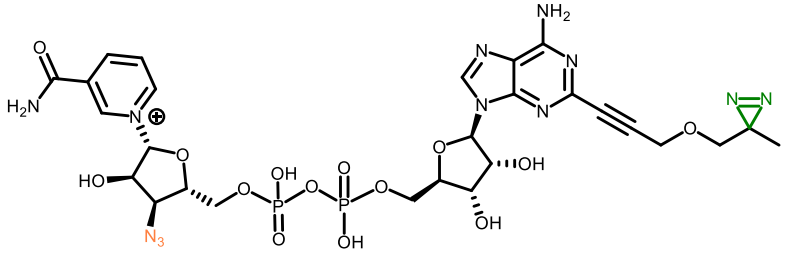
Table 1.2. Overview of NAD^+ analogues developed and used in literature studies. A summary of their applications is included.

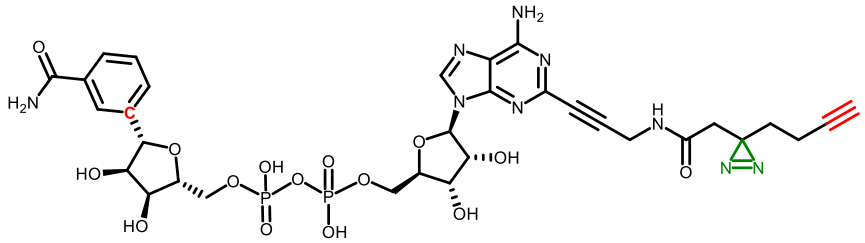
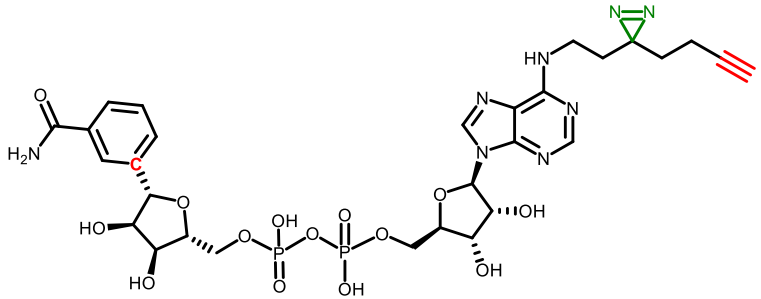
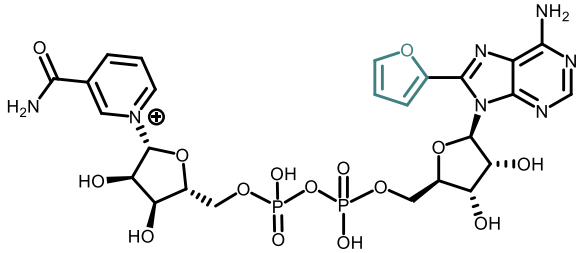
Probe	Type	Applications	Reference
 **1**	^{32}P-labelled NAD^+ (**^{32}P-NAD$^+$**; **Section 1.2.5**)	Detection of free PAR chains, ADP-ribosylated proteins and DNA and RNA by autoradiography (cell lysates, recombinant PARPs)	5,6,101-103
 **2**	Biotinylated NAD^+ analogue (**Section 1.2.5.1**)	Enrichment of ADP-ribosylated proteins (recombinant proteins or cell lysates)	104
 **3**	Clickable alkyne NAD^+ analogue (**6Yn-NAD$^+$**; **Section 1.2.5.1**)	Capture of labelled ADP-ribosylated proteins *via* CuAAC (**Section 1.3.2**). Identification of ADP-ribosylated proteins by proteomics (cell lysates)	105-107

 **4**	Fluorescent NAD^+ analogue (**Section 1.2.5.1**)	Visualisation of ADP-ribosylation by fluorescence microscopy (fixed cells)	107-109
 **5**	Clickable azide NAD^+ analogue (**Section 1.2.5.1**)	Employed for capture of labelled ADP-ribosylated proteins *via* CuAAC but was found not to be a substrate of PARP1 (due to its larger group at N6 position)	110
 **6**	A non-hydrolysable NAD^+ analogue, benzamide adenine dinucleotide (BAD); NAD^+ mimic (**Section 1.2.5.1**)	Cocrystallisation with PARP1 and resolving of the NAD^+ binding mode in the PARP1 active site	111

 **7**	Clickable strained alkyne NAD^+ analogue (**Section 1.2.5.1**)	Capture of labelled ADP-ribosylated proteins *via* SPAAC (**Section 1.3.3**). Visualisation of ADP-ribosylation by fluorescence microscopy (fixed cells)	110
 **8**	Clickable strained alkene NAD^+ analogue (**Section 1.2.5.1**)	Capture of labelled ADP-ribosylated proteins *via* inverse electron demand DAC (**Section 1.3.4**). Visualisation of ADP-ribosylation by fluorescence microscopy (fixed cells)	110
 **9**	Clickable alkyne NAD^+ analogue (**2Yn-NAD$^+$**; **Section 1.2.5.1**)	Capture of labelled ADP-ribosylated proteins *via* CuAAC (**Section 1.3.2**). Visualisation of ADP-ribosylation by fluorescence microscopy (fixed cells)	110,112

 **10**	Clickable azide NAD^+ analogue (**Section 1.2.5.1**)	Capture of labelled ADP-ribosylated proteins *via* CuAAC (**Section 1.3.2**). Visualisation of ADP-ribosylation by fluorescence microscopy (fixed cells)	113
 **11**	'Bumped' alkyne NAD^+ analogue (**Section 1.2.5.2**)	Capture of labelled ADP-ribosylated proteins *via* CuAAC (**Section 1.3.2**). Target profiling of PARP1 and 2 by proteomics (cell lysates)	114
 **12**	'Bumped' alkyne NAD^+ analogue (**Section 1.2.5.2**)	Capture of labelled ADP-ribosylated proteins *via* CuAAC (**Section 1.3.2**). Target profiling of PARP7, 10, 11 and 14 by proteomics (cell lysates)	**115,116**

 **13**	'Bumped' alkyne NAD^+ analogue (**Section 1.2.5.2**)	Capture of labelled ADP-ribosylated proteins *via* CuAAC (**Section 1.3.2**). Target profiling of PARP7 by proteomics (cell lysates)	117
 **14**	'Bumped' alkyne NAD^+ analogue (**8But-Yn-NAD^+**; **Section 1.2.5.2**)	Capture of labelled ADP-ribosylated proteins *via* CuAAC (**Section 1.3.2**). Target profiling of PARP1, 2, 3 and 7 by proteomics (cell lysates)	118,119
 **15**	Photoclickable NAD^+ analogue (**Section 1.2.5.3**)	Capture of labelled ADP-ribosylated and NAD^+ interacting proteins *via* photoclicking (**Section 1.2.5.3**) and CuAAC (**Section 1.3.2**). Identification of ADP-ribosylated proteins and MAR/PAR readers by proteomics (cell lysates)	120

 **16**	Photoclickable NAD^+ mimic BAD analogue (**Section 1.2.5.3**)	Capture of NAD^+ interacting proteins *via* photoclicking (**Section 1.2.5.3**) and CuAAC (**Section 1.3.2**). Identification of MAR/PAR readers by proteomics (cell lysates)	121
 **17**	Photoclickable NAD^+ mimic BAD analogue (**Section 1.2.5.3**)	Capture of NAD^+ interacting proteins *via* photoclicking (**Section 1.2.5.3**) and CuAAC (**Section 1.3.2**). Identification of MAR/PAR readers by proteomics (cell lysates)	121
 **18**	Fluorescent NAD^+ analogue (**Section 1.2.5.4**)	Identification of a novel 5'-NAD^+-RNA decapping mechanism by ADP-ribosyl cyclase CD38; Monitoring the extent of 5'-NAD^+-RNA decapping in assays with purified enzymes	122

1.2.5.1 Biotinylated and Clickable NAD^+ Analogues for Studying ADP-ribosylation

Introduction of functional groups on NAD^+ analogues has been traditionally performed on the adenine ring since the nicotinamide moiety is removed during ADP-ribosylation, and therefore functionalisation at this moiety would be lost. Similarly, introducing modifications at OH groups or replacing them on the ribose rings are likely to partially, or completely, block PARylation since branching of PAR chains occurs through OH ribose groups (**Figure 1.1**). Given that the adenine moiety is conserved in ADP-ribosylation, that it is not involved in PARylation branching and the availability of multiple sites for its functionalisation, the adenine moiety is considered the most appropriate part on the NAD^+ molecule for incorporation of additional functional groups.

Biotinylated NAD^+ analogues incorporating a biotin group at the N6 or C8 positions of the adenine ring, through an elongated linker, were first developed by Zhang *et al.*,[104] where their utilisation for ADP-ribosylation of elongation factor 2 (EF2) and glyceraldehyde-3-phosphate dehydrogenase (GAPDH) was demonstrated. These were the first NAD^+ analogues developed for the selective purification of labelled ADP-ribosylated proteins through streptavidin affinity chromatography, and N6-biotinylated NAD^+ analogues, such as **2**, were subsequently commercialised. However, the relatively large biotin group and long linker were expected to perturb efficient utilisation by NAD^+ consuming enzymes such as PARPs, due to steric hindrance, hence Du *et al.* and Jiang *et al.* developed the first NAD^+ analogues possessing a small clickable group.[105,106] Jiang *et al.* introduced a small, three carbon atom tag incorporating an alkyne group at the N6 position of NAD^+ (**3,** 6Yn-NAD^+) and subsequently demonstrated its utilisation by PARP1 for ADP-ribosylation.[106]

In addition to the small size of a clickable group relative to biotinylated analogues, a major advantage of clickable NAD^+ analogues, such as 6Yn-NAD^+ (**3**), is their ability to be captured through click chemistry reactions, which are discussed in more detail in **Section 1.3.1** (**Table 1.3**). This allows for further functionalisation of an analogue thus allowing for a single analogue-treated sample to be employed for various applications. Jiang *et al.* demonstrated this by conjugating automodified PARP1 labelled with 6Yn-NAD^+ (**3**) to a bifunctional azide-rhodamine fluorophore capture reagent, allowing for its visualisation by in-gel fluorescence (IGF).[106] Furthermore, Jiang *et al.* synthesised a trifunctional azide-biotin-rhodamine capture reagent, which following click conjugation allowed for visualisation of labelled proteins through the rhodamine moiety as well as their enrichment through the biotin moiety for subsequent MS applications.[106] By following this approach and employing mass spectrometry,

Jiang *et al.* identified 79 potential PARP1 substrates following labelling of human breast cancer MCF7 PARP1 KD cell lysates with 6Yn-NAD^+ (**3**) by recombinant PARP1.[106]

Following on from the success of employing 6Yn-NAD^+ (**3**) for ADP-ribosylation and the demonstrated scope of downstream applications with NAD^+ analogues, multiple subsequent studies explored their utility by derivation of the position at which a clickable/functional group is attached. Buntz *et al.* showed histone labelling by PARP1 through utilisation of a fluorescent NAD^+ analogue possessing a carboxytetramethylrhodamine (TAMRA) fluorophore at the C2 position (**4**),[107] demonstrating that large substituents at this position were tolerated and did not impede ADP-ribosylation by PARP1. A subsequent study by Wallrodt S *et al.* looking at the derivation of N7 and C8 positions on NAD^+ analogues showed that WT PARPs did not tolerate modifications at these positions.[108] Wallrodt S *et al.* further demonstrated that although 6Yn-NAD^+ (**3**) was used for ADP-ribosylation, larger groups at N6, such as in analogue **5**, were not well tolerated by PARP1.[110] This was surprising considering that N6-biotinylated-NAD^+ (**2**) was used by PARPs for ADP-ribosylation.[104] However, a possible explanation for this was the presence of the long linker in **2**, which likely allowed for flexibility around this position thus minimising steric hindrance in the active site of PARP1, when compared to NAD^+ analogue **5**. The observation was later supported by crystallographic data of PARP1 with benzamide adenine dinucleotide (**6**, BAD), a non-hydrolysable NAD^+ analogue, which showed that the N6 position was only partially solvent-exposed (see **Section 2.3.1**).[111] Furthermore, the data showed that the C2 position was completely solvent exposed, allowing for the incorporation of large groups at this position without affecting the catalytic activity of PARP1. Wallrodt S *et al.* explored this by introducing various substituents at the C2 position, such as for analogues **7 – 9**, and demonstrated their suitability for use in PARP1 *in vitro* assays as well as for fluorescent imaging in transiently permeabilised paraformaldehyde-fixed HeLa cells following click capture to a Cy3 or a Cy5 fluorophore.[110]

Zhang *et al.* undertook the challenge to synthesise and validate the first ribose-functionalised azide-NAD^+ analogue (**10**) through a combination of chemical and enzymatic reactions.[113] Through the synthesis of multiple NAD^+ analogues *via* modification/replacement of the 2' and 3' OH groups of the β-nicotinamide mononucleotide (β-NMN) moiety, Zhang *et al.* demonstrated that analogue **10**, where its 3' OH group was replaced by an azide group, was utilised for PARP1 automodification in recombinant PARP1 *in vitro* assays.[113] Furthermore, the analogue was successfully utilised intracellularly following transient permeabilisation, cell

fixing and click capture. This was demonstrated by visualisation of nuclear ADP-ribosylation, after 1 h treatment with **10**, through imaging by confocal fluorescence microscopy.[113]

It should be noted that the replacement of the 3' OH group in **10** by an azide group resulted in increased resistance to degradation of PAR chains by PARG. The reduced ability of PARG to hydrolyse PARylation chains is expected to lead to a rapid build-up of PAR chains under oxidative stress thus making the analogue cytotoxic to cells after transient permeabilisation. Although cytotoxicity of transient permeabilisation without the analogue was explored in the study, cytotoxicity following co-treatment with the analogue was not performed.

1.2.5.2 Clickable 'Bumped' NAD^+ Analogues for PARP Target Profiling

A major leap in the scope of applications of NAD^+ analogues was the development of 'bumped' NAD^+ analogues for profiling ADP-ribosylation protein targets of individual PARP proteins through the 'bump-hole' approach (**Figure 1.4**).[114-119] This approach has been previously successfully applied for target identification of kinases, methyl transferases and lysine acetyltransferases.[123-125] The term 'bumped' NAD^+ analogues arises from the observation that these structural NAD^+ analogues are not utilised by WT PARPs, due to inability of WT PARPs to accommodate such analogues in their active site as a result of the additional steric hindrance of the introduced 'bump' modification onto NAD^+. However, by engineering PARP variants through chemical genetics approaches allows for the introduction of a pocket, termed 'hole', in the active site of a PARP protein thus making it possible for the 'bumped' analogue to be accommodated in the active site.[114-119] Due to the structural similarity of PARPs active sites, as a result of high sequence homology and their functional redundancy, it is difficult to identify PARP-specific protein targets. The 'bump-hole' approach therefore allows for the specific identification of ADP-ribosylation targets of a PARP variant since only the mutated PARP variant can utilise the analogue and therefore catalyse ADP-ribosylation with it, and not WT PARPs.

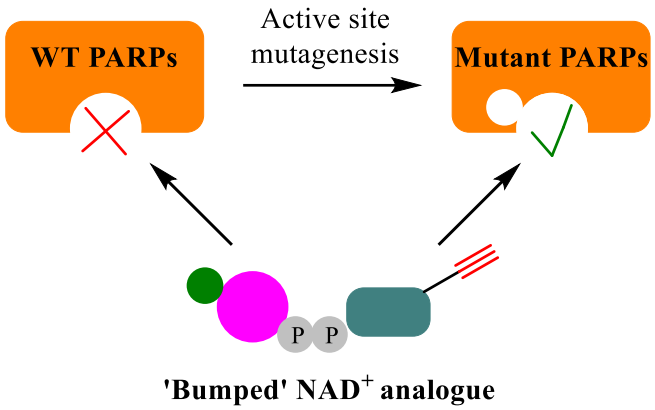


Figure 1.4. Principle behind the 'bump-hole' approach for PARP target profiling. Introduction of a pocket in the active site allows for utilisation of 'bumped' (highlighted in green) NAD^+ analogues as substrates by mutant PARPs only.

The approach was first investigated by Carter-O'Connell *et al.*, where a 'bumped' version of the 6Yn-NAD^+ (**3**) analogue was synthesised by introduction of an ethyl group at the C5" position on the nicotinamide ring (**11**).[114] Given the high sequence homology of PARPs, K903A mutants were generated for PARPs 1 and 2, which introduced a sufficiently big pocket in the active site of both PARPs to accommodate the additional ethyl group on **11**. Carter-O'Connell *et al.* validated the utility of the analogues by the two PARP variants for ADP-ribosylation through *in vitro* labelling of human embryonic kidney (HEK) 293T nuclear extracts.[114] The analogues resulted in extensive protein labelling, as visualised by western blotting for biotinylation following click reaction with an azide-biotin (AzB) capture reagent (see **Section 1.3.1**). After protein enrichment with neutravidin agarose resin and LC-MS/MS analysis, O'Connell *et al.* identified 42 targets of PARP1 and 301 targets of PARP2,[114] demonstrating the potential of the approach for proteome-wide PARP target profiling albeit the limitation of labelling taking place in cell lysates.

Carter-O'Connell *et al.* and Rodriguez *et al.* further expanded on the use of this approach by synthesising two additional 'bumped' analogues (**12** and **13**) for target profiling of other PARP proteins. These were successfully used for target profiling of PARPs 7, 10, 11 and 14 in combination with LC-MS/MS analysis.[115-117] Carter-O'Connell *et al.* engineered L296G variants of PARP10 and PARP11, which, following treatment with **12** and LC-MS/MS analysis, led to the identification of 803 and 260 protein targets from HEK293T lysates, respectively.[115] Carter-O'Connell *et al.* then applied **12** for profiling PARP14 MARylation targets in HEK293T cell lysates, which resulted in the identification of 114 targets by proteomics, among which was the catalytically inactive PARP13 known to play a role in RNA

regulation and metabolism.[116] Subsequently, Rodriguez *et al.* explored the utility of the C2-modified 'bumped' analogue **13** for profiling of PARP7 targets of an I631G PARP7 variant that was unable to use **12** as a substrate.[117] By employing analogue **13**, 250 MARylation targets of PARP7 were identified in HEK293T cell lysates by LC-MS/MS, among which was also the catalytically inactive PARP13, previously identified as a PARP14 MARylation target.[117]

The 'bump-hole' approach for PARP target profiling was also explored by Gibson *et al.* who developed a different type of analogue for which a clickable alkyne group was incorporated within the 'bumped' group at the C8 position on the adenine ring (**14**).[118] This was in contrast to analogues **12** and **13**, where the 'bumped' and clickable groups were separate.[115-117] Employing analogue **14**, Gibson *et al.* successfully profiled PARP1, PARP2 and PARP3 targets in HeLa cell lysates, resulting in the identification of 167, 87 and 401 proteins targets, respectively.[118] By performing a gene ontology analysis, Gibson *et al.* showed that the identified PARP targets largely clustered as DNA repair, transcription regulation and DNA/RNA metabolism proteins.[118] Palavalli *et al.* subsequently utilised **14** for PARP7 target profiling with an S563G PARP7 variant and identified 974 and 1054 PARP7 protein targets in HeLa and OVCAR4 cell lysates, respectively, by LC-MS/MS.[119] A gene ontology analysis illustrated that ~30% of all identified PARP7 targets clustered in at least one of the three categories: translation, cell-cell adhesion and rRNA processing (with ~10% for each individual category),[119] which differed from the protein targets identified for PARPs 1, 2 and 3, thus illustrating the diversity of molecular processes that the different PARPs regulate.

1.2.5.3 Photoclickable NAD^+ Analogues for Identification of NAD^+ Readers

Beyond the utility of NAD^+ analogues for labelling, enrichment and identification of ADP-ribosylated proteins, photoclickable NAD^+ analogues, such as **15 – 17**, have been developed and their use explored for identification of NAD^+-interacting proteins, also known as NAD^+ readers.[120,121] NAD^+ readers can recognise MAR or PAR chains, or both, through recognition motifs and domains, which include the PAR-binding motif (PBM), WWE motif, PAR-binding zing finger motifs, KR-rich domains and macrodomains. Examples include x-ray repair cross-complementing protein 1 (XRCC1), which is recruited in the DDR by recognising PAR chains on histones through its PBM, and the serine/threonine kinase Chk1, which has been shown to be activated upon recognition of PAR chains due to PARP1 activity, a prerequisite for triggering the S-phase checkpoint during DNA replication.[126,127]

Gagné *et al.* used the anti-PAR 10H antibody for immunoprecipitation of PARylated proteins and in combination with LC-MS/MS analysis performed the first proteome-wide study focused on defining NAD^+-interacting proteins, leading to the identification of 334 potential PARylation readers from human neuroblastoma cells.[128] Functional grouping of the identified readers showed that the identified PARylation readers were involved in DNA damage signalling and repair, transcription regulation, DNA replication, RNA metabolism, cell cycle regulation, modification chromatin structure and apoptosis.[128] Given the large number and diverse roles of ADP-ribosylation readers, the study of NAD^+-interacting proteins is important for elucidating their relevance in biological processes.

Although identification of ADP-ribosylation readers has been performed with clickable NAD^+-like polymer probes,[129,130] the development and use of clickable photoaffinity diazirine NAD^+ analogues for identification of readers was first performed by Lam *et al.*[120] and Šileikytė *et al.*[121]. Upon irradiation of a photoclickable diazirine group with UV light (typically 365 nm), a reactive carbene species is generated, which crosslinks to an immediately available protein through insertion of itself into a nearby C-H bond (**Figure 1.5**), and the resulting covalent linkage is irreversible.

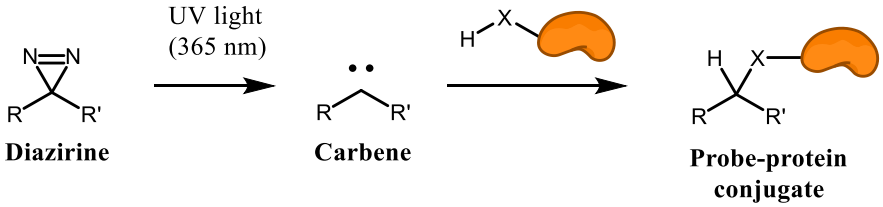


Figure 1.5. Mechanism of diazirine-protein photocrosslinking (photoaffinity labelling). Irradiation of diazirine at 365 nm generates a highly reactive carbene intermediate that inserts itself into C-H bonds of proteins in the molecule's immediate proximity.

Given that NAD^+-interacting proteins are in close proximity to MAR/PAR chains while the interaction is occurring, irradiation of the diazirine group with UV light will irreversibly capture this interaction by forming a stable photocrosslinked conjugate complex. The complex can then be immunoprecipitated or clicked to biotin and enriched by streptavidin affinity chromatography for downstream processing for LC-MS/MS analysis. By employing this approach with analogue **15**, Lam *et al.* identified 247 potential PARylation binding proteins from HEK293T cells through PARP1 competition binding and LC-MS/MS.[120] A potential caveat of using the diazirine azide-NAD^+ analogue **15** for reader identification is that the analogue could still be utilised by PARPs for ADP-ribosylation, therefore potentially leading

to self-photocrosslinking of long PAR chains with the proteins the chains are found on. This would preclude the specific identification of ADP-ribosylation readers only.

This issue was overcome by Šileikytė *et al.*, who developed clickable photoaffinity BAD analogues (**16** and **17**), non-hydrolysable NAD^+ analogues that cannot be utilised by PARPs for ADP-ribosylation.[121] Photocrosslinking would therefore only take place between the analogues and the proteins that recognise them, thus making the approach specific towards identification of NAD^+-interacting proteins. By employing **16** and **17**, Šileikytė *et al.* identified 36 and 48 NAD^+-interacting proteins, respectively.[121] It was noted, however, that only 10 of the identified NAD^+-interacting proteins overlapped with both probes, thus showing that the position of the photoclickable group was important for capturing NAD^+-protein interactions since it affected selectivity. Furthermore, the use of BAD analogues **16** and **17** likely resulted in a reduction of the scope of PARylation readers identified, due to the lack of photoclickable PAR chains and the potential inability of PAR-interacting proteins to interact with non-PAR (MAR) chains, thus introducing selectivity bias.

1.2.5.4 Fluorescent NAD^+ Analogues for Labelling Nucleic Acids

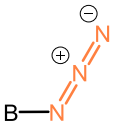
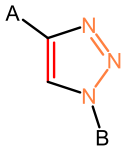
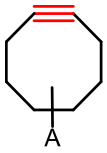
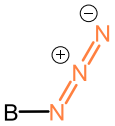
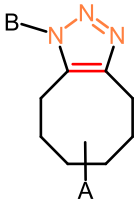
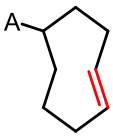
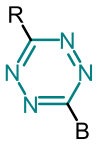
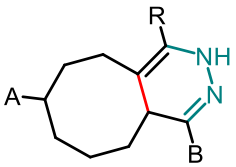
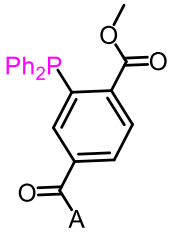
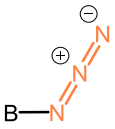
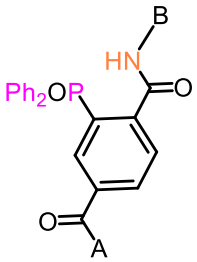
The study of 5'-RNA capping/decapping mechanisms is important due to their role in regulating RNA translation, degradation and translocation across cellular compartments.[131,132] The use of NAD^+ analogues, such as **18**, has been investigated for monitoring the extent of 5' decapping of NAD^+-capped RNA, which led to the discovery of a novel NAD^+-RNA decapping mechanism by the ADP-ribosyl cyclase CD38, a glycohydrolase.[122] To identify this novel mechanism, Abele *et al.* synthesised and employed NAD^+ analogue **18** by introducing a furan ring at the C8 position of NAD^+. Due to the extensive conjugation between the furan ring and the adenine moiety, the modified adenine moiety in **18** fluoresces upon excitation at a wavelength of 304 nm. However, fluorescence emission is quenched by the presence of the nicotinamide ring when **18** is intact. Abele *et al.* demonstrated that by treating NAD^+-capped RNA with CD38, the nicotinamide moiety was cleaved and therefore fluorescence emission upon excitation at $\lambda = 304$ nm was no longer quenched. Thus, Abele *et al.* proved that NAD^+-RNA was a substrate of CD38 and that **18** can be applied for real-time monitoring of NAD^+-RNA decapping.[122]

1.3 Capturing of ADP-ribosylation *via* Click Chemistry

1.3.1 Overview of Click Chemistry Reactions and Ligation Handles

Click chemistry reactions are a powerful approach towards further functionalisation of small molecules and biomolecules incorporating a 'clickable' group, such as those summarised in **Table 1.3**.[133-135] These reactions allow the introduction of secondary labels (**Figure 1.6**), such as a fluorophore (e.g., TAMRA) or an enrichment handle (e.g., biotin), or both, onto lipids, nucleic acids or proteins tagged with a clickable compound.[133-135] Click chemistry groups are typically small, non-polar and do not have an overall charge such that they do not affect, for example, cellular permeability of a probe or disrupt the relevant biological functions upon labelling of a biomolecule.

Table 1.3. Summary of click reactions commonly used for click probe capture and bioconjugation applications.

Reaction type	Fragment A	Fragment B	Product
Copper-catalysed azide-alkyne cycloaddition (CuAAC)			
Strain-promoted azide-alkyne cycloaddition (SPAAC)			
Diels-Alder Cycloaddition (DAC)			
Staudinger ligation			

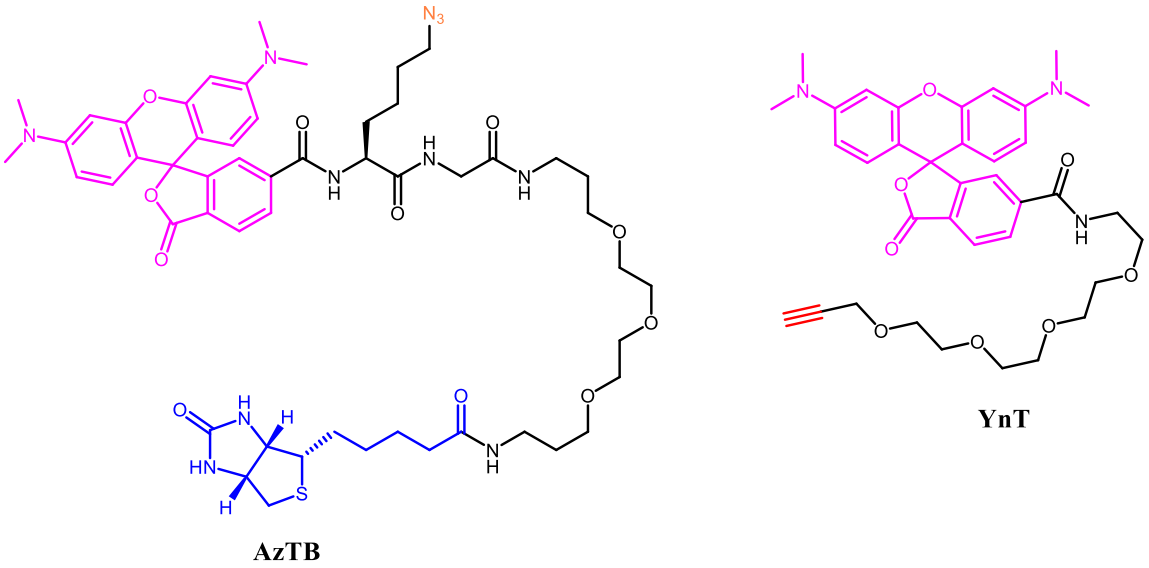


Figure 1.6. Example bifunctional (YnT) and trifunctional (AzTB) click chemistry capture reagents. A full list of all capture reagents used in this project is included in **Appendix Figure A.2**. TAMRA fluorophore (pink), biotin (blue), azide (orange) and alkyne (red) moieties are highlighted.

In the context of protein labelling in cells or cell lysates, click reactions allow for distinguishing of labelled proteins over the unlabelled background proteome, therefore permitting for analysis and further downstream applications of the tagged proteins only.[133] Incorporation of a fluorophore allows for visualisation of labelled proteins by IGF and identification of labelled proteins based on their molecular weight.[105-107] Furthermore, it allows for fluorescence microscopy in live or fixed cells, which is a powerful technique to visualise the cellular compartmentalisation and labelled protein distribution in a cell, thus aiding the study of cellular pathway dynamics.[110,134,135] Alternatively, the introduction of an enrichment handle, such as biotin, through click conjugation permits the selective pull-down of proteins, also known as protein enrichment, that are labelled with a clickable probe.[114-120] This is typically performed *via* streptavidin or neutravidin affinity purifications, where cell lysates containing biotinylated proteins are incubated with streptavidin/neutravidin immobilised onto magnetic or agarose beads.

Streptavidin is a 66 kDa protein isolated from *Streptomyces avidinii*, which has a very high affinity for binding to biotin, with an estimated dissociation constant (K_d) of ~1×10^{-14} M for the biotin-streptavidin complex.[136] Similarly, neutravidin, a deglycosylated form of avidin, has an estimated K_d of ~1×10^{-15} M, and this extremely high affinity towards biotin ensures the efficient enrichment of biotinylated proteins. Protein enrichment prior to analysis is highly desirable due to the expanded range of downstream applications as well as overall boost in

signal during analysis. In IGF analysis following protein pull-down, the fluorescence signal of labelled proteins is significantly boosted relative to the background proteome and easier to observe. In the context of studying ADP-ribosylation by IGF, protein enrichment is important since this PTM is typically low abundant in cells relative to the background proteome. Similarly, a pull-down step is necessary for analysis by western blotting as it allows for separation and therefore distinction of probe labelled proteins from the corresponding non-labelled proteins natively found in cells.

Protein enrichment is particularly important for mass spectrometry applications and the study of proteins *via* LC-MS analysis (proteomics, see **Section 4.5)**. In the absence of a pull-down step prior to analysis, the MS signal arising from the overwhelming background proteome typically largely, or entirely, overshadows the signal arising from the protein(s) of interest studied. This is especially the case for low abundant proteins or PTMs, such as ADP-ribosylation,[137] therefore, protein enrichment is necessary for reliable analysis of such a PTM and for improved data quality. Once enriched, biotinylated proteins are subsequently digested by a protease, typically trypsin, to release the corresponding peptides that are then analysed by LC-MS. A summary of the different workflows utilising non-clickable or clickable NAD^+ analogues, click conjugation, enrichment, IGF, WB and proteomics analysis can be seen in **Figure 1.7**.

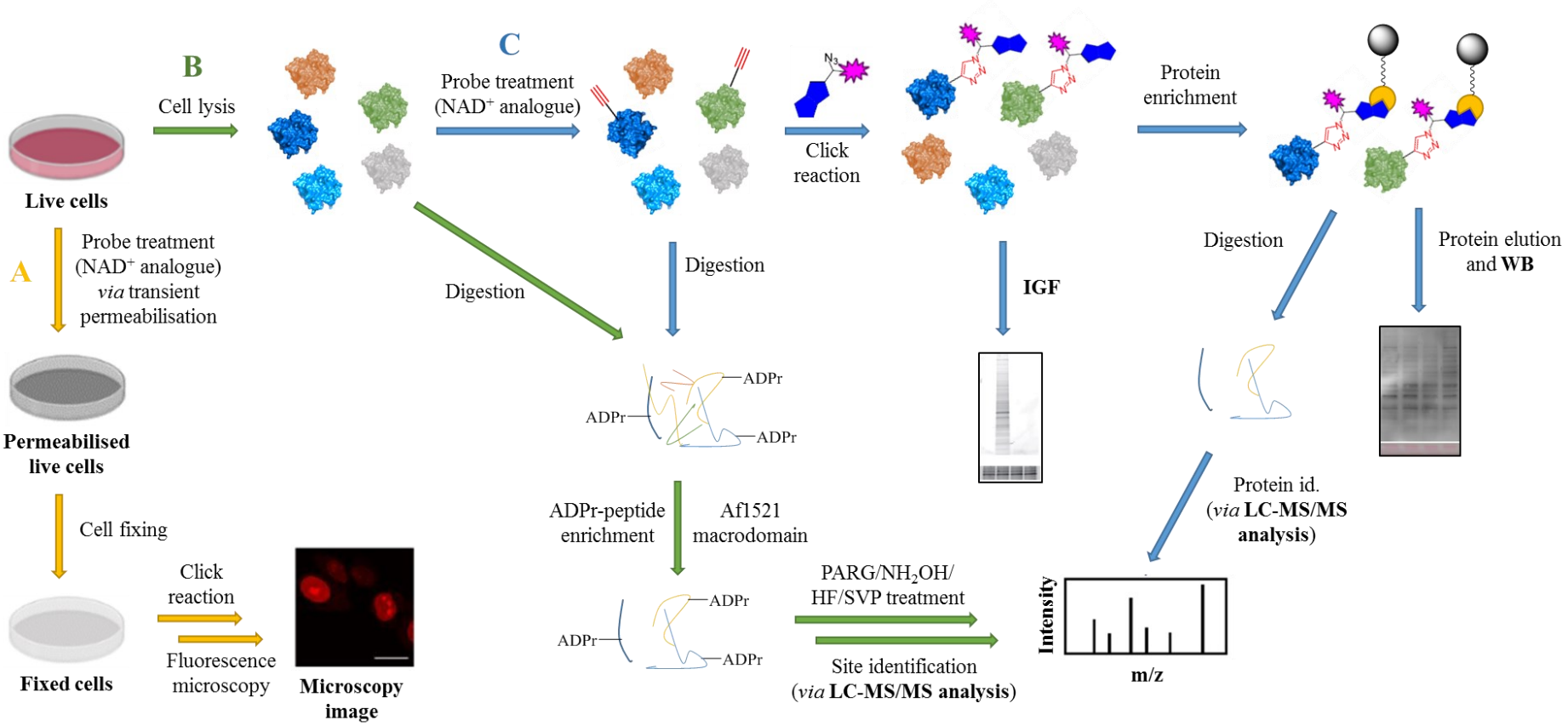


Figure 1.7. Applications of NAD^+ analogues for the study and analysis of ADP-ribosylation. Pathway A: intracellular delivery of NAD^+ analogues by transient permeabilisation followed by cell fixing and click reaction to a fluorophore allows for visualisation of cellular ADP-ribosylation by fluorescence microscopy.[110] Pathway B: cell lysis followed by enrichment of ADP-ribosylated (ADPr) peptides using Af1521 macrodomain, PARG/NH_2OH/HF/SVP treatment (**Section 1.4.2**) and LC-MS/MS analysis allows for site identification of ADP-ribosylated residues (**Section 1.4.1**). Pathway C: cell lysis followed by treatment of lysates with NAD^+ analogues and click reaction to a trifunctional capture reagent allows for visualisation of protein labelling *via* its fluorophore by IGF, or enrichment (pull-down) of labelled proteins *via* its biotin moiety by streptavidin affinity chromatography. Enriched proteins can then be analysed by WB or digested and the corresponding peptides analysed by LC-MS/MS for protein identification.

Given the large scope for downstream applications and analysis, the ability to further functionalise NAD^+ analogue-tagged ADP-ribosylated proteins *via* click chemistry represents a powerful approach towards studying ADP-ribosylation and its biological functions.

1.3.2 Copper-catalysed Azide-alkyne Cycloaddition

The most widespread type of click reaction employed for click chemistry bioconjugations is the copper-catalysed azide-alkyne cycloaddition (CuAAC, **Table 1.3**).[133,138,139] Among the advantages of CuAAC are the small size and the linearity of the alkyne and azide groups present on the probe, such as in NAD^+ analogues **3**, **5**, **9** and **11 – 17**, and on the capture reagent (fragments A and B). The small size of the groups largely avoids disruption to protein function upon probe labelling. It is also unlikely to negatively affect probe utilisation by catalytic enzymes due to the minimal additional steric hindrance at a protein active site, which is important for the successful catalysis of PTMs.

CuAAC is specific, efficient and easy to set up. However, the reaction requires the presence of a copper (II) catalyst in all cases due to the extremely slow reaction rate between linear alkynes and azides at room temperature (r.t.).[134,138,139] This imposes limitations on the utility of CuAAC, which cannot be used for conjugation reactions in live cells due to the cytotoxicity induced by copper. Furthermore, the reaction also requires the addition of a reducing agent, such as tris(2-carboxyethyl)phosphine (TCEP), to generate the catalytically active Cu(I) species *in situ*, and the addition of a ligand, such as tris((1-benzyl-4-triazolyl)methyl)amine (TBTA), which stabilises the Cu(I) species.[139] Although these additives allow CuAAC conjugation to proceed rapidly and with high efficiency at r.t. at physiological conditions, such as in cell lysates, their addition further limits the applicability of CuAAC for live-cell click chemistry (e.g., TCEP is non-membrane permeable).

1.3.3 Strain-promoted Azide-alkyne Cycloaddition

To overcome the limitations of CuAAC for utilisation in non-living systems only, an alternative click conjugation reaction was developed by Agard *et al.*, named strain-promoted azide-alkyne cycloaddition (SPAAC, **Table 1.3**).[140] The conjugation takes place between strained alkynes, typically octyne groups, such as in NAD^+ analogue **7**, and azides. The major advantages of SPAAC over CuAAC ligation is that the SPAAC reaction occurs spontaneously upon addition of the appropriate azide/alkyne capture reagent, therefore it does not require a copper catalyst or the presence of TCEP and TBTA additives, while proceeding at a similar rate to CuAAC.[140] As a result, the reaction is compatible for click bioconjugation in live cells,[140,141] which expands

the scope of applications of click chemistry by allowing its utilisation for applications such as live-cell imaging through fluorescence microscopy. However, strained alkynes, such as octyne groups, are much larger than the small linear alkynes that can be used in CuAAC reactions. Consequently, the increased size of a probe upon incorporation of an octyne group often leads to increased steric hindrance in an enzyme active site, which may negatively impact probe utilisation for protein labelling and/or negatively affect protein function following labelling. For SPAAC reactions, particularly in live cells, it is therefore more desirable for the probe to possess an azide group, which after intracellular protein labelling can be clicked to an octyne-containing capture reagent subsequently.[141]

1.3.4 Inverse Electron Demand Diels-Alder Cycloaddition

Among click chemistry conjugation, the inverse electron demand Diels-Alder cycloaddition (DAC, **Table 1.3**) is the fastest click chemistry reaction established to date.[133,142] The use of DAC has significantly increased over the past decade due to its high specificity, fast kinetics and biocompatibility, including for live cell[141] and *in vivo*[143,144] applications. Furthermore, the reaction occurs spontaneously and does not require a catalyst. The mechanism of the reaction relies on the release of structural strain upon conjugation, therefore it typically occurs between a strained trans-cycloalkene, such as a cyclopropene group in NAD^+ analogue **8**, or a trans-cyclooctene group, and a tetrazine capture reagent.[142] Despite its advantages, the use of DAC in biological experiments is somewhat limited due to the difficulties associated with the synthesis of probes incorporating trans-cycloalkenes. Furthermore, due to the high reactivity and unstable nature of strained cycloalkenes, the corresponding probes are often difficult to handle. In addition, the large size of cycloalkenes, similarly to cyclooctyne-containing probes for SPAAC reactions, introduces a steric bulk, which may lead to reduced efficiency or complete absence of probe utilisation by an enzyme.

1.3.5 Staudinger Ligation

Azide-containing probes and capture reagents have also been utilised in Staudinger ligation conjugation reactions for capturing probe-labelled proteins and biomolecules.[145-147] Staudinger ligation has found many applications in biology; similarly to SPAAC and DAC, it is biocompatible and can be used for conjugation reactions in live cells.[145-147] Upon ligation, an amide bond is formed thus generating a stable conjugate. However, in comparison to CuAAC, SPAAC and DAC reactions, the Staudinger reaction suffers from much slower kinetics.[148] In addition, the phosphine-containing species rapidly undergoes oxidation at physiological conditions, and once oxidised, can no longer undergo conjugation, which leads to reduced

ligation efficiency.[148] As a result, Staudinger ligation has not been widely used in combination with NAD^+ analogues for capturing labelled ADP-ribosylated proteins.

1.4 Identification of ADP-ribosylation Sites by Tandem-mass Spectrometry

1.4.1 Principle Behind Tandem-mass Spectrometry

An important aspect in the field of ADP-ribosylation is the identification of ADP-ribosylated residues (sites of modification). Identification of modified sites is pivotal to better understanding the role of ADP-ribosylation in influencing a protein's function and the biological consequences that follow. Furthermore, direct identification of modifications sites brings a higher level of confidence that an identified protein target, by MS analysis, is indeed ADP-ribosylated. The advancement in mass spectrometry technology and the emergence of highly sensitive MS instruments has made the use of mass spectrometry the golden standard for ADP-ribosylation site identification.[95-100,149] The process typically involves the utilisation of liquid chromatography/tandem-mass spectrometry (LC-MS/MS) analysis (**Figure 1.8**), where a modified site possesses a characteristic mass shift relative to the correspondingly non-modified residue.[150] As a result, a peptide incorporating a modified residue (peptide **2**, **Figure 1.8**, will have the mass of the correspondingly non-modified peptide (peptide **1**, **Figure 1.8**) plus the characteristic mass shift. The overall mass of the peptide is detected during MS^1 scanning, and once isolated, a further fragmentation step during MS/MS (MS^2) scanning is performed, where the peptide is fragmented into individual amino acids.[150] By following this approach, the residue that carries the modification can be identified by detecting which residue bears the characteristic mass shift. The approach has been successfully applied for identification of MARylation sites, which possess a mass shift of +541.06 Da units.[95-100] However, the lack of a characteristic mass shift in PARylated peptides, due to the non-homogeneous nature of the PARylation modification, makes it impossible to identify PARylation sites without further processing steps.

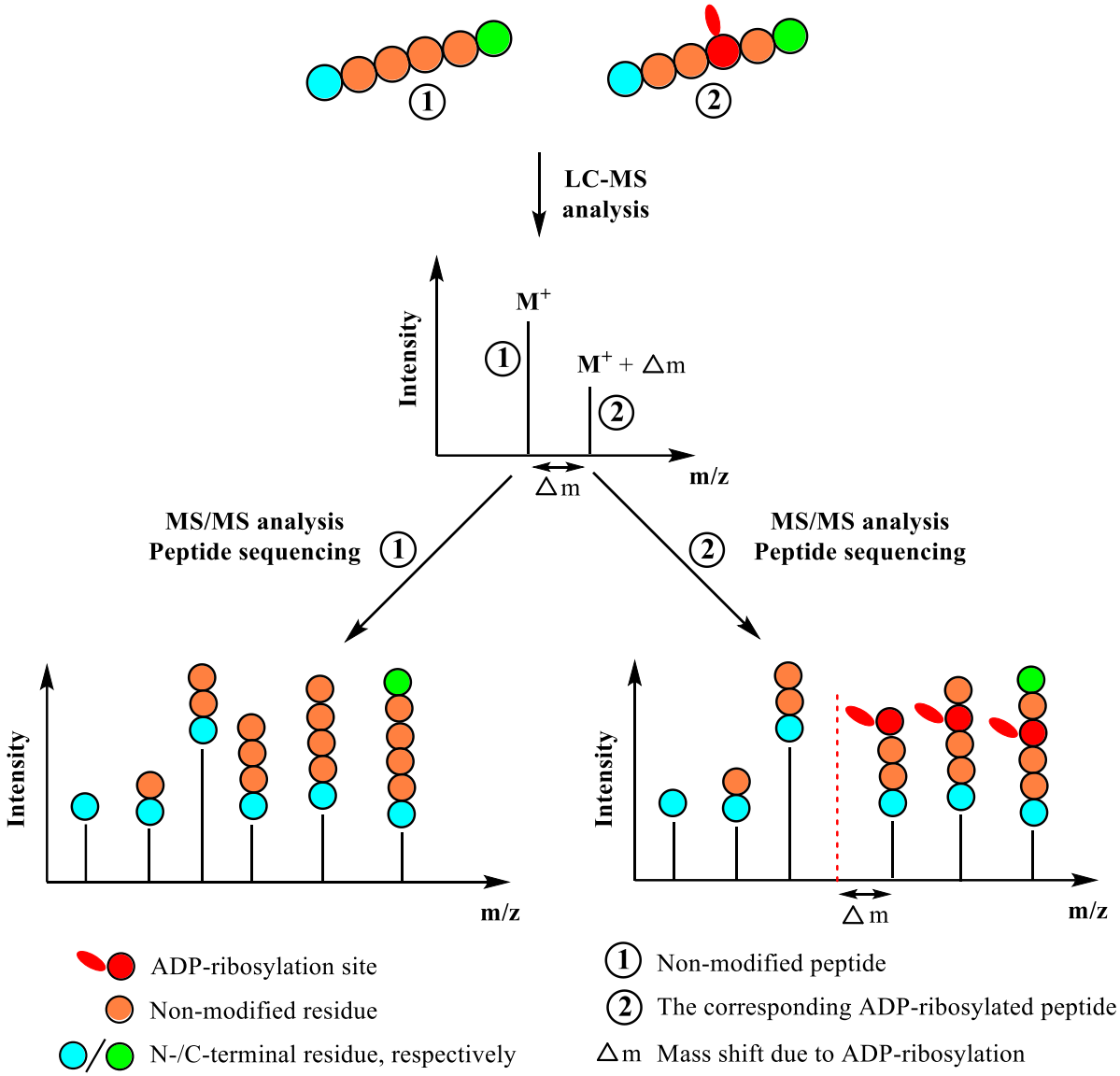


Figure 1.8. Principle of LC-MS/MS analysis for identification of modified sites. Peptides are initially detected during MS scanning and m/z values assigned. Peptide pairs (non-modified and modified) for which a characteristic mass shift (△m) is detected are then selected for peptide backbone fragmentation into individual amino acids during MS^2 scanning, which allows for deconvolution of peptide sequences. The amino acid for which △m is detected relative to the corresponding non-modified residue represents the site bearing the modification.

1.4.2 Methods for Introducing a Characteristic Mass Shift *via* Reduction of the Size of PAR Chains

To overcome the limitation of variable PAR mass, processing steps involving the shortening of PAR chains to MARylation or to simpler modifications that possess a specific mass shift have been developed and employed in ADP-ribosylation proteomics (**Figure 1.9**).

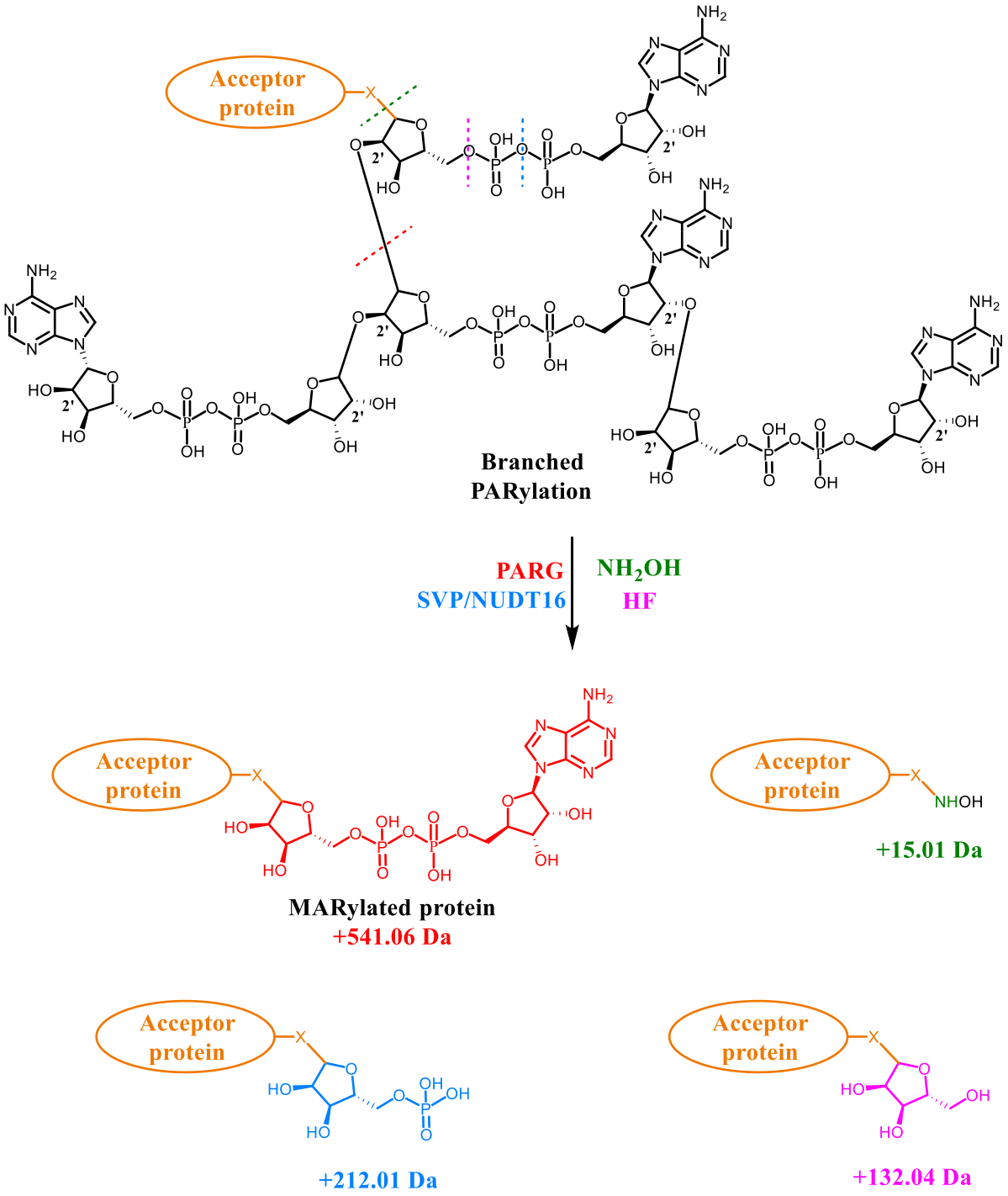


Figure 1.9. Methods for detection of ADP-ribosylation sites by LC-MS/MS analysis *via* reduction of MAR/PAR chains by chemical or enzymatic approaches. After the relevant treatment, a specific mass tag (△m) is left on each modified residue, which can be subsequently detected by LC-MS/MS analysis.

1.4.2.1 Conversion of PARylation to MARylation by PARG

One such approach is the use of PARG[95-100,151-153], which is responsible for hydrolysis of PAR chains intracellularly by cleavage of the O-glycosidic bond between ADP-ribose units and is often used for reducing PAR chains to MAR (**Figure 1.9**). Since PARG is unable to cleave the

last remaining ADP-ribose unit from a modified site, the corresponding product is a MARylated peptide/protein that possesses the characteristic chemical shift of +541.06 Da. This allows for identification of the site during LC-MS/MS analysis. However, it is challenging to reliably detect MARylated residues by LC-MS/MS due to the labile nature of ADP-ribose units, which can lead to complete dissociation or fragmentation of the modification during MS^2 scanning, thus leaving a non-characteristic mass shift. As a result, additional approaches, discussed in the next sections, have been devised and employed for identification of ADP-ribosylation sites.

1.4.2.2 Hydrolysis of ADP-ribosylation Chains by Hydroxylamine Treatment

An alternative approach to PARG treatment is the use of hydroxylamine treatment, which has been utilised in multiple studies.[80,90,154-157] The main advantage of this method is that the PAR modification is displaced by a hydroxylamine tag bearing a characteristic mass shift of only +15.01 Da (**Figure 1.9**), which is easily detected by LC-MS/MS analysis. Furthermore, due to the structural simplicity of hydroxylamine, its use eliminates the undesirable fragmentation of the modification observed with MARylated peptides during MS^2 scanning. However, a major drawback of using hydroxylamine for site identification is that the method can only be used for identification of ADP-ribosylation on the acidic residues glutamate and aspartate, which introduces a bias in the nature of the sites identified. [80,90,154-157] Given that ADP-ribosylation has historically been detected on C, H, K, R, S, T and Y, in addition to E and D residues, a method for non-biased identification of all ADP-ribosylation sites is highly sought after. In addition, a recent study performed by Hendriks *et al.*[100] suggested that hydroxylamine may react non-specifically with E and D residues, thus leading to the identification of non-ADP-ribosylated residues on non-ADP-ribosylated proteins.

1.4.2.3 Reduction of ADP-ribosylation Chains by Hydrofluoric Acid Treatment

Overcoming the innate bias in using hydroxylamine for identification of modified sites has been explored through enzymatic and chemical methods. A recent approach employed by Gagné *et al.* involved the use of hydrofluoric acid (HF) with automodified recombinant PARP1 for reducing its PAR modifications to ribose (**Figure 1.9**), thus generating a tag with a mass shift of +132.04 Da units.[158] The method was used for the identification of ADP-ribosylation sites at D, E, K, R and S residues from PARP1. Owing to the mechanism of MAR/PAR chain reduction by HF, the method should be equally applicable for unbiased identification of all ADP-ribosylation sites. However, this needs to be confirmed by employing HF for identification of modified residues on a proteome-wide level, such as from a cell lysate. A

notable observation from this study was that 45 modified residues on PARP1 were identified,[158] which represents automodification on approximately 4.5% of all residues (PARP1 size is ~1000 residues). The very high % proportion of modified residues identified by this method could potentially suggest the presence of a non-specific/off-target mechanism, on non-ADP-ribosylated residues, through which HF treatment produces the +132.04 Da mass shift, which should warrant further investigation. Furthermore, given the highly hazardous nature of HF, an alternative method is highly preferable to the use of HF.

1.4.2.4 Hydrolysis of ADP-ribosylation Chains by Phosphodiesterases

Enzymatic approaches for cleavage of MAR/PAR chains and unbiased identification of modified residues have been explored. Such methods have utilised phosphodiesterases, such as snake venom protein (SVP), or hydrolases, such as human nudix hydrolase 16 (NUDT16), for cleavage of the phosphodiester bond in ADP-ribose units to produce a phosphoribose tag of +212.01 Da at ADP-ribosylation sites (**Figure 1.9**).[10,159-164] Since cleavage occurs on the modification and not directly on the modified residue, the ability of phosphodiesterases/nudix hydrolases to cleave the ADP-ribose phosphodiester bond is unaffected by the nature of the modified site, thus resulting in an unbiased approach to generating the mass tag of +212.01 Da units on all ADP-ribosylation sites. This mass tag can then be detected by LC-MS/MS analysis for site identification. Although both SVP and human nudix proteins have been used for unbiased identification of ADP-ribosylation sites on automodified PARP1,[159,162] their use for site identification on proteome-wide level, such as from a cell lysate, has been less successful. The primary challenge in achieving this has been attributed to the need for extensive purification of the enzymes, prior to use in cell lysates,[160,163] as well as reduced activity of the enzymes in cell lysates. Furthermore, the endogenous presence of the same phosphoribose modification (+212.01 Da) on proteins in cells has been observed,[165] the origins of which may be different from that of ADP-ribosylation.

1.4.3 Tandem-mass Spectrometry Peptide Fragmentation Approaches for Identification of MARylation Sites

1.4.3.1 Fragmentation by Higher-energy Collision-dissociation

Given the challenges encountered in identification of ADP-ribosylation sites using hydroxylamine, HF or SVP/nudix hydrolyses, and the limitations of each method, the focus on site identification has largely shifted towards utilising PARG for generating MARylation sites on peptides prior to analysis. As previously discussed, PARG allows for non-biased detection

of MARylated residues by subsequent LC-MS/MS analysis.[80,90,154-157] However, their detection and identification has been challenging due to dissociation or fragmentation of the modification during analysis. To overcome these limitations, the use of different fragmentation methods during LC-MS/MS (MS^2) analysis has been explored towards reliable detection of MARylation sites.

MS^2 fragmentation is typically performed in a process known as higher-energy collision-dissociation (HCD),[166] a high energy mode of collision-induced dissociation (CID),[167] to fragment the peptide backbone and allow for peptide sequencing and subsequent modified site identification (**Figure 1.10**).

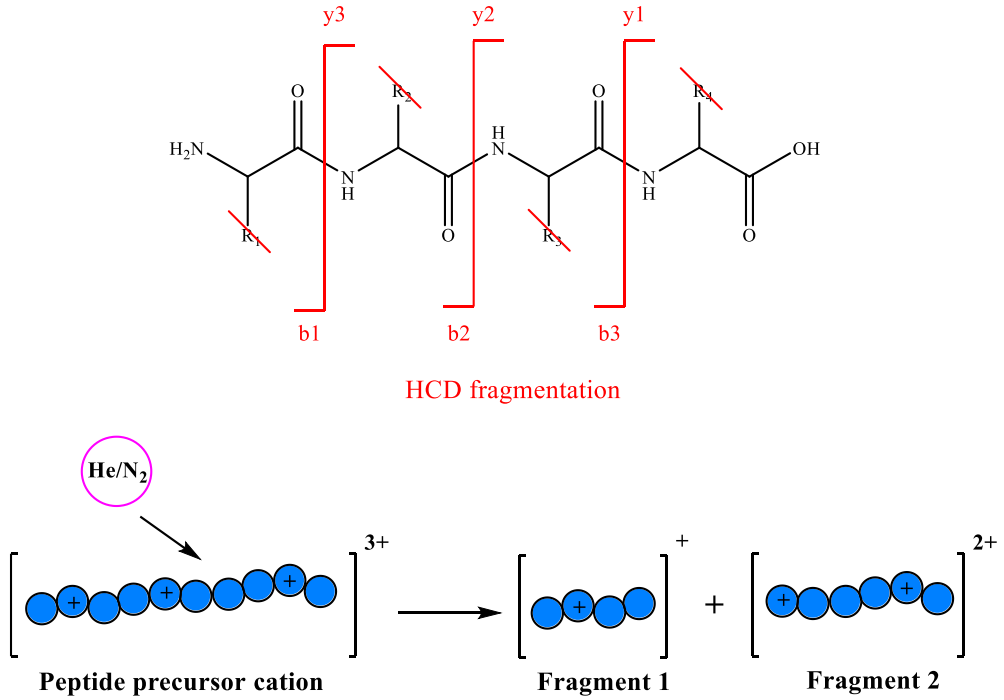


Figure 1.10. Mechanism of fragmentation by HCD. High kinetic energy gas molecules (inert gas) collide with a peptide precursor cation resulting in peptide backbone fragmentation *via* cleavage of amide bonds to generate smaller y- and b- ion fragments. Further fragmentation allows for deconvolution of individual residues.

During HCD, an inert gas is used, typically helium or nitrogen, where the kinetic energy of the gas molecules is increased to a desired value by applying a voltage potential, resulting in their acceleration. Upon collision of the gas molecules with a positively charged peptide (peptide precursor cation), provided that the energy threshold value for bond dissociation is reached, the amide bond between residues breaks. This results in fragmentation of the peptide backbone and the generation of y- and b- ions.[166,167] Fragmentation thus results in the generation of shorter, positively charged peptide fragments, which are subsequently detected and their m/z

value assigned. Given that fragmentation will occur for any amide bond in the peptide backbone for which the threshold fragmentation is reached, various fragment ions of different sizes will be generated from the peptide precursor cation during LC-MS/MS analysis, which allows for deconvolution of the peptide sequence. Although HCD can be used for sequencing of peptide precursor cations possessing a 2+ positive charge, fragmentation may occasionally result in the generation of a non-charged peptide fragment, also known as a 'neutral loss'.[168,169] This results in inability of the neutral fragment to be detected, leading to loss of information. Hence, HCD is most reliably used for detection of peptide precursor cations possessing a charge of ≥3+.

A significant drawback of HCD for peptide sequencing and identification of ADP-ribosylation sites is that the ADP-ribose modification itself (in the context of MARylated peptides) is labile, fragmenting at lower HCD thresholds than amide bonds in a peptide backbone.[97-99] This can result in complete dissociation of the modification from the fragment peptides or lead to partial fragmentation of the modification. As a result, the fragment peptides no longer possess a characteristic mass shift and their masses differ from that of an intact MARylated residue (+541.06 Da), which impedes the identification of ADP-ribosylated residues. The drawbacks of HCD fragmentation for localising ADP-ribosylation sites were demonstrated in the study of Larsen *et al.*, where only in <1% of MS^2 scans the modified site was localised with high confidence.[97] To overcome this limitation, different types of fragmentations methods have been devised, including electron-transfer dissociation (ETD), electron-transfer/higher energy collision dissociation (EThcD) and activated-ion electron-transfer dissociation (AI-ETD).

1.4.3.2 Fragmentation by Electron-transfer Dissociation

In contrast to HCD, which relies on fragmentation of a peptide precursor *via* the transfer of kinetic energy to it upon collision with high-energy gas molecules, ETD relies on the capture of an electron, from an anion molecule, by a peptide precursor cation.[170] The capture of an electron subsequently leads to dissociation of the peptide precursor cation into two corresponding peptide fragments. The mechanism of dissociation results in fragmentation of N-C peptide bonds adjacent to the amide bonds, leading to the generation of z- and c- ions (**Figure 1.11**).[170,171]

A major advantage on the use of ETD over HCD for ADP-ribosylation site identification is that ETD is a low-energy fragmentation method, which leads to fragmentation of the peptide backbone without dissociation of the MARylation modification from the peptide, and without

fragmenting its overall structure. Conservation of the intact modification leads to the generation of a characteristic mass shift of +541.06 Da units on each MARylated residue, which allows identification of all modified residues following LC-MS/MS analysis. The utility of ETD in ADP-ribosylation site identification has been demonstrated by Larsen *et al.*, where ~1300 modification sites in HeLa cells were identified from ETD acquired spectra following H_2O_2 treatment and enrichment of ADPr peptides with Af1521.[97]

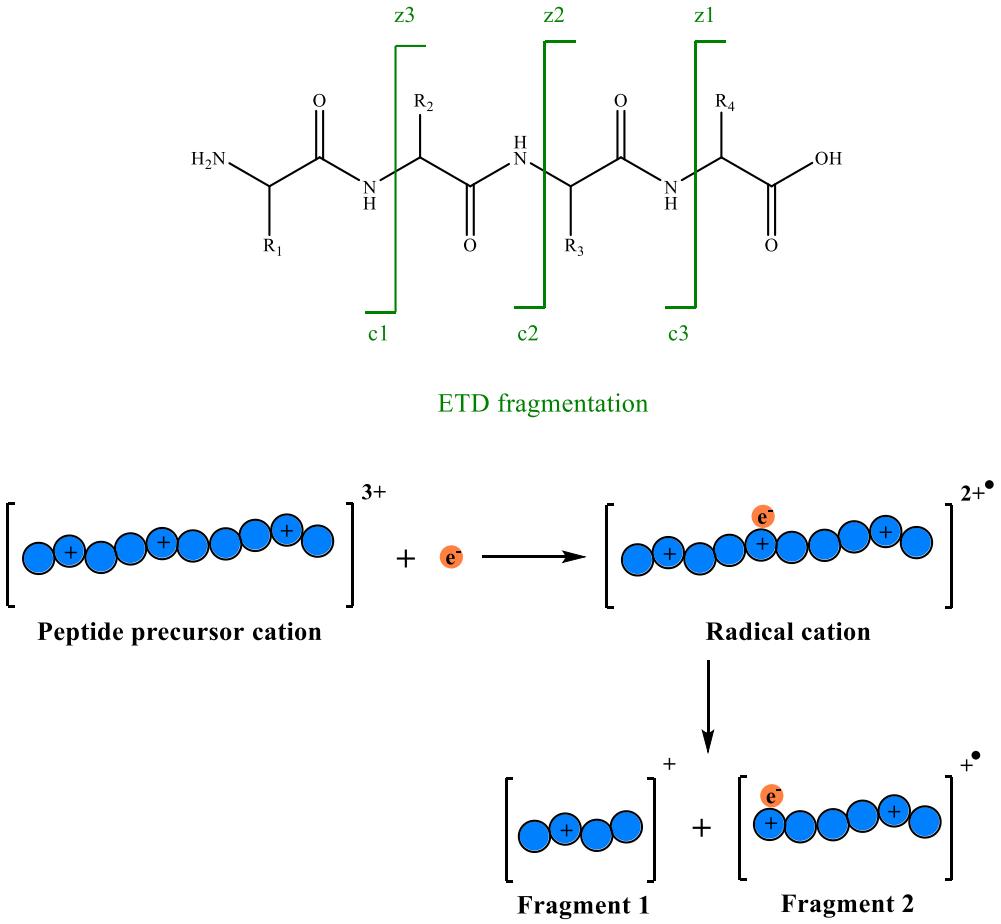


Figure 1.11. Mechanism of fragmentation by ETD. An electron from a radical anion is transferred to a peptide precursor cation, which leads to the generation of a radical cation and its subsequent dissociation into smaller z- and c- ion fragments. Cleavage occurs at C-N bonds, adjacent to amide bonds, and further fragmentation allows for deconvolution of individual residues.

Although ETD is preferred over HCD for site identification, its main limitation in peptide sequencing is that ETD may result in non-dissociative electron-transfer, which effectively reduces the charge of the peptide precursor cation without fragmenting it.[172] Furthermore, following electron capture by the peptide precursor cation, its overall charge is reduced by 1, which further decreases the charge on the corresponding peptide fragments upon dissociation. Consequently, this increases the prevalence of neutral peptide fragments (neutral losses)

following fragmentation. These events are especially common for peptide precursor cations of 2+ charge, where one fragment will always possess no overall charge. Given the high abundance of peptides of relatively low charge (3+, 4+) following digestion with a protease (e.g., trypsin), the overall negative charge of an ADP-ribose unit and further reduction of positive charge upon electron capture, ETD typically results in a higher prevalence of neutral peptide fragments over HCD.

1.4.3.3 Fragmentation by Electron-transfer/Higher-energy Collision-dissociation

The limitations arising from the use of HCD and ETD fragmentation for peptide sequencing and site identification have been minimised with the development of a hybrid fragmentation method that combines the two, termed electron-transfer/higher-energy collision-dissociation (EThcD).[173,174] The hybrid nature of EThcD minimises non-dissociative electron-transfer and neutral losses during fragmentation by ETD-only, due to the supplemental energy provided by the simultaneously applied HCD mode. This allows for sequencing of peptides bearing a low positive charge while maintaining the integrity of the modification, hence aiding site identification.[173,174] Given the advantages of this hybrid fragmentation method, EThcD has been successfully employed for the study and site identification of different PTMs, including ADP-ribosylation,[98,175] N-glycosylation,[176] and phosphorylation sites,[174,177] with the latter two also traditionally difficult to detect by LC-MS/MS analysis. A study performed in 2019 by Hendriks *et al.* comparing the utility of ETD and EThcD for identification of ADP-ribosylated residues showed that EThcD, overall, was superior to ETD in identifying and localising modified sites.[98] It must be noted, however, that not every MS instrument can perform simultaneous/sequential HCD and ETD fragmentation, and EThcD is generally available on higher-end instruments.

1.4.3.4 Fragmentation by Activated-ion Electron-transfer Dissociation

Similarly to EThcD, other hybrid fragmentation methods have been applied for the study and identification of ADP-ribosylation sites. Activated-ion electron-transfer dissociation (AI-ETD) was developed as a novel method to reduce the undesirable formation of secondary structure of peptide fragments that result in non-dissociative electron-transfer during ETD.[178-180] This is achieved by photoactivation of peptide precursor cations and the corresponding fragments through infrared (IR) irradiation, which disrupt non-covalent peptide interactions during ETD fragmentation. Buch-Larsen *et al.* successfully adapted the method for localising and identifying ADP-ribosylation sites in an unbiased manner following ADPr peptide enrichment with Af1521.[99] The study resulted in the highest number of identified ADP-ribosylation sites

from a single study, ~9000 sites, and proved to be superior to both ETD and EThcD fragmentation for site identification.[99] Despite the promising results of AI-ETD as a highly sought-after unbiased site identification approach, this particular fragmentation method is generally difficult to implement. Access to AI-ETD instruments is limited due to the need to physically equip an MS instrument with the appropriate IR laser source. As a result, in many laboratories it is not possible to routinely perform AI-ETD for the study of ADP-ribosylation.

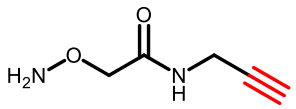
1.5 Studying intracellular ADP-ribosylation

The study of ADP-ribosylation intracellularly, its dynamics and the identification of intracellular ADP-ribosylated protein targets has been impeded by the lack of chemical tools that can cross the cell lipid bilayer. Although NAD^+ analogues have vastly expanded the range of known ADP-ribosylated proteins, these analogues are not cell-permeable, and their use has been restricted to cell lysates, recombinant proteins or fluorescence microscopy experiments following transient permeabilisation and cell fixing.[104-119] Their inability to traverse the negatively charged lipid bilayer arises from their permanent overall negative charge. It has therefore been proposed that masking of one of the phosphate groups or the introduction of a positively charged moiety such that NAD^+ no longer has an overall negative charge might overcome this limitation. The concept has been demonstrated by Fouda *et al.*, who successfully synthesised a biotinylated ATP analogue incorporating a positively charged linker on the phosphate chain, which was shown to be cell-permeable.[181] However, due to the synthetic challenges associated with NAD^+ synthesis and the labile nature of NAD^+, neither prodrugs *via* masking of the phosphates nor NAD^+ analogues incorporating a positively charged moiety have been synthesised to date.

1.5.1 Aminooxy Probe for Capturing ADP-ribosylation on D and E Residues

The concept of targeting intracellular ADP-ribosylation by employing small molecules was first explored by Morgan *et al.*, who synthesised a clickable aminooxy probe (**19**) incorporating an alkyne group (**Figure 1.12**).[182] Morgan *et al.* used **19** in combination with click conjugation to rhodamine fluorophore to show that overexpressed GFP-PARP10 and GFP-PARP11 undergo automodification in HEK293T cells. Subsequently, **19** was employed for fluorescence microscopy in fixed H_2O_2-treated HEK293T cells following intracellular incorporation of the probe and click chemistry. However, a major caveat of utilising the aminooxy probe for studying intracellular ADP-ribosylation is that the probe can only be used to label and capture proteins that undergo ADP-ribosylation on the acidic residues D and E. Given that ADP-

ribosylation has been observed on at least 9 residues,[99] and that the majority of this PTM occurs on serine residues under oxidative stress,[97-100,156] the aminooxy probe would therefore be unable to capture the majority of intracellularly ADP-ribosylated proteins. Furthermore, the specificity of the probe to only modify ADP-ribosylated proteins is being questioned since the mechanism of labelling occurs *via* ribose ring opening to an aldehyde tautomer, which then forms an oxime bond with the probe. This mechanism therefore makes it possible for **19** to also label other proteins possessing a ribose ring as part of a PTM, such as glycoproteins. In addition, the non-selective nature of the primary amine is expected to result in off-target binding *via* modification of non-ADP-ribosylated glutamate and aspartate residues, as has been previously suggested for hydroxylamine[100]. Together, these limitations render **19** unsuitable for reliable monitoring of intracellular ADP-ribosylation.



19

Figure 1.12. Structure of aminooxy probe (**19**).

1.5.2 NAD^+ Biosynthesis Pathway

Taking into consideration the intracellular NAD^+ biosynthesis pathway present in most mammalian cells (**Figure 1.13A**), which is the major source of intracellular NAD^+,[183,184] it had been proposed that treatment of cells with clickable NAD^+ precursor analogues[164,185] could lead to intracellular conversion into the corresponding NAD^+ analogues. The approach appears viable due to the presence of equilibrative nucleoside transporter (ENT) channels on the cell surface in eukaryotic cells, which are responsible for the passive transport of nucleosides, including adenosine, nicotinamide riboside (NR) and reduced nicotinamide riboside (NRH), across the cell lipid bilayer.[186-190] Once in the cell, adenosine undergoes phosphorylation by adenosine kinase (AdK) to produce adenosine monophosphate (AMP) in the cytoplasm,[191] which is subsequently converted into adenosine diphosphate (ADP) by adenylate kinases (AKs),[192] before being transported into the mitochondria. Adenosine triphosphate (ATP) synthase in the mitochondria, responsible for the production of the vast majority of cellular ATP, further phosphorylates ADP to produce ATP.[193] ATP is then transported into the cytoplasm, where it can be used for AMPylation (**Figure 1.13B**), a type of protein PTM,[82] or further transported into the nucleus, where it can be coupled to β-NMN by nicotinamide mononucleotide adenylyltransferase 1 (NMNAT1)[194] for nuclear NAD^+ synthesis. NAD^+ can

then be used by nuclear PARPs for nuclear ADP-ribosylation or transported into the cytoplasm, where it can also be used by cytoplasmic PARPs. Although two more NMNAT isoforms exist (not shown in **Figure 1.13**), namely NMNAT2 and NMNAT3, in the cytoplasm and mitochondria, respectively,[194] neither are expected to significantly contribute towards cellular ADP-ribosylation (in the context of this work). The cytoplasmic NMNAT2 is predominantly expressed in brain tissues[195] (not used in this work), and mitochondrial NAD^+ is in high demand in the Krebs cycle for generation of NADH,[196] for subsequent use in the electron transport chain.

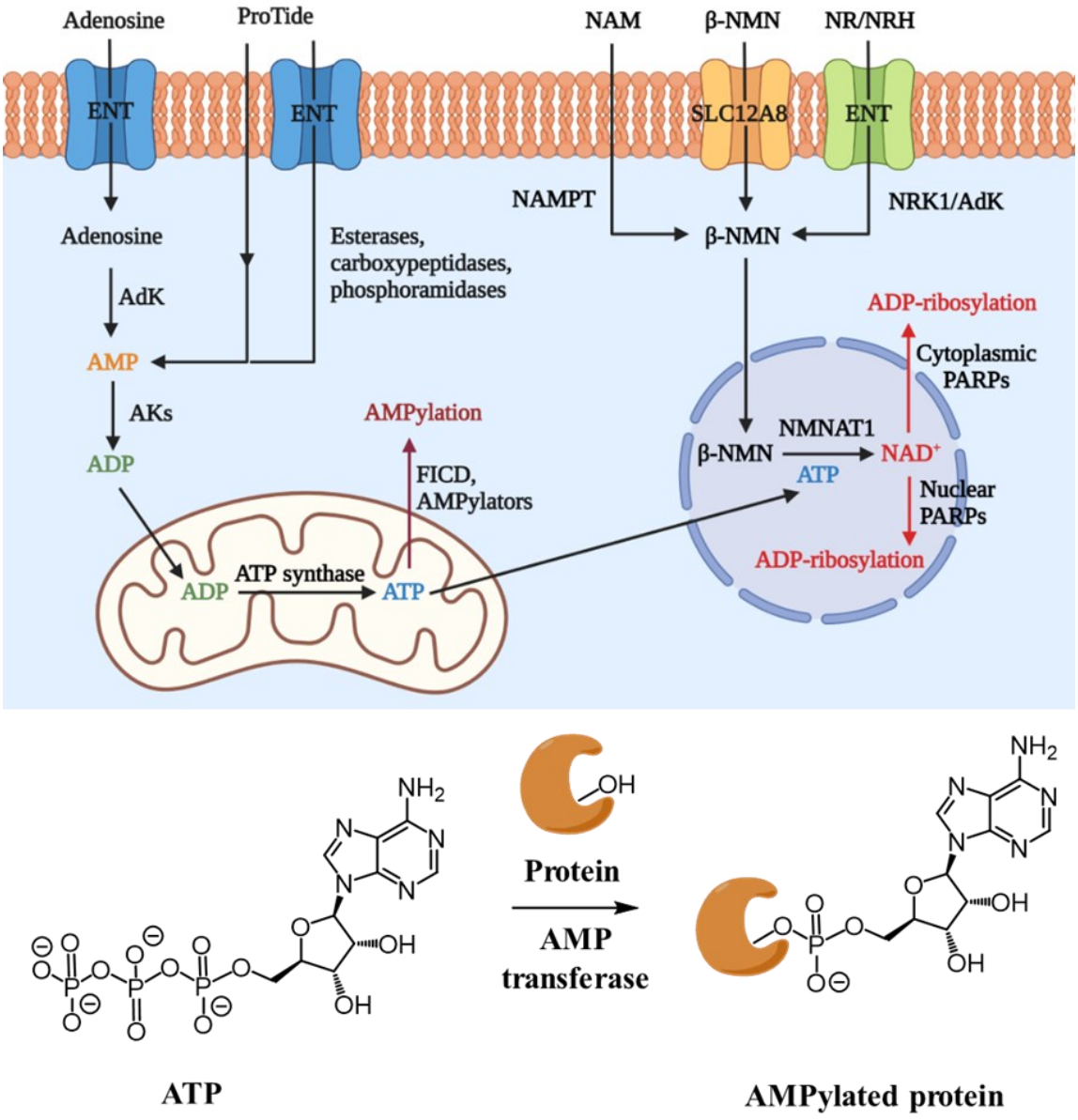


Figure 1.13. Illustration of compartmentalisation of intracellular ATP, β-NMN and NAD^+ biosynthesis. **A.** Extracellular adenosine or ProTide adenosine prodrug is transported into cells through ENTs and converted into AMP and ADP in the cytoplasm. ADP is subsequently transported and converted into ATP in the mitochondria.

ATP can then be used in AMPylation or transported into the nucleus for nuclear NAD^+ synthesis *via* coupling to β-NMN and ADP-ribosylation. **B.** Schematic representation of protein AMPylation.

By utilising the NAD^+ biosynthesis pathway (**Figure 1.13A**), it was hypothesised that intracellular NAD^+ analogues can be metabolically produced following treatment with NAD^+ analogue precursors. However, the NAD^+ precursors AMP, ADP and ATP all possess a permanent negative charge and are therefore non-membrane permeable, thus leaving adenosine analogues as the only NAD^+ analogue precursors that are cell-permeable. Westcott *et al.*[164] and Kalesh *et al.*[185] investigated whether supplementation of cells with clickable adenosine analogues resulted in their metabolic conversion to the corresponding NAD^+ analogues intracellularly, and whether this led to protein labelling due to ADP-ribosylation. The results from both studies were conflicting and are discussed in detail in **Section 4.2**, alongside results generated in this project.

1.5.3 ProTide Adenosine Prodrugs

It has been previously observed that AdK activity was inhibited by native adenosine at high adenosine concentrations,[191] potentially suggesting that the adenosine to AMP conversion step by AdK may be a rate-limiting step in the NAD^+ biosynthesis pathway. Given that typically cell treatment requires high probe concentrations, such as the concentrations of adenosine analogues used by Westcott *et al.*[164] and Kalesh *et al.*[185], it is not clear how efficient intracellular metabolic conversion of adenosine analogues to AMP analogues would be upon cell treatment. However, it is possible to bypass this initial phosphorylation step by supplementing cells with prodrugs of AMP analogues, which, once inside the cell, would be directly converted into the corresponding AMP analogue.

Although multiple prodrug approaches exist for intracellular delivery of monophosphate molecules,[197,198] a well-established approach for generating antiviral and anticancer molecules, that has also been successfully employed in the clinic, is the generation of ProTide nucleoside prodrugs[199-203]. Once in the cell, the ProTide prodrug undergoes a series of enzymatic and hydrolysis reactions to produce the corresponding monophosphorylated molecule (**Figure 1.14**).[199] In this pathway, ProTide undergoes initial ester hydrolysis by esterase or carboxypeptidase type enzyme, generating intermediate **20**. It is then followed by a spontaneous ring cyclisation step, giving rise to intermediate **21**, and a second spontaneous, ring opening hydrolysis step, giving rise to intermediate **22**. Finally, L-alanine moiety in intermediate **22** undergoes enzymatic hydrolysis by a phosphoramidase type enzyme to

generate AMP as the final product. Masking of the phosphate group with L-ala-benzyl ester and phenol is the preferred choice for ProTide synthesis as it has been established in the literature that L-ala-benzyl ester and phenol protected phosphates undergo more efficient intracellular conversion to the unprotected phosphate group compared to other substituents[199,204]

In addition to bypassing an initial phosphorylation step, ProTide nucleoside prodrugs are more lipophilic than their corresponding nucleosides, which results in increased cell permeability through the lipid bilayer. As a result, lower concentrations of probes are typically required for cell treatment. In this work, several adenosine and ProTide adenosine analogues were synthesised (**Chapter Three**), and their utility for intracellular metabolic generation of the corresponding NAD^+ analogues and subsequent protein labelling was investigated (**Chapter Four**).

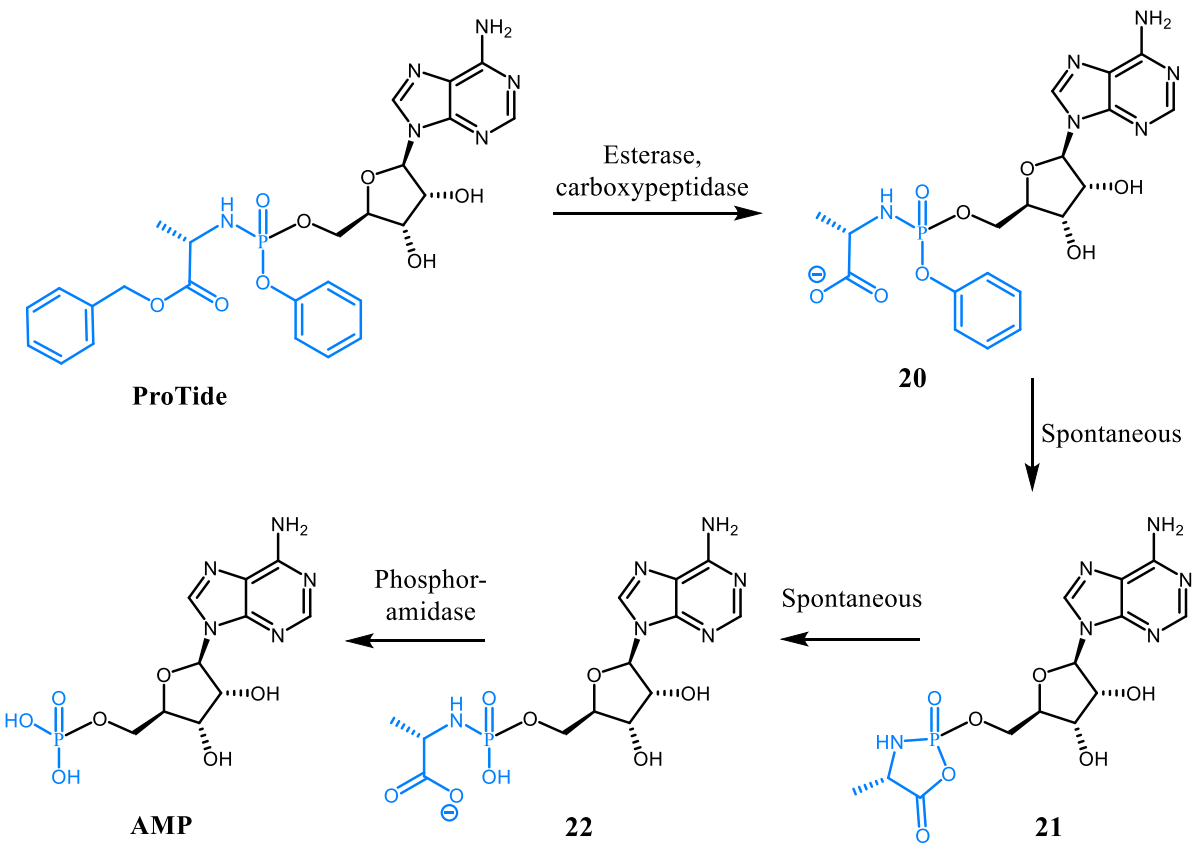


Figure 1.14. Mechanism of intracellular conversion of ProTide prodrug adenosine into AMP. Cleavage of benzyl alanine ester by esterase-type enzymes generates intermediate **20**, followed by spontaneous ring cyclisation generating intermediate **21** and subsequent spontaneous ring opening giving rise to intermediate **22**. A final hydrolysis step by phosphoramidase-type enzymes then generates AMP.

1.5.4 Boosting NAD^+ Levels Through NAD^+ Precursor Supplementation

Literature studies have shown that intracellular NAD^+ production can be boosted by increasing intracellular β-NMN levels. This was achieved through direct supplementation with β-NMN or by stimulating β-NMN production through supplementation with the β-NMN precursors nicotinamide riboside (**23**, NR) and reduced nicotinamide riboside (**24**, NRH) (**Figure 1.15**).[189,190,205-209] Grozio *et al.* identified the presence of the membrane-bound solute carrier family 12 member 8 (SLC12A8) transporter, which was identified as a β-NMN transporter channel, and showed that its knockdown in mouse tissue resulted in ~1.5 – 2 fold decrease in NAD^+ levels.[209] In the same year, a novel β-NMN precursor was discovered, namely NRH (**24**), the supplementation of which was shown to boost intracellular NAD^+ levels between 3-fold and 10-fold in different cell lines, compared to no supplementation.[205-207] Furthermore, Yang *et al.* demonstrated that cells treated with β-NMN or NR (**23**) only had marginally increased NAD^+ levels, up to ~1.5-fold, thus showing that supplementation with NRH (**24**) was superior in boosting NAD^+ levels.[205]

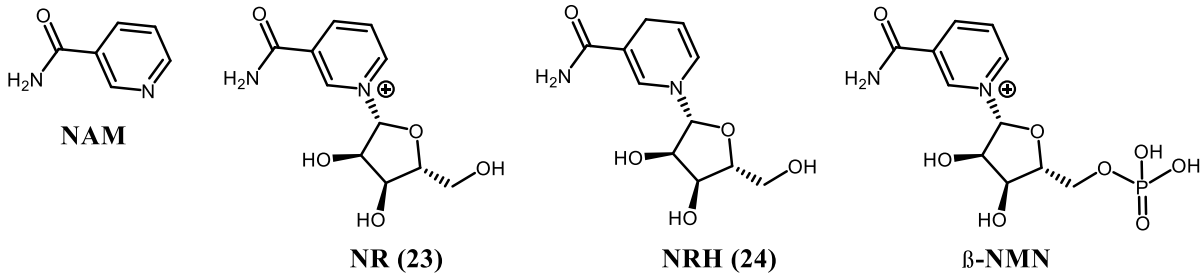


Figure 1.15. Structures of β-NMN and NAD^+ precursors involved in NAD^+ biosynthesis.

It is still up for debate why NRH (**24**) supplementation results in such a substantial increase in NAD^+ levels when compared to the other two precursors. In a subsequent study, Yang *et al.* demonstrated *via* isotope labelling and metabolomics analysis that NRH (**24**) supplementation resulted in the production of reduced β-NMN (β-NMNH).[207] However, it was unclear whether β-NMNH was oxidised to β-NMN prior to conversion into NAD^+, or whether β-NMNH was converted into reduced NAD^+ (NADH) by NMNAT1 and subsequently oxidised to NAD^+, and why either pathway would lead to the drastic increase in NAD^+ levels observed when compared to NR (**23**) supplementation. Regardless, given the literature precedent on the positive effect on NAD^+ levels following supplementation with β-NMN, NR (**23**) or NRH (**24**), the effect of

supplementation with all three precursors on intracellular NAD^+ analogue production was investigated in this work (**Chapter Four**).

1.6 Thesis Aims and Objectives

Development of novel chemical tools for intracellular and *in vivo* study of ADP-ribosylation is essential for better understanding and elucidating the biological consequences of this PTM, particularly its role in the development of cancer and other diseased phenotypes. Such tools will be a great asset for elucidating its intracellular dynamics, identification of the proteins it is found on in a live cell environment and the identification of intracellular protein targets of each individual PARP protein, applications which so far have only been possible in cell lysates, fixed cells, or recombinant protein assays.

We hypothesise that monitoring of intracellular ADP-ribosylation can be achieved through supplementation with clickable NAD^+ analogue precursors, such as adenosine or ProTide prodrug analogues of adenosine, for metabolic conversion into the corresponding clickable NAD^+ analogues inside cells. Thus, the overall aims of this project thesis are to synthesise novel cell-permeable NAD^+ analogue precursors and demonstrate their utility for studying intracellular ADP-ribosylation *via* intracellular labelling of ADP-ribosylated proteins. To achieve this, the following aims and objectives will be the primary focus of this project thesis:

1. *In silico* design of clickable NAD^+ precursor analogues and investigating their potential for utilisation in the NAD^+ biosynthesis pathway and ADP-ribosylation by PARPs. This will be performed using computational modelling and docking experiments using published co-crystal structures of the proteins involved in NAD^+ biosynthesis and PARP proteins (**Chapter Two**).
2. Synthesis of the *in silico* designed NAD^+ precursor analogue probes, the corresponding AMP, ATP and NAD^+ analogues, and the β-NMN/NAD^+ precursors NR (**23**) and NRH (**24**), using novel and literature established synthetic routes (**Chapter Three**).
3. Validation of the synthesised clickable NAD^+ precursor analogue probes. Initial validation will be performed by monitoring probe utilisation for intracellular protein labelling by IGF and WB, and for RNA synthesis (through metabolic conversion into ATP analogues) by IGF (**Chapter Four**).
4. Investigation of the suitability of the probes for studying intracellular ADP-ribosylation. Probe utilisation throughout the NAD^+ biosynthesis pathway and identification of potential conversion bottleneck steps will be monitored by

metabolomics analysis, and proteome-wide identification of intracellularly NAD^+ analogue-labelled ADP-ribosylated proteins will be performed by proteomics analysis (**Chapter Four**).

Chapter 2 *In Silico* Probe Design

2.1 Introduction to Molecular Docking

In this chapter, derivation of clickable NAD^+ analogue precursors that can be employed for intracellular synthesis of the corresponding NAD^+ analogues and subsequent ADP-ribosylation by PARPs was explored by computational molecular modelling. The technique was applied for investigating the suitability of the proposed probes to be fully utilised in the NAD^+ biosynthesis pathway, by probing protein-ligand interactions in each step of the pathway, as well as for identification of any potential bottleneck steps. Overall, five NAD^+ analogue precursor series were tested. The results predicted that at least one of the proposed analogue series, 6Yn-, was likely to be utilised throughout the entire NAD^+ biosynthesis pathway and for subsequent ADP-ribosylation by PARP1.

2.1.1 Overview

Molecular docking is a powerful computational molecular modelling technique used for predicting the binding mode of a ligand with a protein of interest and studying the interactions that can occur.[210,211] Protein-ligand docking is the most common type of molecular docking although the technique can also be applied for predicting protein-peptide, protein-protein and protein-DNA (nucleic acid) interactions.[212] Molecular docking is commonly used as a starting point for drug development in medicinal chemistry and is particularly useful for designing novel compounds where no, or limited, structure-activity relationship (SAR) data is available. In addition, it allows for identification of a protein active site or allosteric binding sites, which can be subsequently targeted for ligand development. Molecular docking software packages,[211] such as the Molecular Operating Environment[213] (MOE, used in this work), can also predict the affinity of binding of a small molecule to a protein target, which is essential for further ligand optimisation.

2.1.2 Homology modelling

Molecular docking requires the availability of protein crystal structures, typically generated by X-ray crystallography, cryo-electron microscopy (cryo-EM) or nuclear magnetic resonance (NMR), however, protein crystallisation is often difficult to achieve. In the case where crystal structures are not available for molecular docking, a protein structure can be generated from its amino acid sequence by homology modelling.[214,215]

The principle behind homology modelling relies on the observation that proteins that share high sequence similarity are also closely resembled in structure. Based on this, a structure for a protein can be generated from its sequence (a homology model) by using a crystal structure of a different protein with a similar amino acid sequence as a template upon which the model is built. Thus, it follows that a higher sequence similarity between a template and the protein to be modelled results in the generation of a higher quality structure, and it is generally accepted that a sequence alignment of >25% is sufficient for generating a good homology model.[214-216]

In the context of ADP-ribosylation, homology modelling is useful for generating 3D structures for PARP proteins, for many of which a resolved crystal structure is incomplete or unavailable. Given the high sequence alignment of the catalytic sites between individual PARylating PARPs and between individual MARylating PARPs,[217] the availability of a crystal structure in either group is generally sufficient to produce a good homology model for each PARP member in that respective group. This could then be applied, for example, for optimisation and design of specific PARP inhibitors. In this project, homology modelling was used to identify potential mutagenesis sites that can be targeted for generation of mutant PARPs (see **Section 2.3.2**), which could then be used for target identification of individual PARPs *via* the 'bump-hole' approach (**Figure 1.4**).

2.1.3 Mutational Analysis

Computational mutation analysis allows for studying the effect of a mutation on protein structure, its catalytic activity and ligand binding.[218,219] Point mutations, particularly in/around a ligand binding site, can alter the overall structure of a binding site to an extent which precludes ligand binding or results in complete loss of catalytic activity.[218,219] Mutational analysis tools, included in most molecular docking software packages, are therefore indispensable tools for identification of residues critical for ligand binding and protein catalytic activity, and for guiding and optimising ligand design.

In the context of PARP point mutations and ADP-ribosylation, mutational analysis in the active site of PARPs has allowed for the successful development of several 'bumped' NAD^+ analogues (**11-14**, **Table 1.2**).[114-119] These ligands have successfully been used for target identification and profiling of individual PARPs, *via* the 'bump-hole' approach (**Figure 1.4**) since they are not utilised by WT PARPs but are substrates for the corresponding active site mutant PARPs.[114-119]

2.1.4 Ligand Pharmacophore Constraints

Structurally complex ligands, such as ATP and NAD^+, have the potential to form multiple interactions in a protein binding site (**Figure 2.1**). This can cause issues during molecular docking, where a ligand might be docked in the 'wrong' orientation compared to its actual binding mode (if known). Essential protein-ligand interactions, critical for binding, can therefore be conserved during molecular docking by setting pharmacophore constraints on the molecule to ensure it is docked in the correct orientation.[220,221] This feature is useful in ligand derivatisation to establish if its binding mode is affected specifically by the part of the ligand being modified, particularly when the derived moiety is spatially distant from the set pharmacophore constraints. Given the structurally complex nature of adenosine analogues and their phosphorylated derivatives (AMP, ADP, ATP, NAD^+), it was necessary to place pharmacophore constraints on the ligands (see **Section 6.5.3.2**) to ensure correct binding mode to their respective protein during the molecular docking experiments described in this chapter.

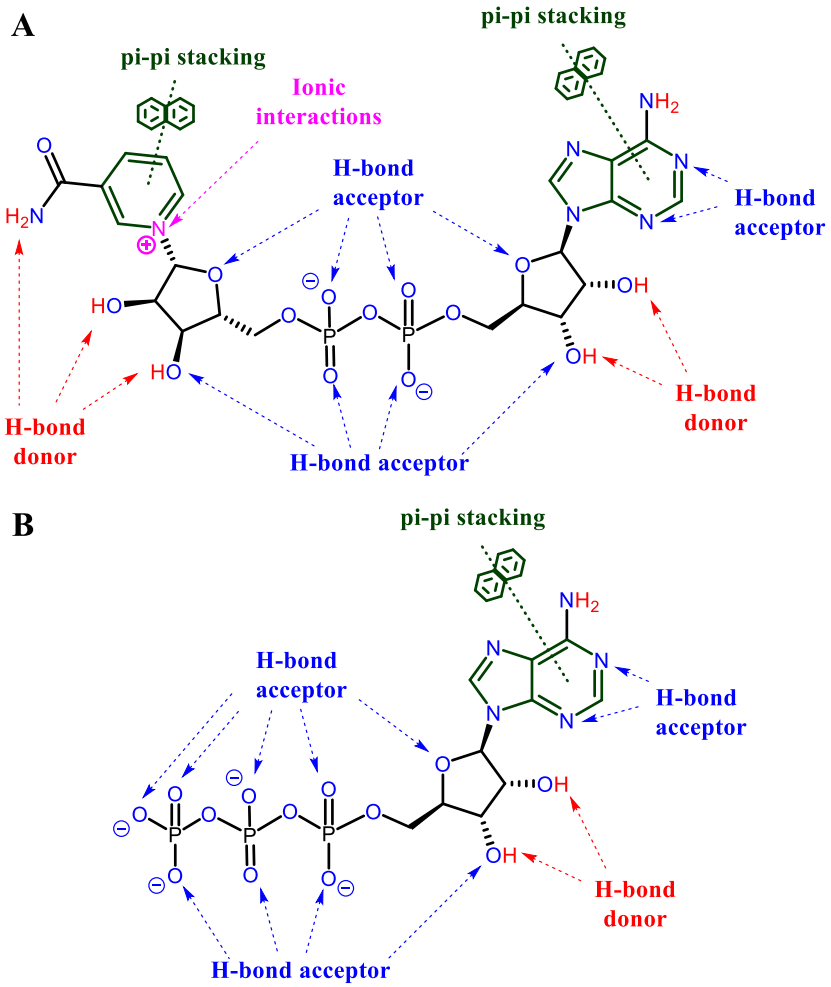


Figure 2.1. Interaction maps of NAD^+ (**A**) and ATP (**B**). H-bond acceptor atoms (blue), H-bond donor atoms (red), pi-pi stacking interactions (green) and ionic interactions (pink) are highlighted.

2.1.5 Limitations of Molecular Docking

2.1.5.1 General Limitations

The main limitation associated with molecular docking is that a crystal structure, such as those generated by X-ray crystallography, represents only one pose/structural conformation at a particular time point.[222] As a result, the generated structure is not representative of the potential dynamic nature of a protein structure/protein-ligand complex. This can be problematic for ligand design for crystal structures where co-crystallisation with a ligand has not been achieved, as it could lead to poor initial ligand design. To overcome this, software packages partially account for the lack of conformational flexibility through an induced fit model-type docking.[213] However, this potential limitation should be taken into account when assessing docking data as molecular docking data may not always translate to in vitro experimental data.

2.1.5.2 Limitations of Homology Modelling

Homology modelling is an excellent tool for generating structural models for protein sequences that do not have a resolved crystal structure. However, computationally derived structures are likely to differ to some degree from actual protein structures. This is especially true for homology models where there is poor sequence alignment relative to a template crystal structure, or for structures that contain extended loops as these can be difficult to model.[214,215] In addition, homology modelling can be resource intensive in terms of the computational power and time required to derive structural models, which can be a limiting factor on the quality of the generated models. Software packages allow for further structural refinement of the derived models,[214,215] however, the more refinement steps are included the more computational power and time are needed.

2.1.5.3 Limitations on the Use of Pharmacophore Constraints

Pharmacophore constraints are useful for conserving critical protein-ligand interactions during molecular docking, however, setting such constraints close to/on derived parts of a ligand may give rise to ligand conformations within a binding site that may not correspond to the actual binding mode *in vitro*. As a result, pharmacophore constraints should be ideally placed on parts of a ligand that are not being modified.

It should be noted that the use of pharmacophore constraints for protein-ligand docking is limited only to co-crystal structures, or homology models derived from co-crystal structures, where a ligand is present at a protein binding site.[220] Owing to the innate difficulties in generating co-crystal structures (e.g. due to high ligand turnover, instability of the protein-

ligand complex) and the structural complexity of ligands capable of forming multiple interactions, it may be difficult to obtain a non-false binding mode for a proposed ligand in the absence of pharmacophore constraints.

2.2 Modelling of Protein-Ligand Interactions in the NAD^+ Biosynthesis Pathway

2.2.1 Rationale for Molecular Docking and Choice of Ligands

The first step in NAD^+ biosynthesis involves conversion of adenosine into AMP by AdK, which is subsequently converted into ADP by AKs and then into ATP by ATP synthase (**Figure 2.2**).[191-193] In the final conversion step, NMNAT proteins couple ATP to β-NMN to produce NAD^+, which is then utilised by PARPs for ADP-ribosylation (**Figure 2.2**).[194]

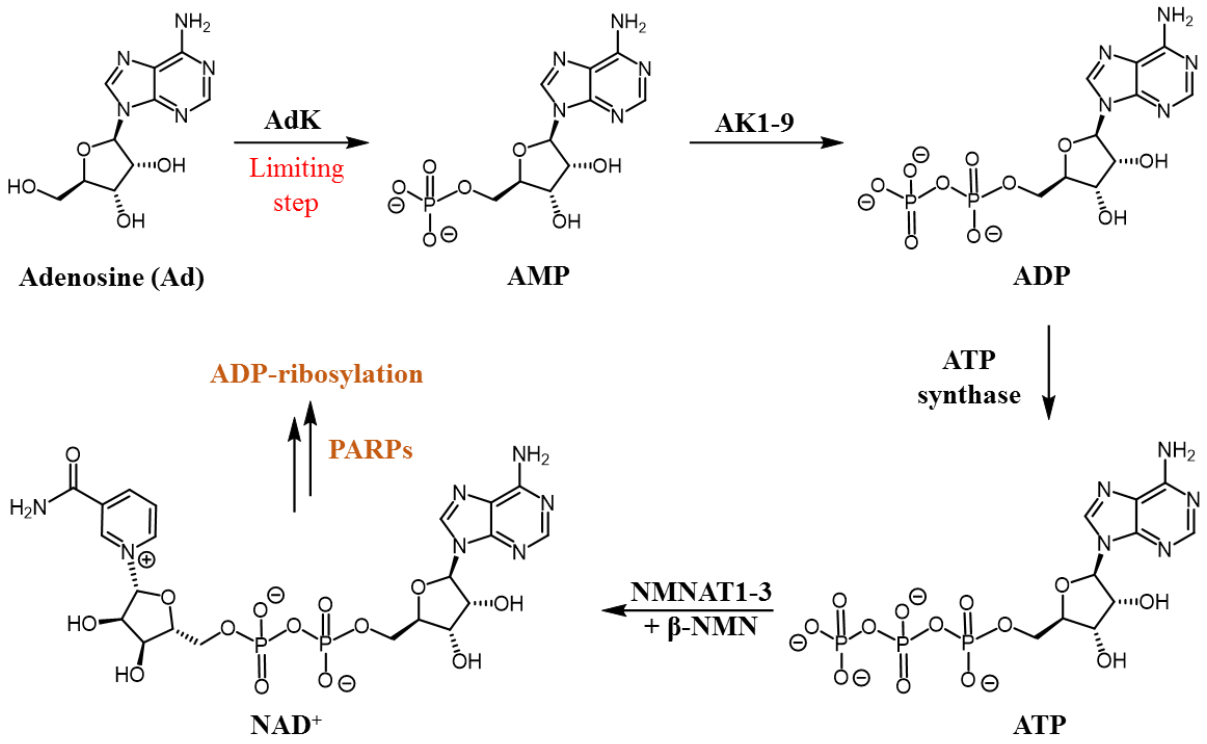


Figure 2.2. Schematic representation of the NAD^+ biosynthesis pathway. Adenosine (Ad) is converted by AdK to AMP, which is subsequently converted into ADP by AK1-9. ATP synthase phosphorylates ADP to produce ATP, which is then converted into NAD^+ by NMNAT1-3 and subsequently utilised by PARPs for ADP-ribosylation.

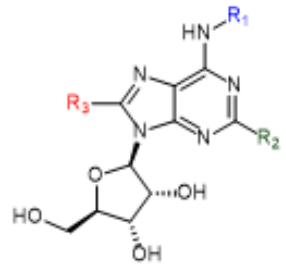
Literature precedent has established that 6Yn-NAD^+ (**3**)[105-107] and 2Yn-NAD^+ (**9**)[110,112] analogues are efficiently used by PARPs as substrates for ADP-ribosylation, and 8But-Yn-NAD^+ (**14**)[118,119] has been successfully used for target identification of mutant PARPs 1, 2, 3 and 7. Furthermore, a ProTide prodrug based on 6Yn-Ad (**25**) (**Section 1.5.3**) for

intracellular delivery was shown to be successfully used in AMPylation[223], which utilises ATP as a cofactor, thus showing that 6Yn- series (**Figure 2.3**), at the very least, undergo metabolic conversion into 6Yn-ATP (**40**) (**Figure 2.3**). Taking this into account, the suitability of these three analogue series and the corresponding NAD^+ precursor analogues (**Figure 2.3**) was investigated for utilisation in the NAD^+ biosynthesis pathway and intracellular production of NAD^+ analogues. In addition, the suitability of two more analogue series for intracellular NAD^+ analogue production, 6Az- and 8Yn- (**Figure 2.3**), was investigated by molecular docking.

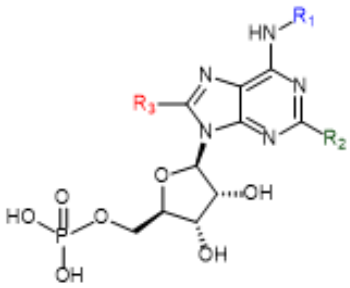
The rationale behind the 6Az- analogue series is the ability of azides to be captured by SPAAC (**Table 1.3**), which can be achieved intracellularly in live cells.[140,141] This would further expand the scope of applications for analysis of ADP-ribosylation as it would allow for live-cell imaging by fluorescence microscopy, which cannot be achieved with the proposed linear alkyne series and the corresponding alkyne NAD^+ analogues. Such applications would allow for monitoring the dynamics and distribution of ADP-ribosylated proteins under the relevant experimental conditions and help dissect the role of the modification in various cellular processes.

NAD^+ analogues possessing bulky clickable groups at the C8 position,[107,118,119,] such as 8But-Yn-NAD^+ (**14**), cannot be utilised by WT PARPs, however, the effect of incorporating a short alkyne group at this position, such as for 8Yn-NAD^+ (**46**), on PARP utilisation has not been previously investigated. It was hypothesised that incorporating a short alkyne group at the C8 position of NAD^+ might be a substrate of PARPs and serve as an additional NAD^+ analogue for labelling ADP-ribosylation. Thus, utilisation of the 8Yn- series in the NAD^+ biosynthesis pathway was investigated.

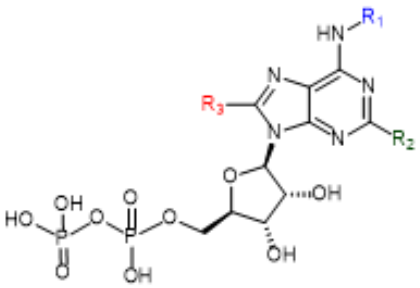
Ultimately, the rationale behind molecular docking was (1) to determine whether the metabolite intermediates for each of the five analogue series were likely to be utilised by the corresponding enzymes in NAD^+ biosynthesis, and (2) help with the identification of any potential bottleneck conversion steps in the pathway. Achieving one (1) would help deciding which NAD^+ precursor analogues to be brought forward for synthesis and subsequent biological validation, and (2) would provide information on whether chemical genetic strategies, such as introduction of active site point mutations, will need to be employed for a particular conversion step for a given metabolite analogue.



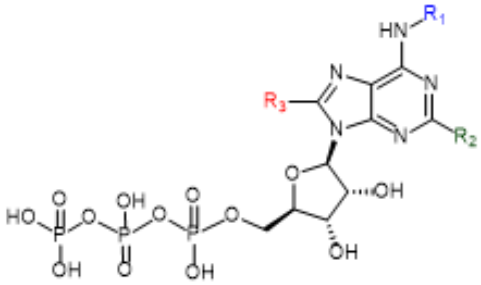
Ad



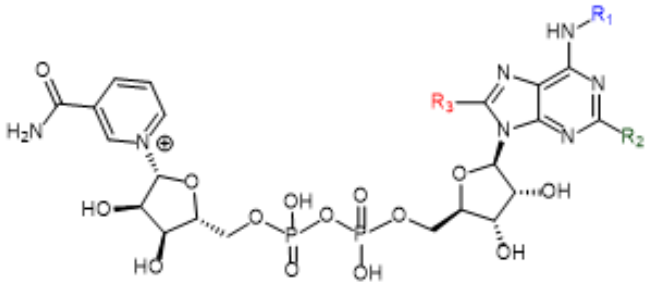
AMP



ADP



ATP



NAD^+

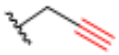
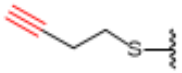
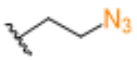
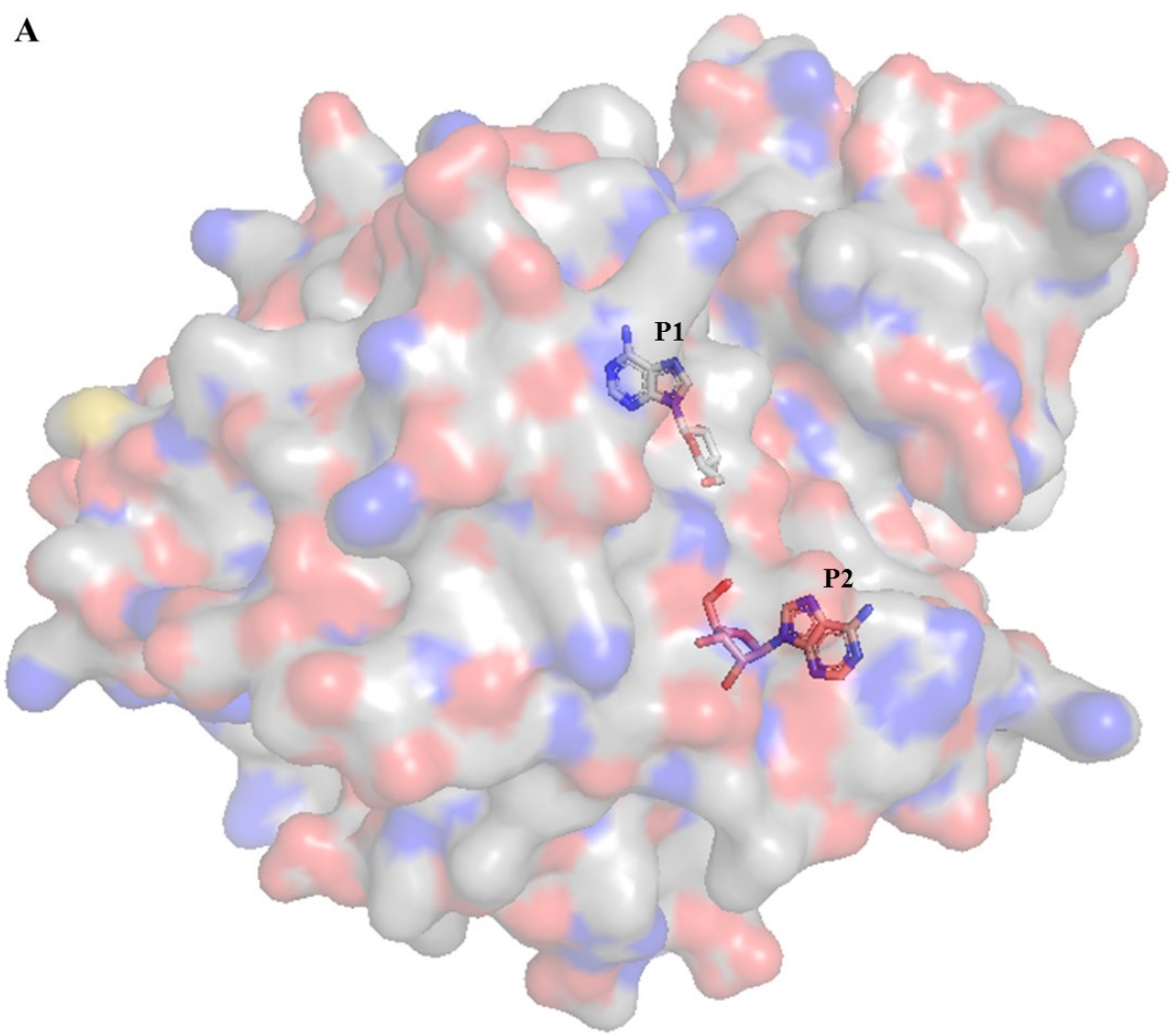
Analogue series	Metabolite	Functional group position		
		R_1	R_2	R_3
6Yn-	Ad (25) AMP (30) ADP (35) ATP (40) NAD^+ (3)		H	H
2Yn-	Ad (26) AMP (31) ADP (36) ATP (41) NAD^+ (9)	H		H
8But-Yn-	Ad (27) AMP (32) ADP (37) ATP (42) NAD^+ (14)	H	H	
6Az-	Ad (28) AMP (33) ADP (38) ATP (43) NAD^+ (45)	H		H
8Yn-	Ad (29) AMP (34) ADP (39) ATP (44) NAD^+ (46)	H	H	

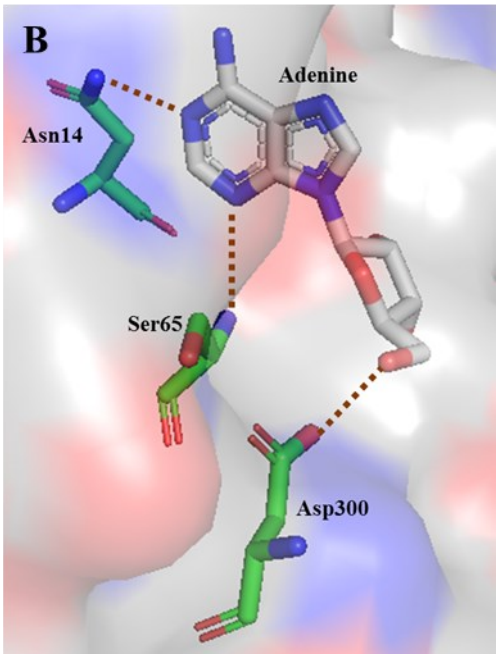
Figure 2.3. Structures of the five metabolite analogue series investigated for utilisation in NAD^+ biosynthesis.

2.2.2 Adenosine Kinase and Adenosine Analogues

The first step in the NAD^+ biosynthesis pathway is the conversion of adenosine into AMP *via* enzymatic addition of a phosphate group at the 5' OH position (**Figure 2.2**), which is often thought to be a rate-limiting step in nucleotide synthesis.[191,197,204] As a result, poor efficiency of phosphorylation of adenosine analogues will likely result in poor/no conversion into the corresponding NAD^+ analogue. It was therefore important to establish whether the proposed adenosine analogues were likely to be utilised in the first step of the pathway.

A co-crystal structure (X-ray crystallography) for AdK with two adenosine ligands (PDB 1BX4)[224] has been published, with the two ligands occupying an adenosine binding site (P1) and an ATP binding site (P2) (**Figure 2.4A**).


A
P1
P2


B
Adenine
Asn14
Ser65
Asp300

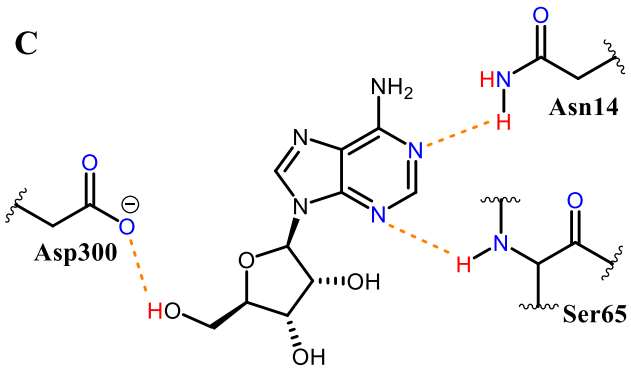

C
NH2
HN
H
O
Asn14
N
N
N
N
Asp300
O
HO
OH
OH
H
N
O
Ser65

Figure 2.4. Co-crystal structure of adenosine kinase. **A.** Overview of AdK showing the binding modes of adenosine ligands at the adenosine binding site (P1) and the ATP binding site (P2). **B.** Binding mode of adenosine at P1 site. Residues important for binding and catalysis (green), and protein-ligand interactions (orange dotted lines) are highlighted. **C.** 2D schematic representation of protein-ligand interactions between AdK and adenosine. H-bond donors (red), H-bond acceptors (blue) and protein-ligand interactions (orange dotted lines) are highlighted.

The co-crystal structure of AdK revealed that residue D300 was essential for catalysis of 5' phosphorylation due to its interaction with the 5' OH group of adenosine (**Figure 2.4B** and **2.4C**). In addition, residues N14 and S65 were shown to form two H-bonding stabilising interactions with the adenine moiety, likely contributing towards ligand binding. The three interactions were therefore considered essential for ligand binding and catalysis, and their loss for a particular adenosine analogue during molecular docking was deemed indicative of partially/completely diminished ability of AdK to utilise that analogue as a substrate.

Results generated from docking experiments with the proposed five adenosine analogues (**25-29**) (**Figure 2.3**) predicted that analogues 6Yn-Ad (**25**) and 2Yn-Ad (**26**) were well accommodated into the AdK active site (**Figures 2.5A and 2.6A**), with an almost identical binding mode to native adenosine, good structural overlap and conservation of key protein-ligand interactions (**Figures 2.5B** and **2.6B**). The results thus predicted that both analogues were likely substrates of AdK for AMP analogue production *in vitro*.

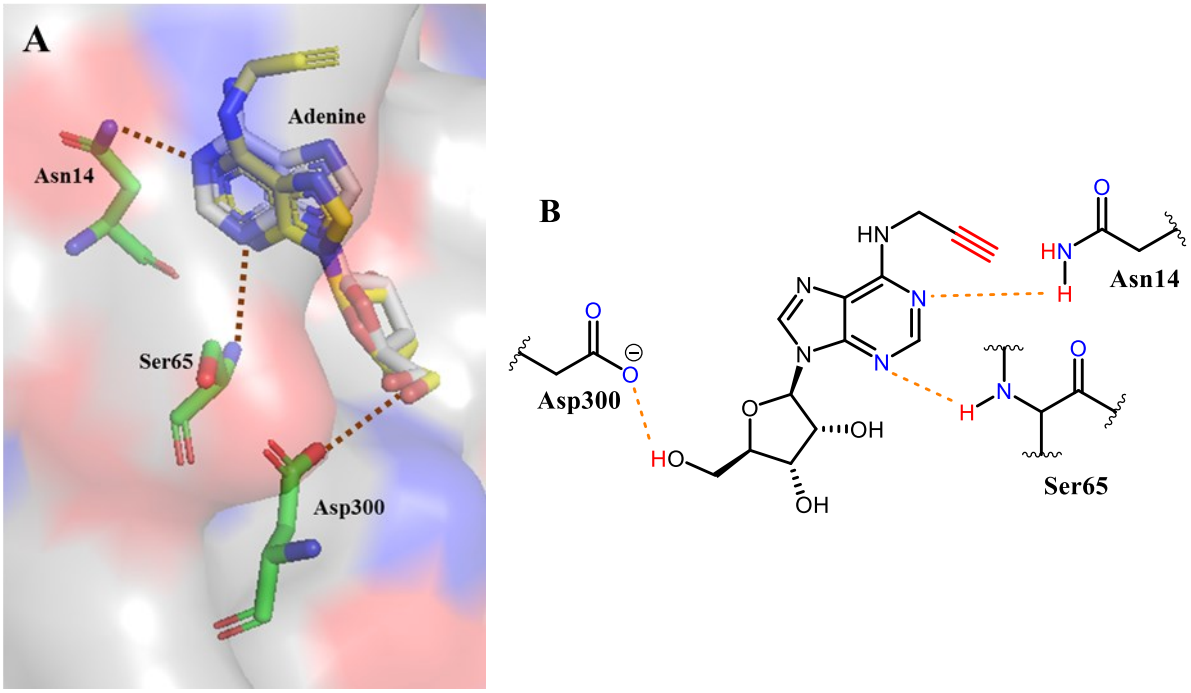


Figure 2.5. Docking of 6Yn-Ad (**25**) with AdK. **A.** The binding modes of adenosine (white) and docked 6Yn-Ad (**25**) (yellow) in the adenosine binding site are shown. Residues important for binding and catalysis (green), and protein-ligand interactions (orange dotted lines) are highlighted. **B.** 2D schematic representation of protein-ligand interactions between 6Yn-Ad (**25**) and AdK. H-bond donors (red), H-bond acceptors (blue) and protein-ligand interactions (orange dotted lines) are highlighted.

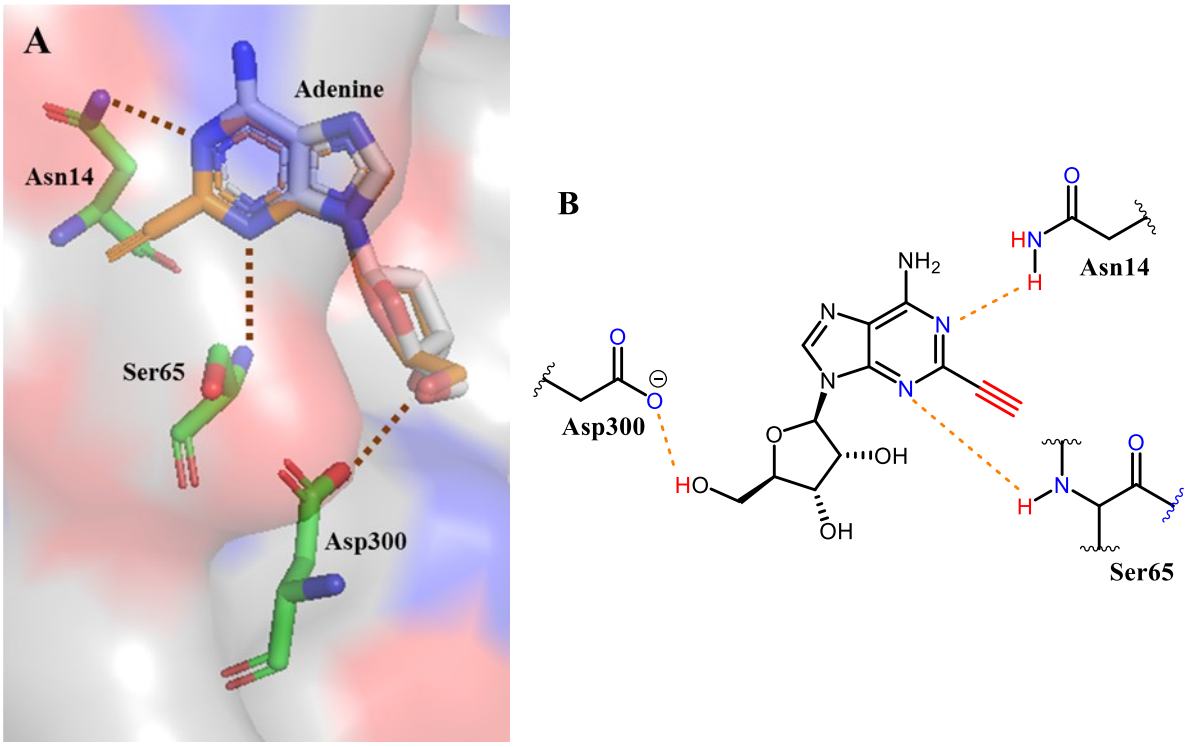


Figure 2.6. Docking of 2Yn-Ad (**26**) with AdK. **A.** The binding modes of adenosine (white) and docked 2Yn-Ad (**26**) (orange) in the adenosine binding site are shown. Residues important for binding and catalysis (green), and protein-ligand interactions (orange dotted lines) are highlighted. **B.** 2D schematic representation of protein-ligand interactions between 2Yn-Ad (**26**) and AdK. H-bond donors (red), H-bond acceptors (blue) and protein-ligand interactions (orange dotted lines) are highlighted.

In contrast to 6Yn-Ad (**25**) and 2Yn-Ad (**26**), the results predicted that analogues 8But-Yn-Ad (**27**) and 8Yn-Ad (**29**) were poorly accommodated into the AdK active site (**Figures 2.7A** and **2.8A**). Incorporation of a clickable group at the C8 position resulted in inversion of the adenine moiety for both analogues, resulting in loss of the two stabilising interactions with residues N14 and S65 (**Figures 2.7B** and **2.8B**). Owing to the significant change in binding mode relative to native adenosine, poor structural overlap and loss of two of the three key protein-ligand interactions, the results predicted that both analogues were unlikely to be substrates of AdK *in vitro*.

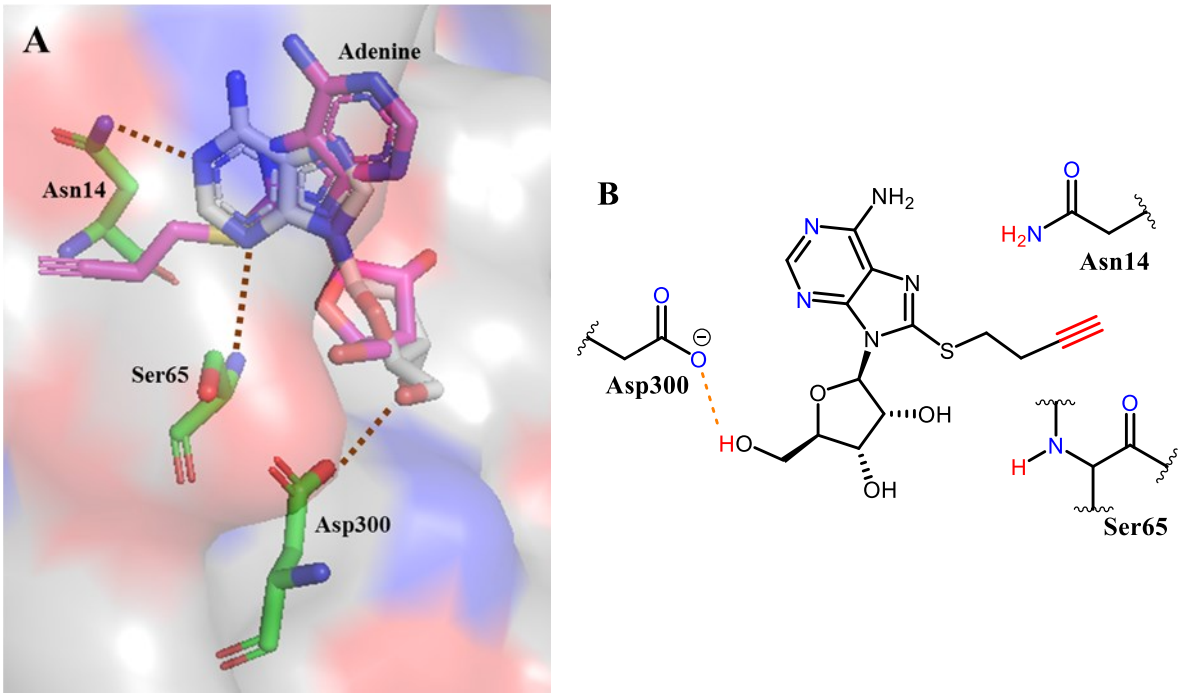


Figure 2.7. Docking of 8But-Yn-Ad (**27**) with AdK. **A.** The binding modes of adenosine (white) and docked 8But-Yn-Ad (**27**) (pink) in the adenosine binding site are shown. Residues important for binding and catalysis (green), and protein-ligand interactions (orange dotted lines) are highlighted. **B.** 2D schematic representation of protein-ligand interactions between 8But-Yn-Ad (**27**) and AdK. H-bond donors (red), H-bond acceptors (blue) and protein-ligand interactions (orange dotted lines) are highlighted.

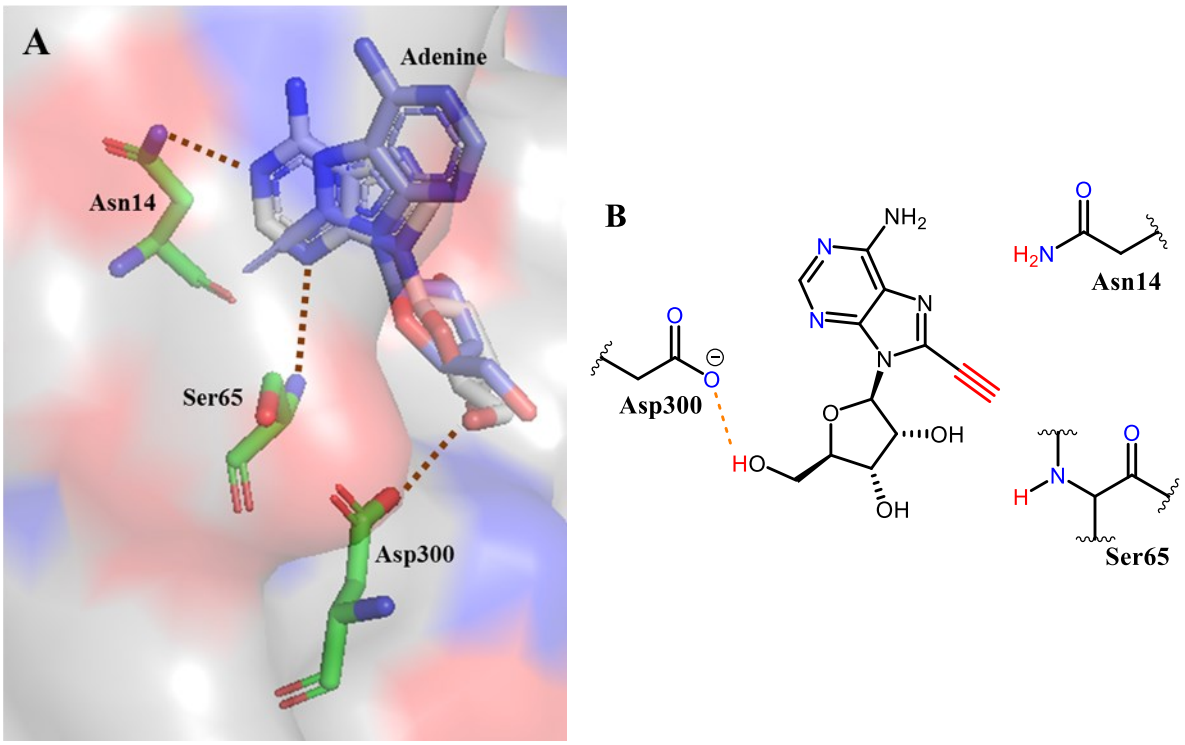


Figure 2.8. Docking of 8Yn-Ad (**29**) with AdK. **A.** The binding modes of adenosine (white) and docked 8Yn-Ad (**29**) (purple) in the adenosine binding site are shown. Residues important for binding and catalysis (green), and protein-ligand interactions (orange dotted lines) are highlighted. **B.** 2D schematic representation of protein-ligand interactions between 8Yn-Ad (**29**) and AdK. H-bond donors (red), H-bond acceptors (blue) and protein-ligand interactions (orange dotted lines) are highlighted.

In comparison to 6Yn-Ad (**25**), which showed good structural overlap with native adenosine (**Figure 2.5A**), molecular docking predicted that the adenosine analogue 6Az-Ad (**28**) was poorly accommodated into the AdK active (**Figure 2.9A)**. Incorporation of the slightly bulkier azide group at the C6 position resulted in inversion of the adenine moiety, in a similar fashion to analogues 8Yn-Ad (**29**) and 8But-Yn-Ad (**27**), which resulted in inversion of the ribose ring. These changes in the binding mode led to loss of all three key protein-ligand interactions (**Figure 2.9B**), therefore the results predicted that 6Az-Ad (**28**) was also unlikely to be a substrate of AdK *in vitro*.

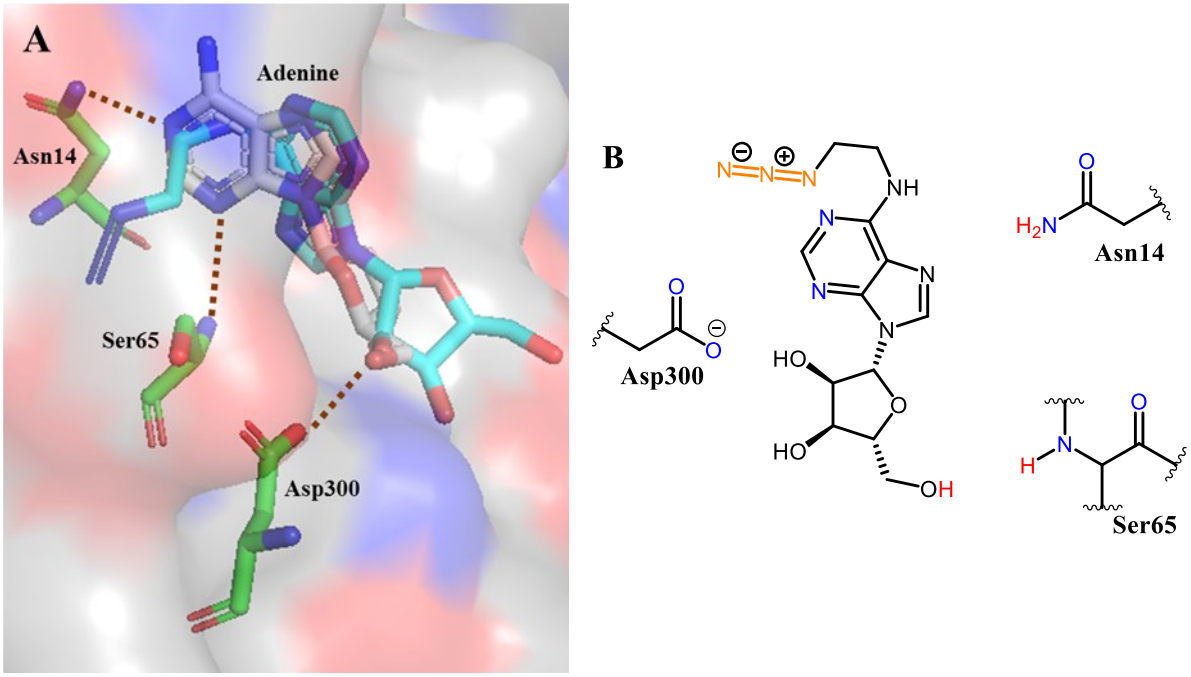


Figure 2.9. Docking of 6Az-Ad (**28**) with AdK. **A.** The binding modes of adenosine (white) and docked 6Az-Ad (**28**) (cyan) in the adenosine binding site are shown. Residues important for binding and catalysis (green), and protein-ligand interactions (orange dotted lines) are highlighted. **B.** 2D schematic representation of protein-ligand interactions between 6Az-Ad (**28**) and AdK. H-bond donors (red), H-bond acceptors (blue) and protein-ligand interactions (orange dotted lines) are highlighted.

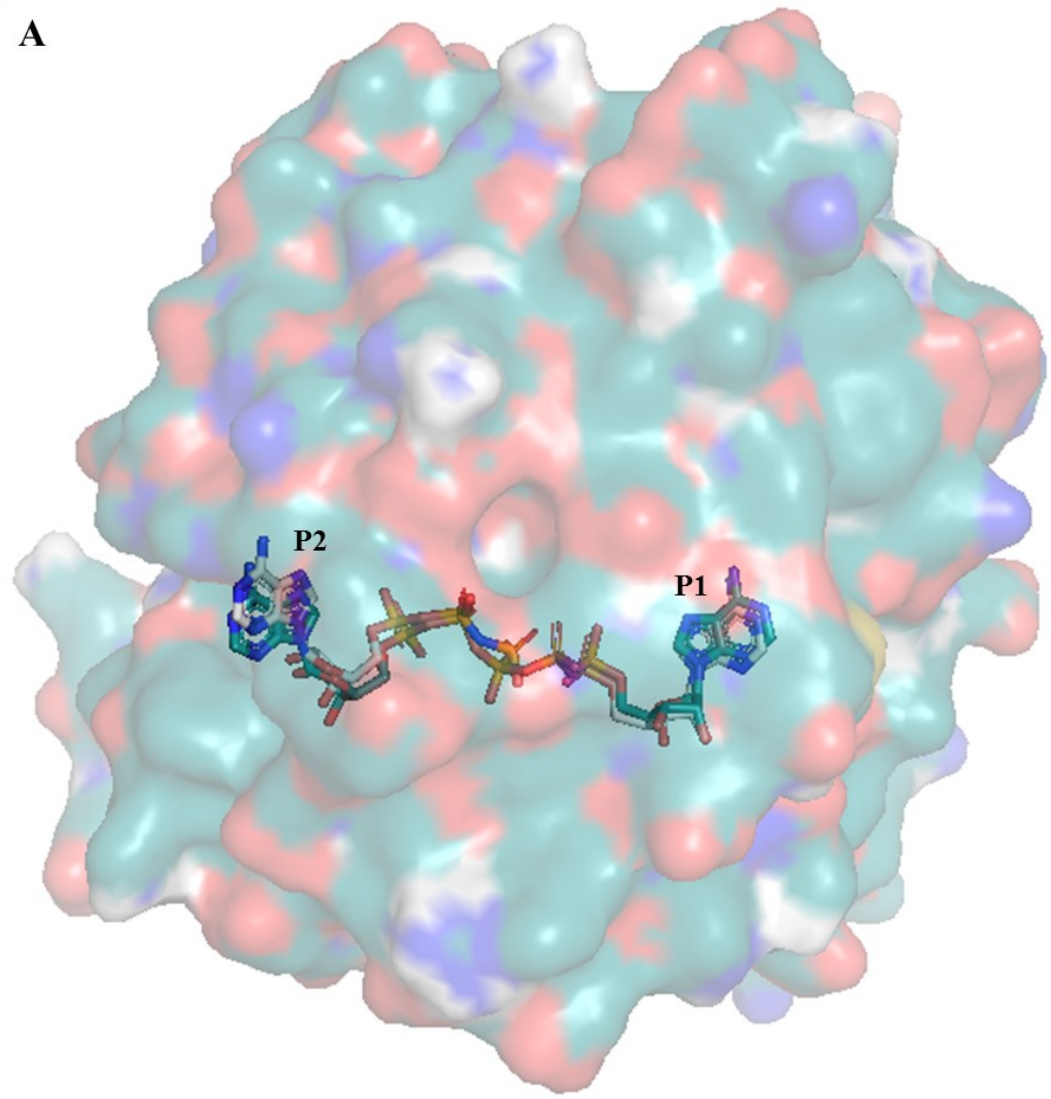
2.2.3 Adenylate Kinases and AMP Analogues

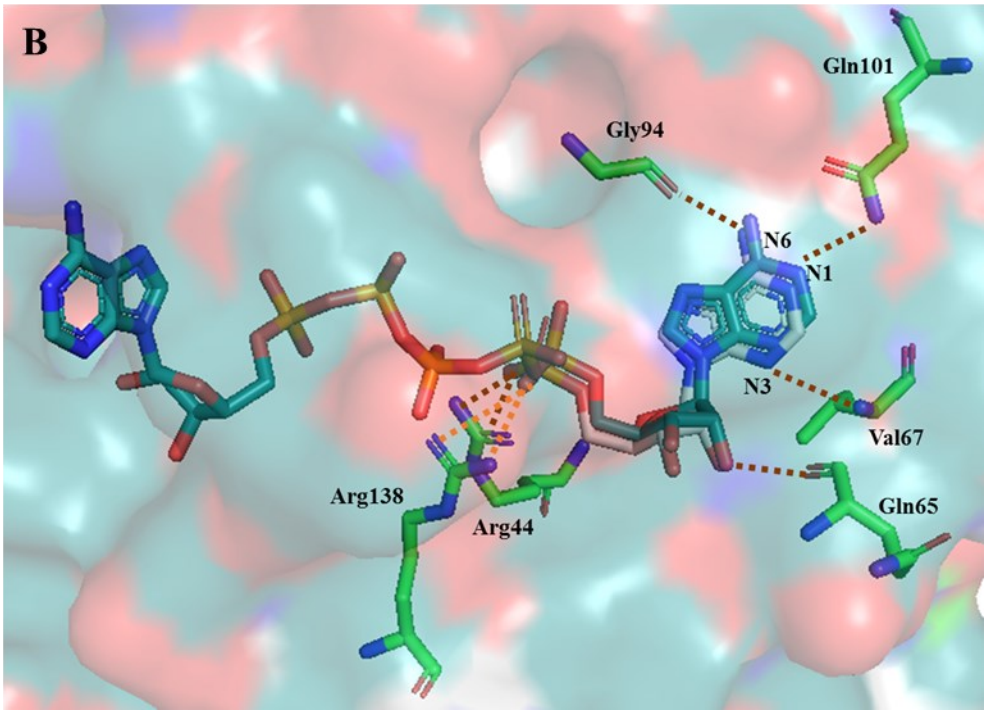
Adenylate kinases are important for balancing cellular concentrations of 5' phosphorylated adenosine derivatives by catalysing reversible transfer of a phosphate group from ATP to AMP to produce ADP.[192] To date, nine AK isoforms (AK1-9) have been identified in humans, with the majority of AKs sharing sequence homology of ~30% (relative to AK1) and each AK localising to a distinct cellular compartment (**Table 2.1**).[192] Adenylate kinases from other species, such as bacteria[225,226] and yeast[227], have also been identified and found to have a similar 30% sequence alignment (relative to AK1) (**Table 2.1**). Since the second step of the NAD^+ biosynthesis pathway involves the conversion of AMP to ADP by adenylate kinases, it was important to establish whether AKs were likely to utilise the proposed AMP analogues as substrates for conversion into the corresponding ADP analogues.

Table 2.1. A summary of adenylate kinases from different species. % alignment and node similarity were obtained relative to AK1.

Type of AK	Species	Cellular localisation	Sequence alignment % relative to AK1	Node similarity % relative to AK1
AK1	Human	Cytosol	100	100
AK2	Human	Mitochondria (intermembrane)	30	49
AK3	Human	Mitochondria	30	48
AK4	Human	Mitochondria (matrix)	27	46
AK5	Human	Cytosol/nucleus	58	77
AK6	Human	Nucleus	17	35
AK7	Human	Cytosol	14	32
AK8	Human	Cytosol	7	22
AK9	Human	Cytosol/nucleus	5	16
AKe (*E. coli*)	*E. coli*	Cytosol	31	51
ADK1 (Yeast)	*Saccharomyces cerevisiae*	Cytosol/Mitochondria	28	51

Crystal structures of some human AKs have been published in the literature, however, co-crystal structures with their native AMP and ATP ligands have not been successfully generated. On the other hand, human AK1 has been previously co-crystallised with diadenosine pentaphosphate (A5PA, **Figure 2.10A**),[228] an AK inhibitor that mimics AMP and ATP ligands, which simultaneously occupies the AMP and ATP binding sites. To establish which site in AK1 was AMP-binding and which ATP-binding, human AK1 bound to AP5A inhibitor (PDB 1Z83)[228] was structurally aligned with a co-crystal structure of AKe from *E. coli* (**Figure 2.10A**),[226] which has been successfully co-crystallised with both AMP and ATP ligands (PDB 1ANK)[226].


A
P2
P1


B
Gln101
Gly94
N6
N1
N3
Val67
Gln65
Arg138
Arg44

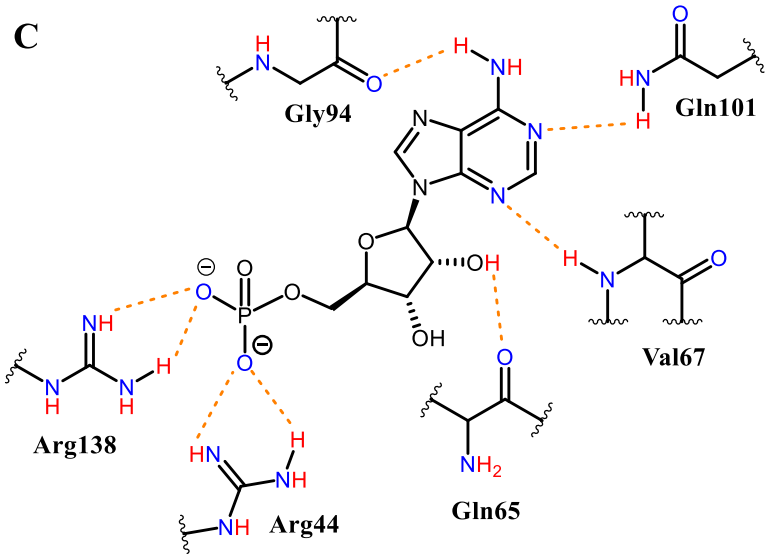


Figure 2.10. Co-crystal structure of adenylate kinase 1. **A.** Overview of AK1 showing the binding modes of AP5A (blue-green) at the AMP binding site (P1) and the ATP binding site (P2). Structures of AK1 and AKe were superposed to show the binding sites and modes of AMP and ATP ligands (white, ligands from AKe co-crystal). **B.** Binding modes of AP5A and docked AMP at P1. Residues important for binding and catalysis (green), and protein-ligand interactions (orange dotted lines) are highlighted. **C.** 2D schematic representation of protein-ligand interactions between AK1 and AMP. H-bond donors (red), H-bond acceptors (blue) and protein-ligand interactions (orange dotted lines) are highlighted.

Structural alignment of human AK1 and *E. coli* AKe revealed that site P1 is an AMP binding site and site P2 is an ATP binding site (**Figure 2.10A**). It further revealed excellent structural overlap between the two proteins, which have a sequence alignment of 31% and node similarity of 51%. Owing to the high degree of structural overlap and the finding that the majority of human AKs have a sequence alignment of ~30% and node similarity of ~50% relative to AK1 (**Table 2.1**), it was reasoned that if AK1 could accommodate an AMP analogue in its active site then these AK isoforms should be able to similarly accommodate the same AMP analogue.

The co-crystal structure of AK1 with A5PA revealed that residues R44, Q65, V67, G94, Q101 and R138 form H-bonding interactions with AMP, which were important for ligand binding (**Figure 2.10B** and **2.10C**). These interactions were therefore considered essential for ligand binding and catalysis, and their loss for a particular AMP analogue during molecular docking was deemed indicative of partially/completely diminished ability of AK1 to utilise that analogue as a substrate.

Results generated from docking of the five AMP analogues (**30-34**) (**Figure 2.3**) predicted that all AMP analogues were well accommodated into the AK1 active site (**Figures 2.11 – 2.15**),

with a largely identical binding mode to native AMP, good structural overlap and conservation of all key protein-ligand interactions. The results thus predicted that all five AMP analogues (**30**-**34**) were likely substrates of AK1 for ADP analogue production *in vitro*.

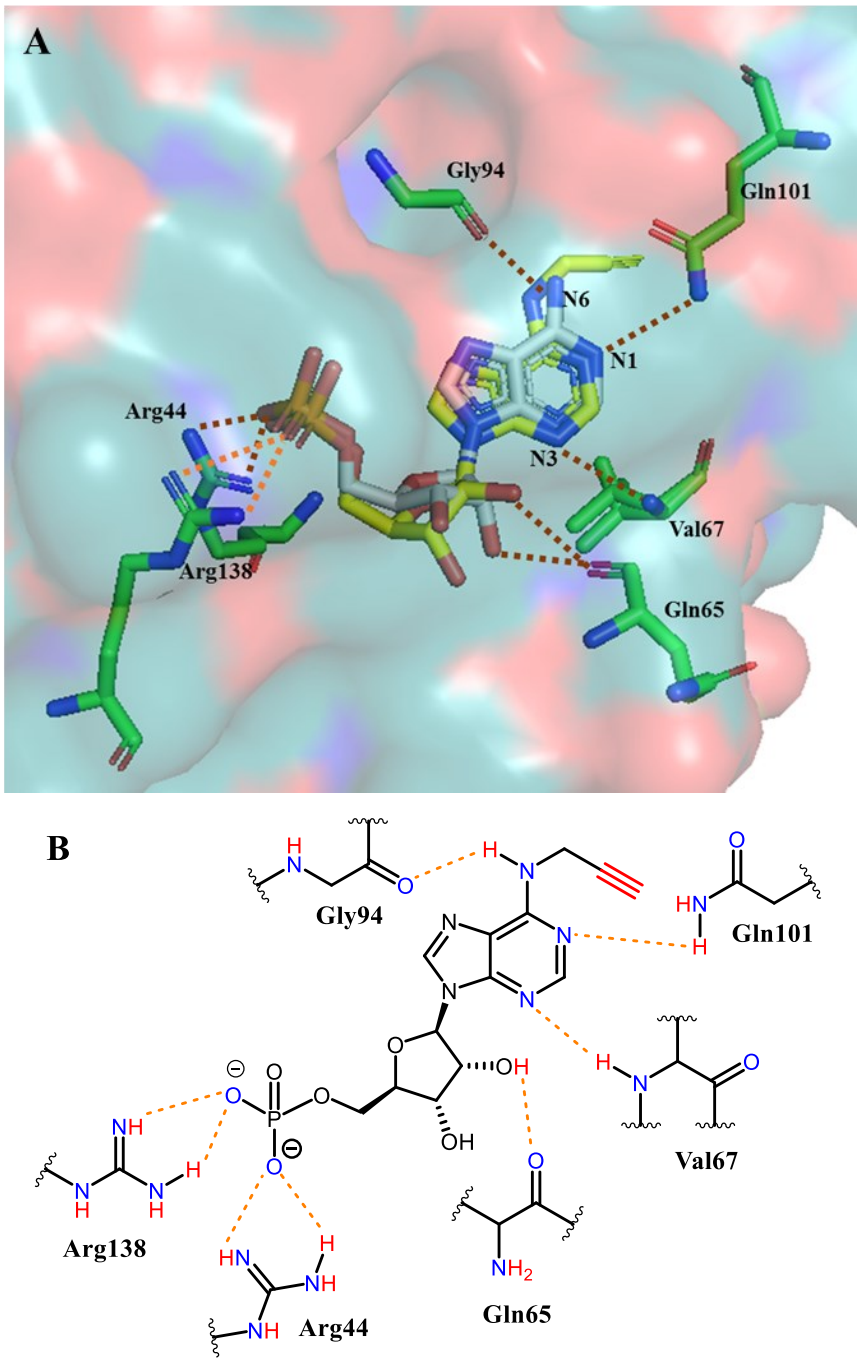


Figure 2.11. Docking of 6Yn-AMP (**30**) with AK1. **A.** The binding modes of AMP (white) and docked 6Yn-AMP (**30**) (yellow) in the AMP binding site are shown. Residues important for binding and catalysis (green), and protein-ligand interactions (orange dotted lines) are highlighted. **B.** 2D schematic representation of protein-ligand interactions between 6Yn-AMP (**30**) and AK1. H-bond donors (red), H-bond acceptors (blue) and protein-ligand interactions (orange dotted lines) are highlighted.

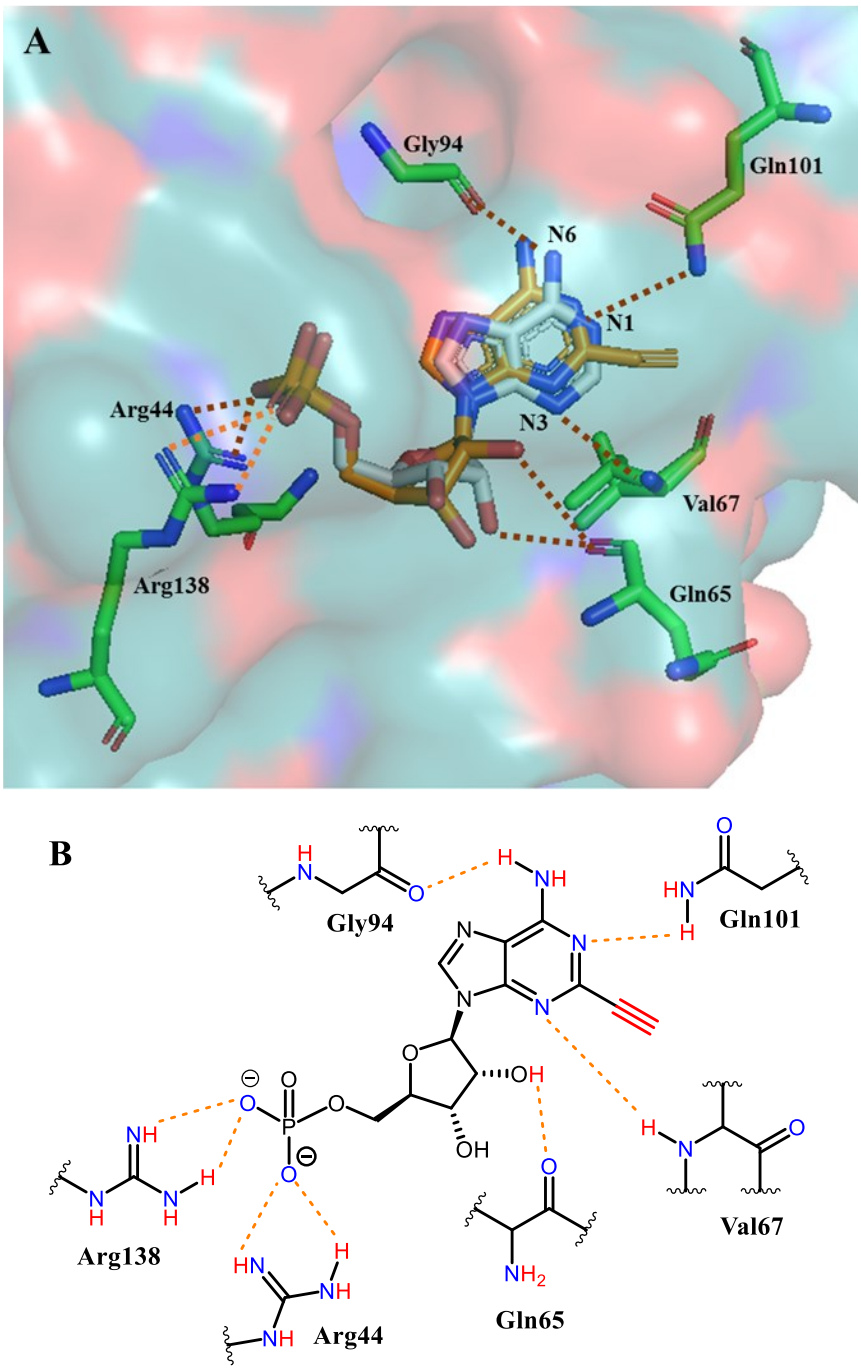


Figure 2.12. Docking of 2Yn-AMP (**31**) with AK1. **A.** The binding modes of adenosine (white) and docked 2Yn-AMP (**31**) (orange) in the AMP binding site are shown. Residues important for binding and catalysis (green), and protein-ligand interactions (orange dotted lines) are highlighted. **B.** 2D schematic representation of protein-ligand interactions between 2Yn-AMP (**31**) and AK1. H-bond donors (red), H-bond acceptors (blue) and protein-ligand interactions (orange dotted lines) are highlighted.

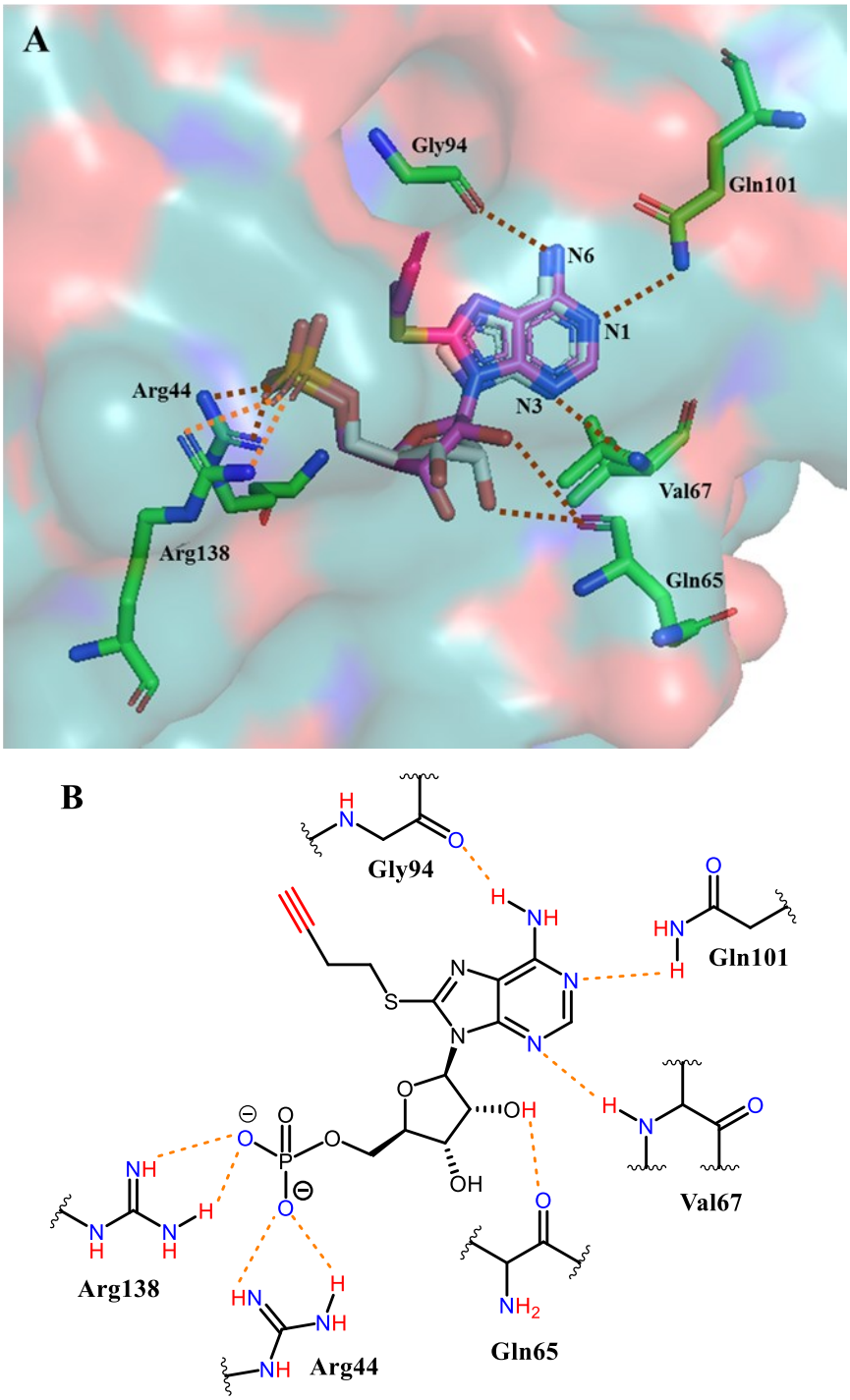


Figure 2.13. Docking of 8But-Yn-AMP (**32**) with AK1. **A.** The binding modes of adenosine (white) and docked 8But-Yn-AMP (**32**) (pink) in the AMP binding site are shown. Residues important for binding and catalysis (green), and protein-ligand interactions (orange dotted lines) are highlighted. **B.** 2D schematic representation of protein-ligand interactions between 8But-Yn-AMP (**32**) and AK1. H-bond donors (red), H-bond acceptors (blue) and protein-ligand interactions (orange dotted lines) are highlighted.

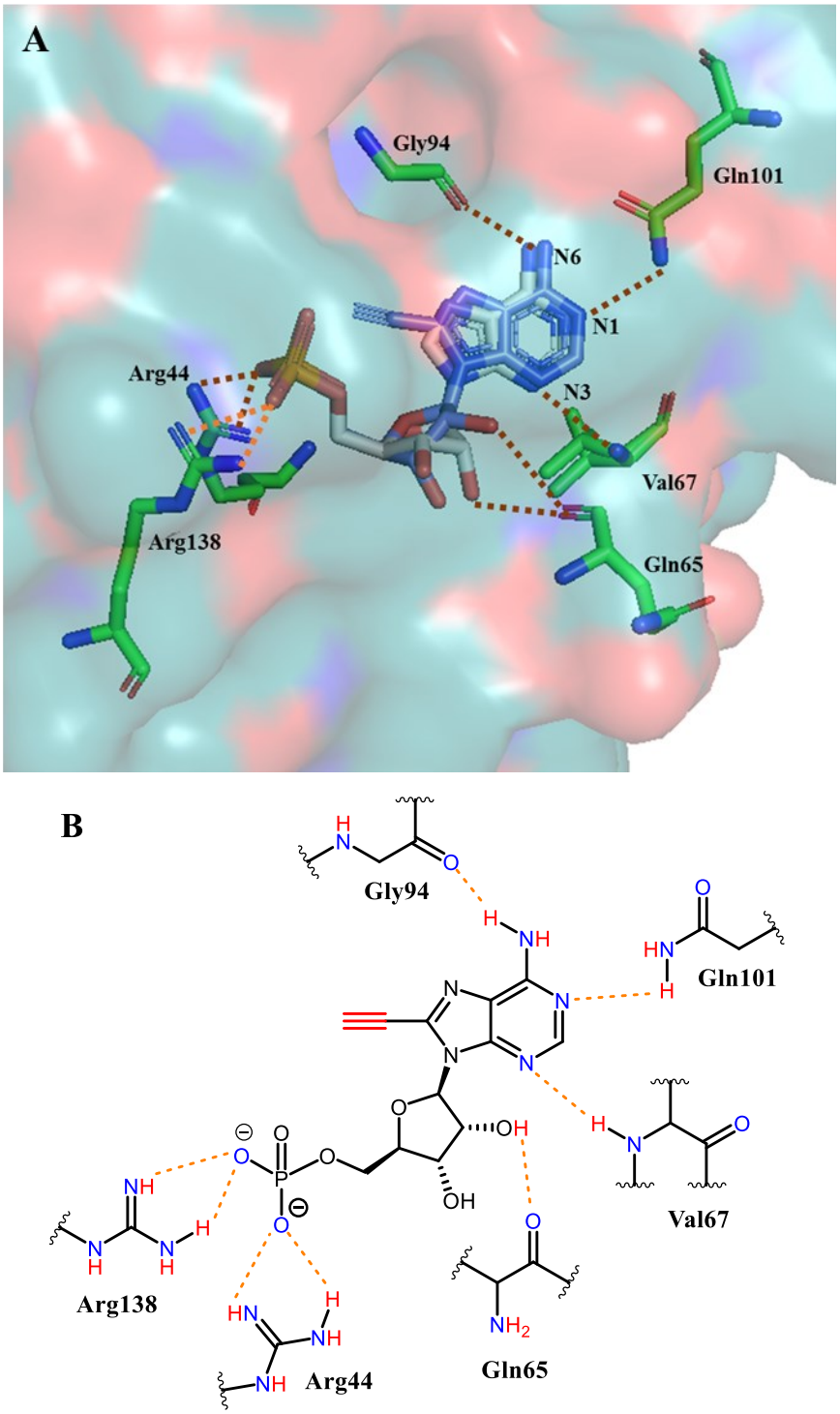


Figure 2.14. Docking of 8Yn-AMP (**34**) with AK1. **A.** The binding modes of adenosine (white) and docked 8Yn-AMP (**34**) (purple) in the AMP binding site are shown. Residues important for binding and catalysis (green), and protein-ligand interactions (orange dotted lines) are highlighted. **B.** 2D schematic representation of protein-ligand interactions between 8Yn-AMP (**34**) and AK1. H-bond donors (red), H-bond acceptors (blue) and protein-ligand interactions (orange dotted lines) are highlighted.

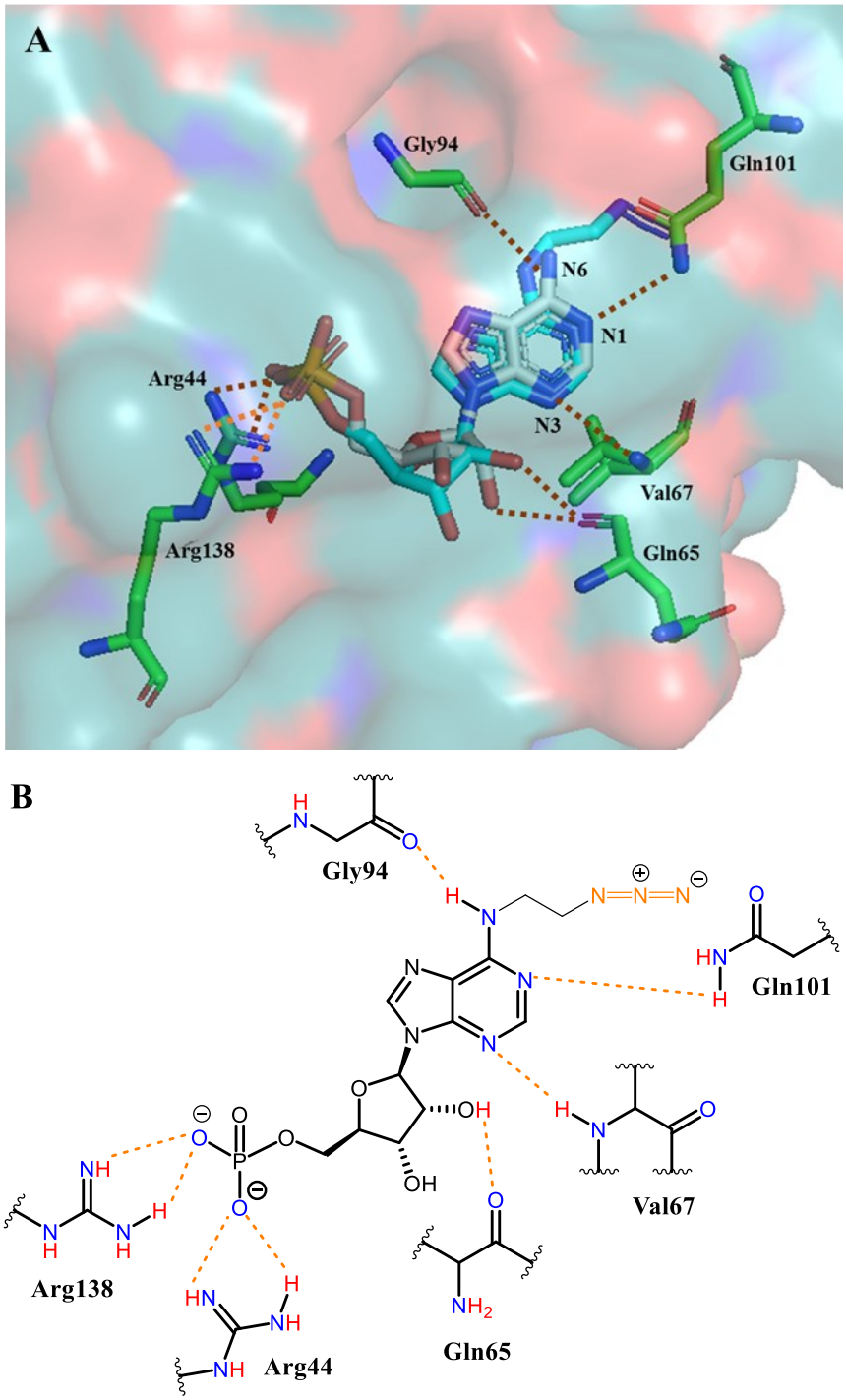


Figure 2.15. Docking of 6Az-AMP (**33**) with AK1. **A.** The binding modes of adenosine (white) and docked 6Az-AMP (**33**) (cyan) in the AMP binding site are shown. Residues important for binding and catalysis (green), and protein-ligand interactions (orange dotted lines) are highlighted. **B.** 2D schematic representation of protein-ligand interactions between 6Az-AMP (**33**) and AK1. H-bond donors (red), H-bond acceptors (blue) and protein-ligand interactions (orange dotted lines) are highlighted.

The AMP binding site P1 is enclosed within the structure of AK1, regardless, sufficient space around the adenine ring allows for accommodation of the clickable groups tested at the N6, C2

and C8 positions, without disrupting key protein-ligand interactions (**Figures 2.11 – 2.13**). This is in contrast to AdK, which only allowed for accommodation of the small alkyne groups in the 6Yn- and 2Yn- analogue series (**Figures 2.5** and **2.6**), and resulted in ligand misalignment for the 8Yn-, 8But-Yn- and 6Az- series (**Figures 2.7 – 2.9**). It was thus hypothesised that AMP analogues were likely to serve as more effective NAD^+ analogue precursors for intracellular NAD^+ analogue production than the corresponding adenosine analogues. This concept was explored by synthesising and validating ProTide prodrugs for direct production of AMP analogues intracellularly (**Chapters Three** and **Four**).

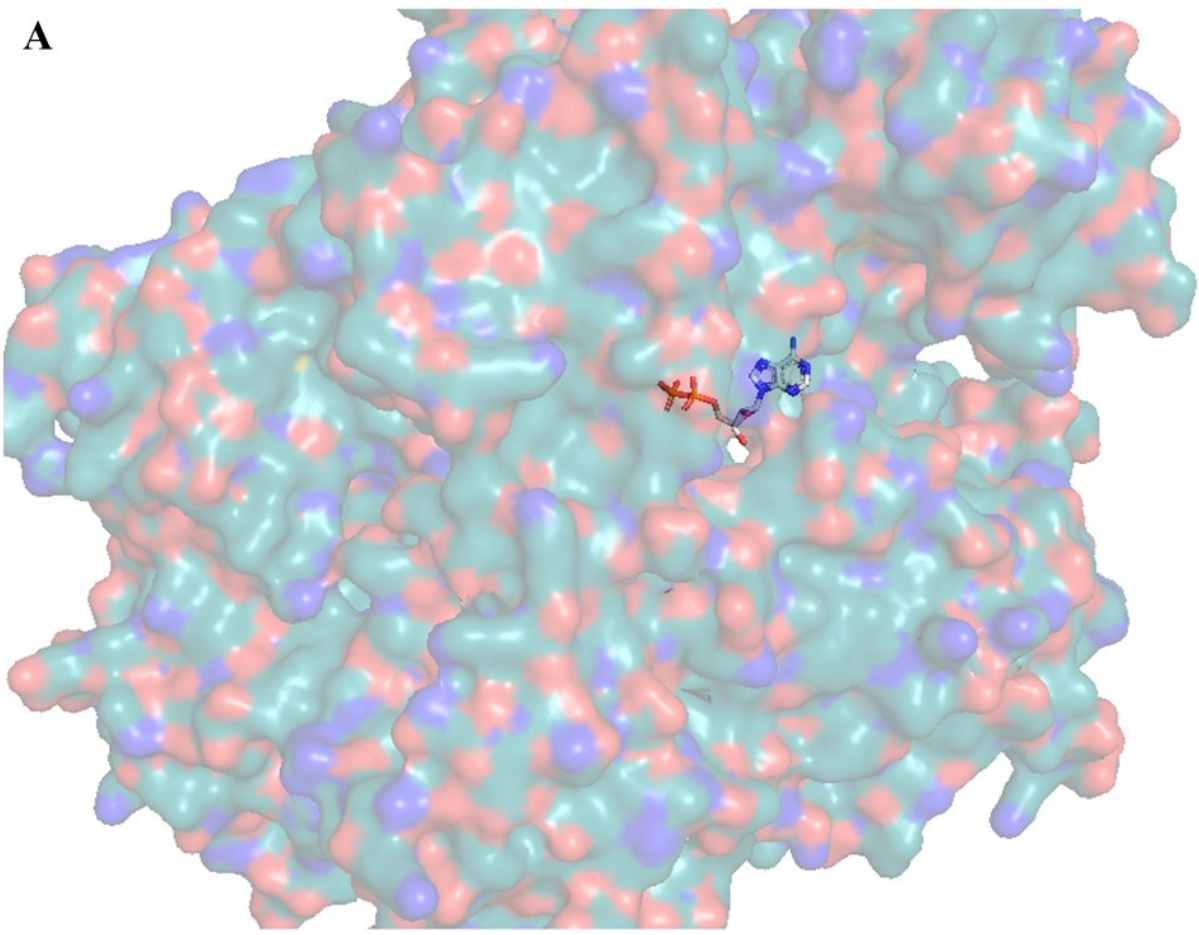
Taking into account the good sequence alignment and structural overlap between AK1 and the majority of AK isoforms (**Table 2.1**), the five AMP analogues were considered likely to be substrates of at least four other human AKs. This was particularly expected to be the case for AKs 2-5, which have a sequence alignment of ~30% and node similarity of ~50% (both relative to AK1), which are comparable to those of AKe (relative to AK1, **Table 2.1**), where excellent structural overlap with AK1 was revealed (**Figure 2.10**). Given the cellular distribution of these AKs, including the mitochondria, cytosol and nucleus, it was expected that intracellular ADP analogue production for the five AMP analogues will be widespread and taking place across most cellular compartments.

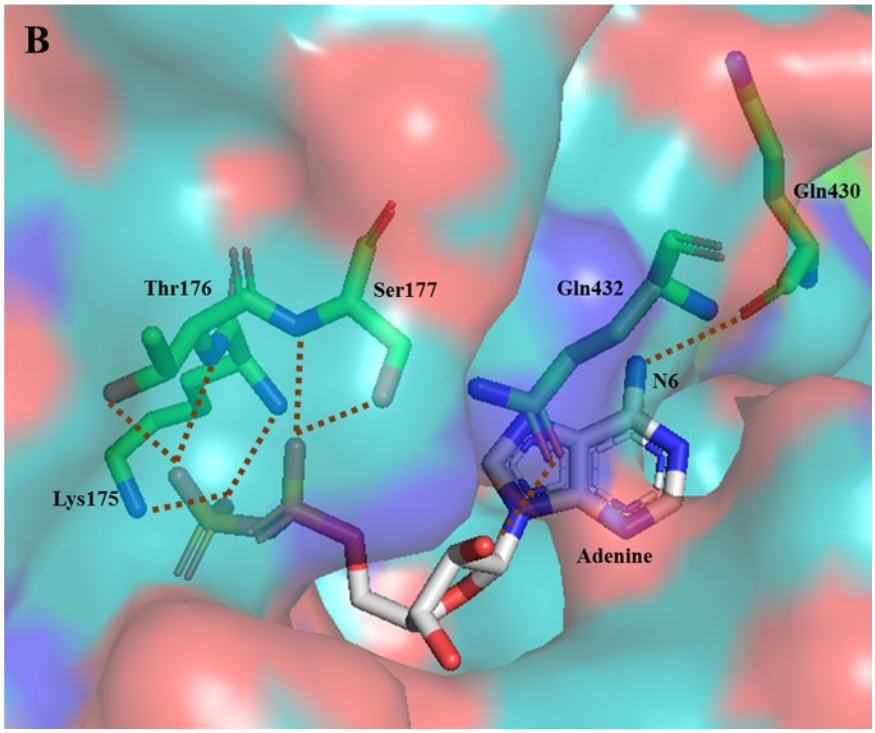
2.2.4 ATP Synthase and ADP Analogues

The third step of the NAD^+ biosynthesis pathway involves the conversion of ADP to ATP by ATP synthase (**Figure 2.2**), a mitochondrial protein responsible for the production of the vast majority of cellular ATP.[193] It was therefore important to establish whether ATP synthase was likely to utilise the proposed ADP analogues as substrates for intracellular conversion into the corresponding ATP analogues. ATP synthase consists of multiple subunits, however, the F1-ATPase alpha subunit is responsible for the catalytic conversion of ADP to ATP.[193] Thus, docking experiments were performed only with F1-ATPase alpha.

The crystal structure of human F1-ATPase has not been published to date, however, co-crystal structures of bovine[229] and yeast[230] F1-ATPase (**Figure 2.16A**) with a bound ADP ligand have been generated and resolved (PDBs 1H8E and 2HLD, respectively). The structures of F1-ATPase between the two species share a sequence alignment of 74%, with excellent structural overlap, showing that F1-ATPase is very highly conserved between different species. It was therefore expected, and assumed, that molecular docking results with bovine F1-ATPase

(**Figure 2.16A**) would mirror those with human F1-ATPase. Molecular docking of the five ADP analogues was therefore performed only with bovine F1-ATPase (PDB 1H8E)[229].





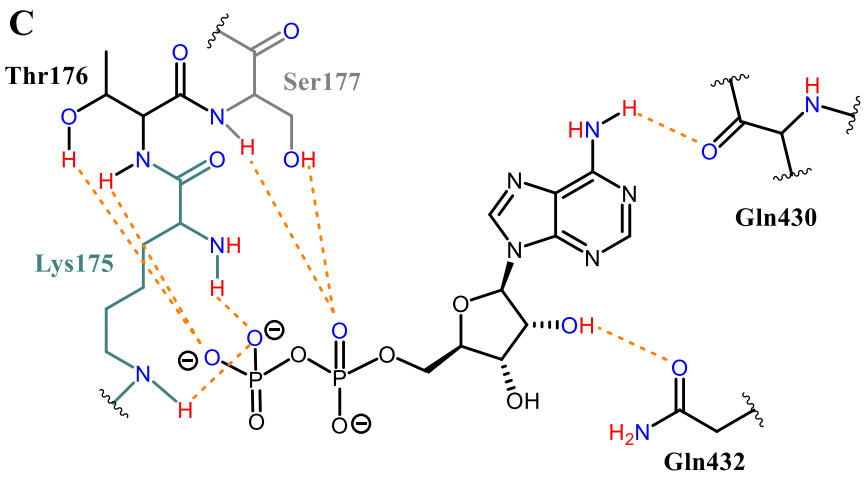


Figure 2.16. Co-crystal structure of bovine F1-ATPase. **A.** Overview of F1-ATPase with ADP at the ADP binding site. **B.** Binding mode of ADP is shown. Residues important for binding and catalysis (green), and protein-ligand interactions (orange dotted lines) are highlighted. **C.** 2D schematic representation of protein-ligand interactions between F1-ATPase and ADP. H-bond donors (red), H-bond acceptors (blue) and protein-ligand interactions (orange dotted lines) are highlighted.

The co-crystal structure of bovine F1-ATPase revealed that residues K175, T176 and S177 each formed two H-bonding interactions with the phosphate chain of ADP and were important for phosphate binding, and residues Q430 and Q432 were important for nucleotide binding through single H-bonding interactions with ADP (**Figure 2.16B** and **2.16C**). These interactions were therefore considered essential for ligand binding and catalysis, and their loss for a particular ADP analogue during molecular docking was deemed indicative of partially/completely diminished ability of F1-ATPase to utilise that analogue as a substrate.

Results generated from molecular docking predicted that four of the five ADP analogues, 6Yn- (**35**), 2Yn- (**36**), 8But-Yn- (**37**) and 6Az- (**38**), were well accommodated into the F1-ATPase active site, with a largely identical binding mode to native ADP, good structural overlap and conservation of all key protein-ligand interactions (**Figures 2.17 – 2.20**). The results thus predicted that these four ADP analogues were likely substrates of ATP synthase for ATP analogue production *in vitro*.

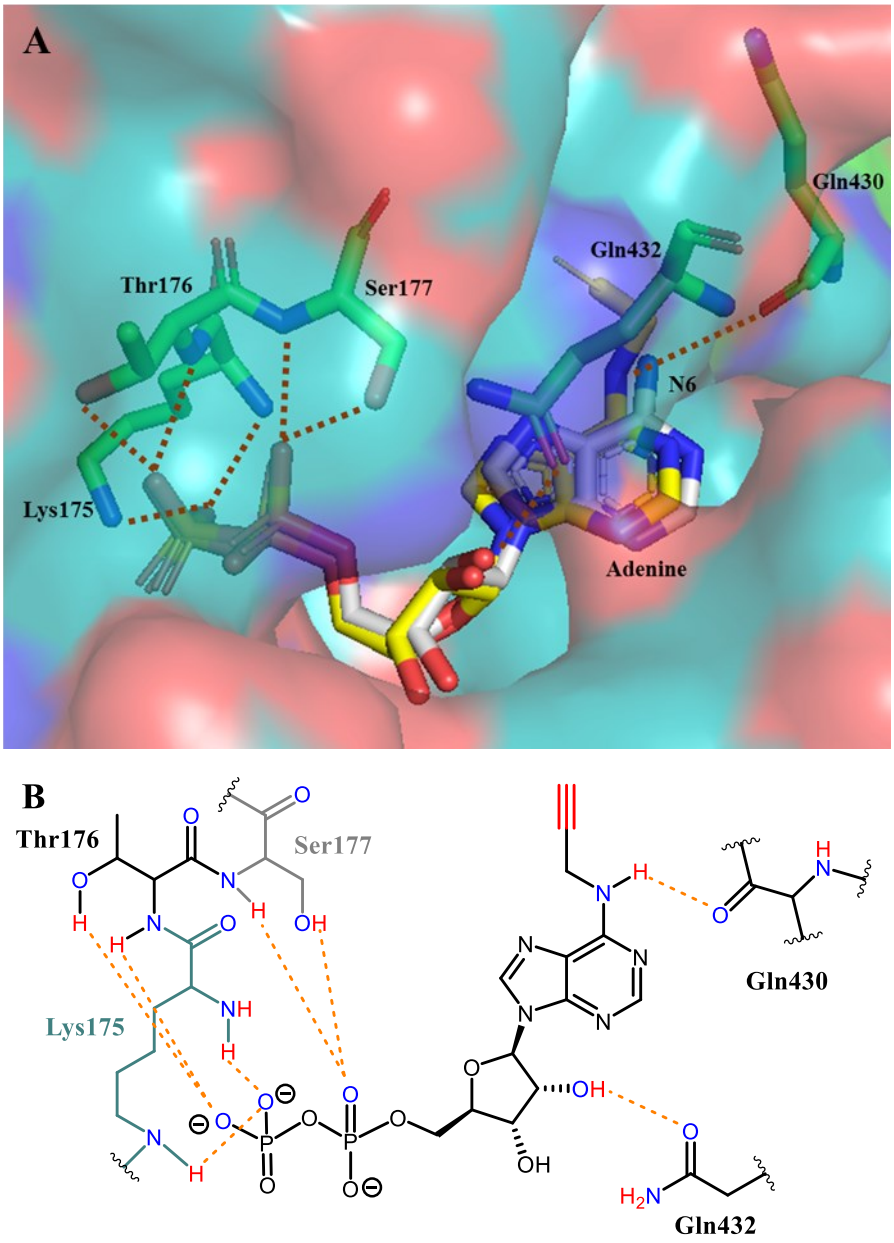


Figure 2.17. Docking of 6Yn-ADP (**35**) with F1-ATPase. **A.** The binding modes of ADP (white) and docked 6Yn-ADP (**35**) (yellow) in the ADP binding site are shown. Residues important for binding and catalysis (green), and protein-ligand interactions (orange dotted lines) are highlighted. **B.** 2D schematic representation of protein-ligand interactions between 6Yn-ADP (**35**) and F1-ATPase. H-bond donors (red), H-bond acceptors (blue) and protein-ligand interactions (orange dotted lines) are highlighted.

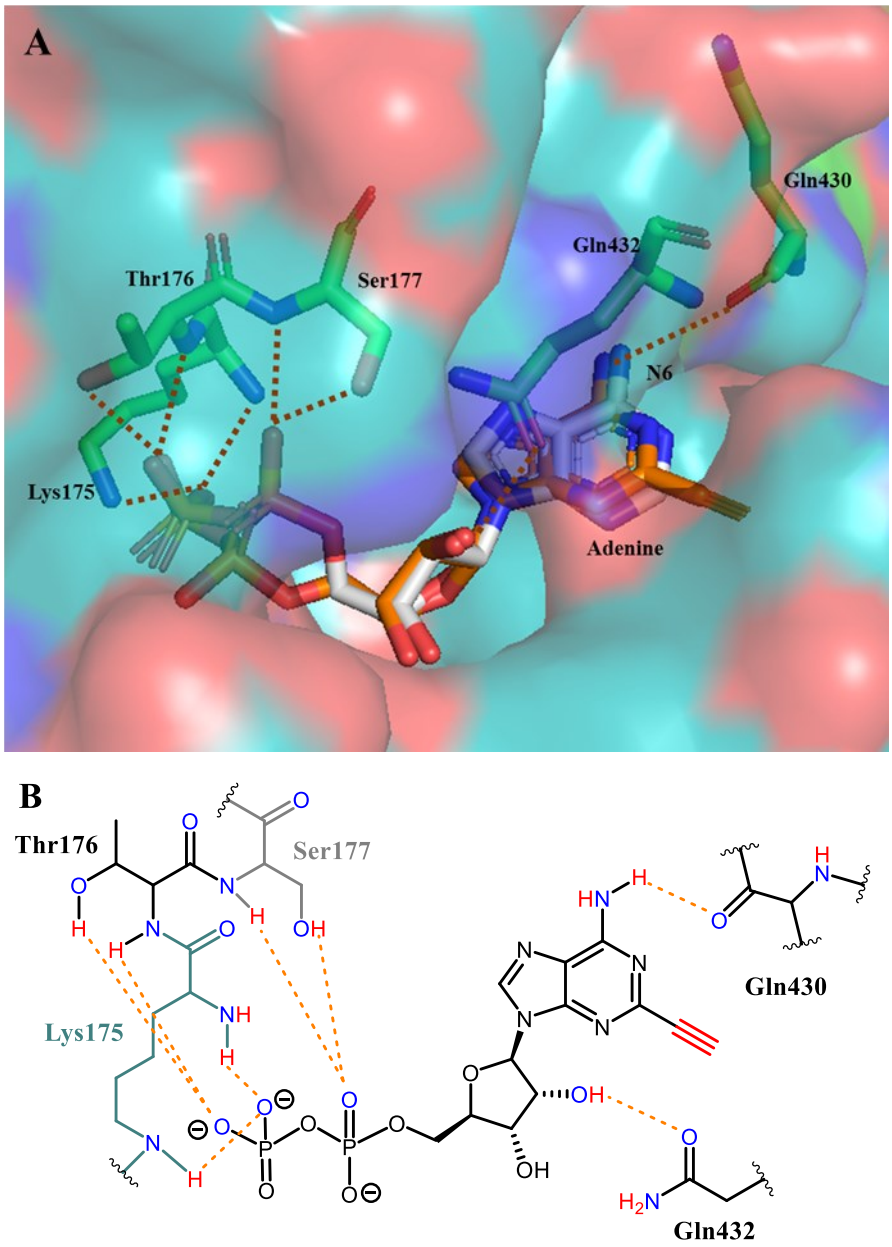


Figure 2.18. Docking of 2Yn-ADP (**36**) with F1-ATPase. **A.** The binding modes of ADP (white) and docked 2Yn-ADP (**36**) (orange) in the ADP binding site are shown. Residues important for binding and catalysis (green), and protein-ligand interactions (orange dotted lines) are highlighted. **B.** 2D schematic representation of protein-ligand interactions between 2Yn-ADP (**36**) and F1-ATPase. H-bond donors (red), H-bond acceptors (blue) and protein-ligand interactions (orange dotted lines) are highlighted.

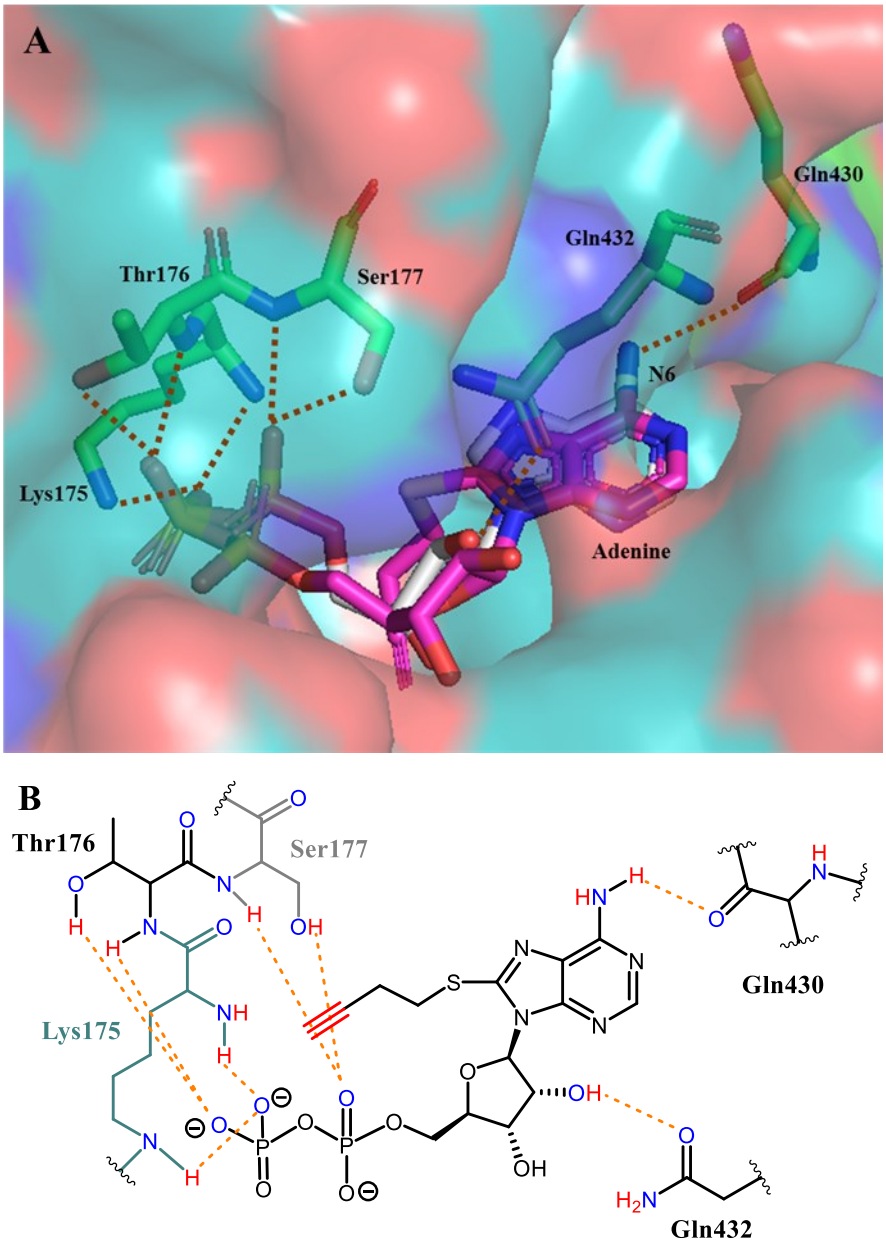


Figure 2.19. Docking of 8But-Yn-ADP (**37**) with F1-ATPase. **A.** The binding modes of ADP (white) and docked 8But-Yn-ADP (**37**) (pink) in the ADP binding site are shown. Residues important for binding and catalysis (green), and protein-ligand interactions (orange dotted lines) are highlighted. **B.** 2D schematic representation of protein-ligand interactions between 8But-Yn-ADP (**37**) and F1-ATPase. H-bond donors (red), H-bond acceptors (blue) and protein-ligand interactions (orange dotted lines) are highlighted.

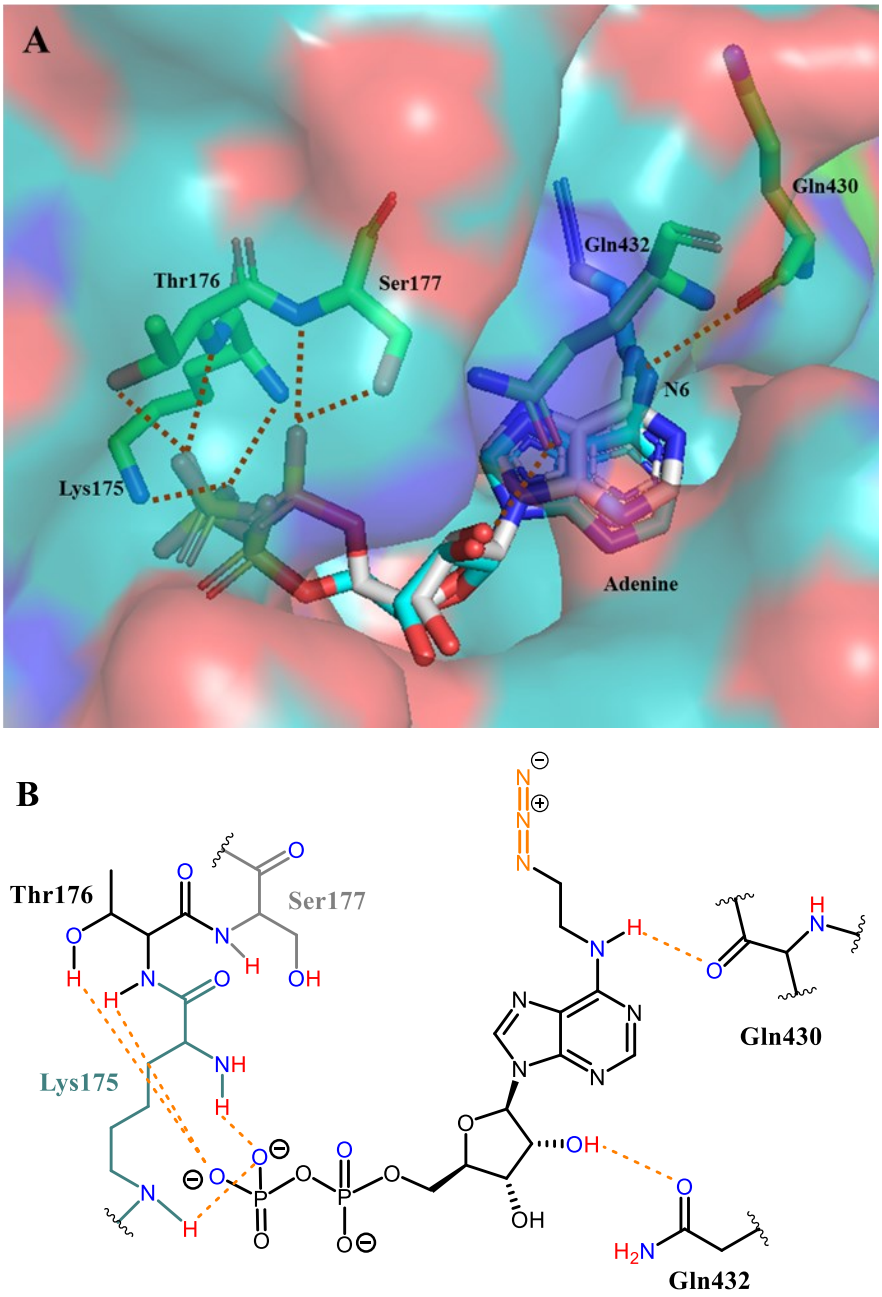


Figure 2.20. Docking of 6Az-ADP (**38**) with F1-ATPase. **A.** The binding modes of ADP (white) and docked 6Az-ADP (**38**) (cyan) in the ADP binding site are shown. Residues important for binding and catalysis (green), and protein-ligand interactions (orange dotted lines) are highlighted. **B.** 2D schematic representation of protein-ligand interactions between 6Az-ADP (**38**) and F1-ATPase. H-bond donors (red), H-bond acceptors (blue) and protein-ligand interactions (orange dotted lines) are highlighted.

On the other hand, the results predicted that analogue 8Yn-ADP (**39**) was less well accommodated into the F1-ATPase active site (**Figure 2.21A**). Incorporation of a clickable group at the C8 position resulted in displacement of the phosphate chain relative to native ADP, resulting in loss of the two H-bond stabilising interactions of the 5' phosphate group with residue S177 (**Figure 2.21B**). The displacement of the phosphate chain further resulted in

displacement of the ribose ring, leading to loss of the interaction between the ribose ring and residue Q432, and a slight displacement of the adenine moiety. This would likely weaken the H-bonding interaction with residue Q320 (**Figure 2.21B)**.

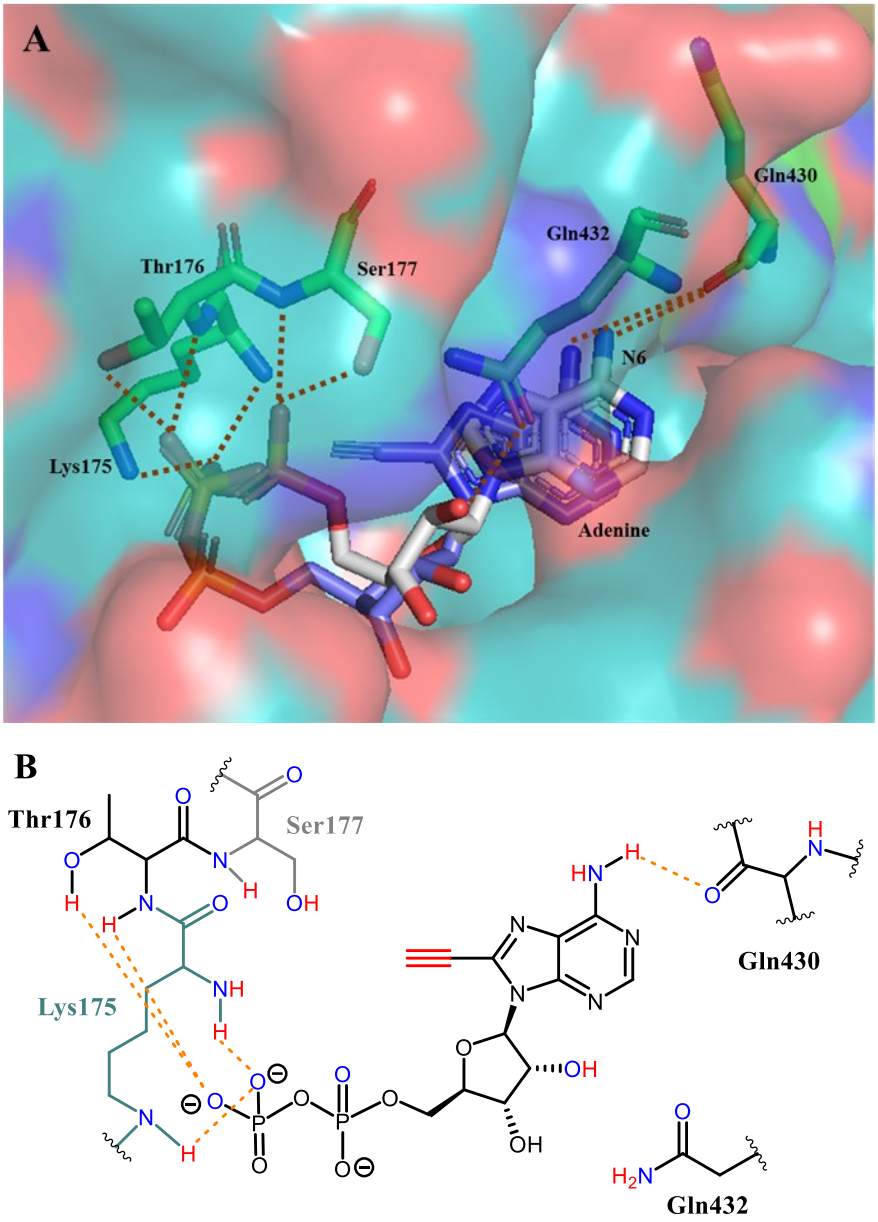


Figure 2.21. Docking of 8Yn-ADP (**39**) with F1-ATPase. **A.** The binding modes of ADP (white) and docked 8Yn-ADP (**39**) (purple) in the ADP binding site are shown. Residues important for binding and catalysis (green), and protein-ligand interactions (orange dotted lines) are highlighted. **B.** 2D schematic representation of protein-ligand interactions between 8Yn-ADP (**39**) and F1-ATPase. H-bond donors (red), H-bond acceptors (blue) and protein-ligand interactions (orange dotted lines) are highlighted.

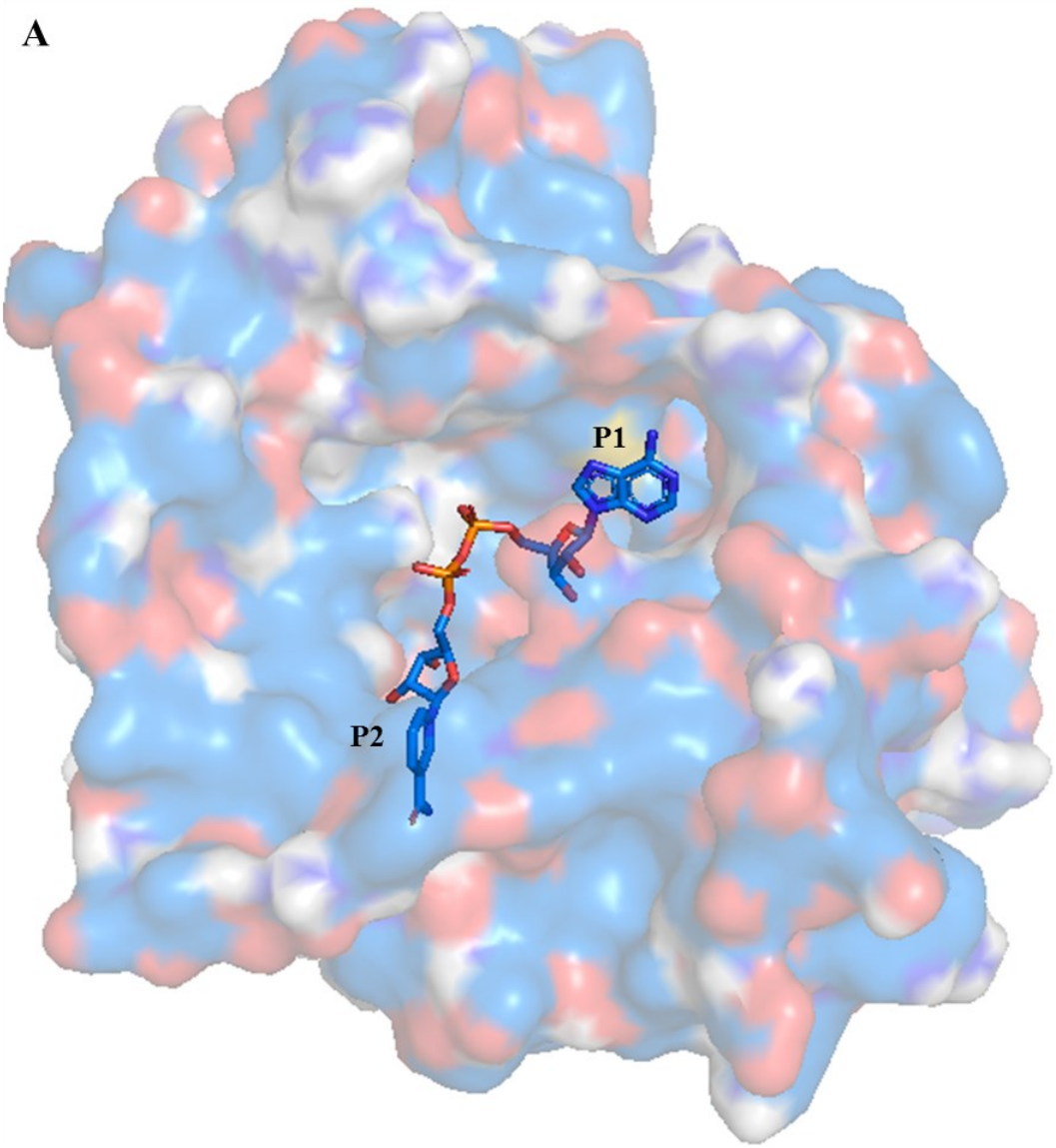
Owing to the moderate change in binding mode relative to native ADP, poor structural overlap between phosphate chains and loss of three of the seven key protein-ligand interactions as well

as weakening of a fourth one, the results predicted that 8Yn-ADP (**39**) was either unlikely to be a substrate of F1-ATPase *in vitro*, or may be a substrate with significantly reduced affinity for F1-ATPase.

2.2.5 NMNAT1 and ATP Analogues

NMNAT proteins are involved in the final step of the NAD^+ biosynthesis pathway (**Figure 2.2**), where they are responsible for conversion of ATP into NAD^+ *via* coupling to β-NMN.[194] There are three NMNAT isoforms in humans with distinct cellular distribution: NMNAT1 is found in the nucleus, NMNAT2 is localised in the cytoplasm and NMNAT3 is a mitochondrial protein.[194] Considering that PARP1 is responsible for consumption of ~90% of all cellular NAD^+,[20] and that it is localised in the nucleus, the vast majority of ADP-ribosylation would therefore occur in the nucleus. As a result, it was imperative to establish whether the nuclear NMNAT1 could generate NAD^+ analogues from the corresponding ATP analogues.

A co-crystal structure of human NMNAT1 with an ATP ligand has not been published, however, a co-crystal structure of human NMNAT1 with NAD^+ as the ligand is available (PDB 1KQN)[231], which reveals the binding modes and binding sites of ATP (P1 site) and β-NMN (P2 site) within the active site (**Figure 2.22A**).


A
P1
P2

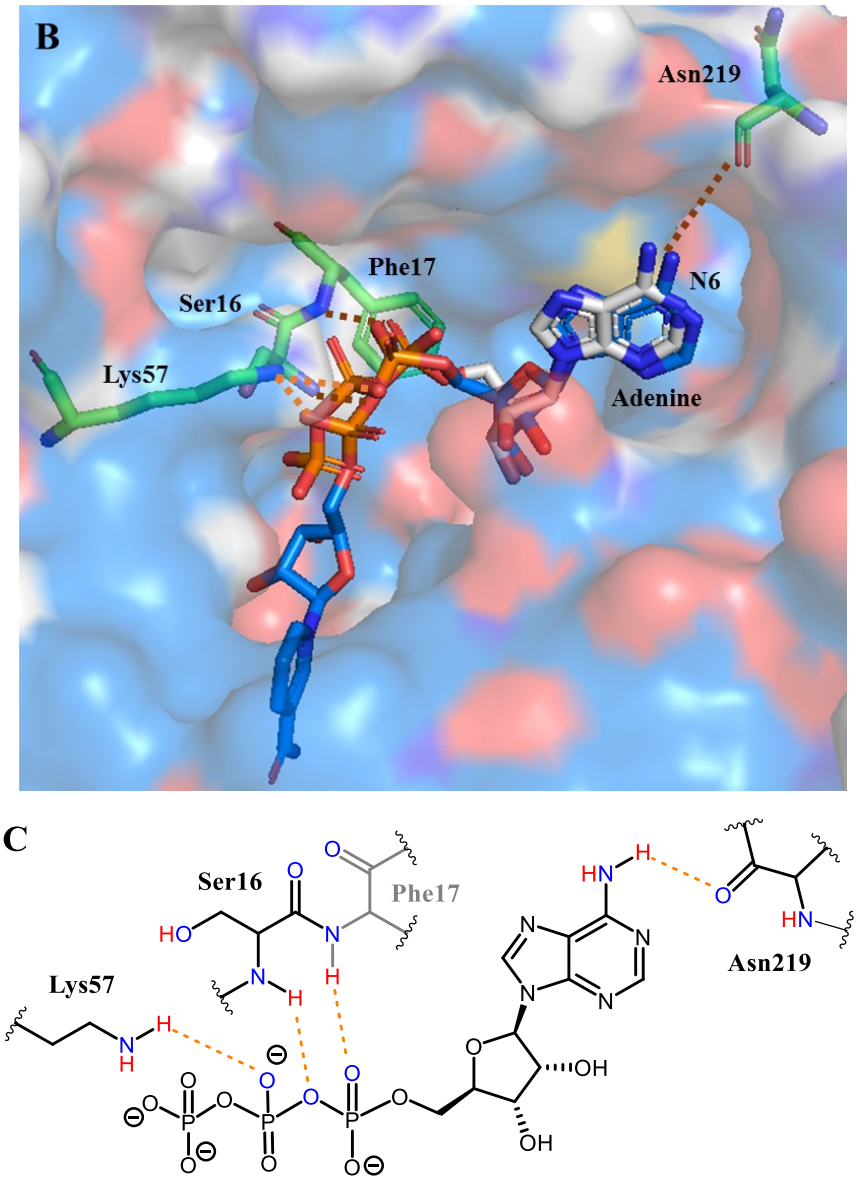


Figure 2.22. Co-crystal structure of NMNAT1. **A.** Overview of NMNAT1 showing NAD^+ binding mode at the ATP binding site (P1) and β-NMN binding site (P2). **B.** Binding modes of NAD^+ (blue) and docked ATP (white) at the ATP binding site. Residues important for binding and catalysis (green), and protein-ligand interactions (orange dotted lines) are highlighted. **C.** 2D schematic representation of protein-ligand interactions between NMNAT1 and ATP. H-bond donors (red), H-bond acceptors (blue) and protein-ligand interactions (orange dotted lines) are highlighted.

The co-crystal structure of NMNAT1 with NAD^+ revealed that residues S16, F17 and K57 each formed a single H-bonding interaction with the ATP phosphate chain, and residue N219 formed a single interaction with the adenine moiety (**Figure 2.22B** and **2.22C**). These interactions were therefore considered essential for ligand binding and catalysis, and their loss

for a particular ATP analogue during molecular docking was deemed indicative of partially/completely diminished ability of NMNAT1 to utilise that analogue as a substrate.

Results generated from docking predicted that three of the five ATP analogues, 6Yn- (**40**), 8But-Yn- (**42**) and 8Yn- (**44**), were well accommodated into the ATP binding site, with a largely identical binding mode to native ATP, good structural overlap and conservation of all key protein-ligand interactions (**Figures 2.23 – 2.25**). The results thus predicted that these three ATP analogues were likely substrates of NMNAT1 for nuclear NAD^+ analogue production *in vitro*.

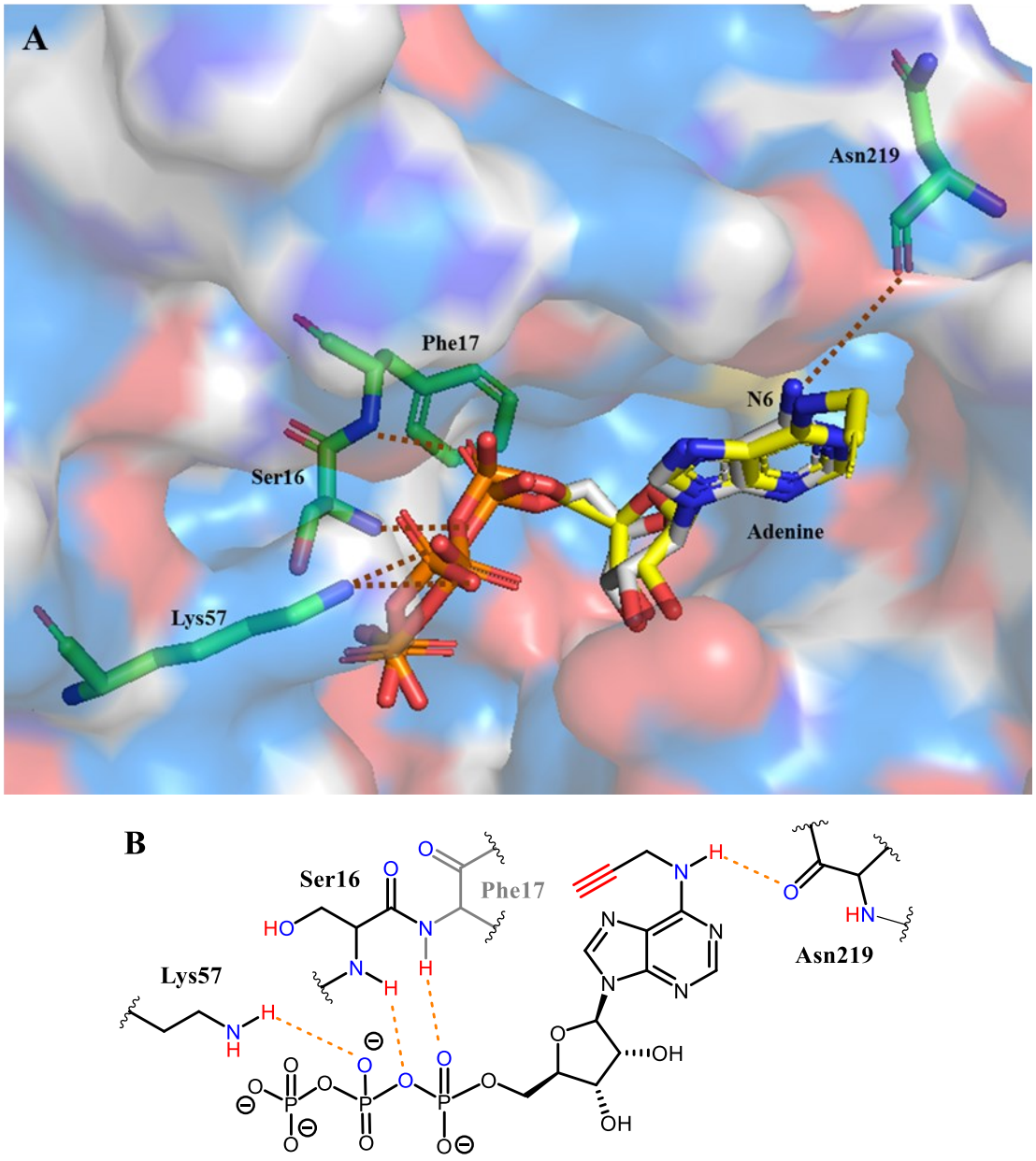


Figure 2.23. Docking of 6Yn-ATP (**40**) with NMNAT1. **A.** The binding modes of ATP (white) and docked 6Yn-ATP (**40**) (yellow) in the ATP binding site are shown. Residues important for binding and catalysis (green),

and protein-ligand interactions (orange dotted lines) are highlighted. **B.** 2D schematic representation of protein-ligand interactions between 6Yn-ATP (**40**) and NMNAT1. H-bond donors (red), H-bond acceptors (blue) and protein-ligand interactions (orange dotted lines) are highlighted.

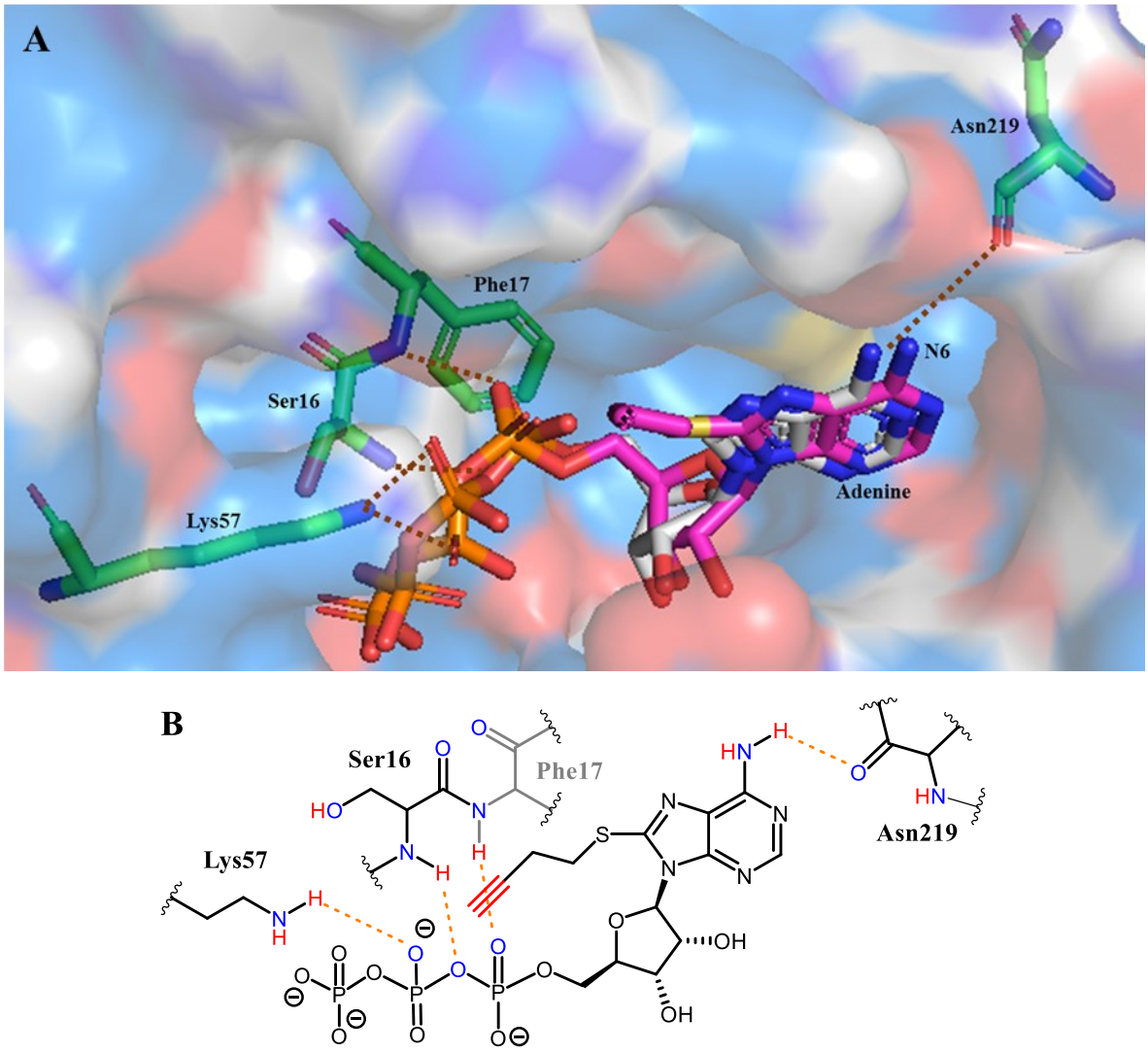


Figure 2.24. Docking of 8But-Yn-ATP (**42**) with NMNAT1. **A.** The binding modes of ATP (white) and docked 8But-Yn-ATP (**42**) (pink) in the ATP binding site are shown. Residues important for binding and catalysis (green), and protein-ligand interactions (orange dotted lines) are highlighted. **B.** 2D schematic representation of protein-ligand interactions between 8But-Yn-ATP (**42**) and NMNAT1. H-bond donors (red), H-bond acceptors (blue) and protein-ligand interactions (orange dotted lines) are highlighted.

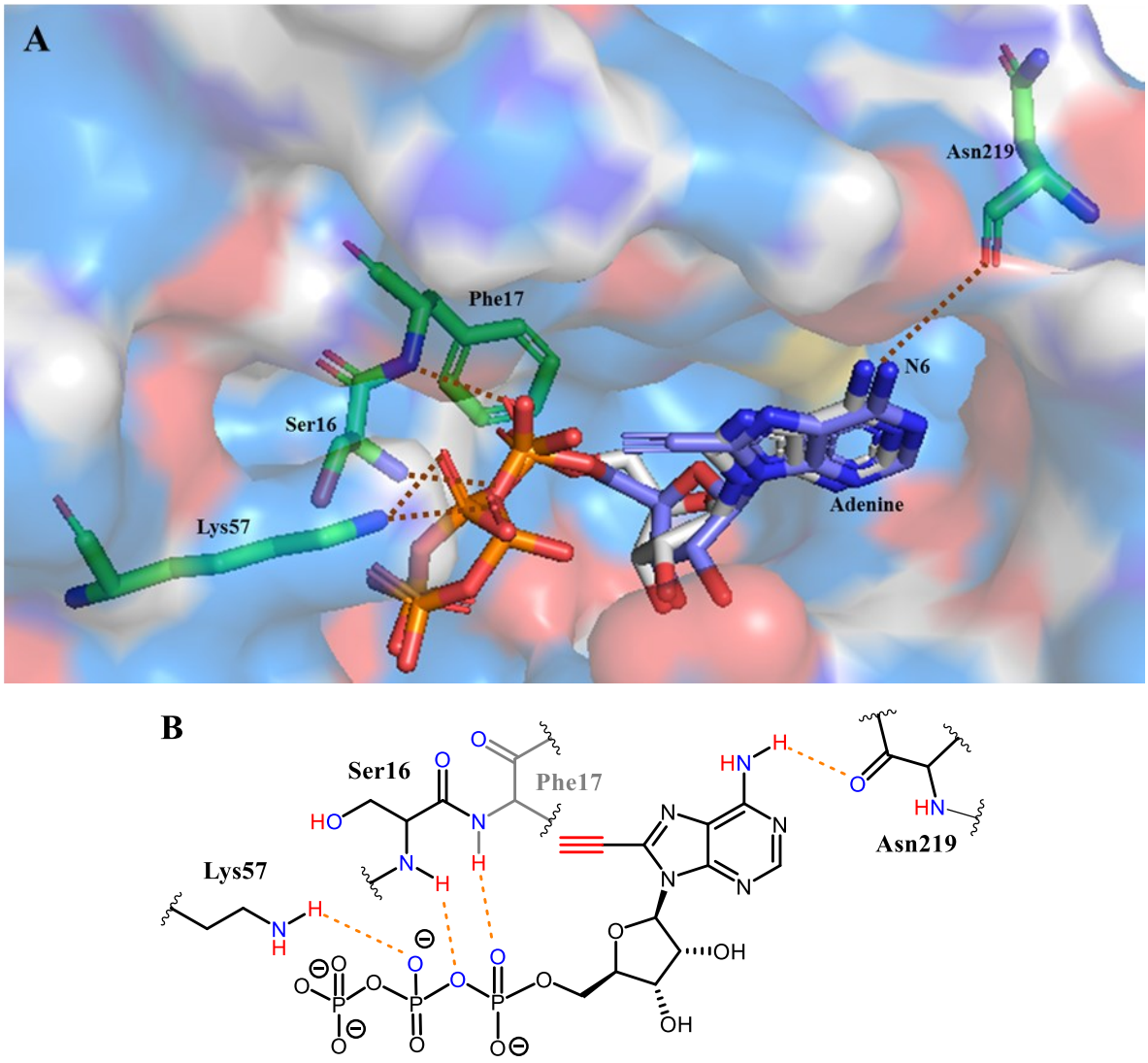


Figure 2.25. Docking of 8Yn-ATP (**44**) with NMNAT1. **A.** The binding modes of ATP (white) and docked 8Yn-ATP (**44**) (purple) in the ATP binding site are shown. Residues important for binding and catalysis (green), and protein-ligand interactions (orange dotted lines) are highlighted. **B.** 2D schematic representation of protein-ligand interactions between 8Yn-ATP (**44**) and NMNAT1. H-bond donors (red), H-bond acceptors (blue) and protein-ligand interactions (orange dotted lines) are highlighted.

In contrast, the results predicted that the analogue 2Yn-ATP (**41**) was poorly accommodated into the ATP binding site of NMNAT1 (**Figure 2.26A**). Although seemingly 2Yn-ATP was well accommodated and all four protein-ligand interactions were conserved (**Figure 2.26B**), the clickable group at the C2 position underwent significant structural distortion from its expected linear structure (180º angle, **Figure 2.26A**). Such structural distortion would not occur *in vitro*, implying that 2Yn-ATP (**41**) was unlikely to be a substrate of WT NMNAT1. On the other hand, mutational analysis revealed that a V186G mutation, adjacent to the C2 position of the alkyne group, allowed for its accommodation into the NMNAT1 ATP binding

site without any structural distortion while conserving protein-ligand interactions (**Figure 2.27A** and **2.27B**). The results thus implied that V186G NMNAT1 mutant, but not WT NMNAT1, was likely to utilise 2Yn-ATP (**41**) as a substrate.

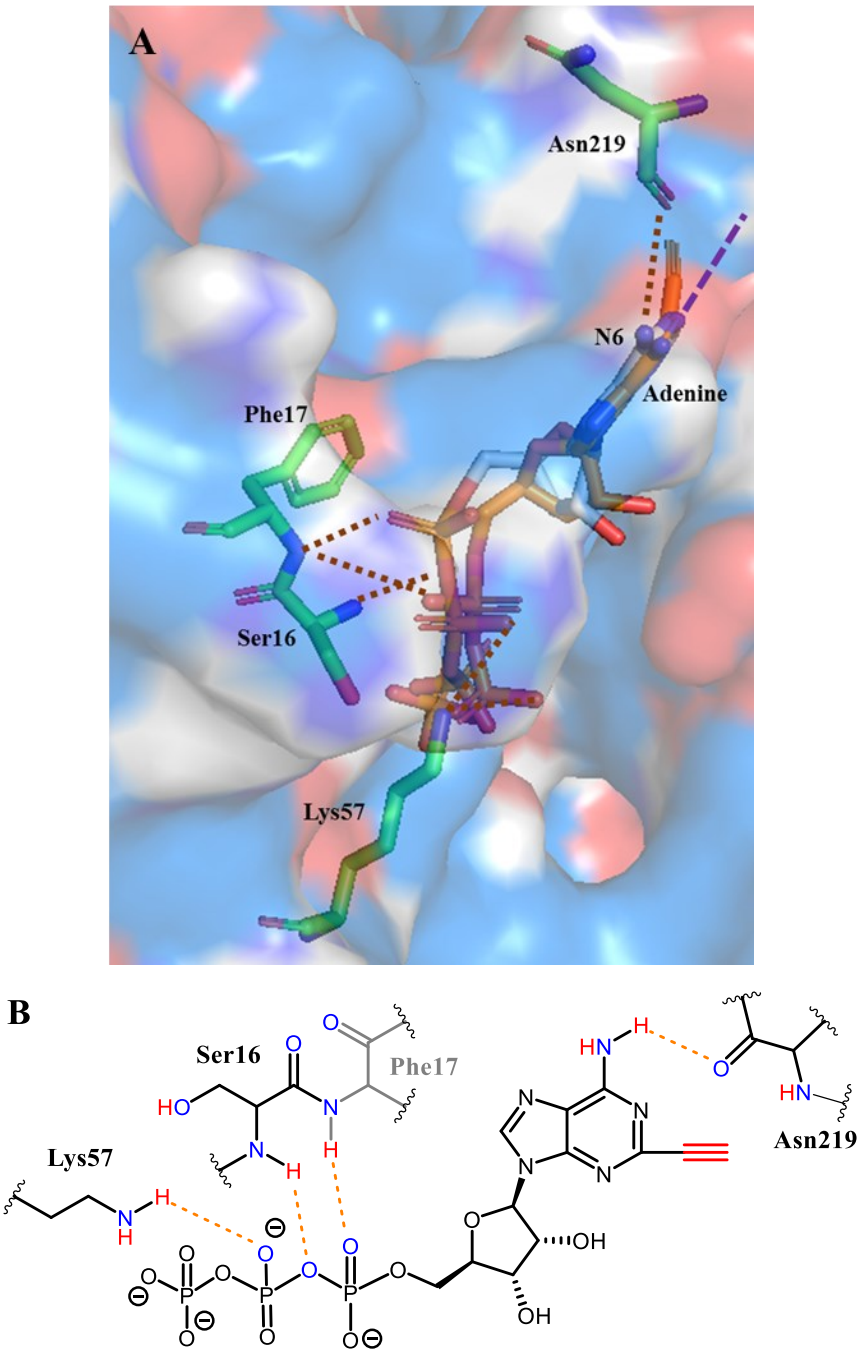


Figure 2.26. Docking of 2Yn-ATP (**41**) with NMNAT1. **A.** The binding modes of ATP (white) and docked 2Yn-ATP (**41**) (orange) in the ATP binding site are shown. Residues important for binding and catalysis (green), and protein-ligand interactions (orange dotted lines) are highlighted. Purple dotted line represents directionality of the alkyne group in the absence of structural distortion. **B.** 2D schematic representation of protein-ligand interactions between 2Yn-ATP (**41**) and NMNAT1. H-bond donors (red), H-bond acceptors (blue) and protein-ligand interactions (orange dotted lines) are highlighted.

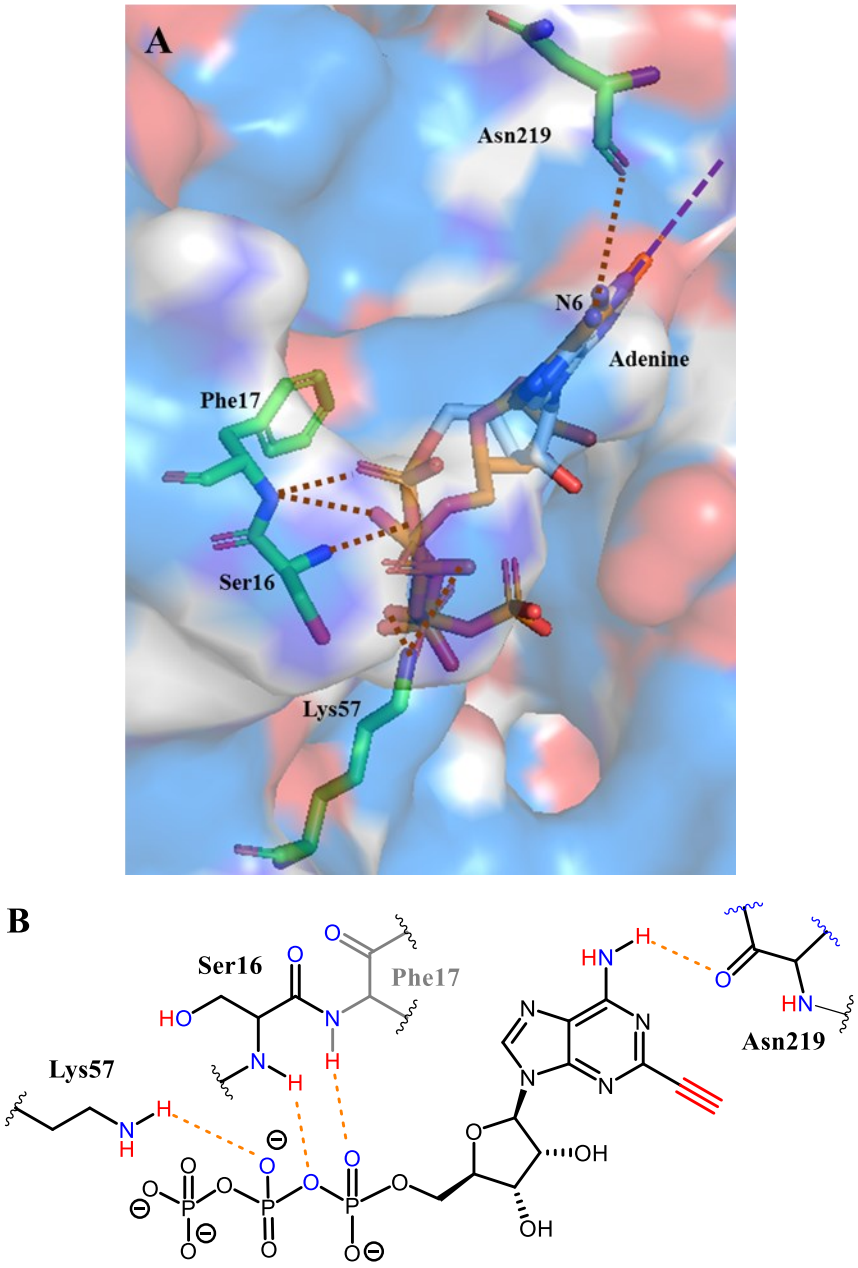


Figure 2.27. Docking of 2Yn-ATP (**41**) with V186G NMNAT1. **A.** The binding modes of ATP (white) and docked 2Yn-ATP (**41**) (orange) in the ATP binding site are shown. Residues important for binding and catalysis (green), and protein-ligand interactions (orange dotted lines) are highlighted. Purple dotted line represents directionality of the alkyne group in the absence of structural distortion. **B.** 2D schematic representation of protein-ligand interactions between 2Yn-ATP (**41**) and V186G NMNAT1. H-bond donors (red), H-bond acceptors (blue) and protein-ligand interactions (orange dotted lines) are highlighted.

For 6Az-ATP (**43**), incorporation of the azide group at the N6 position resulted in inversion of the adenine moiety (**Figure 2.28A**), leading to its displacement and loss of the H-bonding interaction with residue N219 (**Figure 2.28B**). The resulting significantly reduced affinity for binding as well as the general inability of the analogue to be accommodated at the ATP binding

site implied that the 6Az-ATP analogue (**43**) was unlikely to be a substrate of NMNAT1 *in vitro*.

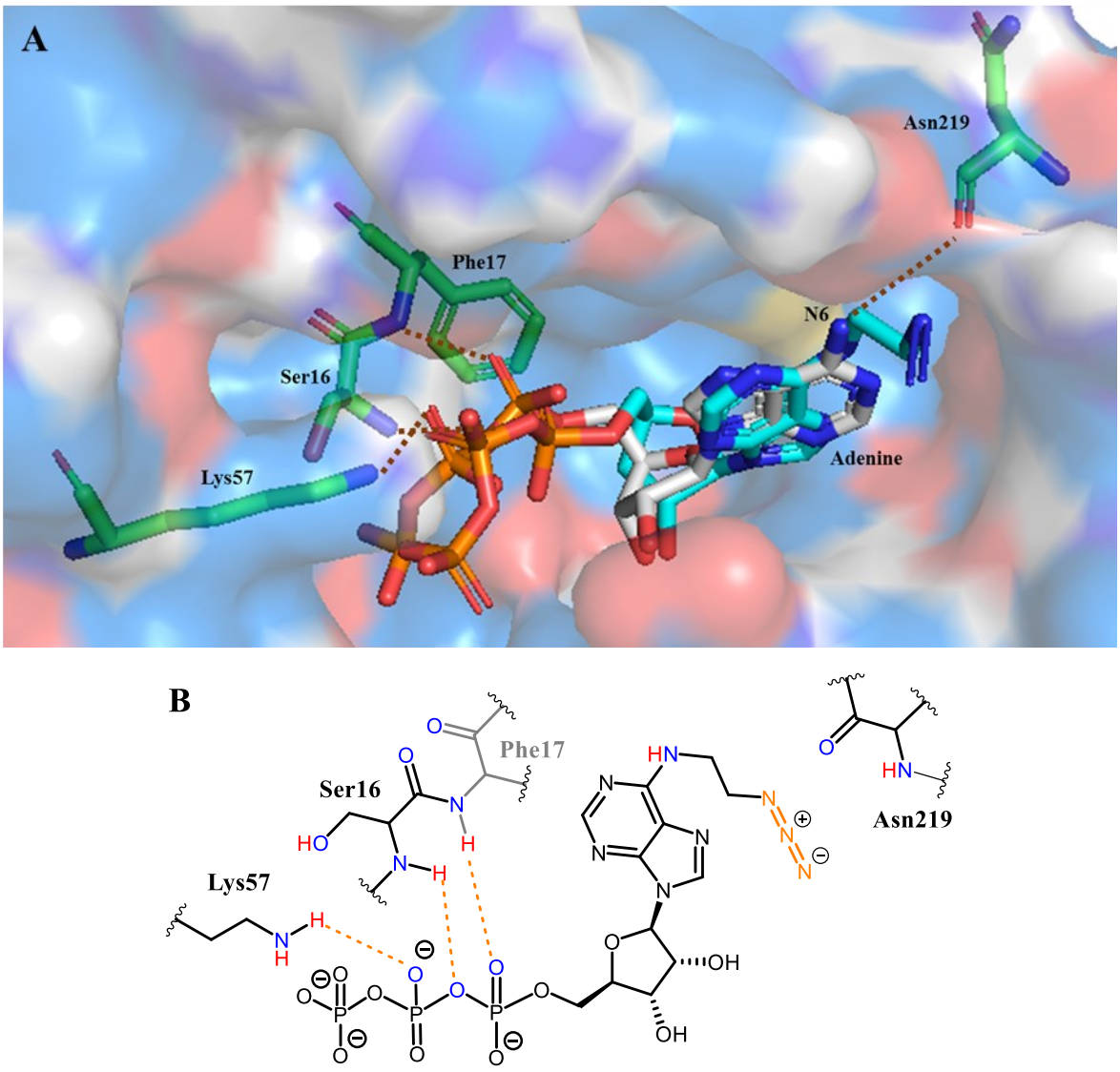


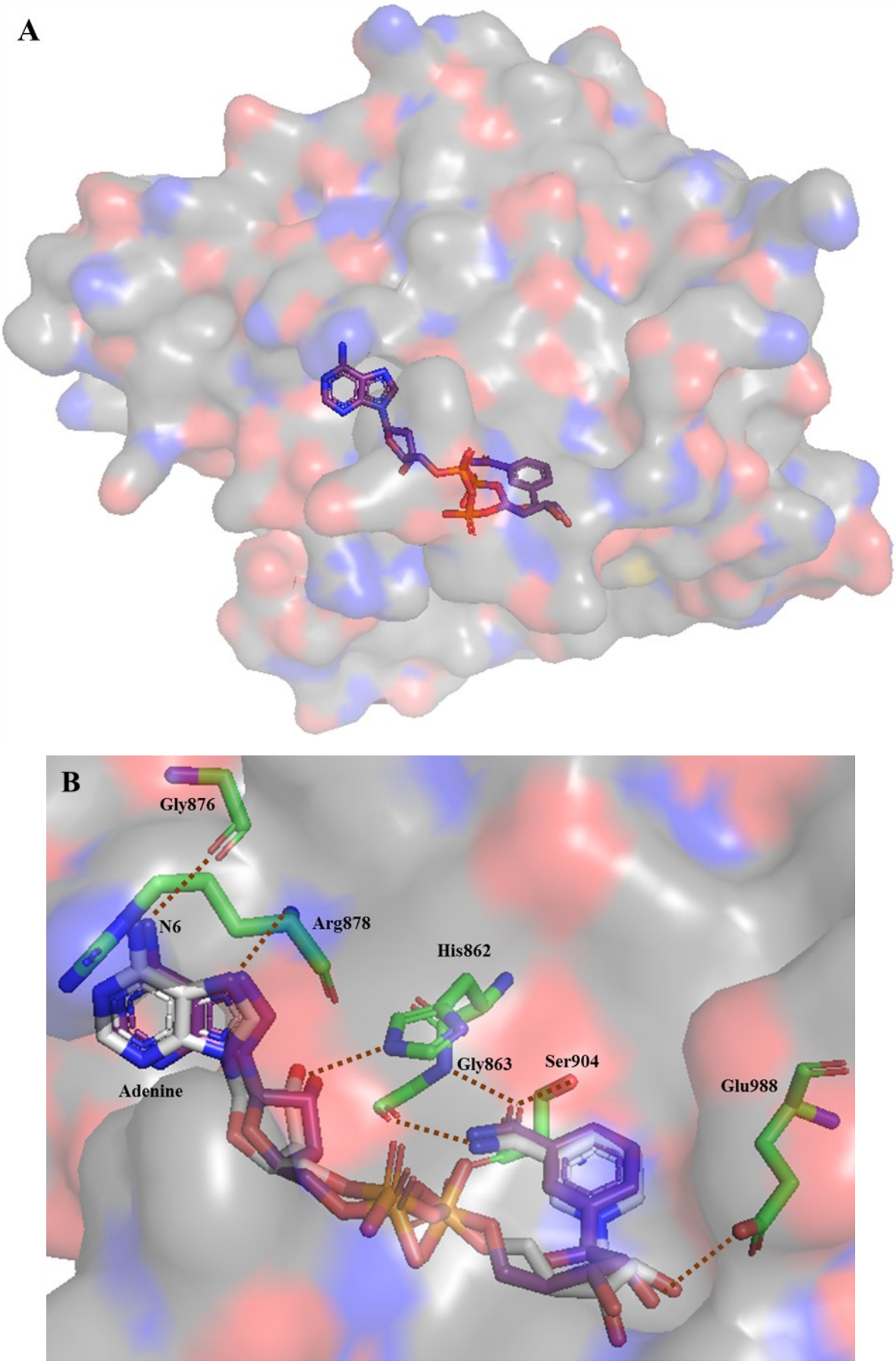
Figure 2.28. Docking of 6Az-ATP (**43**) with NMNAT1. **A.** The binding modes of ATP (white) and docked 6Az-ATP (**43**) (cyan) in the ATP binding site are shown. Residues important for binding and catalysis (green), and protein-ligand interactions (orange dotted lines) are highlighted. Purple dotted line represents directionality of the alkyne group in the absence of structural distortion. **B.** 2D schematic representation of protein-ligand interactions between 6Az-ATP (**43**) and NMNAT1. H-bond donors (red), H-bond acceptors (blue) and protein-ligand interactions (orange dotted lines) are highlighted.

2.3 Modelling of Protein-Ligand Interactions of PARPs and NAD^+ Analogues

2.3.1 PARP1 and NAD^+ Analogues

Following on from intracellular NAD^+ analogue biosynthesis, the corresponding NAD^+ analogues will be used by PARPs for intracellular ADP-ribosylation (**Figure 2.2**).[1-3] Investigating the ability of PARPs to utilise such analogues as substrates was therefore pivotal in establishing whether they could be employed for labelling ADP-ribosylated proteins in live cells. Since PARP1 catalyses the majority of cellular ADP-ribosylation,[19,20] it was important to establish whether the proposed NAD^+ analogues could be accommodated in the PARP1 active site. Furthermore, given the high sequence and structural homology between active sites of different PARPs,[217] ability of PARP1 to utilise a particular NAD^+ analogue as a substrate would be highly indicative of whether other PARPs were also able to employ that analogue for ADP-ribosylation. Molecular docking experiments were therefore only performed with PARP1.

A co-crystal structure for PARP1 with a BAD ligand (**6**) (PDB 6BHV)[111], an NAD^+-mimic, has been published (**Figure 2.29A**), which revealed seven protein-ligand interactions taking place between BAD (**6**) and PARP1 (**Figure 2.29B** and **2.29C**).


A
B
Gly876
N6
Arg878
His862
Gly863
Ser904
Glu988
Adenine

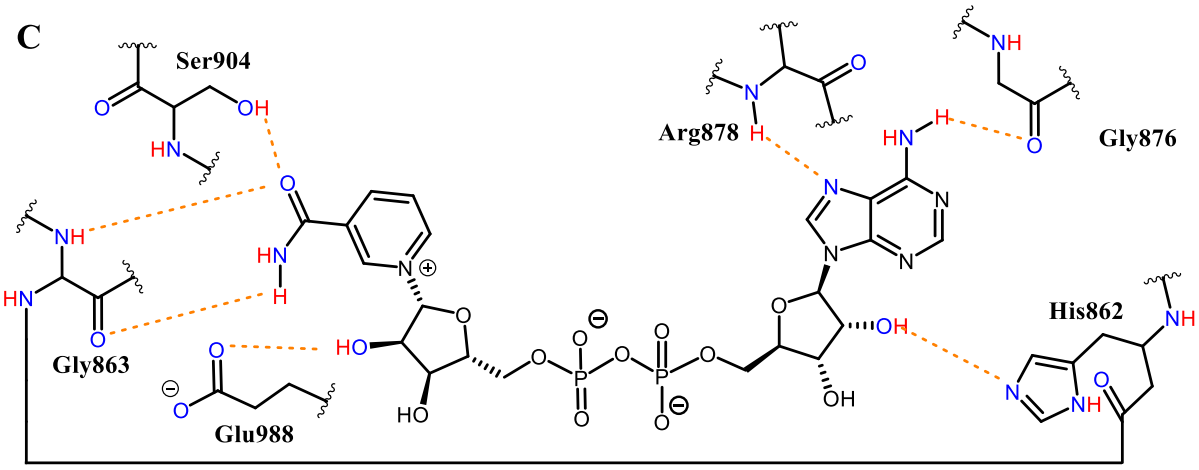


Figure 2.29. Co-crystal structure of PARP1. **A.** Overview of PARP1 showing binding mode of BAD at the NAD^+ binding site. **B.** Binding modes of BAD (purple) and docked NAD^+ (white) at the NAD^+ binding site. Residues important for binding and catalysis (green), and protein-ligand interactions (orange dotted lines) are highlighted. **C.** 2D schematic representation of protein-ligand interactions between PARP1 and NAD^+. H-bond donors (red), H-bond acceptors (blue) and protein-ligand interactions (orange dotted lines) are highlighted.

The co-crystal structure revealed that residues G863, S904 and E988 formed four H-bonding interactions with the β-NMN moiety, and residues H862, G876 and R878 formed three additional ones with the adenosine moiety of NAD^+ (**Figure 2.29B** and **2.29C**). These interactions were therefore considered essential for ligand binding and catalysis, and their loss for a particular NAD^+ analogue during molecular docking was deemed indicative of partially/completely diminished ability of PARP1, and by extension of other PARPs, to utilise that analogue as a substrate for ADP-ribosylation.

Results generated from docking predicted that two of the five NAD^+ analogues, 2Yn- (**9**) and 8Yn- (**46**), were well accommodated into the NAD^+ binding site, with a largely identical binding mode to native NAD^+, good structural overlap and conservation of all key protein-ligand interactions (**Figures 2.30B** and **2.31B**). The results thus predicted that these two NAD^+ analogues were likely substrates of PARP1 for ADP-ribosylation *in vitro*. Indeed, previous studies have shown that 2Yn-NAD^+ (**9**) is efficiently utilised for labelling of ADP-ribosylated proteins in cell lysates and *in vitro* assays with recombinant proteins.[107,110,112]

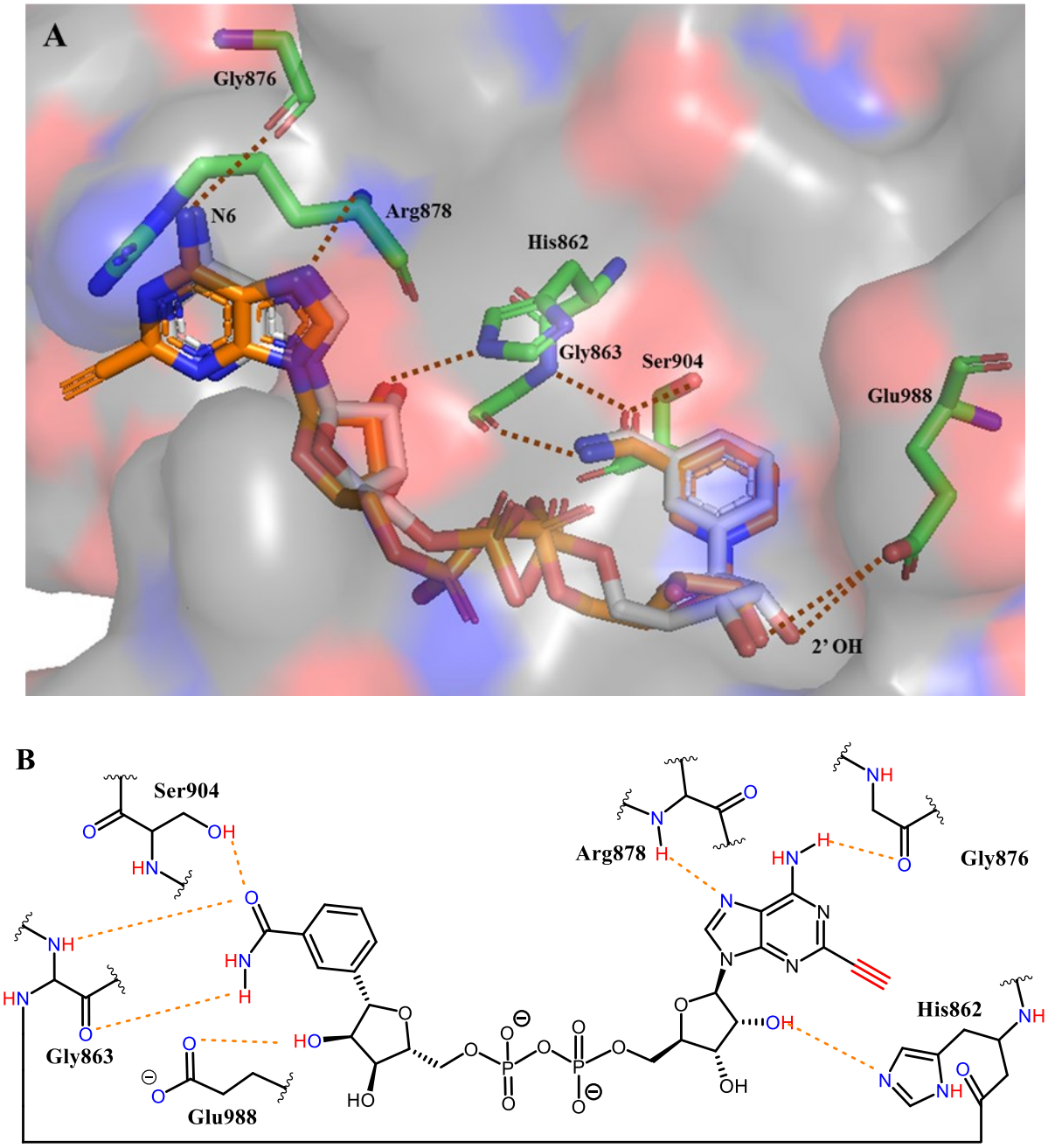


Figure 2.30. Docking of 2Yn-NAD$^+$ (**9**) with PARP1. **A.** The binding modes of NAD$^+$ (white) and docked 2Yn-NAD$^+$ (**9**) (orange) in the NAD$^+$ binding site are shown. Residues important for binding and catalysis (green), and protein-ligand interactions (orange dotted lines) are highlighted. **B.** 2D schematic representation of protein-ligand interactions between 2Yn-NAD$^+$ (**9**) and PARP1. H-bond donors (red), H-bond acceptors (blue) and protein-ligand interactions (orange dotted lines) are highlighted.

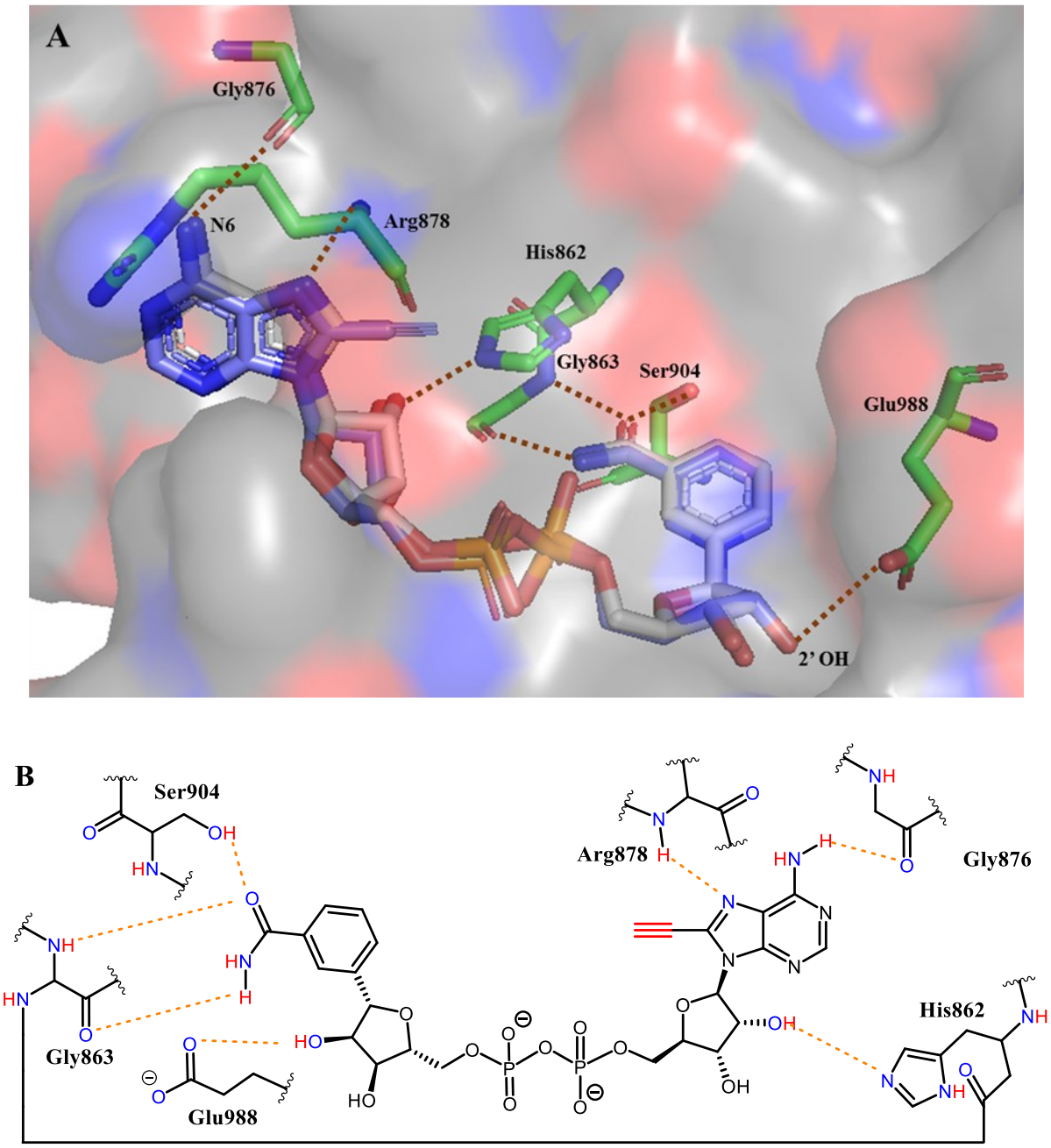


Figure 2.31. Docking of 8Yn-NAD$^+$ (**46**) with PARP1. **A.** The binding modes of NAD$^+$ (white) and docked 8Yn-NAD$^+$ (**46**) (purple) in the NAD$^+$ binding site are shown. Residues important for binding and catalysis (green), and protein-ligand interactions (orange dotted lines) are highlighted. **B.** 2D schematic representation of protein-ligand interactions between 8Yn-NAD$^+$ (**46**) and PARP1. H-bond donors (red), H-bond acceptors (blue) and protein-ligand interactions (orange dotted lines) are highlighted.

On the other hand, although 6Yn-NAD$^+$ (**3**) appears to be well accommodated into the PARP1 active site (**Figure 2.32A**) with conservation of all seven protein-ligand interactions (**Figure 2.32B**), it was noted that the small alkyne group partially protrudes through the protein surface (**Figure 2.33**). This would inevitably lead to some steric clash between the binding site and the

ligand, likely leading to partial displacement of the analogue from the optimal binding mode. Indeed, 6Yn-NAD$^+$ (**3**) has been shown to be utilised *in vitro* by PARPs in cell lysates and recombinant proteins, however, the efficiency of protein labelling was lower relative to that of 2Yn-NAD$^+$ (**9**),[107,112] where such steric clash was absent given that the C2 position is solvent exposed.

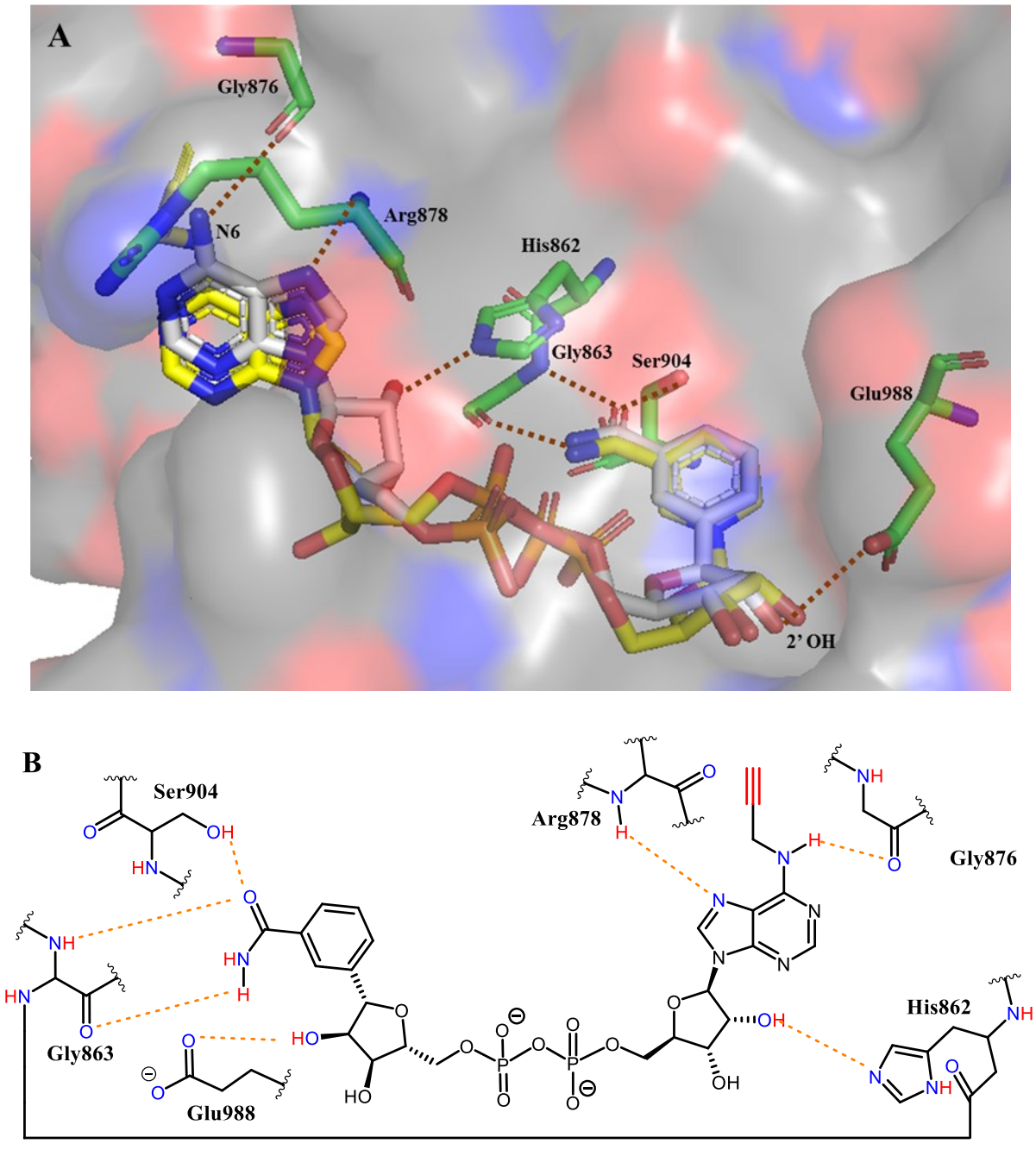


Figure 2.32. Docking of 6Yn-NAD$^+$ (**3**) with PARP1. **A.** The binding modes of NAD$^+$ (white) and docked 6Yn-NAD$^+$ (**3**) (yellow) in the NAD$^+$ binding site are shown. Residues important for binding and catalysis (green), and protein-ligand interactions (orange dotted lines) are highlighted. **B.** 2D schematic representation of protein-

ligand interactions between 6Yn-NAD$^+$ (**3**) and PARP1. H-bond donors (red), H-bond acceptors (blue) and protein-ligand interactions (orange dotted lines) are highlighted.

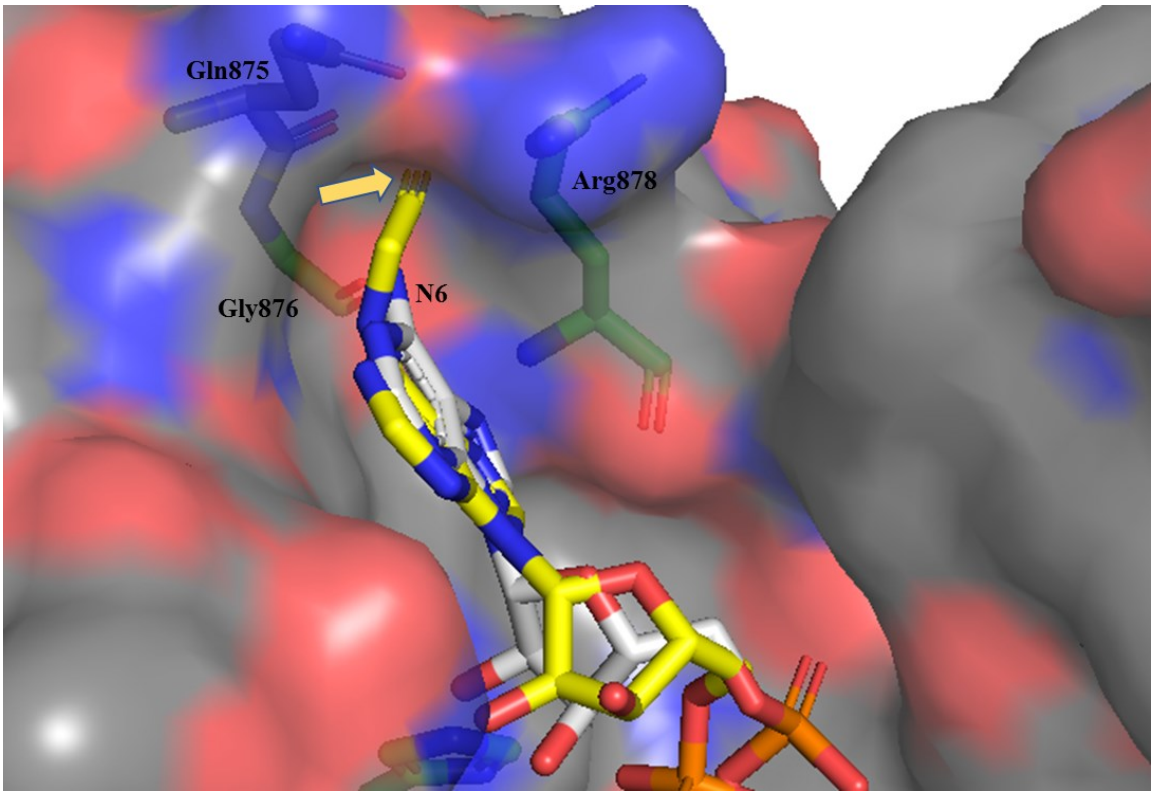


Figure 2.33. Side view of the binding modes of NAD$^+$ (white) and docked 6Yn-NAD$^+$ (**3**) (yellow) in the NAD$^+$ binding site. Residues important for binding and catalysis are shown in green. Arrow indicates site of steric clash with residue N875 shown in grey.

For analogues 8But-Yn-NAD$^+$ (**14**) and 6Az-NAD$^+$ (**45**) docking results predicted that neither analogue was well accommodated into the NAD$^+$ binding site, as indicated by the significant displacement of the ligands relative to native NAD$^+$, leading to loss of all protein-ligand interactions (**Figures 2.34B** and **2.35B**). For 8But-Yn-NAD$^+$ (**14**), these findings support results from previous literature studies, which have demonstrated that the analogue cannot be utilised by WT PARPs although it can be utilised by active site mutant PARPs *via* the 'bump-hole' approach (**Section 1.2.5.2**).[118,119] 6Az-NAD$^+$ (**45**) has not been previously described in the literature. However, similar N6 NAD$^+$ analogues, such as NAD$^+$ analogue **5** (**Table 1.2**), were not successfully employed by PARP1 for ADP-ribosylation thus supporting the finding that larger groups at the N6 position were not well tolerated by PARPs.[112]

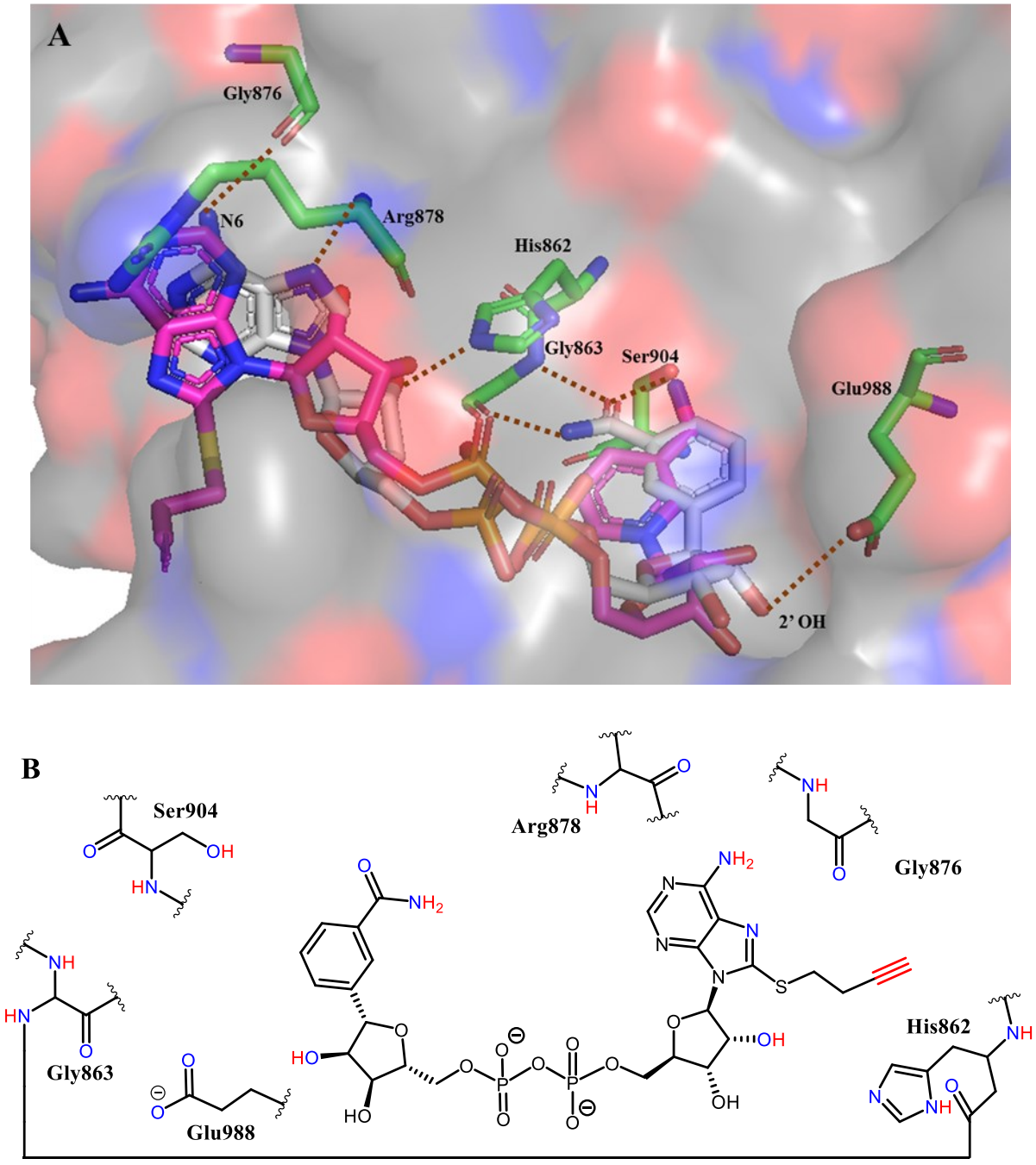


Figure 2.34. Docking of 8But-Yn-NAD$^+$ (**14**) with PARP1. **A.** The binding modes of NAD$^+$ (white) and docked 8But-Yn-NAD$^+$ (**14**) (pink) in the NAD$^+$ binding site are shown. Residues important for binding and catalysis (green), and protein-ligand interactions (orange dotted lines) are highlighted. **B.** 2D schematic representation of protein-ligand interactions between 8But-Yn-NAD$^+$ (**14**) and PARP1. H-bond donors (red), H-bond acceptors (blue) and protein-ligand interactions (orange dotted lines) are highlighted.

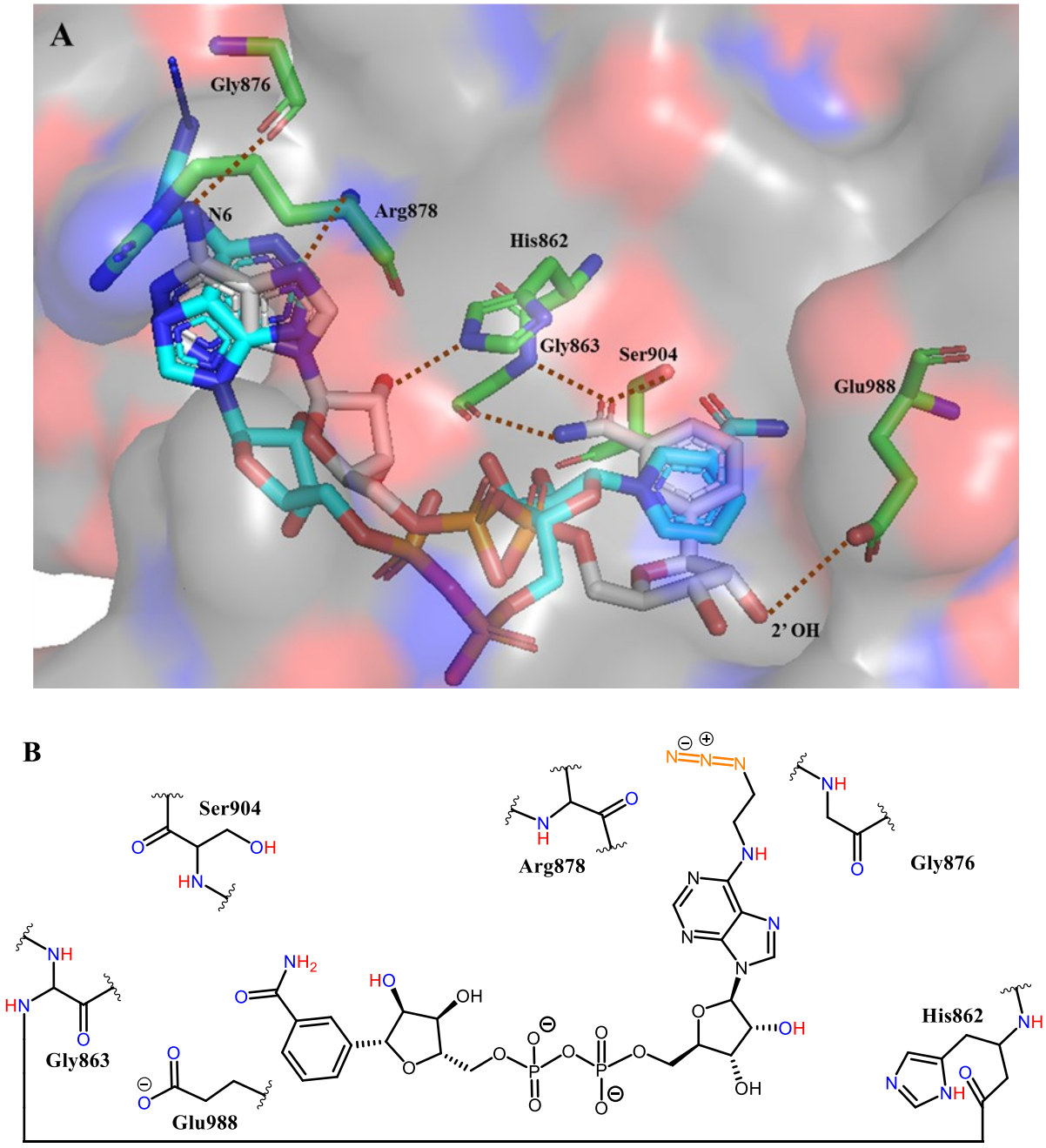


Figure 2.35. Docking of 6Az-NAD$^+$ (**45**) with PARP1. **A.** The binding modes of NAD$^+$ (white) and docked 6Az-NAD$^+$ (**45**) (cyan) in the NAD$^+$ binding site are shown. Residues important for binding and catalysis (green), and protein-ligand interactions (orange dotted lines) are highlighted. **B.** 2D schematic representation of protein-ligand interactions between 6Az-NAD$^+$ (**45**) and PARP1. H-bond donors (red), H-bond acceptors (blue) and protein-ligand interactions (orange dotted lines) are highlighted.

2.3.2 Target Profiling of PARPs *via* the 'Bump-Hole' Approach

Gibson *et al.*[118] and Parsons *et al.*[119] have previously demonstrated that 8But-Yn-NAD$^+$ (**14**) cannot be utilised by WT PARPs as a substrate. These findings were explained by molecular docking, which predicted that this was due to inability of the binding site to accommodate the long clickable group at the C8 position (**Figure 2.34A**). Knowing this, Gibson *et al.*[118] and Parsons *et al.*[119] successfully generated PARP1, 2, 3 and 7 mutants by introducing a hydrophobic pocket into the NAD$^+$ binding site *via* mutational analysis, which were subsequently employed for target identification of individual PARPs. For PARP1, an L877A mutant was predicted to possess a pocket in its active site large enough to accommodate the clickable group of 8But-Yn-NAD$^+$ (**14**), without negatively affecting its binding mode, and conserving all protein-ligand interactions.[118] This was confirmed in the herein performed docking experiments (**Figures 2.36** and **2.37**).

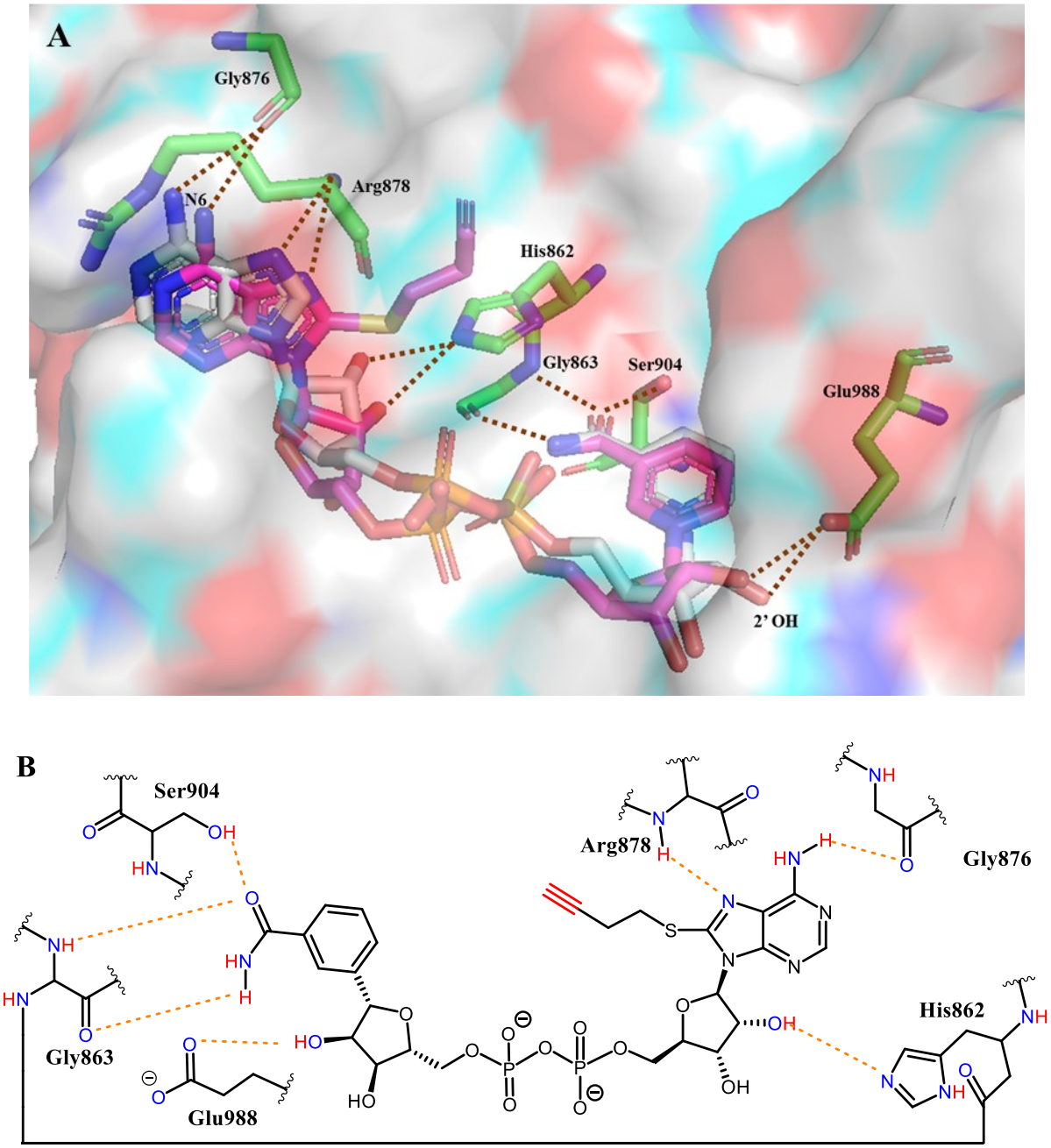


Figure 2.36. Docking of 8But-Yn-NAD$^+$ (**14**) with L877A PARP1. **A.** The binding modes of NAD$^+$ (white) and docked 8But-Yn-NAD$^+$ (**14**) (purple) in the NAD$^+$ binding site are shown. Residues important for binding and catalysis (green), and protein-ligand interactions (orange dotted lines) are highlighted. **B.** 2D schematic representation of protein-ligand interactions between 8But-Yn-NAD$^+$ (**14**) and L877A PARP1. H-bond donors (red), H-bond acceptors (blue) and protein-ligand interactions (orange dotted lines) are highlighted.

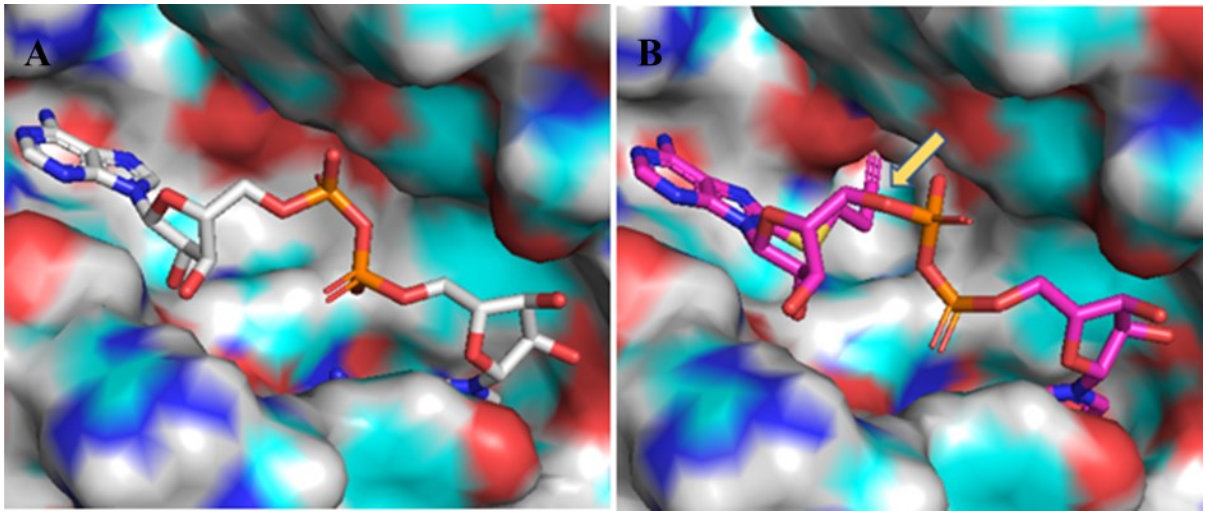


Figure 2.37. Binding modes of docked NAD^+ in the NAD^+ binding site of WT PARP1 (**A**) and 8But-Yn-NAD^+ (**14**) in the NAD^+ binding site of L877A PARP1 mutant (**B**). Arrow indicates L877A pocket formation.

Taking this into account, it was of interest to establish whether 8But-Yn-NAD^+ (**14**) could be similarly employed for target profiling of all other PARP proteins. This was performed *via* sequence and structural alignment of PARP1 with published crystal structures or homology models generated for all PARPs.

Sequence and structural alignment resulted in the identification of four two-amino acid motifs, GL, GF, NF and FL, in the active sites of PARPs that can be targeted for mutagenesis (**Table 2.2**). Specifically, mutation of the latter residue (L or F) in each motif, to A or G, such as the L877A or L877G mutations in PARP1, was expected to introduce a pocket large enough for accommodation of the clickable group at the C8 position. This should allow a corresponding mutant PARP to utilise 8But-Yn-NAD^+ (**14**) as a substrate.

Table 2.2. Active site sequence alignment comparison for all PARPs relative to the PARP1 residue region 873 – 881. Highlighted residues indicate X→A sites of mutation to allow for accommodation of analogue 8But-Yn-NAD^+ (**14**).

PARP	**Sequence alignment** **873 877 881**	**ADP-ribosylation activity**
PARP1	LSQGLRIAP	Poly-
PARP2	LSHGLRIAP	Poly-
PARP3	LTSGLRIMP	Mono-

PARP4	LCRGLLLPK	Mono-
PARP5a	IHKGFDERH	Poly-
PARP5b	IHKGFDEMF	Poly-
PARP6	LRNGLVNAS	Mono-
PARP7	CKHNFDPRV	Mono-
PARP8	LRNGLVVAS	Mono-
PARP9	-	Mono-
PARP10	CAHGFNRSF	Mono-
PARP11	CIHNFDWRI	Mono-
PARP12	CQQNFDWRV	Mono-
PARP13	Inactive	Inactive
PARP14	NRNGFNRSY	Mono-
PARP15	NQHGFNRSC	Mono-
PARP16	IHNGLHCHL	Mono-

Docking results predicted that the 8But-Yn- precursor series was likely to be utilised throughout the NAD^+ biosynthesis pathway for intracellular generation of 8But-Yn-NAD^+ (**14**). Provided that this is the case *in vitro*, 8But-Yn-Ad (**27**) or its corresponding ProTide (**49**) (**Figure 2.38**) could therefore be employed for identification of intracellular, physiologically relevant, protein targets of individual PARPs. This would be performed by generating and expressing individual mutant PARP proteins possessing the active site mutations described in **Table 2.2**.

2.4 Summary and Conclusions

Molecular docking tools for probing protein-ligand interactions are indispensable for the identification and derivation of novel protein-binding ligands. Accordingly, the technique was utilised in this chapter for identification of suitable NAD^+ precursor analogue probes (**Figure 2.3**) that could be utilised in the NAD^+ biosynthesis pathway for intracellular production of NAD^+ analogues.

Results from docking experiments predicted that 6Yn-metabolites were likely to be utilised in all steps of the NAD^+ biosynthesis pathway, and that 6Yn-NAD^+ precursors were the most promising candidates for intracellular generation of an NAD^+ analogue out of the five analogue series tested. In addition, previous studies have established that 6Yn-NAD^+ (**3**) is utilised by PARPs for protein ADP-ribosylation *in vitro*.[105-107] Taking all of these findings into account, 6Yn-NAD^+ precursor probes, such as 6Yn-Ad (**25**) or its corresponding ProTide prodrug (**47**) (**Figure 2.38**), appear as suitable candidates for intracellular protein labelling and studying of ADP-ribosylation in live cells.

Literature studies have demonstrated that 2Yn-NAD^+ (**9**) is a PARP1 substrate,[107,110,112] however, results from docking experiments predicted that conversion of 2Yn-ATP (**41**) to 2Yn-NAD^+ (**9**) by WT NMNAT1 was a likely bottleneck step in 2Yn-NAD^+ biosynthesis (**Figure 2.26A**). This was attributed to the observation that the alkyne group of 2Yn-ATP (**41**) underwent structural distortion, arising from steric clash of the ligand with the ATP binding site in NMNAT1, thus demonstrating inability of this analogue to be accommodated in the NMNAT1 active site (**Figure 2.26A**). It was established, however, *via* mutational analysis, that a V186G mutation resulted in the generation of a pocket in the binding site sufficiently big to accommodate the alkyne group of 2Yn-ATP (**41**) (**Figure 2.27A**). The results thus predicted that although the 2Yn- precursor series was unlikely to be utilised fully in the NAD^+ pathway, expression of V186G NMNAT1 mutant may overcome this limitation and result in the generation of 2Yn-NAD^+ (**9**) for intracellular labelling of ADP-ribosylated proteins.

For the 8Yn- series, molecular docking predicted high likelihood of encountering two bottleneck steps in NAD^+ biosynthesis. Docking results predicted 8Yn-Ad (**29**) to be poorly accommodated in the active site of AdK (**Figure 2.8A**), suggesting inability to catalyse 5' phosphorylation to produce 8Yn-AMP (**34**). In addition, the rigid alkyne group was also predicted to partially displace the phosphate chain of 8Yn-ADP (**39**) in the F1-ATPase binding site (**Figure 2.21A**), thus likely impeding 8Yn-ATP (**44**) generation. Overall, the results

suggested that 8Yn- series was unlikely to be utilised throughout the NAD^+ biosynthesis pathway.

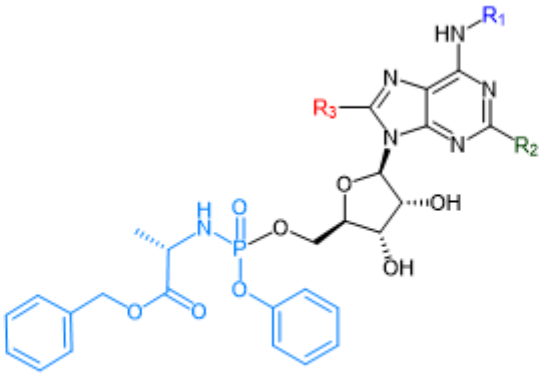
In a similar fashion, docking results predicted poor accommodation of 6Az-Ad (**28**) in the active site of AdK (**Figure 2.9A**). Furthermore, 6Az-ATP was predicted to be poorly accommodated into the ATP binding site of NMNAT1 (**Figure 2.28A**) as well as inability of PARP1 to utilise 6Az-NAD^+ (**45**) as a substrate (**Figure 2.35A**) for ADP-ribosylation. The presence of multiple bottleneck steps thus strongly suggested that the 6Az- series, similarly to 8Yn-, was unlikely to be fully utilised throughout NAD^+ biosynthesis and for subsequent protein ADP-ribosylation.

For the final analogue series, 8But-Yn-, results predicted inability of AdK to catalyse phosphorylation of 8But-Yn-Ad (**27**) into 8But-Yn-AMP (**32**) (**Figure 2.7A**). On the other hand, docking results suggested that this analogue series was likely to be utilised in the remaining steps of NAD^+ biosynthesis for intracellular 8But-Yn-NAD^+ (**14**) production. Given that 8But-Yn-NAD^+ (**14**) has been previously used for PARP target identification using mutant PARPs *via* the 'bump-hole' approach (**Section 1.2.5.2**),[118,119] and the identification of motifs for mutagenesis in the catalytic domains of all PARPs (**Table 2.2**), 8But-Yn-NAD^+ precursors could potentially be applied for identification of intracellular, physiologically relevant protein targets of individual PARPs. In particular, employing the ProTide prodrug of 8But-Yn-Ad (**49**) (**Figure 2.38**) will likely prove useful since it would directly generate 8But-Yn-AMP (**32**) intracellularly, thus bypassing the initial phosphorylation step by AdK, predicted to be a bottleneck step (**Figure 2.7**).

Overall, for three of the five analogue series (8Yn-, 8But-Yn- and 6Az-), the initial phosphorylation step by AdK was identified as a likely bottleneck step in NAD^+ analogue biosynthesis. Taking this into account, the results strongly support the use of adenosine ProTide prodrugs (**Figure 2.38**) in cell-based experiments over adenosine analogues. Employing this approach would provide the advantage of direct intracellular conversion of the probes into the corresponding AMP analogues and bypassing of the initial phosphorylation step. Furthermore, ProTide probes are less polar than adenosine analogues thus expected to exhibit improved permeability into cells.

Finally, although results predicted that not all analogue series were likely to be converted into their corresponding NAD^+ analogue, four of the five analogue series (6Yn-, 2Yn, 8But-Yn-, 6Az-) were identified as likely to undergo metabolic conversion from AMP analogues to ATP

analogues, and one (8Yn-) as ambiguous. ProTide prodrugs could therefore also find applications in studying intracellular AMPylation, which utilises ATP as a cofactor (**Figure 1.13B**). As a result, ProTide prodrugs of all five proposed adenosine analogues (**47-51**) (**Figure 2.38**) were proposed for subsequent biological validation in cells, the synthesis of which is discussed in **Chapter Three**.



ProTide adenosine (Pro)

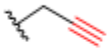
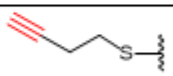
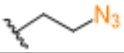
Analogue series	Metabolite	Functional group position		
		R_1	R_2	R_3
6Yn-	**Pro (47)**		H	H
2Yn-	**Pro (48)**	H		H
8But-Yn-	**Pro (49)**	H	H	
6Az-	**Pro (50)**	H		H
8Yn-	**Pro (51)**	H	H	

Figure 2.38. Structures of proposed ProTide prodrugs of adenosine analogues.

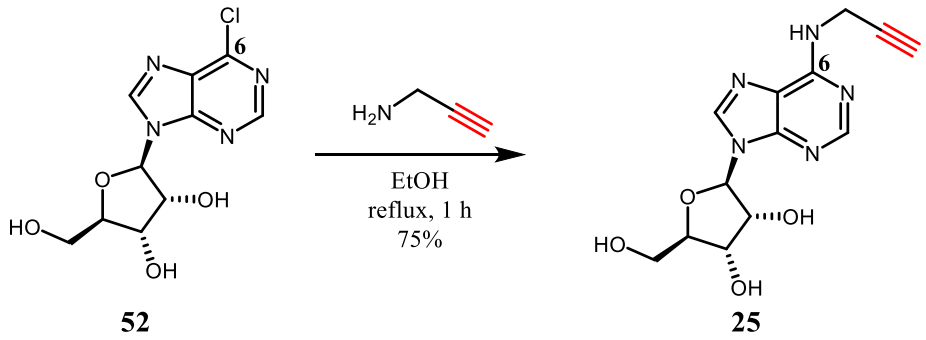
Chapter 3 Synthesis of NAD$^+$ Precursors, Probes and Metabolites

Protein-ligand molecular docking experiments with the five proposed adenosine analogues, and their corresponding phosphorylated analogue metabolites (**Figure 2.3**), were performed in **Chapter Two**. Following on from this, the next step in this project was to bring forward the proposed molecules for synthesis. In this chapter, the synthesis of adenosine analogues and the correspondingly derived ProTide analogue probes for the five analogue series is described. In addition, the synthesis of phosphorylated metabolites for the 6Yn- and ^{15}N- series (see **Section 3.3**) is also described. The phosphorylated 6Yn- and ^{15}N- metabolites were subsequently employed for optimisation of metabolomics experiments in **Chapter Four** (**Section 4.4**).

3.1 Synthesis of Adenosine Analogues

3.1.1 Synthesis of 6Yn-Ad

The synthesis of probe 6Yn-Pro (**47**) and 6Yn-metabolites (**30**, **35**, **40**, **3**) required 6Yn-Ad (**25**) as the starting material, therefore, 6Yn-Ad (**25**) was synthesised. The proposed synthesis was based on a previously published procedure for functionalisation of adenosine analogues at the 6-position (**Scheme 3.1**).[110] Literature suggested that the reaction between 6-chlororiboside (**52**) and propargylamine should be performed at 90 °C for 3 hours, however, the synthesis was complete in 1 h. The precipitated product was then filtered and washed to obtain pure 6Yn-Ad (**25**).

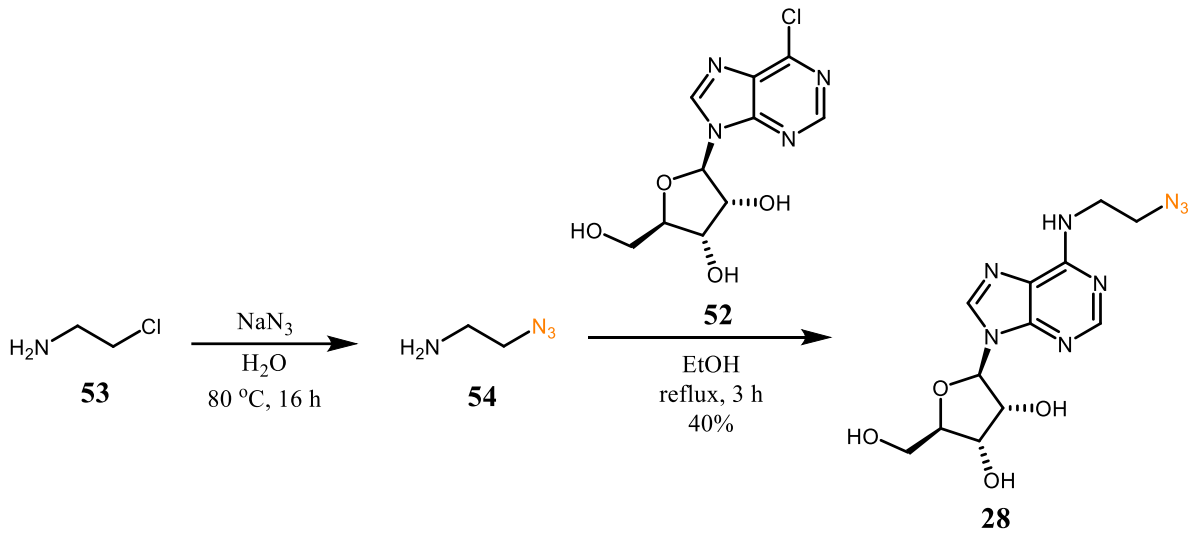


Scheme 3.1. Synthetic route for 6Yn-Ad (**25**).

3.1.2 Synthesis of 6Az-Ad

In a similar manner, probe 6Az-Pro (**50**) was synthesised from its corresponding azide adenosine analogue (**28**). A two-step synthetic route for 6Az-Ad (**28**) was therefore proposed (**Scheme 3.2**). Synthesis of azide **54** was performed following literature precedent between

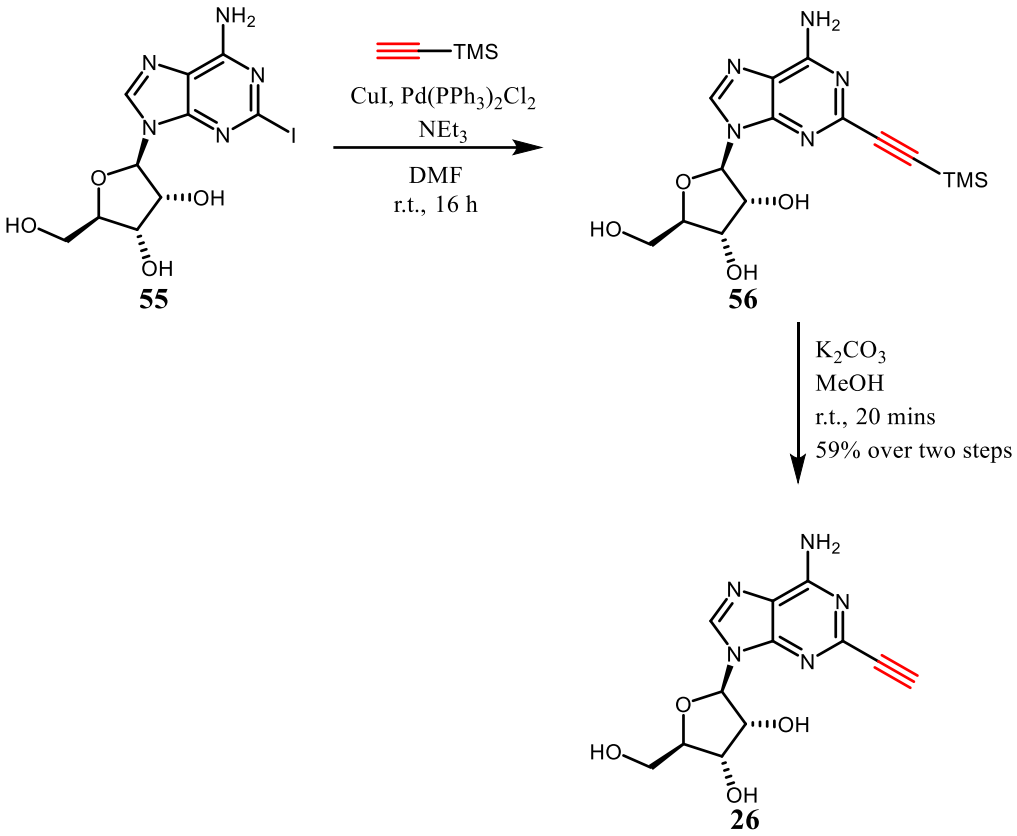
NaN_3 and 1-chloroethanolamine (**53**), and subsequently coupled to **52** without further purification.[232] The resulting 6Az-Ad (**28**) did not precipitate in ethanol (EtOH), likely due to its increased polarity, and was therefore purified by reverse-phase column chromatography.



Scheme 3.2. Synthetic route for 6Az-Ad (**28**).

3.1.3 Synthesis of 2Yn-Ad

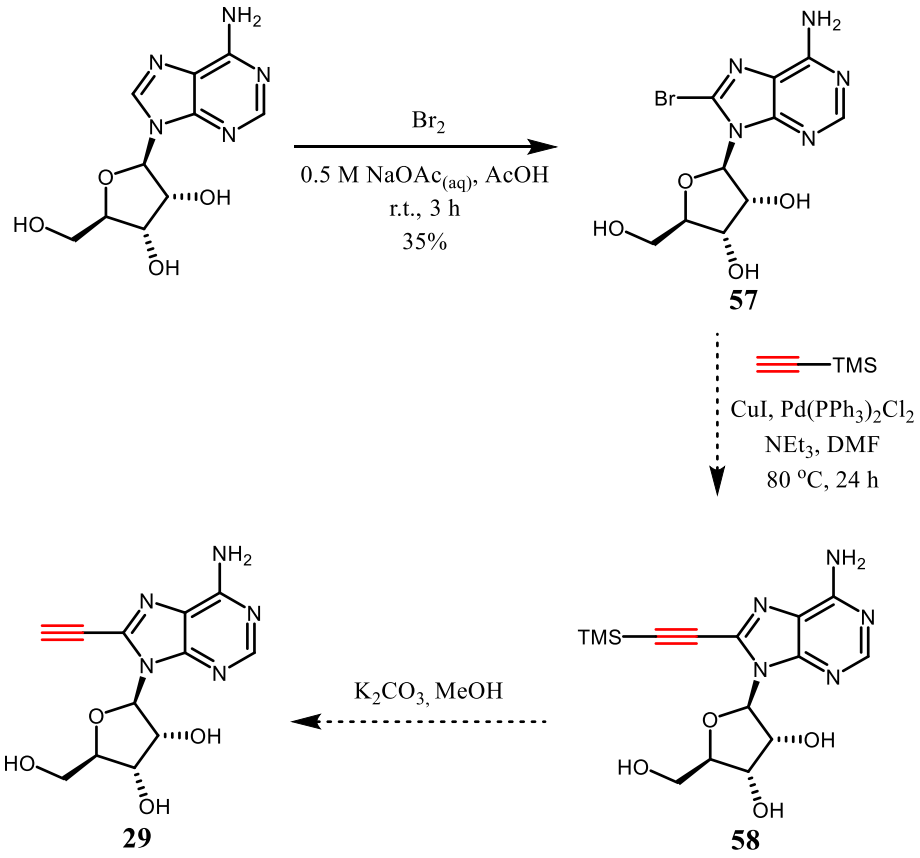
Given that 2Yn-Ad (**26**) was required for the synthesis of probe 2Yn-Pro (**48**), 2Yn-Ad (**26**) was synthesised *via* the two-step reaction route outlined (**Scheme 3.3**). The first step involved a Sonogashira coupling between 2-iodoadenosine (**55**) and TMS protected ethylene to produce **56**, as described in the literature.[110] However, for subsequent TMS deprotection of **56**, careful consideration of deprotection conditions and monitoring of reaction time was required; the deprotected 2Yn-Ad product (**26**) was prone to degradation under the basic TMS deprotection conditions used. Monitoring of the reaction by thin-layer chromatography (TLC) showed that TMS deprotection using methanol/potassium carbonate ($MeOH/K_2CO_3$) mixture was complete within 20 mins, and reaction times beyond 30 mins or heating above r.t. led to spontaneous degradation of the 2Yn-Ad (**26**) product. To maximise TMS deprotection and minimise product degradation, the deprotection reaction was allowed to proceed for 20 mins. The reaction mixture was subsequently loaded on a prepacked normal phase column for immediate purification.



Scheme 3.3. Synthetic route for 2Yn-Ad (**26**).

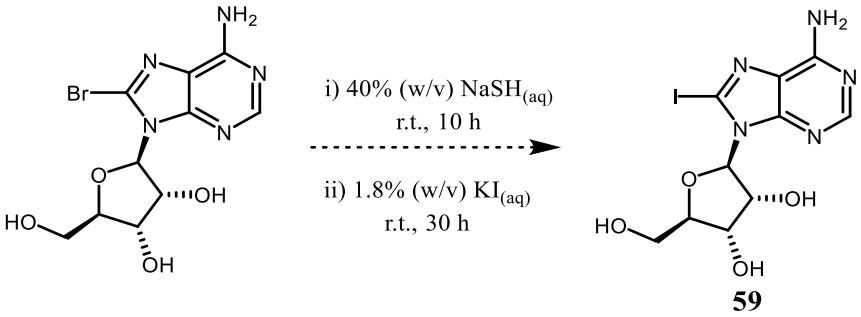
3.1.4 Attempted Synthesis of 8Yn-Ad

The adenosine analogue 8Yn-Ad (**29**) was required for the synthesis of 8Yn-Pro (**51**), therefore, synthesis of 8Yn-Ad (**29**) was attempted *via* the three-step reaction outlined (**Scheme 3.4**). In the first step, 8-bromoadenosine (**57**) was synthesised *via* bromination of the C8 position of adenosine, as described in the literature.[233] Next, coupling of **57** to ethylene TMS to produce **58** was attempted *via* Sonogashira coupling, however, the reaction failed to progress at r.t. for 16 hours and at 50 °C for 16 hours. Further heating of the reaction mixture at 80 °C for 24 hours resulted in minimal conversion to **58** (<10% isolated yield following purification), and the obtained amount was insufficient for subsequent deprotection to **29** and conversion to the corresponding ProTide (**51**).



Scheme 3.4. Synthetic route for 8Yn-Ad (**29**).

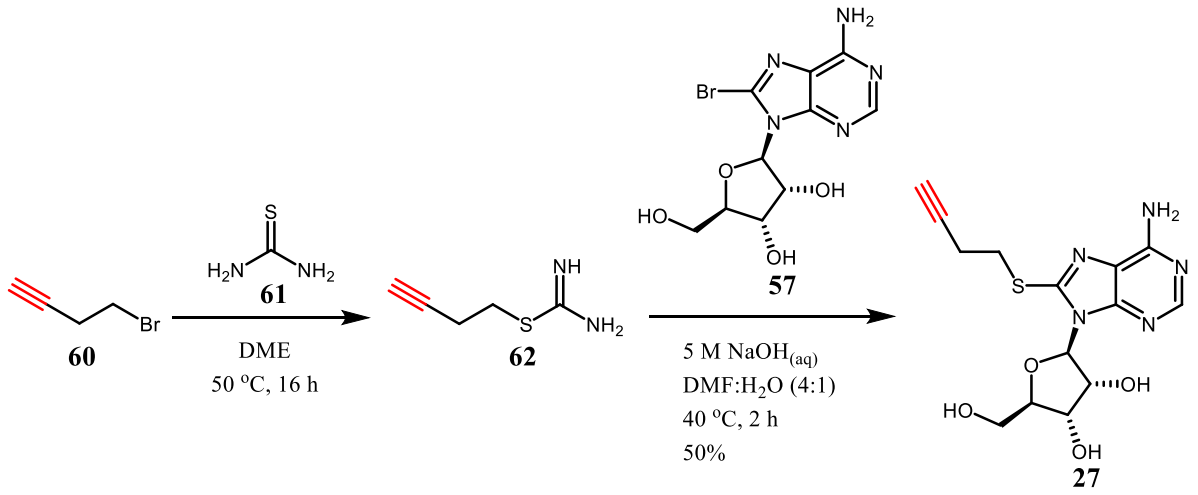
Given that Sonogashira coupling was successfully performed with aryl iodide **55**, replacement of the bromine atom in **57** for an iodine atom was attempted *via* an established literature route (**Scheme 3.5**).[234] However, conversion of **57** to 8-iodoadenosine (**59**) was unsuccessful. Owing to the synthetic challenges in obtaining 8Yn-Ad (**29**) for 8Yn-Pro (**51**) synthesis, along with the findings in **Sections 2.2.2** and **2.2.4** that this analogue was unlikely to be utilised throughout the NAD^+ biosynthesis pathway, the synthesis of 8Yn-Ad (**29**) was abandoned.



Scheme 3.5. Synthetic route for 8-iodoadenosine (**59**).

3.1.5 Synthesis of 8But-Yn-Ad

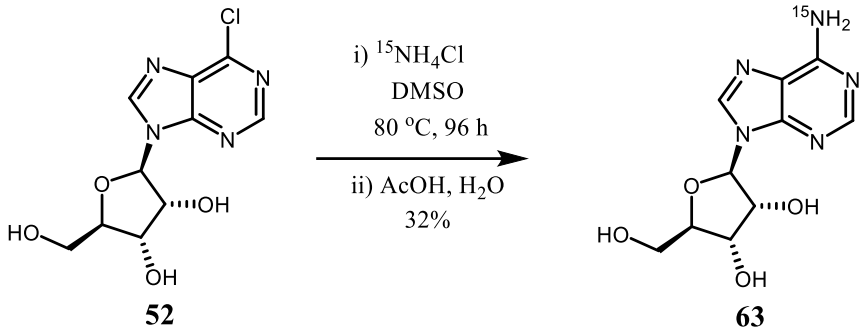
The synthesis of 8But-Yn-Pro (**49**) required 8But-Yn-Ad (**27**) as the starting material, hence a two-step synthesis for the adenosine analogue 8But-Yn-Ad (**27**) *via* coupling of **57** and **62** was proposed (**Scheme 3.6**). Synthesis of **62** was performed by coupling **60** and **61**, as described in the literature[235] and used for coupling to **57** without further purification. Although coupling of **57** to reactive thiols has been performed in the literature before,[236] attempting to couple **62** and **57** using the described literature procedure was unsuccessful. As suggested by LC-MS analysis, polymerisation/side reactions of **57** had occurred, likely through reactivity of 2', 3' and/or 5' OH groups. In the published procedure,[236] 1 eq. of **57** was coupled to 0.7 eq. of thiol ligand in the presence of 4 eq. of 5 M NaOH solution. It was thus reasoned that reduction of the equivalents of 5 M NaOH added and an excess of the thiol ligand **62** might prevent side reactions/polymerisation of the starting materials. A subsequent repeat of the reaction with 2 eq. of **62** and 2 eq. of 5 M NaOH was successfully attempted and a 50% yield was obtained for 8But-Yn-Ad (**27**).



Scheme 3.6. Synthetic route for 8But-Yn-Ad (**27**).

3.1.6 Synthesis of ^{15}N-Ad

The final adenosine analogue to be synthesised was ^{15}N-Ad (**63**) (**Scheme 3.7**), which was required for the synthesis of probe ^{15}N-Pro (**64**) (see **Section 3.3**). Following literature precedent, **52** was reacted with $^{15}NH_4Cl_{(s)}$ in DMF at 80 °C for 7 days.[237] As evidenced by LC-MS analysis, the reaction did not progress beyond 48 h and the addition of further equivalents of $^{15}NH_4Cl_{(s)}$ failed to push the reaction to completion. The desired product (**63**) was purified by reverse-phase and isolated in 32% yield following purification.



52 **63**

Scheme 3.7. Synthetic route for ^{15}N-Ad (**63**).

3.1.7 Summary of Adenosine Analogues Synthesised

The synthesis of six adenosine analogues was attempted, however, only five were successfully synthesised (**25**-**28**, **63**) (**Figure 3.1**). Adenosine analogues 6Yn-Ad (**25**), 6Az-Ad (**28**) and ^{15}N-Ad (**63**) were synthesised according to previously described literature procedures. For 2Yn-Ad (**26**) and 8But-Yn-Ad (**27**), modifications to existing procedures were necessary to obtain the desired products. Despite multiple attempts and employing different approaches for the synthesis of 8Yn-Ad (**29**), the reactions were unsuccessful and 8Yn-Ad (**29**) was not obtained.

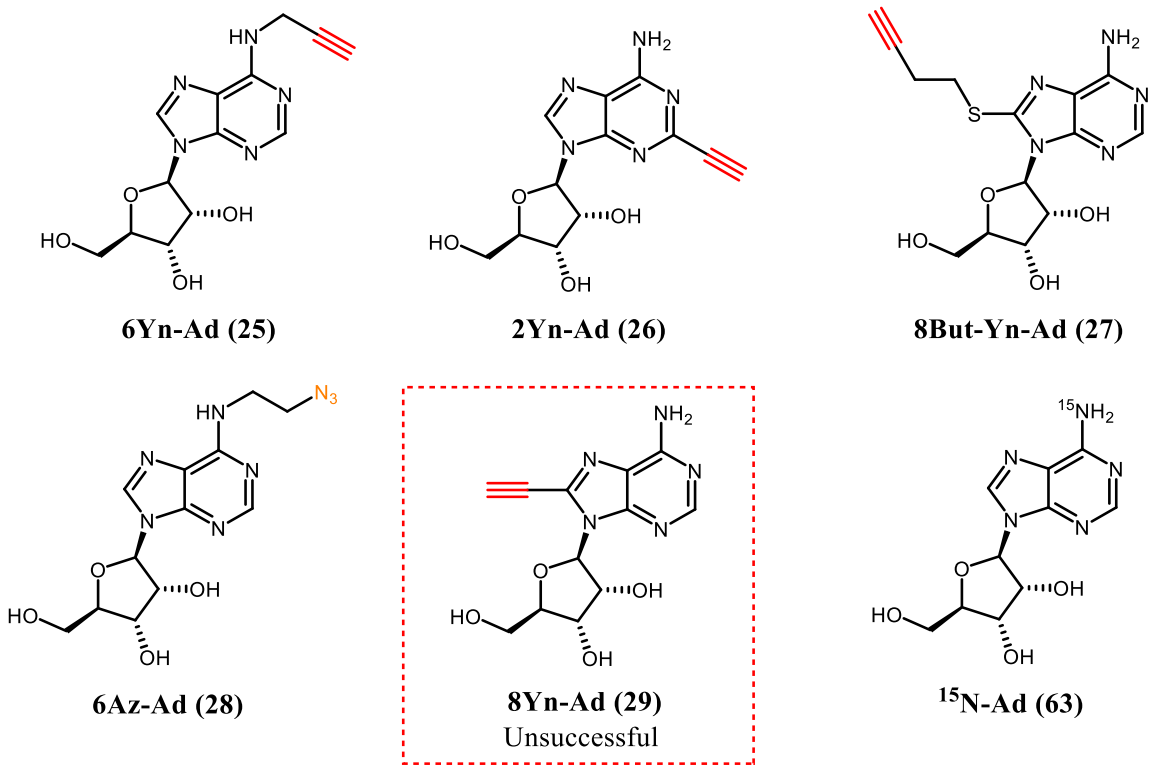
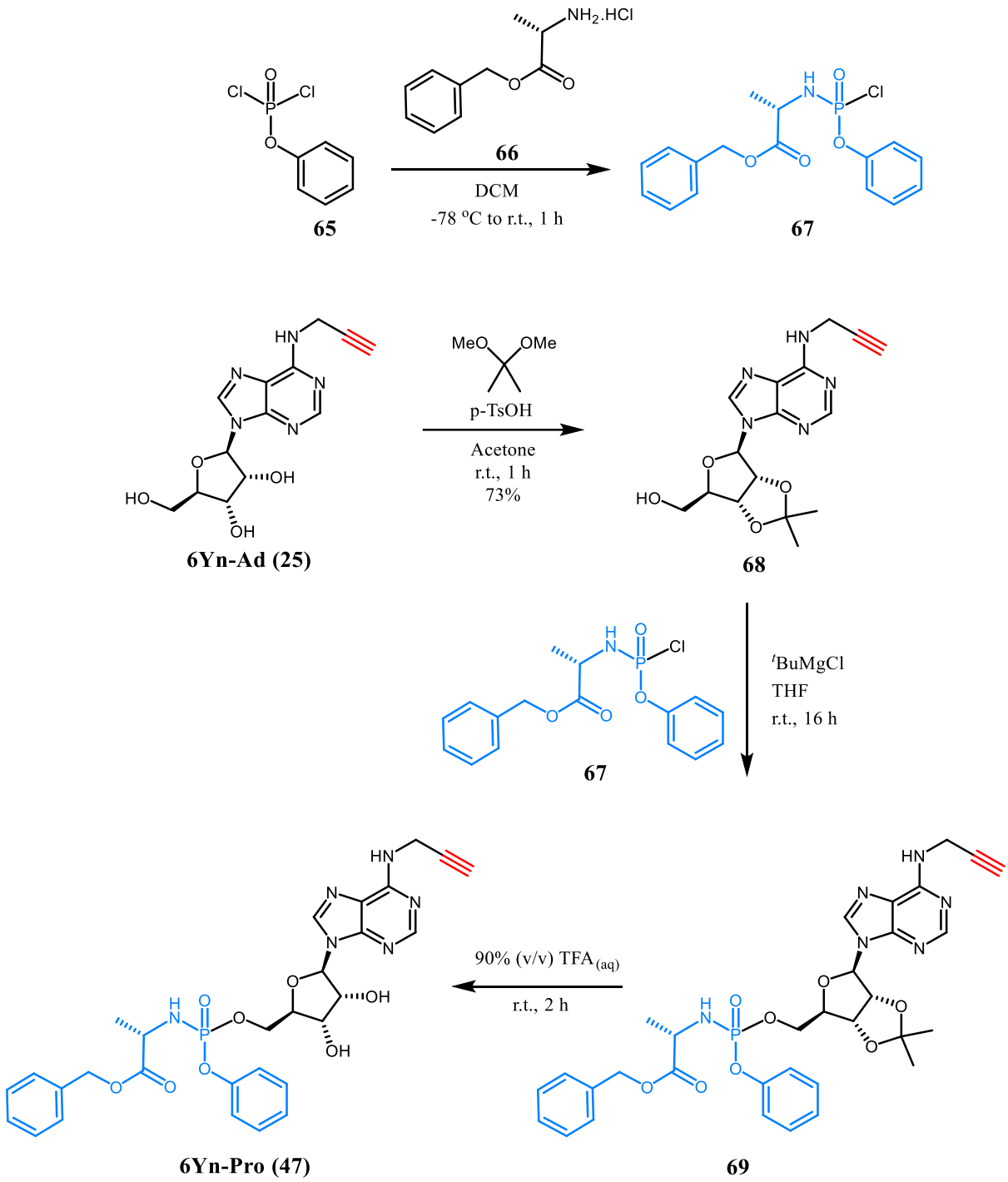


Figure 3.1. Summary of adenosine analogues attempted for synthesis. The synthesis of 8Yn-Ad (**29**) was unsuccessful.

3.2 Synthesis of ProTide Probes

3.2.1 Synthesis of ProTides *via* Protection of 2' and 3' OH Groups

The use of ProTide prodrugs for intracellular delivery of masked phosphorylated molecules and conversion into active molecules has been well established in the literature as well as in the clinic (**Section 1.5.3**).[199-203] For adenosine, a common approach to ProTide synthesis involves initial protection of the 2' and 3' OH groups to produce **68** followed by coupling of the 5' OH to the appropriate protected phosphoryl monochloride (**67**), analogous to the approach described for the synthesis of 6Yn-Pro (**47**) by Kielkowski *et al.*[223] (**Scheme 3.8**). This approach eliminates possible coupling of **67** to the 2' or 3' OH groups of **68** and allows for purification of each intermediate, which is desirable considering the highly reactive nature of phosphoryl chlorides and the generation of multiple side products. In the final step, 2' and 3' diol deprotection of **69** is performed in 90% TFA $_{(aq)}$ to afford the desired ProTide product.



Scheme 3.8. Synthesis of 6Yn-Pro (**47**) *via* 2' and 3' diol protection.

Considerations need to be taken into account with respect to functional group compatibility under these reaction conditions. For example, the need to use ^{t}BuMgCl in THF for coupling of the protected phosphoryl monochloride (**67**) and the use of aqueous TFA for deprotection could lead to undesirable modifications of the clickable groups, particularly for azides, thus rendering them non-functional. In addition, generation and handling of **67** from phenyl phosphoryl dichloride (**65**) is non-trivial. Reaction monitoring and purification are incredibly challenging;

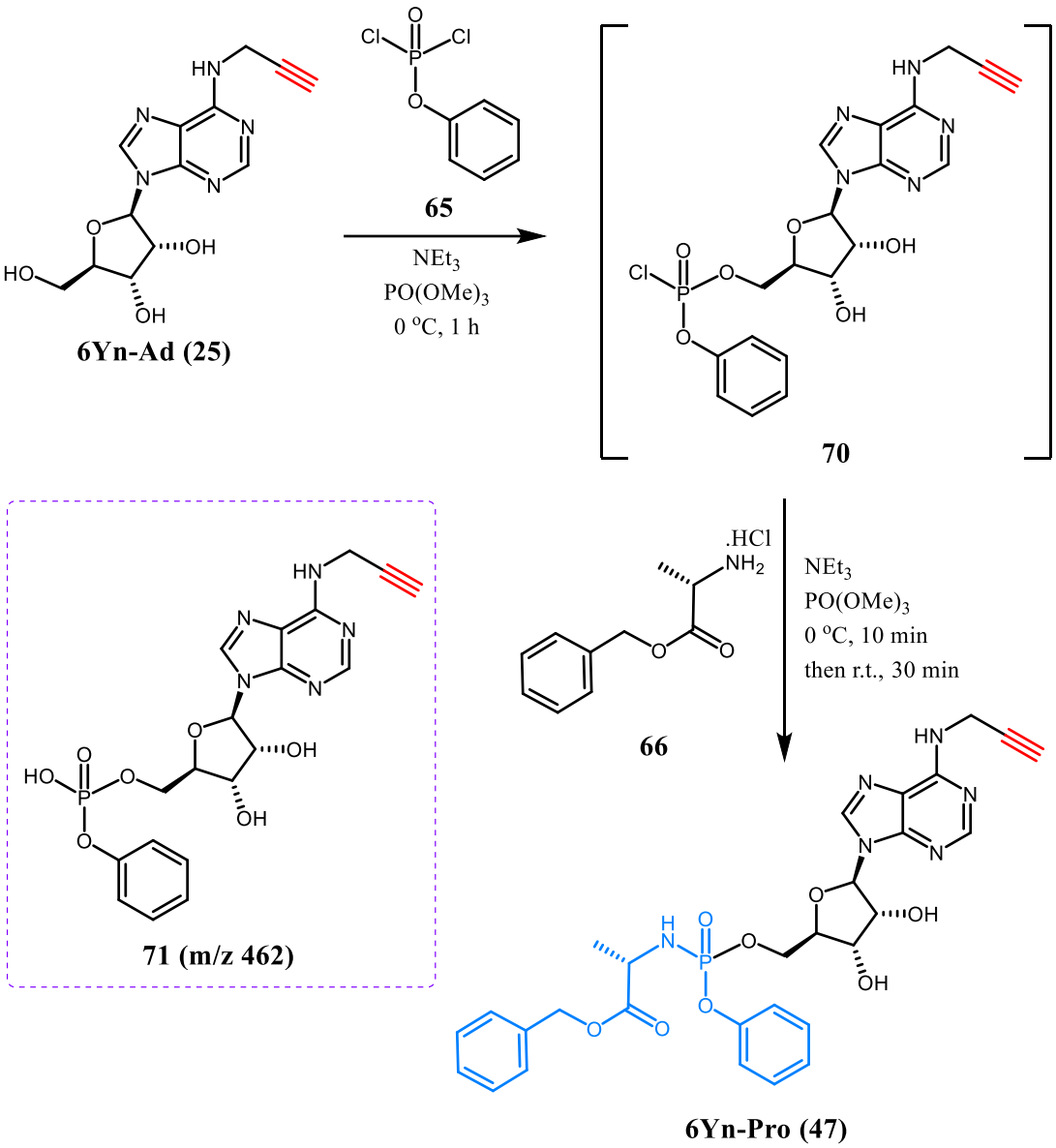
the product is highly unstable and susceptible to hydrolysis. Nevertheless, this approach was attempted for initial synthesis of 6Yn-Pro (**47**), following the success of Kielkowski *et al.* in synthesising **47** (Kielkowski *et al.* reported a yield of 35% over all four steps)[223].

Protection of 2' and 3' OH groups of **25** to produce **68** was monitored by TLC and the starting material was mostly consumed within 1 h. In parallel, synthesis of **67** was performed by coupling L-ala-benzyl ester (**66**) and **65** according to literature precedent,[223] however, monitoring of the production of **67** by LC-MS was difficult owing to its hydrolysis during analysis. Purification by flash column chromatography was equally challenging despite following literature precedent.[238] Product **67** quickly hydrolysed upon contact with air, as evidenced by inability of the product to be eluted from the column, thus indirectly implying that it had been hydrolysed into the highly polar phosphoric acid during purification.

In a subsequent attempt, **67** was instead filtered *via* a cannula, under nitrogen, and used directly for coupling to **68** without further purification. The coupling reaction was attempted in the presence of ^{t}BuMgCl in THF, as described by Kielkowski *et al.*,[223] however, the reaction failed to progress, as indicated by the lack of consumption of **68** by TLC. The failure of the reaction to proceed was attributed either due to the presence of excess phenyl phosphoryl dichloride (**65**), which is less sterically hindered and could react with ^{t}BuMgCl, thus leading to its depletion, or due to degradation of ^{t}BuMgCl in THF stock reagent over time, which was needed to facilitate the coupling reaction.

3.2.2 Synthesis of ProTides *via* Direct 5' Activation

Owing to the difficulties associated with the outlined synthetic route in **Scheme 3.8**, an alternative route consisting of two-step one-pot synthesis was proposed (**Scheme 3.9**). In this approach, the 5' OH group of **25** was activated *via* direct coupling to **65** to generate intermediate **70**, followed by a second coupling step of **70** with **66** to produce ProTide **47**. This approach was advantageous due to the shortened synthesis (one step compared to four steps for the route in **Scheme 3.8**) thus saving considerable amount of time (~half a day compared to ~3 – 4 days required for the route in **Scheme 3.8**). In addition, only a single purification step was required by reverse-phase to obtain the final ProTide product. Furthermore, it bypassed the use of moisture sensitive ^{t}BuMgCl, and the use of aqueous TFA, which could affect functionality of clickable groups. Overall, fewer reagents were required for this synthetic route (**Scheme 3.9**).



Scheme 3.9. Proposed two-step one-pot synthetic route for the synthesis of 6Yn-Pro (**47**). All other ProTide analogues (**48-51**, **64**) were synthesised in the exact same manner from their corresponding adenosine analogue starting material (**25-28**, **63**).

A drawback associated with this shortened route (**Scheme 3.9**) was the generation of multiple side products owing to the highly reactive nature of **65**, which complicated purification. Furthermore, the coupling reactions were strictly performed at 0 °C to prevent activation of 2' and 3' OH groups, and degradation of intermediate **70**. By employing LC-MS, it was noted that performing the reaction at 0 °C and dropwise addition of **65** to **25** resulted in predominantly 5' OH activation (as seen by the generation of **71**, the hydrolysis product of intermediate **70**) and in negligible 2' and 3' activation (**Appendix Figure A.3**). This observation agreed with the

findings from established literature procedures for direct phosphorylation of 5' OH, without 2' and 3' OH protection.[110,114,239]

To improve reaction efficiency and minimise the formation of hydrolysis side products, the solvent for the reaction trimethyl phosphate ($PO(OMe)_3$) was distilled prior to each use. Distillation of $PO(OMe)_3$ improved isolated yields for 6Yn-Pro (**47**) synthesis, raising from 3% before distillation to 23% after distillation. In addition, minimising the abundance of hydrolysis side products as a result of distillation of $PO(OMe)_3$ eased separation and purification of the desired ProTide probe. Further optimisation for 6Yn-Pro (**47**) synthesis revealed that the efficiency of the reaction decreased when <50 mg of 6Yn-Ad (**25**) starting material was used, as evidenced by the decrease in isolated yield following purification. It was therefore reasoned that synthesis of any ProTide probes should be attempted with a minimum of 50 mg of the corresponding adenosine starting material.

Although the obtained yield for 6Yn-Pro (**47**) using direct 5' activation (**Scheme 3.9**) was lower than for the approach established by Kielkowski *et al.*[223] (**Scheme 3.8**) (23% vs 35%, respectively), the time needed to obtain the product was reduced significantly and synthesis was less complex. As a result, synthesis of all ProTides (**Table 3.1, Figure 3.2**) was performed by following the route outlined in **Scheme 3.9**.

Table 3.1. Summary of the isolated % yield obtained for each synthesised ProTide probe.

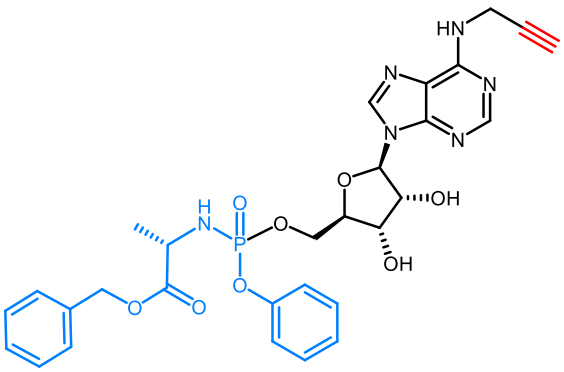
ProTide Probe	Yield (%)
6Yn-Pro (**47**)	23
2Yn-Pro (**48**)	2
8But-Yn-Pro (**49**)	16 (after double purification)
6Az-Pro (**50**)	23
^{15}N-Pro (**64**)	19

It was noted that, although this synthetic route worked well for the synthesis of most ProTide analogues, the yield for 2Yn-Pro (**48**) was very low (~2%) despite multiple synthetic attempts. The difficulties in synthesising 2Yn-Pro (**48**) were associated with the earlier observation for 2Yn-Ad (**26**) that, under basic conditions, the product underwent spontaneous degradation at

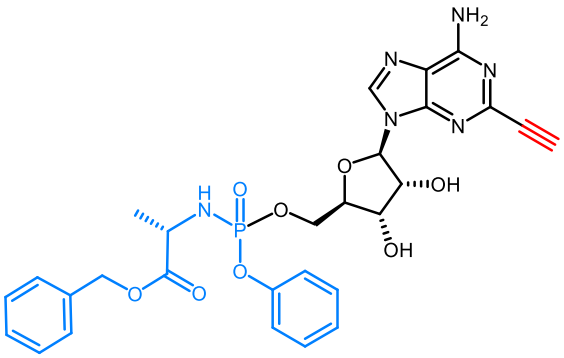
reaction times of >30 min. It was therefore reasoned that the ProTide reaction conditions outlined in **Scheme 3.9** were incompatible with synthesis of 2Yn-Pro (**48**), given that the combined reaction time under basic conditions exceeded 1 h 30 mins.

3.2.3 Summary of ProTide Probes Synthesised

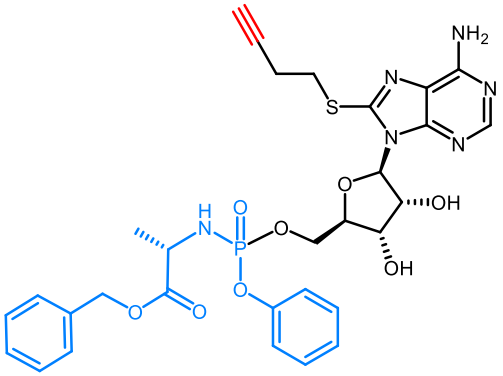
The synthesis of five ProTide analogue probes (**47**-**50**, **64**) was attempted, and all five probes were successfully synthesised (**Table 3.1, Figure 3.2**). Although a literature precedent has been established for the synthesis of 6Yn-Pro (**47**) (**Scheme 3.8**),[223] an initial attempt to reproduce it was unsuccessful. As a result, a shorter synthetic route was proposed (**Scheme 3.9**) and all ProTide probes were synthesised in accordance with this new route, in largely comparable yields (16 – 23%, **Table 3.1**). The synthesis of 2Yn-Pro (**48**), however, was more challenging than expected due to incompatibility of the functionality of the starting material (2Yn-Ad (**26**)) and product (2Yn-Pro (**48**)) with the reaction conditions used. Overall, all ProTide probes were synthesised in sufficient amounts for use in biological testing (**Chapter Four**).



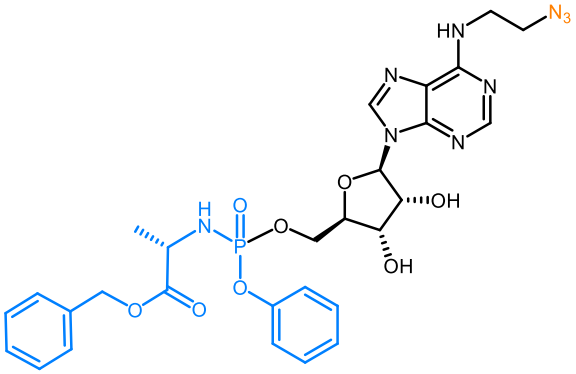
6Yn-Pro (47)



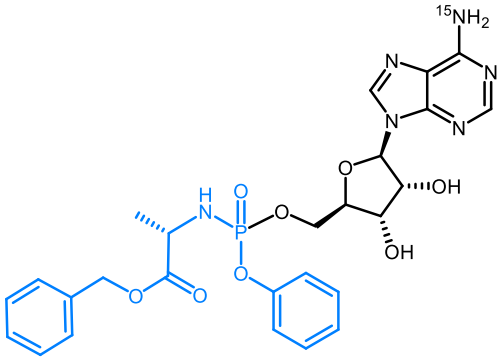
2Yn-Pro (48)



8But-Yn-Pro (49)



6Az-Pro (50)



^{15}N-Pro (64)

Figure 3.2. Summary of successfully synthesised ProTide analogue probes.

3.3 Synthesis of 6Yn- and ^{15}N-Metabolites

To investigate the utilisation of ProTide probes for intracellular metabolic conversion into their corresponding NAD^+ analogues *via* targeted metabolomics (see **Section 4.4.3**), the various metabolites that arise in the NAD^+ biosynthesis pathway were synthesised and used as purified stocks for optimisation of metabolomics methods. Given the innate challenges in synthesis of phosphorylated metabolites, in addition to the difficulties associated with execution and

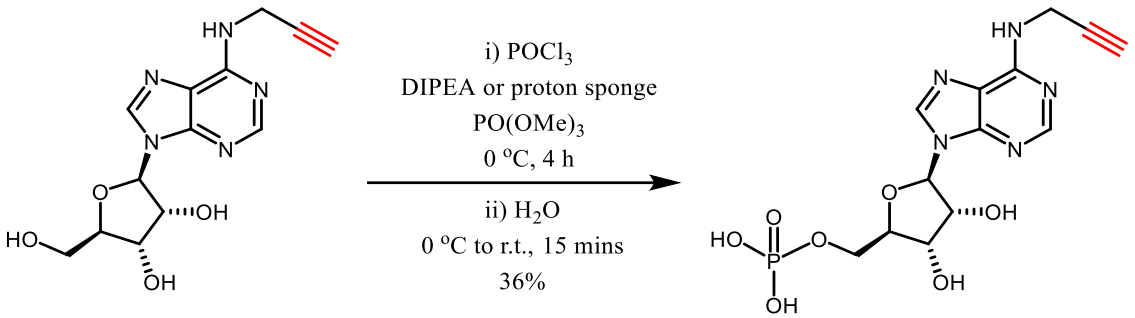
analysis of metabolomics experiments, the focus of metabolomics studies was primarily on the intracellular utilisation of the 6Yn-Pro (**47**) and ^{15}N-Pro (**64**) probes for NAD^+ biosynthesis.

Utilisation of 6Yn-Pro (**47**) and ^{15}N-Pro (**64**) in the NAD^+ pathway was deemed more informative than for the other ProTide probes. For ^{15}N-Pro (**64**), this was reasoned since ^{15}N-Pro (**64**) and its associated ^{15}N-AMP (**72**), ^{15}N-ATP (**73**) and ^{15}N-NAD^+ (**74**) metabolites are structurally identical to native AMP, ATP and NAD^+, respectively (see **Figure 3.4**, **Section 3.3.4**). Hence, this approach could be used to establish whether there are inherent limitations in utilising NAD^+ precursor probes for NAD^+ biosynthesis due to cellular metabolite dynamics, rather than due to the structural modifications present on the clickable analogues. Similarly, 6Yn-Pro (**47**), as predicted by molecular docking data (**Chapter 2**), was the clickable analogue most likely to be utilised in the pathway out of the four structural analogues, due to its small alkyne group and the alkyne group's position. Synthesis of metabolite analogues 6Yn-AMP (**30**), 6Yn-ATP (**40**), 6Yn-NAD^+ (**3**), and ^{15}N-AMP (**72**), ^{15}N-ATP (**73**), ^{15}N-NAD^+ (**74**), for subsequent use in metabolomics experiments (**Section 4.4.3**), was therefore attempted.

3.3.1 Synthesis of 6Yn-AMP and ^{15}N-AMP

3.3.1.1 Direct Phosphorylation at 5′OH

The first step in NAD^+ biosynthesis (**Figure 2.2**) involves conversion of adenosine or ProTide probes into AMP, therefore, 6Yn-AMP (**30**) and ^{15}N-AMP (**72**) were synthesised. Synthesis of AMP analogues *via* 5' phosphorylation of the corresponding adenosine analogues, without protection of 2' and 3' OH groups, is well established in the literature and has been performed in multiple published studies.[110,114,239] The approach typically involves coupling of adenosine to phosphoryl chloride ($POCl_3$) in the presence of a bulky base (**Scheme 3.10**), such as 'proton sponge' (**75**) (**Figure 3.3**), in dry $PO(OMe)_3$, and is strictly performed at 0 °C to avoid phosphorylation at the 2' and 3' OH groups. The reaction is then quenched by the addition of H_2O and AMP analogues are purified by reverse-phase high-performance liquid chromatography (HPLC) or anion exchange chromatography (AXC).

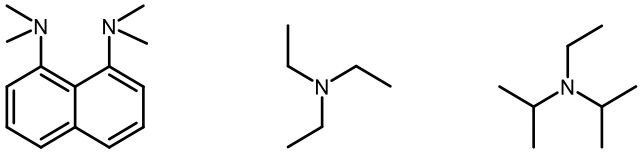


6Yn-Ad (25) **6Yn-AMP (30)**

Scheme 3.10. Synthesis of 6Yn-AMP (**30**) *via* direct 5' OH phosphorylation.

In a manner similar to ProTide synthesis, it was observed by LC-MS that performing the reaction at 0 °C resulted in negligible phosphorylation at 2' and 3' positions of 6Yn-Ad (**25**) (**Appendix Figure A.4**), thus protection of the 2' and 3' OH groups was not necessary. This observation agreed with the findings from established literature procedures for direct phosphorylation of 5' OH, without 2' and 3' OH protection.[110,114,239]

For AMP synthesis from adenosine, the presence of a bulky base, such as proton sponge (**75**), was required to neutralise *in situ* generated HCl, which can lead to product degradation, while simultaneously avoiding unwanted coupling to the highly reactive $POCl_3$. The presence of proton sponge, however, complicated purification of 6Yn-AMP (**30**) due to co-elution during reverse-phase purification. In addition, the low solubility of **75** in $PO(OMe)_3$ resulted in its precipitation in the reaction mixture when the solvent volume was reduced (<0.5 mL). To circumvent these issues, alternative bulky bases that were more soluble and easily separated during purification were pursued, such as triethylamine (NEt_3, **76**) and diisopropylethylamine (DIPEA, **77**) (**Figure 3.3**). By replacing proton sponge (**75**) with NEt_3 (**76**) it was established that NEt_3 (**76**) reacted with $POCl_3$, therefore no product was generated. On the other hand, attempting the reaction in the presence of DIPEA (**77**) revealed that it did not react with $POCl_3$ and conversion of 6Yn-Ad (**25**) to 6Yn-AMP (**30**) (and ^{15}N-Ad (**63**) to ^{15}N-AMP (**72**)) was successful. Further optimisation of the reaction revealed that distillation of $PO(OMe)_3$ was necessary for the reaction to proceed efficiently, with yields of <20% for 6Yn-AMP (**30**) before distillation rising to >35% after distillation.



Proton sponge (75) **NEt_3 (76)** **DIPEA (77)**

Figure 3.3. Structures of bulky bases tested for AMP analogue synthesis.

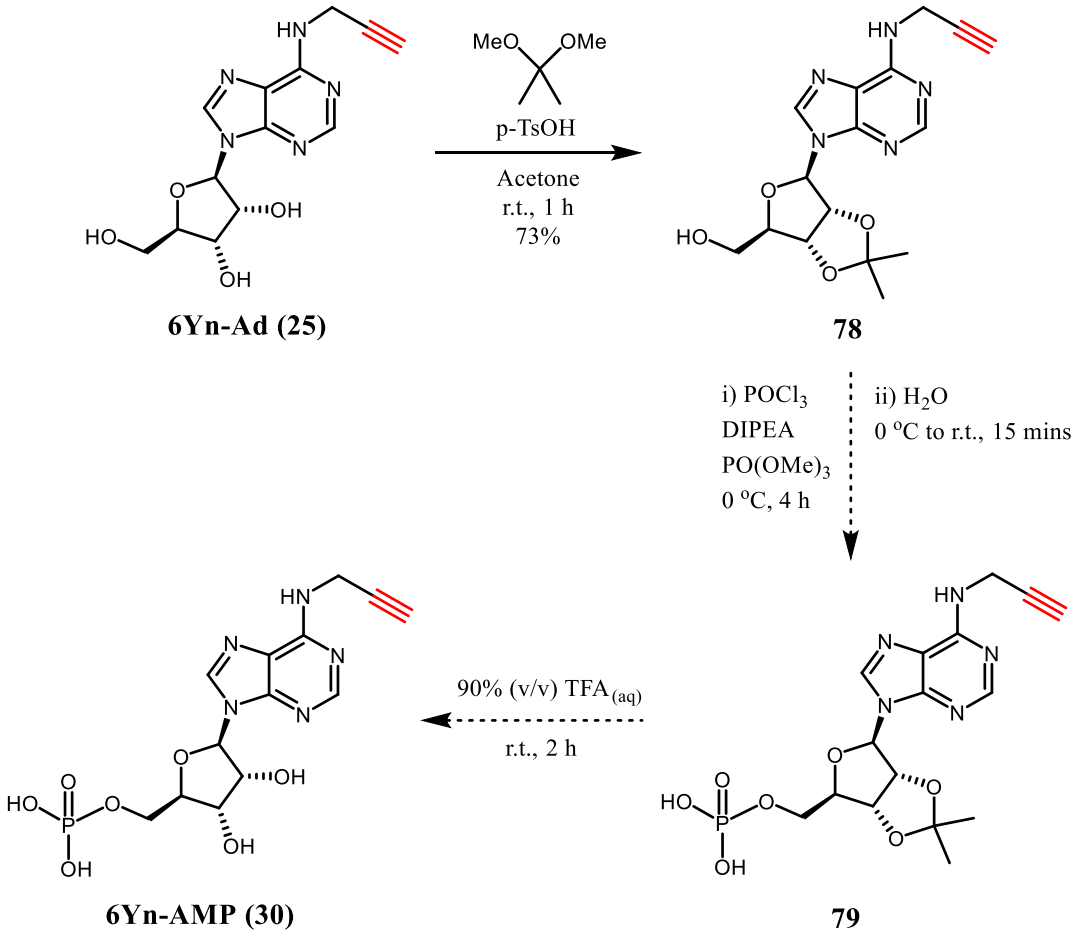
3.3.1.2 Purification via Reverse-phase and Anion Exchange Chromatography

Owing to the highly polar nature of the 6Yn-AMP (**30**) and ^{15}N-AMP (**72**) analogues, issues were encountered with their purification. When reverse-phase purification of both compounds was attempted at acidic pH using H_2O:acetonitrile (MeCN) solvent system (supplemented with 0.1% FA), both compounds co-eluted with the solvent front even at 2% (v/v) MeCN gradient. It was thus hypothesised that purification at basic pH might improve retention of the compounds on the column. For 6Yn-AMP (**30**), successful purification was achieved when attempted at basic pH using 25 mM ammonium bicarbonate (AMBIC):MeCN as the solvent system, due to improved retention. However, ^{15}N-AMP (**72**) still co-eluted with the solvent front and could not be successfully purified by reverse-phase. Considering this, purification of ^{15}N-AMP (**72**) by AXC was attempted and successfully performed with an increasing gradient of AMBIC (up to 0.4 M, **Section 6.1.3**). As a result of the high AMBIC concentration, however, multiple lyophilisation cycles were required to remove the salt (which gradually dissociates into ammonia (NH_3) and CO_2), taking at least two days to obtain pure ^{15}N-AMP (**72**) following purification.

3.3.1.3 Protection of 2' and 3' OH Groups Followed by 5' Phosphorylation

Although direct 5' phosphorylation proceeded relatively well for AMP analogue synthesis (36% yield for 6Yn-AMP (**30**)), protection of the 2' and 3' OH groups was considered to help improve isolated yields (**Scheme 3.11**). To test this, diol protection of 6Yn-Ad (**25**) with 2,2-dimethoxypropane was performed as described in the literature[223] (73% isolated yield for **78**), followed by 5' phosphorylation of **78** with $POCl_3$ to produce **79**. The attempted 5' phosphorylation, however, failed to proceed. This observation was surprising considering that 2' and 3' OH group protection with 2,2-dimethoxypropane should not result in steric hindrance around the 5' OH group of **78**. It was therefore hypothesised that 2' and 3' diol protection with 2,2-dimethoxypropane, resulting in the generation of a 5-membered ring merged to the ribose ring in **78**, forced the ribose ring to adopt a conformation that made the 5' OH group inaccessible for phosphorylation by $POCl_3$. An alternative OH group protection approach that

leads to individual OH group protection and thus avoids the formation of a 5-membered ring merged to ribose, such as the use of the TBDMS-Cl protecting group, may be able to overcome this issue, however, this was not investigated further.

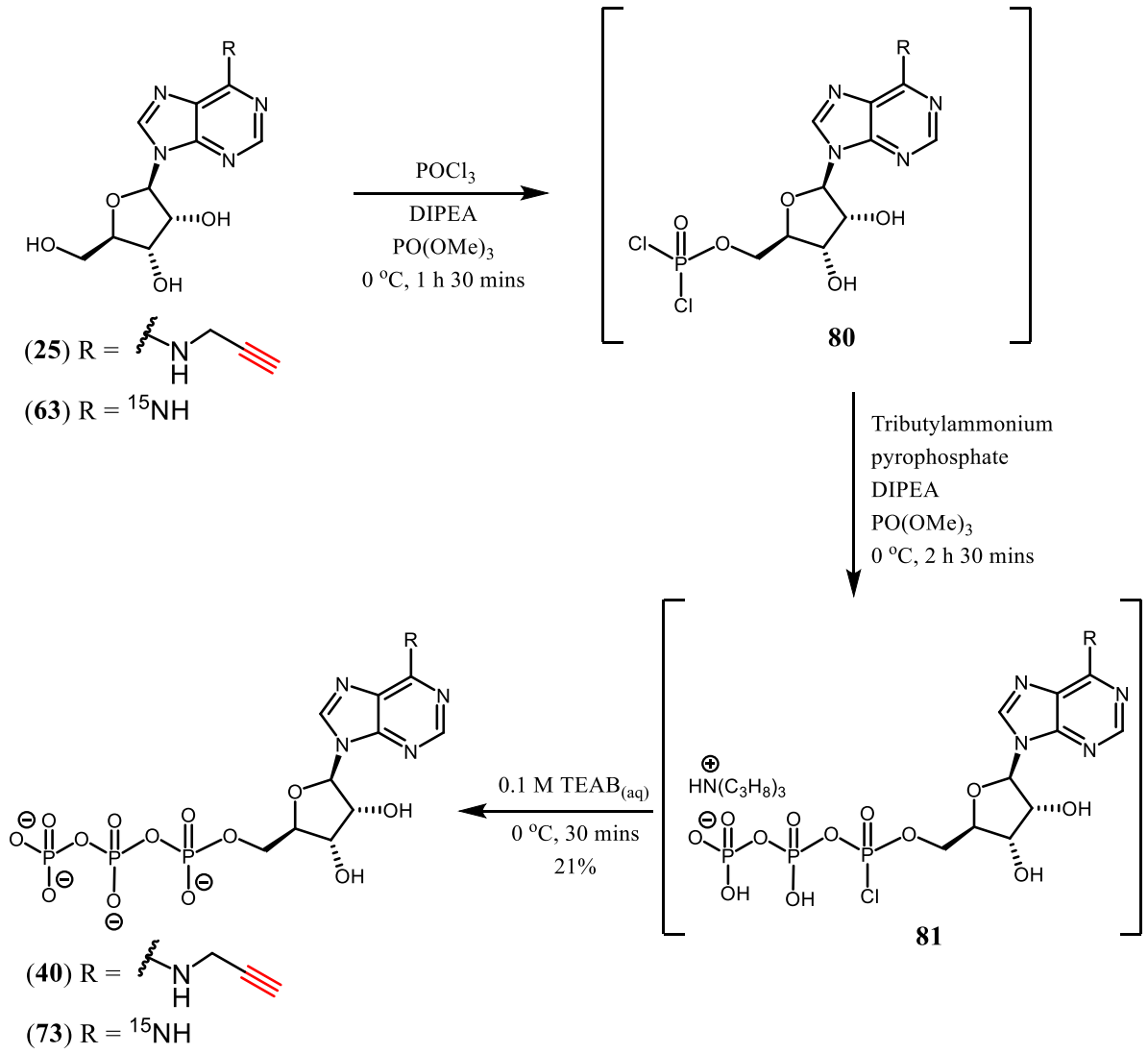


Scheme 3.11. Proposed three-step synthesis of 6Yn-AMP (**30**) *via* 2' and 3' diol protection.

3.3.2 Synthesis of 6Yn-ATP and ^{15}N-ATP Metabolites

3.3.2.1 Synthesis via Direct 5' Activation and Pyrophosphate Coupling

In the third step of the NAD^+ biosynthesis pathway ADP is converted into ATP (**Figure 2.2**), therefore, 6Yn-ATP (**40**) and ^{15}N-ATP (**73**) were synthesised next and used for method optimisation in metabolomics experiments (**Section 4.4.3**). Synthesis of the two ATP analogues was performed *via* activation of the 5' OH group of the corresponding adenosine analogues (**25**, **63**) with $POCl_3$ to intermediate **80** (**Scheme 3.12**). Tributylammonium pyrophosphate was then coupled to intermediate **80** to produce intermediate **81**, and **81** was subsequently hydrolysed in the presence of 0.1 M triethylammonium bicarbonate (TEAB) $_{(aq)}$ to generate the ATP analogues **40** and **73** (**Scheme 3.12**), as described in the literature.[240,241]



Scheme 3.12. Synthetic route for 6Yn-ATP (**40**) and ^{15}N-ATP (**73**).

In a similar manner to ProTide and AMP analogue synthesis, the reaction was very moisture-sensitive due to the presence of $POCl_3$ and the generation of activated phosphoryl chloride intermediates **80** and **81**. To maximise reaction yields, freshly distilled $PO(OMe)_3$ was therefore used for each reaction attempt.

Synthesis of ATP analogues using this approach was limited by the high costs of tributylammonium pyrophosphate (1 g ~ £150). A significant amount of the pyrophosphate was consumed by excess unreacted $POCl_3$ during the course of the reaction, therefore, a large excess of the pyrophosphate (6 eq.) was used to ensure efficient coupling to intermediate **80** for generation of intermediate **81**. In addition to this, to ensure sufficient activation of 5' OH with $POCl_3$, >50 mg of the corresponding adenosine starting material (**25**, **63**) were used per reaction, translating to ~540 mg of pyrophosphate for a single reaction attempt.

Nevertheless, reactions for both ATP analogues were successfully attempted. Coupling of $POCl_3$ (2 eq.) to **25** or **63** for generation of the corresponding activated intermediate **80** was performed at 0 °C for 1 h 30 mins, followed by subsequent coupling of tributylammonium pyrophosphate (6 eq. for 6Yn-ATP (**40**), 4 eq. for ^{15}N-ATP (**73**)) at 0 °C for 2 h 30 mins to produce intermediate **81**. Disappearance of starting material and generation of each ATP product was monitored by LC-MS, and quenching of each reaction was performed with 0.1 M $TEAB_{(aq)}$ at 0 °C for 30 mins.

3.3.2.2 Purification via Reverse-phase and Anion Exchange Chromatography

Purification of the two ATP analogues was challenging due to their extremely polar nature and inability of reverse-phase C18 columns to retain the products. Both 6Yn-ATP (**40**) and ^{15}N-ATP (**73**) were purified by AXC, however, this was challenging to perform due to slow elution of the ATP products and the need to apply a 100% elution gradient of 0.4 M AMBIC. Owing to the high salt concentration following elution and the slow degradation of AMBIC, multiple lyophilisation cycles were required to obtain each product. This led to a time gap of at least two days between purification of an ATP product and obtaining it free of solvent and salt.

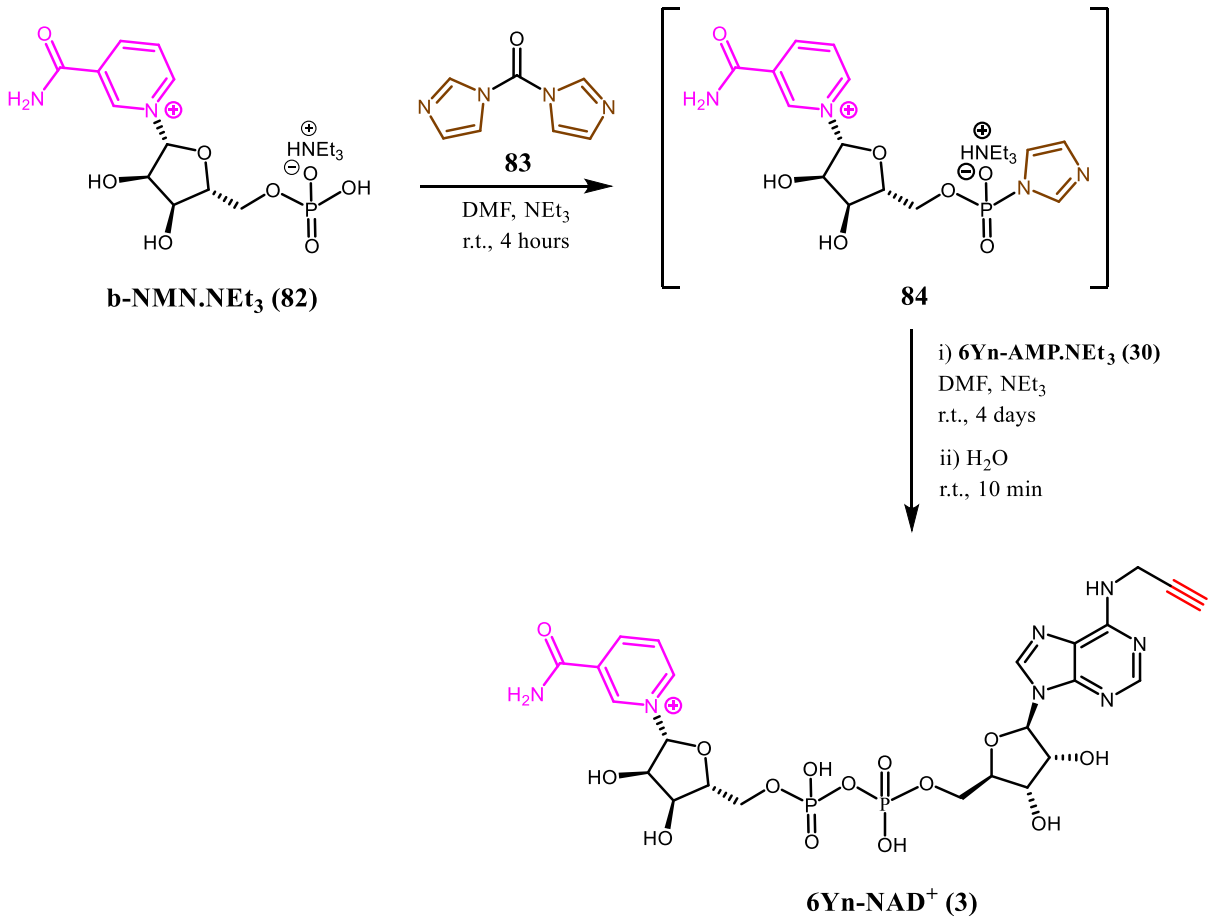
A notable observation for both purified ATP analogues was that they were both extremely hygroscopic and quickly absorbed moisture when exposed to air, which made them difficult to handle subsequently. Lyophilised ATP products were therefore stored under nitrogen at -20 °C to avoid absorption of moisture.

3.3.3 Synthesis of 6Yn-NAD$^+$ and ^{15}N-NAD$^+$

3.3.3.1 Synthesis of 6Yn-NAD$^+$

In the final step of NAD$^+$ biosynthesis, NAD$^+$ is synthesised from ATP (**Figure 2.2**). Since 6Yn-NAD$^+$ (**3**) and ^{15}N-NAD$^+$ (**74**) were necessary for optimisation of metabolomics experiments, the synthesis of both NAD$^+$ analogues was attempted.

Multiple approaches towards NAD$^+$ analogue synthesis have been described in the literature, as outlined by Wallrodt *et al.*[110], Carter-O'Connell *et al.*[114] and Du *et al.*[105]. For synthesis of 6Yn-NAD$^+$ (**3**), the procedure described by Wallrodt *et al.*[110] was initially attempted (**Scheme 3.13**). In this approach, initial activation of triethylammonium β-NMN salt (β-NMN.NEt_3, **82**) was attempted *via* coupling to 1,1'-carbonyldiimidazole (CDI, **83**) for 4 hours to produce intermediate **84**, followed by subsequent coupling to 6Yn-AMP (**30**), over 4 days, to generate product 6Yn-NAD$^+$ (**3**).

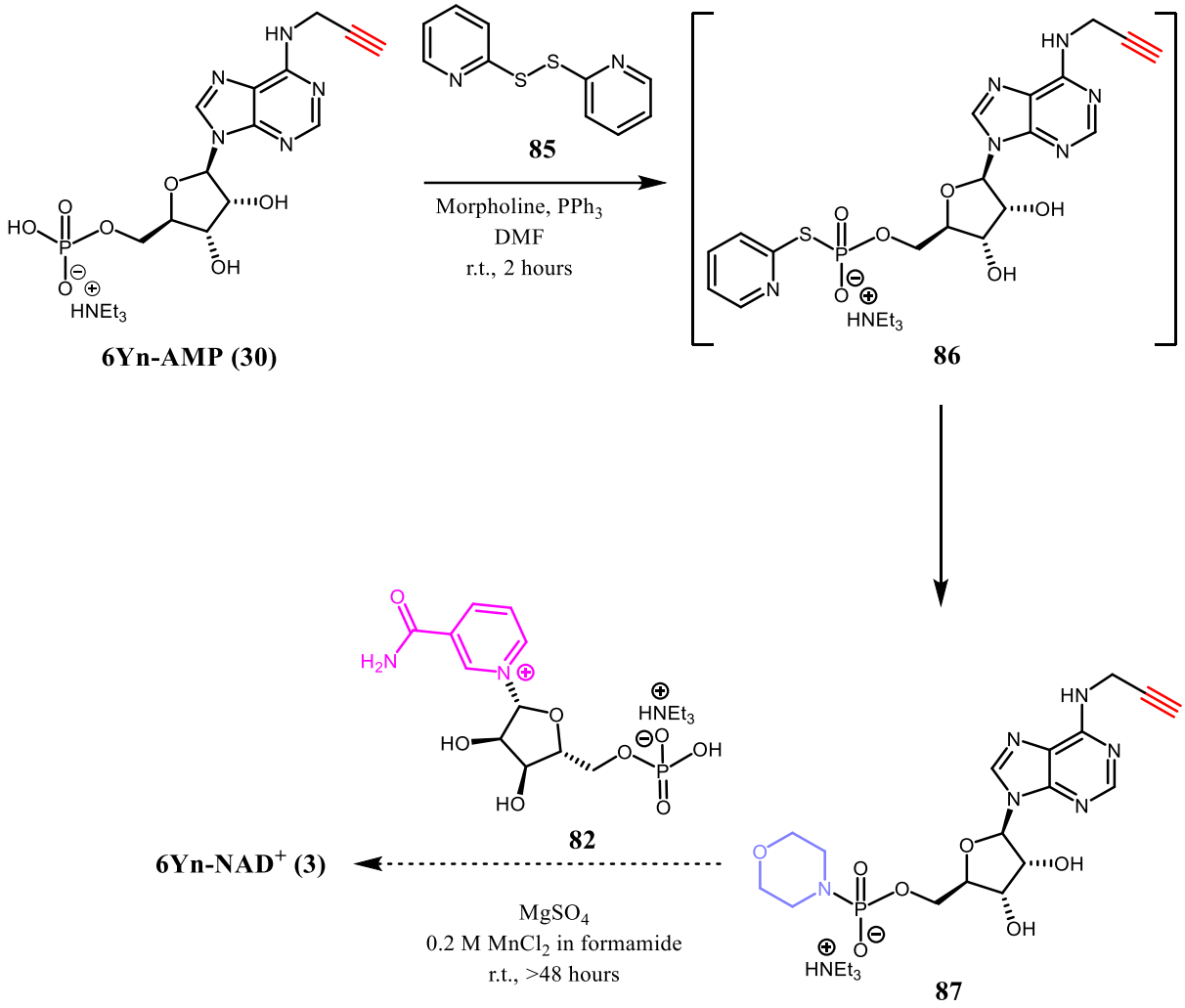


Scheme 3.13. Proposed two-step synthesis of 6Yn-NAD$^+$ (**3**) *via* activation of b-NMN.NEt$_3$ (**82**) with CDI (**83**).

Despite multiple optimisation attempts, such as optimisation of the reaction time, solvent volume and equivalents of reagents used, activation of β-NMN.NEt$_3$ (**82**) progressed with little efficiency in all cases. This was evidenced by LC-MS analysis, which revealed no/trace amounts of intermediate **84** (m/z 411) in the reaction mixture. It was hypothesised that perhaps the activation reaction proceeded but that intermediate **84** hydrolysed during LC-MS analysis. Thus, subsequent coupling of **84** with 6Yn-AMP (**30**) was attempted in all reaction attempts. However, only trace amounts of 6Yn-NAD$^+$ (**3**) were observed by LC-MS analysis in all cases, suggesting that initial activation of **82** did not proceed efficiently. Given the challenges encountered with coupling β-NMN.NEt$_3$ (**82**) and **83**, it was reasoned that either CDI was not an effective reagent for initial activation of the phosphoryl group of β-NMN.NEt$_3$ (**82**), or a key step in the published procedure had been accidentally omitted.

Subsequent synthesis of 6Yn-NAD$^+$ (**3**) was attempted by following the approach described by Carter-O'Connell *et al.*[114] (**Scheme 3.14**). In this approach, 6Yn-AMP (**30**) was activated by 2,2'-dipyridyldisulfide (DPS, **85**) to produce activated intermediate (**86**) for subsequent *in situ*

coupling to morpholine to yield 6Yn-AMP morpholidate (**87**). In the final step, **87** was coupled to β-NMN.NEt_3 (**82**) to generate product 6Yn-NAD^+ (**3**).



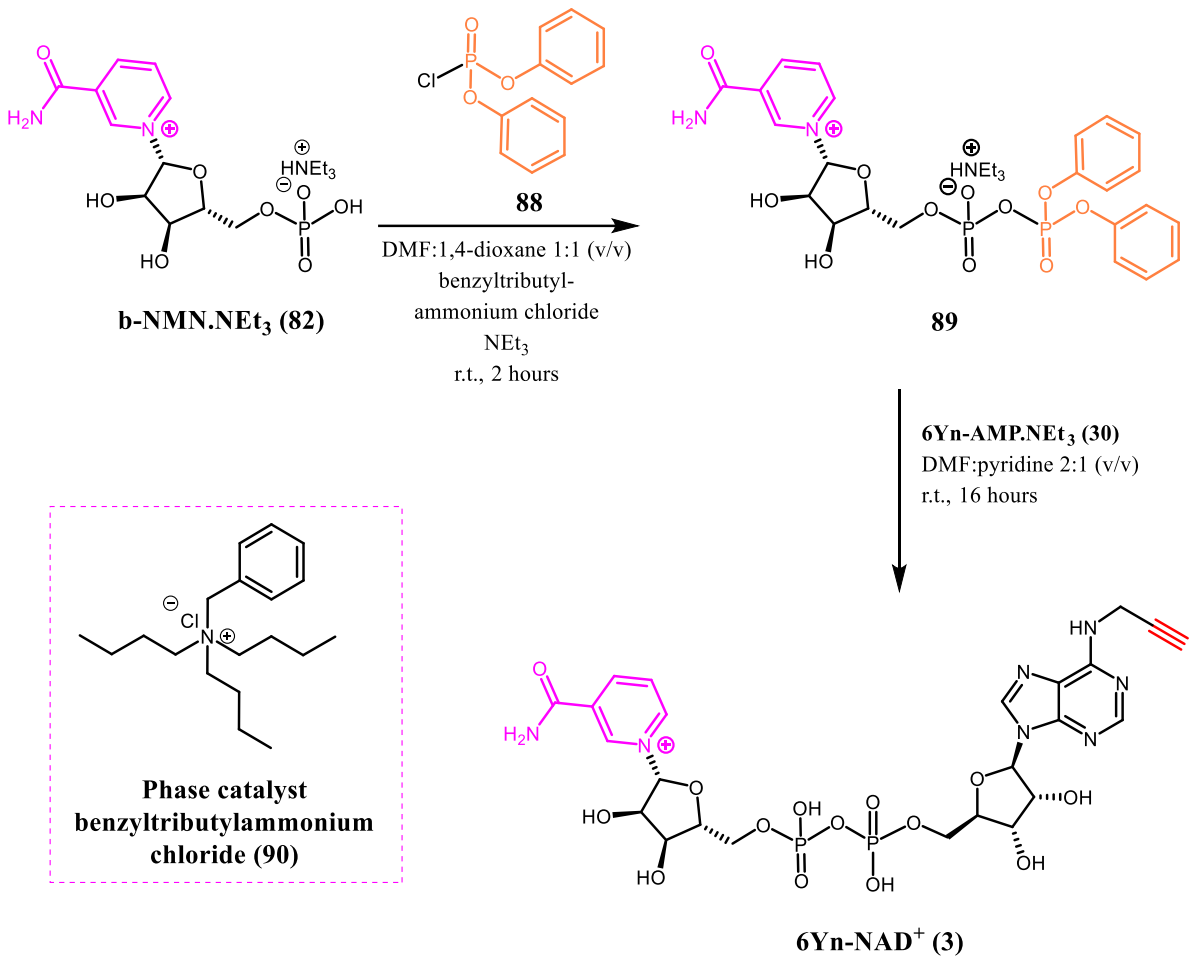
Scheme 3.14. Proposed synthetic route for 6Yn-NAD^+ (**3**) *via* coupling to DPS (**85**) and generation of 6Yn-AMP morpholidate (**87**).

An initial attempt at generating 6Yn-AMP morpholidate (**87**) *via* activation of 6Yn-AMP (**30**) with DPS (**85**) was successful, as evidenced by LC-MS analysis. **87** was subsequently purified by precipitation with MeCN, and LC-MS analysis revealed the presence of a single peak (m/z 455), corresponding to product **87** (**Appendix Figure A.5**). Despite the absence of impurities, the attempted subsequent coupling of product **87** and β-NMN.NEt_3 (**82**) did not proceed.

It was noted that 6Yn-AMP morpholidate (**87**) exhibited relatively high stability, as evidenced by its ability to withstand hydrolysis during LC-MS analysis. It was reasoned that, owing to this high stability, β-NMN.NEt_3 was unable to displace the morpholine moiety in product **87**. Thus, it was hypothesised that, instead of generating the morpholidate product **87**, a more

optimal approach towards NAD^+ synthesis might be to bypass the morpholidate product generation step altogether and attempt direct coupling of β-NMN.NEt_3 (**82**) with intermediate (**86**) (akin to the CDI coupling approach in **Scheme 3.13**). However, direct coupling of **86** and **82** was not attempted, therefore the feasibility of the approach was not investigated.

Synthesis of 6Yn-NAD^+ (**3**) was lastly explored by utilising the approach described by Du *et al.*[105]. In this procedure, product **3** was generated in a two-step reaction (**Scheme 3.15**).



Scheme 3.15. Proposed synthetic route for 6Yn-NAD^+ (**3**) *via* activation of b-NMN.NEt_3 (**82**) with diphenyl phosphoryl chloride (**88**).

In the proposed route, β-NMN.NEt_3 (**82**) was initially activated *via* coupling to diphenyl phosphoryl chloride (**88**) to generate intermediate product **89**, in the presence of the phase catalyst benzyltributylammonium chloride (**90**). **89** was then coupled to 6Yn-AMP (**30**) to produce 6Yn-NAD^+ (**3**).

When attempted, initial activation of β-NMN.NEt_3 (**82**) proceeded efficiently within 3 hours, both in the presence and absence of phase catalyst **90**, as evidenced by the emergence of a peak

for intermediate product **89** (m/z 567) during LC-MS analysis. Partial purification of **89** was then performed by precipitation in diethyl ether (Et_2O), and the product was subsequently coupled to 6Yn-AMP (**30**) in DMF:pyridine 2:1 (v/v) for 16 hours, to generate 6Yn-NAD^+ (**3**).

Monitoring of the reaction by LC-MS revealed that the coupling reaction between **89** and **30** was complete within 16 hours, which was of significantly shorter duration than for the routes proposed by Wallrodt *et al.*[110] and Carter-O'Connell *et al.*[114], where reaction times of >3 days were required. Furthermore, the approach by Du *et al.*[105] was the only one of the three approaches tested which resulted in successful synthesis of 6Yn-NAD^+ (**3**). The robustness of the method was further confirmed by successfully synthesising 6Yn-NAD^+ (**3**) in multiple attempts as well as its successful utilisation for the synthesis of C2-modified NAD^+ analogues (not discussed in this thesis).

3.3.3.2 Purification of 6Yn-NAD^+

In published literature procedures, the purification of NAD^+ analogues has been typically performed by reverse-phase HPLC or AXC.[105,110,114] Reverse-phase purifications are suitable for NAD^+ analogues incorporating larger clickable groups, such as in NAD^+ analogues **7** and **8**, since these moieties increase their hydrophobicity, which improves compound retention on a C18 column. On the other hand, for highly polar analogues such as 6Yn-NAD^+ (**3**), purification by reverse-phase at acidic pH (<7) is difficult to achieve owing to their poor retention. When purification of 6Yn-NAD^+ (**3**) was attempted in the presence of 0.1% FA, the product co-eluted with the solvent front.

Although purification by reverse-phase HPLC at basic pH (>7), or AXC at basic pH, has been previously described in the literature,[110] a major concern with those approaches was that NAD^+ analogues rapidly hydrolyse at pH levels >7. Thus, purification at basic pH was expected to lead to substantial/complete product hydrolysis, especially for small scale reactions (typically, 3.8 mg of 6Yn-AMP (**30**) were used for 6Yn-NAD^+ (**3**) synthesis in a reaction attempt). The use of AXC for purification of 6Yn-NAD^+ (**3**) was also deemed unsuitable based on the observations from AXC purifications of 6Yn-ATP (**40**), ^{15}N-ATP (**73**) and ^{15}N-AMP (**72**). The purification process was slow and multiple lyophilisation cycles were required to remove high salt concentrations. Given the high risk of product hydrolysis arising from the purification of 6Yn-NAD^+ (**3**) by reverse-phase (basic pH) or AXC (basic pH), purification using these methods was not performed. Instead, a partial purification step was performed by precipitating the product in Et_2O. Considering that 6Yn-NAD^+ (**3**) was used only as a standard stock solution

for optimisation of LC-MS methods for metabolomics experiments (S**ection 4.4**), trace amounts of impurities remaining following precipitation were not a concern as these did not co-elute with 6Yn-NAD^+ (**3**).

3.3.3.3 Attempted Synthesis of ^{15}N-NAD^+

Synthesis of ^{15}N-NAD^+ (**74**) was attempted employing the reaction conditions that were used for synthesis of 6Yn-NAD^+ (**3**) (**Scheme 3.15**), however, despite multiple reaction attempts, coupling of ^{15}N-AMP (**72**) to activated intermediate **89** did not take place. This was attributed to the observation that ^{15}N-AMP (**72**) was insoluble in the DMF:pyridine solvent mixture, likely as a result of its increased hydrophilicity due to exposure of the polar N6 amine group.

3.3.4 Summary of 6Yn- and ^{15}N-Metabolites Synthesised

Synthesis and purification of phosphorylated metabolite analogues for the 6Yn- and ^{15}N-metabolite series was attempted and successfully performed for five metabolites (^{15}N-AMP (**72**), ^{15}N-ATP (**73**), 6Yn-AMP (**30**), 6Yn-ATP (**40**), 6Yn-NAD^+ (**3**), **Figure 3.4**). The synthesised metabolites were then used for optimisation of LC-MS methods in metabolomics experiments (**Section 4.4**).

Despite multiple attempts, synthesis of metabolite ^{15}N-NAD^+ (**74**) was unsuccessful, which was attributed to the low solubility of the starting material ^{15}N-AMP (**72**) in the reaction solvent used. Overall, the successfully synthesised five metabolite analogues were of sufficient amounts for use in metabolomics experiments.

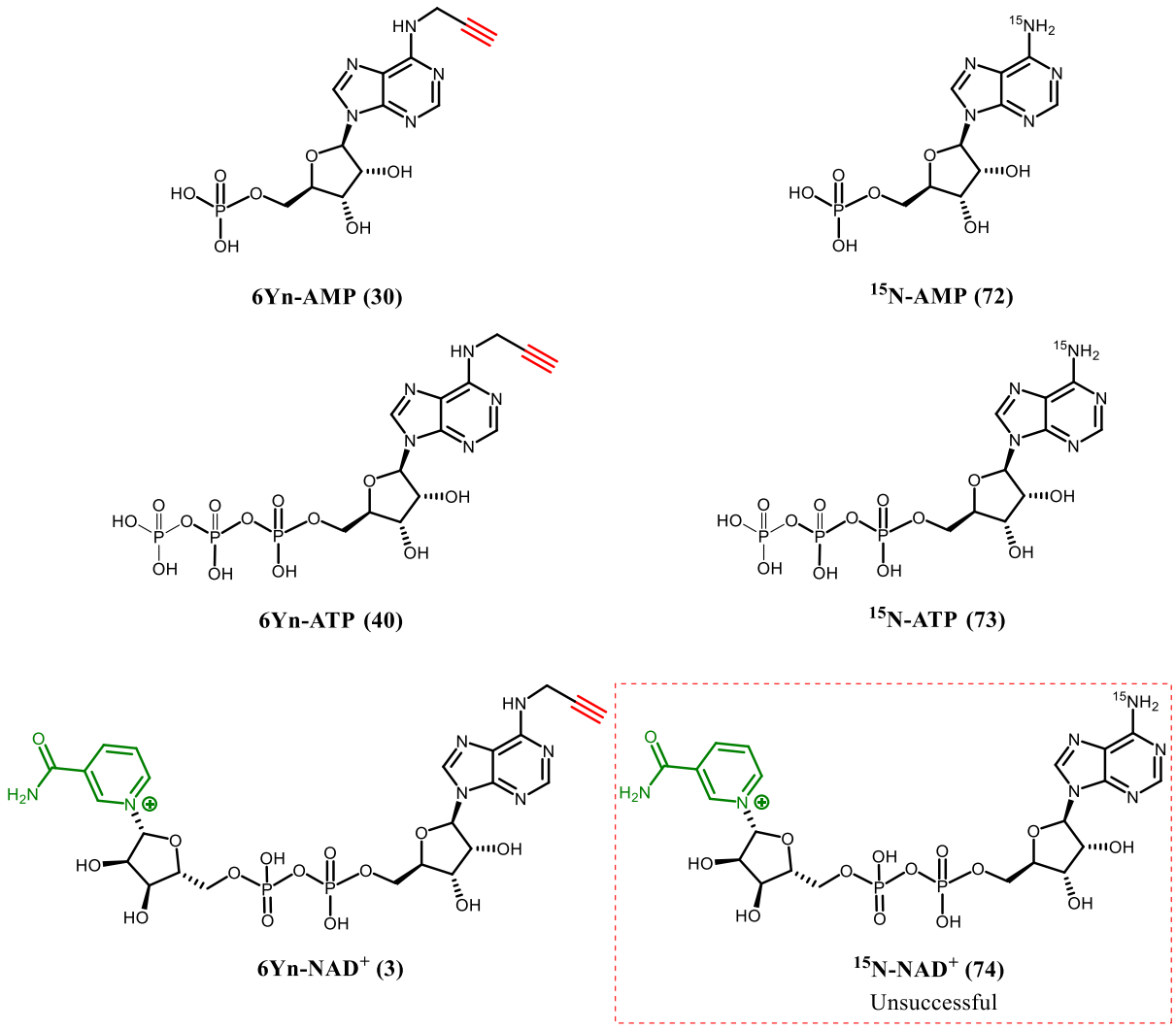


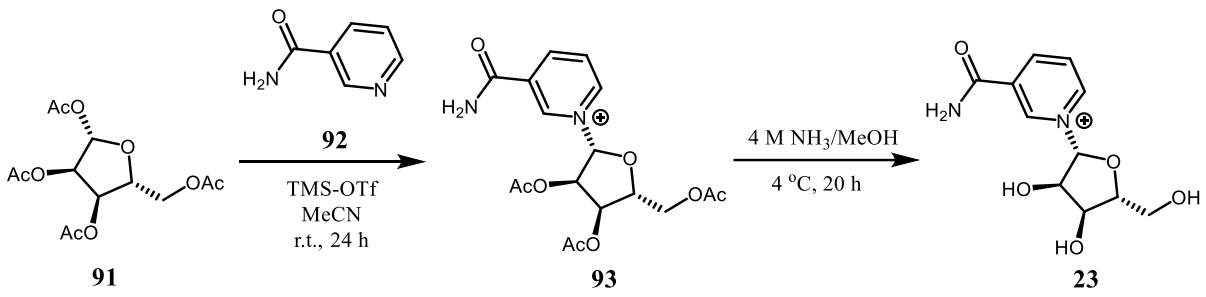
Figure 3.4. Summary of 6Yn- and ^{15}N- phosphorylated metabolites attempted for synthesis. The synthesis of ^{15}N-NAD$^+$ (**74**) was unsuccessful.

3.4 Synthesis of the NAD$^+$ Precursors NR and NRH

Supplementation of cells with the NAD$^+$ precursors NR (**23**) and NRH (**24**) has been shown in literature studies to result in an increase in intracellular NAD$^+$ levels through a boost of β-NMN/NMNH levels. [189,190,205-209] As a result, the two NAD$^+$ precursors NR (**23**) and NRH (**24**) were synthesised for use in subsequent biological experiments.

3.4.1 Synthesis of NR

Synthesis of the NAD$^+$ precursor NR (**23**) was performed in a two-step reaction (**Scheme 3.16**) by adapting a previously described literature procedure.[242]

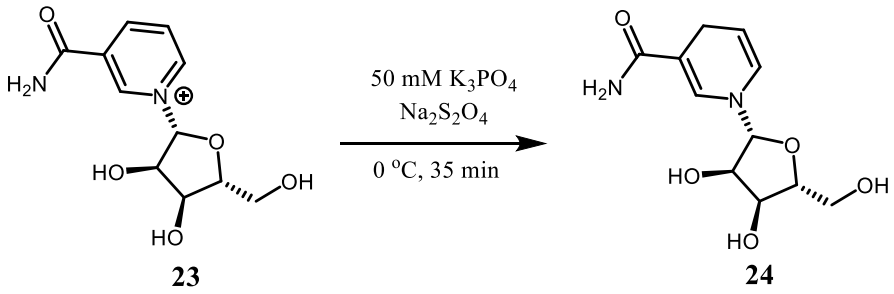


Scheme 3.16. Synthetic route for NR (**23**).

In the first step, β-D-ribofuranose 1,2,3,5-tetraacetate was reacted with nicotinamide **92** in the presence of TMS trifluoromethanesulfonate (TMS-OTf) to generate the acetyl protected nicotinamide riboside **93**. Following purification by reverse-phase, hydrolysis of the acetyl groups was performed in the presence of 4 M NH_3 in MeOH at 4 ˚C and subsequently purified by reverse-phase with 0.1% FA to obtain NR (**23**) (the product was found to hydrolyse at pH levels >7). It was noted that NR (**23**) was very hygroscopic, therefore, to avoid hydrolysis of the nicotinamide moiety during storage, **23** was stored under nitrogen at -20 ˚C.

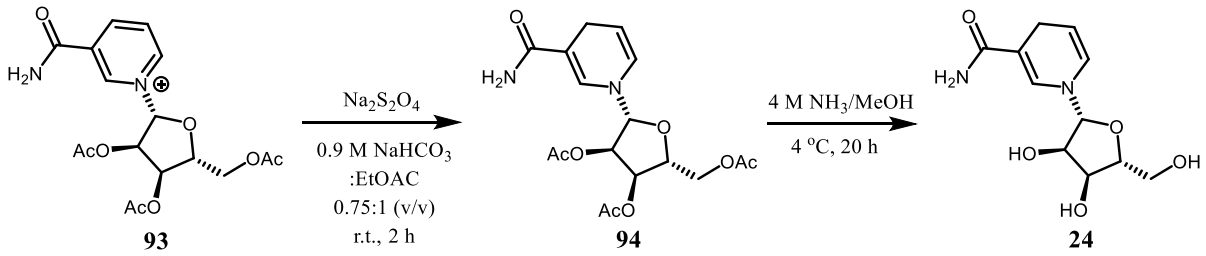
3.4.2 Synthesis of NRH

Synthesis of the NAD^+ precursor NRH (**24**) has been previously described in the literature from NR (**23**) in a one-step reduction reaction (**Scheme 3.17**).[205]



Scheme 3.17. Synthesis of NRH (**24**) *via* reduction of NR (**23**).

Initial synthesis of NRH (**24**) was attempted *via* direct reduction of NR (**23**) in the presence of sodium dithionite ($Na_2S_2O_4$) in 50 mM $K_3PO_{4\ (aq.)}$ solution (**Scheme 3.17**). Monitoring of the reaction by LC-MS indicated consumption of NR (**23**), however, formation of product NRH (**24**) was not observed, implying that NR (**23**) underwent hydrolysis. An alternative route for NHR (**24**) synthesis was therefore proposed (**Scheme 3.18**), which was adapted from a literature procedure employed for the synthesis of amino acid-conjugated NR derivatives.[243]



Scheme 3.18. Two-step synthesis of NRH (**24**).

In this route, acetyl protected NR (**93**) was first reduced to acetyl protected NRH (**94**), followed by subsequent hydrolysis of the acetyl groups in 4 M NH_3 in MeOH to generate **24**. It was reasoned that since **93** was significantly less hygroscopic than NR (**23**), the nicotinamide moiety was less likely to undergo hydrolysis and more likely to undergo reduction to **94**. Furthermore, generation of **94** was expected to improve product yield following the subsequent acetyl deprotection in 4 M NH_3 in MeOH, since the reduced nicotinamide moiety in **94** was not prone to hydrolysis by NH_3. In addition, purification of **94** by reverse-phase prior to its reduction to **24** was not required, unlike for **23**, since product **94** was successfully extracted in EtOAc from the excess inorganic reagents in the reaction mixture. By employing this approach, NRH (**24**) was successfully synthesised.

3.5 Conclusions

In this chapter, the successful synthesis of four clickable alkyne/azide adenosine analogues (**25**-**28**) and of a ^{15}N-isotopically labelled adenosine analogue (**63**) (**Figure 3.1**) was described (**Sections 3.1.1 – 3.1.6**). These were used as starting materials for the synthesis of the corresponding ProTide probes (**47**-**50**, **64**) (**Figure 3.2**), described in **Section 3.2.2**, which were used for biological validation in **Chapter Four**. In addition, the successful synthesis of five phosphorylated metabolites of the 6Yn- and ^{15}N- series (**Figure 3.4**) was described (**Sections 3.3.1 – 3.3.3**), which were applied for optimisation of metabolomics experiments in **Chapter Four**. Finally, the NAD^+ precursors NR (**23**) and NRH (**24**) were synthesised, and their effect on intracellular native NAD^+ and NAD^+ analogue levels in supplemented cells was investigated by metabolomics.

Chapter 4 Biological Validation of Clickable NAD^+ Precursor Probes

In this chapter, the four clickable ProTide probes (**47**-**50**) and two clickable adenosine analogues (6Yn-Ad (**25**), 2Yn-Ad (**26**)), synthesised in **Chapter Three**, were brought forward for biological validation in live cells. Initial validation of the probes was performed by IGF, which demonstrated widespread protein labelling in multiple cell lines (MDA-MB-231, MDA-MB-435, HEK293T, T47D) following treatment with each ProTide probe. Treatment of cells with 6Yn-Ad (**25**) and 2Yn-Ad (**26**), however, failed to reproduce protein labelling previously reported in two separate studies, the origin of which was uncovered in IGF experiments, described in this chapter, to be non-specific and unrelated to probe activity. Despite the lack of intracellular protein labelling following treatment with 6Yn-Ad (**25**) by IGF, metabolomics experiments revealed that both NAD^+ precursors, 6Yn-Ad (**25**) and 6Yn-Pro (**47**), were successfully utilised throughout the entire NAD^+ biosynthesis pathway for intracellular conversion into 6Yn-NAD^+ (**3**). In subsequent proteomics experiments, it was confirmed that 6Yn-Pro (**47**) treatment resulted in labelling of automodified PARP1 as well as of multiple known ADP-ribosylation targets. These findings confirmed the suitability of intracellular 6Yn-NAD^+ (**3**), derived from cell-permeable 6Yn-NAD^+ precursors, to be employed by PARPs for intracellular labelling of ADP-ribosylated proteins.

4.1 Importance of Studying ADP-ribosylation Intracellularly

4.1.1 Identification of Physiological ADP-ribosylation Targets

Over the past decade, novel approaches have been developed for studying ADP-ribosylation and identification of the protein targets it is found on. These include the development of functionalised NAD^+ analogues[101-119] (**Section 1.2**) and enzymatic and chemical approaches for facilitating the identification of modified sites[95-100,151-164] (**Section 1.4**) by tandem mass spectrometry methods. The newly developed methodologies, however, have largely focused on the identification of ADP-ribosylation targets in cell lysates or assays involving recombinant proteins. Although current methodologies have greatly expanded the scope of novel ADP-ribosylation targets, they provide little opportunity to study the dynamics of this modification in a live cell environment and to identify physiologically ADP-ribosylated proteins in their native environment.

Overcoming these limitations could, in principle, be achieved *via* the development of tools that allow for studying intracellular ADP-ribosylation. One such tool being explored in this chapter was the use of the cell-permeable NAD^+ precursor analogue 6Yn-Pro (**47**), with key objectives being to establish whether the probe could be used to identify upregulated (e.g. due to oxidative stress by H_2O_2) as well as baseline ADP-ribosylation levels in the absence of cellular stress. This was explored *via* a combination of biochemical techniques and mass spectrometry-based metabolomics and proteomics analyses, and the relevant data is discussed in this chapter.

4.1.2 Monitoring Live Cell Dynamics of Physiological ADP-ribosylation

Studying ADP-ribosylation dynamics intracellularly *via* confocal fluorescence microscopy is essential to better understanding the compartmentalisation of the modification as well as its role in different cellular processes. The technique has been applied for visualisation of ADP-ribosylated proteins in fixed cells with NAD^+ analogues following transient permeabilisation with Triton X-100 and staining with fluorescent dyes (see **Section 1.2.5**).[107-110] Unfortunately, cell fixing induces cell death therefore dynamic monitoring of protein compartmentalisation is not possible. In addition, the process of membrane permeabilisation likely induces significant cellular stress, thus making it difficult to study endogenous ADP-ribosylation. It was hypothesised that a cell-permeable NAD^+ precursor incorporating an azide group, such as probe 6Az-Pro (**50**), that can be captured intracellularly *via* SPAAC[140,141] (**Table 1.3**) could overcome this limitation. It was therefore important to establish whether cell treatment with 6Az-Pro (**50**) could lead to intracellular generation of the corresponding NAD^+ analogue and subsequent ADP-ribosylation.

4.1.3 Profiling of Intracellular PARP Targets

Target profiling of PARPs is pivotal for studying the cellular processes they are involved in and elucidating their roles in the development of diseased phenotypes. Although this has been performed in cell lysates with recombinant PARP mutants and 'bumped' NAD^+ analogues (see **Section 1.2.5.2**),[114-119] proteome-wide target profiling of PARPs has not been previously attempted in living cells. Limitations of performing ADP-ribosylation PARP target profiling in cell lysates include a PARP protein potentially modifying non-endogenous protein targets, such as those residing in separate compartments to the PARP of interest in an intact cell. Likewise, endogenous PARP targets might be 'missed' under non-physiological conditions.

It was hypothesised that the use of 'bumped' NAD^+ precursor analogues for intracellular generation of 'bumped' NAD^+ analogues, such as 8But-Yn-NAD^+ (**14**) from the precursor

probe 8But-Yn-Pro (**49**), could be applied for physiological PARP target profiling thus bypassing these potential drawbacks. Given that the viability of the approach was supported by molecular docking data (**Chapter Two**), which predicted utilisation of 8But-Yn-AMP (**32**) in NAD^+ biosynthesis for intracellular production of 8But-Yn-NAD^+ (**14**), it was important to determine whether the same results translated to *in vitro* experiments involving cell treatment with 8But-Yn-Pro (**49**).

4.2 Evaluation of Previous Studies with 6Yn-Ad, 2Yn-Ad and 6Yn-Pro

4.2.1 Protein Labelling Following 6Yn-Ad Treatment

The NAD^+ biosynthesis pathway is the major source of intracellular NAD^+,[183,184] which utilises adenosine as the starting material into a series of phosphorylation reactions to produce the relevant metabolites and ultimately NAD^+ (**Figure 4.1**). Given that adenosine is membrane permeable, it had been proposed in previous studies[164,185] that supplementing cells with clickable adenosine analogues could lead to their intracellular conversion into the corresponding NAD^+ analogues, and thus lead to intracellular ADP-ribosylation.

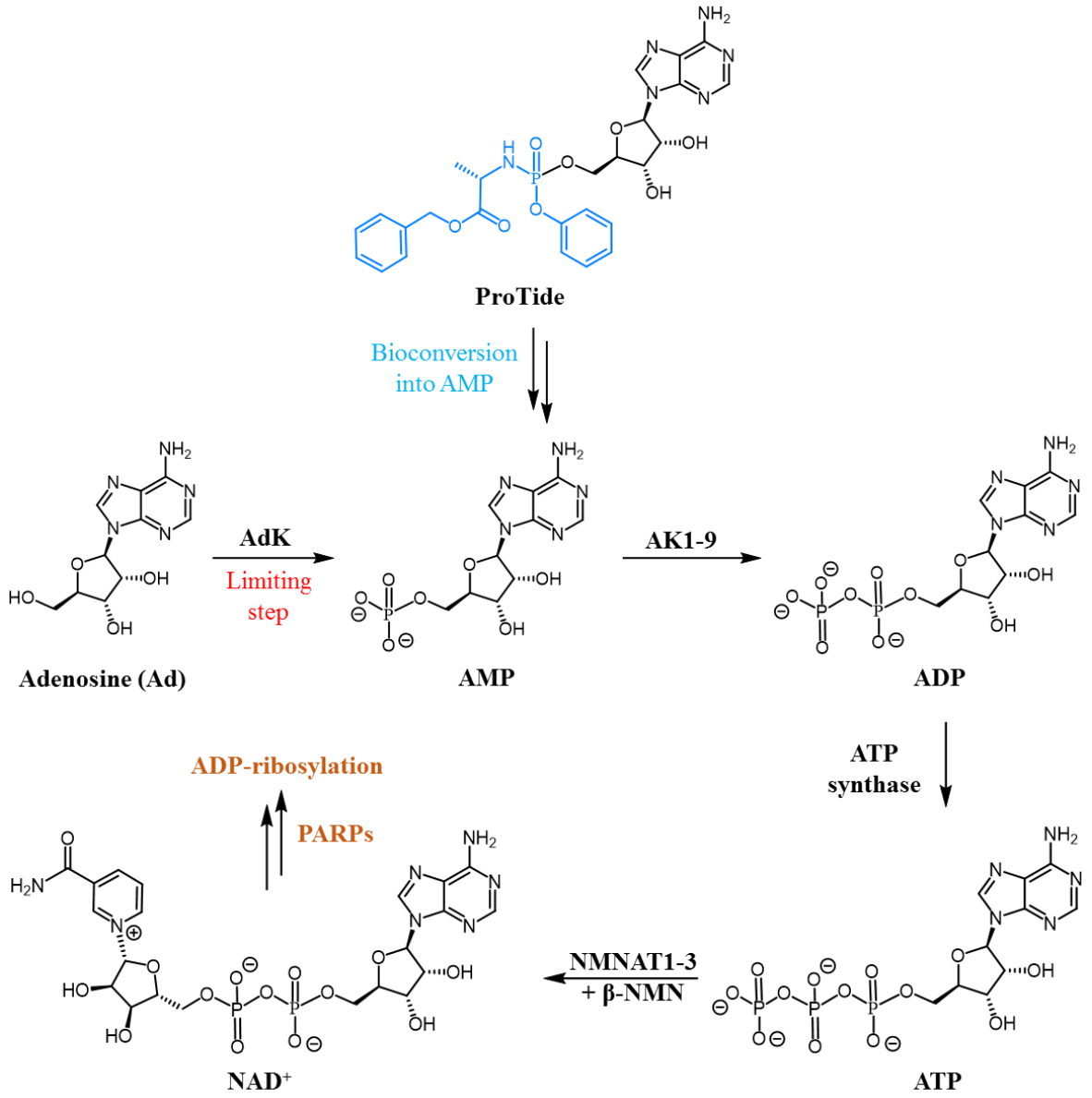


Figure 4.1. NAD^+ biosynthesis pathway starting from adenosine or adenosine ProTide prodrug. ProTide prodrug (ProTide moiety is highlighted in blue) is converted into AMP through a series of enzymatic and chemical steps (see **Figure 1.4**) and adenosine is converted into AMP by AdK. ADP is subsequently produced from AMP by AK1-9 and converted into ATP by ATP synthase. In the final step, ATP is converted into NAD^+ by NMNAT1-3. NAD^+ is then used by PARPs for ADP-ribosylation.

The first study to look at the feasibility of this approach was performed by Westcott *et al.*, where HeLa and HEK293T cells were treated for 1 h with DMSO or 6Yn-Ad (**25**) (also known as N^6pA) or co-treated with 6Yn-Ad (**25**) and olaparib (Ola)/3-aminobenzamide (ABA).[164] Following cell lysis and capturing of labelled proteins by CuAAC (**Table 1.3**), protein labelling was analysed by IGF. Under those experimental conditions, Westcott *et al.* observed that 6Yn-Ad (**25**) resulted in substantial protein labelling in HeLa cells, which disappeared upon

treatment with the PARP inhibitors ABA and olaparib (**Figure 4.2A**).[164] This led to the reasoning that all labelled proteins were ADP-ribosylated proteins, arising from 6Yn-NAD^+ (**3**), and that PARP1 and/or PARP2 were primarily responsible for this, given that olaparib is a potent inhibitor of PARP1 and PARP2. However, when we tested the same experimental conditions in breast cancer MDA-MB-231 cells, the data shown in Westcott *et al.* (**Figure 4.2A**)[164] could not be reproduced. Despite multiple attempts, no protein labelling was observed following 6Yn-Ad (**25**) treatment when compared to the DMSO control (**Figure 4.2B** and **4.2C**). This led to the conclusion that treatment with probe 6Yn-Ad (**25**) did not result in sufficient protein labelling to be detected by IGF. Consequently, this raised some concerns about the nature of the protein labelling that Westcott *et al.*[164] had observed following cell treatment with 6Yn-Ad (**25**). Particularly, we questioned how olaparib/ABA treatment could result in complete disappearance of all protein bands.

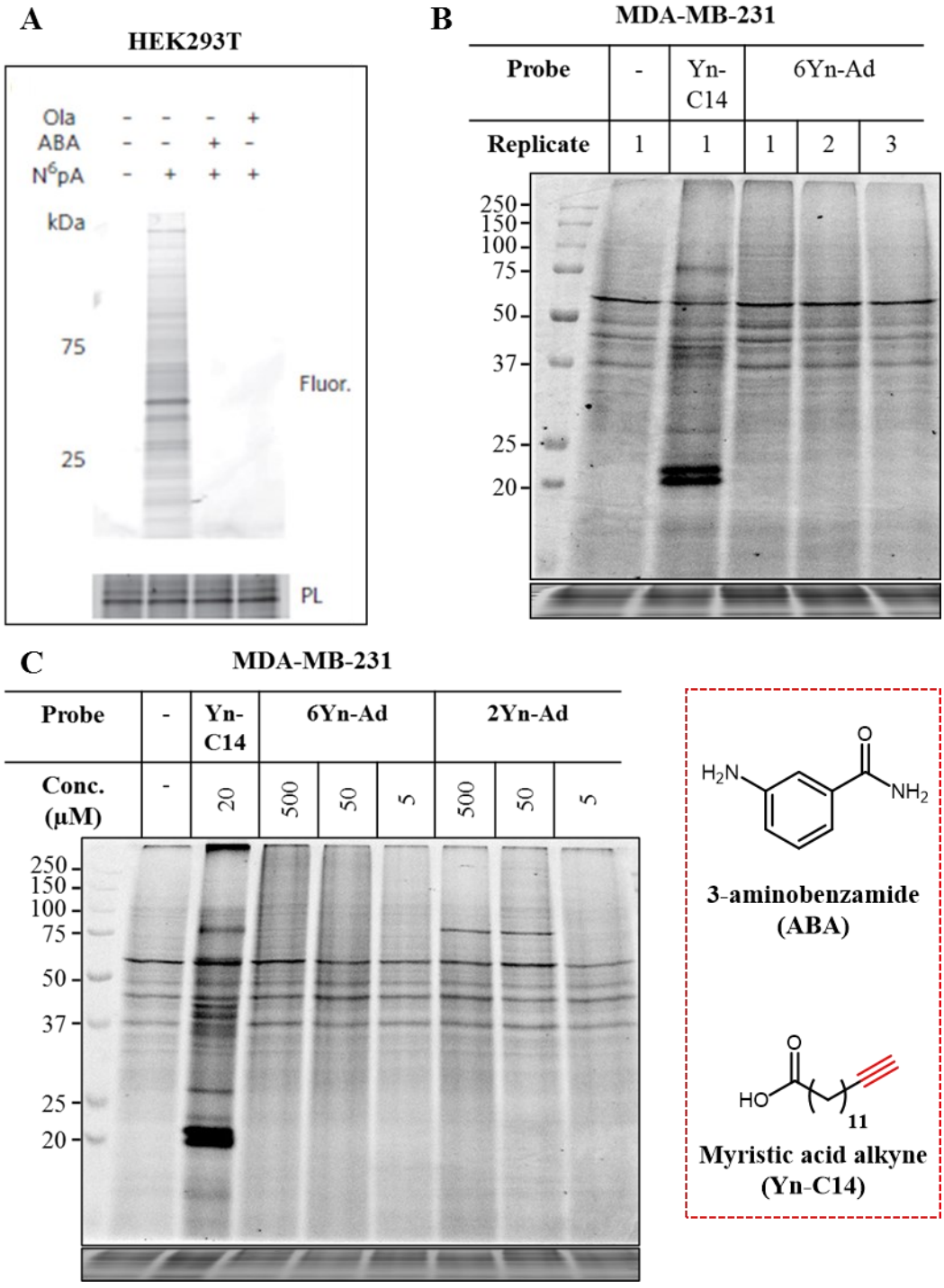


Figure 4.2. In-gel fluorescence images showing protein labelling in live-cell samples after treatment with 6Yn-Ad (N^6pA, (**25**)), 2Yn-Ad (**26**) or Yn-C14 (positive control). Coomassie staining = loading control. **A**: protein labelling in HeLa-treated samples with 6Yn-Ad (1 mM, 1 h) in the presence/absence of pre-treatment with olaparib (10 µM, 1 h) or ABA (20 mM, 1 h) in Westcott *et al*. The image is presented as illustrated in '**Figure 2d**' in Westcott *et al*[164]. **B**: protein labelling in MDA-MB-231-treated samples with 6Yn-Ad (1 mM, 1 h) or Yn-C14 (positive control, 20 µM, 24 h). Treated MDA-MB-231 were lysed (4% (w/v) SDS lysis buffer), protein precipitation was performed and tagged proteins ligated to AzT by CuAAC. **C**: protein labelling in MDA-MB-231-treated samples with 6Yn-Ad (1 h) or 2Yn-Ad (1 h) at different concentrations, or Yn-C14 (positive control,

20 µM, 24 h). Treated MDA-MB-231 were lysed (4% (w/v) SDS lysis buffer), protein precipitation was performed and tagged proteins ligated to AzT by CuAAC.

Upon closer inspection of the workflow followed by Westcott *et al.*[164] and comparison with the workflow employed in our experiments, from cell treatment to analysis by IGF, it was established that our workflow consisted of an additional protein precipitation step that was performed right after cell lysis and right before click reaction (**Figure 4.3**). The additional protein precipitation step was required to exchange the 4% (w/v) SDS lysis buffer (used in Westcott *et al.*[164]) for a 0.2% (w/v) SDS in phosphate-buffered saline (PBS) buffer. The reasoning for the precipitation step was that CuAAC click reaction is inhibited by high percentages of SDS, with click efficiency decreasing at SDS concentrations of >1% (w/v).

Protein precipitation in MeOH:H_2O:$CHCl_3$ is highly efficient, with very high protein recovery and is not expected to result in significant protein loss. Even in the occurrence of minor protein loss, this is not expected to occur to the extent that all widespread protein labelling, ranging from 10 kDa to 250 kDa, would disappear. Furthermore, after protein precipitation, protein loading overall (by Coomassie staining) appeared unaffected compared to no precipitation (**Figures 4.4A** and **4.5B**). Nevertheless, it was hypothesised that this additional protein precipitation step was responsible for the observed change in protein labelling and that perhaps leftover traces of propargylamine from the 6Yn-Ad (**25**) synthesis, which would be removed during protein precipitation, might cause non-specific protein labelling.

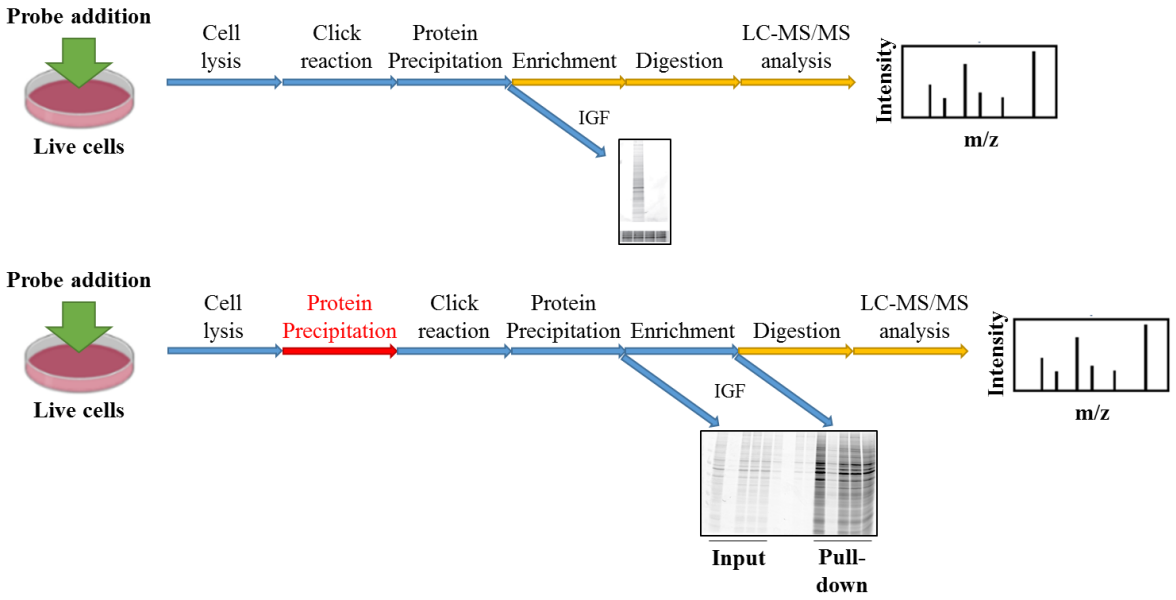


Figure 4.3. Overview of the sample processing workflows employed for analysis by IGF and proteomics in Westcott *et al.*[164] (top), and in this work (bottom). Yellow arrows represent steps followed in proteomics

experiments. Red arrow represents an additional protein precipitation step performed in this work but not performed in Westcott *et al*.[164].

Cells experiments were therefore performed following 6Yn-Ad (**25**) or propargylamine treatment, where a protein precipitation step after cell lysis was not performed (**Figure 4.4**). Propargylamine treatment alone resulted in no protein labelling compared to DMSO control, demonstrating that traces of propargylamine did not result in non-specific protein labelling. However, in 6Yn-Ad (**25**) treated samples, in the absence of a protein precipitation step after cell lysis (in 4% (w/v) SDS lysis buffer) and prior to click reaction, widespread protein labelling was observed (**Figure 4.4A**), which was identical to that showed by Westcott *et al*.[164] (**Figure 4.2A**). Furthermore, it was also established that treatment with 2Yn-Ad (**26**) (**Figure 4.4B**) and 6Yn-Pro (**47**) (**Figure 4.4C**) resulted in the same labelling pattern to that of 6Yn-Ad (**Figure 4.4C**). Although all three probes were expected to undergo similar metabolic conversions and produce similar active metabolites, in the case of 6Yn-Ad (**25**) and 2Yn-Ad (**26**), the two probes were expected to result in different labelling profiles. This was expected based on protein labelling profiles of 6Yn-NAD^+ (**3**) and 2Yn-NAD^+ (**9**) obtained in previous studies showing that protein labelling with the two probes differed, and that 2Yn-NAD^+ (**9**) typically resulted in more protein labelling.[107,113] Furthermore, docking results predicted that 2Yn-NAD^+ (**9**) was better accommodated in the active site of PARP1 (**Figure 2.30A**) than 6Yn-NAD^+ (**3**) (**Figure 2.32A** and **2.33**), thus 2Yn-NAD^+ (**9**) would be expected to be a more efficient substrate of PARP1 for protein ADP-ribosylation.

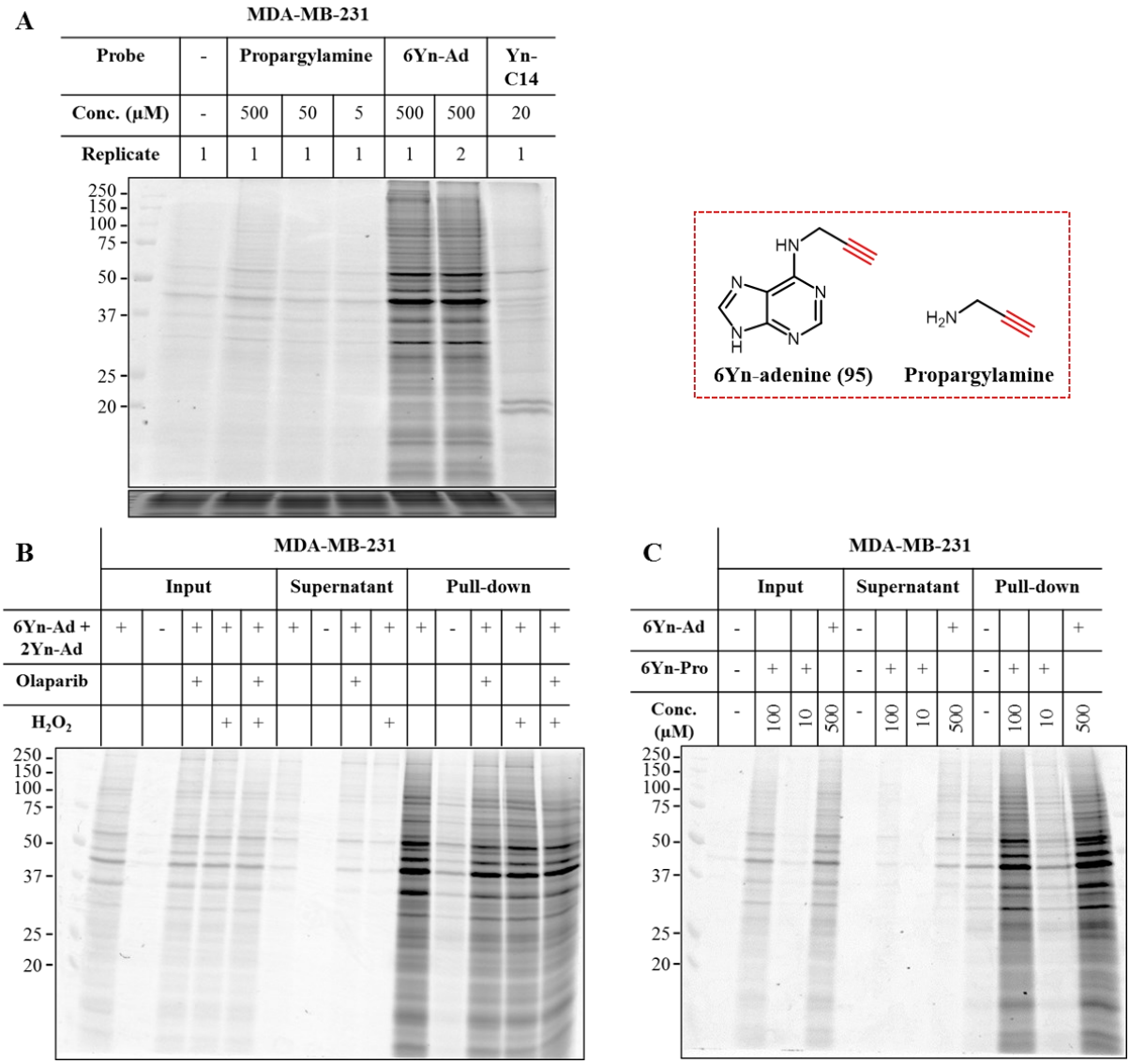


Figure 4.4. In-gel fluorescence images showing protein labelling in live-cell MDA-MB-231 samples treated with 6Yn-Ad (**25**), 6Yn-Pro (**47**), co-treated with 6Yn-Ad (**25**) and 2Yn-Ad (**26**), or Yn-C14 (positive control). All samples were lysed (4% (w/v) SDS lysis buffer) and tagged proteins ligated to AzT by CuAAC. Protein precipitation after cell lysis and before CuAAC click was not performed for any sample. Input shows protein labelling before enrichment, pull-down shows protein labelling after enrichment, supernatant shows depletion of protein labelling from input sample after the enrichment step. **A**: Protein labelling in MDA-MB-231 samples treated with 6Yn-Ad (500 µM, 1 h), propargylamine (1 h) or Yn-C14 (positive control, 20 µM, 24 h). Coomassie staining = loading control. **B**: Protein labelling in MDA-MB-231 samples co-treated with 6Yn-Ad (250 µM, 1 h) and 2Yn-Ad (250 µM, 1 h) with/without olaparib pre-treatment (10 µM, 2 h), with/without H_2O_2 treatment (2 mM, 10 min) prior to cell lysis. **C**: Protein labelling in MDA-MB-231 samples treated with 6Yn-Ad (500 µM, 1 h) or 6Yn-Pro (24 h).

We questioned why a precipitation step after cell lysis affected protein labelling to such a large extent, considering the minimal loss of protein during precipitation, and why 6Yn-Ad (**25**),

2Yn-Ad (**26**) and 6Yn-Pro (**47**) probe treatment produced the exact same labelling profile. Taking these considerations into account, it was proposed that possibly the probes resulted in substantial non-specific labelling of proteins following cell lysis. Given that prior to cell lysis intact cells were washed with PBS multiple times to remove excess extracellular probe remaining from the culture media (see **Section 6.2.1**), residual extracellular probe was excluded as the origin. Furthermore, the highly denaturing 4% (w/v) SDS lysis buffer employed for cell lysis results in loss of all residual enzymatic activity in lysates within minutes. Thus, conversion of the inactive adenosine/ProTide probes into active compounds following cell lysis was not possible. This led to the hypothesis that upon cell treatment, the probes permeated into cells, and following cell lysis, they were released into the lysates subsequently leading to non-covalent non-specific interactions with proteins and thus non-specific labelling. The protein precipitation step, therefore, removed traces of excess probe after cell lysis thus preventing the non-covalent non-specific labelling of proteins and their subsequent ligation during click chemistry by CuAAC.

To test this hypothesis, we generated denatured MDA-MB-231 cell lysates and treated them with 6Yn-Ad (**25**), 2Yn-Ad (**26**) or 6Yn-Pro (**47**). Denatured MDA-MB-231 lysates were generated by lysing MDA-MB-231 cells in 4% (w/v) SDS lysis buffer at r.t. for 1 h. The denatured lysates were treated with DMSO (control), 6Yn-Ad (**25**), 2Yn-Ad (**26**) or 6Yn-Pro (**47**) at r.t. for 1 h. CuAAC click reaction was subsequently performed at r.t. for 3 hours followed by protein precipitation to remove excess click reagents. Subsequent analysis of these samples by IGF revealed that the exact same protein labelling pattern was produced in these denatured, enzymatically inactive and probe inactive samples (**Figure 4.5A**) as compared to treatment of live cells (**Figures 4.2A, 4.4** and **4.5B**). This hinted to the fact that the observed protein labelling in Westcott *et al.*[164] was not due to genuine intracellular metabolic utilisation of the 6Yn-Ad (**25**) probe but rather non-specific in nature. Furthermore, it confirmed that other adenosine analogues, such as 2Yn-Ad (**26**), and adenosine ProTide probes, such as 6Yn-Pro (**47**), also suffered from this major drawback (**Figure 4.5**).

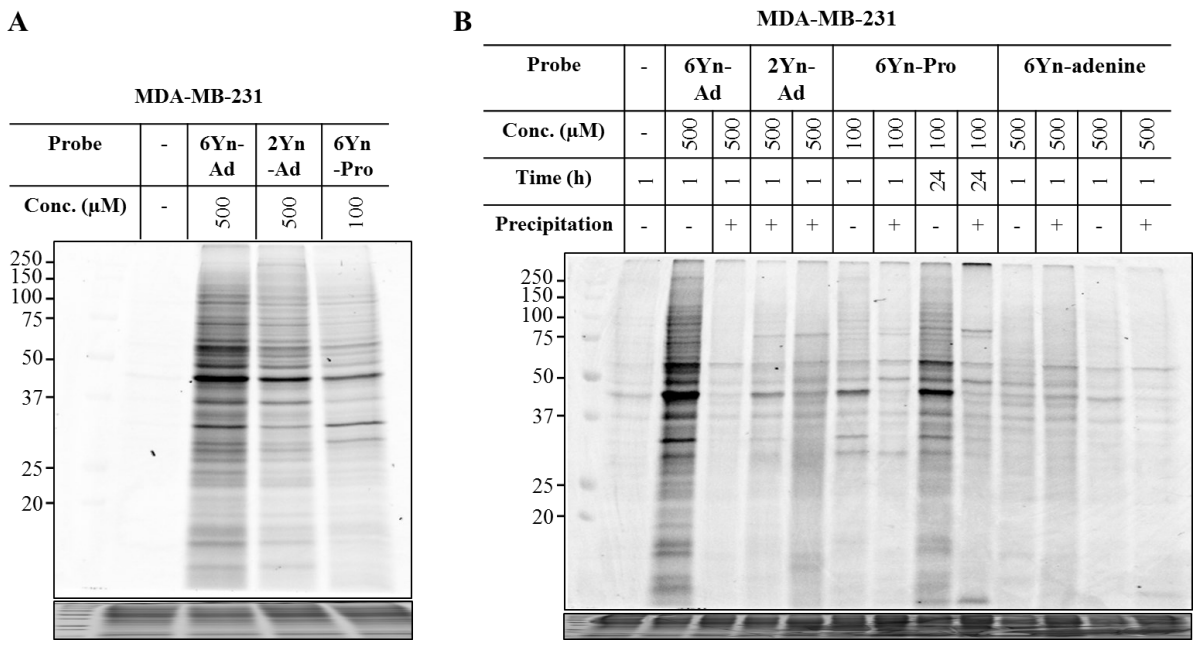


Figure 4.5. In-gel fluorescence images showing protein labelling in denatured MDA-MB-231 lysates (**A**) and live-cell MDA-MB-231 samples (**B**). Samples were treated with 6Yn-Ad (**25**), 2Yn-Ad (**26**), 6Yn-Pro (**47**) or 6Yn-adenine (**95**) at the appropriate concentration for the appropriate duration. Samples for which protein precipitation has been performed after cell lysis/prior to CuAAC are indicated (+). Coomassie staining = loading control.

Moreover, protein labelling did not disappear following co-treatment with olaparib (**Figure 4.4B**), suggesting that none of the labelled proteins seen in Westcott *et al.*[164] were, in fact, ADP-ribosylated.

The finding that adenosine probes non-specifically label proteins in denatured lysates also questions the reliability of subsequent proteomics analyses data. Given that a protein enrichment step was performed as part the proteomics workflow in Westcott *et al.*[164], all non-specifically labelled proteins were very likely enriched, as demonstrated in **Figure 4.4B** and **4.4C**. These would have therefore shown up as significantly enriched hits in Westcott *et al.*[164], since protein labelling would be absent in the corresponding DMSO-treated control samples.

Considering the observation that non-specific labelling occurred with all three clickable analogues (**25**, **26**, **47**), we next investigated whether the alkyne-adenine moiety (6Yn-adenine, **93**) was promoting these non-specific interactions. For this purpose, 6Yn-adenine (**95**) was synthesised, and MDA-MB-231 cells or cell lysates were treated with the compound for 1 h. Subsequent comparison of protein labelling in the absence or presence of a protein precipitation step was then made (**Figure 4.5B**). It was observed that, unlike for the other three probes,

6Yn-adenine (**95**) did not result in non-specific protein labelling following treatment of live cells (**Figure 4.5B, lanes 11 and 12**) or cell lysates (**Figure 4.5B, lanes 13 and 14**), as evidenced by the lack of fluorescent bands in unprecipitated samples (**Figure 4.5B, lanes 11 and 13**). This finding suggested that the ribose ring in adenosine facilitated non-specific protein-probe interactions, possibly due to hydrophilic H-bonding interactions between the ribose ring and proteins. Although not further investigated in this project, this finding could have significant implications on the use of other nucleoside-based clickable analogues in proteomics and other applications. Thus, it would be important to establish whether non-specific protein-probe interactions with clickable nucleoside probes, other than adenosine, also take place.

4.2.2 Protein Labelling Following 2Yn-Ad Treatment

A subsequent study by Kalesh *et al*. employed 6Yn-Ad (**25**) and 2Yn-Ad (**26**) for visualisation and identification of ADP-ribosylated proteins *via* IGF, WB and proteomics in MDA-MB-231 cells.[185] Similarly to the approach adopted by Westcott *et al*.[164], the study by Kalesh *et al*.[185] was shown to suffer from the same drawbacks; protein labelling arising from non-specific protein-probe interactions. Demonstrated in **Figure 4.5A**, treatment of denatured lysates with 2Yn-Ad (**26**) resulted in non-specific protein labelling, as observed for 6Yn-Ad (**25**). In Kalesh *et al*.[185], the same protein labelling pattern was observed, *via* IGF, following co-treatment of MDA-MB-231 cells with 6Yn-Ad (**25**) and 2Yn-Ad (**26**) (**Figure 4.6A**). Similarly to Westcott *et al*.[164], a protein enrichment step was also performed as part of the proteomics workflow, potentially enriching all non-specifically labelled proteins (c.f. **Figure 4.6B)** and showing as significantly enriched hits relative to the corresponding DMSO-treated control samples.

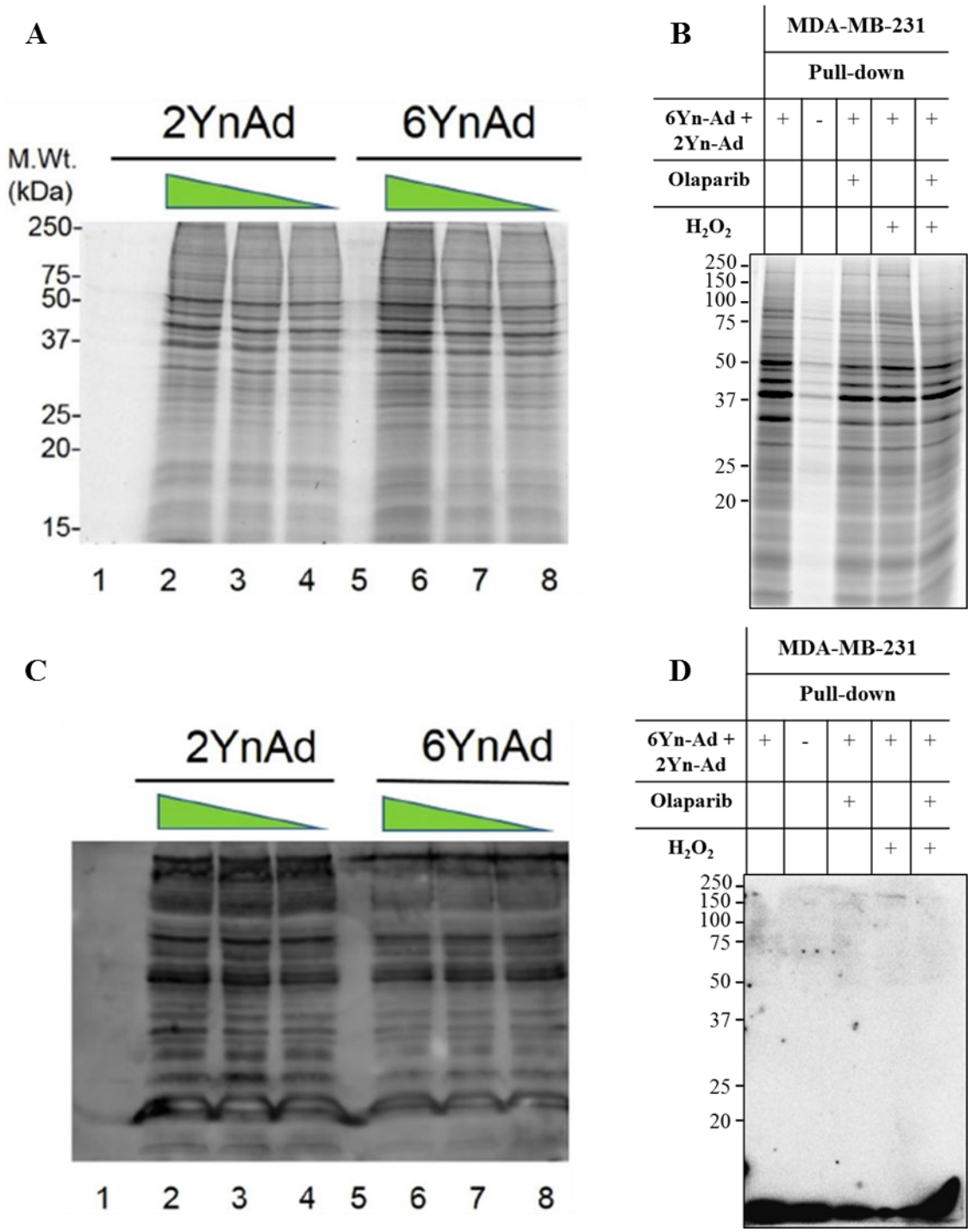


Figure 4.6. In-gel fluorescence and western blot images showing protein labelling in live-cell MDA-MB-231 samples treated with 6Yn-Ad (**25**) and 2Yn-Ad (**26**). **A**: protein labelling in MDA-MB-231-treated samples with 6Yn-Ad (1 mM, 500 µM, 250 µM in lanes 2, 3, 4, respectively, 1 h) or 2Yn-Ad (1 mM, 500 µM, 250 µM in lanes 6, 7, 8, respectively, 1 h) in Kalesh *et al.*[185]. The image is presented as illustrated in '**Figure 1C**' in Kalesh *et al.*[185]. **B**: Protein labelling in MDA-MB-231-co-treated samples with 6Yn-Ad (250 µM, 1 h) and 2Yn-Ad (250 µM, 1 h) after pull-down. This pull-down section was extracted from **Figure 4.4B** for head-to-head comparison. **C**: protein labelling of ADP-ribosylated proteins in MDA-MB-231-treated samples after pull-down, visualised by western blotting in Kalesh *et al*[185]. This blot was generated by blotting the gel shown in **A** with an

anti-pan-ADP-ribose binding reagent (MABE1016). The image is presented as illustrated in '**Figure 1D**' in Kalesh *et al.*[185]. **D**: protein labelling of ADP-ribosylated proteins in MDA-MB-231-treated samples after pull-down, visualised by western blotting with an anti-MAR/PAR antibody (Cell Signalling Technology).

Following treatment of MDA-MB-231 cells with 6Yn-Ad (**25**) and 2Yn-Ad (**26**), CuAAC click reaction, protein pull-down and subsequent WB with anti-pan-ADPr binding reagent (see **Section 1.2.4**), Kalesh *et al.*[185] concluded that they had observed ADP-ribosylated proteins arising from labelling with 6Yn-NAD^+ (**3**) and 2Yn-NAD^+ (**9**) (**Figure 4.4C**). However, from our experiments, when labelled proteins following co-treatment with 6Yn-Ad (**25**) and 2Yn-Ad (**26**) were enriched (**Figure 4.4B**) and blotted with the anti-MAR/PAR antibody (Cell Signalling Technology, see **Section 1.2.3**), no ADPr proteins were seen (**Figure 4.4D**). It was thus hypothesised that the ADP-ribosylated proteins observed in **Figure 4.4C** from Kalesh *et al.*[185] showed endogenous ADP-ribosylation levels arising from native NAD^+, before a pull-down step was performed, hence labelling was not due to metabolically generated 6Yn-NAD^+ (**3**) and 2Yn-NAD^+ (**9**). Indeed, the labelling pattern observed in **Figure 4.4C** was identical to that obtained when we investigated endogenous ADP-ribosylation levels (i.e., cells were not treated with 6Yn-Ad (**25**) or 2Yn-Ad (**26**), and an enrichment step was not performed) of MDA-MB-231 cells upon H_2O_2 treatment, by WB with the same anti-pan-ADPr binding reagent used by Kalesh *et al.*[185] (**Figure 4.7A**). Furthermore, the pattern very closely resembled that generated by the anti-MAR/PAR antibody (**Figure 4.7B**), which we previously used to show that no ADP-ribosylated proteins were detected following protein pull-down of 6Yn-Ad (**25**) and 2Yn-Ad (**26**) treated cells (**Figure 4.6D**). Taken together, these findings strongly suggest that the western blot in **Figure 4.4C** from Kalesh *et al.*[185] shows endogenous ADP-ribosylation levels from native NAD^+, before protein pull-down, and that the observed labelling pattern was not due to implied ADP-ribosylation from metabolically generated 6Yn-NAD^+ (**3**) and 2Yn-NAD^+ (**9**).

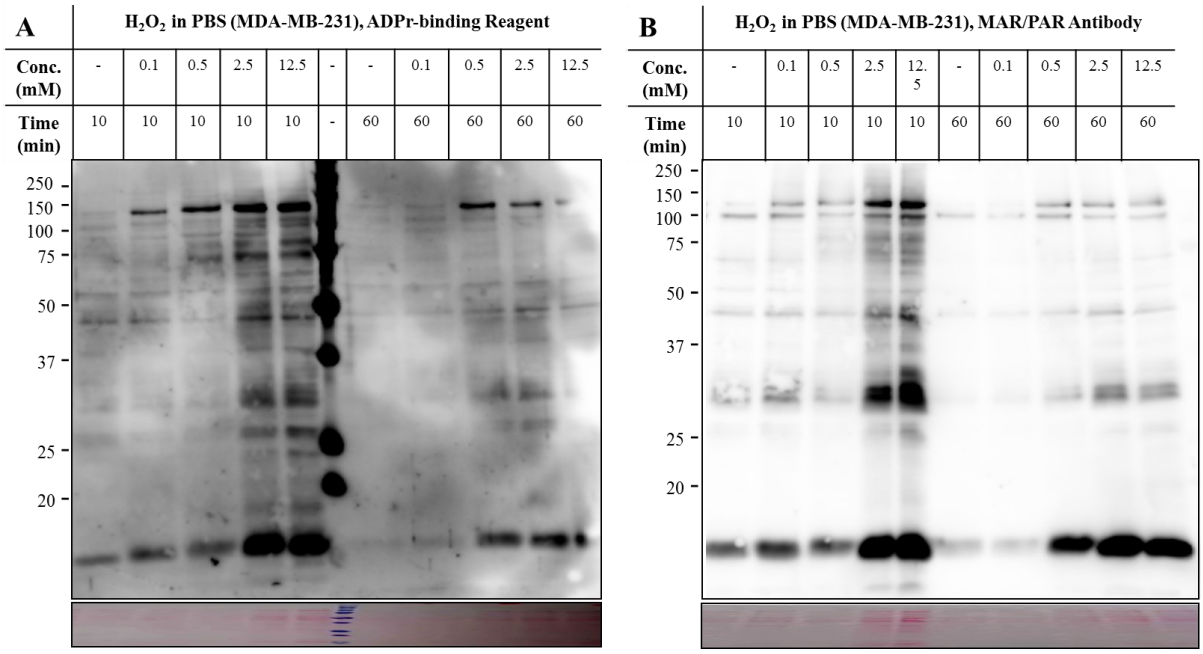


Figure 4.7. Screening of overall MARylation/PARylation protein levels in MDA-MB-231 cells by western blotting. Prior to cell lysis, culture media was aspirated and MDA-MB-231 cells were treated with the appropriate concentration of H_2O_2 for the appropriate duration. Ponceau S staining = loading control. **A**: Blotting was performed with anti-MAR/PAR antibody (Cell Signalling Technology). **B**: Blotting was performed with anti-pan-ADP-ribose binding reagent (MABE1016). Ponceau S (bottom left and right) staining loading control.

4.2.3 Protein Labelling Following 6Yn-Pro Treatment

Moving on from the use of clickable adenosine analogues, Kielkowski *et al.*[223] synthesised and employed 6Yn-Pro (**47**) for the study of protein AMPylation (**Figure 4.8A**) in multiple cell lines. This was achieved through metabolic conversion of 6Yn-Pro (**47**) to 6Yn-ATP (**40**), which was used as a co-factor for AMPylation. Subsequent identification of AMPylated proteins was performed by proteomics analysis, leading to the identification of 162 potential AMPylation targets. Our earlier findings that 6Yn-Pro (**47**) also resulted in non-specific labelling following cell treatment and in denatured lysates (**Figure 4.5**), imply that at least some of the identified protein hits are unlikely to be genuine AMPylation targets, as demonstrated by the (non-specific) labelling pattern obtained by Kielkowski *et al.*[223] *via* IGF following cell treatment (**Figure 4.8B**). On the other hand, Kielkowski *et al.*[223] employed an azide-TEV-cleavable biotin linker (**Figure 4.8C**) for identification of AMPylation sites by detecting a characteristic mass shift of +694.27 Da on modified residues by LC-MS. Using this strategy, Kielkowski *et al.*[223] identified AMPylation sites due to 6Yn-ATP (**40**) labelling on cathepsin B (CTSB), C (CTSC) and L (CTSL), as well as on three additional proteins. The successful identification of AMPylation sites on at least six proteins implied that 6Yn-Pro (**47**)

can be converted into 6Yn-ATP (**40**), which is a single step away from bioconversion into 6Yn-NAD$^+$ by NMNAT1/2/3, and subsequent utilisation by PARPs for intracellular ADP-ribosylation (**Figure 4.1**).

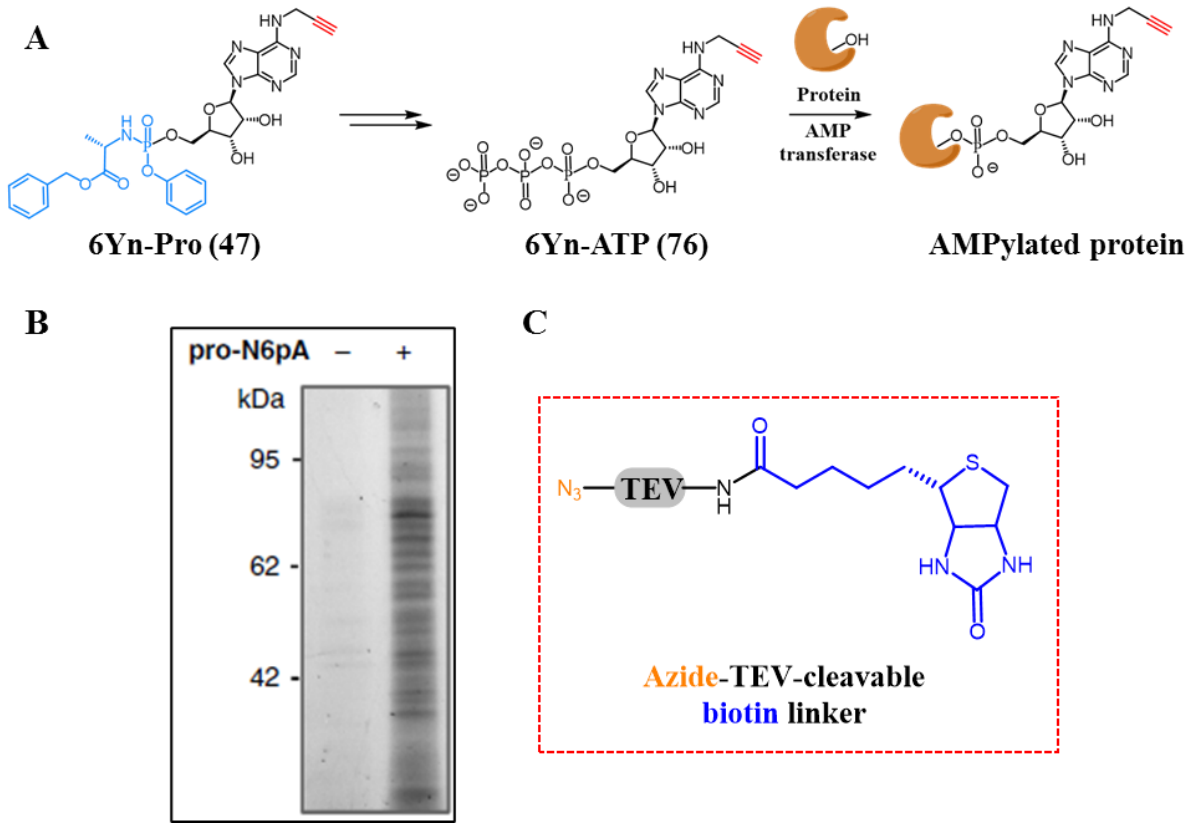


Figure 4.8. Utilisation of 6Yn-Pro (**47**) for protein AMPylation. **A**: schematic representation of protein AMPylation with 6Yn-ATP (**40**) *via* metabolic conversion of 6Yn-Pro (**47**). ProTide moiety is highlighted in blue. **B**: protein labelling in HeLa-treated sample with 6Yn-Pro (also known as pro-N^{6}pA, 100 μM, 24 h) in Kielkowski *et al.*[223]. The image is presented as illustrated in '**Figure 1C**' in Kielkowski *et al.*[223]. **C**: Structure of the azide-TEV-cleavable biotin linker used for identification of AMPylation sites due to labelling with 6Yn-ATP (**40**). The relevant functional groups are highlighted (azide in orange, biotin in blue).

4.2.4 Conclusions on Previously Published Work

The use of the clickable adenosine analogues 6Yn-Ad (**25**) and 2Yn-Ad (**26**) has been previously explored in two separate studies by Westcott *et al.*[164] and Kalesh *et al.*[185] for identification of intracellularly ADP-ribosylated proteins *via* IGF, WB and proteomics. However, we have established that the two probes resulted in non-specific protein labelling in denatured, enzymatically inactive cell lysates (**Figure 4.5A**), which produced the same protein labelling pattern *via* IGF to that obtained following treatment of cells (**Figures 4.4B** and **4.5B**). Furthermore, adenosine analogues are inactive molecules; they cannot be directly utilised for protein labelling, unless converted into the corresponding ATP or NAD$^+$ analogue co-factors,

which is not possible in denatured, enzymatically inactive lysates. To uncover the origin of the non-specific protein labelling, we synthesised the ribose-deficient 6Yn-adenine (**95**) probe and treated cells or denatured cell lysates with the compound, however, 6Yn-adenine (**95**) treatment did not result in protein labelling in either case (**Figure 4.5B**). Collectively, these findings provided evidence that adenosine-based probes can lead to the formation of substantial non-specific probe-protein interactions. We showed that the resulting non-specific protein labelling, possibly facilitated by H-bonding interactions with the ribose ring of the adenosine moiety, can be subsequently captured by click chemistry reactions. Furthermore, we showed that the non-specifically labelled proteins were enriched following protein pull-down (**Figure 4.4B** and **4.4C**) and thus carried through subsequent downstream processing steps. Consequently, our findings questioned the reliability of the obtained biological data, including by proteomics, in the two studies[164,185].

Considering the origin of the observed protein labelling *via* IGF in the study of Westcott *et al.*[164] (**Figure 4.2A**), we could not reproduce, nor explain, the complete disappearance of all protein labelling of 6Yn-Ad (**25**) treated samples following treatment with the PARP inhibitors olaparib and ABA. In addition, we provided evidence that in Kalesh *et al.*[185] the observed ADP-ribosylation by WB following treatment with 6Yn-Ad (**25**) and 2Yn-Ad (**26**) and subsequent protein enrichment (**Figure 4.6A** and **4.6C**), was highly likely, in fact, endogenous ADP-ribosylation by native NAD^+ before protein pull-down, and not due to implied metabolic conversion to 6Yn-NAD^+ (**3**) and 2Yn-NAD^+ (**9**).

Despite the observation that treatment of cells and denatured lysates with 6Yn-Pro (**47**) also resulted in non-specific protein labelling, Kielkowski *et al.*[223] identified AMPylation sites on at least six proteins arising from metabolically derived 6Yn-ATP (**40**). This provided evidence that 6Yn-Pro (**47**) was utilised in NAD^+ biosynthesis at least until the 6Yn-ATP (**40**) production stage (**Figure 4.1**). Given that conversion of 6Yn-ATP (**40**) to 6Yn-NAD^+ (**3**) requires a single enzymatic step performed by NMNAT proteins, probe 6Yn-Pro (**47**) appears to be a suitable candidate for intracellular production of 6Yn-NAD^+ and for subsequent intracellular ADP-ribosylation by PARPs.

Finally, to disrupt non-specific adenosine-based probe-protein interactions, we established that an initial protein precipitation step must be performed after cell lysis and prior to click chemistry. This ensured the removal of any residual probe released from cells upon cell lysis

thus preventing subsequent non-specific protein labelling from arising (**Figure 4.1B** and **4.1C**, and **Figure 4.5B**).

4.3 Screening of Cell Lines and Probe Validation by In-gel Fluorescence and Western Blotting

4.3.1 Screening of Protein Expression Profiles *via* Western Blotting

Considering the complexity of the NAD^+ biosynthesis pathway (**Figure 4.1**), it was important to find a suitable cell line to use for initial validation experiments of the synthesised clickable ProTide probes (**47**-**50**). An important consideration for choosing a suitable cell line was the protein expression profiles of the various enzymes involved in each biocatalytic conversion step, hence a panel of cell lines was screened (**Figures 4.9** and **4.10**).

The panel included the cell lines HEK293T and MDA-MB-231, which have been used in the work of Westcott *et al.*[164] and Kalesh *et al.*[185], respectively. HEK293T cells have also been shown to express endogenously high PARP1 RNA levels (Human Protein Atlas, **Appendix Figure A.6A**). Similarly, the breast cancer cell line T47D has been shown to endogenously express high RNA levels of the β-NMN transporter channel SLC12A8 (Human Protein Atlas, **Appendix Figure A.6B**). In addition, the breast cancer/melanoma cell line MDA-MB-435 has been shown to express high levels of NMNAT1,[245] and the ovarian cancer cell line COV318 was a cell line of interest in ADP-ribosylation studies in our collaborator's lab (Prof Hector Keun, Imperial College).

Considering that ProTide probes are converted into AMP thus bypassing initial phosphorylation by AdK (**Figure 4.1**), and the high energy cellular demand for ATP, it was reasoned that most cell lines would express sufficiently high levels of AKs and ATP synthase for ATP synthesis. Cell line screening thus focused on protein expression profiling of the β-NMN transporter channel SLC12A8[209], NMNAT1[194] for conversion of ATP into NAD^+, PARP1 for subsequent protein ADP-ribosylation and overall MARylation/PARylation cellular levels (**Figures 4.9** and **4.10**). All protein expression profiles were obtained by WB, by incubation with the appropriate primary and secondary antibodies (see **Table 6.3**). The effect of supplementation of cells with the NAD^+ precursors β-NMN, NR (**23**), NRH (**24**), (**Figure 1.15**) on the protein expression profiles was also investigated, given that all the three precursors have been previously shown to boost NAD^+ production in cells[205-209].

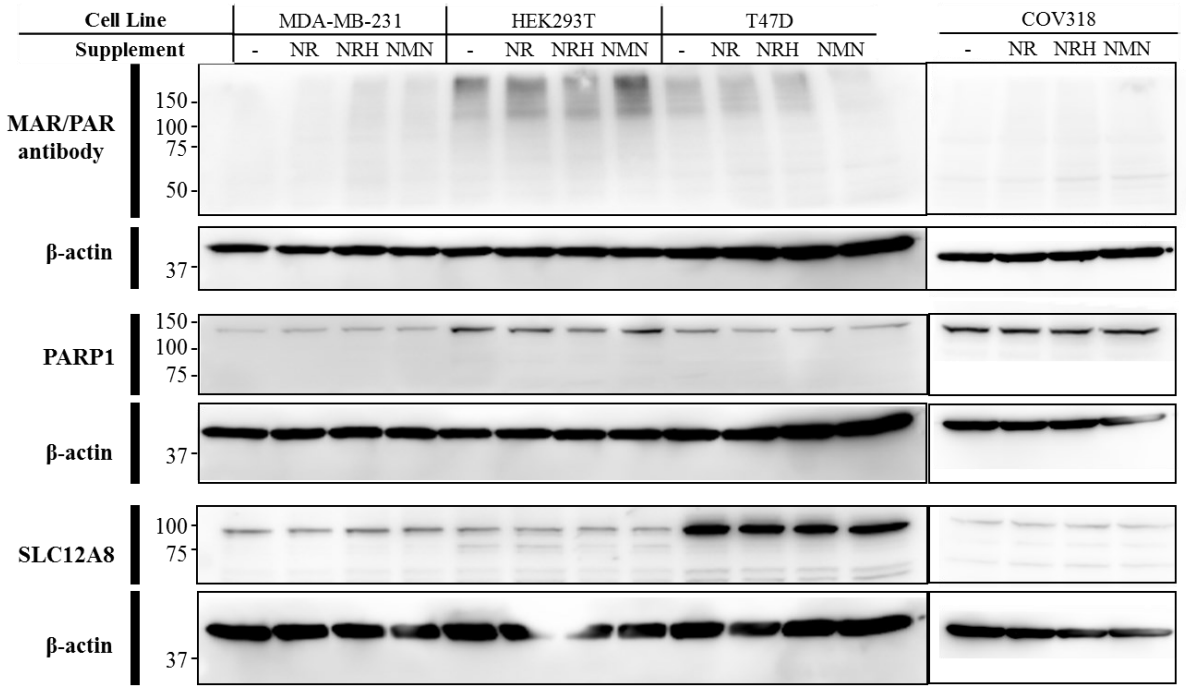


Figure 4.9. Screening of protein expression levels in MDA-MB-231, HEK293T, T47D and COV318 cells. Protein expression profiles were obtained by western blotting for the proteins SLC12A8 and PARP1, and for overall MARylation/PARylation protein levels following incubation with the appropriate antibodies. Cells were either untreated (-) or supplemented with the NAD^+ precursors NR (500 μM, 24 h), NRH (500 μM, 24 h) or β-NMN (500 μM, 24 h). β-actin = loading control.

WB experiments for the relevant proteins revealed that in all tested cell lines, supplementing cells with any of the three precursors did not affect protein expression levels relative to non-supplemented samples, except for T47D cells treated with β-NMN, which saw a slight decrease in overall MARylation/PARylation levels. The observation for T47D cells was surprising considering that it showed the highest expression level of SLC12A8, and the assumption that increased transport of β-NMN through SLC12A8 would result in higher overall levels of MARylation/PARylation. The screening also revealed that HEK293T and COV318 cell lines expressed the highest PARP1 levels. Interestingly, despite the observed high PARP1 expression, the overall MARylation/PARylation levels for COV318 cells were among the lowest of all tested cell lines, comparable to those seen in MDA-MB-231 cells, whereas MARylation/PARylation levels in HEK293T were the highest.

Initial blotting for NMNAT1 was unsuccessful due to poor quality of the NMNAT1 antibody used (Thermo Fisher), hence a second protein profiling experiment was performed with a new NMNAT1 antibody (Santa Cruz Biotechnology), and for PARP1, SLC12A8 and MARylation/PARylation for the cell line MDA-MB-435 (**Figure 4.10**).

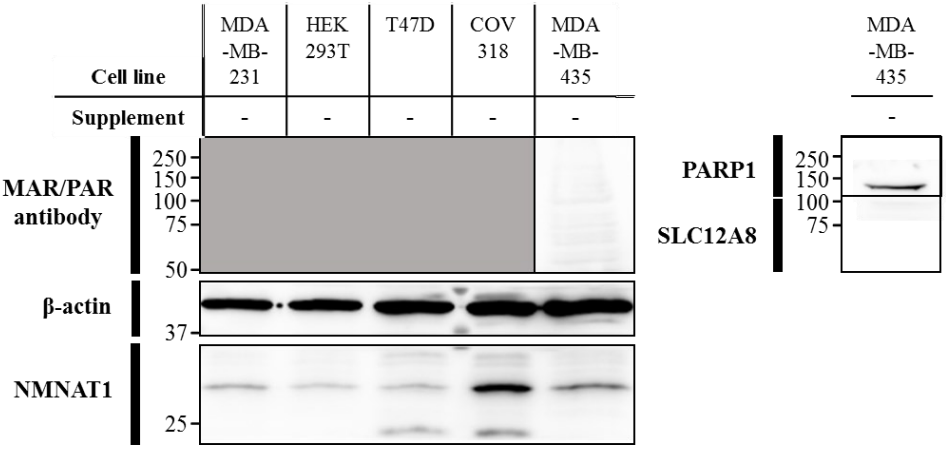


Figure 4.10. Screening of NMNAT1 expression levels in MDA-MB-231, HEK293T, T47D, COV318 and MDA-MB-435 cells by western blotting. Protein expression levels for SLC12A8 and PARP1, and for overall MARylation/PARylation protein levels in MDA-MB-435 cells were also obtained. All screening was performed in the absence of NAD^+ precursor supplementation. β-actin = loading control.

Profiling protein expression levels in MDA-MB-435 cells revealed that PARP1 expression was comparable to that of HEK293T and COV318 cells, but overall MARylation/PARylation levels were among the lowest of all five cell lines, comparable to those of COV318. The findings from COV318 and MDA-MB-435 cells thus showed that PARP1 expression levels do not necessarily correlate with overall ADP-ribosylation levels in cells.

Blotting for NMNAT1 (Santa Cruz Biotechnology) revealed that COV318 cells expressed the highest level of NMNAT1, with the remaining four cell lines largely expressing similar NMNAT1 levels. Interestingly, despite the cell line COV318 exhibiting the highest expression levels of both NMNAT1 and PARP1 of all five cells lines, its MARylation/PARylation levels were among the lowest. In contrast, HEK293T cells exhibited among the lowest NMNAT1 levels but the largest expression of MARylation/PARylation proteins levels. These findings thus contradict the assumption that high expression levels of NMNAT1, PARP1 or both proteins will directly lead to high intracellular ADP-ribosylation levels.

Overall, HEK293T, MDA-MB-435 and COV318 cells expressed similarly high levels of PARP1. Despite HEK293T cells expressing the lowest NMNAT1 levels of all cell lines, it nevertheless exhibited the highest MARylation/PARylation protein levels. Taking this into account, along with the relative ease of culturing HEK293T cells, this cell line was considered the most suitable cell line to use in future optimisation and biological experiments.

4.3.2 Probe Validation *via* In-gel Fluorescence and Western Blotting

Initial validation of the synthesised clickable ProTide probes (**47**-**50**) was performed by treating MDA-MB-231, HEK293T, T47D and MDA-MB-435 cells overnight, precipitating proteins following cell lysis (to remove non-specific protein labelling) and looking at protein labelling by IGF (**Figure 4.11**) following CuAAC click reaction. COV318 cells were excluded from this experiment due to difficulties with culturing the cell line at the time of the experiment, and on consideration that COV318 cells express low MARylation/PARylation levels.

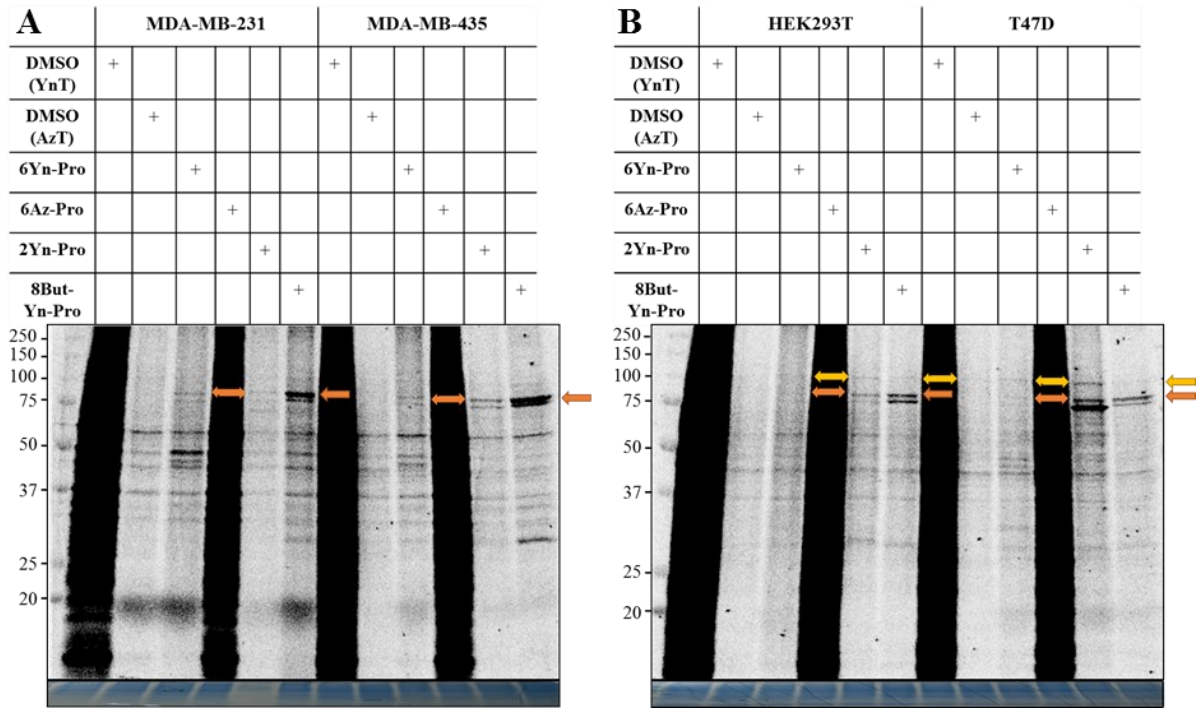


Figure 4.11. In-gel fluorescence images showing protein labelling in live-cell MDA-MB-231, MDA-MB-435, HEK293T and T47D samples treated with DMSO (0.1% v/v), 6Yn-Pro (100 µM, 24 h), 6Az-Pro (100 µM, 24 h), 2Yn-Pro (100 µM, 24 h) or 8But-Yn-Pro (100 µM, 24 h). All samples were lysed (4% (w/v) SDS lysis buffer), protein precipitation was performed and tagged proteins were ligated to AzT (for samples DMSO, 6Yn-Pro (**47**), 2Yn-Pro (**48**), 8But-Yn-Pro (**49**)) or YnT (for samples DMSO, 6Az-Pro (**50**)). **A**: protein labelling in MDA-MB-231 and MDA-MB-435 cells. **B**: protein labelling in HEK293T and T47D cells. Coomassie staining = loading control.

Unfortunately, for samples treated with DMSO (YnT) and 6Az-Pro (**50**), visualisation of protein bands was not possible. This was attributed to non-specific labelling of the lysates by the YnT capture reagent (**Figure 1.6**), the origin of which was attributed to degradation/chemical modification of the capture reagent over time, likely due to its storage beyond its expiry date. The resulting non-specific labelling by YnT led to extremely high

background fluorescence for both DMSO and 6Az-Pro (**50**) treated samples, which made it impossible to distinguish genuine protein labelling by 6Az-Pro (**50**) compared to background.

Comparison of protein labelling for the remaining three probes 6Yn-Pro (**47**) (lanes 4, 10), 2Yn-Pro (**48**) (lanes 6, 12) and 8But-Yn-Pro (**49**) (lanes 7, 13) with the corresponding DMSO (AzT) control (lanes 3, 9) (**Figure 4.11**) revealed the presence of additional fluorescent protein bands in all four treated cells lines. Furthermore, it was observed that all three probes produced a similar protein labelling profile to one another, which was expected as ProTide probes should be utilised in the same biosynthetic pathway. The observation that the three probes produced similar protein labelling profiles further suggested that all three probes were, at the very least, metabolically converted into the corresponding ATP analogues. This conclusion was based on the knowledge that covalent PTMs, such as AMPylation (**Figure 4.8A**), ADP-ribosylation (**Figure 1.1**) and other potential nucleotide-based PTMs[245], require ATP, or co-factors derived from ATP (such as NAD^+), for covalent modification/labelling of their protein targets. This was further supported by molecular docking data presented in **Chapter Two**, which predicted that all three ProTide-derived AMP analogues (**30**-**32**) were likely to be utilised by AKs and ATP synthase for production of the corresponding ATP analogues (**40**-**42**).

It was not possible to determine from IGF alone if any of the labelled proteins in **Figure 4.11** were, in fact, ADPr-ribosylated. However, bands appearing just above 100 kDa, indicated by yellow arrows, and the two bands above 75 kDa, indicated by orange arrows, could potentially correspond to labelling of full-length PARP1 (~113 – 116 kDa) and PARP1 fragments[246] (89 kDa and ~75 kDa), respectively (**Figure 4.11**). The ~100 kDa band was most noticeable in HEK293T and T47D treated samples, both of which produced the highest MARylation/PARylation protein levels by WB (**Figure 4.9**). The labelling intensity of this band also followed the expected trend of full-length PARP1 auto-modification labelling by the three NAD^+ analogues, 2Yn-NAD^+ (**9**) > 6Yn-NAD^+ (**3**) > 8But-Yn-NAD^+ (**14**), based on literature evidence that 2Yn-NAD^+ (**9**) is a more efficient substrate of PARP1 than 6Yn-NAD^+ (**3**),[107,113] and that 8But-Yn-NAD^+ (**14**) is a poor substrate of WT PARP1[118,119].

To determine whether the ~100 kDa and ~75 kDa bands corresponded to PARP1 or its fragments in HEK293T and T47D cells, IGF and western blotting with anti-PARP1 antibody (Santa Cruz Biotechnology) were performed following protein enrichment (**Figure 4.12**). The PARP1 antibody can detect both full-length PARP1 and PARP1 fragments, thus it was used to uncover if those bands were PARP1-related.

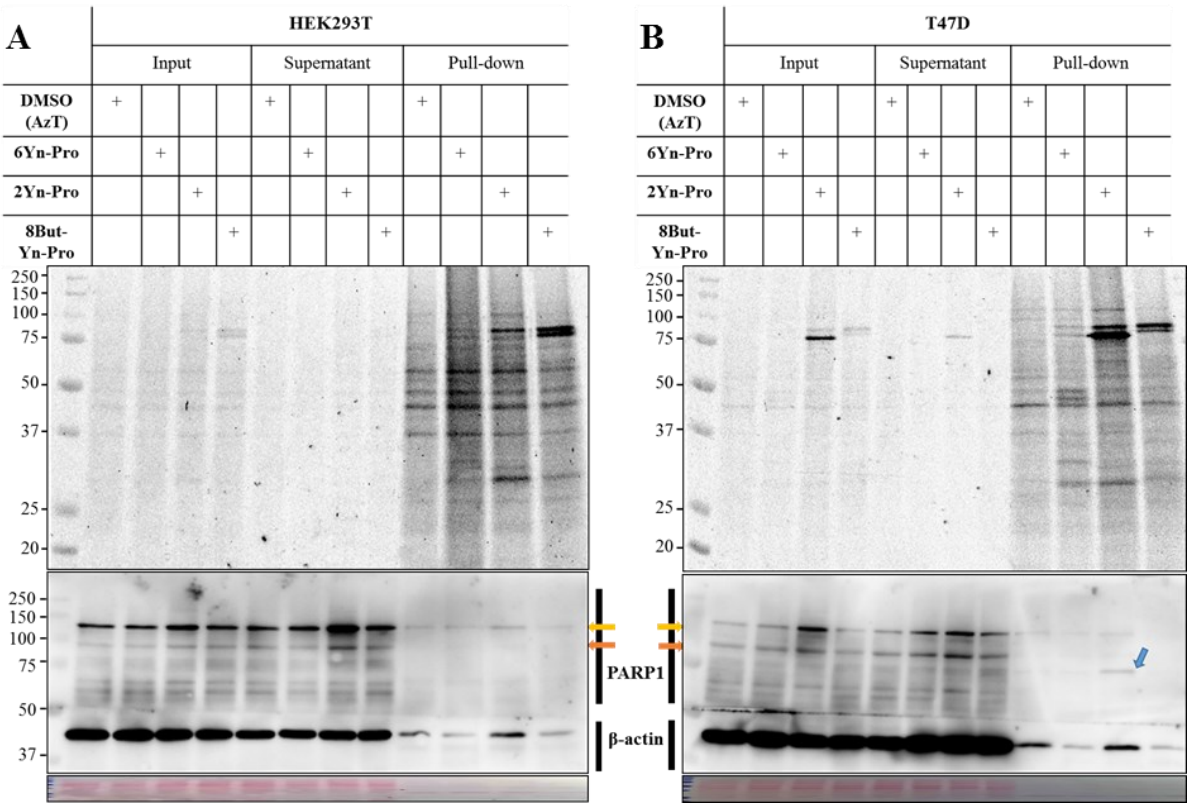


Figure 4.12. In-gel fluorescence (top panels) and western blot (bottom panels) images showing protein labelling in live-cell HEK293T and T47D samples. Cell treatment was performed with DMSO (0.1% v/v), 6Yn-Pro (100 µM, 24 h), 2Yn-Pro (100 µM, 24 h) or 8But-Yn-Pro (100 µM, 24 h) followed by cell lysis (4% (w/v) SDS lysis buffer), protein precipitation and ligation of tagged proteins to AzTB by CuAAC. Input shows protein labelling before enrichment, pull-down shows protein labelling after enrichment, supernatant shows depletion of protein labelling from input samples after the enrichment step. Western blotting was performed using PARP1 antibody. β-actin and Ponceau S staining = loading controls. **A**: protein labelling in HEK293T cells. **B**: protein labelling in T47D cells.

A protein enrichment step using magnetic neutravidin beads was performed to separate probe-labelled proteins from natively ADP-ribosylated proteins. IGF (**Figure 4.12A** and **4.12B**, top panels) showed that the supernatant was fully depleted (lanes 6-9), indicating that the enrichment step was successful. In addition, protein enrichment enhanced the fluorescent signal of labelled protein bands (lanes 10-13) compared to before pull-down (input, lanes 2-5), demonstrating the need for incorporating a pull-down step for more reliable visualisation of protein labelling by IGF.

Blotting for PARP1 (**Figure 4.12A** and **4.12B**, bottom panels) revealed labelling of a band at ~75 kDa (blue arrow) in T47D 2Yn-Pro (**48**) treated samples (**Figure 4.12B**, bottom panel), which likely corresponded to a PARP1 cleavage fragment, however, labelling of this band was not observed in HEK293T samples. In addition, full-length PARP1 (~100 kDa) labelling

following probe treatment was comparable to that in the DMSO control sample in all cases, thus it was not possible to determine by WB whether full-length PARP1 labelling was observed following treatment with any of the ProTide probes.

The lack of labelling of PARP1 in probe treated samples, compared to the DMSO control sample, could be explained by low extent of labelling by metabolically derived NAD^+ analogues. This would consequently result in a marginal increase of PARP1 following protein enrichment, relative to background PARP1 (DMSO control), and this marginal increase could be below the sensitivity of detection by western blotting. An equally likely alternative explanation for the lack of observed PARP1 labelling compared to background levels was the possibility that, following click reaction with the bulky capture reagent AzTB (**Figure 1.6**), the captured protein was modified to an extent such that the used PARP1 antibody could no longer bind to this modified protein. Indeed, this was suspected to be the case since the use of another anti-PARP1 antibody (Cell Signalling Technology) resulted in a similar lack of labelling (data not shown). This observation would suggest that, prior to analysis by WB, additional processing steps may be necessary to remove the bulky modification following click capture, to ensure antibody binding is not impeded.

4.3.3 Incorporation of Probes into RNA

To confirm if the tested ProTide probes were converted into their corresponding ATP analogues, we next looked at whether the probes were metabolically incorporated into RNA *via* conversion into ATP analogues (**Figure 4.13**). RNA synthesis requires ATP as a building block, therefore, incorporation of ATP analogues into RNA molecules and their subsequent capture by CuAAC to a fluorophore would allow for visualisation of fluorescent RNA bands by IGF. Particularly, 28S and 18S rRNA molecules are the most abundant in cells,[247] hence these were used as a marker for incorporation of metabolically derived ATP analogues into RNA.

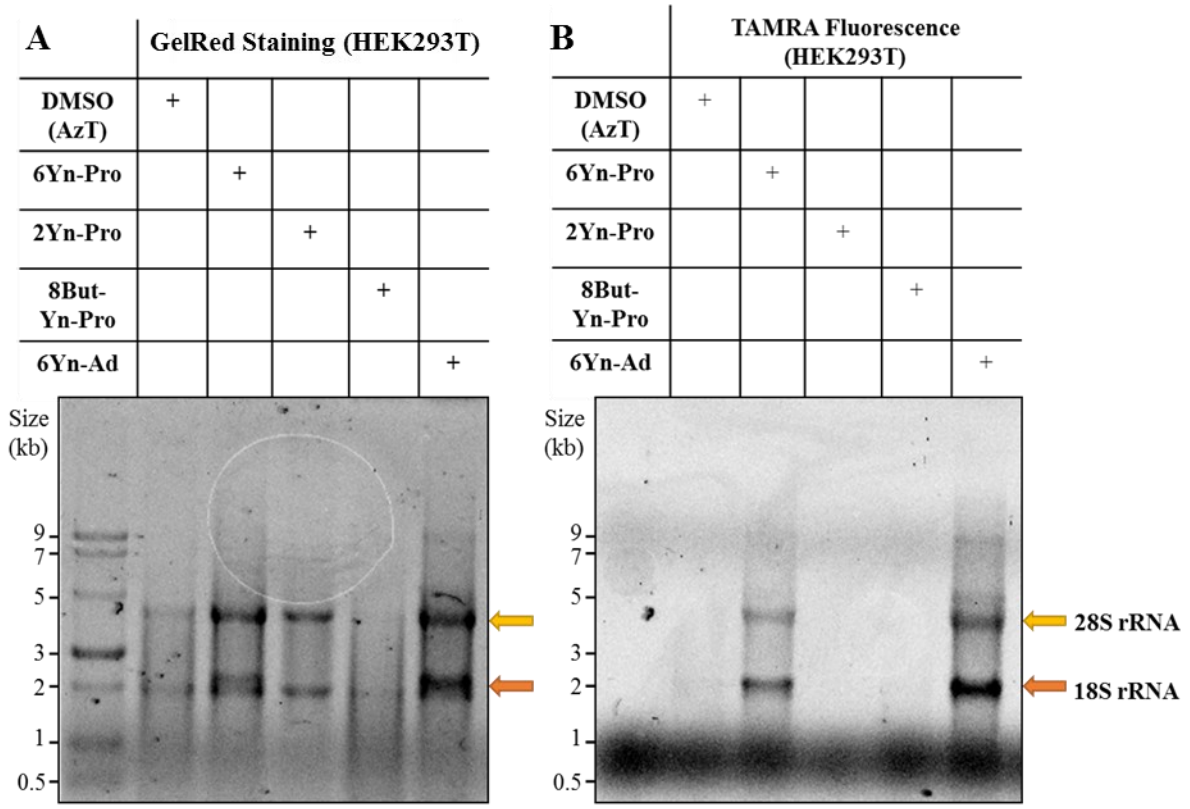


Figure 4.13. In-gel fluorescence images showing RNA loading (**A**) and RNA labelling (**B**) in HEK293T-probe treated samples. Cell treatment was performed with DMSO (0.1% v/v), 6Yn-Pro (100 μM, 24 h), 2Yn-Pro (100 μM, 24 h), 8But-Yn-Pro (100 μM, 24 h) or 6Yn-Ad (500 μM, 24 h). RNA was subsequently extracted (see **Section 5.2.5.3**) and ligation of tagged RNA molecules with AzT was performed. Yellow and orange arrows indicate positions of 28S rRNA and 18S rRNA, respectively. **A**: GelRed staining = loading control. **B**: visualisation of RNA labelling through TAMRA fluorescence.

HEK293T cells were treated with the relevant probe (6Yn-Pro (**47**), 2Yn-Pro (**48**), 8But-Yn-Pro (**49**), 6Yn-Ad (**25**)) or DMSO, RNA was extracted and subsequently 'clicked' to AzT (see **Appendix Figure A.2**) by CuAAC, and samples were analysed on a formaldehyde-agarose gel. Staining of the gel was performed with GelRed nucleic acid stain, which revealed loading of intact RNA for all samples, although for the 8But-Yn-Pro (**49**) treated sample the loading was lower than for other samples (**Figure 4.13A**). Interestingly, samples treated with probes 6Yn-Pro (**47**) and 6Yn-Ad (**25**) were the only ones that showed labelling of 28S rRNA (yellow arrow) and 18S rRNA (orange arrow) (**Figure 4.13B**), demonstrating that the probes were successfully converted into the corresponding 6Yn-ATP (**40**) analogue and used in RNA synthesis. In contrast, for samples treated with 2Yn-Pro (**48**) and 8But-Yn-Pro (**49**), no fluorescent bands were observed. This observation could imply that either the two probes were not metabolically converted into their corresponding ATP analogues (**41**, **42**), or the two ATP

analogues could not be utilised by RNA polymerase for RNA synthesis. Although this experiment could not determine the cause for this observation, protein labelling following treatment with 2Yn-Pro (**48**) and 8But-Yn-Pro (**49**) (**Figures 4.11** and **4.12**) implied their successful metabolic conversion into co-factors, typically derived from ATP, for use in covalent PTMs. Further to this, inability of RNA polymerase to employ these ATP analogues (**41**, **42**) for RNA synthesis could prove advantageous for their conversion into NAD^+ analogues (**9**, **14**), since less incorporation into RNA would be expected to result in a more abundant ATP analogue pool for conversion into NAD^+ analogues by NMNAT1.

4.3.4 Utilisation of 6Yn-Pro for AMPylation

The observation that treatment of HEK293T cells with 6Yn-Pro (**47**) resulted in RNA labelling and its subsequent capture by CuAAC, implied that 6Yn-Pro (**47**) was metabolically converted into 6Yn-ATP (**40**), which was then used in RNA synthesis. This led to the hypothesis that, following metabolic conversion, the probe should be similarly utilised for protein labelling for AMPylation since this PTM requires ATP as a co-factor. To uncover whether this was the case, HEK293T cells were treated with 6Yn-Pro (**47**), 'clicked' by CuAAC and a protein enrichment step was performed prior to analysis by IGF and western blotting with anti-AMPylated tyrosine antibody (**Figure 4.14**), which binds to AMPylation on tyrosine residues (Sigma-Aldrich).

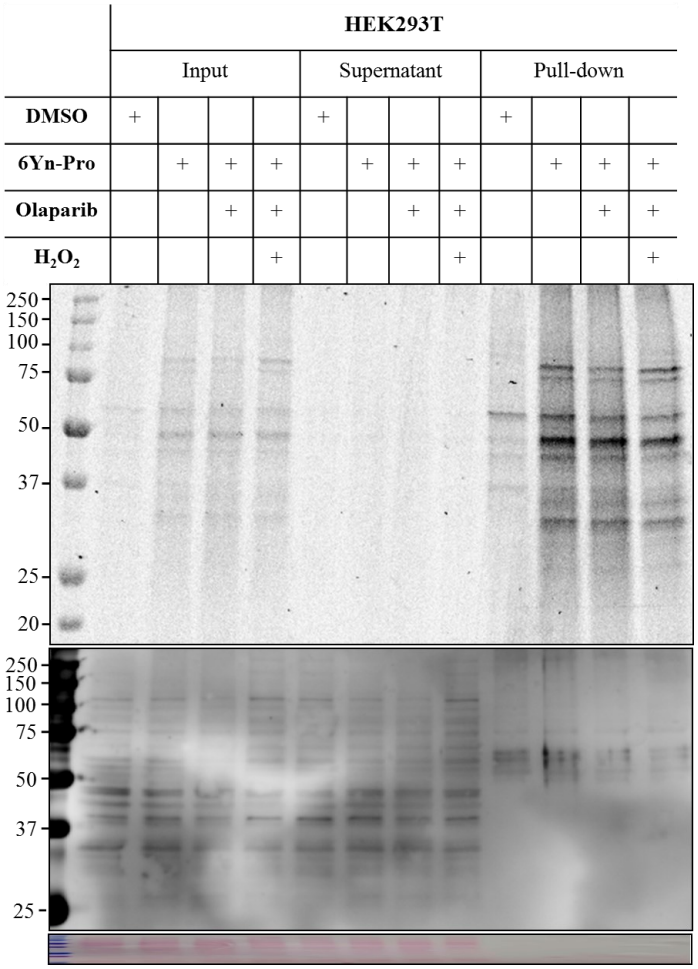


Figure 4.14. In-gel fluorescence (top panel) and western blot (bottom panel) images showing protein labelling in live-cell HEK293T samples. Cell treatment was performed with DMSO (0.1% v/v) or 6Yn-Pro (100 μM, 24 h) with/without olaparib pre-treatment (10 μM, 2 h), with/without H_2O_2 treatment (2 mM, 10 min) prior to cell lysis. Cells were lysed (4% (w/v) SDS lysis buffer), protein precipitation was performed and tagged proteins were ligated to AzT by CuAAC. Input shows protein labelling before enrichment, pull-down shows protein labelling after enrichment, supernatant shows depletion of protein labelling from input samples after the enrichment step. Western blotting was performed using anti-AMPylated tyrosine antibody. Ponceau S staining = loading control.

Similarly to **Figure 4.12**, protein labelling by IGF was reliably detected following pull-down (**Figure 4.14**, lanes 10-13). The extent of protein labelling was unaffected in the presence of olaparib (lanes 12, 13), showing that the observed fluorescent protein bands were not due to ADP-ribosylation by PARP1 or PARP2. In addition, the induced oxidative stress due to H_2O_2 treatment (lane 13) did not result in an increase of protein labelling, which would be expected to occur as a result of upregulation of cellular ADP-ribosylation. Despite ruling out ADP-ribosylation as the origin of protein labelling by IGF (**Figure 4.14**, top panel), subsequent blotting for AMPylation with an anti-AMPylated tyrosine antibody (**Figure 4.14**, bottom panel) revealed no enhanced labelling in probe-treated samples, relative to DMSO control, after

pull-down. This was surprising considering the utilisation of 6Yn-Pro (**47**) for metabolic conversion into 6Yn-ATP (**40**), as illustrated by its incorporation into RNA (**Figure 4.13B**).

A possible explanation could be that the efficiency of labelling of AMPylated proteins with metabolically derived 6Yn-ATP was low and below the detection limit of WB, as potentially observed for WB with PARP1 (**Figure 4.12**, bottom panels). Additionally, it was possible that the bulky modification on AMPylated proteins following CuAAC click reaction impeded the ability of the anti-AMPylated tyrosine antibody to recognise its target proteins, thus tyrosine AMPylated proteins were not detected. A further explanation could be the presence of an alternative PTM, that either directly used ATP as a co-factor or used an alternative co-factor derived from ATP for covalent labelling of proteins. Regardless, the data suggested that western blotting may not be an effective technique for monitoring protein ADP-ribosylation (**Figure 4.12**) and AMPylation (**Figure 4.14**) using metabolically derived clickable co-factor analogues. Thus, a more sensitive approach, such as proteomics analysis, was required for reliable detection and identification of modified proteins (see **Section 4.5**).

4.3.5 Effect of NMNAT1 Overexpression on Protein Labelling and ADP-ribosylation Levels

Owing to the role of NMNAT1 in the final step of (nuclear) NAD^+ biosynthesis (**Figure 4.1**), it was important to determine if NMNAT1 expression levels affected the metabolic utility of the ProTide probes (**47**-**49**) for intracellular ADP-ribosylation. Initially, we looked at the levels of cellular ADP-ribosylation following NMNAT1 overexpression (OE, see **Appendix Figure A.7** and **A.8**) in plasmid transfected HEK293T cells by blotting for MARylation/PARylation protein levels using the anti-MAR/PAR antibody (**Figure 4.15A**). Contrary to the expectation that high NMNAT1 expression levels would stimulate ADP-ribosylation *via* increased NAD^+ biosynthesis, overexpression of NMNAT1 (lanes 3, 5) resulted in a decrease of overall MARylation/PARylation levels compared to baseline NMNAT1 levels (lanes 1, 2). This finding implied the presence of a negative feedback mechanism between NMNAT1 expression levels and activity of nuclear PARPs, and that very high levels of NMNAT1 negatively affect cellular ADP-ribosylation levels. Indeed, baseline NMNAT1 levels were between two to three orders of magnitude lower compared to overexpression NMNAT1 levels (**Figure 4.15A**).

Next, we investigated whether NMNAT1 overexpression impacted protein labelling upon cell treatment with the ProTide probes (**Figure 4.15B**). Considering molecular docking data presented in **Chapter Two**, for the 2Yn- series the mutant V186G NMNAT1 was employed,

which was predicted to catalyse conversion of 2Yn-ATP (**41**) into 2Yn-NAD^+ (**9**) (**Figure 2.27**). Due to unavailability of probe 2Yn-Pro (**48**) at the time of experiment, it was substituted for the corresponding non-Protide probe 2Y-Ad (**26**). For the 6Yn- and 8But-Yn- series, 6Yn-ATP (**40**) and 8But-Yn-ATP (**42**) were predicted to be substrates of WT NMNAT1 (**Figure 2.23** and **Figure 2.24**, respectively), therefore WT NMNAT1 was overexpressed in cells treated with 6Yn-Pro (**47**) and 8But-Yn-Pro (**49**). For 8But-Yn-Pro (**49**) treated cells, the PARP1 mutant L877A was also overexpressed given literature evidence that WT PARP1 (**Appendix Figure A.9**) cannot utilise the corresponding 8But-Yn-NAD^+ analogue (**14**)[118,119] as a substrate for ADP-ribosylation. Following overexpression of NMNAT1, and of L877A PARP1 for cells to be treated with 8But-Yn-Pro (**49**), probe treatment and cell lysis (overexpression, probe treatment, cell lysis were performed by PhD student Michael Gruet), proteins were subsequently precipitated, CuAAC click reaction was performed and protein labelling visualised by IGF.

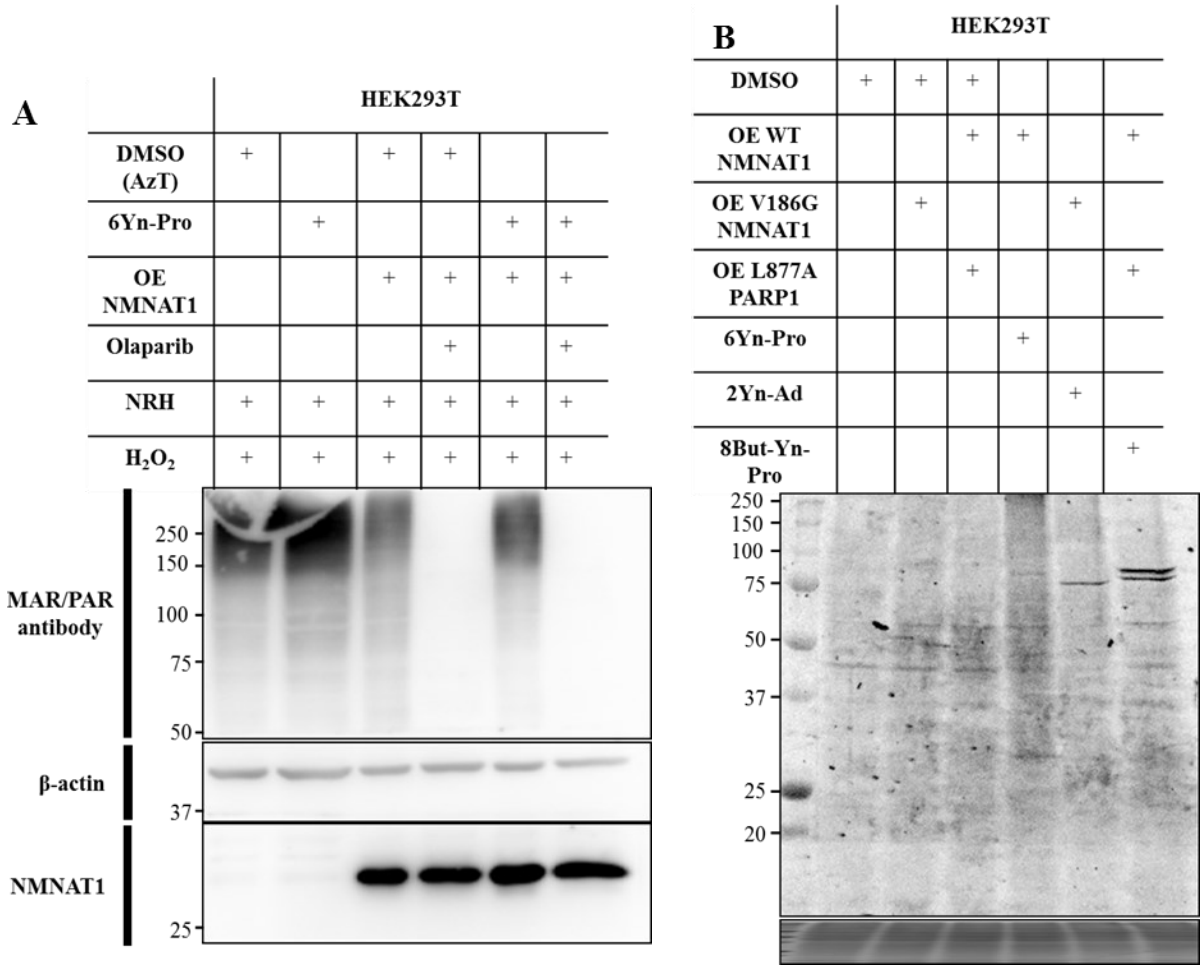


Figure 4.15. Western blot (**A**) and in-gel fluorescence (**B**) images showing protein labelling in live-cell HEK293T samples after probe treatment and NMNAT1 overexpression. **A**: NMNAT1 was overexpressed for 24 h prior to

cell treatment with DMSO (0.1% v/v) or 6Yn-Pro (100 μM, 24 h), with/without olaparib pre-treatment (10 μM, 2 h). All cells were co-treated with NRH (500 μM, 24 h) and finally treated with H_2O_2 (2 mM, 10 min) prior to cell lysis. Blotting for MARylation/PARylation protein levels and NMNAT1 expression was performed with the relevant antibodies. β-actin antibody = loading control. **B**: Expression of the relevant NMNAT1 form or L877A PARP1 was performed for 24 h prior to cell treatment with DMSO (0.1% v/v), 6Yn-Pro (100 μM, 24 h), 2Yn-Ad (500 μM, 6 h) or 8But-Yn-Pro (100 μM, 24 h). Cells were lysed (4% (w/v) SDS lysis buffer), protein precipitation was performed and tagged proteins were ligated to AzT by CuAAC. Coomassie staining = loading control.

IGF data showed that overexpression of WT NMNAT1 in HEK293T cells followed by 6Yn-Pro (**47**) probe treatment (**Figure 4.15B**, lane 5) did not increase protein labelling when compared to protein labelling with 6Yn-Pro (**47**) in HEK293T cells expressing baseline NMNAT1 levels (**Figure 4.12A**, lanes 3, 11). In a similar manner, overexpression of V186G NMNAT1 followed by 2Yn-Ad (**26**) treatment (**Figure 4.15B**, lane 6) did not result in additional protein labelling relative to baseline NMNAT1 HEK293T cells treated with the corresponding 2Yn-Pro (**48**) probe (**Figure 4.12A**, lanes 4, 12). The obtained data similarly showed that following co-expression of WT NMNAT1 and L877A PARP1 for 8But-Yn-Pro (**49**) treated HEK293T cells (**Figure 4.15B**, lane 7), there was no increase in protein labelling when compared to protein labelling in 8But-Yn-Pro (**49**) treated HEK293T cells expressing baseline levels of NMNAT1 and PARP1 (**Figure 4.12A**, lanes 5, 13). The obtained data thus suggested that either protein labelling changes were too small to be detected by IGF following NMNAT1 overexpression, thus requiring a more sensitive method for detection (e.g., proteomics), or that NMNAT1 overexpression did not affect overall ADP-ribosylation levels arising from metabolically derived NAD^+ analogues. It should be noted that IGF data in **Figure 4.15B** was obtained in the absence of protein enrichment, which was shown to significantly enhance protein labelling signal by IGF (**Figure 4.12A**, lanes 10-13).

4.3.6 NMNAT1 *In Vitro* Assay with ATP and 6Yn-ATP

NMNAT1 overexpression did not increase protein labelling following treatment with 6Yn-Pro (**47**) (**Figure 4.15B**), despite the observation that the probe was metabolically converted into 6Yn-ATP (**40**) for use in RNA synthesis (**Figure 4.13B**). To determine whether NMNAT1 was able to use 6Yn-ATP (**40**) as a substrate for conversion into 6Yn-NAD^+ (**3**), an *in vitro* assay with recombinant NMNAT1 and 6Yn-ATP (**40**) was performed. The assay involved conversion of (6Yn-)ATP into (6Yn-)NAD^+ by NMNAT1, followed by subsequent conversion of (6Yn-)NAD^+ into (6Yn-)NADH by alcohol dehydrogenase (ADH). NADH (**96**) exhibits a strong absorbance at 340 nm, which can be detected on a plate reader and was used as a readout for the assay (**Figure 4.16A**).

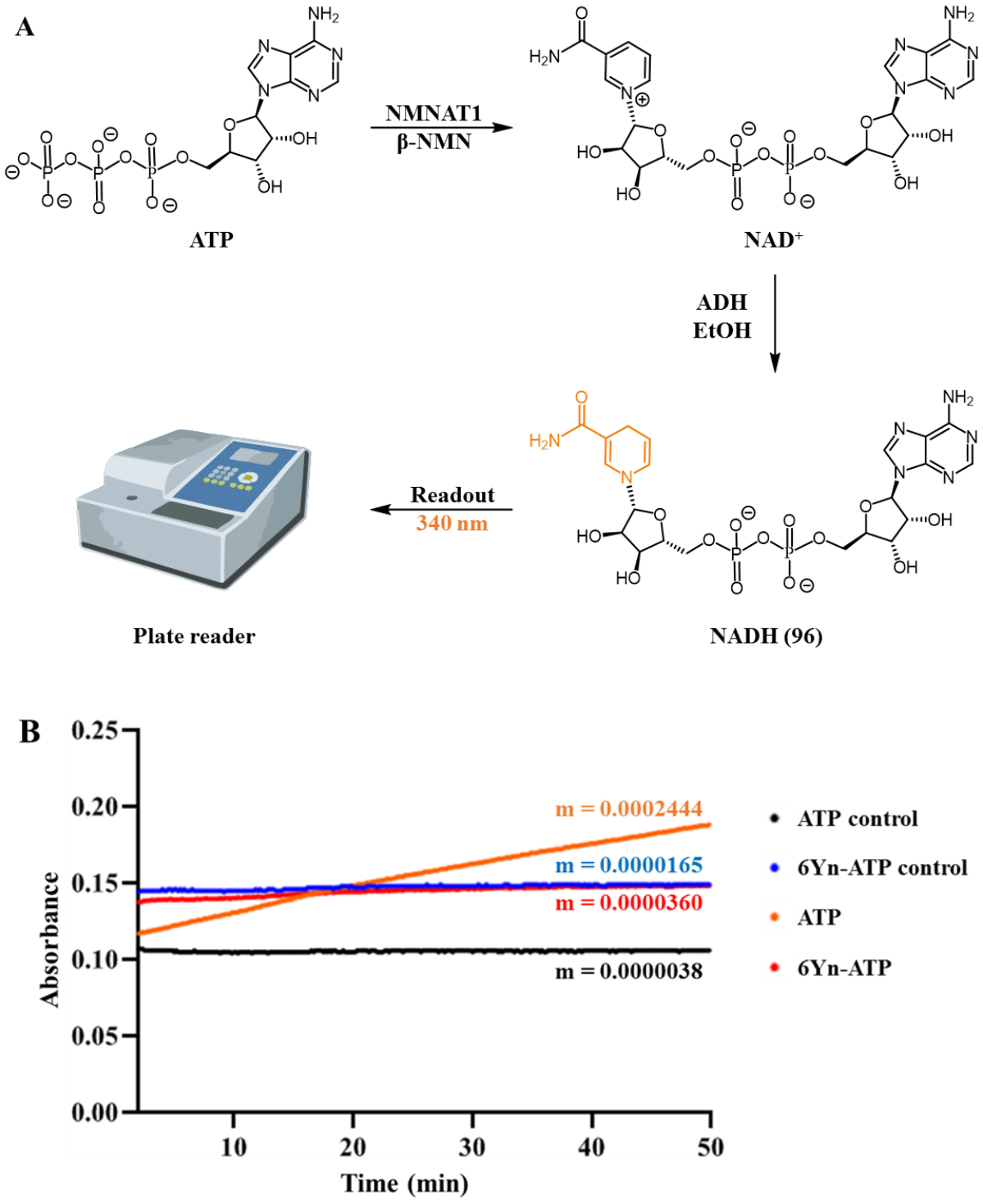


Figure 4.16. *In vitro* assay with recombinant NMNAT1 and (6Yn-)ATP. **A**: Schematic representation of the assay workflow. (6Yn-)ATP is initially coupled to β-NMN by NMNAT1 to produce (6Yn-)NAD^+, which is subsequently reduced to (6Yn-)NADH by ADH in the presence of EtOH. Generation of (6Yn-)NADH is monitored by measuring the absorbance at 340 nm. **B**: Data obtained and plotted (absorbance as a function of time) after performing the assay with the substrates ATP or 6Yn-ATP (**40**). For the ATP/6Yn-ATP controls NMNAT1 was not added. After initiation of the assay, absorbance was measured every 10 s for 50 min. m = line gradient. The assay was performed as described in Section **6.2.4**.

Table 4.1. Summary of absorbance gradients (see **Figure 4.16B**). Gradient normalisation was performed for each sample relative to the corresponding control sample.

	Absorbance line gradient	**Gradient normalisation (relative to corresponding control)**
ATP control	0.0000038	1 (0.0000038/0.0000038)
ATP	0.0002444	64.3 (0.0002444/0.0000038)
6Yn-ATP control	0.0000165	1 (0.0000165/0.0000165)
6Yn-ATP	0.0000360	2.2 (0.0000360/0.0000165)

Once the assay was initiated (see **Section 6.2.4** for exact protocol), absorbance measurements were taken every 10 s for a total of 50 mins (**Figure 4.16B**). For the relevant ATP and 6Yn-ATP (**40**) control samples, recombinant NMNAT1 was not added, hence absorbance measurements in those samples represented background absorbance. In the ATP and 6Yn-ATP (**40**) samples, recombinant NMNAT1 was added, hence absorbance measurements in those samples represented conversion of (6Yn-)ATP into (6Yn-)NADH. Due to the different absorbance values at the starting point (0 min) in all four samples, direct comparison of absorbance values for the ATP and 6Yn-ATP (**40**) samples with their relevant control was not possible. Thus, to compare the efficiency of conversion of ATP and 6Yn-ATP (**40**) into (6Yn-)NADH, the gradient of increase in absorbance over the duration of the assay for each of the two samples was normalised relevant to that of the corresponding control sample (**Table 4.1**).

Normalisation of the gradients revealed that the rate of increase of absorbance, due to NADH (**96**) production, for the ATP sample was 64.3 times higher compared to the ATP control. In contrast, the rate of increase of absorbance, due to 6Yn-NADH production, for the 6Yn-ATP (**40**) sample was 2.2 times higher compared to the 6Yn-ATP (**40**) control. Comparison of these ratios thus revealed that the rate of conversion of 6Yn-ATP (**40**) into 6Yn-NADH was approximately 30-fold lower (64.3/2.2) than that of native ATP into NADH (**96**). Therefore, the results demonstrated that NMNAT1 exhibited a significantly higher preference (~30-fold higher affinity) for native ATP than for the clickable analogue 6Yn-ATP (**40**).

A potentially major caveat of this assay was that a second enzymatic step, catalysed by ADH, was required for conversion of (6Yn-)NAD^+ into (6Yn-)NADH for the assay readout. Although

ADH readily catalysed conversion of NAD^+ into NADH (**96**), this might not be the case for structural NAD^+ analogues such as 6Yn-NAD^+ (**3**). Possibly, NMNAT1 converted 6Yn-ATP (**40**) into 6Yn-NAD^+ (**3**) with higher efficiency than estimated but subsequent detection of 6Yn-NADH was hindered by the ability of ADH to catalyse the reduction of 6Yn-NAD^+ (**3**) into 6Yn-NADH. An alternative approach to detecting the low quantities of 6Yn-NAD^+ (**3**) being produced in this assay would be to use UPLC-MS for analysis, however, an LC-MS-based approach would require further sample clean up as well as access to the appropriate equipment on-demand, which was not available in this work.

4.3.7 Conclusions from Initial Validation Experiments

To select an appropriate cell line for biological validation of the ProTide probes (**47**-**50**) synthesised in **Chapter Three**, a panel of five cell lines was screen by profiling of protein expression levels of the relevant enzymes involved in NAD^+ biosynthesis by WB (**Figures 4.9** and **4.10**). The screening experiments revealed that HEK293T cells expressed the highest endogenous level of PARP1 as well as the highest levels of MARylated/PARylated proteins (**Figure 4.9**). Taking these findings into account, along with the relative ease of culturing HEK293T cells and their ability to be efficiently transfected, the cell line HEK293T was deemed the most suitable for use in future optimisation and validation experiments. HEK293T cells were therefore included in most metabolomics experiments (see **Section 4.4**) and used in all proteomics experiments (see **Section 4.5**) described in this chapter. Additionally, supplementation of the cell line panel with β-NMN, NR (**23**) or NRH (**24**) was found to have no effect on expression levels of the profiled proteins by WB (**Figure 4.9**), including on overall MARylation/PARylation levels, despite literature evidence that supplementation with NAD^+ precursors was found to boost cellular NAD^+ levels[205-209].

Initial validation of ProTide probes (**47**-**49**) was performed in the cell lines MDA-MB-231, MDA-MB-435, HEK293T and T47D by IGF, which revealed widespread protein labelling in all cases (**Figures 4.11** and **4.12**). This was suspected to be due to protein AMPylation, ADP-ribosylation or another nucleotide-based PTM, which use ATP, or co-factors derived from ATP (e.g., NAD^+), for protein labelling, thus indirectly implying potential metabolic conversion of the tested ProTide probes into the corresponding ATP analogues. In the case of 6Yn-Pro (**47**) (and 6Yn-Ad (**25**)), its metabolic conversion into 6Yn-ATP (**40**) was confirmed in HEK293T cells through its incorporation into RNA molecules, subsequent ligation to a fluorophore by CuAAC and the observation of fluorescent RNA bands (**Figure 4.13B**). Despite these observations, treatment of HEK293T and T47D cells with 6Yn-Pro (**47**), 2Yn-Pro (**48**) and

8But-Yn-Pro (**49**) followed by protein pull-down and WB for PARP1 did not result in PARP1 labelling when compared to background levels (DMSO control) (**Figure 4.12**). Similarly, treatment of HEK293T cells with for 6Yn-Pro (**47**) followed by protein pull-down and WB for AMPylation did not result in labelling of AMPylated proteins (relative to DMSO control) (**Figure 4.14**). It was thus reasoned that possibly levels of AMPylated or ADP-ribosylated (PARP1) proteins following metabolic labelling were too low to be detected by WB, and that a more sensitive method, such as proteomics analysis, may be required. Additionally, the lack of protein labelling by WB could be explained by the relevant antibodies no longer binding to ligated proteins following CuAAC due to the presence of the bulky capture reagent modification (**Table 1.3**, **Figure 1.6**). Alternatively, the observed protein labelling by IGF (**Figure 4.14**) could be due to the presence of an additional PTM. This observation was supported by the finding that protein labelling following 6Yn-Pro (**47**) treatment was unaffected following treatment with the PARP inhibitor olaparib, or under oxidative stress induced by H_2O_2 (**Figure 4.14**), thus ruling out ADP-ribosylation by PARP1 and PARP2 as the origin of the observed protein labelling.

To investigate whether NMNAT1 expression levels affected overall MARylation/PARylation levels as well as utilisation of ProTide probes (**47**-**49**) for protein labelling, WT NMNAT1 (for 6Yn-Pro (**47**) and 8But-Yn-Pro (**49**) treatment) or mutant V186G NMNAT1 (for 2Yn-Ad (**26**) treatment)) was overexpressed. It was noted that NMNAT1 levels increased between two to three orders of magnitude due to overexpression when compared to baseline levels (**Figure 4.15A**). The high NMNAT1 expression levels resulted in a slight decrease of overall MARylation/PARylation levels in HEK293T cells (**Figure 4.15A**) although protein labelling following probe treatment appeared unaffected (**Figure 4.15B**). This led to the hypothesis that a negative feedback mechanism between NMNAT1 expression levels and PARP1 activation for ADP-ribosylation was present, and that possibly a moderate increase in NMNAT1 levels may instead increase MARylation/PARylation levels. This was, however, not investigated further.

Finally, utilisation of 6Yn-ATP (**40**) by recombinant NMNAT1 for conversion into 6Yn-NAD^+ (**3**) was investigated *in vitro* **(Figure 4.16A)**. The findings from the assay demonstrated that potentially NMNAT1 exhibited a 30-fold increased affinity for ATP as a substrate in comparison to the analogue 6Yn-ATP (**40**) (**Table 4.1, Figure 4.16B)**. It was noted, however, that the perceived higher affinity of NMNAT1 for ATP than for 6Yn-ATP (**40**) could possibly be due to subsequent inability of ADH to use 6Yn-NAD^+ (**3**) as a substrate for conversion into

6Yn-NADH, which was used as a readout for the assay. Regardless, the data demonstrated the ability of NMNAT1 to employ 6Yn-ATP for conversion into 6Yn-NAD^+.

Collectively, the findings show that 6Yn-Pro (**47**) and 6Yn-Ad (**25**) were converted into 6Yn-ATP (**40**) for use in RNA synthesis (**Figure 4.13B**), and that NMNAT1 can utilise 6Yn-ATP (**40**) as a substrate to produce 6Yn-NAD^+ (**3**) (**Figure 4.16B**). The precursor analogue 6Yn- series thus appear to be promising candidates for use in cells for metabolic generation of 6Yn-NAD^+ (**3**) and its subsequent use for intracellular protein ADP-ribosylation.

4.4 Validation of 6Yn-Pro and 6Yn-Ad by Metabolomics

4.4.1 Importance of Metabolomics in Studying NAD^+ Biosynthesis

Metabolomics is a powerful LC-MS-based analytical technique used in the study of metabolic processes *via* identification of the metabolites involved (**Figure 4.17A**).[248,249] The technique is useful in identifying metabolic bottleneck steps and establishing whether a proposed metabolic pathway is viable. Metabolomics can be untargeted,[250] where all metabolites from a sample are analysed and their identification is performed *via* subsequent filtering of data (**Figure 4.17B**), or targeted,[251] where detection is tailored towards specific metabolites of interest (**Figure 4.17C**).

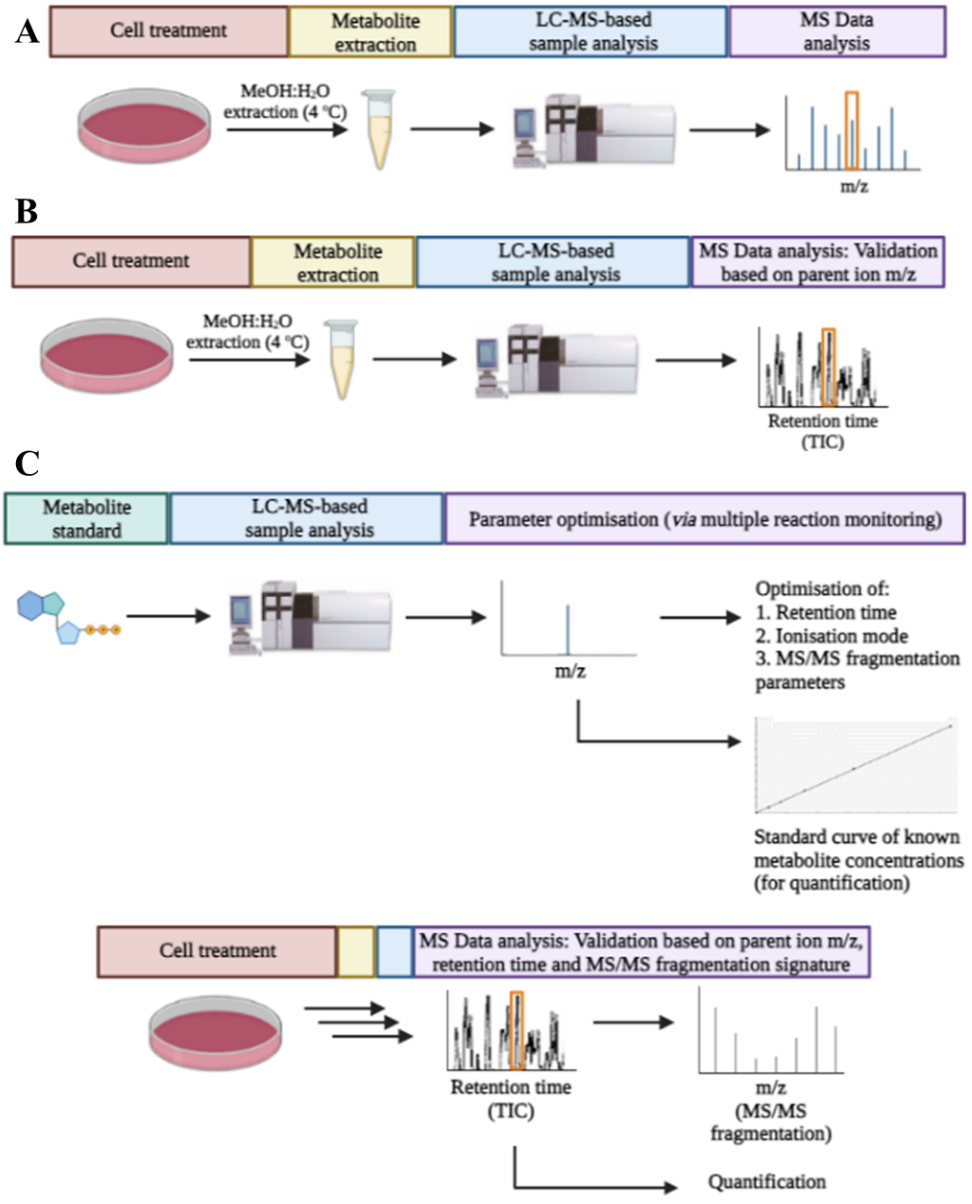


Figure 4.17. Workflows followed in metabolomics experiments. **A.** Overview of a typical workflow employed in metabolomics experiments. Live cells are treated with the appropriate probe and sample metabolites are

subsequently extracted in the appropriate solvent (e.g., MeOH:H_2O) at 4 ˚C. The extracted metabolites are then analysed by LC-MS for identification based on their m/z ratio, retention time, fragmentation patterns. **B.** Untargeted metabolomics workflow. Sample treatment, metabolite extraction and LC-MS analysis are performed as described in **A**. Subsequent metabolite identification relies predominantly on the parent m/z ratio. **C.** Targeted metabolomics workflow. Prior to sample generation and analysis, LC-MS method development and optimisation, and metabolite parameter optimisations are performed using pure stock solutions of known concentrations of the metabolites of interest. A standard curve is also typically generated for subsequent quantification of metabolite amounts from a biological sample. After sample generation, processing and analysis, metabolites are identified based on m/z ratio, retention time and fragmentation patterns. Overall, analysis is tailored towards detection of metabolites of interest.

In the context of ADP-ribosylation, untargeted metabolomics can be used for studying the utilisation of clickable ProTide or adenosine analogue probes in the NAD^+ biosynthesis pathway upon cell treatment since the technique allows detection of all the arising metabolites. The metabolites can then be identified by filtering of the acquired data and searching for the appropriate m/z ratio of each metabolite. Unfortunately, detection of phosphorylated nucleotide metabolites, such as AMP, ADP, ATP, and NAD^+, including their structural analogues, is difficult to achieve due to their chemically unstable nature and overall low abundance in a cellular context. In addition, these metabolites are also challenging to detect due to their innate physical properties; their permanent negative charge requires significant optimisation of the MS ionisation detection mode, and their highly polar nature makes them difficult to retain on an analytical column during LC-MS analysis. Consequently, their identification and accurate quantification by untargeted metabolomics[250] is difficult to achieve and unreliable.

To overcome these drawbacks, purified stock solutions of metabolites of interest are typically used for LC-MS method development to improve their retention time and establish an optimal MS ionisation detection mode, prior to analysing biological samples. In addition, parameter optimisation (see **Table 6.22**, **Section 6.4.2.1**) helps with establishing fragmentation patterns for the metabolites of interest and the generation of daughter ions (fragments) carrying signature m/z ratios. This brings an extra level of confidence during metabolite identification since identification is no longer based only on the m/z value of a metabolite, but also takes into account whether the presence of the corresponding daughter ions is observed. Furthermore, the retention time of the suspected metabolite is compared to the known retention time of the metabolite stock solution. Overall, detection is suited towards the metabolites of interest, which makes their identification more reliable and allows for their accurate quantification from a biological sample. This process is known as targeted metabolomics.[251]

In **Section 4.4**, targeted metabolomics was used to investigate whether probes 6Yn-Pro (**47**) and 6Yn-Ad (**25**) were utilised throughout the entire NAD^+ biosynthesis pathway for metabolic generation of 6Yn-NAD^+ (**3**) upon cell treatment, as well as the identification of potential conversion bottleneck steps. The effect of supplementing cells with NAD^+ precursors on native NAD^+ and 6Yn-NAD^+ (**3**) levels was also investigated, as well as the effect of NMNAT1 overexpression, H_2O_2 treatment, or a combination of all three.

4.4.2 Utilisation of 6Yn-Pro for Intracellular 6Yn-AMP Production

For initial validation of 6Yn-Pro (**47**) by metabolomics, intracellular concentration of 6Yn-AMP (**30**) was measured upon treatment of COV318 cells with 6Yn-Pro (**47**) alone, or in combination with methyl methanesulfonate[95] (MMS, a DNA damaging agent), FK866[252,253] (an inhibitor of nicotinamide phosphoribosyltransferase (NAMPT)), or olaparib (a PARP inhibitor) (**Figure 4.18**). This experiment and subsequent data analysis was performed by PhD student Michael Gruet (Keun Lab), who was provided with the probe 6Yn-Pro (**47**).

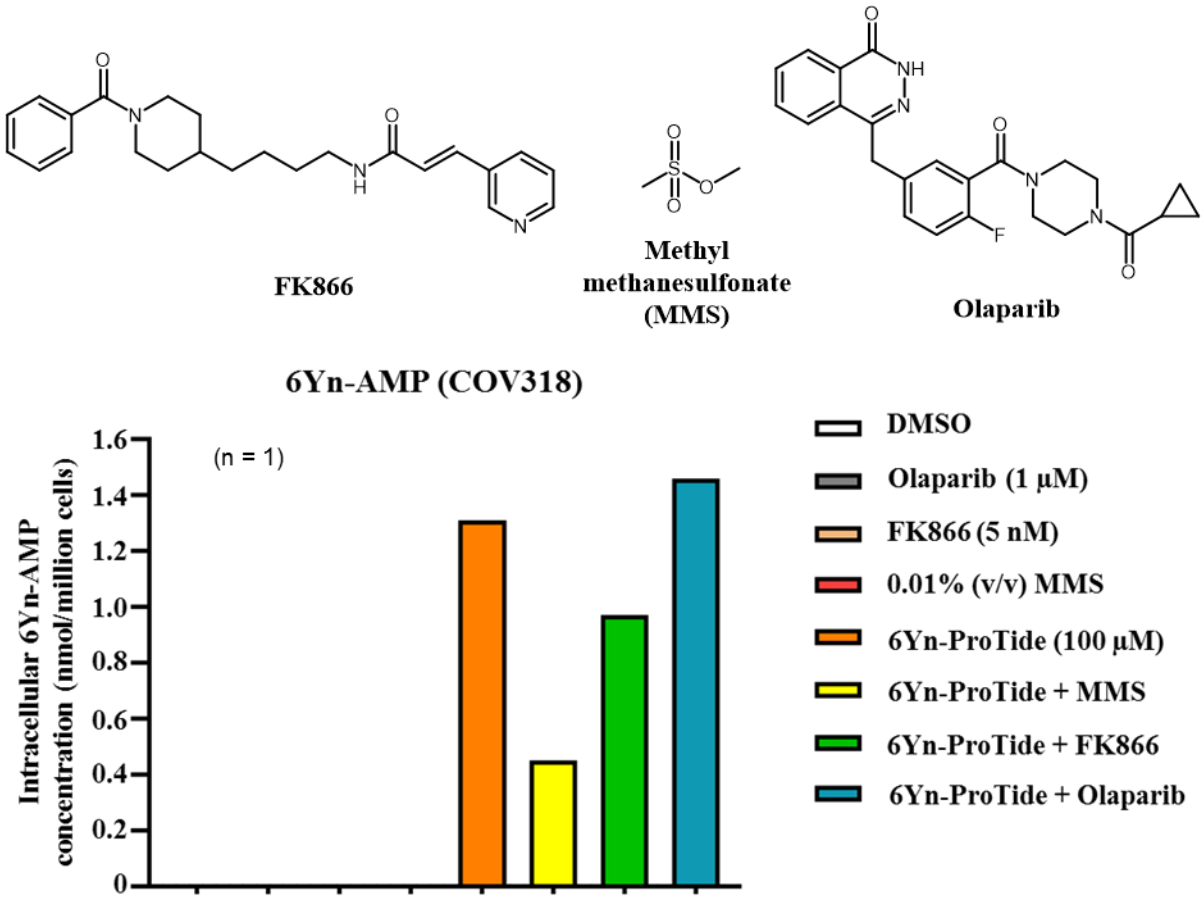


Figure 4.18. Intracellular metabolic production of 6Yn-AMP (**30**) in probe-treated COV318 cells. COV318 cells were treated with 6Yn-Pro (100 µM, 24 h) with/without olaparib pre-treatment (1 µM, 2 h), or in combination with the additives MMS (0.01% v/v, 1 h prior to metabolite extraction) and FK866 (5 nm, 24 h). Control samples

were generated by treating cells with DMSO (0.1% v/v) or each additive in the absence of 6Yn-Pro (**47**). Metabolites were subsequently extracted (MeOH:H_2O 80:20, 4 ˚C), samples analysed by LC-MS and 6Yn-AMP (**30**) levels measured. 6Yn-AMP concentrations were calculated (mmol/million cells) and plotted for each treatment condition.

Following sample analysis and data processing (see **Section 6.4**), it was observed that treatment of COV318 cells with 6Yn-Pro (**47**) alone resulted in its conversion to 6Yn-AMP (**30**), to an intracellular concentration of 1.3 nmol/million cells (**Figure 4.18**). On the other hand, co-treatment with 6Yn-Pro (**47**) and MMS or FK866 resulted in a 3-fold and 1.4-fold decrease in 6Yn-AMP (**30**) concentration, respectively, compared to treatment with 6Yn-Pro (**47**) alone. The observation upon MMS co-treatment was expected since it was hypothesised that co-treatment with MMS would upregulate ADP-ribosylation by PARP1/2 due to the induced DNA damage. Similarly, inhibition of NAMPT by FK866 would lead to depletion of cellular NAD^+ levels, as demonstrated in previous literature studies.[252,253] Consequently, both treatments would lead to a decrease of (6Yn-)NAD^+ concentrations, which would be expected to stimulate consumption of 6Yn-AMP (**30**) for production of 6Yn-NAD^+ (**3**), thus leading to a decrease in 6Yn-AMP (**30**) concentrations, as observed (**Figure 4.18**). In contrast, co-treatment with 6Yn-Pro (**47**) and olaparib restored the overall 6Yn-AMP (**30**) concentration relative to 6Yn-Pro (**47**) treatment alone. This observation was expected since inhibition of PARPs would decrease demand for intracellular (6Yn-)NAD^+ thus resulting in decreased consumption of 6Yn-AMP (**30**) for production of 6Yn-NAD^+ (**3**) *via* NAD^+ biosynthesis.

4.4.3 Utilisation of 6Yn-Ad in 6Yn-NAD^+ Biosynthesis

To investigate whether 6Yn-Ad (**25**) and the corresponding 6Yn- metabolites were utilised in all stages of 6Yn-NAD^+ (**3**) biosynthesis, PhD student Michael Gruet was provided with 6Yn-Ad (**25**), who performed a time course experiment in COV318 cells. COV318 cells were treated with 6Yn-Ad (**25**) for 1, 3, 6 or 24 hours, metabolites were extracted and the abundance of each measured metabolite (6Yn-AMP (**30**), 6Yn-ATP (**40**), 6Yn-NAD^+ (**3**) was plotted as a function of the metabolite peak area (area under the curve (AUC), see **Section 6.4.4**) for each metabolite at each extraction time point (**Figure 4.19**).

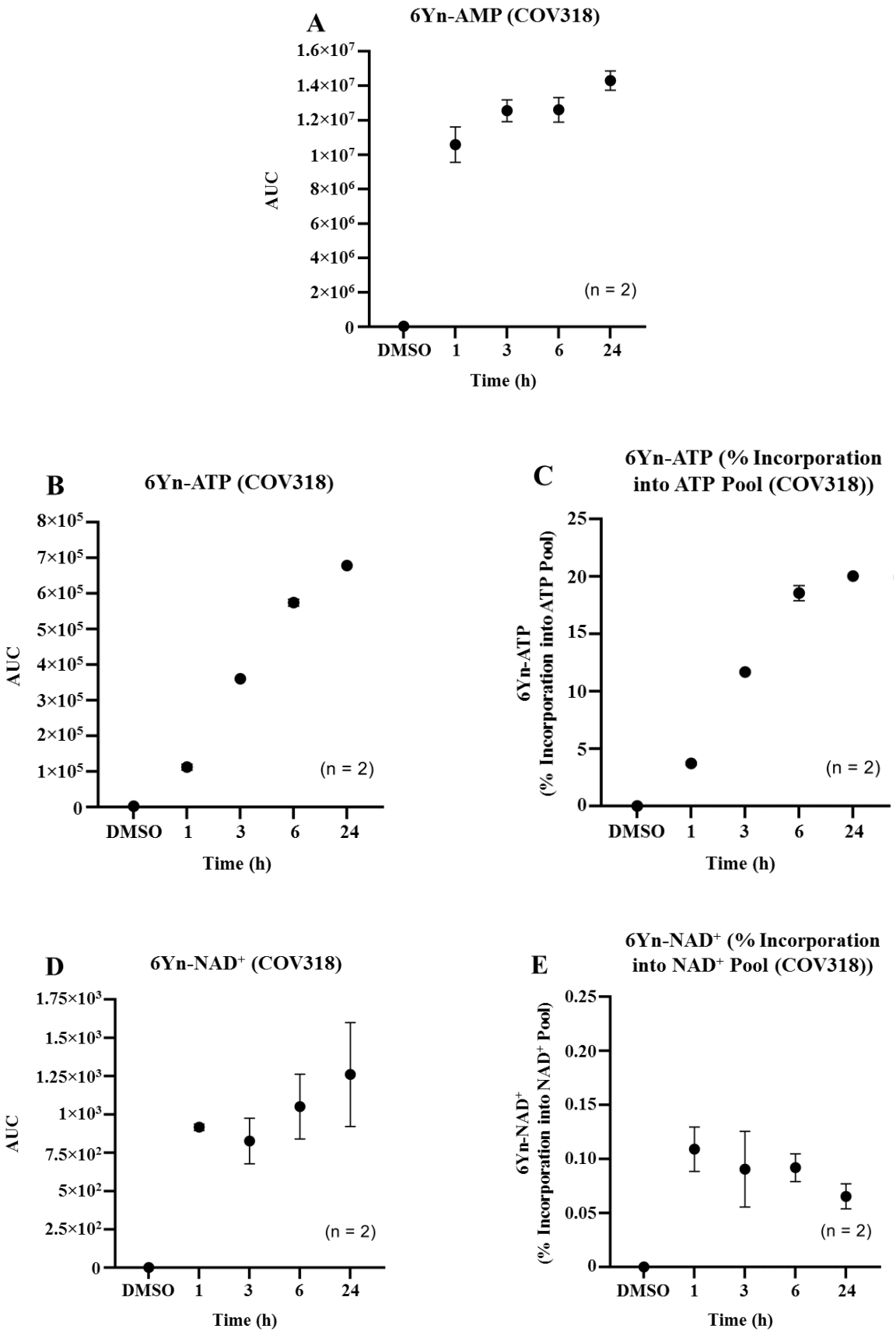


Figure 4.19. Time course experiment for COV318 cells treated with 6Yn-Ad (**25**). COV318 cells were treated with DMSO (0.1% v/v) or 6Yn-Ad (500 μM) for 1 h, 3 h, 6 h and 24 h. Metabolites were extracted (MeOH:H_2O

80:20, 4 ˚C) and analysed by LC-MS. Metabolite abundance was shown in absolute values (area under the curve (AUC)) or relative (% incorporation into relevant native metabolite pool) **A**: absolute abundance (AUC) for 6Yn-AMP (**30**). **B**. absolute abundance (AUC) for 6Yn-ATP (**40**). **C**. % incorporation of 6Yn-ATP (**40**) into native ATP pool. **D**. absolute abundance (AUC) for 6Yn-NAD^+ (**3**). **E**. % incorporation of 6Yn-NAD^+ (**3**) into native NAD^+ pool.

Following treatment with 6Yn-Ad (**25**), it was observed that the probe was readily converted into 6Yn-AMP (**30**) within the first hour, as evidenced by the rapid increase in 6Yn-AMP (**30**) abundance, compared to the DMSO control, and the relative plateauing beyond the 1 h time point (**Figure 4.19A**). In contrast, conversion into 6Yn-ATP (**40**) was gradual and maximum abundance was reached after 24 hours (**Figure 4.19B**). This gradual increase was reflected in the incorporation of 6Yn-ATP (**40**) into the overall ATP pool, which reached a maximum of ~20% after 24 hours, although % incorporation started to plateau after 6 hours (**Figure 4.19C**). These findings provided evidence that maximum 6Yn-ATP (**40**) production and % incorporation into ATP pool was achieved between 6 and 24 hours, thus an optimum time point for treatment of cells with the probe was determined to be between 6 and 24 h. On the other hand, the observed increase in 6Yn-ATP (**40**) production over 24 hours was not reflected in the incorporation of 6Yn-NAD^+ (**3**) into the overall NAD pool. The measured abundance of 6Yn-NAD^+ (**3**) was low, in the 10^3 range, which was close to the measured background, and only marginally increased between 1 h and 24 hours (by ~30%) (**Figure 4.19D**). When compared with % incorporation of 6Yn-NAD^+ (**3**) into the overall NAD^+, however, incorporation decreased from 0.11% at 1 h to 0.07% after 24 hours (**Figure 4.19E**).

The data presented in **Figure 4.19** showed that 6Yn-Ad (**25**) was readily converted into 6Yn-AMP (**30**), within 1 h (**Figure 4.19A**), and 6Yn-ATP (**40**), within 6 to 24 hours (**Figure 4.19B**), as illustrated by the observed ~20% incorporation of 6Yn-ATP (**40**) into the entire ATP pool (**Figure 4.19C**). However, subsequent conversion of 6Yn-ATP (**40**) into 6Yn-NAD^+ (**3**) was poor, as evidenced by the low absolute abundance of 6Yn-NAD^+ (**3**) (**Figure 4.19D**) and low overall incorporation into the NAD^+ pool (**Figure 4.19E**). The data thus suggested that the metabolic conversion of 6Yn-ATP (**40**) into 6Yn-NAD^+ (**3**) was a bottleneck step in 6Yn-NAD^+ (**3**) biosynthesis, which was attributed to at least one of the factors below:

1. Reduced affinity of NMNAT1 for 6Yn-ATP (**40**), compared to native ATP
2. Low expression levels of NMNAT1, resulting in low conversion of 6Yn-ATP (**40**) into 6Yn-NAD^+ (**3**)

3. Significantly lower cellular abundance of the metabolite β-NMN relative to metabolically generated 6Yn-ATP (**40**), which was required for coupling with 6Yn-ATP (**40**) to produce 6Yn-NAD^+ (**3**) (see **Figure 4.1**)

Docking results in **Chapter Two** predicted that NMNAT1 should be able to use 6Yn-ATP (**40**) as a substrate, therefore factor one listed above was considered unlikely to be the origin of low 6Yn-NAD^+ (**3**) biosynthesis. Thus, our focus shifted on establishing how the latter two factors affected biosynthesis of 6Yn-ATP (**40**) and 6Yn-NAD^+ (**3**).

4.4.4 Effect of NMNAT1 Overexpression on 6Yn-NAD^+ Biosynthesis

The effect of NMNAT1 expression levels on 6Yn-NAD^+ (**3**) biosynthesis was investigated by overexpressing NMNAT1 in HEK293T cells and measuring the abundance of the relevant metabolites (6Yn-AMP (**30**), 6Yn-ATP (**40**), 6Yn-NAD^+ (**3**)) before and after NMNAT1 overexpression, and treatment with 6Yn-Ad (**25**). The experiment was performed in HEK293T cells due to the high efficiency of lipofectamine transfection of the cell line, in comparison to COV318 cells, which were difficult to transfect. This experiment and subsequent data analysis was performed by PhD student Michael Gruet.

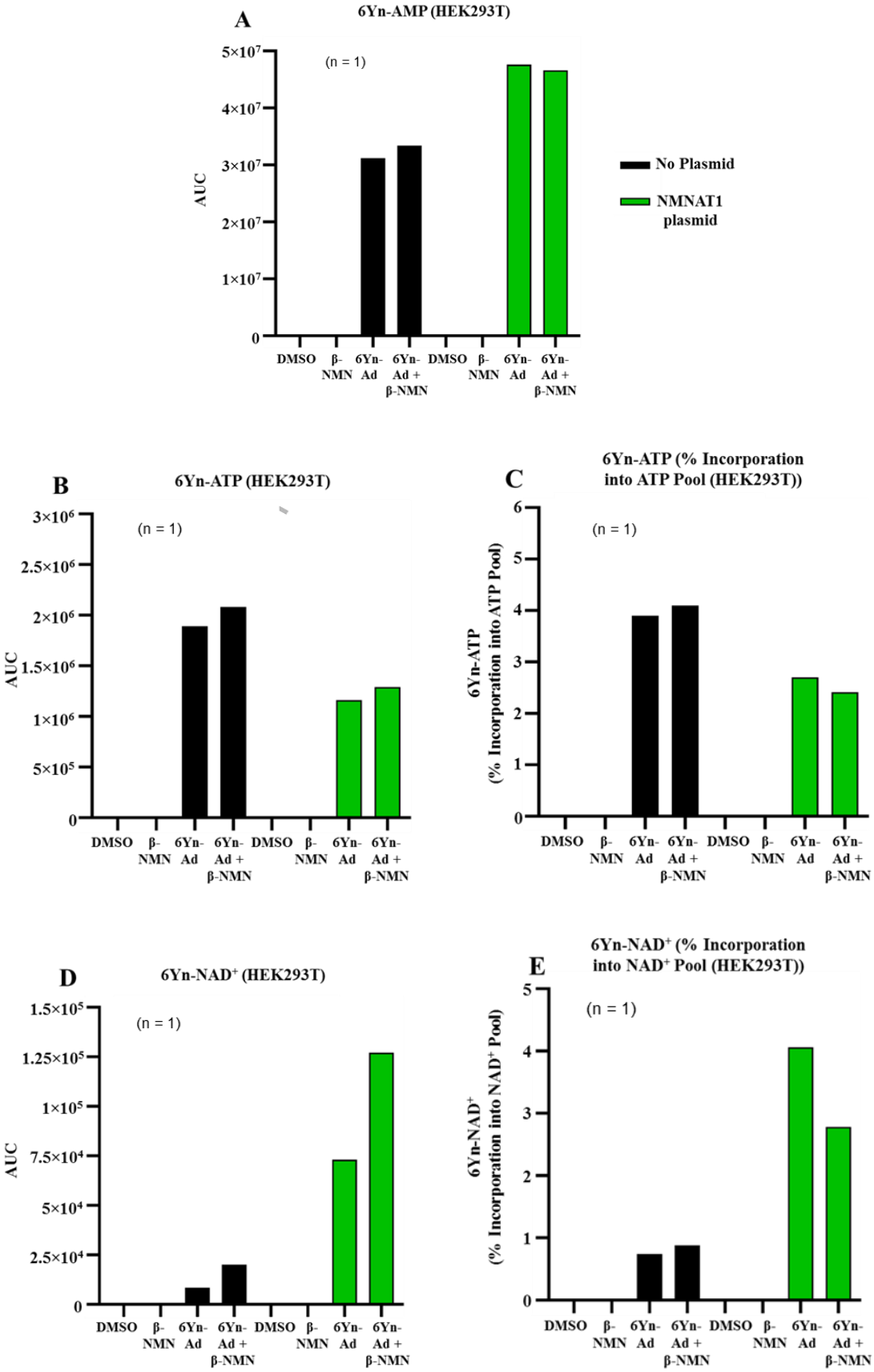


Figure 4.20. Metabolite profiling in HEK293T cells following NMNAT1 overexpression and treatment with 6Yn-Ad (**25**). Metabolite levels for 6Yn-AMP (**30**), 6Yn-ATP (**40**) and 6Yn-NAD$^+$ (**3**) were measured in non-

transfected cells (baseline NMNAT1 levels) or NMNAT1 plasmid transfected cells (NMNAT1 overexpression, 24 h) following treatment with DMSO (0.1% v/v) or 6Yn-Ad (500 μM, 24 h). In co-treated samples, cells were supplemented with β-NMN (500 μM, 24 h). **A.** absolute abundance (AUC) for 6Yn-AMP (**30**). **B.** absolute abundance (AUC) for 6Yn-ATP (**40**). **C.** % incorporation of 6Yn-ATP (**40**) into native ATP pool. **D.** absolute abundance (AUC) for 6Yn-NAD^+ (**3**). **E.** % incorporation of 6Yn-NAD^+ (**3**) into native NAD^+ pool.

Following overexpression of NMNAT1 and treatment with 6Yn-Ad (**25**), it was observed that NMNAT1 overexpression resulted in a 1.5-fold increase in 6Yn-AMP (**30**) levels compared to cells for which NMNAT1 was not overexpressed (**Figure 4.20A**). In contrast, overexpression of NMNAT1 resulted in a 1.5-fold decrease of absolute 6Yn-ATP (**40**) levels (**Figure 4.20B**) and a 1.5-fold decrease of its % incorporation into ATP pool when compared to no overexpression (2.8% vs 4.0%, respectively, **Figure 4.20C**). This observation was expected since it was hypothesised that higher NMNAT1 levels would increase consumption of 6Yn-ATP (**40**) to produce 6Yn-NAD^+ (**3**). It was also observed that supplementation of cells with β-NMN did not have a significant effect on 6Yn-AMP (**30**) and 6Yn-ATP (**40**) abundance.

Upon measuring 6Yn-NAD^+ (**3**) levels, it was revealed that NMNAT1 overexpression resulted in a ~5-fold increase in 6Yn-NAD^+ (**3**) levels when compared to no overexpression (**Figure 4.20D**). Furthermore, supplementation with β-NMN resulted in a further 1.8-fold increase compared to non-supplemented cells (**Figure 4.20D**). The 5-fold increase following NMNAT1 overexpression was reflected in the overall 6Yn-NAD^+ (**3**) % incorporation into the NAD^+ pool, where a similar ~5-fold increase was observed, raising from 0.75% to 4.0% (**Figure 4.20E**). It was observed that β-NMN supplemented cells also experienced increased % incorporation of 6Yn-NAD^+ (**3**) into the NAD^+ pool, although to a lower extent, of ~3-fold, from 0.9% to 2.8%. This was surprising considering that overall 6Yn-NAD^+ (**3**) levels were higher in supplemented cells, which suggested that β-NMN supplementation boosted native NAD^+ levels higher than for metabolically derived 6Yn-NAD^+. Potentially, this could imply a decrease in subsequent utilisation of 6Yn-NAD^+ (**3**) by PARPs due to its dilution in the overall NAD^+ pool.

4.4.5 Effect of NR/NRH/β-NMN Supplementation on NAD^+ Biosynthesis

Previous literature studies have provided evidence that supplementation of cells with the NAD^+ precursors NR (**23**), NRH (**24**) and β-NMN resulted in an increase of cellular NAD^+ levels as soon as 1 h following supplementation, by boosting cellular β-NMN/ β-NMNH concentrations.[205-209] To establish the extent to which each supplement boosted native NAD^+ production over the typical 24-hour treatment employed in 6Yn-Ad (**25**) and 6Yn-Pro (**47**)

experiments, NAD^+ levels were measured at 1 h and 24 hours in the cell lines HEK293T, T47D and MDA-MB-435 (**Figure 4.21**).

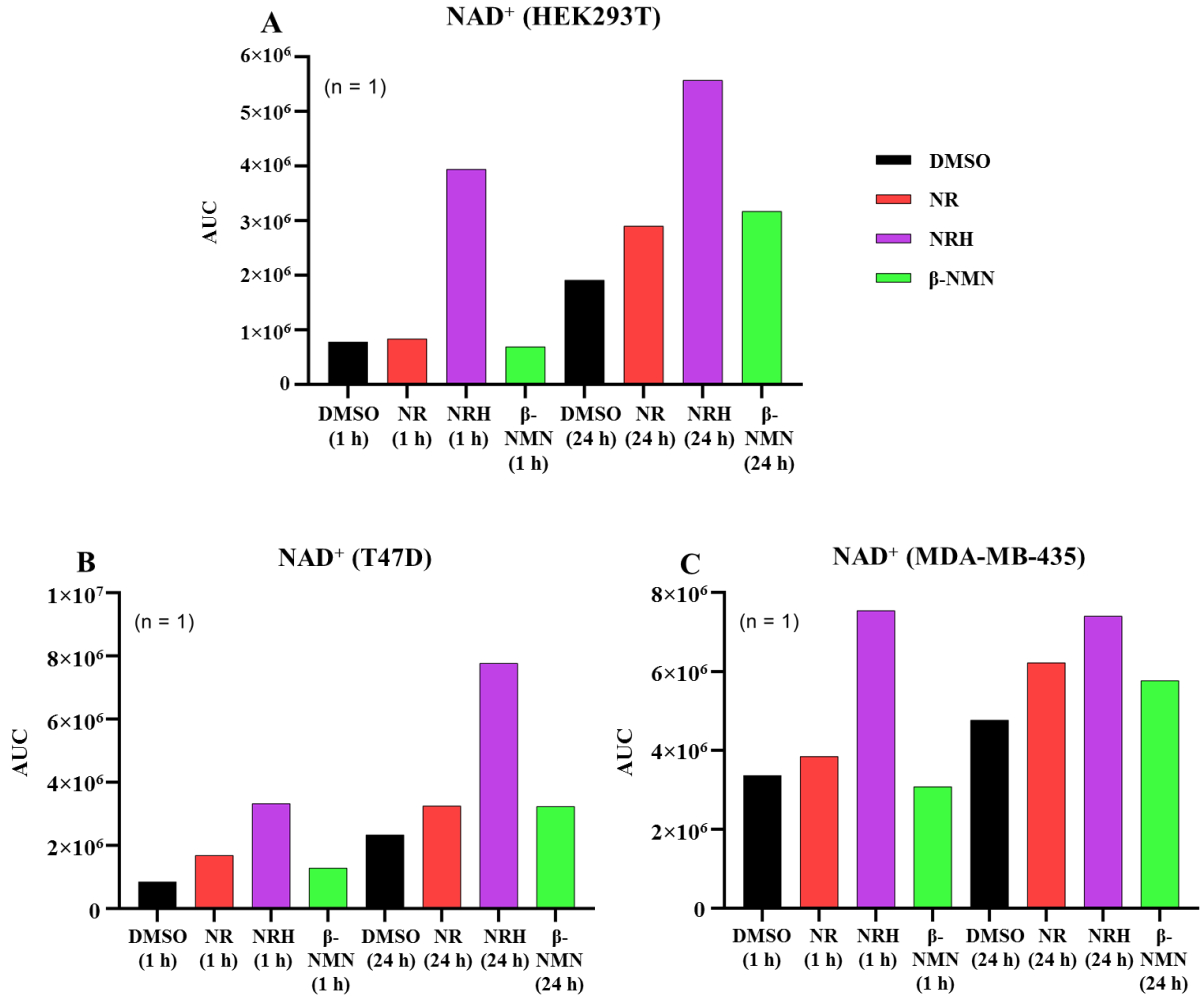


Figure 4.21. Effect of supplementation of NAD^+ precursors on intracellular NAD^+ levels. Cells were treated with DMSO (0.1% v/v), NR (500 µM), NRH (500 µM) or β-NMN (500 µM) for 1 h or 24 h prior to metabolite extraction and analysis. **A**: absolute abundance (AUC) for NAD^+ in HEK293T cells. **B**: absolute abundance (AUC) for NAD^+ in T47D cells. **C**: absolute abundance (AUC) for NAD^+ in MDA-MB-435 cells.

Treatment of all three cell lines with NR (**23**) or β-NMN revealed that the two supplements did not affect NAD^+ levels after 1 h treatment relative to the corresponding DMSO control (**Figure 4.21**). In contrast, a 1 h treatment with NRH (**24**) resulted in a 4-fold increase in NAD^+ levels in HEK293T (**Figure 4.21A**) and T47D (**Figure 4.21B**) cells, and a 2-fold increase in MDA-MB-435 cells (**Figure 4.21C**). Extending the treatment to 24 hours resulted in a ~1.5-fold increase in NAD^+ levels for both NR (**23**) and β-NMN treated cells relative to DMSO control (24 h). Regardless, NRH (**24**) treatment still resulted in the highest increase in NAD^+ levels in

all cell lines, of 3-fold, 3.2-fold and 1.7-fold for HEK293T (**Figure 4.21A**), T47D (**Figure 4.21B**) and MDA-MB-435 (**Figure 4.21C**) cells, respectively.

The data supported previous literature findings that NRH (**24**) was superior in boosting NAD^+ levels when compared to NR (**23**) and β-NMN.[205-207] Furthermore, the increase was largely maintained over 24 hours, which was the typical duration of treatment with the adenosine and ProTide analogue probes used in this work. It was also observed that HEK293T and T47D cells responded with the highest fold-change as well as highest absolute increase in NAD^+ levels following NRH treatment. Taken together, these findings suggested that NRH supplementation in the two cell lines may be beneficial for boosting metabolic production of NAD^+ analogues following treatment with the relevant NAD^+ precursor probes.

4.4.6 Effect of NR/NRH/β-NMN Supplementation on 6Yn-NAD^+ Biosynthesis

To determine whether the boost in native cellular NAD^+ levels observed in **Figure 4.21**, due to supplementation with NAD^+ precursors, was reciprocated for 6Yn-NAD^+ (**3**) biosynthesis, HEK293T, T47D and MDA-MB-435 cells were co-treated with 6Yn-Pro (**47**) and β-NMN, NR (**23**) or NRH (**24**) (**Figure 4.22**).

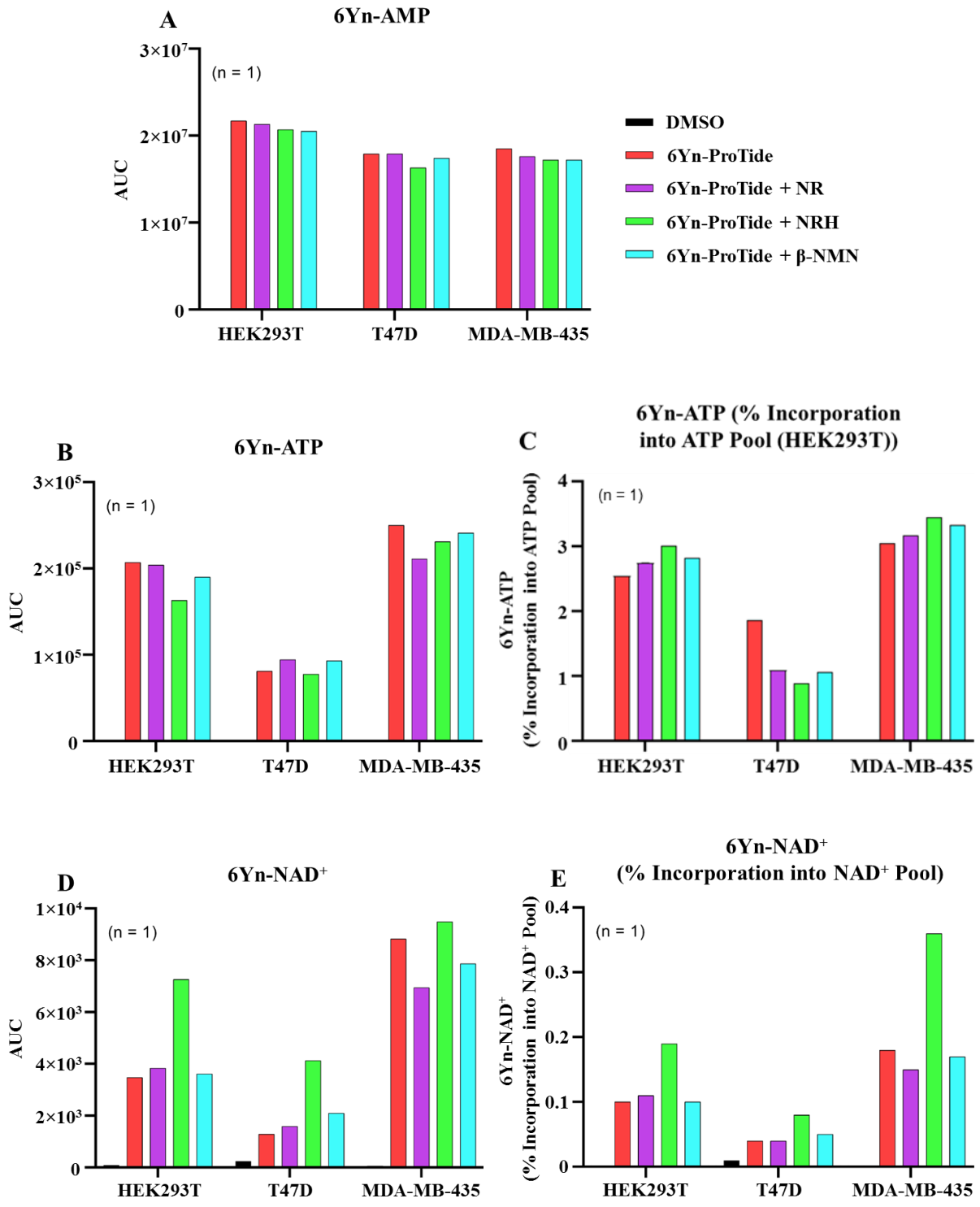


Figure 4.22. Effect of supplementation of NAD^+ precursors on intracellular 6Yn-metabolites levels. HEK293T, T47D and MDA-MB-435 cells were treated with DMSO (0.1% v/v) or 6Yn-Pro (100 µM, 24 h) alone, or co-treated with 6Yn-Pro (100 µM, 24 h) and NR (500 µM, 24 h), NRH (500 µM, 24 h) or β-NMN (500 µM, 24 h) prior to metabolite extraction and analysis. **A**: absolute abundance (AUC) for 6Yn-AMP (**30**). **B**: absolute abundance (AUC) for 6Yn-ATP (**40**). **C**: % incorporation of 6Yn-ATP (**40**) into native ATP pool. **D**: absolute abundance (AUC)) for 6Yn-NAD^+ (**3**). **E**: % incorporation of 6Yn-NAD^+ (**3**) into native NAD^+ pool.

Following data analysis (performed by PhD student Michael Gruet), it was determined that supplementation of 6Yn-Pro-treated cells with β-NMN, NR (**23**) or NRH (**24**) did not influence 6Yn-AMP (**30**) levels in all three cell lines, when compared to no supplementation (**Figure 4.22A**). Similarly, the precursors did not appear to have a significant effect on absolute 6Yn-ATP (**40**) levels when compared to no supplementation (**Figure 4.22B**). Although % incorporation of 6Yn-ATP (**40**) into the overall ATP pool in HEK293T and MDA-MB-435 cells was largely comparable before and after precursor supplementation, T47D cells exhibited a 2-fold drop in % incorporation in all cases, from ~2% to ~1% (**Figure 4.22C**), which could be indicative of increased consumption of 6Yn-ATP (**40**) in this cell line.

Surprisingly, although NRH (**24**) supplementation did not appear to affect overall 6Yn-ATP (**40**) levels in any of the cell lines (**Figure 4.22C**), absolute 6Yn-NAD^+ (**3**) levels increased 2-fold in HEK293T cells and 2.5-fold in T47D cells following NRH (**24**) supplementation compared to no supplementation (**Figure 4.22D**). These observations were reflected in the % incorporation of 6Yn-NAD^+ (**3**) into the NAD^+ pool, which showed a corresponding 2-fold increase (from 0.1% to 0.2%) for HEK293T cells and a similar 2-fold increase (from 0.05% to 0.1%) for T47D cells (**Figure 4.22E**). On the other hand, β-NMN and NR supplementation did not have a significant effect on absolute 6Yn-NAD^+ (**3**) levels or % incorporation of 6Yn-NAD^+ (**3**) into the NAD^+ pool.

The observation that a similar 2-fold increase (from 0.18% to 0.36%) was seen following supplementation with NRH (**24**) in MDA-MB-435 cells (**Figure 4.22E**) was puzzling considering that there was no increase observed in absolute 6Yn-NAD^+ levels (**Figure 4.22D**). Regardless, the presented data provided evidence that supplementation of 6Yn-Pro-treated cells with NRH (**24**) was beneficial for promoting 6Yn-NAD^+ (**3**) biosynthesis. This was concluded based on the observations that NRH (**24**) supplementation boosted absolute 6Yn-NAD^+ (**3**) levels 2-fold and 2.5-fold in HEK293T and T47D cells, respectively (**Figure 4.22D**), and 2-fold in the % incorporation of 6Yn-NAD^+ (**3**) into the overall NAD^+ pool in all three cell lines, when compared to no supplementation.

4.4.7 Effect of H_2O_2 on 6Yn-NAD^+ Biosynthesis

Considering the role of oxidative stress, due to H_2O_2 treatment, in the upregulation of ADP-ribosylation, it was important to investigate how H_2O_2 treatment affected 6Yn-NAD^+ biosynthesis. In this experiment, 6Yn-Pro-treated samples were either treated with H_2O_2 alone

or in combination with NRH supplementation. In all cases, NMNAT1 was overexpressed (experiment, sample and data analysis were performed by PhD student Michael Gruet).

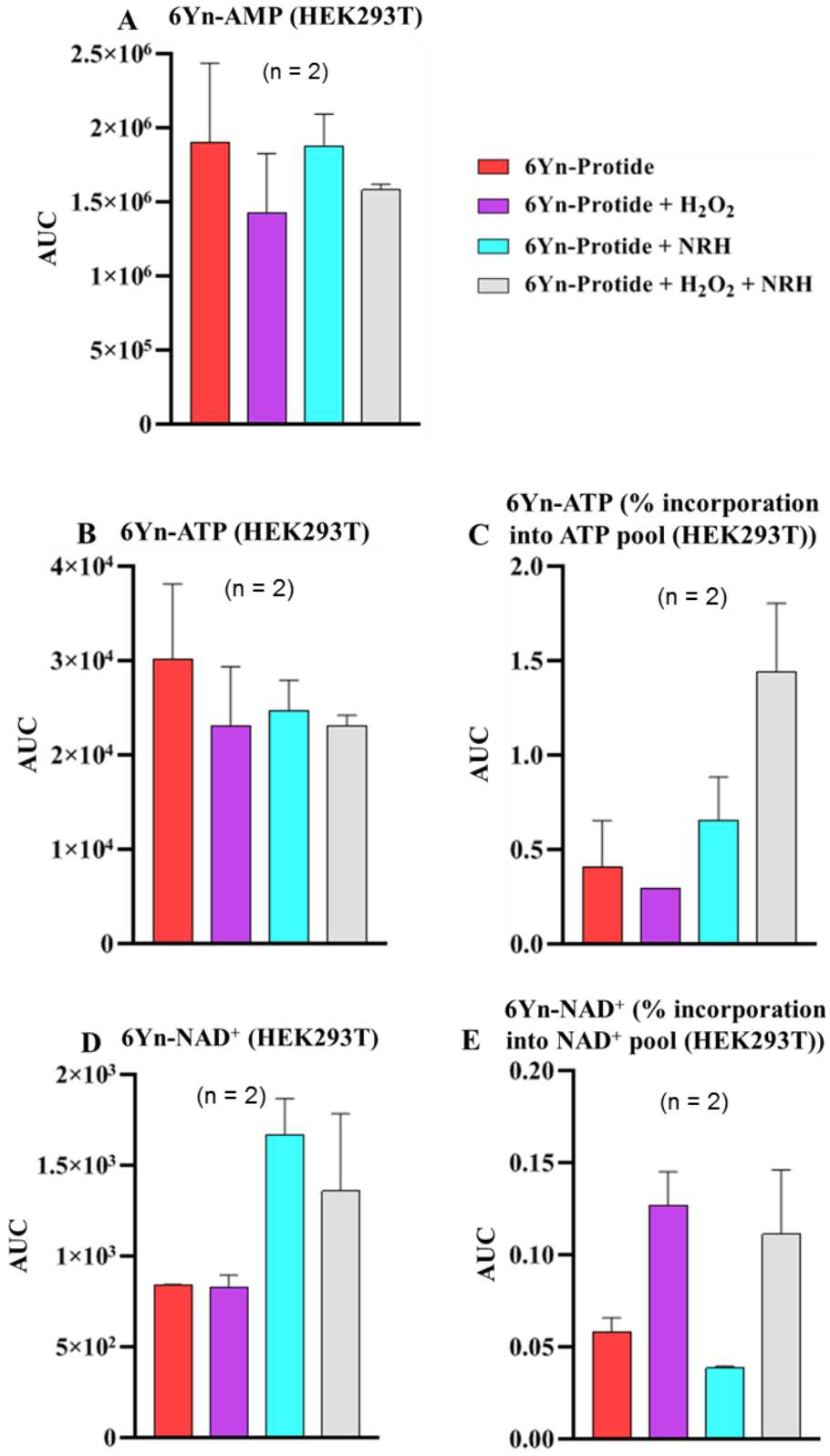


Figure 4.23. Effect of H_2O_2 treatment on intracellular 6Yn-metabolites levels in the presence/absence of NRH (**24**) supplementation. HEK293T cells were treated with 6Yn-Pro (100 µM, 24 h) alone or co-treated with

6Yn-Pro (100 µM, 24 h) and NRH (500 µM, 24 h), followed by H_2O_2 treatment (2 mM, 10 min) prior to metabolite extraction and analysis. **A**: absolute abundance (AUC) for 6Yn-AMP (**30**). **B**: absolute abundance (AUC) for 6Yn-ATP (**40**). **C**: % incorporation of 6Yn-ATP (**40**) into native ATP pool. **D**: absolute abundance (AUC)) for 6Yn-NAD^+ (**3**). **E**: % incorporation of 6Yn-NAD^+ (**3**) into native NAD^+ pool.

Treatment of HEK293T cells with 6Yn-Pro (**47**) followed by H_2O_2 resulted in a ~25% reduction of 6Yn-AMP (**30**) abundance when compared to 6Yn-Pro (**47**) treatment alone (**Figure 4.23A**). In the presence of NRH (**24**), the decrease was ~15%. Similarly, 6Yn-ATP (**40**) abundance decreased by ~20% following H_2O_2 treatment or NRH (**24**) and H_2O_2 co-treatment (**Figure 4.23B**) when compared to 6Yn-Pro (**47**) treatment alone. On the other hand, the % incorporation of 6Yn-ATP (**40**) into the ATP pool decreased by ~20% after H_2O_2 treatment alone but increased 3.5-fold after co-treatment with NRH (**24**) + H_2O_2 (**Figure 4.23C**). This observation was surprising because it suggested that NRH (**24**) led to increased consumption of native ATP relative to 6Yn-ATP (**40**), thus leading to a reduction in the native ATP pool size and a perceived increase in % incorporation of 6Yn-ATP (**40**). Such preference for native ATP was not observed in the previously described experiment in **Section 4.4.6** (**Figures 4.22B** and **4.22C**) thus its origin could not be explained in this experiment. Overall, the decrease in 6Yn-AMP (**30**) and 6Yn-ATP (**40**) levels (**Figures 4.23A** and **4.23B**) was expected in the presence of H_2O_2 due to PARP1 activation and increased demand for NAD^+ from NAD^+ biosynthesis.

Treatment of cells with 6Yn-Pro (**47**), NRH (**24**) and H_2O_2 resulted in no change of 6Yn-NAD^+ (**3**) abundance compared to 6Yn-Pro (**47**) treatment alone (**Figure 4.23D**). On the other hand, co-treatment with 6Yn-Pro (**47**) and NRH (**24**) followed by H_2O_2 treatment resulted in a 1.6-fold increase in 6Yn-NAD^+ (**3**) abundance compared to 6Yn-Pro (**47**) treatment alone (**Figure 4.23D**), which translated into a 1.9-fold increase of 6Yn-NAD^+ % incorporation into NAD^+ pool, from 0.06% to 0.115% (**Figure 4.23E**). These findings were surprising since H_2O_2 treatment was expected to result in a decrease of absolute 6Yn-NAD^+ (**3**) levels compared to 6Yn-NAD^+ (**3**) levels in its absence, given the increased cellular demand for NAD^+ due to PARP1 activation. Thus, the observed increase in overall 6Yn-NAD^+ (**3**) levels and its % incorporation into the NAD^+ pool potentially suggested that ADP-ribosylation with native NAD^+ was still favoured over ADP-ribosylation with 6Yn-NAD^+ (**3**) even under oxidative stress.

4.4.8 Conclusions from Metabolomics Experiments and Future Work

Targeted metabolomics[251] was employed to study the utilisation of the probes 6Yn-Ad (**25**) and 6Yn-Pro (**47**) in the NAD^+ biosynthesis pathway. This was performed by monitoring for their metabolic conversion, by LC-MS analysis, into the corresponding 6Yn-AMP (**30**), 6Yn-ATP (**40**) and 6Yn-NAD^+ (**3**) metabolites in several cell lines. The presented data provided evidence that both probes 6Yn-Pro (**47**) and 6Yn-Ad (**25**) were membrane permeable and efficiently converted into 6Yn-AMP (**30**) intracellularly (**Figures 4.18** and **4.19A**, respectively). Furthermore, both probes were metabolically converted into the metabolite 6Yn-ATP (**40**) (**Figures 4.19B, 4.20B** and **4.22B)**, although the extent of conversion into 6Yn-ATP (**40**), as well as its % incorporation into overall ATP pool, appeared to be dependent on the type of cell line used (**Figures 4.19C, 4.20C** and **4.22C**). For COV318 cells, a ~20% incorporation of 6Yn-ATP into the cellular ATP pool was observed (**Figure 4.19C**) after treatment with 6Yn-Ad (**25**), whereas for HEK293T, T47D and MDA-MB-435 cells this was ~3%, 2% and 3%, respectively (**Figure 4.22C**), after treatment with 6Yn-Pro (**47**). The data thus suggested that probe utilisation in NAD^+ biosynthesis can be significantly affected by the type of cell line used in an experiment.

Subsequent metabolic conversion of 6Yn-ATP (**40**) into 6Yn-NAD^+ (**3**) by NMNAT1 was identified as a bottleneck step in the pathway. This was evidenced by the low extent of conversion of 6Yn-ATP (**40**) into 6Yn-NAD^+ (**3**) in 6Yn-Ad-treated COV318 cells, both in terms of absolute abundance levels (**Figure 4.19D**) and as a % incorporation of 6Yn-NAD^+ (**3**) into the cellular NAD^+ pool (**Figure 4.19E**). As a result, this step was targeted for further optimisation, such as stimulating conversion of 6Yn-ATP (**40**) into 6Yn-NAD^+ (**3**) through overexpression of NMNAT1 and increasing intracellular β-NMN/β-NMNH levels by supplementation with the NAD^+ precursors β-NMN, NR (**23**) and NRH (**24**).

Consequently, supplementation of probe-treated cell lines with the NAD^+ precursor NRH (**24**) was shown to result in a 2-fold increase in metabolic levels of 6Yn-NAD^+ (**3**) (**Figure 4.22D**). This was further reflected in its % incorporation into the NAD^+ pool, which also raised 2-fold in all three cell lines tested (**Figure 4.22E**). Similarly, NMNAT1 overexpression in HEK293T cells boosted overall 6Yn-NAD^+ (**3**) levels, leading to a 5-fold increase in 6Yn-Ad-treated cells in comparison to baseline NMNAT1 levels (**Figure 4.20D**). The increase was in turn reflected in the % incorporation of 6Yn-NAD^+ (**3**) into the entire NAD^+ pool, which raised from 0.75% before NMNAT1 overexpression, to 4% after NMNAT1 overexpression (**Figure 4.20E**).

These findings thus demonstrated that supplementing cells with NRH (**24**) and overexpressing NMNAT1 promoted metabolic conversion of 6Yn-ATP (**40**) into 6Yn-NAD^+ (**3**).

Finally, the effect H_2O_2 treatment on 6Yn-NAD^+ (**3**) was investigated. H_2O_2 treatment resulted in a decrease of 6Yn-ATP (**40**) levels in 6Yn-Pro-treated HEK293T cells, likely due to increased consumption of 6Yn-ATP (**40**) for 6Yn-NAD^+ (**3**) biosynthesis as a result of PARP1 activation (**Figure 4.23B**). This was evidenced by a ~20% decrease in 6Yn-ATP (**40**) abundance levels when compared to samples not treated with H_2O_2 (**Figure 4.23B**). However, the decrease was not reflected in the overall 6Yn-NAD^+ (**3**) % incorporation into the cellular NAD^+ pool; instead, a 1.9-fold increase was noted, which could suggest that, even under oxidative stress, RARPs have a preference for native NAD^+ over 6Yn-NAD^+ (**3**) for subsequent ADP-ribosylation.

Overall, the data presented in **Section 4.4** provided evidence that probes 6Yn-Ad (**25**) and 6Yn-Pro (**47**) can be metabolically converted into the corresponding 6Yn-NAD^+ (**3**) upon cell treatment.

It should be noted that, unfortunately, it was not possible to perform analysis of HEK293T, T47D and MDA-MB-435 cell line samples treated with the isotopically labelled probe ^{15}N-Pro (**64**) (see **Appendix Table A.1**) in the time frame of this project. Isotopically labelled ^{15}N- metabolites (**Figure 3.4**) are structurally identical to native NAD^+ biosynthesis metabolites. Consequently, metabolomics experiments with ^{15}N-Ad (**63**) or ^{15}N-Pro (**64**) would have provided information as to whether there were innate limitations to metabolic flux of metabolite molecules due to cellular dynamics, and not due to increased steric bulk on clickable metabolites because of the presence of clickable groups, such as in the 6Yn- metabolite series. Because of challenges that were encountered during LC-MS method development and metabolite parameter optimisation of ^{15}N-metabolites, analysis of the ^{15}N-Pro (**64**) treated samples (see **Appendix Table A.1**) was delayed and has not yet been performed.

4.5 Validation of ProTide Probes by Proteomics

4.5.1 Importance of Chemical Proteomics in Studying ADP-ribosylation

Proteomics is a powerful LC-MS-based analytical technique used for identification and quantification of proteins in a biological system[254-256]. The technique allows for proteome-wide monitoring of protein expression profiles, which permits comparison of the global proteome across different experimental conditions. Recent technological advancements have led to the development of highly sensitive MS instruments, which allow for identification and accurate quantification of very low abundant proteins. This provides significant advantages over the use of less sensitive biochemical techniques such as western blotting, for which identification of low abundant proteins may be difficult, or impossible, to achieve and accurate quantification is unreliable.

Chemical proteomics has been applied in the study of various post-translational modifications by using tagged co-factors, typically by incorporating a clickable group onto them.[257,258] The tagged co-factor probes are then typically used for intracellular metabolic protein labelling, or for labelling in cell lysates. For ADP-ribosylation, co-factor tagging has been achieved through the development and use of clickable NAD^+ analogues (**Table 1.2**) for protein labelling in cell lysates and in recombinant protein assays (**Figure 1.7**).[104-119] The presence of a clickable group, such as azide or alkyne, allows for ligation of the labelled proteins to functional moieties by click chemistry reactions, such as CuAAC (**Table 1.3**). Such functional moieties include fluorophores, such as TAMRA, which allow for visualisation of protein labelling by IGF or fluorescence microscopy, and biotin, which allows for subsequent selective enrichment of the labelled proteins only (protein pull-down). Once enriched, labelled proteins are then digested using proteases such as trypsin, which release corresponding shorter length peptides that are more easily separated by LC and readily detectable by MS. This approach, in combination with tandem mass tag (TMT) labelling, has been employed in this work for the identification and quantification of metabolically labelled proteins following cell treatment with the clickable ProTide (**47**-**50**) or clickable adenosine (**25**, **26**) probes under different experimental conditions. An illustration of the overall workflow used in proteomics experiments in this work is shown in **Figure 4.24**.

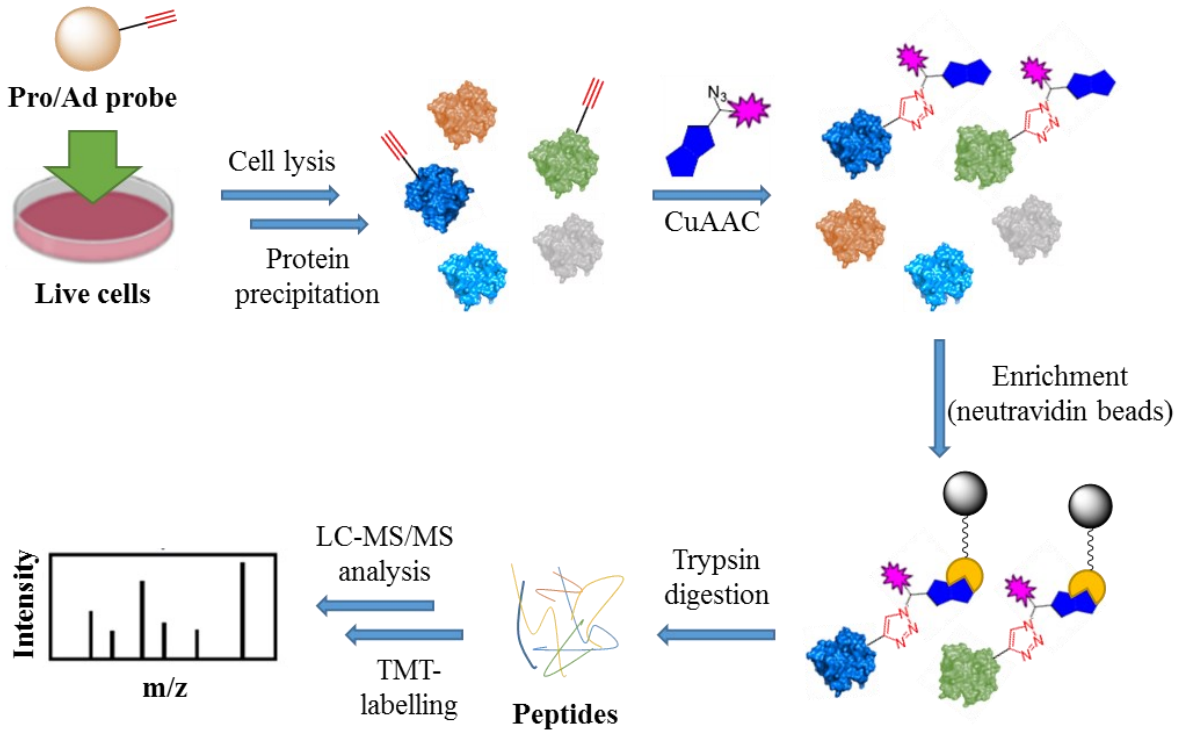


Figure 4.24. Overview of the proteomics workflow followed for protein identification. Live cells are treated with the relevant ProTide (100 µM, 24 h) or adenosine probe (500 µM, 24 h) along with NRH (500 µM, 24 h). Cells are then lysed (RIPA buffer), protein precipitation is performed and tagged proteins are ligated to AzTB, AzRB, AzB or YnB (see **Appendix Figure A.2**) by CuAAC. Captured proteins are subsequently enriched using neutravidin beads and digested using trypsin. The corresponding released peptides are then TMT-labelled and submitted for LC-MS/MS analysis for identification and quantification.

4.5.2 Protein Quantification Using TMT-labelling

The use of TMT-labelling has been an indispensable tool for relative protein quantification in samples analysed by proteomics.[259,260] The principle behind TMT-labelling relies on the use of isobarically labelled TMT reagents, which result in the addition of a tag of the same mass in each TMT-labelled peptide (**Figure 4.25A**).[259,260] As a result, the same peptide from each distinct sample is labelled with a different TMT-reagent, but it will still have the same mass upon labelling with each TMT-reagent, thus combining distinct samples will result in the generation of a single MS^1 peak for that peptide (**Figure 4.25B**). This leads to signal boosting for the peptide at the MS^1 level, which aids peptide (and protein) identification. However, due to the different distribution of the isotope labels in each TMT-reagent, fragmentation of the reagent during MS^2 scanning at the fragmentation site leads to the subsequent generation of TMT tags of different masses (**Figure 4.25B**).[259,260] Thus, the same TMT-labelled peptide can be distinguished across the different samples, which allows for relative quantification of the

peptide, and hence the protein it originates from, across the different experimental conditions used for each distinct sample. However, ion suppression during MS^2 analysis is common and can lead to peptide ratio compression during quantification,[261] which can affect the detection of statistically significant changes for a protein from different samples and should be taken into account when using TMT-labelling.

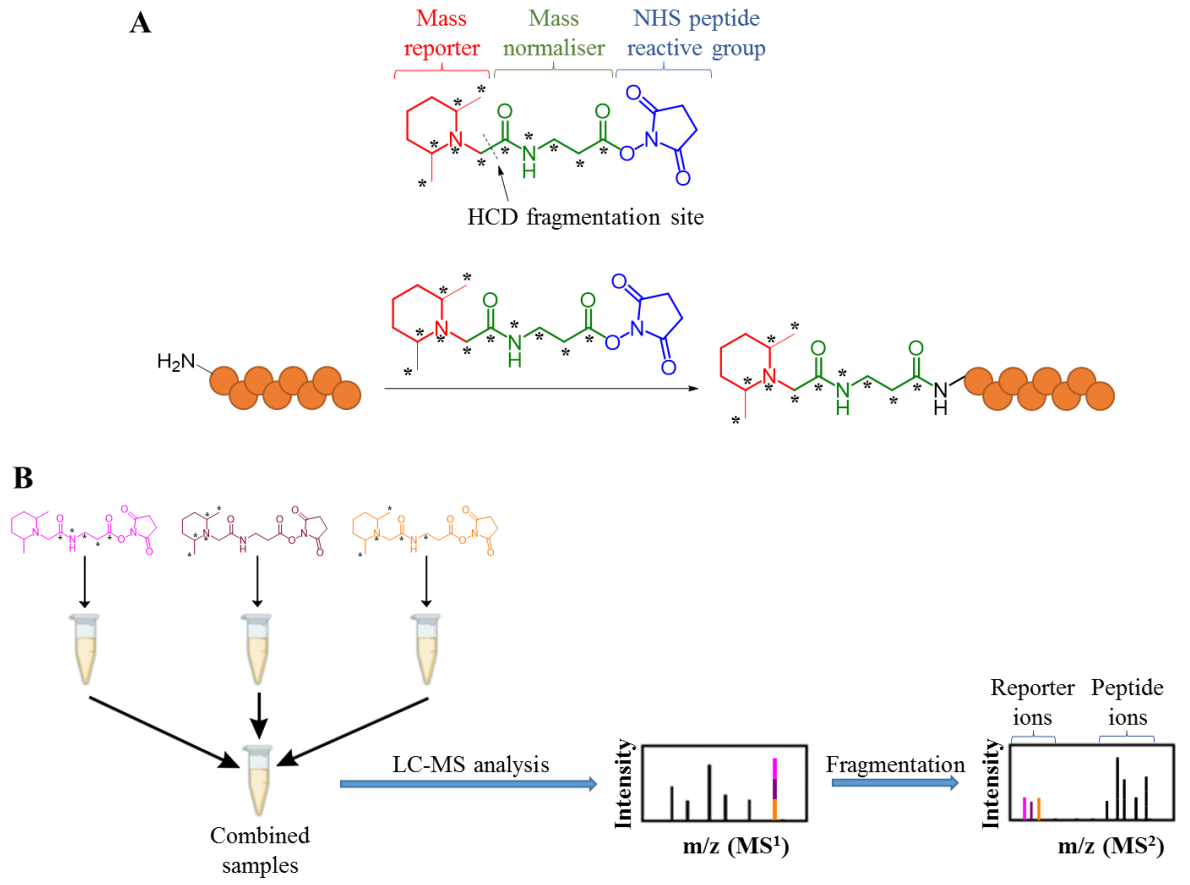


Figure 4.25. Overview of TMT-labelling for peptide quantification. **A**: generic structure of TMT-labelling reagents (10plex) is shown. * represents the position of isotopically labelled ^{13}C or ^{15}N atoms and the mass normaliser ensures a uniform mass of different TMT reagents in MS^1 spectra (prior to fragmentation). A TMT reagent reacts with a peptide at a lysine residue or the N-terminus through displacement of the NHS reactive group. **B**: following trypsin digestion, separate peptide samples are labelled by different TMT reagents and then combined. The same peptide from each sample co-elutes during LC-MS (MS^1) analysis (due to uniform mass of TMT-labels by the mass normaliser) and appears as a single peak in MS^1 spectra. During HCD fragmentation, the mass reporter from each TMT-labelled peptide dissociates from the mass normaliser and reporter ions of different mass are generated. Comparison of the intensity of mass reporter ions thus allows for relative quantification of the corresponding peptide from each sample.

4.5.3 Initial Screening of Probes by Proteomics

To investigate the intracellular protein labelling profiles of each clickable ProTide probe (6Yn-Pro (**47**), 2Yn-Pro (**48**), 8But-Yn-Pro (**49**), 6Az-Pro (**50**)) and the 2Yn-Ad (**26**) probe, HEK293T cells were treated with each probe alone or in the presence of the additives NRH (**24**), H_2O_2 or both. Following proteomics analysis and data processing, the extent of protein labelling and enrichment for each probe and set of conditions (compared to the relevant DMSO control) was visualised by generating profile plots (**Figure 4.26**).

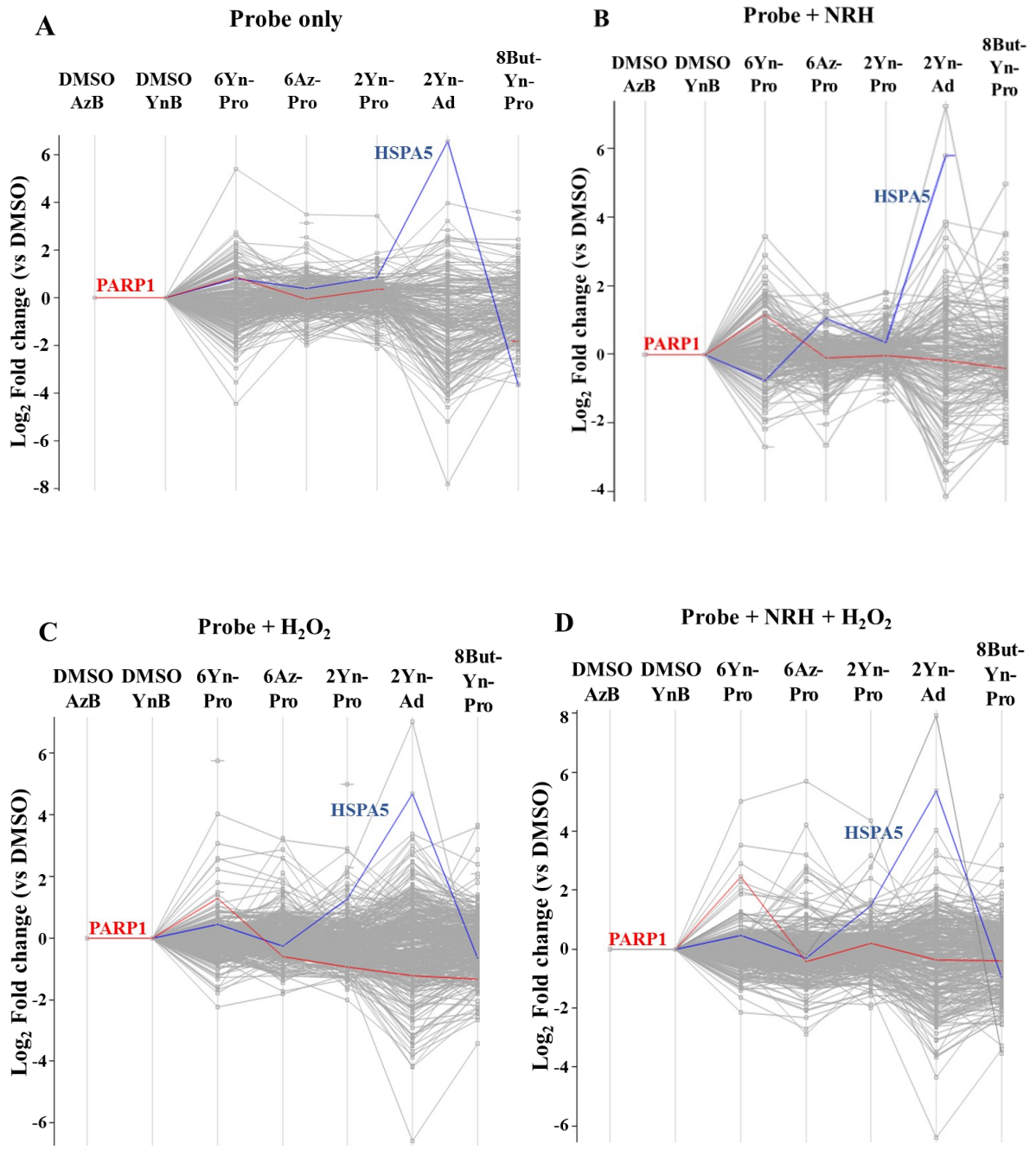


Figure 4.26. Profile plots showing protein labelling profiles in HEK293T cells. Protein labelling profiles were obtained in HEK293T cells following treatment with DMSO (0.1% v/v) or a ProTide probe (100 μM, 24 h), or

2Yn-Ad (500 µM, 24 h). Where relevant, NRH supplementation (500 µM, 24 h) and H_2O_2 treatment (2 mM, 6 min) were performed. Cells were lysed (RIPA buffer), precipitated, captured by CuAAC, enriched (neutravidin beads), trypsin digested and TMT-labelled prior to LC-MS/MS analysis. Log_2 Fold change (y-axis) corresponds to the extent of protein enrichment relative to the appropriate DMSO control, which represents the degree of protein labelling in a sample. Highlighted lines in red and blue represent PARP1 and HSPA enrichment, respectively, in each sample. **A**. Protein labelling in probe-only treated samples. **B**. Protein labelling in probe and NRH co-treated samples. **C**. Protein labelling in probe-treated samples followed by H_2O_2 treatment prior to cell lysis. **D**. Protein labelling in probe and NRH co-treated samples followed by H_2O_2 treatment prior to cell lysis.

The data presented in the profile plots illustrate that, under all four experimental conditions, PARP1 was only enriched (relative to DMSO AzB control) following treatment with the probe 6Yn-Pro (**47**) (**Figure 4.26**). The extent of PARP1 enrichment under each of the four conditions, summarised in **Table 4.2**, was shown to be higher in the presence of NRH (**24**) (**Figure 4.26B**) or H_2O_2 (**Figure 4.26C**) (2.22- and 2.46-absolute fold change over DMSO control, respectively) when compared to treatment with 6Yn-Pro (**47**) alone (1.84-absolute fold change over DMSO control, **Figure 4.26A**). The highest increase was observed when HEK293T cells were co-treated with 6Yn-Pro (**47**) and NRH (**24**), followed by H_2O_2 treatment, where PARP1 was the 4th most enriched protein, with an absolute 5.5-fold increase in abundance compared to DMSO control background levels (**Figure 4.26D**).

Table 4.2. Summary of PARP1 enrichment in 6Yn-Pro-treated samples compared to DMSO (AzB) control (see **Figure 4.26**).

Condition	Log_2 Fold change (PARP1)	Absolute Fold increase (PARP1)
6Yn-Pro	0.883	1.84
6Yn-Pro + NRH	1.15	2.22
6Yn-Pro + H_2O_2	1.30	2.46
6Yn-Pro + NRH + H_2O_2	2.46	5.51

Co-treatment with 6Yn-Pro (**47**) and NRH (**24**), followed by H_2O_2 treatment, also resulted in the highest total number of proteins identified (97), out of all four tested conditions, that match known ADP-ribosylated proteins (**Table 4.3**). In addition, co-treatment with 6Yn-Pro (**47**) and NRH (**24**), followed by H_2O_2 treatment, resulted in the highest proportion of proteins that match known ADP-ribosylated proteins, represented as % of all detected proteins in a sample

(**Table 4.3**). The database of literature known ADP-ribosylated proteins was compiled from eight previous ADP-ribosylation (ADPr) studies.[80,97-100,175,262,263]

Table 4.3. Summary of the total number of proteins enriched (Log_2 Fold change >0) in 6Yn-Pro-treated samples compared to DMSO (AzB) control (see **Figure 4.26**). The number of proteins previously identified as ADP-ribosylated proteins is shown for each sample along with their fraction of the total number of proteins enriched (shown as %).

	6Yn-Pro	**6Yn-Pro + NRH**	**6Yn-Pro + H_2O_2**	**6Yn-Pro + NRH + H_2O_2**
Total number of proteins enriched	104	114	155	189
No. of proteins identified in at least one ADPr study	41 (39%)	51 (45%)	79 (51%)	97 (51%)
No. of proteins identified in two or more ADPr studies	31 (30%)	38 (33%)	56 (36%)	71 (38%)

The combined findings supported cell supplementation with NRH (**24**) and H_2O_2 treatment for stimulating PARP1 activation and promotion of protein ADP-ribosylation. This was evidenced by the observation that supplementation of 6Yn-Pro-treated HEK293T cells with NRH (**24**), followed by H_2O_2 treatment, was shown to result in the highest extent of PARP1 activation due to PARP1 automodification, as evidenced by the highest extent of PARP1 labelling and enrichment (**Table 4.2, Figure 4.26D**). In turn, the highest number of potential ADP-ribosylated proteins, in terms of absolute number as well as highest % proportion of all identified proteins, was observed under this experimental condition (**Table 4.3**).

The detection of PARP1 by proteomics was also interesting given that PARP1 enrichment was not detected by western blotting (relative to DMSO control) following CuAAC click reaction and protein enrichment (**Figure 4.12**). This observation thus provided evidence that following click reaction, potentially ADP-ribosylated proteins, such as PARP1, were modified to an extent where they were no longer recognised by the corresponding antibodies, thus making analysis and identification by WB unreliable. The observation could be equally applicable to

proteins modified by other PTMs, such as AMPylation, which would explain the lack of labelling by WB with the anti-AMPylation antibody (**Figure 4.14**).

Interestingly, the profile plots potentially revealed conversion of 2Yn-Ad (**26**) into 2Yn-ATP (**41**) metabolically and its utilisation for protein AMPylation in 2Yn-Ad-treated HEK293T cells. This was evidenced by the observation that heat shock 70-kDa protein 5 (HSPA5), a 78 kDa protein which is a known target for AMPylation,[264] was the most or 2nd most enriched protein under all the tested conditions in 2Yn-Ad-treated samples (**Table 4.4, Figure 4.26**). In the absence of NRH (**24**) and H_2O_2 treatment, HSPA5 showed ~94-fold enrichment over background levels (DMSO control). This contrasted well with the highly intense labelled band seen by IGF at ~75 kDa following treatment of HEK293T cells with 2Yn-Ad (**26**) (**Figure 4.15B**) as well as in MDA-MB-231 2Yn-Ad-treated cells (**Figure 4.2C**), which was within the mass range of HSPA5 (~78 kDa).

Table 4.4. Summary of HSPA5 enrichment in 2Yn-Ad-treated samples compared to DMSO (AzB) control (see **Figure 4.26**).

Condition	Log_2 Fold change	Absolute Fold change
2Yn-Ad	6.56	94.4
2Yn-Ad + NRH	5.80	55.7
2Yn-Ad + H_2O_2	4.69	25.8
2Yn-Ad + NRH + H_2O_2	5.38	41.6

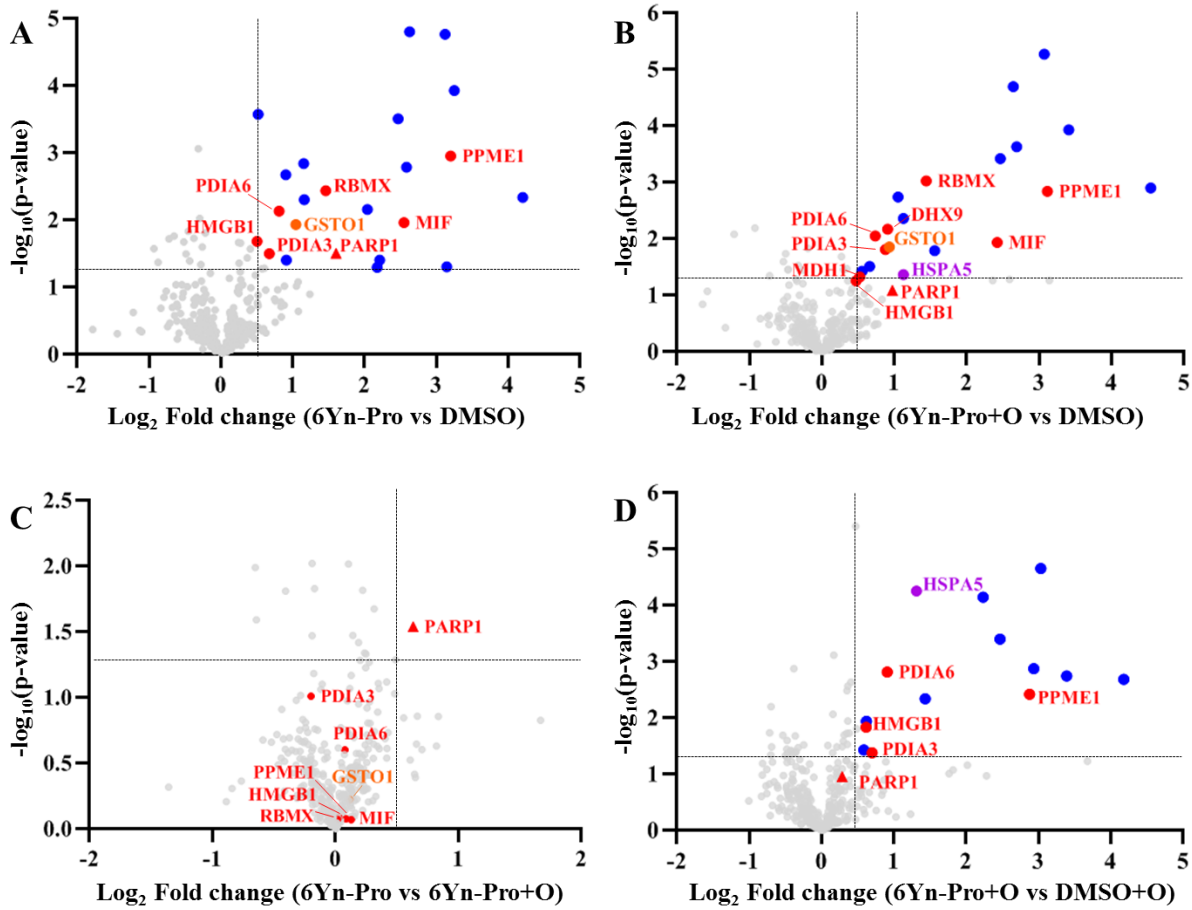
Although treatment of cells with probes 2Yn-Pro (**48**), 8But-Yn-Pro (**49**) and 6Az-Pro (**50**) did not result in PARP1 labelling and enrichment, substantial labelling and enrichment was observed for other proteins, suggesting that the probes were likely utilised for AMPylation and/or other PTMs.

4.5.4 Further Validation of 6Yn-Pro by Proteomics

Considering the observation that PARP1 labelling and enrichment were only observed following treatment with 6Yn-Pro (**47**), further validation of the probe for labelling of protein ADP-ribosylation was undertaken by performing additional proteomics experiments in triplicates. Performing experiments in triplicates was important because it allowed for

visualisation of proteomics data on volcano plots (**Figure 4.27**), which allowed for subsequent identification of labelled proteins that were statistically significant hits.

A cut-off limit of 1.3 for $-\log_{10}$(p-value) (y-axis) corresponded to 95% confidence interval, representing significance (with respect to replicates). In contrast, a cut-off limit of 0.5 for Log_2 Fold change (x-axis) corresponded to a 1.4-fold enrichment for an experimental condition relative to another experimental condition, thus representing the extent of protein enrichment in the former condition compared to the latter. Log_2 Fold change (x-axis) was therefore calculated by subtracting the Log_2 Fold value of the latter condition from the former condition, which was illustrated in volcano plots on the x-axis as 'Log_2 Fold change (former condition vs latter condition)'. A hit was therefore considered to be statistically significant for a given experimental condition relative to another experimental condition if both values, for significance and extent of enrichment, for a given protein were above the cut-off limits.



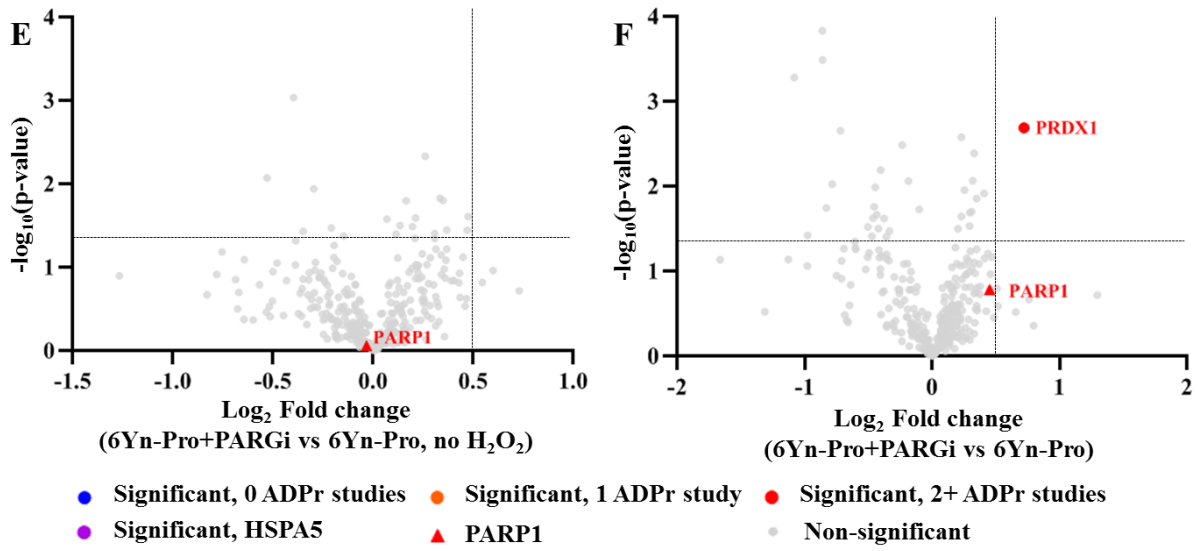


Figure 4.27. Protein labelling profiles of 6Yn-Pro-treated HEK293T cells. Cells were treated in triplicate with DMSO (0.1% v/v) or 6Yn-Pro (100 µM, 24 h) alone, or co-treated with PARG inhibitor (10 µM, 24 h), or pre-treated with olaparib (10 µM, 2 h). All samples were treated with NRH (500 µM, 24 h) and H_2O_2 (2 mM, 6 min) prior to cell lysis, unless otherwise stated. Cells were lysed (RIPA buffer), precipitated, captured by CuAAC, enriched (neutravidin beads), trypsin digested and TMT-labelled prior to LC-MS/MS analysis. Data was visualised on volcano plots allowing for direct comparison of significance (y-axis) and enrichment (x-axis) between two experimental conditions. O = olaparib treatment, PARGi = treatment with PARG inhibitor (see **Figure 4.28**). **A.** Comparison of 6Yn-Pro and DMSO-treated samples. **B**: comparison of co-treated 6Yn-Pro+olaparib and DMSO-treated samples. **C**: comparison of 6Yn-Pro-treated and co-treated 6Yn-Pro+olaparib samples. **D**: comparison of 6Yn-Pro+olaparib and DMSO+olaparib co-treated samples. **E**: comparison of co-treated 6Yn-Pro+PARGi and 6Yn-Pro-treated samples. These samples were not treated with H_2O_2. **F**: comparison of co-treated 6Yn-Pro+PARGi and 6Yn-Pro-treated samples (H_2O_2 treatment was included).

Comparison of protein labelling in 6Yn-Pro-treated cells with the DMSO control (**Figure 4.27A**) revealed a total of 23 significantly enriched proteins, 8 of which were identified as ADP-ribosylated proteins in the previous ADPr studies database[80,97-100,175,262,263], including PARP1. Subsequent co-treatment with olaparib resulted in reduced enrichment of PARP1 when compared to the DMSO control, presumably due to reduced PARP1 labelling *via* automodification, while the extent of enrichment for the other 7 known ADP-ribosylated proteins was generally unaffected (**Figure 4.27B**). The change in extent of enrichment following treatment with the PARP inhibitor olaparib was more easily observed in **Figure 4.27C**, where the only significantly enriched protein following 6Yn-Pro (**47**) treatment, compared to co-treatment of 6Yn-Pro (**47**) and olaparib, was PARP1. This was a surprising observation considering that PARP1 enrichment could only be achieved through PARP1 automodification with 6Yn-NAD^+ (**3**), which was a sign that PARP1 was indeed activated.

Thus, PARP1 was expected to lead to widespread protein ADP-ribosylation with 6Yn-NAD^+ (**3**) considering that PARP1 is responsible for majority of cellular ADP-ribosylation and consumption of ~90% of all NAD^+.[20] The observed lack of other statistically significant hits when comparing 6Yn-Pro (**47**) treatment in the absence and presence of olaparib could be explained by one or more of the following reasons:

1. Some of the significantly enriched proteins observed in **Figure 4.27A** were targets of PARPs 3-16, since olaparib is a highly potent inhibitor of PARP1 and PARP2
2. Low extent of labelling of a protein with 6Yn-NAD^+ (**3**) by PARP1 relative to labelling with endogenous NAD^+, resulting in low extent of protein enrichment and non-significant change in enrichment upon olaparib treatment (**Figure 4.27B** and **4.27C**)
3. Olaparib possibly worked well for monitoring PARP1 activation by 6Yn-NAD^+ (**3**) in cells treated with 6Yn-Pro (**47**) but was inappropriate for use as a control for monitoring proteome-wide ADP-ribosylation. This was investigated and discussed in more detail in **Section 4.5.7**.

The data shown in **Figure 4.27D** supported the assertion that potentially PARPs, other than PARP1 (and PARP2), were also utilising 6Yn-NAD^+ (**3**) for ADP-ribosylation. This was based on the observed protein labelling when comparing 6Yn-Pro (**47**)+olaparib co-treated samples vs DMSO+olaparib co-treated samples (i.e. olaparib was present in both samples, **Figure 4.27D**). The comparison revealed statistically significant enrichment of 4 of the 8 hits (known ADP-ribosylated proteins) originally identified as statistically significant in **Figure 4.27A** (HMGB1, PDIA3, PDIA6 and PPME1, highlighted in red) when PARP1 and PARP2 were inhibited by olaparib.

Another interesting observation was that HSPA5, a known AMPylation target,[264] was significantly enriched only following co-treatment with olaparib (**Figure 4.27B** and **4.27D**). This observation thus suggested that the decreased consumption of (6Yn-)NAD^+ due to PARP1 (and PARP2) inhibition resulted in decreased demand for 6Yn-NAD^+ (**3**) biosynthesis from 6Yn-ATP (**40**), likely leading to an increase in the 6Yn-ATP (**40**) pool for protein AMPylation. The findings thus illustrated the importance of optimising experimental conditions towards NAD^+ biosynthesis and utilisation of 6Yn-Pro (**47**) for metabolic production of 6Yn-NAD^+ (**3**).

Degradation of PARylation chains to MARylation by PARG (**Figure 1.9**) is essential for metabolism of ADP-ribosylation.[151,265] Treatment of HEK293T cells with the PARG inhibitor (PARGi) PDD00017273[265], performed by PhD student Michael Gruet, was shown to result in

significant retention of PARylation chains by WB (**Figure 4.28**). Hence, it was hypothesised that co-treatment of 6Yn-Pro (**47**) and PARGi might lead to an increase in the number of identified significantly enriched ADP-ribosylated proteins.

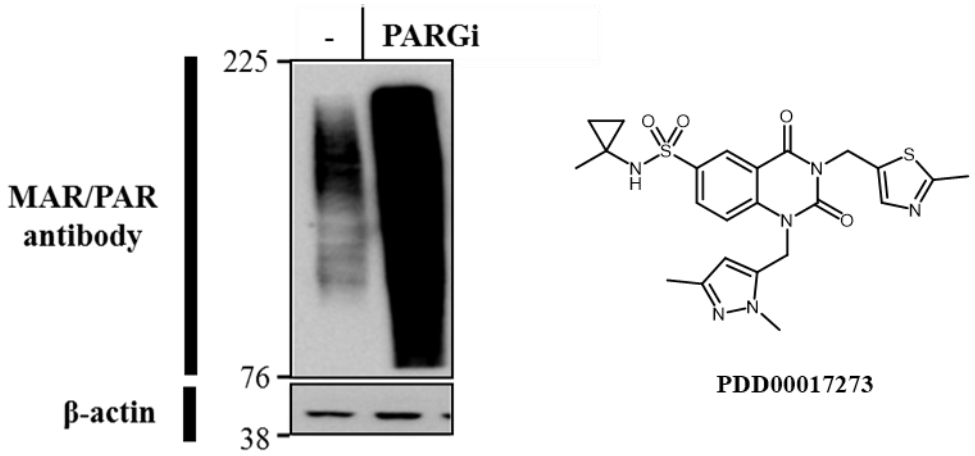


Figure 4.28. Screening of MARylation/PARylation protein levels by western blotting before and after treatment with the PARG inhibitor PDD00017273 (1 μM, 24 h). β-actin = loading control.

Despite the substantial increase seen in MARylation/PARylation labelling by western blotting, co-treatment of 6Yn-Pro (**47**) and PARGi, in the absence of H_2O_2 treatment, did not result in any statistically significant enrichment of proteins by proteomics (**Figure 4.27E**). Surprisingly, even after H_2O_2 treatment (**Figure 4.27F**), only a single protein was significantly enriched (peroxiredoxin-1 (PRDX1), a modulator of cellular H_2O_2 concentrations). These findings thus showed that addition of PARGi did not provide any benefits in the identification of ADP-ribosylated proteins by metabolically generated 6Yn-NAD^+ (**3**) following 6Yn-Pro (**47**) treatment.

4.5.5 Effect of NMNAT1 Overexpression on Protein Identification by Proteomics

Data obtained from metabolomics experiments following NMNAT1 overexpression demonstrated that NMNAT1 overexpression resulted in an increase in overall abundance levels of 6Yn-NAD^+ (**3**) (**Figures 4.20D** and **4.22D**) as well as in increased % incorporation of 6Yn-NAD^+ (**3**) into the NAD^+ pool (**Figures 4.20E** and **4.22E**). Taking these findings into account, it was hypothesised that NMNAT1 overexpression may lead to an increase in protein ADP-ribosylation by 6Yn-NAD^+ (**3**) following cell treatment with 6Yn-Pro (**47**). NMNAT1 was therefore overexpressed in HEK293T cells prior to co-treatment with 6Yn-Pro (**47**) and NRH (**24**), and H_2O_2 treatment subsequently (**Figure 4.29**).

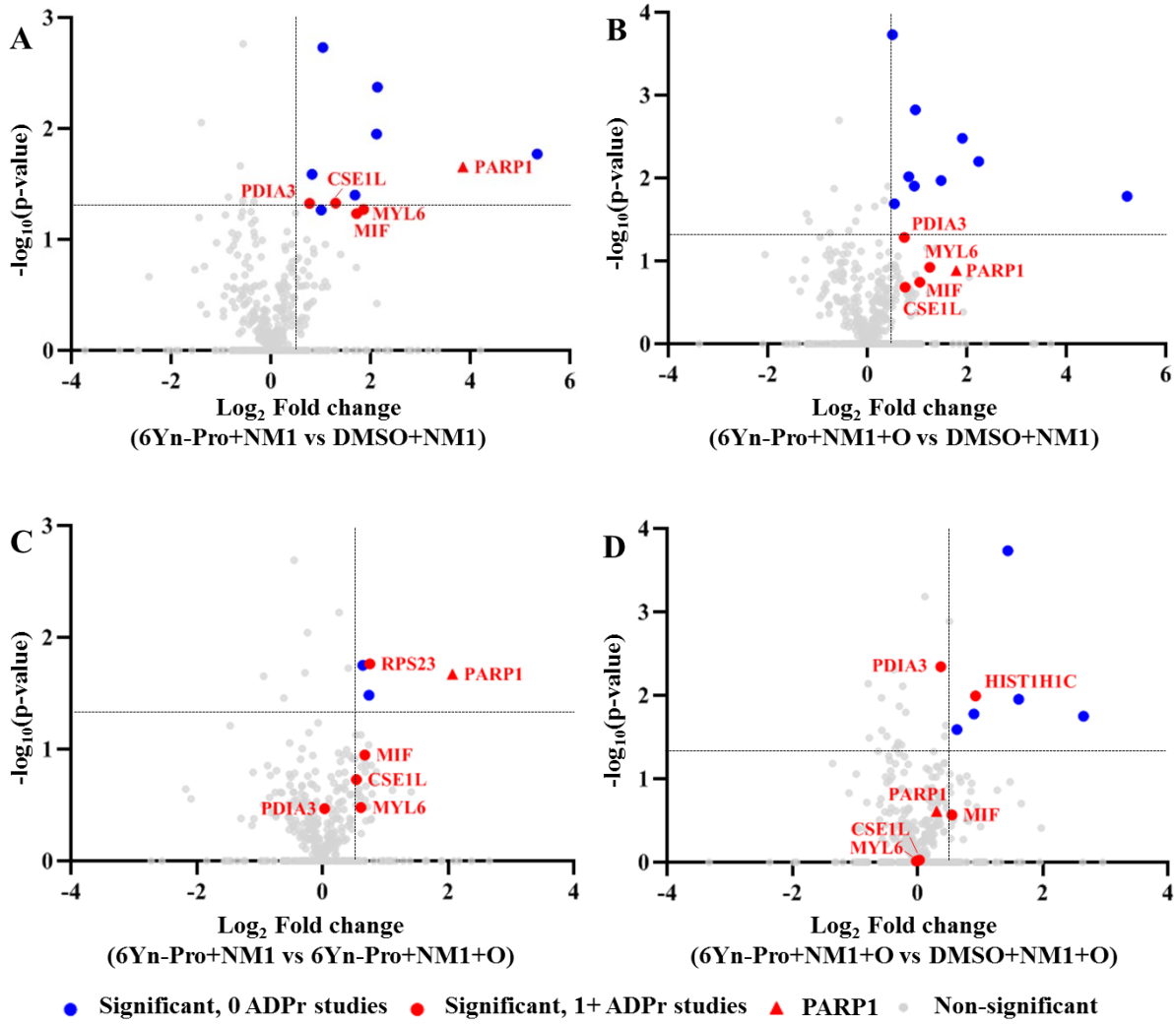


Figure 4.29. Protein labelling profiles of 6Yn-Pro-treated HEK293T cells following NMNAT1 overexpression. All cell samples were transfected with NMNAT1 plasmid (1000 ng/mL culture media, 24 h) prior to probe treatment. Cells were subsequently treated in triplicate with DMSO (0.1% v/v) or 6Yn-Pro (100 µM, 24 h) alone, or pre-treated with olaparib (10 µM, 2 h). All samples were treated with NRH (500 µM, 24 h) and H_2O_2 (2 mM, 6 min) prior to cell lysis. Cells were treated in triplicate, lysed (RIPA buffer), precipitated, captured by CuAAC, enriched (neutravidin beads), trypsin digested and TMT-labelled prior to LC-MS/MS analysis. Data was visualised on volcano plots allowing for direct comparison of significance (y-axis) and enrichment (x-axis) between two experimental conditions. O = olaparib treatment, NM1 = NMNAT1 overexpression. **A**: comparison of 6Yn-Pro+NM1 and DMSO+NM1 treated samples. **B**: comparison of co-treated 6Yn-Pro+NM1+olaparib and DMSO+NM1 treated samples. **C**: comparison of 6Yn-Pro+NM1 treated and 6Yn-Pro+NM1+olaparib co-treated samples. **D**: comparison of 6Yn-Pro+NM1+olaparib and DMSO+NM1+olaparib co-treated samples.

Comparison of 6Yn-Pro+NMNAT1 overexpression samples with DMSO+NMNAT1 overexpression revealed a total of 10 significantly enriched proteins (**Figure 4.29A**). 3 of the proteins were known ADP-ribosylated proteins (PARP1, PDIA3, CSE1L), with additional two known ADP-ribosylated proteins (MYL6, CSE1L) observed just below the significance cut-

off value (**Figure 4.29A**). Subsequent comparison of these results with results obtained in the absence of NMNAT1 overexpression (6Yn-Pro vs DMSO, **Figure 4.27A**) showed that NMNAT1 overexpression led to a decrease in the total number of significantly enriched proteins compared to no overexpression (10 vs 23, respectively). In addition, NMNAT1 overexpression resulted in a decrease in the total number of identified significantly enriched known ADP-ribosylated proteins compared to no overexpression (3 vs 8, respectively). These observations were surprising considering that the higher absolute 6Yn-NAD^+ (**3**) levels and higher % incorporation of 6Yn-NAD^+ (**3**) into the NAD^+ pool seen following NMNAT1 overexpression were expected to result in an increase of protein labelling with 6Yn-NAD^+ (**3**). On the other hand, the observations contrasted well with WB data obtained following NMNAT1 overexpression where a decrease in overall MARylation/PARylation levels were seen in HEK293T cells compared to MARylation/PARylation levels in the absence of no NMNAT1 overexpression (**Figure 4.15A**). Thus, the acquired proteomics data reinforced the hypothesis that a negative feedback mechanism exists between high NMNAT1 expression levels and overall ADP-ribosylation levels. Nevertheless, after NMNAT1 overexpression, Log_2 Fold change for PARP1 enrichment increased to 4 (compared to 1.6 without NMNAT1 overexpression, (**Figure 4.27A**)), corresponding to a 16-fold increase in absolute enrichment (compared to 3-fold increase without NMNAT1 overexpression, (**Figure 4.27A**)). These results demonstrated an increase in PARP1 labelling by automodification despite an overall decrease in cellular MARylation/PARylation levels.

NMNAT1 overexpression appeared to affect susceptibility of inhibition of PARP1 activity by olaparib. Co-treatment of 6Yn-Pro (**47**) and olaparib resulted in a decrease of the extent of enrichment of four of the five known ADP-ribosylated proteins seen in **Figure 4.29A** (PARP1, MYL6, MIF, CSE1L, **Figure 4.29B**). A similar decrease was not seen in the absence of NMNAT1 overexpression for the seven known ADP-ribosylated proteins in **Figure 4.27A**, when compared to the corresponding olaparib co-treated sample (**Figure 4.27B**).

Finally, a comparison of 6Yn-Pro (**47**) treated and 6Yn-Pro+olaparib co-treated samples, all after NMNAT1 overexpression, showed enrichment of three proteins above the enrichment cut-off value (MYL6, MIF, CSE1L, **Figure 4.29C**). When a subsequent comparison was performed for 6Yn-Pro+olaparib co-treated and DMSO+olaparib co-treated samples, all after NMNAT1 overexpression, it was noted that both the significance and enrichment for two of three proteins (MYL6, CSE1L) decreased to zero (**Figure 4.29D**). Given that the labelling of the two proteins was abolished upon olaparib co-treatment, the results implied that the proteins

myosin light polypeptide 6 (MYL6) and chromosome segregation 1-like protein (CSE1L, also known as exportin-2) were likely targets of PARP1 (and/or possibly PARP2). On the other hand, the histone protein HIST1H1C was significantly enriched following olaparib co-treatment, suggesting that HIST1H1C was an ADP-ribosylation target of other PARPs.

A further interesting observation was that NMNAT1 overexpression appeared to influence whether the 6Yn-Pro (**47**) probe was utilised for protein AMPylation or ADP-ribosylation. A comparison of **Figure 4.27D** (no NMNAT1 overexpression) and **Figure 4.29D** (NMNAT1 overexpression) revealed that the known AMPylation target HSPA5 was significantly enriched only in the absence of NMNAT1 overexpression (**Figure 4.27D**). Since the comparison was performed for 6Yn-Pro+olaparib co-treated and DMSO+olaparib co-treated samples, the finding showed that HSPA5 was not an ADP-ribosylation of PARP1 and PARP2. This was in agreement with metabolomics data, showing that absolute 6Yn-ATP (**40**) levels (**Figure 4.20B**) and its % incorporation into the ATP pool (**Figure 4.20C**) were higher in the absence of NMNAT1 overexpression, implying greater availability of 6Yn-ATP (**40**) for use in protein AMPylation. Collectively, this shows that low NMNAT1 expression levels are expected to favour AMPylation over ADP-ribosylation.

Overall, NMNAT1 overexpression was shown to result in increased PARP1 labelling by automodification (**Figure 4.29A**) in 6Yn-Pro-treated cells, compared to baseline NMNAT1 levels (**Figure 4.27A**). Similarly, NMNAT1 overexpression was shown to promote protein ADP-ribosylation with 6Yn-NAD^+ (**3**) instead of protein AMPylation by 6Yn-ATP (**40**), as evidenced by the disappearance of the AMPylation marker HSPA5. On the other hand, NMNAT1 overexpression overall led to fewer significantly enriched proteins (**Figure 4.29A**) compared to baseline NMNAT1 levels (**Figure 4.27A**), and lower overall ADPr levels (**Figure 4.15A**). The findings thus suggest that intermediate NMNAT1 levels may be optimal for stimulating PARP1 activation and protein ADP-ribosylation over AMPylation, while maintaining or increasing overall MARylation/PARylation levels, instead of decreasing them. To achieve this, optimisation of NMNAT1 transfection of HEK293T cells is required.

4.5.6 Effect of Sequential Pull-downs on Protein Enrichment

The observation that metabolically generated 6Yn-ATP (**47**) was used for RNA synthesis (**Figure 4.13B**) led us to hypothesise that high degree of incorporation of 6Yn-ATP (**47**) into nucleic acids could result in saturation of neutravidin beads during protein pull-down, potentially preventing enrichment of labelled proteins. This would lower the efficiency of

protein enrichment and result in a decrease in the number of significantly enriched protein hits. To investigate whether potential saturation of neutravidin beads occurred due to the presence of nucleic acids, a second pull-down step (PD2) was performed with supernatants from samples generated following an initial pull-down step (PD1), and samples were analysed by western blotting (**Figure 4.30A**) and proteomics (**Figure 4.30B** and **4.30C**). Experimental conditions were identical to those in **Section 4.5.5**, with the only exception that in this experiment H_2O_2 treatment was not performed for any sample prior to cell lysis.

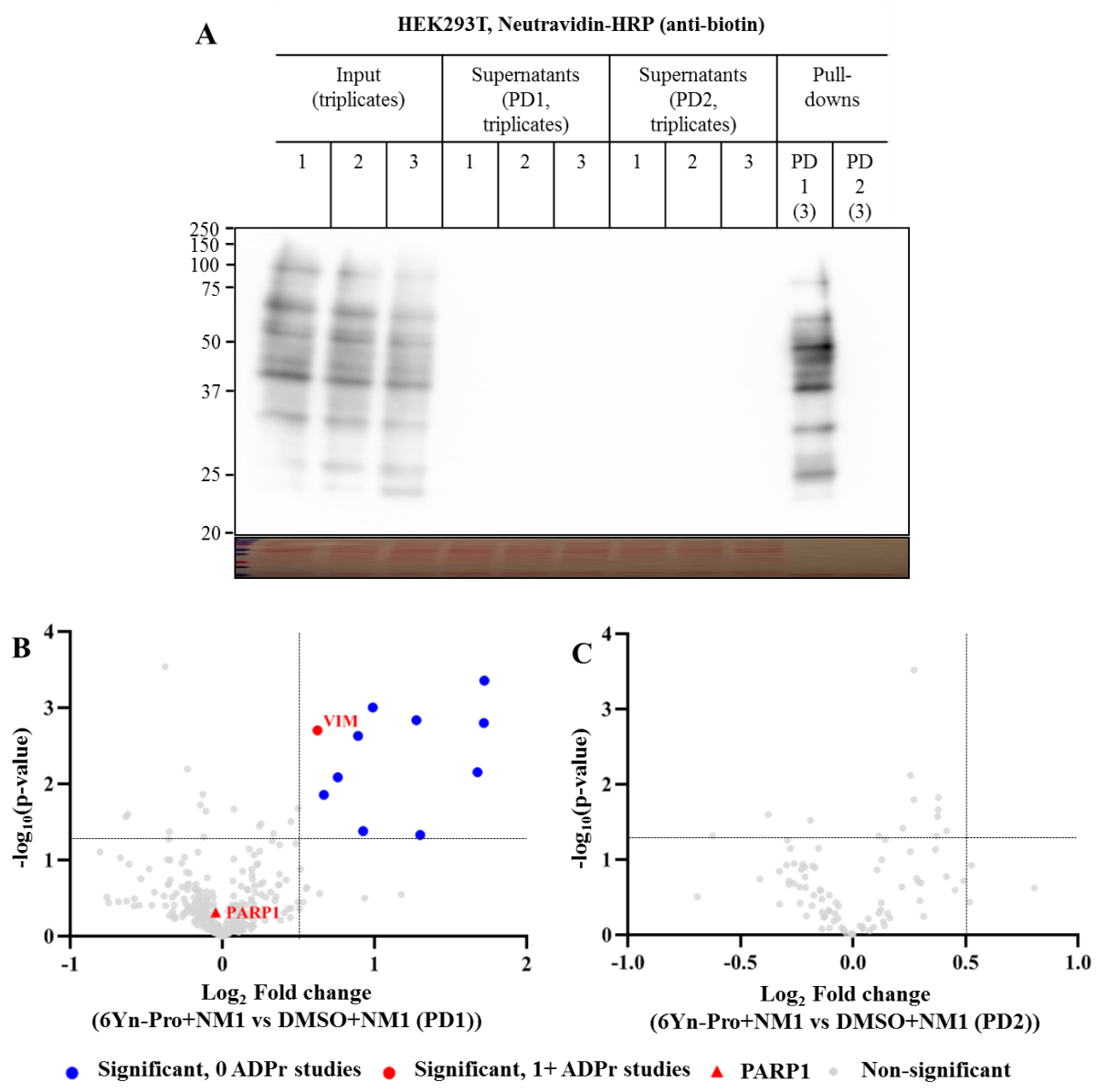


Figure 4.30. Protein labelling profiles of 6Yn-Pro-treated HEK293T cells following NMNAT1 overexpression and sequential protein pull-down steps. All cell samples were transfected with NMNAT1 plasmid (1000 ng/mL culture media, 24 h) prior to probe treatment. Cells were subsequently treated in triplicate with DMSO (0.1% v/v) or 6Yn-Pro (100 µM, 24 h). All samples were treated with NRH (500 µM, 24 h). For proteomics experiments,

cells were treated in triplicate, lysed (RIPA buffer), precipitated, captured by CuAAC, enriched twice (neutravidin beads), trypsin digested and TMT-labelled prior to LC-MS/MS analysis. Data was visualised on volcano plots allowing for direct comparison of significance (y-axis) and enrichment (x-axis) between two experimental conditions. NM1 = NMNAT1 overexpression. For western blotting, proteins were analysed following the two enrichment steps. **A**: biotinylated labelled proteins following CuAAC. Input shows protein labelling before enrichment, PD1 and PD2 show protein labelling after first and second pull-down enrichment step, respectively, supernatant shows depletion of protein labelling from input samples after each the enrichment step. Western blotting was performed using Neutravidin-HRP. Ponceau S staining = loading control. **B**: comparison of 6Yn-Pro+NM1 and DMSO+NM1 treated samples after the first pull-down step (PD1). **C**: comparison of 6Yn-Pro+NM1 and DMSO+NM1 treated samples after the second pull-down step (PD2).

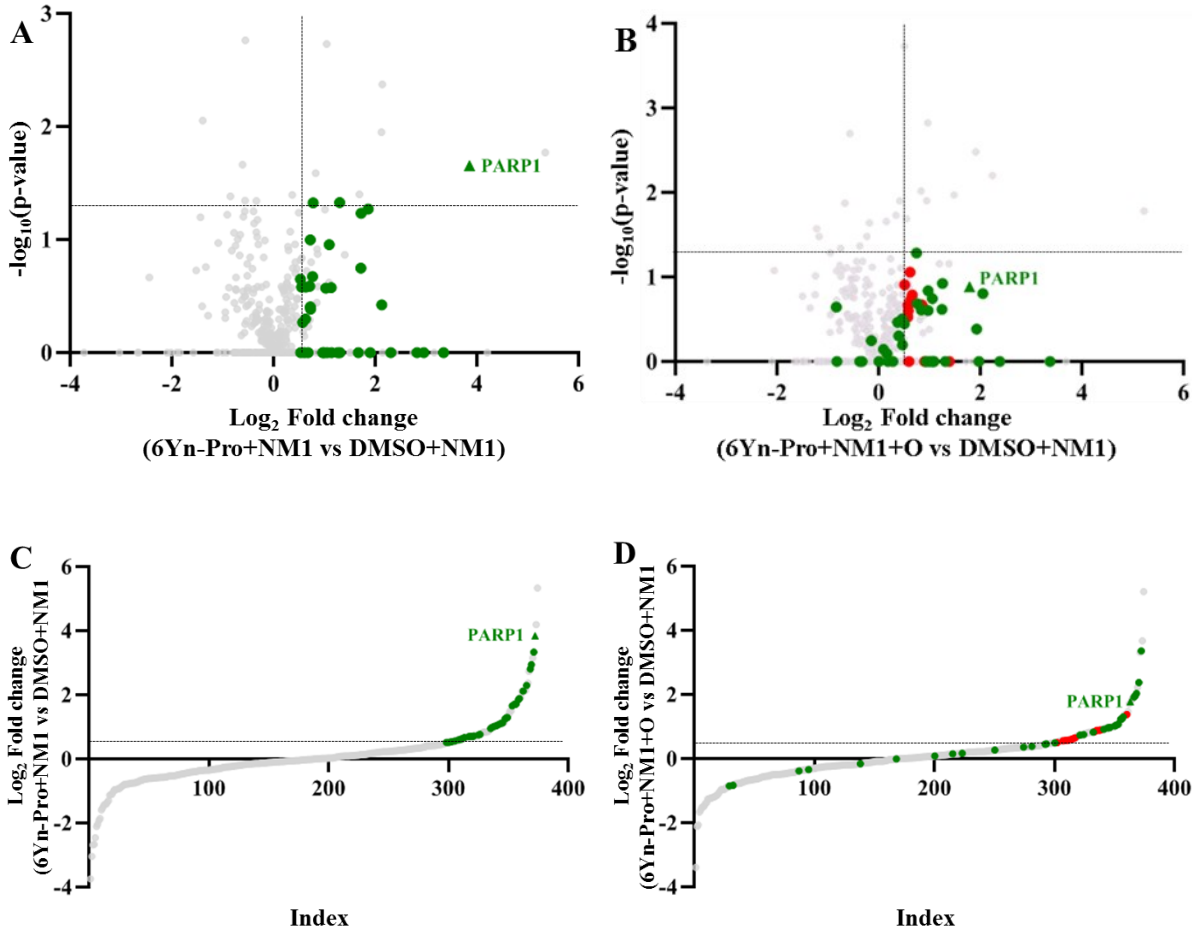
Analysis by WB using Neutravidin-HRP (**Figure 4.30A**) to detect for biotinylated proteins revealed that all biotinylated proteins from before pull-down (input, lanes 1-3) were enriched in the PD1 step (pull-down, lane 10), as evidenced by complete depletion of biotinylated proteins in the supernatants of PD1 samples (lanes 4-6). Consequently, no biotinylated proteins were observed following the second pull-down step PD2 (lane 11). Taken together, the results demonstrated that neutravidin beads did not become saturated by biotinylated RNA/nucleic acids in the PD1 step. Subsequent proteomics analysis also showed that 11 proteins were statistically significantly enriched in PD1, whereas no statistically significantly enriched proteins were seen after PD2.

4.5.7 Suitability of Olaparib for Monitoring ADP-ribosylome

Cell samples co-treated with olaparib were used in the previous experiments as a comparison reference for monitoring the extent of labelling and enrichment of ADP-ribosylated proteins arising from 6Yn-NAD^+ (**3**) after treatment with 6Yn-Pro (**47**). However, it was noted that in olaparib-treated samples a statistically significant change in enrichment was mostly only detected for PARP1 (**Figures 4.27C** and **4.29C**). Thus, it was hypothesised that olaparib was suitable for monitoring PARP1 activation by automodification but was not suitable for monitoring proteome-wide ADP-ribosylation arising from metabolically derived 6Yn-NAD^+ (**3**). It was therefore important to establish whether olaparib was indeed a suitable reference treatment in these experiments.

To investigate this, the data presented in **Figure 4.29A** was reanalysed to show all 35 proteins above the enrichment cut-off value (0.5), regardless of statistical significance, that have been previously identified as known ADP-ribosylated proteins (highlighted in green, **Figure 4.31A** and **4.31C**; see **Appendix Table A.2)**. A comparison of **Figure 4.31A** and **4.31C** with data obtained after co-treatment with 6Yn-Pro+olaparib (**Figure 4.31B** and **4.31D**; see **Appendix**

Table A.3) showed that, although the extent of enrichment decreased below the cut-off for 14 of the 35 proteins, the remaining 21 proteins were still enriched above the cut-off limit with little/no change in their extent of enrichment, except for PARP1. Furthermore, this decrease was offset after olaparib treatment where 13 additional proteins that were known to be ADP-ribosylated proteins (highlighted in red, **Figure 4.31B** and **4.31D**; see **Appendix Table A.4**), were found to be above the 0.5 enrichment cut-off, whereas they were below the cut-off limit in **Figure 4.31A** and **4.31C**. The data presented thus suggested that although olaparib was suitable for monitoring PARP1 activation and the extent of enrichment of certain individual ADP-ribosylated proteins, it was not suitable for monitoring proteome-wide ADP-ribosylation due to 6Yn-NAD^+ (**3**) labelling following 6Yn-Pro (**47**) treatment.

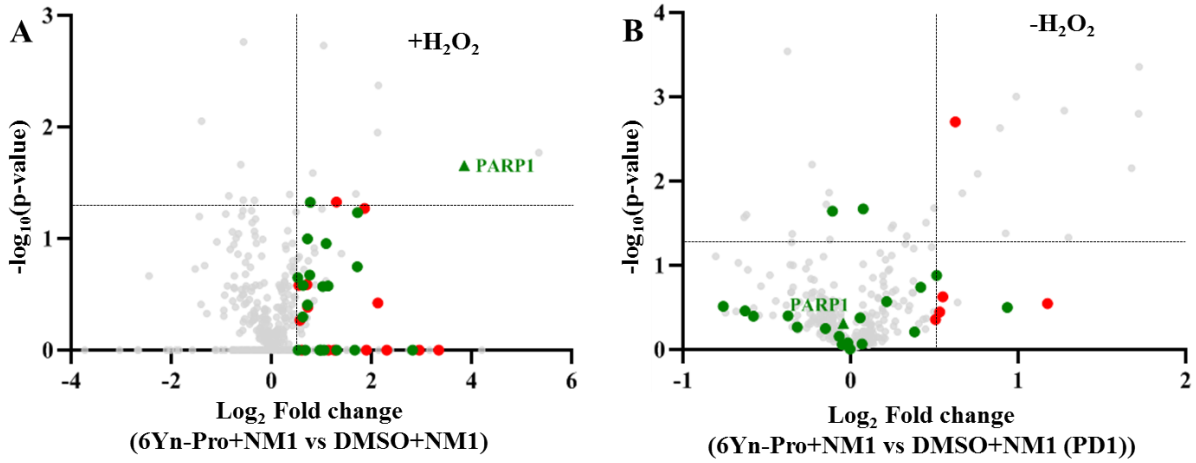


- **1+ ADPr studies with enrichment >0.5 in Figures A and C. These proteins were matched in Figures B and D, respectively.**
- **1+ ADPr studies with enrichment >0.5 in Figures B and D only (i.e. enrichment >0.5 only after olaparib treatment, hence these proteins were not matched in Figures A and C).**
- **PARP1**
- **Not identified in ADPr studies or enrichment <0.5.**

Figure 4.31. Protein labelling profile of 6Yn-Pro-treated HEK293T cells following NMNAT1 overexpression (reanalysis). **A**: reanalysis of the data in **Figure 4.29A**. All known ADP-ribosylated proteins with an enrichment value (Log_2 Fold change) >0.5 are highlighted in green. **B**: reanalysis of the data in **Figure 4.29B**. All known ADP-ribosylated proteins with an enrichment value (Log_2 Fold change) >0.5 from **A** were matched in this data set (highlighted in green). Proteins with an enrichment value (Log_2 Fold change) >0.5 in **B** that were not matched in **A** are also shown (highlighted in red). **C**: illustration of protein enrichment (Log_2 Fold change) for the data in **A** on an S-plot as a function of protein index (significance is excluded). **D**: illustration of protein enrichment (Log_2 Fold change) for the data in **B** on an S-plot as a function of protein index (significance is excluded).

4.5.8 Effect of H_2O_2 Treatment on Protein Identification by Proteomics

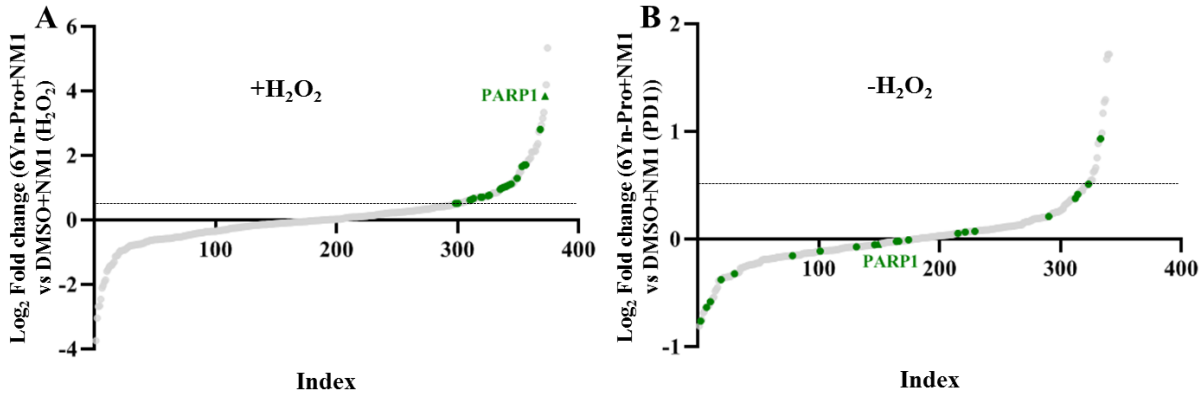
Following the conclusion that olaparib treatment was not a suitable reference control for monitoring proteome-wide ADP-ribosylation with metabolically derived 6Yn-NAD^+ (**3**), our focus shifted towards finding an alternative reference control treatment. Considering the high extent of upregulation of ADP-ribosylation due to PARP1 activation under oxidative stress e.g., due to H_2O_2 treatment, we set to establish whether H_2O_2 treatment could be used as a suitable reference control. For this purpose, the data presented in **Figure 4.29** (see **Section 4.5.5**) and **Figure 4.31** (see **Section 4.5.7**) where all samples were treated with H_2O_2 prior to cell lysis, and the data presented in **Figure 4.30** (see **Section 4.5.6**) where H_2O_2 treatment was not performed prior to cell lysis, were compared (**Figures 4.32** and **4.33**).



- **1+ ADPr studies with enrichment >0.5 in Figure A. These proteins were matched in Figure B.**
- **1+ ADPr studies with enrichment >0.5 in Figures A and B. These proteins do not match with each other between the two figures.**
- **PARP1**
- **Not identified in ADPr studies or enrichment <0.5.**

Figure 4.32. Comparison of protein labelling profiles of 6Yn-Pro-treated HEK293T cells following NMNAT1 overexpression, with (**A**) and without (**B**) H_2O_2 treatment prior to cell lysis. All known ADP-ribosylated proteins with an enrichment value (Log_2 Fold change) >0.5 in **A** that matched the data set in **B** are highlighted in green. All known ADP-ribosylated proteins with an enrichment value of (Log_2 Fold change) >0.5 in **A** that do not match the data set in **B**, and vice versa, are highlighted in red. **A**: reanalysis of the data in **Figure 4.29A**. **B**: reanalysis of the data in **Figure 4.30B**.

The set of 35 known ADP-ribosylated proteins above the enrichment cut-off value (0.5) from **Figure 4.31A** (samples treated with H_2O_2), were compared with all proteins from **Figure 4.30A** (samples not treated with H_2O_2). The comparison revealed that a total of 21 proteins matched across the two data sets (highlighted in green, **Figure 4.32A** and **Figure 4.32B**, respectively; **Appendix Table A.5** and **Table A.6**, respectively). This data was also visualised on S-plot figures, where enrichment was shown only as a function of protein index in ascending order thus excluding significance values (**Figure 4.33A** and **Figure 4.33B**).



- **1+ ADPr studies with enrichment >0.5 in Figure A. These proteins were matched in Figure B.**
- **PARP1**
- **Not identified in ADPr studies or enrichment <0.5.**

Figure 4.33. Comparison of protein labelling profiles of 6Yn-Pro-treated HEK293T cells following NMNAT1 overexpression, with (**A**) and without (**B**) H_2O_2 treatment prior to cell lysis (S-plots). **A**: illustration of protein enrichment (Log_2 Fold change) for the data set in **Figure 4.32A** on an S-plot as a function of protein index (significance is excluded). **B**: illustration of protein enrichment (Log_2 Fold change) for the data set in **Figure**

4.32B on an S-plot as a function of protein index (significance is excluded). All known ADP-ribosylated proteins with an enrichment value (Log_2 Fold change) >0.5 in **A** that matched the data set in **B** are highlighted in green.

A visual comparison of **Figures 4.32A/4.33A** with **Figures 4.32B/4.33B** revealed, that in the absence of H_2O_2, there was a clear shift of this set of 21 proteins towards the origin, corresponding to a substantial reduction in their labelling and enrichment (**Figures 4.32B/4.33B**). In the absence of H_2O_2, only 2 of the 21 proteins were found at or above the enrichment cut-off limit of 0.5, and 16 of the 21 proteins were found either very close to 0 or below 0 (**Figures 4.32B/4.33B**). Furthermore, in the presence of H_2O_2 (**Figure 4.32A**) there were additional 14 known ADP-ribosylated proteins above the cut-off enrichment value (0.5), with an average Log_2 fold change of >1.5 (highlighted in red, these did not match in **Figure 4.32B;** see **Appendix Table A.7**). When compared to the absence of H_2O_2 (**Figure 4.32B**), there were only five additional proteins above the cut-off enrichment value (0.5), with an average Log_2 fold change ~0.6 (highlighted in red, these did not match in **Figure 4.32A;** see **Appendix Table A.8**). Such a substantial decrease in enrichment, both for matching (green) and non-matching (red) known ADP-ribosylated proteins, was not observed following olaparib treatment (**Figure 4.31**). These findings thus demonstrated that H_2O_2 treatment was a suitable comparison reference for proteome-wide monitoring of protein ADP-ribosylation arising from metabolically generated 6Yn-NAD^+ (**3**), instead of olaparib treatment.

To further quantify the results, the mean enrichment along with the 25^{th} and 75^{th} percentiles for the mean enrichment (interquartile range), of the set of 21 proteins for H_2O_2-treated and untreated samples were calculated and illustrated in **Figure 4.34**. The lowest absolute enrichment value (lowest abundant protein) and highest absolute enrichment value (highest abundant protein) were also shown; these were individual absolute values of the least and most abundant protein in the samples and do not represent error bars of the mean enrichment.

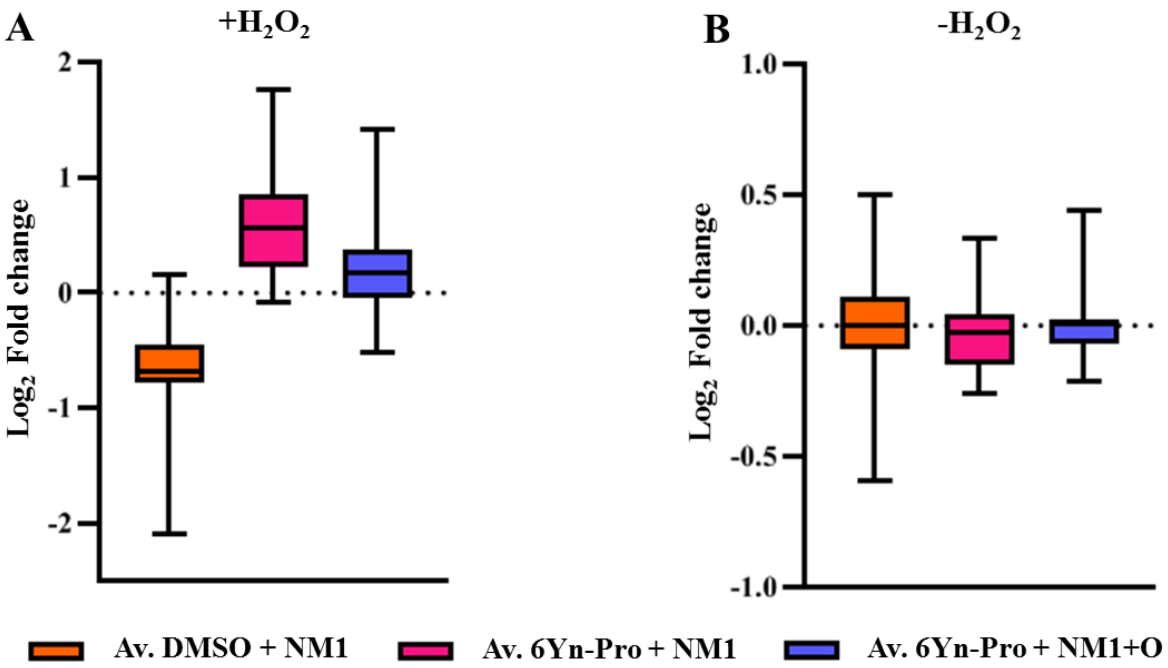


Figure 4.34. Summary statistics for the mean enrichment (Log_2 Fold change) for the data set of 21 known ADP-ribosylated proteins (highlighted in green) from **Figure 4.32** and **Figure 4.33**. **A**: mean enrichment (Log2 Fold change) for the data set of 21 proteins from HEK293T samples treated with H_2O_2 (2 mM, 6 min) prior to cell lysis (see **Figures 4.32A** and **4.33A**). **B**: mean enrichment (Log2 Fold change) for the data set of 21 proteins from HEK293T samples not treated with H_2O_2 prior to cell lysis (see **Figures 4.32A** and **4.33A**).

The summary statistics for H_2O_2 treated samples showed that mean protein enrichment for the set of 21 known ADP-ribosylated proteins increased after 6Yn-Pro (**47**) treatment, to 0.555, when compared to the mean enrichment for the corresponding DMSO control, which was -0.678 (**Figure 4.34A**). These findings illustrated that the set of proteins were, on average, enriched 2.4-fold after co-treatment with 6Yn-Pro (**47**) and H_2O_2. On the other hand, co-treatment with 6Yn-Pro+olaparib showed that, on average, the enrichment of this set of proteins only decreased 1.3-fold when compared to treatment with 6Yn-Pro (**47**) alone (**Figure 4.34A)**, where a 2.4-fold increase was observed, and did not return to baseline levels (DMSO control, **Figure 4.34A**). These observations were in agreement with earlier findings in **Figure 4.31** (see **Section 4.5.7**), which showed that olaparib treatment resulted in reduction of labelling and enrichment only in a small subset of ADP-ribosylated proteins.

The summary statistics for samples not treated with H_2O_2, however, revealed that there was no change in the mean enrichment for the set of 21 known ADP-ribosylated proteins following treatment with 6Yn-Pro (**47**), when compared to the DMSO control (**Figure 4.34B**). These findings suggested that detection of baseline ADP-ribosylation levels following 6Yn-Pro (**47**)

treatment is likely difficult to achieve without H_2O_2 treatment, and that an alternative reference control treatment is necessary to monitor for baseline ADP-ribosylation levels arising from 6Yn-NAD^+ (**3**) labelling. In addition, olaparib co-treatment exhibited no effect on mean enrichment when compared to the DMSO control or 6Yn-Pro (**47**) treatment (**Figure 4.34B**) thus providing evidence that olaparib only exhibited a noticeable effect on overall labelling and enrichment of ADP-ribosylated proteins at high cellular ADP-ribosylation levels.

4.5.9 Conclusions from Proteomics Experiments

To investigate the overall intracellular protein labelling profile upon cell treatment with each of the synthesised clickable ProTide probes (**47**-**50**) and the 2Yn-Ad (**26**) probe, proteomics experiments, in combination with TMT-labelling for protein quantification, were performed in HEK293T cells. Initial proteomics experiments revealed that PARP1 labelling (by automodification) and enrichment only occurred in cells treated with the probe 6Yn-Pro (**47**) (**Figure 4.26**). The data also revealed that the extent of PARP1 labelling and enrichment in 6Yn-Pro-treated cells increased following co-treatment with NRH (**24**) or H_2O_2, with the highest extent of enrichment observed when both NRH (**24**) and H_2O_2 treatments were applied (**Table 4.2**). Furthermore, co-treatment of 6Yn-Pro (**47**) and NRH (**24**) followed by H_2O_2 treatment resulted in the identification of the highest number of known ADP-ribosylated proteins (**Table 4.3**). Taken together, these findings demonstrated the importance of supplementing cells with the NAD^+ precursor NRH (**24**) and performing H_2O_2 treatment prior to cell lysis for boosting intracellular ADP-ribosylation by metabolically derived 6Yn-NAD^+ (**3**). It was further noted that 2Yn-Ad (**26**) treatment led to labelling and enrichment of the AMPylation marker HSPA5 (**Table 4.4**, **Figure 4.26**), thus suggesting that 2Yn-Ad (**26**) was metabolically converted into 2Yn-ATP (**41**) and used for protein AMPylation instead of 2Yn-NAD^+ (**9**) biosynthesis.

Probe 6Yn-Pro (**47**) was further validated by performing protein labelling proteomics experiments in triplicates in the presence or absence of olaparib treatment (**Figure 4.27**). These showed that PARP1 was statistically significantly enriched in 6Yn-Pro-treated samples (**Figure 4.27A**), and that PARP1 labelling (by automodification) was abrogated upon olaparib treatment (**Figure 4.27B**). Surprisingly, despite presumed PARP1 activation, there was no significant change observed in the enrichment of other labelled proteins (**Figure 4.27C**), leading us to hypothesise that olaparib was not a suitable reference control for monitoring ADP-ribosylation arising from metabolically derived 6Yn-NAD^+ (**3**).

Considering that NMNAT1 overexpression was shown to boost intracellular 6Yn-NAD^+ (**3**) levels (**Figure 4.20D**) and its % incorporation into the overall NAD^+ pool (**Figure 4.20E**) by metabolomics, we explored whether NMNAT1 overexpression resulted in increased protein labelling in HEK293T cells by proteomics. NMNAT1 overexpression was shown to increase the extent of PARP1 labelling and enrichment (**Figure 4.29A**), thus suggesting an increase in its activation, however, the overall number of statistically significantly enriched known ADP-ribosylated proteins decreased, compared to no NMNAT1 overexpression (**Figure 4.27A**). This was in agreement with the decrease of MARylation/PARylation levels after NMNAT1 overexpression (**Figure 4.15A**), suggesting that there was a negative feedback mechanism between high NMNAT1 expression levels and cellular ADP-ribosylation, and that optimisation of NMNAT1 expression levels was required. It was also noted that in olaparib-treated NMNAT1 overexpression samples the AMPylation marker HSPA5 was not significantly enriched (**Figure 4.29B**). On the other hand, HSPA5 was statistically significantly enriched in the absence of NMNAT1 overexpression in olaparib-treated samples (**Figure 4.27B**), thus suggesting that high NMNAT1 levels stimulate 6Yn-NAD^+ (**3**) biosynthesis over AMPylation with 6Yn-ATP (**40**).

A potential concern that significant utilisation of 6Yn-ATP (**40**) in RNA synthesis impeded subsequent protein pull-down of labelled proteins *via* saturation of neutravidin beads was investigated. This was performed by sequential pull-down of 6Yn-Pro-treated samples (**Figure 4.30**). WB analysis for biotinylation of labelled proteins showed that all biotinylated proteins were successfully enriched in the first pull-down step (**Figure 4.30A**), which was subsequently confirmed by proteomics data (**Figure 4.30B** and **4.30C**). The results showed that the extent of labelling of nucleic acids was not substantial enough to affect the efficiency of protein enrichment during pull-down.

Finally, the suitability of olaparib treatment for use as a reference control for monitoring protein ADP-ribosylation due to 6Yn-NAD^+ (**3**) labelling was investigated. Comparison of the enrichment of a set of 35 known ADP-ribosylated proteins was compared before and after olaparib treatment. The results showed that olaparib treatment decreased the extent of enrichment to below the cut-off limit for 14 of the proteins, but increased it to above the cut-off limit for other 13 proteins (**Figure 4.31**). The extent of enrichment for 21 proteins, overall, appeared unaffected (**Figure 4.31**). The findings thus suggested that although olaparib was suitable for monitoring the extent of enrichment of certain individual ADP-ribosylated proteins

e.g., PARP1, it was not suitable for monitoring proteome-wide ADP-ribosylation changes due to 6Yn-NAD^+ (**3**) labelling in the performed experiments.

On the other hand, comparison of H_2O_2-treated and untreated cells revealed a global shift for a set of 21 known ADP-ribosylated proteins that were enriched above the cut-off limit following H_2O_2 treatment. In the absence of H_2O_2 treatment, a decrease in the enrichment for 19 of the 21 proteins to below the cut-off value was observed, with the remaining two also experiencing an overall decrease in enrichment towards no enrichment. The findings thus demonstrated that H_2O_2 treatment served as a suitable reference control for monitoring protein ADP-ribosylation due to 6Yn-NAD^+ (**3**) labelling. However, this raised the question whether the probe 6Yn-Pro (**47**) can be indeed used for monitoring of baseline ADP-ribosylation levels in the absence of conditions that upregulate ADP-ribosylation.

Overall, the presented proteomics data provided evidence for successful utilisation of 6Yn-Pro (**47**) for metabolic generation of 6Yn-NAD^+ (**3**) and subsequent intracellular labelling of ADP-ribosylated proteins, such as PARP1. The results also demonstrated the importance of using relevant reference controls for appropriate monitoring of protein enrichment due to 6Yn-NAD^+ (**3**) labelling, as well as the need for experimental conditions promoting NAD^+ biosynthesis and ADP-ribosylation over other PTMs, such as AMPylation.

Chapter 5 Conclusions and Future Perspectives

The PTM ADP-ribosylation plays a role in many biological processes and has been implicated in the development of pathological conditions and diseased phenotypes. However, identification of the relevant proteins that possess this modification has been limited due to the lack of chemical tools to study ADP-ribosylation in live cells and in *vivo*. This PhD project aimed to develop novel chemical probes that could be used for identification of physiological intracellular ADP-ribosylation targets and for intracellular target profiling of the different PARP proteins.

The first step undertaken in this work was the design of appropriate clickable cell-permeable NAD^+ precursor probes that can be utilised in the NAD^+ biosynthesis pathway in live cells. This was performed *in silico*, using molecular modelling, to probe protein-ligand interactions of five different analogue precursor series with the relevant enzymes in the pathway. The technique identified three potential analogue precursor candidates, 6Yn-Ad (**25**) and 6Yn-Pro (**47**), and 8But-Yn-Pro (**49**), that were predicted to be utilised throughout the entire NAD^+ biosynthesis pathway for metabolic conversion into the NAD^+ analogues 6Yn-NAD^+ (**3**) and 8But-Yn-NAD^+ (**14**), respectively. Subsequent biological validation of the probes by IGF revealed their ability to label proteins through conversion into biologically relevant cofactors intracellularly. For the probes 6Yn-Ad (**25**) and 6Yn-Pro (**47**), this was confirmed by metabolomics analysis, which demonstrated that both probes were successfully converted intracellularly into 6Yn-ATP (**40**) and 6Yn-NAD^+ (**3**). Ultimately, the utility of 6Yn-Pro (**47**) for labelling of ADP-ribosylated proteins *via* metabolically generated 6Yn-NAD^+ (**3**) was confirmed by proteomics analysis, which revealed labelling and enrichment of automodified PARP1 and of multiple known ADP-ribosylation targets under oxidative stress (**Section 4.5.8**). Given that PARP1 catalyses the vast majority of cellular ADP-ribosylation, these data demonstrate the suitability of the probe to be used for identification of intracellular protein ADP-ribosylation arising from PARP1.

While the methodology described herein was primarily validated *via* identification of known ADP-ribosylated proteins, the same principle could be applied for the identification of new, unknown ADP-ribosylated proteins. Of particular interest is the use of the precursor probe 8But-Yn-Pro (**49**), which could find applications in intracellular target profiling of each PARP protein using the 'bump-hole' approach. Although in previous studies the method has been applied for identification of PARP targets in lysates, PARP target profiling has never been

performed intracellularly. Encouragingly, validation of 8But-Yn-Pro (**49**) by IGF through protein labelling demonstrated its conversion into biologically active cofactors. However, the precise nature of the observed intracellular protein labelling requires further exploration by metabolomics and proteomics methods. Ultimately, it is hoped that the use of probe 8But-Yn-Pro (**49**) will serve as a tool to dissect the roles of individual PARPs in different cellular processes in live cells, and thus lead to the identification of specific protein targets that could be targeted for therapeutic purposes.

An equally important finding during this PhD project was the observation that adenosine-based clickable probes, including the corresponding clickable ProTide probes, are capable of forming non-specific protein-ligand interactions in denatured, enzymatically inactive cell lysates (**Section 4.2**). Their removal is therefore pivotal for the identification of truly ADP-ribosylated proteins. Off-target protein labelling due to non-specific protein-probe interactions was observed in two previous studies that aimed to explore the use of 6Yn-Ad (**25**) and 2Yn-Ad (**26**) for studying intracellular protein ADP-ribosylation. The off-target labelling was not identified as such in those studies, and was taken forward in subsequent proteomics experiments, thus casting doubts on the reliability of the acquired data. In our experimental workflow, we found that the inclusion of a protein precipitation step following cell lysis and prior to click reaction was necessary for removal of non-specific protein labelling. These findings therefore have implications for published and potential future studies on PTMs looking to explore utilisation of adenosine-based clickable probes for protein identification and target validation. Further to this, it would be of much research interest to establish whether similar non-specific labelling occurs in denatured lysates with other, non-adenosine nucleoside-based clickable probes and prodrugs.

Future perspectives on the project include metabolomics analysis of the biological samples obtained following cell treatment with probe ^{15}N-Pro (**64**). Performing this analysis is vital to establishing whether there are innate limitations, due to cellular dynamics, on the utilisation of NAD^+ precursor probes for intracellular NAD^+ biosynthesis. Achieving this would help establish new approaches towards optimising NAD^+ biosynthesis and further elucidate whether the presence of clickable groups plays a limiting role on utilisation of the different metabolite analogues in the pathway.

Among the primary aims of this project was to determine whether the proposed clickable NAD^+ precursor probes could be used to study baseline, physiological ADP-ribosylation. To achieve

this, we attempted to compare the protein labelling profiles of 6Yn-Pro (**47**) treated HEK293T cells, by proteomics, in the presence or absence of olaparib pre-treatment. However, we found that olaparib treatment was not reliable for monitoring labelling and enrichment of potential ADP-ribosylated proteins, other than for automodified PARP1. As a result, upregulation of ADP-ribosylation under oxidative stress, by H_2O_2 treatment, was necessary in proteomics experiments to establish if 6Yn-Pro (**47**) treatment, indeed, resulted in metabolic labelling of ADP-ribosylated proteins by 6Yn-NAD^+ (**3**). Future work thus needs to focus on the development of appropriate experiments (e.g., by site identification) that can establish whether treatment with clickable NAD^+ precursor probes can be used to study baseline, physiological ADP-ribosylation in a native cell environment, in the absence of artificial upregulation.

Future perspectives also include further validation of the probe 8But-Yn-Pro (**49**), by metabolomics and proteomics methods, to determine whether it can be metabolically converted into 8But-Yn-NAD^+ (**14**) and subsequently employed by mutant PARPs for intracellular PARP target profiling. Similarly, validation of 6Az-Pro (**50**) should be performed in future experiments. Given its potential to be used for live-cell imaging applications, such as fluorescence microscopy, successful utilisation of the probe for intracellular labelling of ADP-ribosylation will be a much-needed tool for monitoring the modification's cellular distribution and for the study of its involvement in the relevant biological processes.

Overall, this PhD project provided novel chemical probes for the study of intracellular ADP-ribosylation, and the probes should find applications in future studies. We hope that the herein developed tools will provide fundamental insights into the role of ADP-ribosylation in biological processes and help with the identification of novel therapeutic protein targets in disease.

Chapter 6 Experimental, Materials and Methods

6.1 Chemical Synthesis

6.1.1 General Synthetic Methods

All reagents and solvents were purchased from VWR, Sigma-Aldrich UK, Fluorochem, Tokyo Chemical Industry and Alfa Aesar and used without further purification, unless otherwise stated. All reactions under anhydrous conditions were performed under a nitrogen atmosphere in oven-dried glassware. All anhydrous solvents were obtained from the departmental SolvTM solvent towers (Innovative Technology Inc.) and freshly used. For reversed-phase purifications, HPLC grade acetonitrile (VWR, Merck) and ultrapure water from MilliQ Millipore purification system were used. $^{\circ}$C

6.1.2 Analytical Techniques

Reaction monitoring was performed by thin-layer chromatography (TLC) on Merck aluminium plates pre-coated with silica gel 60 F254. Visualisation of spots was performed either by using a UV lamp (at 254 nm) or by TLC plate staining using potassium permanganate, vanillin or ninhydrin. Monitoring of reactions with phosphorylated compounds was performed by LC-MS on a Waters 3100 Mass Detector system equipped with a photodiode array and an XBridge reverse phase C18 column (5 μm, 4.6 × 100 mm, operating at a flow rate of 1.2 mL/min). Unless otherwise stated, LC-MS analysis was performed using MeCN (solvent B) and H_2O (solvent A) as the eluents (both containing 0.1% FA) over 18 mins using the following linear gradient: 5-98% MeCN (in H_2O)0-10 mins, 98% MeCN 10-12 mins, 98-5% 12-13 mins and 5% MeCN 13-18 mins. ^{1}H and ^{13}C NMR spectra were recorded on a 400 MHz Bruker AV NMR instrument at room temperature in chloroform-*d*, methanol-d_4, D_2O or DMSO-*d*6 at 400 MHz and 101 MHz for ^{1}H and ^{13}C NMR respectively. NMR data is reported in the following manner: chemical shift (δ) recorded in ppm relative to trimethylsilane (δ_H and δ_C set at 0 ppm); multiplicity (s = singlet, d = doublet, t = triplet, q = quartet, m = multiplet); coupling constant (*J*) stated in Hz; number of protons (integration).

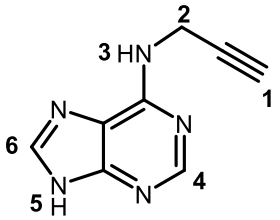
6.1.3 Purification Techniques

Purification was generally performed by manual column chromatography over normal phase silica gel 60 F254. For phosphorylated compounds, selected nucleosides and all ProTide analogues, purification was performed on a Biotage Isolera Prime automated system equipped with a reverse-phase Biotage SNAP Ultra C18 column (12 g, column volume = 17 mL). Unless

otherwise stated, reverse-phase purification was performed using MeCN and H_2O as the eluents (both containing 0.1% FA) over 25 column volumes (CV) at 12 mL/min using the following linear gradient: 5% MeCN (in H_2O) over 3 CV, 5-95% MeCN over 20 CV, 95% over 2 CV. Some AMP analogues, where specified, and all ATP analogues were purified by anion exchange chromatography (AXC). AXC purifications were performed on a Biotage Isolera Prime automated system equipped with a SNAP cartridge (12 g, column volume = 17 mL), manually packed with activated DEAE Sephadex A-25 (chloride form) weak anion exchange resin. Activation of the resin was performed by dissolving the resin (7.5 g) in 1 M $NaHCO_{3\,(aq)}$ (100 mL) at 4 °C with mild shaking over 24 hours. The swollen resin was then washed with distilled H_2O and packed into the empty SNAP cartridge described above. Unless otherwise stated, AXC purification was performed using 0.4 M $NH_4HCO_{3\,(aq)}$ and H_2O as the eluents over 30 column volumes (CV) at 12 mL/min using the following linear gradient: 0-100% $NH_4HCO_{3\,(aq)}$ over 20 CV and then 100% $NH_4HCO_{3\,(aq)}$ over 10 CV. At the end, the column was flushed and the resin reactivated by washing subsequently with 2 M $NaCl_{(aq)}$ (100 mL), H_2O (100 mL) and 1 M $NH_4HCO_{3\,(aq)}$ (50 mL). The column was stored at 4 °C and reused in future purifications.

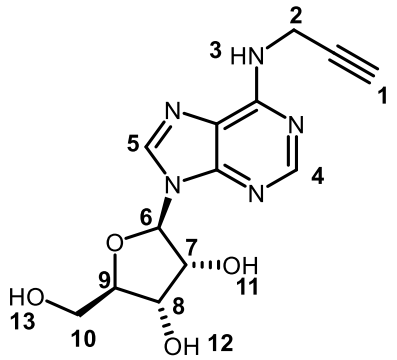
6.1.4 Synthesis of Adenosine Analogues

6.1.4.1 N-(prop-2-yn-1-yl)-9H-purin-6-amine (6Yn-adenine, 93)



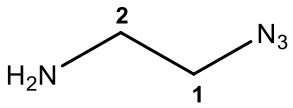
To a solution of 6-chloropurine (200 mg, 1.29 mmols) in EtOH (2 mL) was added propargylamine (414 µL, 6.47 mmols) and the reaction mixture was heated under reflux for 3 hours. The pale-yellow precipitate was filtered and washed with H_2O and EtOH to afford **93** a pale-yellow powder (156 mg, 0.903 mmols, 70%). R_f = 0.15 (DCM:MeOH 9:1); ^{1}H NMR (400 MHz, DMSO-*d*$_6$) δ 13.01 (s, 1H, 5), 8.26 (s, 1H, 6), 8.15 (s, 1H, 4), 8.02 (s, 1H, 3), 4.28 (s, 2H, 2), 3.04 (s, 1H, 1); ^{13}C NMR (101 MHz, DMSO-*d*$_6$) δ 154.2, 152.7, 150.0, 139.8, 119.3, 82.5, 72.9, 29.6; LC-MS (ESI$^+$) m/z found $[M+H]^+$ = 174.09 at R_t = 2.33 mins. Analytical data consistent with that reported in literature.[266]

6.1.4.2 (2R,3S,4R,5R)-2-(hydroxymethyl)-5-(6-(prop-2-yn-1-ylamino)-9H-purin-9-yl)tetrahydrofuran-3,4-diol (6Yn-Ad, 25)



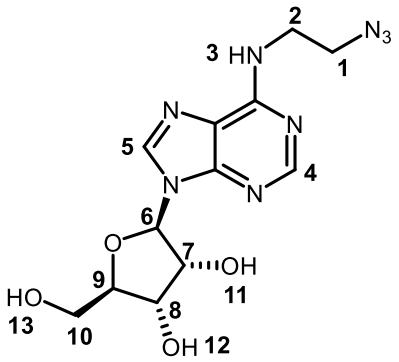
To a solution of 6-chloropurine riboside (1.00 g, 3.49 mmols) in EtOH (10 mL) was added propargylamine (1.12 mL, 17.4 mmols) and the reaction mixture was heated under reflux for 1 hour. The yellow-orange precipitate was filtered and washed with H_2O and EtOH to afford **25** as a white powder (799 mg, 2.61 mmols, 75%). R_f = 0.2 (DCM:MeOH 9:1); ^{1}H NMR (400 MHz, DMSO-d_6) δ 8.42 (s, 1H, 5), 8.29 (s, 1H, 4), 5.91 (d, J = 6.0, 1H, 6), 5.49 (s, 1H, 11), 5.37 (s, 1H, 12), 5.23 (s, 1H, 13), 4.61 (t, J = 5.5, 1H, 7), 4.26 (s, 2H, 2), 4.16 (t, J = 4.0, 1H, 8), 3.97 (q, J = 3.5, 1H, 9), 3.68 – 3.65 (m, 1H, 10), 3.60 – 3.52 (m, 1H, 10), 3.05 (s, 1H, 1); ^{13}C NMR (101 MHz, DMSO-d_6) δ 154.4, 152.7, 147.6, 140.7, 120.4, 88.3, 86.3, 82.3, 78.3, 74.0, 71.1, 62.1, 28.7; LC-MS (ESI$^+$) m/z found $[M+H]^+$ = 306.08 at R_t = 7.55 mins; HRMS (ESI+) found 306.1193 ($C_{13}H_{15}N_5O_4$, $[M+H]^+$ requires 306.1202). Analytical data consistent with that reported in literature.[239,266]

6.1.4.3 2-azidoethan-1-amine (54)



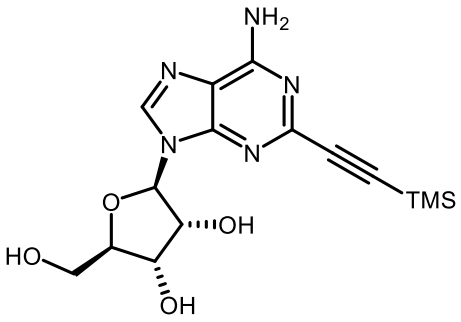
To a solution of 2-chloroethylamine hydrochloride (3.00 g, 25.9 mmols) in H_2O (20 mL) was added sodium azide (5.05 g, 77.6 mmols) and the dark orange-red reaction mixture was heated at 80 °C for 16 hours. The solution was basified to pH 13 using NaOH $_{(s)}$ followed by dilution with H_2O (30 mL) and extraction with Et_2O (3 × 50 mL). The combined organic layers were dried over anhydrous Na_2SO_4, filtered and evaporated under reduced pressure to afford **54** as a colourless oil. The crude product was used in the subsequent step without further purification. ^{1}H NMR (400 MHz, $CDCl_3$) δ 3.42 (t, J = 5.9, 2H, 1), 2.80 (t, J = 5.8, 2H, 2); ^{13}C NMR (101 MHz, $CDCl_3$) δ 53.3, 40.2. Analytical data consistent with that reported in literature.[232]

6.1.4.4 (2R,3R,4S,5R)-2-(6-((2-azidoethyl)amino)-9H-purin-9-yl)-5-(hydroxymethyl) tetrahydrofuran-3,4-diol (6Az-Ad, 28)



To a solution of 6-chloropurine riboside (1.00 g, 3.49 mmols) in EtOH (15 mL) was added 2-azidoethan-1-amine **54** (1.20 g, 13.9 mmols) followed by NEt_3 (1.94 mL, 13.9 mmols), and the reaction mixture was heated under reflux for 3 hours. Removal of solvent under reduced pressure afforded a pale-yellow powder which was washed with H_2O and purified by automated reverse-phase column chromatography, as described in section **6.1.3**. Removal of solvent under reduced pressure afforded **28** as a white powder (469 mg, 1.40 mmols, 40%). R_f = 0.2 (DCM:MeOH 9:1); ^{1}H NMR (400 MHz, DMSO-d_6) δ 8.40 (s, 1H, 5), 8.26 (s, 1H, 4), 8.10 (s, 1H, 3), 5.90 (d, J = 6.2, 1H, 6), 5.48 (d, J = 6.2, 1H, 11), 5.40 (dd, J = 7.1 and 4.6, 1H, 13), 5.22 (d, J = 4.5, 1H, 12), 4.62 (q, J = 5.9, 1H, 7), 4.15 (q, J = 4.4, 1H, 8), 3.97 (q, J = 3.4, 1H, 9), 3.72 – 3.65 (m, 3H, 1, 10), 3.59 – 3.54 (m, 3H, 2, 10); ^{13}C NMR (101 MHz, DMSO-d_6) δ 155.1, 152.8, 150.0, 140.5, 120.4, 88.3, 86.4, 74.0, 71.1, 62.1, 50.2; LC-MS (ESI$^+$) m/z found $[M+H]^+$ = 337.21 at R_t = 8.14 mins; HRMS (ESI$^+$) found 337.1360 ($C_{12}H_{16}N_8O_4$, $[M+H]^+$ requires 337.1373). Analytical data consistent with that reported in literature.[232]

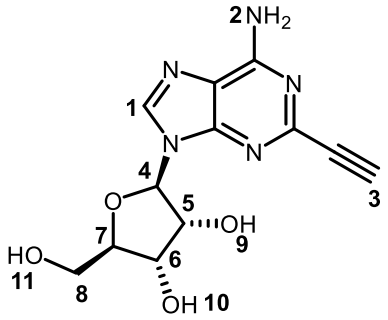
6.1.4.5 (2R,3R,4S,5R)-2-(6-amino-2-((trimethylsilyl)ethynyl)-9H-purin-9-yl)-5-(hydroxy methyl)tetrahydrofuran-3,4-diol (56)



To a solution of 2-iodoadenosine (200 mg, 0.509 mmols) in dry and degassed DMF (2.5 mL) under nitrogen were added CuI (19.3 mg, 0.101 mmols), $Pd(PPh_3)_2Cl_2$ (35.6 mg,

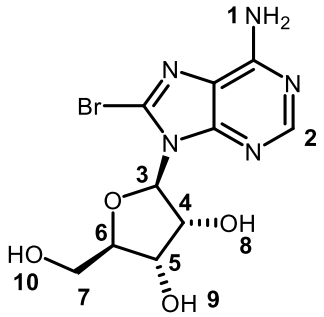
0.0508 mmols) and dry and degassed trimethylamine (426 µL, 3.06 mmols). To the resulting dark orange solution degassed trimethylsilylacetylene (106 µL, 0.762 mmols) was added and the reaction mixture was stirred at r.t. for 16 hours. Upon addition of trimethylsilylacetylene, the reaction mixture immediately changed colour to clear yellow and gradually (over 30 mins) changed to black. Removal of solvent under reduced pressure afforded a black residue which was purified by manual column chromatography (DCM:MeOH 9:1) to afford **56** as a dark yellow-brown residue. The presence of trace amounts and black inorganic impurities was noted and the crude product was used in the subsequent TMS deprotection reaction without further purification. R_f = 0.5 (DCM:MeOH 9:1); LC-MS (ESI^+) m/z found $[M+H]^+$ = 364.36 at R_t = 10.18 mins. This compound is known.[112]

6.1.4.6 (2R,3R,4S,5R)-2-(6-amino-2-ethynyl-9H-purin-9-yl)-5-(hydroxymethyl)tetra hydrofuran-3,4-diol (2Yn-Ad, 26)



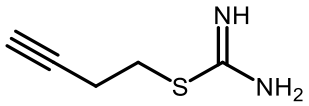
To a solution of **56** in dry MeOH (3 mL) was added K_2CO_3 (491 mg, 3.56 mmols) and the reaction was stirred for 20 mins at r.t. (>30 mins reaction time leads to product degradation). The reaction mixture was diluted with DCM (27 mL) and purified (DCM:MeOH 9:1) to afford **26** as a yellow powder (87 mg, 0.299 mmols, 59% over 2 steps). R_f = 0.2 (DCM:MeOH 9:1); ^{1}H NMR (400 MHz, DMSO-d_6) δ 8.44 (s, 1H, 1), 7.54 (s, 2H, 2), 5.87 (d, *J* = 6.1, 1H, 4), 5.48 (d, *J* = 6.3, 1H, 9), 5.20 (d, *J* = 4.8, 1H, 10), 5.19 (d, *J* = 4.8, 1H, 11), 4.56 (q, *J* = 5.9, 1H, 5), 4.14 (ddd, *J* = 7.3 and 5.2 and 2.8, 1H, 6), 4.03 (s, 1H, 3), 3.96 (q, *J* = 3.6, 1H, 7), 3.68 (dt, *J* = 12.0 and 4.4, 1H, 8), 3.56 (ddd, *J* = 12.1 and 6.8 and 3.8, 1H, 8); ^{13}C NMR (101 MHz, DMSO-d_6) δ 156.4, 149.6, 145.1, 141.2, 119.5, 88.0, 86.2, 83.7, 75.5, 74.1, 70.9, 61.9; LC-MS (ESI^+) m/z found $[M+H]^+$ = 292.03 at R_t = 7.22 mins; HRMS (ESI^+) found 292.1040 ($C_{12}H_{16}N_8O_4$, $[M+H]^+$ requires 292.1046). Analytical data consistent with that reported in literature.[112]

6.1.4.7 (2R,3R,4S,5R)-2-(6-amino-8-bromo-9H-purin-9-yl)-5-(hydroxymethyl)tetra hydrofuran-3,4-diol (57)



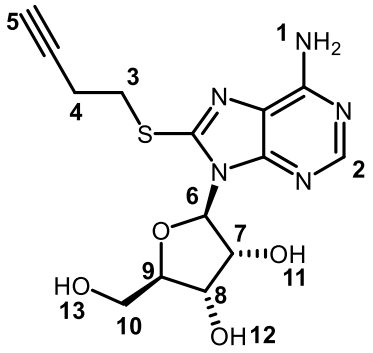
To a solution of 0.5 M NaOAc $_{(aq)}$ (22 mL) and AcOH (2.2 mL) was added adenosine (560 mg, 2.10 mmols) and the mixture was heated to 50 °C and stirred until complete dissolution of adenosine. Bromine solution (161 μL, 3.15 mmols) was then added to the reaction mixture at r.t. and the reaction was stirred at r.t. for 3 hours. The resulting dark red solution changed colour to yellow and was quenched by addition of excess sodium bisulphite, and neutralised (to pH 7) by the addition of 5M NaOH $_{(aq)}$ (~10 mL). The orange precipitate was filtered and washed with H_2O and acetone to afford **57** as a pale-yellow powder (253 mg, 0.730 mmols, 35%). R_f = 0.15 (DCM:MeOH 9:1); ^{1}H NMR (400 MHz, DMSO-d_6) δ 8.12 (s, 1H, 2), 5.85 (d, J = 6.9, 1H, 3), 5.08 (q, J = 6.9, 1H, 4), 4.20 (dd, J = 5.2 and 2.2, 1H, 5), 4.00 (q, J = 3.6, 1H, 6), 3.69 (dd, J = 12.3 and 3.7, 1H, 7), 3.53 (dd, J = 12.2 and 4.0, 1H, 7); ^{13}C NMR (101 MHz, DMSO-d_6) δ 155.5, 152.8, 150.3, 127.6, 120.1, 90.9, 87.2, 71.6, 71.3, 62.5; LC-MS (ESI$^+$) m/z found $[M+H]^+$ = 346.2, 348.2 (isotope) at R_t = 7.12 mins. Analytical data consistent with that reported in literature.[233]

6.1.4.8 But-3-yn-1-yl carbamimidothioate (62)



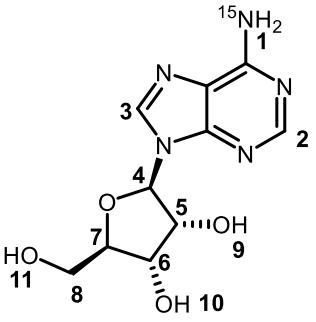
To a solution of 4-bromo-1-butyne (93.9 μL, 1.00 mmols) in dimethoxyethane (2.0 mL) was added thiourea (76.0 mg, 1.00 mmols) and the reaction mixture was heated at 50 °C for 16 hours. The solvent was evaporated under reduced pressure, the resulting yellow slurry was washed with Et_2O, and the crude product **62** was used in the next step without further purification. LC-MS (ESI$^+$) m/z found $[M+H]^+$ = 129.11 at R_t = 1.96 mins. This compound is known.[235]

6.1.4.9 (2R,3R,4S,5R)-2-(6-amino-8-(but-3-yn-1-ylthio)-9H-purin-9-yl)-5-(hydroxy methyl)tetrahydrofuran-3,4-diol (8But-Yn-Ad, 27)



To a solution of 8-bromoadenosine **57** (100 mg, 0.289 mmols) in DMF (2 mL) was added a solution of but-3-yn-1-yl carbamimidothioate **62** (76.9 mg, 0.6 mmols) in H_2O (600 μL). 5 M NaOH $_{(aq)}$ (115.6 μL, 0.578 mmols) was added and the reaction mixture was stirred at 40 °C for 2 hours. The reaction was neutralised by addition of formic acid and the crude mixture was purified by automated reverse-phase column chromatography as described in section **6.1.3**. Removal of solvent under reduced pressure, followed by lyophilisation afforded **27** as a white powder (51 mg, 0.144 mmols, 50%). R_f = 0.2 (DCM:MeOH 9:1); ^{1}H NMR (400 MHz, DMSO-d_6) δ 8.07 (s, 1H, 2), 7.35 (s, 2H, 1), 5.75 (d, *J* = 6.9, 1H, 6), 5.68 (d, *J* = 8.8, 1H, 11), 5.46 (d, *J* = 6.3, 1H, 12), 5.24 (d, *J* = 4.4, 1H, 13), 5.00 (q, *J* = 5.9, 1H, 7), 4.16 (t, *J* = 4.3, 1H, 8), 3.98 (q, *J* = 3.4, 1H, 9), 3.68 (dt, *J* = 12.4 and 3.7, 1H, 10), 3.56 – 3.44 (m, 1H, 3, 10), 2.97 (t, *J* = 2.7, 1H, 5), 2.71 (td, *J* = 7.0 and 2.7, 2H, 4); ^{13}C NMR (101 MHz, DMSO-d_6) δ 155.1, 151.8, 150.9, 148.6, 120.1, 89.3, 87.1, 82.9, 73.3, 71.8, 71.5, 62.7, 31.6, 19.3; LC-MS (ESI$^+$) m/z found $[M+H]^+$ = 352.14 at R_t = 7.23 mins; HRMS (ESI$^+$) found 352.1078 ($C_{14}H_{17}N_5O_4S$, $[M+H]^+$ requires 352.1079). This compound is known but no analytical data is available in the literature.

6.1.4.10 (2R,3R,4S,5R)-2-(6-(amino-15N)-9H-purin-9-yl)-5-(hydroxymethyl)tetrahydro furan-3,4-diol (^{15}N-Ad, 63)

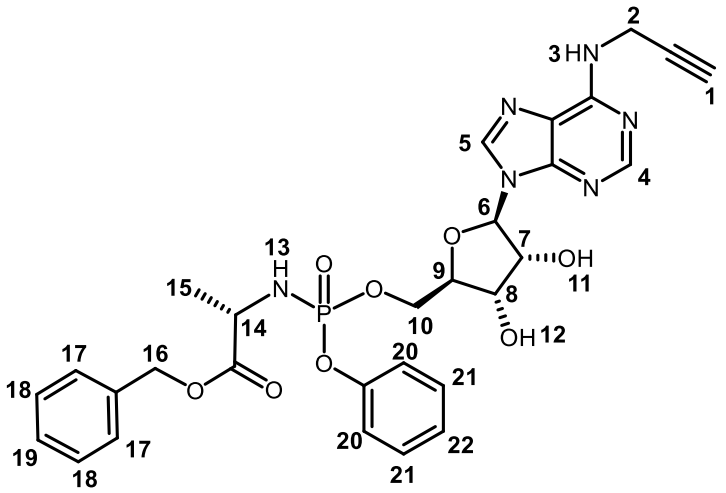


To a solution of 6-chloropurine riboside (600 mg, 2.10 mmols) and $NaHCO_3$ (794 mg, 9.46 mmols) in DMSO (3.5 mL) was added $^{15}NH_4Cl$ (344 mg, 6.30 mmols) and the reaction mixture was heated at 80 °C for 96 hours. The reaction was quenched by the dropwise addition of 10% (v/v) AcOH in H_2O (5 mL) and the crude mixture was purified by automated reverse-phase column chromatography as described in section **6.1.3**. Removal of solvent under reduced pressure, followed by lyophilisation afforded **63** as a white solid (175 mg, 0.663 mmols, 32%). R_f = 0.1 (DCM:MeOH 9:1); ^1H NMR (400 MHz, D_2O) δ 8.14 (s, 1H, 3), 7.99 (s, 1H, 2), 5.89 (d, *J* = 6.1, 1H, 4), 4.63 (m, 1H, 5), 4.29 (dd, *J* = 5.2 and 3.3, 1H, 6), 4.16 (q, *J* = 3.2, 1H, 7), 3.79 (dd, *J* = 12.9 and 2.7, 1H, 8), 3.70 (dd, *J* = 12.9 and 3.5, 1H, 8); ^{13}C NMR (101 MHz, D_2O-d_6) δ 155.5, 152.4, 148.2, 140.5, 118.9, 88.3, 85.7, 73.6, 70.6, 61.4; LC-MS (ESI^+) m/z found $[M+H]^+$ = 269.2 at R_t = 2.96 mins; HRMS (ESI^+) found 269.1013 ($C_{13}H_{15}N_4{}^{15}NO_4$, $[M+H]^+$ requires 269.1016). Analytical data consistent with that reported in literature.[237]

6.1.5 Synthesis of ProTide Analogues

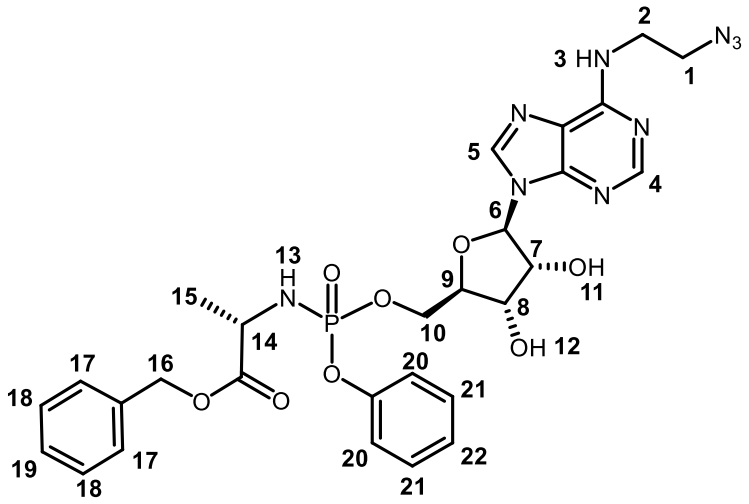
All ProTide analogues were synthesised according to the following general procedure: To a solution of 50 mg (1 eq.) of the corresponding adenosine analogue in freshly distilled trimethyl phosphate $PO(OMe)_3$ (500 µL) under nitrogen was added dry NEt_3 (4 eq.) at 0 °C. After 2 – 3 mins, phenyl dichlorophosphate (2 eq.) was added and the reaction mixture was stirred at 0 °C for 30 mins - 1 hour. Disappearance of the starting material and formation of the (hydrolysed) activated intermediate was monitored by LC-MS. In a separate flask, to a solution of L-alanine benzyl ester hydrochloride (4 eq.) in freshly distilled $PO(OMe)_3$ (800 µL) under nitrogen was added dry NEt_3 (4 eq.) and the solution was transferred to the reaction mixture dropwise using a syringe. The flask was washed with $PO(OMe)_3$ (500 µL) and the washing was also transferred to the reaction mixture. The reaction was allowed to proceed at 0 °C for 10 mins and then at r.t. for 30 mins. The reaction was quenched with H_2O (3 mL) and the resulting solution was purified by automated reverse-phase column chromatography as described in section **6.1.3**. Removal of solvent under reduced pressure, followed by lyophilisation afforded all ProTide products as fluffy white powders.

6.1.5.1 Benzyl ((((2R,3S,4R,5R)-3,4-dihydroxy-5-(6-(prop-2-yn-1-ylamino)-9H-purin-9-yl)tetrahydrofuran-2-yl)methoxy)(phenoxy)phosphoryl)-L-alaninate (6Yn-Pro, 47)



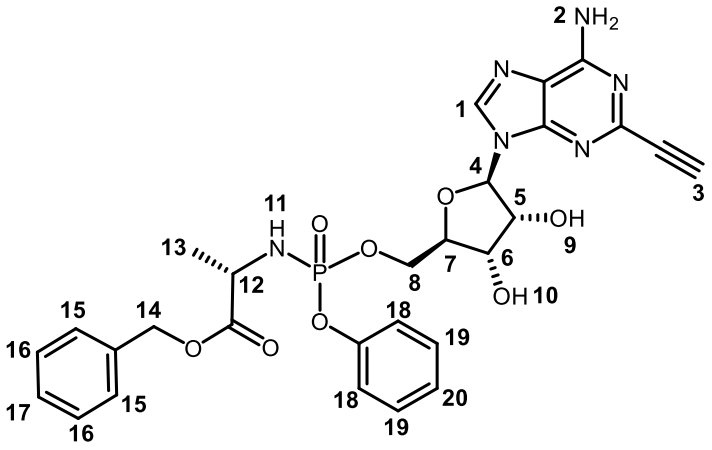
Synthesised according to the general procedure described. **47** (23 mg, 0.0376 mmols, 23%). R_f = 0.7 (DCM:MeOH 9:1); ^{1}H NMR (400 MHz, methanol-d_4) δ 8.31 (s, 1H, 5), 8.28 (s, 1H, 4), 8.24 (s, 1H, 3), 7.35 – 7.27 (m, 7H, 17-19, 21), 7.22 – 7.16 (m, 3H, 20, 22), 6.06 (t, *J* = 4.9, 1H, 6), 5.12 (d, *J* = 3.3, 1H, 16), 5.09 (d, *J* = 7.5, 1H, 16), 4.65 (dt, *J* = 12.8 and 5.0, 1H, 7), 4.44 – 4.37 (m, 4H, 2, 8, 14), 4.37 – 4.29 (m, 1H, 10), 4.25 (q, *J* = 3.4, 1H, 9), 4.03 – 3.89 (m, 1H, 10), 2.66 (t, *J* = 2.9, 1H, 1), 1.30 (dd, *J* = 19.8 and 7.1, 3H, 15); ^{13}C NMR (101 MHz, methanol-d_4) δ 174.8, 155.1, 153.4, 152.0, 141.1, 137.2, 130.8, 129.6, 129.3, 129.3, 126.2, 121.4, 121.4, 121.0, 90.0, 84.4, 81.0, 75.4, 72.4, 71.5, 67.9, 67.1, 51.7, 30.9, 20.2; 31P NMR (162 MHz, methanol-d_4) δ 3.91, 3.65; LC-MS (ESI$^+$) m/z found $[M+H]^+$ = 623.24 at R_t = 11.28 mins; HRMS (ESI$^+$) found 623.2014 ($C_{29}H_{31}N_6O_8P$, $[M+H]^+$ requires 623.2019). Analytical data consistent with that reported in literature.[223]

6.1.5.2 Benzyl ((((2R,3S,4R,5R)-5-(6-((2-azidoethyl)amino)-9H-purin-9-yl)-3,4-dihydroxytetrahydrofuran-2-yl)methoxy)(phenoxy)phosphoryl)-L-alaninate (6Az-Pro, 50)



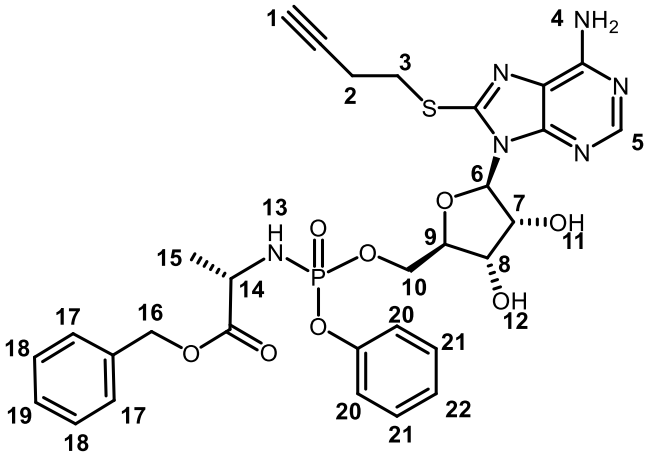
Synthesised according to the general procedure described. **50** (22 mg, 0.0324 mmols, 23%). R_f = 0.7 (DCM:MeOH 9:1); ^{1}H NMR (500 MHz, methanol-d_4) δ 8.29 (s, 1H, 5), 8.26 (s, 1H, 4), 8.23 (s, 1H, 3), 7.35 – 7.26 (m, 7H, 17-19, 21), 7.22 – 7.14 (m, 3H, 20, 22), 6.05 (d, *J* = 5.1, 1H, 6), 5.13 – 5.10 (m, 1H, 16), 5.08 (d, *J* = 11.2, 1H, 16), 4.65 (dt, *J* = 14.0 and 5.1, 1H, 7), 4.39 (m, 2H, 8, 14), 4.31 (m, 1H, 10), 4.27 – 4.22 (m, 1H, 9), 4.03 – 3.91 (m, 1H, 10), 3.85 – 3.71 (m, 2H, 1), 3.58 (td, *J* = 5.9 and 2.2, 2H, 2), 1.37 – 1.24 (m, 3H, 15); ^{13}C NMR (101 MHz, methanol-d_4) δ 174.6, 155.8, 153.6, 152.1, 140.8, 137.2, 130.8, 129.6, 129.3, 129.3, 126.2, 121.5, 121.4, 121.4, 90.0, 84.4, 75.4, 71.6, 67.9, 67.5, 67.1, 51.7, 51.6, 20.4; 31P NMR (162 MHz, methanol-d_4) δ 3.90, 3.65; LC-MS (ESI$^+$) m/z found $[M+H]^+$ = 654.18 at R_t = 11.54 mins; HRMS (ESI$^+$) found 654.2207 ($C_{29}H_{31}N_6O_8P$, $[M+H]^+$ requires 654.2189). Analytical data consistent with that reported in literature.[232]

6.1.5.3 Benzyl ((((2R,3S,4R,5R)-5-(6-amino-2-ethynyl-9H-purin-9-yl)-3,4-dihydroxy tetrahydrofuran-2-yl)methoxy)(phenoxy)phosphoryl)-L-alaninate (2Yn-Pro, 48)



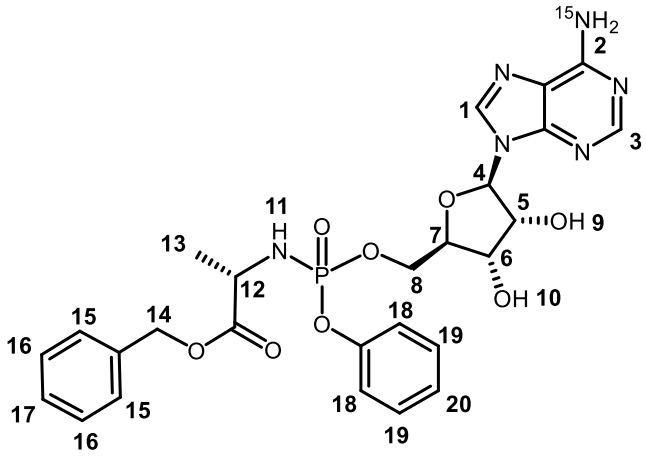
Synthesised according to the general procedure described. **48** (2.1 mg, 0.00345 mmols, 2%). R_f = 0.7 (DCM:MeOH 9:1); ^{1}H NMR (500 MHz, methanol-d_4) δ 8.29 (s, 1H, 1), 8.25 (s, 1H, 2), 7.30 – 7.22 (m, 8H, 2, 15-17, 19), 7.21 – 7.12 (m, 3H, 18, 20), 6.00 (d, J = 4.6, 1H, 4), 5.10 (d, J = 6.0, 1H, 14), 5.08 – 5.05 (m, 1H, 14), 4.55 (dt, J = 14.8 and 4.9, 1H, 5), 4.39 – 4.34 (m, 2H, 6, 12), 4.33 – 4.26 (m, 1H, 8), 4.25 – 4.19 (m, 1H, 7), 4.03 – 3.91 (m, 1H, 8), 1.32 – 1.24 (m, 3H, 13); ^{13}C NMR (101 MHz, methanol-d_4) δ 173.6, 155.5, 150.6, 149.1, 140.5, 135.9, 129.4, 128.1, 128.0, 127.9, 124.8, 120.1, 120.0, 118.9, 88.7, 82.8, 74.2, 69.9, 66.5, 66.5, 66.0, 65.6, 50.0, 22.8; 31P NMR (162 MHz, methanol-d_4) δ 3.91, 3.66; LC-MS (ESI$^+$) m/z found $[M+H]^+$ = 609.25 at R_t = 10.97 mins; HRMS (ESI$^+$) found 609.1863 ($C_{29}H_{31}N_6O_8P$, $[M+H]^+$ requires 609.1862). Synthesis of this molecule was previously unreported.

6.1.5.4 Benzyl ((((2R,3S,4R,5R)-5-(6-amino-8-(but-3-yn-1-ylthio)-9H-purin-9-yl)-3,4-dihydroxytetrahydrofuran-2-yl)methoxy)(phenoxy)phosphoryl)-L-alaninate (8But-Yn-Pro, 49)



Synthesised according to the general procedure described. **49** (8.0 mg, 0.0120 mmols, 8%). R_f = 0.75 (DCM:MeOH 9:1); ^{1}H NMR (500 MHz, methanol-d_4) δ 8.11 (s, 1H, 5), 7.32 – 7.19 (m, 9H, 4, 17-19, 21), 7.17 – 6.99 (m, 3H, 20, 22), 5.93 (d, J = 4.7, 1H, 6), 5.09 – 5.01 (m, 2H, 16), 4.59 – 4.52 (m, 1H, 7), 4.42 – 4.33 (m, 1H, 10), 4.32 – 4.21 (m, 1H, 10), 4.19 – 4.10 (m, 1H, 8), 3.99 – 3.85 (m, 1H, 9), 3.51 – 3.41 (m, 2H, 3), 2.70 (td, J = 7.1 and 2.6, 2H, 2), 2.38 (t, J = 2.6, 1H, 1), 1.27 (dd, J = 7.1 and 1.1, 3H, 15); ^{13}C NMR (101 MHz, methanol-d_4) δ 174.6, 155.2, 153.9, 152.3, 150.2, 137.2, 130.7, 129.6, 129.3, 129.3, 126.0, 121.4, 121.3, 121.0, 91.1, 84.4, 82.6, 73.0, 71.6, 71.5, 67.9, 67.6, 51.5, 32.5, 24.2, 20.2; 31P NMR (162 MHz, methanol-d_4) δ 3.53, 3.42; LC-MS (ESI$^+$) m/z found $[M+H]^+$ = 669.23 at R_t = 11.16 mins; HRMS (ESI$^+$) found 669.1911 ($C_{30}H_{33}N_6O_8PS$, $[M+H]^+$ requires 669.1896). Synthesis of this molecule was previously unreported.

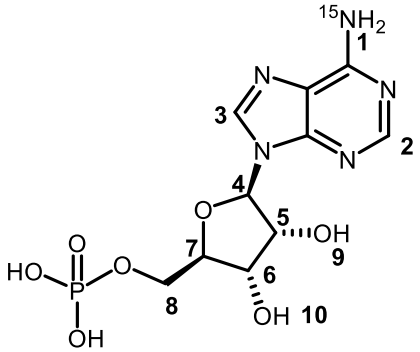
6.1.5.5 Benzyl ((((2R,3S,4R,5R)-5-(6-(amino-15N)-9H-purin-9-yl)-3,4-dihydroxytetra hydrofuran-2-yl)methoxy)(phenoxy)phosphoryl)-L-alaninate (^{15}N-Pro-Ad, 64)



Synthesised according to the general procedure described. **64** (21 mg, 0.0359 mmols, 19%). R_f = 0.6 (DCM:MeOH 9:1); ^{1}H NMR (400 MHz, methanol-d_4) δ 8.42 (s, 1H, 1), 8.39 (s, 1H, 3), 8.27 (s, 1H, 2), 7.35 – 7.28 (m, 8H, 2, 15-17, 19), 7.21 – 7.17 (m, 3H, 18, 20), 6.13 – 6.05 (m, 1H, 4), 5.13 (d, *J* = 2.8, 1H, 14), 5.10 (d, *J* = 3.7, 1H, 14), 4.64 (dt, *J* = 14.7 and 5.2, 1H, 5), 4.43 – 4.36 (m, 2H, 6, 12), 4.35 – 4.30 (m, 1H, 8), 4.29 – 4.25 (m, 1H, 7), 4.04 – 3.92 (m, 1H, 8), 1.33 – 1.28 (m, 3H, 13); ^{13}C NMR (101 MHz, methanol-d_4) δ 174.6, 152.1, 150.1, 147.8, 142.9, 137.2, 130.8, 130.3, 129.5, 129.2, 126.2, 121.7, 121.4, 120.4, 90.2, 84.6, 75.6, 71.5, 67.9, 67.4, 51.6, 20.4; 31P NMR (162 MHz, methanol-d_4) δ 3.88, 3.64; LC-MS (ESI$^+$) m/z found $[M+H]^+$ = 586.20 at R_t = 11.09 mins; HRMS (ESI$^+$) found 586.1821 ($C_{29}H_{31}N_5{}^{15}NO_8P$, $[M+H]^+$ requires 586.1833). Synthesis of this molecule was previously unreported.

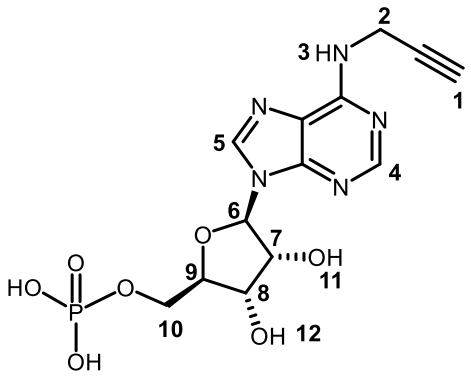
6.1.6 Synthesis of AMP, ATP and NAD$^+$ Analogues

6.1.6.1 ((2R,3S,4R,5R)-5-(6-(amino-15N)-9H-purin-9-yl)-3,4-dihydroxytetrahydrofuran-2-yl)methyl dihydrogen phosphate (^{15}N-AMP, 72)



To a solution of ^{15}N-Ad **63** (49.3 mg, 0.183 mmols) in freshly distilled $PO(OMe)_3$ (750 µL) under nitrogen was added dry DIPEA (95.6 µL, 0.549 mmols) at 0 °C. After 5 mins, $POCl_3$ (34.2 µL, 0.367 mmols) was added and the reaction mixture was stirred at 0 °C for 2 hours. The reaction was quenched with H_2O (2.5 mL) and the resulting solution was purified by automated anion exchange chromatography as described in section **6.1.3**. Removal of solvent under reduced pressure, followed by lyophilisation afforded **72** as a pale-yellow solid (17 mg, 0.0476 mmols, 26%). ^{1}H NMR (400 MHz, D_2O) δ 8.37 (s, 1H, 3), 8.04 (s, 1H, 2), 5.96 (d, J = 5.8, 1H, 4), 4.63 – 4.60 (m, 1H, 5), 4.36 (t, J = 4.4, 1H, 6), 4.23 (d, J = 3.5, 1H, 7), 3.93 (d, J = 2.6, 2H, 8); ^{13}C NMR (101 MHz, D_2O) δ 153.1, 150.4, 146.7, 137.7, 116.4, 84.7, 82.0, 72.2, 68.3, 61.7; ^{31}P NMR (162 MHz, D_2O) δ 0.66; LC-MS (ESI^+) m/z found $[M+H]^+$ = 349.18 at R_t = 2.0 mins; HRMS (ESI^+) found 349.0688 ($C_{10}H_{14}N_4{}^{15}NO_7P$, $[M+H]^+$ requires 349.0601). Synthesis of this molecule was previously unreported.

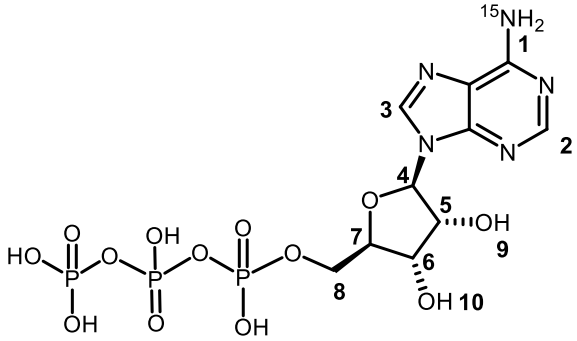
6.1.6.2 ((2R,3S,4R,5R)-3,4-dihydroxy-5-(6-(prop-2-yn-1-ylamino)-9H-purin-9-yl)tetra hydrofuran-2-yl)methyl dihydrogen phosphate (6Yn-AMP, 30)



To a solution of 6Yn-Ad **25** (200 mg, 0.656 mmols) in freshly distilled $PO(OMe)_3$ (2.4 mL) under nitrogen was added dry DIPEA (340 µL, 1.96 mmols) at 0 °C. After 5 mins, $POCl_3$ (120 µL, 1.30 mmols) was added and the reaction mixture was stirred 0 °C for 3 hours. Dry DIPEA (85.0 µL, 0.490 mmols) and $POCl_3$ (30.0 µL, 0.325 mmols) were subsequently added and the reaction was further stirred at 0 °C for 1 hour. The reaction was quenched with H_2O (7.5 mL) and the resulting solution was purified by automated reverse-phase column chromatography, eluting with MeCN and 25 mM $NH_4HCO_{3\ (aq)}$ over 23 CV at 12 mL/min using the following linear gradient: 2% MeCN (in 25 mM $NH_4HCO_{3\ (aq)}$) over 3 CV, 2-5% MeCN over 5 CV, 5-10% MeCN over 5 CV and 10-50% MeCN over 10 CV. Removal of solvent under reduced pressure, followed by lyophilisation afforded **30** as a white powder (90 mg, 0.235 mmols, 36%). ^{1}H NMR (400 MHz, D_2O) δ 8.38 (s, 1H, 5), 8.12 (s, 1H, 4), 5.98 (d, J = 5.8, 1H, 6), 4.63

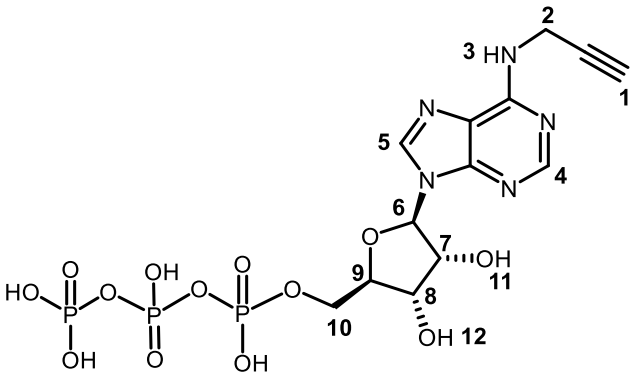
(t, *J* = 5.4, 1H, 7), 4.37 (dd, *J* = 5.1 and 3.6, 1H, 8), 4.28 – 4.22 (m, 1H, 9), 4.21 – 4.13 (m, 2H, 2), 3.98 – 3.87 (m, 2H, 10), 2.49 (t, *J* = 2.5, 1H, 1); ^{13}C NMR (101 MHz, D_2O) δ 153.8, 152.6, 148.3, 139.8, 119.0, 86.9, 84.3, 80.3, 74.4, 71.8, 70.5, 63.8, 30.1; ^{31}P NMR (162 MHz, D_2O) δ 2.16; LC-MS (ESI^+) m/z found $[M+H]^+$ = 386.29 at R_t = 2.7 mins; HRMS (ESI^+) found 386.0870 ($C_{13}H_{16}N_5O_7P$, $[M+H]^+$ requires 386.0787). Analytical data consistent with that reported in literature.[114,239]

6.1.6.3 ((2R,3S,4R,5R)-5-(6-(amino-15N)-9H-purin-9-yl)-3,4-dihydroxytetrahydrofuran-2-yl)methyl tetrahydrogen triphosphate (^{15}N-ATP, 73)



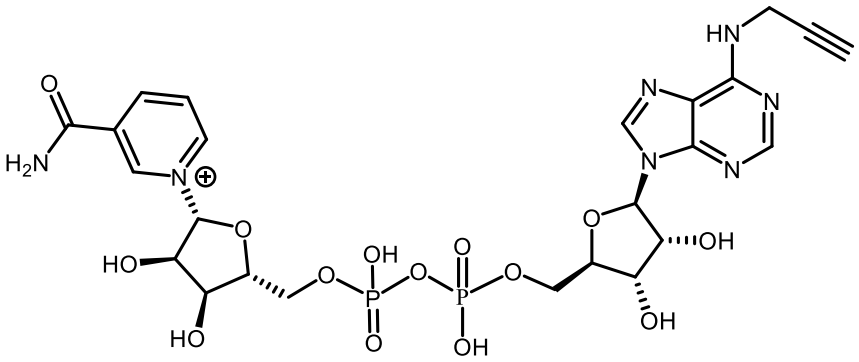
To a solution of ^{15}N-Ad **63** (50 mg, 0.186 mmols) in freshly distilled $PO(OMe)_3$ (800 μL) under nitrogen was added dry DIPEA (97.2 μL, 0.558 mmols) at 0 °C. After 5 mins, $POCl_3$ (34.7 μL, 0.372 mmols) was added and the reaction mixture was stirred at 0 °C for 1 hour 30 mins. In a separate flask, to a solution of tributylammonium pyrophosphate (408 mg, 0.744 mmols) in distilled $PO(OMe)_3$ (1.0 mL) under nitrogen was added dry DIPEA (97.2 μL, 0.558 mmols) and the solution was added dropwise to the reaction mixture at 0 °C over 5 mins. The reaction was allowed to proceed at 0 °C for 2 hours and was quenched by the addition of 0.1 M $TEAB_{(aq)}$ (2 mL) at 0 °C for 30 mins. The resulting solution was purified by automated anion exchange chromatography as described in **Section 6.1.3**. Removal of solvent under reduced pressure, followed by lyophilisation afforded **73** as a pale yellow solid (14 mg, 0.0283 mmols, 15%). ^{1}H NMR (400 MHz, D_2O) δ 8.45 (s, 1H, 3), 8.15 (s, 1H, 2), 6.09 – 6.01 (m, 1H, 4), 4.57 – 4.49 (m, 1H, 5), 4.31 (s, 1H, 6), 4.24 – 4.16 (m, 1H, 7), 4.15 – 4.07 (m, 1H, 8), 3.93 (dt, *J* = 15.0 and 4.3, 1H, 8); ^{13}C NMR (101 MHz, D_2O) δ 155.8, 152.9, 149.2, 139.9, 86.7, 80.6, 74.2, 70.2, 65.1; ^{31}P NMR (162 MHz, D_2O) δ -6.04, -11.17, -21.55; LC-MS (ESI^+) m/z found $[M+H]^+$ = 509.02 at R_t = 2.3 mins; HRMS (ESI^+) found 509.0020 ($C_{10}H_{16}N_4{}^{15}NO_{13}P_3$, $[M+H]^+$ requires 509.0006. Synthesis of this molecule was previously unreported.

6.1.6.4 ((2R,3S,4R,5R)-3,4-dihydroxy-5-(6-(prop-2-yn-1-ylamino)-9H-purin-9-yl)tetra hydrofuran-2-yl)methyl tetrahydrogen triphosphate (6Yn-ATP, 40)



To a solution of 6Yn-Ad **25** (50 mg, 0.164 mmols) in freshly distilled $PO(OMe)_3$ (0.75 mL) under nitrogen was added dry DIPEA (85.6 μL, 0.493 mmols) at 0 °C. After 5 mins, $POCl_3$ (30.5 μL, 0.328 mmols) was added and the reaction mixture was stirred at 0 °C for 1 hour 45 mins. In a separate flask, to a solution of tributylammonium pyrophosphate (539 mg, 0.984 mmols) in freshly distilled $PO(OMe)_3$ (1.25 mL) under nitrogen was added dry DIPEA (85.6 μL, 0.493 mmols) and the solution was added dropwise to the reaction mixture at 0 °C over 5 mins. The reaction was allowed to proceed at 0 °C for 2 hours 30 mins and was quenched by the addition of 0.1 M $TEAB_{(aq)}$ (2 mL) at 0 °C for 30 mins. The resulting solution was purified by automated anion exchange chromatography as described in **Section 6.1.3**. Removal of solvent under reduced pressure, followed by lyophilisation afforded **40** as a white crystalline solid (19 mg, 0.0347 mmols, 21%). ^{1}H NMR (400 MHz, D_2O) δ 8.26 (s, 1H, 5), 8.03 (s, 1H, 4), 5.91 (d, J = 5.5, 1H, 6), 4.59 – 4.57 (m, 1H, 7), 4.39 (t, J = 4.7, 1H, 8), 4.25 – 4.18 (m, 1H, 9), 4.11 – 4.07 (m, 3H, 2, 10), 3.90 (t, J = 13.4, 1H, 10), 2.46 (s, 1H, 1); ^{13}C NMR (101 MHz, D_2O) δ 153.6, 152.5, 148.2, 139.5, 118.9, 86.8, 83.6, 80.3, 74.2, 71.8, 70.1, 65.1, 30.1; ^{31}P NMR (162 MHz, D_2O) δ -10.68, -11.39, -23.01; LC-MS (ESI^+) m/z found $[M+H]^+$ = 546.1 at R_t = 2.34 mins; HRMS (ESI^+) found 546.0170 ($C_{13}H_{18}N_5O_{13}P_3$, $[M+H]^+$ requires 546.0192). Analytical data consistent with that reported in literature.[240]

6.1.6.5 3-carbamoyl-1-((2R,3R,4S,5R)-5-(((((((2R,3S,4R,5R)-3,4-dihydroxy-5-(6-(prop-2-yn-1-ylamino)-9H-purin-9-yl)tetrahydrofuran-2-yl)methoxy)(hydroxy)phosphoryl)oxy)(hydroxy)phosphoryl)oxy)methyl)-3,4-dihydroxytetrahydrofuran-2-yl)pyridin-1-ium (6Yn-NAD, 3)

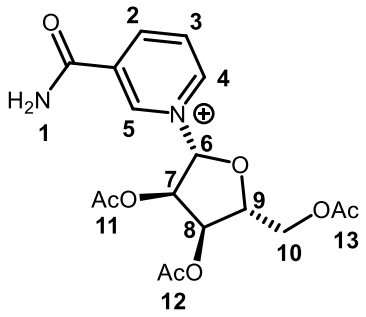


6Yn-AMP **30** (3.8 mg, 0.0100 mmols) and β-nicotinamide mononucleotide (β-NMN) (10.2 mg, 0.0300 mmols) were added to separate flasks followed by addition of dry NEt_3 (1.0 mL) and stirred for 16 – 20 hours under nitrogen to afford the corresponding triethylammonium salts. After removal of NEt_3 under reduced pressure, to a solution of β-NMN.NEt_3 **82** in dry DMF (210 µL) and dry 1,4-dioxane (150 µL) under nitrogen was added dry NEt_3 (30.0 µL, 0.216 mmols) followed by diphenyl phosphoryl chloride **88** (12.5 µL, 0.0600 mmols) and benzyl tributyl ammonium chloride **90** (9.4 mg, 0.0300 mmols). The yellow reaction mixture was stirred at r.t. for 3 hours and formation of the activated intermediate **89** was monitored by LC-MS. The reaction mixture was transferred into a 15 mL falcon tube, precipitated by addition of dry Et_2O (10 mL) and centrifuged at 4000 g at 4 °C for 2 mins. A pale-yellow pellet formed at the bottom of the tube and the supernatant was discarded. Washing of the pellet was repeated with Et_2O, centrifuged at 4000 g at 4 °C for 2 mins and then dried under a flow of nitrogen for 15 mins and under vacuum for 3 hours. In a separate flask, a solution of 6Yn-AMP.NEt_3 in dry DMF (150 µL) under nitrogen was prepared and added to the dried pellet under nitrogen. A solution of dry pyridine (150 µL) in dry DMF (200 µL) under nitrogen was prepared and added to the reaction mixture, and the reaction was allowed to proceed at r.t. for 16 hours. The reaction mixture was transferred into a 15 mL falcon tube, precipitated by the addition of dry Et_2O (12 mL) and centrifuged at 4000 g at 4 °C for 2 mins. A pale-yellow pellet formed at the bottom of the tube and the supernatant was discarded. Washing of the pellet was repeated with Et_2O, centrifuged at 4000 g at 4 °C for 2 mins and then dried under a flow of nitrogen for 15 mins to afford crude **3** as a pale-yellow powder. Because of the highly polar nature of 6Yn-NAD^+ (**3**) and its tendency to easily

hydrolyse, it could not be successfully separated from other components in the reaction mixture such as excess 6Yn-AMP (**30**) and was not further purified. LC-MS (ESI^+) m/z found $[M+H]^+$ = 702.37 at R_t = 2.2 mins. There was insufficient compound for full characterisation. This compound is known.[105]

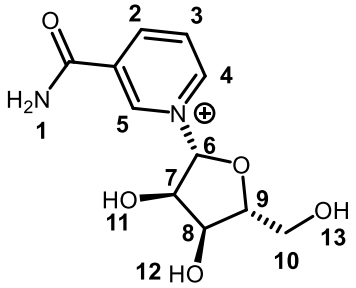
6.1.7 Synthesis of NR and NRH

6.1.7.1 3-carbamoyl-1-((2R,3R,4R,5R)-3,4-diacetoxy-5-(acetoxymethyl)tetrahydrofuran-2-yl)pyridin-1-ium (93)



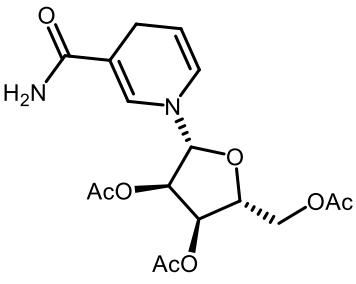
To a solution of nicotinamide **92** (208 mg, 1.65 mmols) in dry MeCN (11 mL) under nitrogen was added β-D-ribofuranse 1,2,3,5-tetraacetate **91** (350 mg, 1.10 mmols) followed by dropwise addition of TMS-OTf (239 μL, 1.32 mmols) over 10 mins and the reaction mixture was stirred at r.t. for 24 hours. The solvent was removed under reduced pressure, the crude residue was dissolved in MeOH (25 mL) and extracted with hexane (3 × 25 mL). Removal of the MeOH layer under reduced pressure afforded a pale yellow residue which was dissolved in H_2O (3 mL) and purified by automated reverse-phase column chromatography as described in **Section 6.1.3**. Removal of solvent under reduced pressure, followed by lyophilisation afforded **93** as a fluffy white powder (218 mg, 0.572 mmols, 52%). ^1H NMR (400 MHz, D_2O) δ 9.40 (t, *J* = 1.6, 1H, 5), 9.16 (dt, *J* = 6.6 and 1.4, 1H, 4), 8.94 (dt, *J* = 8.1 and 1.5, 1H, 2), 8.22 (dd, *J* = 8.1 and 6.3, 1H, 3), 6.54, (d, *J* = 3.9, 1H, 6), 5.52 (dd, *J* = 5.4 and 3.8, 1H, 7), 5.40, (t, *J* = 5.4, 1H, 8), 4.84 (dt, *J* = 5.4 and 2.7, 1H, 9), 4.48 (t, *J* = 2.5, 2H, 10), 2.11 (s, 3H, 11), 2.08 (s, 3H, 12), 2.04 (s, 3H, 13); ^{13}C NMR (101 MHz, D_2O) δ 173.3, 172.4, 172.4, 165.5, 146.2, 143.1, 140.4, 134.2, 128.6, 97.3, 82.6, 76.4, 69.4, 62.6, 20.1, 19.8, 19.8; LC-MS (ESI^+) m/z found $[M+H]^+$ = 381.25 at R_t = 7.31 mins. Analytical data consistent with that reported in literature.[242]

6.1.7.2 3-carbamoyl-1-((2R,3R,4S,5R)-3,4-dihydroxy-5-(hydroxymethyl)tetrahydrofuran-2-yl)pyridin-1-ium (NR, 23)



93 (72.8 mg, 0.191 mmols) was dissolved in 4 M ammonia in MeOH solution (1.7 mL) and stirred at 4 °C for 20 hours. Removal of solvent under reduced pressure afforded a pale-yellow residue which was dissolved in H_2O (3 mL) and purified by automated reverse-phase column chromatography, eluting with MeCN (+0.1% FA) and H_2O (+0.1% FA) over 25 CV at 12 mL/min using the following linear gradient: 2-5% MeCN (in H_2O) over 3 CV, 5-95% MeCN over 20 CV, 95% over 2 CV. Removal of solvent under reduced pressure, followed by lyophilisation afforded **23** as a highly hygroscopic colourless crystalline solid (16 mg, 0.0638 mmols, 33%). ^{1}H NMR (400 MHz, DMSO) δ 9.50 (t, *J* = 2.0, 1H, 5), 9.16 (dt, *J* = 6.4 and 1.5, 1H, 4), 8.87 (dt, *J* = 8.1 and 1.5, 1H, 2), 8.17 (dd, *J* = 8.1 and 6.3, 1H, 3), 6.14 (d, *J* = 4.4, 1H, 6), 4.42 – 4.35 (m, 2H, 7, 8), 4.27 – 4.23 (m, 1H, 9), 3.95 (dd, *J* = 12.9 and 2.9, 1H, 10), 3.79 (dd, *J* = 12.9 and 3.6, 1H, 10); ^{13}C NMR (101 MHz, D_2O) δ 165.8, 145.7, 142.6, 140.4, 134.0, 128.4, 99.9, 87.7, 77.5, 69.8, 60.2; LC-MS (ESI$^+$) m/z found $[M+H]^+$ = 255.30 at R_t = 2.18 mins. Analytical data consistent with that reported in literature.[242]

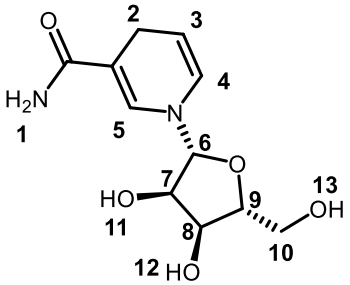
6.1.7.3 (2R,3R,4R,5R)-2-(acetoxymethyl)-5-(3-carbamoylpyridin-1(4H)-yl)tetrahydrofuran-3,4-diyl diacetate (94)



Synthesis of **93** was scaled up 5× and the crude product was used for the synthesis of **94** without further purification. To a solution of crude **93** (1.68 g assumed to contain ~800 mg of product, 2.10 mmols) in H_2O (15 mL) was added $NaHCO_3$ (1.15 g, 13.7 mmols) followed by sodium dithionite (915 mg, 5.26 mmols). The reaction mixture was stirred at r.t. for 2 mins, EtOAc

(20 mL) was then added and the reaction mixture was stirred at r.t. for 2 hours. The EtOAc layer was extracted, followed by extraction of the aqueous layer with EtOAc (3x25 mL) and all EtOAc layers were combined. Acetone (25 mL) was added to completely dissolve the product, due to borderline solubility of the desired product in EtOAc, and the combined EtOAc and acetone layers were dried over anhydrous Na_2SO_4, filtered and evaporated under reduced pressure to afford crude **94** as a yellow residue. The product was used in the subsequent reaction step without further purification. LC-MS (ESI^+) m/z found $[M+H]^+ = 383.01$ at $R_t = 9.93$ mins. Synthesis of this molecule was previously unreported.

6.1.7.4 1-((2R,3R,4S,5R)-3,4-dihydroxy-5-(hydroxymethyl)tetrahydrofuran-2-yl)-1,4-dihydropyridine-3-carboxamide (NRH, 24)



Crude **94** (assuming quantitative yield ~800 mg, 2.10 mmols) was dissolved in 4 M ammonia in MeOH solution (17 mL) and stirred at 4 °C for 20 hours. Removal of solvent under reduced pressure afforded a yellow residue which was dissolved in H_2O (2 mL) and purified by automated reverse-phase column chromatography, eluting with MeCN and 25 mM $NH_4HCO_{3\,(aq)}$ over 25 CV at 12 mL/min using the following linear gradient: 2-5% MeCN (in 25 mM $NH_4HCO_{3\,(aq)}$) over 3 CV, 5-70% MeCN over 20 CV and 70% MeCN over 2 CV. The use of basic pH (>7) for the elution gradient was necessary to prevent the product from hydrating at position **4**, which occurs at pH <7. Removal of solvent under reduced pressure, followed by lyophilisation afforded **24** as a bright yellow powder (56 mg, 0.219 mmols, 5% over three reaction steps). ^1H NMR (400 MHz, DMSO) δ 6.98 (d, *J* = 1.3, 1H, 5), 6.67 (s, 2H, 1), 6.11 (dd, *J* = 8.3 and 1.8, 1H, 4), 4.73 – 4.65 (m, 1H, 3), 4.60 (d, *J* = 6.7, 1H, 6), 4.16 – 3.92 (m, 3H, 11-13), 3.92 – 3.86 (m, 1H, 7), 3.83 (dd, *J* = 5.4 and 2.6, 1H, 8), 3.70 – 3.64 (m, 1H, 9), 3.51 – 3.40 (m, 2H, 10), 2.95 (d, *J* = 3.4, 2H, 2); ^{13}C NMR (101 MHz, D_2O) δ 169.6, 136.3, 127.1, 102.9, 102.1, 95.7, 84.4, 71.7, 70.8, 62.3, 23.3; LC-MS (ESI^+) m/z found $[M+H]^+ =$ 257.13 at $R_t = 2.00$ mins. Analytical data consistent with that reported in literature.[205,206]

6.2 Biological Methods

6.2.1 Tissue Culture

HEK293T, MDA-MB-231 and COV318 (provided by Prof Hector Keun's lab at Imperial College London) cells were cultured in high glucose (4.5 g/L D-glucose, 4.0 mM L-glutamine, 1.0 mM sodium pyruvate) Dulbecco's Modified Eagle's Medium (DMEM) supplemented with 10% (v/v) Fetal Bovine Serum (FBS). MDA-MB-435 (provided by Prof Julian Downward's lab at the Francis Crick Institute) and T47D cells were cultured in high glucose (4.5 g/L D-glucose, 4.0 mM L-glutamine, 1.0 mM sodium pyruvate, 17.9 mM $NaHCO_3$, 10 mM HEPES) Roswell Park Memorial Institute (RPMI)-1640 medium at 37 °C in a humidified 5% CO_2 incubator. Mycoplasma testing was performed every four weeks and cells were regularly inspected under a microscope to ensure appropriate confluency before passaging, and to eliminate the presence of an infection. Cells were passaged up to 30 times (for proteomics experiments) or up to 40 times for IGF and WB experiments. Cell stocks at low passage number were created by freezing ~2×10^6 cells in FBS (1 mL) containing 10% (v/v) DMSO at -80 °C and storing them at -150 °C until required.

Cell passaging was performed by removing old cell media, washing cells with phosphate-buffered saline (PBS) solution once (5 mL) and dissociation of cells from culture flask by subsequent addition of trypsin-ethylenediaminetetraacetic acid (trypsin-EDTA, 0.25%, w/v) and incubation at 37 °C for 3 mins. Quenching of the trypsin was performed by addition of fresh media into the flask, cell counting was performed on a Countess™ II FL Automated Cell Counter (Invitrogen) and the appropriate number of cells were transferred to a new flask (for cell propagation) or seeded into an appropriate number of 96-well plates/6-well plates/6 cm dishes for subsequent cell experiments. Number of cells seeded per plate type and volume of lysis buffer used are shown in **Table 6.1**. For cell experiments, stocks of all compounds were made up in DMSO and left at -80 °C for at least 2 hours prior to cell treatment to ensure sterility of the DMSO stock.

Table 6.1. Volumes of appropriate media/buffer used for cell seeding, cell assays, cell washing and cell lysis.

Plate type	Number of cells seeded	Volume of media (seeding)	Volume of media (assay)	Volume of PBS (wash)	Volume of lysis buffer
6 cm dish	1×10^6	5 mL	3 mL	2 × 3 mL	400 µL
6-well plate	$4\text{-}6 \times 10^5$	2 mL	1 mL	2 × 2 mL	200 µL
96-well plate	1×10^4	100 µL	100 µL	-	-

Prior to cell lysis, media assay was aspirated and cells were washed with PBS twice (see **Table 6.1**). Cell lysis was performed by treating cells either with RIPA lysis buffer (25 mM Tris, 150 mM NaCl, 1% (v/v) Triton X100, 0.1% (w/v) SDS, 1% (w/v) sodium deoxycholate, protease inhibitor cocktail (1X, cOmplete), benzonase (50 units/mL of buffer, 10 mM olaparib, pH 7.6) or 4% (w/v) SDS lysis buffer (50 mM HEPES, 4% (w/v) SDS, 150 mM NaCl, protease inhibitor (1X), benzonase (50 units/mL of buffer), 10 mM olaparib) (see **Table 6.1**). Cells lysed with RIPA lysis buffer were incubated on ice for 30 mins and cells lysed with 4% (w/v) SDS lysis buffer were incubated at r.t. for 30 mins, unless otherwise stated. Lysates were scraped, transferred into Eppendorf tubes and cleared by centrifugation for 10 mins at 16 000 g. The supernatants for all samples (containing dissolved proteins) were then transferred into clean Eppendorf tubes. Protein precipitation was performed (as described in the next paragraph), unless otherwise stated, and protein concentrations were subsequently measured.

Protein precipitation was performed by the sequential addition of MeOH (4 vol), H_2O (2 vol) and chloroform $CHCl_3$ (1 vol), where vol represents the volume of the lysis buffer. Samples were then centrifuged at 4 °C (for lysates generated in RIPA lysis buffer) or at r.t. (for lysates generated in 4% (w/v) SDS lysis buffer) for 5 mins at 6000 g. The supernatant (containing the MeOH/ H_2O layer) was aspirated for each sample without disturbing the protein pellet (forming at the $CHCl_3$ – MeOH/H_2O interface) and discarded. MeOH (500 µL) was added to each protein pellet in $CHCl_3$, the samples were sonicated to break up the pellets and the proteins were pelleted by centrifugation at r.t. for 5 mins at 16 000 g. The supernatant was discarded, protein pellets were washed with MeOH (500 µL), sonicated until broken up and then centrifuged at 16 000 g. An additional washing with MeOH (500 µL) was performed once more and proteins were pelleted in the exact same manner. The resulting pellets were allowed to air

dry for 10 mins at r.t. and subsequently dissolved in 1% (w/v) SDS in PBS (pH 7.4). For samples from 6-well plates or 6 cm dishes, 40 µL or 100 µL, respectively, of 1% (w/v) SDS in PBS (pH 7.4) were added to each sample for dissolution of the protein pellets. The samples were then vortexed and sonicated for 5 – 10 mins to ensure complete dissolution of the proteins pellet into the buffer. Subsequently, each solution was diluted 5-fold to a 0.2% (w/v) SDS final concentration by the addition of 160 µL or 400 µL of PBS to 6-well plate or 6 cm dish samples, respectively.

Protein concentrations were estimated in triplicates using Bio-Rad DC Protein Assay kit and following the protocol supplied with the product. Absorbance measurements were performed at 750 nm on an EnVision 2104 plate reader. Bovine serum albumin (BSA) standard curve for known BSA concentrations was created and used for estimation of protein concentrations.

6.2.2 Biochemical Techniques

6.2.2.1 Click Reaction (CuAAC)

For a typical click reaction, a freshly prepared "click mix" must be assembled. This was done by mixing the following stock reagents in a ratio 2:2:1:1 (v/v/v/v) – tris(2-carboxyethyl)phosphine hydroxide (TCEP, 50 mM in H_2O), copper sulphate ($CuSO_4$, 50 mM in H_2O), tris(benzyltriazolylmethyl)amine (TBTA, 10 mM in DMSO) and AzT or AzTB or AzRB or YnT (depending on the experiment being performed, 10 mM in DMSO). In a typical click reaction, 6 µL of the "click mix" was added to every 100 µL of protein sample (at a 1 – 2 mg/mL protein concentration). Samples were then briefly vortexed and the click reaction was allowed to proceed for 1 – 3 hours at r.t. with shaking at 750 – 800 rpm. Quenching of the reaction was performed by the addition of 0.5 M EDTA $_{(aq)}$ stock to a final concentration of 5 mM, with shaking at r.t. for 2 mins. Protein precipitation was performed exactly as described in **Section 6.2.1**, where vol represents the volume of the sample click reaction. Proteins were initially dissolved in 1% (w/v) SDS in PBS to a concentration of 5 mg/mL and then diluted in PBS to a final protein concentration of 1 mg/mL. Samples were subsequently stored at -80 $^{\circ}$C until further use.

6.2.2.2 Gel Electrophoresis and In-Gel Fluorescence

Sodium dodecyl sulphate-polyacrylamide (SDS-PAGE) gels used for gel electrophoresis were prepared in-house by following the recipes in **Table 6.2**. For the relevant % gel, components were mixed in the order of appearance in the table (top to bottom). All SDS-PAGE gels were casted as 10- or 15-well gels.

Table 6.2. Recipes for the preparation of SDS-PAGE gels of different gradients.

Reagent type	10% Resolving gel	12% Resolving gel	4% Stacking gel
H_2O	4 mL	3.4 mL	3.05 mL
Resolving/Stacking buffer (National Diagnostics)	2.5 mL	2.5 mL	1.25 mL
Protogel 30% (National Diagnostics)	3.4 mL	4 mL	0.65 mL
N,N,N',N'-tetramethylethylenediamine	10 µL	10 µL	5 µL
Ammonium persulfate (10% (w/v) in H_2O)	100 µL	100 µL	25 µL

First, the appropriate resolving gel mixture was prepared. The gel was subsequently casted into glass plates (1.0 mm spacing) and allowed to solidify for 10 – 15 mins at r.t. Next, the stacking gel mixture was prepared. It was subsequently casted on top of the resolving gel (into the same glass plates, 1.0 mm spacing) and a 10 or 15-well comb was immediately inserted into the stacking gel portion. The gel was then allowed to solidify for 15 mins at r.t.

For IGF/WB analysis in a 10-well gel, typically 20 µg of protein in a final volume of 25 µL were loaded per lane. For IGF/WB analysis in a 15-well gel, typically 10 – 15 µg of protein in a final volume of 15 – 20 µL were loaded per lane. A molecular weight ladder (MWL), either Precision Plus Protein™ All Blue Prestained Protein Standards (Bio-Rad) or Precision Plus Protein Dual Color Standards (Bio-Rad), was included in at least one lane in all gels, and 2 – 3 µL of ladder were typically loaded.

Protein samples (excluding MWL) for gel electrophoresis were prepared by adding a loading buffer mixture, consisting of 4X (v/v) Laemmli loading buffer and 20% (v/v) β-mercaptoethanol, to protein samples in a ratio 3:1 (v/v) of protein sample:loading buffer mixture. Samples were then boiled by heating at 95 °C for 10 mins, allowed to cool down to

r.t. and briefly centrifuged. Subsequently, samples were loaded on a gel and running buffer (25 mM Tris (base), 192 mM glycine, 0.1% (w/v) SDS) was added until the gel was entirely submerged in the running buffer. Finally, the gel was run at 90 V for 10 mins and then at 150 V for 50 mins – 1 hour. Running of the gel was performed on a PowerPac^{TM} Basic Power Supply (Bio-Rad) equipped with a Mini-PROTEAN Tetra Cell (Bio-Rad).

For in-gel fluorescence, following a successful run the gel was briefly rinsed with H_2O and subsequently imaged for TAMRA fluorescence (λ_{abs} = 532 nm; λ_{em} = 583 nm) on a Typhoon^{TM} FLA 9500 imager (GE Healthcare). The gel was then either stained by InstantBlue Coomassie Protein Stain (Abcam) or Coomassie Brilliant Blue (Sigma-Aldrich), to check for protein loading, or used for western blotting as described in the next section. Gels that were stained were imaged by trans-illumination on an ImageQuant LAS 4000 (Fujifilm) instrument and MWL was imaged by detecting for Cy5 (λ_{abs} = 635 nm; λ_{em} = 670 nm) fluorescence. Unless otherwise stated, all MWL values were shown in kDa units.

6.2.2.3 Western Blotting

SDS-PAGE gels that were run (and not Coomassie stained) were transferred onto a nitrocellulose membrane. This was performed in a wet transfer buffer (25 mM Tris (base), 192 mM glycine, 20% (v/v) MeOH) for 1 hour at 100 V on a PowerPac^{TM} Basic Power Supply (Bio-Rad) equipped with a Mini-PROTEAN Tetra Cell (Bio-Rad). To check for protein loading and confirm that the wet transfer was successful, the membrane was stained by Ponceau S stain (Sigma-Aldrich) for 5 mins at r.t. The membrane was then rinsed with H_2O, images were taken (by phone) and the membrane was blocked in 5% (w/v) BSA in TBS-T (1X Tris-buffered saline, 0.1% (v/v) Tween-20) buffer (blocking buffer) for 1 hour at r.t. with mild shaking. After 1 hour, the membrane was quickly washed once with blocking buffer and incubated with primary antibody (appropriate dilution (v/v) of antibody stock in blocking buffer, see **Table 6.3**) for 16 – 20 hours at 4 $^{\circ}$C. Following incubation, the membrane was washed with TBS-T three times (5 mins each). The membrane was then either incubated with a secondary antibody (appropriate dilution (v/v) of antibody stock in blocking buffer, see **Table 6.3**) for 1 hour at r.t. (for non-HRP-linked primary antibodies), or directly imaged (for HRP-linked primary antibodies). After incubation with a secondary antibody the membrane was washed with TBS-T three times (5 mins each) and then imaged. Imaging was performed by chemiluminescence following addition of Immobilon Crescendo Western HRP onto the entire surface of the membrane on an ImageQuant LAS 4000 (Fujifilm) instrument. MWL was imaged by detecting

for Cy5 (λ_{abs} = 635 nm; λ_{em} = 670 nm) fluorescence. Unless otherwise stated, all MWL values were shown in kDa units.

Table 6.3. Types of antibodies and reagents used for western blotting applications. The appropriate dilution in TBS-T blocking buffer (v/v) and commercial supplier for each antibody is included.

Antibody	Supplier	Dilution (v/v)
α-Poly/Mono-ADP ribose (anti-MAR/PAR antibody)	Cell Signalling Technology	1:1000
Anti-pan-ADP-ribose binding reagent	Sigma-Aldrich	1:1000
α-PARP1	Santa Cruz Biotechnology	1:1000
α-PARP1	Cell Signalling Technology	1:1000
α-NMNAT1	Santa Cruz Biotechnology	1:500
α-SLC12A8	Aviva Systems Biology	1:1000
α-AMPylated tyrosine	Sigma-Aldrich	1:1000
Neutravidin-HRP (α-biotin)	Invitrogen	1:1000
α-biotin-HRP	Cell Signalling Technology	1:1000
α-β-actin	Sigma-Aldrich	1:5000 – 1:10 000
α-mouse-HRP	Advansta	1:10 000
α-rabbit-HRP	Advansta	1:10 000

6.2.2.4 Protein Pull-down (Protein Enrichment*)*

For western blotting, protein pull-down was typically performed by incubating 200 µg (200 µL) of protein sample (0.2% (w/v) SDS in PBS pH 7.4, 1 mg/ml) with 20 µL streptavidin magnetic beads (Thermo Scientific Pierce^{TM}) for 3 hours at r.t., with shaking (750 – 800 rpm). Prior to pull-down incubation, the streptavidin magnetic beads were washed three times with 0.2% (w/v) SDS in PBS. Following pull-down incubation, the bead samples were placed on a magnetic rack, supernatants were transferred into clean Eppendorf tubes (the supernatants were

then stored at -80 °C) and the bead samples were washed three times with 0.2% (w/v) SDS in PBS (500 µL each). The washings were discarded and the enriched proteins were eluted from the beads by adding 15 µL of 2X Laemmli loading buffer and 10% (v/v) β-mercaptoethanol mixture to each bead sample and subsequent boiling by heating at 95 °C for 10 mins. Samples were allowed to cool down to r.t., briefly centrifuged and directly loaded on an SDS-PAGE gel for subsequent western blot analysis.

For proteomics analysis, protein pull-down was typically performed by incubating 500 – 1000 µg (500 – 1000 µL) of protein sample (0.2% (w/v) SDS in PBS pH 7.4, 1 mg/ml) with 50 – 100 µL Neutravidin agarose beads (Thermo Scientific Pierce™) for 3 hours at r.t., with shaking (750 – 800 rpm). Prior to the pull-down incubation, the Neutravidin agarose beads were washed five times with 0.2% (w/v) SDS in PBS, pelleted by centrifugation (3500 g for 2 mins) and supernatant aspirated by pipetting. Beads were suspended to their original volume and appropriate volume of beads added to each sample. Following the incubation, the bead samples were pelleted by centrifugation (3500 g for 3 mins), supernatants aspirated, samples washed with 0.2% (w/v) SDS in 50 mM HEPES (pH 8.0) four times (1 mL each) and then washed three more times with 50 mM HEPES (pH 8.0). Peptides were then eluted from enriched proteins bound to the beads by trypsin digestion (see **Section 6.3.1.2**).

6.2.3 Molecular Cloning

6.2.3.1 General Methods

All equipment and workspace was sterilised by spraying with 70% (v/v) EtOH prior to carrying out bacterial work, or autoclaving at 115 °C for at least 15 mins where appropriate. Cell growth media were also sterilised by autoclaving at 115 °C for at least 15 mins. Lysogeny broth (LB) growth medium (Merck) was prepared by dissolving 37.0 g of LB powder in 1L distilled H_2O and was subsequently autoclaved. LB agar (Merck) for bacterial plate preparation was prepared by dissolving 25.0 g of LB agar powder in 1 L of distilled H_2O and was also autoclaved. Stocks of antibiotics were prepared as 1000X stocks in distilled H_2O (100 mg/mL ampicillin and 50 mg/mL kanamycin) and diluted to 1X in LB growth medium or LB agar, as required. Antibiotic stocks were stored at -20 °C until further use. LB agar plates were prepared by pouring ~15 – 20 mL of molten LB agar containing 1X antibiotic into a sterile 10 cm plate and letting it solidify at r.t. for 10 mins. NMNAT1 plasmid was obtained from Addgene as a bacterial stab. 3xFLAG-PARP1 plasmid was provided by Prof Hector Keun's lab as a purified stock in H_2O. Plasmid sequencing (Sanger sequencing) was carried out by GENEWIZ and

plasmid concentration measurements were performed on a NanoDrop™ One^{c} (Thermo Scientific).

6.2.3.2 Bacterial Selection, Plasmid Production and Harvesting

Individual colony selection for plasmids in a bacterial stab or following transformation was performed by spreading the corresponding bacterial stab/transformed bacteria onto an LB agar plate containing the appropriate antibiotic. Plates were incubated at 37 °C in a humidified incubator for 24 – 48 hours. Individual colonies were picked and grown in 5 mL or 200 mL of LB medium in separate 12 mL sterile round-bottom Falcon tubes or 1 L autoclaved conical flasks, respectively, at 37 °C for 16 – 18 hours. Following overnight incubation, cells were pelleted by centrifugation at 4 °C for 10 mins at 350 g and media discarded. Plasmids were extracted and purified using Qiagen's QIAprep Spin Miniprep Kit (for 5 mL cultures) or Qiagen's HiSpeed Plasmid Maxi Kit (for 200 mL cultures) following the manufacturer's protocol. DNA concentrations were then measured and plasmids were submitted (600 ng per plasmid) for Sanger sequencing.

6.2.3.3 Polymerase Chain Reaction (PCR) Amplification and Primer Design

PCR reactions were performed on a SureCycler 8800 (Agilent) using Q5 High-Fidelity DNA Polymerase (New England Biolabs) by assembling a PCR reaction mixture using the volumes and thermocycling conditions used in **Table 6.4** and **Table 6.5**, respectively.

Table 6.4. Summary of the reagents and the corresponding amounts used in PCR amplification reactions.

Reagent	Volume	Final reagent concentration
5X Q5 Reaction buffer	10 µL	1X
Nuclease-free H_2O	32.5 µL	-
10 mM dNTPs	1 µL	200 µM
Template DNA	1 µL (1 ng DNA)	1 ng
10 µM Forward primer	2.5 µL	0.5 µM
10 µM Reverse primer	2.5 µL	0.5 µM

Q5 HiFi DNA polymerase	0.5 µL	0.2 U/µL

Table 6.5. Summary of the thermocycling conditions used for PCR amplification reactions.

Step	Temperature	Duration
Denaturation	98 °C	30 s
30 cycles	98 °C	10 s
	*50 – 72 °C (Ta)	**30 s/kb
	72 °C	30 s
Elongation (final)	72 °C	2 mins
Storage	4 °C	-

*Annealing temperature (Ta) depends on the length of the primers used in the reaction. **30 seconds is the required duration for annealing per 1000 base pairs of fragment length per one cycle.

PCR primers were generated using the following tools:

https://nebuilder.neb.com/#!/ - Used to generate sequence alignment primers, with overhang (non-aligning) sequences, for extracting specific (complementary) sequence fragments from plasmids. Overhang sequences were used for recombination of fragments via Gibson Assembly. Aligning (annealing) sequences (highlighted in red and orange, see **Tables 6.6, 6.7** and **6.12**) for all primers were at least 20 nucleotides long to ensure good binding to the complementary plasmid sequence.

https://tmcalculator.neb.com/#!/main - Used to check the annealing temperature for the highlighted aligning (annealing) sequences for primers. To ensure good binding to the complementary plasmid sequence, annealing temperatures must be in the range 60 – 72 °C.

http://www.bioinformatics.org/sms2/pcr_primer_stats.html - Used to check for additional properties, listed below, of the aligning (annealing) sequences of the primers. Generally, an

annealing sequence possessing one or more of the following properties increases the risk of the amplification PCR reaction failing (e.g., hairpins and self-annealing bases can lead to a primer forming a secondary structure instead of aligning with a complementary sequence). If possible, the three properties listed below should be avoided in an annealing sequence:

1. Possessing >3 G and C bases in the last 5 bases of the annealing sequence
2. Possessing >3 self-annealing bases in a row, particularly towards the end of the annealing sequence
3. Possessing >3 hairpin bases in a row, particularly towards the end of the sequence

6.2.3.3.1 Primer Sequences and Thermocycling Conditions for Generating CMV N-FLAG-NMNAT1 Plasmid

In this section, the forward and reverse primer sequences and thermocycling conditions used for the generation of a CMV N-FLAG-NMNAT1 plasmid, where a FLAG tag is incorporated on the N-terminus of NMNAT1, are described.

Table 6.6. Forward primer and reverse primer sequences for retroviral NMNAT1 and CMV FLAG plasmids. These primers were used in subsequent PCR amplification reactions for generating a CMV N-FLAGNMNAT1 plasmid. Annealing sequences for retroviral NMNAT1 plasmid (in red) and CMV FLAG plasmid (in orange) are highlighted.

Primer type	Primer sequence
NMNAT1 Forward	5'-TGACGACAAGgaaaattccgagaagactgaag-3'
NMNAT1 Reverse	5'-cGAATTCTCAtgtcttagcttctgcagtg-3'
CMV FLAG Plasmid Forward	5'-agctaagacaTGAGAATTCGACTCTAGAGGATC-3'
CMV FLAG Plasmid Reverse	5'-cggaattttcCTTGTCGTCATCGTCTTTGTAGTC-3'

NMNAT1 sequence fragment was extracted from the pMXs_FLAG-NMNAT1 plasmid template (Addgene) by incubating the plasmid template with the two NMNAT1 primers (see **Table 6.6**) in a PCR reaction. Ta for the reaction was set to 63 °C. Duration of annealing was set to 25 s per one cycle (NMNAT1 fragment length = 837 base pairs).

CMV FLAG plasmid template was incubated with the two CMV FLAG plasmid primers (see **Table 6.6**) in a PCR reaction. Ta for the reaction was set to 64 °C. Duration of annealing was set to 186 s per one cycle (CMV Flag plasmid length = 6.2 kb).

6.2.3.3.2 Primer Sequences and Thermocycling Conditions for Generating CMV NMNAT1 Plasmid

In this section, the forward and reverse primer sequences and thermocycling conditions used for the generation of a CMV NMNAT1 plasmid are described.

Table 6.7. Forward primer and reverse primer sequences for retroviral NMNAT1 and CMV plasmids. These primers were used in subsequent PCR amplification reactions for generating a CMV NMNAT1 plasmid. Annealing sequences for retroviral NMNAT1 plasmid (in red) and CMV plasmid (in orange) are highlighted

Primer type	Primer sequence
NMNAT1 Forward	5'-ATCTACcatggaaaattccgagaagactgaag-3'
NMNAT1 Reverse	5'-CGAATTCTCatgtcttagcttctgcagtg-3'
CMV Plasmid Forward	5'-agctaagacaTGAGAATTCGACTCTAGAGGATC-3'
CMV Plasmid Reverse	5'-cggaattttcCATGGTAGATCGATCTGAATTAATTC-3'

NMNAT1 sequence fragment was extracted from the pMXs_FLAG-NMNAT1 plasmid template (Addgene) by incubating the plasmid template with the two NMNAT1 primers (see **Table 6.7**) in a PCR reaction. Ta for the reaction was set to 63 °C. Duration of annealing was set to 25 s per one cycle (NMNAT1 fragment length = 837 base pairs).

CMV plasmid template was incubated with the two CMV plasmid primers (see **Table 6.7**) in a PCR reaction. Ta for the reaction was set to 64 °C. Duration of annealing was set to 186 s per one cycle (CMV plasmid length = 6.2 kb).

6.2.3.4 DNA Gel Electrophoresis

To ensure that PCR amplification reactions were successful (see **Sections 6.2.3.3.1** and **6.2.3.3.2**), each PCR product was loaded on a DNA gel and analysed by gel electrophoresis in the following manner:

DNA gel preparation: agarose (600 mg) was dissolved in 60 mL of 1X Tris-acetate-EDTA (TAE) buffer (prepared from a 50X commercial stock diluted in MilliQ H_2O, Sigma-Aldrich). The mixture was heated in a microwave initially for 30 s followed by heating for another 15 s, and then gently swirled to ensure no solid agarose was seen. The agarose solution was allowed to cool down for 2 – 3 mins and was then casted into an electrophoresis chamber (SERVA). A 20-well comb was inserted, the gel was allowed to solidify for 20 mins and 1X TAE buffer was added to cover the entire gel.

Sample preparation: 2 µL of a PCR product were mixed with 6X loading dye (2 µL, New England Biolabs) and autoclaved nuclease-free H_2O (8 µL) were added.

Sample loading, analysis and imaging: 1 kb DNA ladder (3 µL, (500 bp – 10 kb range, New England Biolabs) were added to at least one well on the gel. 8 µL of each sample were loaded in separate wells and the gel was run at 100 V for 50 mins – 1 hour on a PowerPac^{TM} Basic Power Supply (Bio-Rad). The gel was transferred to a plastic container and stained with 3X GelRed Nucleic Acid Stain (Biotum) for 15 mins at r.t. with mild shaking. After 15 mins, the gel was imaged for ethidium bromide (EtBr) fluorescence (λ_{abs} = 532 nm; λ_{em} = 605 nm) on a Typhoon^{TM} FLA 9500 imager (GE Healthcare).

6.2.3.5 PCR Product Purification, Gibson Assembly and Plasmid Transformation

6.2.3.5.1 PCR Product Purification Protocol

To ensure the initial DNA templates were removed from the PCR products prior to Gibson Assembly, DNA template digestion was performed with DpnI enzyme. This was performed by incubating 43 µL of each PCR product with 10X Cutsmart^{R} Buffer (5 µL, New England Biolabs) and DpnI enzyme (2 µL, 40 units, New England Biolabs) at 37 $^{\circ}$C for 2 hours. After the incubation, DpnI was inactivated by heating at 80 $^{\circ}$C for 20 mins. The samples were subsequently purified using the QIAquick PCR Purification Kit (QIAGEN) and fragment DNA concentrations (**Table 6.8**) were measured on a NanoDrop^{TM} One^{c} (Thermo Scientific).

Table 6.8. Measured concentrations of NMNAT1 fragments, non-ligated CMV plasmid and non-ligated CMV FLAG plasmid after PCR amplification. The fragments were subsequently used in Gibson Assembly.

Fragment	Concentration
NMNAT1 (for CMV Plasmid)	77.5 ng/µL
NMNAT1 (for CMV FLAG Plasmid)	69.8 ng/µL
CMV Plasmid	33.3 ng/µL
CMV FLAG Plasmid	55.6 ng/µL

6.2.3.5.2 Gibson Assembly Protocol

Each pair of purified PCR fragments, insert + plasmid, was assembled into a single plasmid vector via Gibson Assembly. 100 ng of vector backbone, CMV plasmid or CMV FLAG plasmid, were used for Gibson Assembly. Amounts of NMNAT1 insert fragments used for the assembly (27 ng) were based on the use of 100 ng of vector backbone and were calculated using the online tool available at https://nebiocalculator.neb.com/#!/ligation. The exact amounts of all reagents used are summarised in **Table 6.9**. Gibson Assembly was performed by incubating the appropriate fragments at 50 °C for 1 hour and the product mixtures were stored at -20 °C until transformation.

Table 6.9. Summary of the reagents and the corresponding amounts used in Gibson Assembly.

Vector:insert molar ratio	1:2
Amounts (NMNAT1:CMV plasmid)	0.348 µL:3.00 µL (27 ng:100 ng)
Amounts (NMNAT1:CMV FLAG plasmid)	0.387 µL: 1.80 µL (27 ng:100 ng)
NEBilder HiFi DNA Assembly Master Mix	10 µL
H_2O	Make up to 20 µL final volume
Final Volume	20 µL

6.2.3.5.3 Plasmid Transformation Protocol

Transformation was performed with either High Efficiency NEB 5-α Competent *E. coli* C2987H cells (for Gibson Assembly products) or Subcloning Efficiency NEB 5-α Competent *E. Coli* C2988 cells (for general scale-up plasmid production for Mini/MaxiPrep purifications). For a typical transformation of a Gibson Assembly reaction, 2 µL of a Gibson Assembly product were added to 20 µL suspension of C2987H cells and gently mixed by slowly pipetting up and down 4 – 5 times. The mixture was incubated on ice for 30 mins and was then placed in a water bath at 42 °C for exactly 30 s. The sample was placed on ice for 2 mins and room temperature Stable Outgrowth (SOC) medium (400 µL, New England Biolabs) was then added. Incubation of the mixture was performed at 37 °C for 1 hour with shaking at 400 rpm and after the incubation 200 µL of the suspension were added dropwise to a pre-heated (to 37 °C) LB agar plate containing the appropriate antibiotic. The cells were spread onto the plates using a bacterial spreader and incubated for 20 – 24 hours at 37 °C in a humidified incubator.

For a transformation using a purified plasmid (instead of a Gibson Assembly product) the same protocol was followed as described, with the only exception that 1 ng (1 µL from a 1 ng/µL stock) of pure plasmid material was mixed with C2988 cells (instead of 2 µL of a Gibson Assembly product).

6.2.3.6 FLAG-NMNAT1 and 3x-FLAG-PARP1 Plasmid Mutagenesis

Introduction of point mutations into CMV FLAG-NMNAT1 and CMV 3x-FLAG-PARP1 plasmids was performed using the Q5 Site-Directed Mutagenesis Kit (New England Biolabs), in accordance with their recommended protocol. PCR amplification was used as the method for introduction of the point mutations, with the appropriate reagents and amounts, and thermocycling conditions used summarised in **Table 6.10** and **Table 6.11**, respectively. The alignment (annealing) primers containing the desired point mutations (**Tables 6.12** and **6.13**) were generated using the online tool available at https://nebasechanger.neb.com/.

Table 6.10. Summary of the reagents and the corresponding amounts used for plasmid mutagenesis by PCR amplification.

Reagent	Volume	Final reagent concentration
Q5 Hot Start HiFi 2X Master Mix	12.5 µL	1X
Nuclease-free H_2O	6.0 µL	-
Template DNA	(1 ng DNA)	1 ng
10 µM Forward primer	1.25 µL	0.5 µM
10 µM Reverse primer	1.25 µL	0.5 µM

Table 6.11. Summary of the thermocycling conditions used for plasmid mutagenesis PCR amplification reactions.

Step	Temperature	Duration
Denaturation	98 °C	30 s
30 cycles	98 °C	10 s
	*50 – 72 °C (Ta)	**30 s/kb
	72 °C	30 s
Elongation (final)	72 °C	2 mins
Storage	4 °C	-

*Annealing temperature (Ta) depends on the length of the primers used in the reaction. **30 seconds is the required duration for annealing per 1000 base pairs of fragment length per one cycle.

Table 6.12. Forward primer and reverse primer sequences for retroviral NMNAT1 and CMV FLAG plasmids. These corresponding ligated CMV N-FLAG-NMNAT1 plasmids were used in subsequent mutagenesis PCR

amplification reactions for generating point mutant CMV N-FLAG-NMNAT1 plasmids. Annealing sequences for retroviral NMNAT1 plasmid (in red) and CMV FLAG plasmid (in orange) are highlighted

Primer type	Primer sequence
NMNAT1 Forward	5'-TGACGACAAGgaaaattccgagaagactgaag-3'
NMNAT1 Reverse	5'-cGAATTCTCAtgtcttagcttctgcagtg-3'
CMV FLAG Plasmid Forward	5'-agctaagacaTGAGAATTCGACTCTAGAGGATC-3'
CMV FLAG Plasmid Reverse	5'-cggaattttcCTTGTCGTCATCGTCTTTGTAGTC-3'

Table 6.13. Forward primer and reverse primer sequences possessing the relevant point mutation 3-base long sequence (highlighted in red). The sequences are complementary for ligated CMV N-FLAG-NMNAT1 plasmids. These primers were used in subsequent mutagenesis PCR amplification reactions for generating point mutant CMV N-FLAG-NMNAT1 plasmids.

Plasmid mutant	Primer type	Primer Sequence
CMV FLAG NMNAT1 V186G	Forward	5'-GCTCATATGTggcACTCGGGCTG-3'
	Reverse	5'-CCATAGTTGGCCACGATT-3'
CMV FLAG NMNAT1 S222G	Forward	5'-TAATGACATCggcTCCACAAAAATCCGGAG-3'
	Reverse	5'-GCGATCCATTCATTCACC-3'
CMV FLAG NMNAT1 H24G	Forward	5'-CACCAACATGggcCTCAGGTTGTTTG-3'
	Reverse	5'-ATGGGATTGAATGAACCAC-3'
CMV 3x-FLAG PARP1 L877A	Forward	5'-GTCCCAGGGTgcgCGGATAGCCC-3'
	Reverse	5'-AGGATCCCAGCAAAGTTG-3'

CMV N-FLAG-NMNAT1 point mutant plasmids (V186G, S222G, H24G) were generated by incubating CMV N-FLAG-NMNAT1 plasmid with the appropriate forward and reverse point mutant primers (**Table 6.13**) and with the reagents summarised in **Table 6.10**. The thermocycling conditions for each plasmid point mutant are summarised below:

CMV FLAG NMNAT1 V186G: Ta = 63 °C. Duration of annealing was set to 212 s per one cycle (plasmid length = 7.07 kb).

CMV FLAG NMNAT1 S222G: Ta = 58 °C. Duration of annealing was set to 212 s per one cycle (plasmid length = 7.07 kb).

CMV FLAG NMNAT1 H24G: Ta = 60 °C. Duration of annealing was set to 212 s per one cycle (plasmid length = 7.07 kb).

CMV 3x-FLAG-PARP1 L877A point mutant plasmids was generated by incubating CMV 3x-FLAG-PARP1 plasmid (provided by the Keun Lab, Imperial College) with the appropriate forward and reverse point mutant primers (**Table 6.13**) and with the reagents summarised in **Table 6.10**. The thermocycling conditions for generating the plasmid point mutant are summarised below:

CMV 3x-FLAG PARP1 L877A: Ta = 63 °C. Duration of annealing was set to 214 s per one cycle (plasmid length = 7.15 kb).

To ensure that PCR amplification had successfully worked, the products of all reactions were loaded on a DNA gel and analysed by gel electrophoresis (see **Section 6.2.3.4**).

6.2.3.7 NMNAT1 Overexpression via Transfection of HEK239T Cells

NMNAT1/FLAG-NMNAT1 overexpression was induced by transfection of HEK293T cells with CMV NMNAT1/FLAG-NMNAT1 plasmids. This was performed using Lipofectamine 2000 (Invitrogen) and in accordance with the manufacturer's protocol. Reagents and amounts used for transfection are summarised in **Table 6.14.**

Table 6.14. Volumes/amounts of reagents used for transfection of HEK293T cells in the appropriate volume of seeding media.

Plate type	Seeding media volume	Opti-MEM media volume	Plasmid DNA amount	Lipofectamine 2000 volume
6-well plate	2 mL	2 × 125 µL	2000 ng	5 µL
6 cm dish	5 mL	2 × 250 µL	5000 ng	10 µL

For a typical transfection experiment, HEK293T cells were cultured in DMEM media supplemented with 10% (v/v) FBS in 6-well plates or 6 cm dishes, respectively, until ~90% confluency was reached. The appropriate volume of Lipofectamine 2000 was added to 125 µL or 250 µL of Opti-MEM (GIBCO), mixed gently by pipetting and incubated at r.t. for 5 mins. The appropriate amount of plasmid DNA was added to 125 µL or 250 µL of Opti-MEM (GIBCO) and mixed by pipetting. The plasmid DNA and Lipofectamine mixtures were subsequently combined, mixed gently by pipetting and incubated at r.t. for 20 mins. Following incubation, 250 µL (per well for 6-well plates) or 500 µL (per 6 cm dish) of the combined mixture were added dropwise to cells and incubated for 24 hours. Expression of NMNAT1/FLAG-NMNAT1 was confirmed by western blotting (see **Section 6.2.2.3**).

6.2.4 Recombinant NMNAT1 *in vitro* Assay

A comparison of the catalytic turnover of 6Yn-NAD^+ analogue with wild-type human NMNAT1 relative to endogenous NAD^+ was performed using commercially available recombinant NMNAT1 (R&D Systems). The assay was performed in accordance with the manufacturer's protocol. Reagents and amounts used in the assay are summarised in **Table 6.15**.

Table 6.15. Summary of the reagents and the corresponding amounts used for recombinant NMNAT1 *in vitro* assays.

Reagent	Volume
NMNAT1 (0.5 ng/µL)	50 µL
β-NMN (50 mM)	2 µL
ATP (10 mM)	20 µL
6Yn-ATP (10 mM)	20 µL
Yeast alcohol dehydrogenase (ADH, 5 mg/ml, 25 mM MES, 20% (v/v) glycerol, pH 6.5)	1 µL
Magnesium chloride (1 M)	1.5 µL
100% Ethanol	1 µL
Assay buffer (50 mM HEPES, pH 7.5)	24.5 µL

NAD^+	50 µL

Briefly, NMNAT1 was diluted in assay buffer (50 mM HEPES, pH 7.5) to a stock concentration of 0.5 ng/µL. A separate substrate mixture of 50 µL final volume was prepared by mixing β-NMN (2 µL), ATP **or** 6Yn-ATP (20 µL), ADH (1 µL), $MgCl_2$ (1.5 µL), 100% EtOH (1 µL) and assay buffer (24.5 µL) at the indicated concentrations and volumes. In a 96-well plate, the diluted NMNAT1 stock (50 µL, 0.5 ng/µL) or assay buffer (negative control, 50 µL) and substrate mixture (50 µL) were mixed to initiate the reaction. To confirm ADH enzyme activity, a separate substrate mixture was assembled where β-NMN (50 mM) was replaced by NAD^+ (positive control, 50 mM) and used for the reaction. The assay was performed on an EnVision 2104 plate reader and individual reactions followed for 1 hour with absorbance readings at 340 nm (NADH λ_{em} = 340 nm) recorded every 10 s.

6.2.5 Metabolic Incorporation of Adenosine/ProTide Analogues in Cell Lines

6.2.5.1 General Methods

A summary of the reagents used in metabolic labelling experiments is shown in **Table 6.16**. Stock solutions were prepared by dissolving all reagents in DMSO at the appropriate stock concentration and subsequently used in cell experiments at the appropriate final concentration. All DMSO stock solutions were stored at -20 or -80 °C.

Table 6.16. List of stock compounds and amounts used in cell culture experiments.

Reagent	Stock concentration	Volume of stock	Final concentration
DMSO	-	1 – 3 µL	0.1% (v/v)
6Yn-Pro (**47**)	100 mM	1 – 3 µL	100 µM
2Yn-Pro (**48**)	100 mM	1 – 3 µL	100 µM
8But-Yn-Pro (**49**)	100 mM	1 – 3 µL	100 µM
6Az-Pro (**50**)	100 mM	1 – 3 µL	100 µM
^{15}N-Pro (**64**)	100 mM	1 – 3 µL	100 µM
6Yn-Ad (**25**)	500 mM	1 – 3 µL	500 µM

2Yn-Ad (**26**)	500 mM	1 – 3 µL	500 µM
NR (**23**)	500 mM	1 – 3 µL	500 µM
NRH (**24**)	500 mM	1 – 3 µL	500 µM
β-NMN	500 mM	1 – 3 µL	500 µM
Olaparib	10 mM	1 – 3 µL	10 µM
PARGi	10 mM	1 – 3 µL	10 µM
FK866	5 mM	1 – 3 µL	5 nM
H_2O_2 (in PBS)	2 M	1 – 3 µL	2 mM

Seeding of cells was performed as described in **Section 6.2.1** (see **Table 6.1**). Metabolic labelling was performed at 37 °C in a humidified 5% CO_2 incubator, typically for 24 hours, unless otherwise stated. For experiments requiring pre-treatment with FK866 or olaparib, incubation was performed for 24 hours (FK866) or 2 hours (olaparib), prior to addition of NR/NRH/β-NMN and/or addition of the relevant adenosine/ProTide analogue probe. For co-treatments with NR/NRH/β-NMN and adenosine/ProTide probes, NRH/NR/β-NMN was added to all the appropriate samples first and the relevant adenosine/ProTide probes were added to all the appropriate samples subsequently. Where indicated, PARGi was added as a co-treatment along the relevant probe. For experiments where oxidative stress was induced *via* addition of H_2O_2, unless otherwise stated, treatment was typically performed for 6 mins at 2 mM final concentration in sterile PBS (pH 7.4) at 37 °C.

6.2.5.2 Cytotoxicity Assay in MDA-MB-231 Cells

MDA-MB-231 cells were seeded at a concentration of 10 000 cells in 100 µL DMEM media per well in a 96-well plate. After 24 hours, Sytox green (0.5 µL, 50 µM) was added to each well, and 0.1% (v/v) DMSO (1 µL, 10% (v/v) DMSO stock in DMEM media) or stock compound, 6Yn-Ad (**25**) or 2Yn-Ad (**26**) (1 µL, 500 mM or 50 mM or 5 mM), were added to the appropriate wells. The assay was performed for 24 hours in a dose-dependent manner for stock compounds in triplicate per condition (see **Table 6.17** for an overview of all experimental conditions and final concentrations). Incubation and imaging of the plate was performed for cell confluence (phase setting) and Sytox green fluorescence (λ_{abs} = 450 – 490 nm; λ_{em} =

523 nm) on an IncuCyte S3 Live Cell Analysis System (Sartorius, 37 °C, 5% CO_2, humidified) every 1 hour for 24 hours at a 10× magnification factor. Cytotoxicity data is shown in **Appendix Figure A.10**.

Image analysis was performed in IncuCyte Software v2019B. For phase (confluency) image analyses, a minimum area threshold was set to 100 μm^2 and all other parameters were set to default. For green fluorescence image analyses, a 2 CGU unit threshold was set for Top-Hat segmentation and all other parameters were set to default. Extent of cytotoxicity in each well at each 1 hour time point was measured based on the ratio of 'Total Green Area:Total Phase Area' for each time point normalised to 'Total Green Area:Total Phase Area' for the 0 hours time point, which represented the start of the experiment. Higher 'Total Green Area:Total Phase Area' represented increased green fluorescence from Sytox Green binding to DNA of dead cells, which was indicative of cytotoxicity induced by the compound(s) tested. Cytotoxicity data is shown in **Appendix Figure A.10**.

Table 6.17. Summary of experimental set-up and reagents used in IncuCyte cell viability assays.

	1	2	3	4	5	6	7	8	9
A	DMSO 0.1% Sytox Green 250 nM								
B	6Yn-Ad 500 µM Sytox Green 250 nM			6Yn-Ad 50 µM Sytox Green 250 nM			6Yn-Ad 5 µM Sytox Green 250 nM		
C	2Yn-Ad 500 µM Sytox Green 250 nM			2Yn-Ad 50 µM Sytox Green 250 nM			2Yn-Ad 5 µM Sytox Green 250 nM		

6.2.5.3 RNA Sample Processing – Extraction, Click Reaction and Analysis by RNA Gel Electrophoresis

Metabolic labelling and RNA extraction: HEK293T cells (500 000 cells per well) were seeded into a 6-well plate for 19 hours. Media was then replaced with fresh media (1 mL per well) and metabolic labelling was performed for 24 hours (see **Table 6.18** for reagents summary). RNA extraction was performed using an RNeasy Mini Kit (Part 1, QIAGEN) in accordance with the manufacturer's protocol and RNA concentrations were measured on a NanoDrop™ One^c (Thermo Scientific).

Table 6.18. Summary of the reagents and the corresponding amounts used in cell culture RNA labelling experiments.

Reagent	Stock concentration	Volume of stock	Final concentration
DMSO	-	1 µL	0.1% (v/v)
6Yn-Pro (**47**)	100 mM	1 µL	100 µM
2Yn-Pro (**48**)	100 mM	1 µL	100 µM
8But-Yn-Pro (**49**)	100 mM	1 µL	100 µM
6Yn-Ad (**25**)	500 mM	1 µL	500 µM

Click reaction of metabolically labelled RNA: 3 µg of each RNA sample were separately dissolved in RNase-free H_2O (20 µL final volume). Click reaction was performed by adding "click mix" (1.2 µL, assembled as described in **Section 6.2.2.1**) to each one, mixing by gentle pipetting and incubating at r.t. for 1 hour **without** any shaking. To ensure proper mixing throughout the incubation period, gentle pipetting of each sample was carried out every 20 mins. To quench the reaction, each RNA sample was precipitated after 1 hour reaction time. This was performed by adding NH_4OAc (10 M, 20 µL), followed by the addition of 100% EtOH (360 µL) to each sample, mixing by gentle pipetting and incubation of the samples at -20 °C for 5 mins. RNA samples were pelleted by centrifugation (13 000 g, 4 °C, 15 mins) and supernatants were aspirated. Washing of the samples was performed with 70% (v/v) EtOH in RNase-free H_2O (200 µL) and RNA samples were pelleted again by centrifugation (13 000 g, 4 °C, 3 mins). Supernatants were aspirated, pelleted RNA samples were air dried for 15 mins and stored at -80 °C until further use. Analysis of extracted RNA samples was performed by RNA gel electrophoresis as described below.

RNA gel preparation: This step must be performed in a fume hood. Agarose (1 g) was dissolved in MilliQ H_2O (85 mL). The mixture was heated in a microwave initially for 30 s followed by heating for another 30 s, and then gently swirled to ensure complete dissolution of agarose. 10X MOPS buffer (12.5 mL, 0.2 M MOPS, 0.05 M NaOAc, 0.01 M EDTA, pH 7.0), prepared in-house in MilliQ H_2O, was added to the agarose solution and allowed to cool down

to ~55 – 60 °C. 37% (w/v) formaldehyde in H_2O solution (6.75 mL) was added to the warm agarose solution, quickly mixed by swirling and immediately casted into an electrophoresis chamber (SERVA). A 20-well comb was inserted, the gel was allowed to solidify for 20 mins and 1X MOPS buffer was added to cover the entire gel.

Sample preparation: ssRNA ladder (5 µL, 500 bases – 9 kb range, New England Biolabs) was mixed with 2X RNA loading dye (8 µL, New England Biolabs). Dry RNA pellets were dissolved in 5 µL of autoclaved RNase-free H_2O each and 2X RNA loading dye (5 µL, New England Biolabs) was added. The ssRNA ladder and sample solutions were boiled by heating at 95 °C for 2 mins, allowed to cool down to r.t. and briefly centrifuged.

Sample loading, analysis and imaging: The entire ladder and sample solutions were loaded in separate wells and the gel was run at 100 V for 1 hour on a PowerPac™ Basic Power Supply (Bio-Rad). The gel was transferred to a plastic container and imaged for TAMRA fluorescence (λ_{abs} = 532 nm; λ_{em} = 583 nm) on a Typhoon™ FLA 9500 imager (GE Healthcare). To check for RNA loading, the gel was subsequently stained with 3X GelRed Nucleic Acid Stain (Biotum) for 15 mins at r.t. with mild shaking. After 15 mins, the gel was imaged for ethidium bromide fluorescence (λ_{abs} = 532 nm; λ_{em} = 605 nm) on a Typhoon™ FLA 9500 imager (GE Healthcare).

6.2.5.4 Induction of MARylation/PARylation *via* Hydrogen Peroxide Titration

MDA-MB-231 cells were seeded at a concentration of 6×10^5 cells in 2 mL DMEM media (+10% (v/v/) FBS) per well in two 6-well plates. After 24 hours, media was aspirated and replaced with PBS containing different H_2O_2 concentrations (see **Table 6.19**) for 10 mins or 1 hour. Incubations were performed at 37 °C and cells were subsequently lysed in 4% (w/v) SDS lysis buffer. Lysates were cleared by centrifugation (13 000 g for 10 mins at r.t.) and protein concentrations measured as described in **Section 6.2.1**. 20 µg of protein of each sample were loaded on a 12% SDS-PAGE gel, run at 90 V for 10 mins and then at 150 V for ~1 h, and subsequently analysed by western blotting. For visualisation of MARylation/PARylation protein levels, anti-PARylation/MARylation antibody (α-Poly/Mono-ADP ribose, see **Table 6.3**) at a dilution of 1:1000 (v/v), and anti-pan-ADP-ribose binding reagent (1:1000 (v/v) dilution, see **Table 6.3**) were used. Ponceau S staining was used as a loading control.

Table 6.19. H_2O_2 concentrations and volumes used in H_2O_2 titration cell culture experiments.

Reagent	Concentration	Volume
PBS only	-	2 mL
H_2O_2 (in PBS)	0.1 mM	2 mL
H_2O_2 (in PBS)	0.5 mM	2 mL
H_2O_2 (in PBS)	2.5 mM	2 mL
H_2O_2 (in PBS)	12.5 mM	2 mL

6.3 Proteomics Analysis

6.3.1 Sample Preparation for Proteomics Analysis

6.3.1.1 General Methods

All proteomics experiments were performed with HEK293T cells. Cell seeding was performed for 24 – 48 hours in 6 cm dishes at a concentration of 1×10^6 cells in 5 mL DMEM media (+10% (v/v/) FBS) per dish. Prior to metabolic labelling, media was replaced with 3 mL of fresh media and reagents were added at the appropriate final concentration. After a 24-hour incubation, media was aspirated and cells were washed. For cells treated with 2 mM H_2O_2 (in PBS), cells were washed once with PBS (5 mL) and subsequently incubated with 2 mM H_2O_2 (in PBS) for 6 mins prior to lysis. For cells not treated with 2 mM H_2O_2, cells were washed twice with PBS (5 mL) and directly lysed. Lysates were generated using RIPA lysis buffer and incubation on ice for 30 mins. Clearing of the lysates was performed by centrifugation at 13 000 g at 4 °C for 5 mins and protein precipitation of the lysates was performed with MeOH:H_2O:$CHCl_3$ (see **Section 6.2.1**). Protein pellets were dissolved in 0.2% (w/v) SDS in PBS (500 µL per sample) and protein concentrations were measured using Bio-Rad DC Protein Assay kit (see **Section 6.2.1**).

6.3.1.2 Sample Processing (Click, Pull-down, Reduction and Alkylation, Trypsin Digestion)

Click reaction: Click reaction was performed for 500 µg or 1000 µg of protein sample (2 mg/mL final concentration) for 2 hours at r.t. (see **Section 6.2.2.1**). Following incubation and quenching of the reaction, protein precipitation was performed and pelleted proteins were

dissolved in 0.2% SDS in PBS (500 µL or 1000 µL per sample, 1 mg/mL). Samples were stored at -80 °C until further use.

Pull-down: Protein pull-down with Neutravidin agarose beads and bead washing was performed as described in **Section 6.2.2.4**. Each beads sample was suspended in 50 mM HEPES (pH 8.0) buffer (140 µL).

Reduction and alkylation: Stock solutions of TCEP (50 mM) and 2-chloroacetamide (CAA, 150 mM) were prepared in 50 mM HEPES (pH 8.0). Equal volumes of the stocks were combined and 40 µL of each solution was added to each sample, giving final concentrations of 5 mM (TCEP) and 15 mM (CAA). Samples were subsequently incubated at r.t. with shaking for 15 mins.

Trypsin digestion: Peptides were eluted from beads *via* digestion with trypsin. Following reduction and alkylation, 5 µL of trypsin (0.2 µg/µL) were added to each sample and overnight incubation (16 – 18 hours) at 37 °C with shaking (900 – 1000 rpm) was performed. Trypsin digestion was quenched by the addition of EDTA-free protease inhibitor cocktail (4 µL, 50X) and incubation for 5 mins at r.t. with shaking. Beads were pelleted by centrifugation at 3500 g for 3 mins and supernatants were transferred into clean Eppendorf tubes. Each beads sample was washed once with 50 mM HEPES (pH 8.0, 100 µL), beads were pelleted at 3500 g for 3 mins and each washing combined with its respective supernatant.

Measuring peptide concentrations: Peptide concentration was measured for each sample using the Pierce™ Quantitative Fluorometric Peptide Assay (Thermo Scientific) in accordance with the manufacturer's protocol. The assay was performed in a fluorescence compatible black 96-well plate (Greiner) and fluorescence was measured on an EnVision 2104 plate reader (λ_{abs} = 380 nm, λ_{em} = 460 nm). Total amount of peptide was calculated for each sample and all samples were dried on a vacuum centrifuge overnight.

6.3.1.3 Six(6)-plex/ten(10)-plex Tandem Mass Tag (TMT)-labelling

Samples were dissolved in 50 – 100 µL of MilliQ H_2O and the pH of each sample was checked on pH paper prior to TMT-labelling (TMT-labelling only works at basic pH, ideally between 8.0 and 8.5). TMT-labelling was performed on the same amount of peptide for each sample for a given experiment (4 – 9 µg, ~25 – 30 µL volume), and each sample was labelled with a different 'plex' channel. Generally, each TMT 'plex' vial was enough to label ~100 µg of peptides and each TMT reagent was dissolved in dry MeCN. An aliquot of each dissolved TMT

reagent, enough to label 4 – 9 µg of peptides, was taken out and diluted to ~25 – 30 µL, to approximately match the volume of the peptide sample to be labelled (1:1 (v/v)). Each sample was mixed with its respective TMT channel label and incubated at r.t. for 2 hours with shaking (750 rpm). The TMT labelling reactions were quenched by the addition of 5% (w/v) hydroxylamine in 50 mM HEPES (pH 8.0, 2 µL per sample) and incubating at r.t. for 15 mins with shaking (750 rpm). All samples within a TMT set were combined, acidified by the addition of trifluoroacetic acid (TFA, 2% (v/v) final concentration) and pH level checked on pH paper to ensure pH <7. Combined samples were dried under vacuum overnight and stored at -80 °C until further use.

For the proteomics experiment described in **Section 4.5.6** and the data presented in **Figure 4.30**, ~1/10th (0.4 – 0.9 µg) of each sample for each TMT set were combined in a separate Eppendorf tube and this combined sample was labelled with an extra TMT channel label, distinct from TMT channel labels used for individual sample labelling. ~1/10th of this combined labelled sample (per TMT set) was then added to each individual TMT-labelled sample within that TMT set. By following this approach, missing values between TMT sample replicates were eliminated during data processing and analysis.

6.3.1.4 4-/8-Layer Fractionation

In all proteomics experiments, 4-/8-Layer fractionation was performed. This was performed using the Pierce^{TM} High pH Reversed-Phase Fractionation Kit (Thermo Scientific) in accordance with the manufacturer's protocol (see **Table 6.20** and **Table 6.21** for a summary of the elution solutions and gradients used for 4- and 8-layer fractionation, respectively). Salts in sample buffer and traces of unreacted TMT-reagents were removed in the two washing steps. Following fractionation, samples were dried under vacuum overnight and stored at -80 °C until further use.

Table 6.20. Summary of the elution gradients, reagents and the corresponding amounts used in 4-layer fractionation experiments.

Fraction	Buffer composition	
	Acetonitrile	0.1% (v/v) Triethylamine
Wash (100% H_2O)	-	-
Wash	5.0% (v/v)	95.0% (v/v)

1	12.5% (v/v)	87.5% (v/v)
2	17.5% (v/v)	82.5% (v/v)
3	22.5% (v/v)	77.5% (v/v)
4	50.0% (v/v)	50.0% (v/v)

Table 6.21. Summary of the elution gradients, reagents and the corresponding amounts used in 8-layer fractionation experiments.

Fraction	**Buffer composition**	
	Acetonitrile	**0.1% (v/v) Triethylamine**
Wash (100% H_2O)	-	-
Wash	5.0% (v/v)	95.0% (v/v)
1	10.0% (v/v)	90.0% (v/v)
2	12.5% (v/v)	87.5% (v/v)
3	15.0% (v/v)	85.0% (v/v)
4	17.5% (v/v)	82.5% (v/v)
5	20.0% (v/v)	80.0% (v/v)
6	22.5% (v/v)	77.5% (v/v)
7	25.0% (v/v)	75.0% (v/v)
8	50.0% (v/v)	50.0% (v/v)

6.3.1.5 Desalting

For samples where fractionation was not performed, a separate desalting step following TMT-labelling was performed to remove salts in the sample buffer, as described next. Three layers of polystyrene-divinylbenzene copolymer (SDB-XC) membrane (Empore) were stacked, cut out and inserted into a 200 μL pipette tip. Each tip was placed through a hole on the lid of a

1.5 mL Eppendorf tube and washed with MeOH (150 µL), followed by H_2O (150 µL). For each washing step, tips were centrifuged at 1000 g for 3 mins. Dried peptide samples were dissolved in a H_2O:MeCN:TFA (98.5:1:0.5 v/v/v) mixture (150 µL), vortexed briefly and sonicated for 2 – 3 mins. Samples were loaded on the membrane tips and centrifuged at 1000 g for 3 mins. Each sample tip was washed with H_2O (150 µL), centrifuged at 1000 g for 3 mins and placed into a new clean Eppendorf tube. Peptides were eluted from each tip by loading MeCN:H_2O (3:2 v/v) solution (60 µL) and centrifuging at 1000 g for 3 mins. Tips were washed with an additional 60 µL aliquot of MeCN:H_2O (3:2 v/v), combined with their corresponding elution sample, dried under vacuum for 2 hours or overnight and stored at -80 °C until further use.

6.3.1.6 Sample Dissolution, Filtering and Submission for Analysis

Fractionated/desalted dried peptide samples were dissolved in an appropriate volume of H2O:MeCN:TFA (97.5:2:0.5 v/v/v) LC-MS grade reagent mixture (typically 15 – 40 µL). To ensure complete dissolution, samples were vortexed briefly, placed on a shaker at 750 rpm for 3 mins, sonicated for 2 – 3 mins, vortexed again and very briefly centrifuged. Three layers of polyvinylidene fluoride (PVDF) Durapore 0.1 µm membrane (Millipore) were stacked, cut out and inserted into a 10 µL pipette tip. 10 – 15 µL of each peptide sample were loaded on separate PVDF membrane tips and filtered by centrifugation directly into LC-MS 0.3 mL polypropylene micro-vials (Kinesis). Samples were stored at 4 °C for same day or next day analysis.

6.3.2 LC-MS/MS Proteomics Analysis of TMT-labelled Samples

0.5 – 2 µg of peptides were loaded per sample injection on an EASY-Spray™ Acclaim PepMap C_{18} column with an inner diameter of 50 × 75 µm. Separation of peptides was performed using a 3-hour linear gradient of 0-100% solvent B and a flow rate of 250 nL/min. The following solvent system was used: 80% MeCN supplemented with 0.1% FA (solvent B):2% MeCN supplemented with 0.1% FA (solvent A). Coupling of the LC to a QExactive MS instrument was performed *via* an EASY-Spray™ source (Thermo Fischer Scientific). Operation was set to data-dependent mode. Acquisition of survey scans was performed at a resolution of 70 000 at m/z 200 and in the range 350 – 1800 m/z. The most abundant isotope patterns (upper limit = 10) from the survey scan with a charge +2 or higher were selected for fragmentation by HCD. A 1.6 m/z isolation window was applied and a normalised collision energy for HCD fragmentation was set to 25. Survey scan maximum ion injection time was set to 20 ms. Acquisition of MS/MS scans was performed at a resolution of 35 000 at m/z 200 with a

maximum ion injection time set to 120 ms. MS acquisition ion target value was set to 10^6 and MS/MS acquisition ion target value was set to 10^5.

6.3.3 Data Processing and Analysis in MaxQuant/Perseus/PEAKS

6.3.3.1 Data Processing in MaxQuant

Processing of mass spectrometry raw files was performed in MaxQuant (v1.6.5.0) for all experiments. Peptide searching was performed against human proteome reference list obtained as a FASTA file from UniProt (Taxonomy 9606, downloaded on 20 February 2020). The following were set as variable modifications: Oxidation (M), Acetyl (Protein N-term). The following were set as fixed modifications: Carbamidomethyl (C). Digestion mode was set to Trypsin (maximum missed cleavages = 2, minimum peptide length = 7 residues). For all analyses involving TMT-labelled samples, reporter ion MS^2 option was selected under 'Type' and the appropriate pre-defined TMT6plex or TMT10plex labels were selected for lysine residues and N-termini. For protein quantification, 'unique + razor' peptide option was selected, with minimum label ratio count set to 2. All other parameters were used as set by default in the software.

6.3.3.2 Data Analysis in Perseus

Analysis of processed data from MaxQuant was performed in Perseus (v1.6.15.0) for all experiments. For TMT-labelling, all 'reporter intensity corrected' values for a given experiment were imported into Perseus from the 'proteinGroups' text file generated by MaxQuant. For experiments performed in triplicates, 'reporter intensity corrected' values were grouped ('Categorical Annotation Rows' option) into three categories: per TMT-set, per triplicates and per condition. Data filtering was performed by removing rows identified as 'potential contaminants' and 'reverse' ('Filter Rows Based on Categorical Column' option). Log_2 transformation was performed for all values ('Basic -> Transform' option). Normalisation of protein abundance was performed by first subtracting the mean from each row in each TMT-set ('Normalization -> Subtract -> Rows, TMT-set, Mean') and then subtracting the median from each column ('Normalization -> Subtract -> Columns, Median'). A final filtering step was applied to only include rows with at least two valid values per triplicate condition ('Filter Rows Based on Valid Values -> Number (set to 2), Mode -> In At Least One Group (set to Replicates)'). For statistical analysis, the mean for each row for each set of triplicate was calculated ('Average Groups -> Replicates, Mean') and summary statistics was produced ('Basic -> Summary Statistics (columns)'). Summary statistics data was visualised in

GraphPad Prism (v9.2.0). Processed (non-statistical) data was visualised by either profile plots (log2 values plotted against their corresponding condition) or volcano plots (significance (log(P)) plotted against difference in log2 values for two conditions) generated using Student's t-test (paired two-sample t-test), with the following parameters set: False discovery rate (FDR) = 0.05, S_o = 0.1, Number of randomisations = 250. For principal component analysis (PCA), missing values must be replaced and this was performed by 'Imputation -> Replace Missing Values From Normal Distribution'.

6.3.3.3 Data Processing and Analysis in PEAKS

Processing of MS raw files and data analysis for site identification was performed in PEAKS (v8.5). The following parameters were used: digestion enzyme = trypsin, maximum missed cleavages = 2, TMT quantification selected. Cysteine carbamidomethylation, deamidation, N-terminal acetylation, N-terminal TMT and Lysine TMT tags, methionine oxidation, hydroxylamine modification (+15.0109) and AMPylation-modified with AzRB adducts (+624.1918) were set as variable modifications. Peptide $-\log_{10}(P) \geq 15$ and Ascore >20 cut-offs were used for the identification analysis of modified sites.

6.4 Metabolomics Analysis

6.4.1 Sample Preparation for Metabolite Extraction

6.4.1.1 General Methods

Metabolomics experiments were performed with HEK293T, T47D, MDA-MB-435 or COV318 cells. Cell seeding was performed for 24 hours in 6-well plates at a concentration of 4-6 × 10^5 cells in 2 mL DMEM (HEK293T, COV318) or RPMI-1640 (T47D, MDA-MB-435) media (+10% (v/v/) FBS) per well. Depending on experiment type, metabolic labelling was performed for 1 h or 24 hours and experiments were performed as single or in duplicates. Prior to metabolic labelling, media was replaced with 1 mL of fresh media and reagents were added at the appropriate final concentration.

6.4.1.2 Sample Processing

After appropriate incubation time (37 °C, 5% CO_2 in a humidified incubator), culture media was aspirated and cells were washed once with ice-cold Ringers solution (2 mL, one tablet per 500 mL of MilliQ H_2O, Sigma-Aldrich). The plates were placed on ice, ice-cold proteomics grade MeOH:H_2O solution (4:1 v/v) was added to each well (1 mL) and the plates were incubated on ice for 20 mins. Cells were briefly scraped and the solutions were transferred into clean 2 mL Eppendorf tubes. Each well was washed once with proteomics grade ice-cold

MeOH (500 µL) and the washings were combined with their corresponding extracted solutions. Samples were briefly vortexed and centrifuged at 13 000 g at 4 °C for 20 mins. 1 mL per sample was transferred into a new clean Eppendorf tube and all samples were dried on a vacuum centrifuge at r.t. for 2 – 3 hours. The dried samples were stored at -80 °C until further use.

6.4.2 Targeted Metabolomics LC-MS/MS Method Development

6.4.2.1 Parameter Optimisation for MS^2

Metabolite detection and identification was performed for native metabolites (AMP, ATP, β-NMN, NAD^+) and for the 6Yn-metabolite analogue series (6Yn-Ad (**25**), 6Yn-ProTide (**47**), 6Yn-AMP (**30**), 6Yn-ATP (**40**), 6Yn-NAD^+ (**3**)) by targeted metabolomics. For targeted metabolomics method development, separate stock standard solutions (1 mg/ml) of purified materials were generated in MeOH or H_2O. The samples were diluted in MeCN:H_2O (1:1 v/v) + 0.1% (v/v) FA (infusion solvent) to 10 µg/ml final concentration and used for direct infusion onto a SCIEX 4000 QTRAP (hybrid triple quadrupole/linear ion trap) MS instrument. Declustering potential (DP) and collision energy (CE), which are metabolite-specific parameters, were optimised for fragmentation and identification of each compound from MS^2 scans (performed by PhD student Michael Gruet and Dr Alexis Siskos (Keun Lab)). The optimised parameters, daughter ions (fragments) and retention times for each metabolite are summarised in **Table 6.22**.

Table 6.22. List of all monitored metabolites in LC-MS/MS metabolomics experiments. The corresponding daughter ions (fragments) for each parent ion are shown along with the corresponding metabolite parameters (DP, CE). The retention time (mins) for each metabolite for the appropriate elution gradient (RP, HILIC) is shown as well as the MS ionisation detection mode (ESI^+, ESI^-) employed for detection of ions.

	Positive mode (ESI^+)				**Negative mode (ESI^-)**				**Retention time (mins)**	
Metabolite	**Parent ion**	**Frag-ment**	**DP (V)**	**CE**	**Parent ion**	**Frag-ment**	**DP (V)**	**CE**	**RP**	**HILIC**
6Yn-NAD^+ (**3**)	702.3	580.3	93	24	700.9	579.2	-80	-20	3.80	6.45 (ESI^+)
		562.2	93	28		543.1	-80	-21		
		466.3	93	35		273.2	-80	-50		
		174.2	93	64		249.3	-80	-55		

6Yn-ProTide (**47**)	623.1	432.5	180	26	621.5	527.3	-105	-18	7.75	1.02 (ESI^-)
		288.3	180	36		334.1	-105	-30		
		174.4	180	48		172.1	-105	-34		
		97.2	180	58		104.1	-105	-85		
6Yn-ATP (**40**)	546.4	174.4	85	46	544.2	464.3	-75	-35	-	5.80 (ESI^-)
		-	-	-		445.9	-75	-30		
		-	-	-		177.1	-75	-38		
		-	-	-		159.1	-75	-45		
6Yn-AMP (**30**)	386.3	-	70	28	384.2	-	-	-	3.70	4.92 (ESI^-)
		-	70	92		-	-	-		
		-	70	50		-	-	-		
		-	-	-		-	-	-		
6Yn-Ad (**25**)	306.3	174.3	55	40	-	-	-	-	5.04	-
		135.1	55	60	-	-	-	-		
NAD^+	664.4	136.0	70	70	663.0	540.3	-40	-25	0.86	7.30 (ESI^+)
		97.2	70	85		-	-	-		
β-NMN	335.2	123.1	100	20	-				0.65	6.78 (ESI^-)
[β-NMN + Na]	357.2	235.1	50	14	-					
[β-NMN + 2Na]	-	-	-	-	379.1	257.1	-42	-10		
	-	-	-	-		211.0	-42	-20		
ATP	508.2	410.2	88	24	506.2	159.1	-85	-40	-	6.20 (ESI^-)
		136.2	88	46		-	-	-		
AMP	-	-	-	-	346.2	79	-55	-50	-	5.65 (ESI^-)

6.4.2.2 Liquid Chromatography Optimisation

Retention time of metabolites (see **Table 6.22**) was determined by analysing stock compounds (10 µg/ml) by reversed-phase LC-MS (RP-LC/MS) or by Hydrophilic Interaction Chromatography LC-MS (HILIC-LC/MS), or both.

RP-LC/MS: All RP-LC/MS analyses were performed in ESI^+ mode. Metabolite separation and analysis was performed on an Agilent 1290 Infinity System coupled to a SCIEX 4000 QTRAP (LC/MS/MS) System. 5 µL of stock compound (10 µg/ml) were loaded per sample injection on an ACQUITY UPLC HSS T3 (C18) column (Waters) with dimensions 2.1 × 100 mm and particle size 1.8 µm. Column temperature was set to 40 °C. Analysis was performed using a 15 mins gradient of 0.5-99.5% solvent B (0.5% 0-2 mins, 0.5-15.0% 2-5 mins, 15.0-99.5% 5-10 mins, 99.5% 10-13 mins, 99.5-0.5% 13-13.1 mins, 0.5% 13.1-15 mins) and a flow rate of 600 µL/min. The following solvent system was used: 100% MeCN supplemented with 0.1% FA (solvent B):100% H_2O supplemented with 0.1% FA (solvent A).

HILIC-LC/MS: Most HILIC-LC/MS analyses were performed in ESI^- mode, except for NAD^+ and 6Yn-NAD^+ (**3**), which were analysed in ESI^+ mode (both for HILIC and RP). Metabolite separation and analysis was performed on an Agilent 1290 Infinity System coupled to a SCIEX 4000 QTRAP (LC/MS/MS) System. 5 µL of stock compound (10 µg/ml) were loaded per sample injection on an ACQUITY UPLC BEH Amide (HILIC) column (Waters) with dimensions 3 × 150 mm and particle size 1.7 µm. Column temperature was set to 40 °C. In ESI^- mode, analysis was performed using a 15 mins gradient of 10-55% solvent B (10.0% 0-1 mins, 10.0-55.0% 1-8 mins, 55.0% 8-9 mins, 55.0-10.0% 9-9.10 mins, 10.0% 9.10-15 mins) and a flow rate of 500 µL/min. The following solvent system was used: 20 mM ammonium acetate and 10 mM ammonium hydroxide, both in H_2O (solvent B):MeCN and 10 mM ammonium hydroxide in H_2O (solvent A). In ESI^+ mode, analysis was performed using a 15 mins gradient of 5-50% solvent B (5.0% 0-1 mins, 5.0-50.0% 1-8 mins, 50.0% 8-9 mins, 50.0-5.0% 9-9.10 mins, 5.0% 9.10-15 mins) and a flow rate of 500 µL/min. The following solvent system was used: 20 mM ammonium formate supplemented with 0.1% FA in H_2O (solvent B):MeCN supplemented with 0.1% FA (solvent A).

6.4.3 LC-MS/MS Metabolomics Analysis

Depending on experimental set-up and goals, sample analysis was performed either by RP LC-MS/MS or HILIC LC-MS/MS, or both. Where both analyses were performed, RP LC-MS/MS was carried out on day 1 and HILIC LC-MS/MS was carried out on day 2. Samples were stored

at 10 °C in-between analyses in the instrument autosampler. Dried samples were dissolved in 50 µL of proteomics grade H_2O and 5 µL of sample were loaded on the column per injection. Targeted metabolomics was performed by pre-selecting the desired precursor ion masses of metabolites of interest and selecting those for fragmentation with the corresponding optimal DP and CE parameters for each metabolite pre-specified (see **Table 6.22**).

6.4.4 Data Analysis in Analyst

Processing and analysis of MS raw files was performed in Analyst (v1.6.2, SCIEX) by PhD student Michael Gruet (Keun Lab). Intensity peaks for metabolites of interest were filtered by selecting their corresponding precursor mass. To ensure the correct identification of a metabolite from a sample, the retention time and fragmentation pattern (daughter ions, from MS^2 spectra) for the desired metabolite peak was compared with the retention time and fragmentation pattern for the corresponding purified stock compound.

For calculating metabolite concentrations and % fraction of a metabolite analogue in the entire native metabolite pool within a sample, the peak areas for the metabolite analogue and the corresponding native metabolite were integrated using the in-built peak integration tool. The integrated peak areas were then compared against a standard curve generated for the peak areas of pure stock solutions of known concentrations for each metabolite, thus allowing for calculating the concentration of each metabolite in each sample. % incorporation was in turn calculated by using the formula (metabolite analogue concentration/native metabolite concentration)*100.

6.5 Molecular Docking

6.5.1 General Procedures and Software Information

Molecular docking experiments and homology modelling were performed in Molecular Operating Environment (MOE) software (v2019.0102, CCG). Visualisation of structures was performed directly in MOE or structures were exported to PyMOL (v2.3.4). 2D ligand structures and protein-ligand interaction maps were generated in ChemDraw Professional (v17.0, PerkinElmer).

6.5.2 3D Structure Preparation for Ligands

Structures of ligands used for docking experiments were exported as .sdf file type (ChemDraw Professional), as 2D structures, and imported into MOE for 3D structure preparation. An initial 'Wash' step ('Compute -> Molecule -> Wash') was performed. Protonation was set to

'Enumerate', the option 'Scale to Reasonable Bond Lengths' was selected and all other settings were used as set by default. Subsequently, a 'QuickPrep' step ('Compute -> Molecule -> QuickPrep') was performed and all settings were used as set by default. Next, a 'Partial Charges' step was applied ('Compute -> Molecule -> Partial Charges'). Method was set to 'Current Forcefield', Amber10:EHT, the option 'Adjust Hydrogens and Lone Pairs as Required' was selected and all other settings were used as set by default. Finally, an 'Energy Minimize' step was applied ('Compute -> Molecule -> Energy Minimize'), the 'General' tab was selected and all settings were used as set by default.

6.5.3 Protein-ligand Docking

6.5.3.1 General Methods

Protein-ligand docking was performed using the 'Dock' option ('Compute -> Dock') available within the software. 'Alpha PMI', or 'Pharmacophore' where appropriate, was selected as the placement method. The number of poses to be generated was set to 50 using the London dG scoring system. 'Induced Fit' was selected as the subsequent refinement method, with the number of poses to be generated set to 15 using the GBVI/WSA dG scoring system.

The following PDB IDs were used for molecular docking: AdK (1BX4), human AK1 (1Z83), *E. coli* AKe (1ANK), yeast F1-ATPase (ATP synthase subunit, 2HLD), bovine F1-ATPase (ATP synthase subunit, 1H8E), NMNAT1 (1KQN), PARP1 (6BHV).

6.5.3.2 Pharmacophores and Constraints

For docking experiments with AdK and adenosine ligands, AK1 and AMP ligands, ATP synthase and ADP ligands, and NMNAT1 and ATP ligands, two pharmacophore constraints were placed on the two rings of the adenine moiety in each ligand, based on aromaticity/pi-pi stacking interactions (**Figure 6.1A**). This ensured that the adenine moiety for each ligand was placed in the correct position in its respective binding site during docking experiments. For docking experiments with PARP1, and PARP homology models derived from PARP1, and NAD^+ ligands, three pharmacophore constraints were placed on each NAD^+ ligand: two were placed on the two rings of the adenine moiety and one was placed on the nicotinamide ring (**Figure 6.1B**), based on aromaticity/pi-pi stacking interactions. This ensured that the adenine moiety and nicotinamide moiety for each NAD^+ ligand were placed in the correct position in their respective binding site during docking experiments.

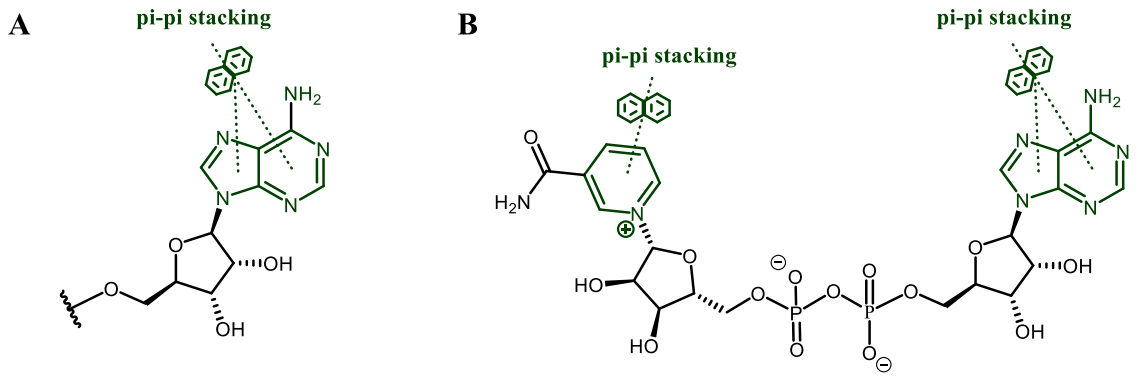


Figure 6.1. Pharmacophore placement (highlighted in green) on adenine moiety on (**A**) adenosine, AMP, ADP and ATP ligands, and (**B**) on adenine and nicotinamide moieties on NAD^+ ligands.

6.5.4 Mutational Analysis

Point mutations were performed using the in-built 'Protein Builder' tool within the software. An amino acid was selected and replaced with the desired residue using the tool. A 'Repack' step followed by an energy minimisation step were performed for the mutated residue. Molecular docking for ligands with mutated proteins was then performed as usual (see **Section 6.5.3.1**).

6.5.5 Homology Modelling of PARPs

Homology modelling was performed using the in-built 'Homology Model' tool within the software. For homology modelling of PARPs, PARP1 (6BHV) was selected as the template structure (template chain #1) and the PARP sequence to be modelled was selected in the 'Sequence' tab. Ligands from the template structure were modelled into the derived homology model by selecting 'Options -> Ligand Atoms'. The number of structures generated was set to 10 ('Settings -> Maximum Number of Mainchain Models'). Refinement of the structures was performed using the GB/VI scoring system and the 'Refinement Gradient Limit' was set to 5. All other settings were used as set by default. Molecular docking for ligands with homology models was then performed as usual (see **Section 6.5.3.1**).

Bibliography

1. Gupte, R., Liu, Z. & Kraus, W. L. PARPs and ADP-ribosylation: recent advances linking molecular functions to biological outcomes. *Genes Dev.* **31**, 101–126 (2017).
2. Hoch, N. C. & Polo, L. M. ADP-ribosylation: from molecular mechanisms to human disease. *Genet. Mol. Biol.* **43**, e20190075 (2020).
3. Lüscher, B., Bütepage M, Eckei L, Krieg S, Verheugd P & Shilton B. H. ADP-Ribosylation, a Multifaceted Posttranslational Modification Involved in the Control of Cell Physiology in Health and Disease. *Chem. Rev.* **118**, 1092–1136 (2018).
4. Vivelo, C. A. & Leung AK. Proteomics approaches to identify mono-(ADP-ribosyl)ated and poly(ADP-ribosyl)ated proteins. *Proteomics*. **15**, 203-217 (2015).
5. Munnur, D. & Ahel, I. Reversible mono-ADP-ribosylation of DNA breaks. *FEBS J*. **284**, 4002-4016 (2017).
6. Munnur, D., Bartlett, E., Mikolčević, P., Kirby, I. T., Rack, J. G. M., Mikoč, A., Cohen, M. S. & Ahel, I. Reversible ADP-ribosylation of RNA. *Nucleic Acids Res*. **47**, 5658-5669 (2019).
7. Groslambert, J., Prokhorova, E. & Ahel, I. ADP-ribosylation of DNA and RNA. *DNA Repair*. **105**, 103144 (2021).
8. Weixler, L., Schäringer, K., Momoh, J., Lüscher, B., Feijs, K. L. H. & Žaja, R. ADP-ribosylation of RNA and DNA: from in vitro characterization to in vivo function. *Nucleic Acids Res*. **49**, 3634-3650 (2021).
9. Hottiger, M. O., Hassa, P. O., Lüscher, B., Schüler, H. & Koch-Nolte, F. Toward a unified nomenclature for mammalian ADP-ribosyltransferases. *Trends Biochem. Sci*. **35**, 208-219 (2010).
10. Vyas, S., Matic, I., Uchima, L., Rood, J., Zaja, R., Hay, R. T., Ahel, I. & Chang P. Family-wide analysis of poly(ADP-ribose) polymerase activity. *Nat. Commun*. **5**, 4426 (2014).
11. Zhou, G. C., Parikh, S. L., Tyler, P. C., Evans, G. B., Furneaux, R. H., Zubkova, O. V., Benjes, P. A. & Schramm, V. L. Inhibitors of ADP-ribosylating bacterial toxins based on oxacarbenium ion character at their transition states. *J. Am. Chem. Soc*. **126**, 5690-5698 (2004).
12. Dudev, T. & Lim, C. Factors controlling the mechanism of NAD+ non-redox reactions. *J. Am. Chem. Soc.* **132**, 16533–16543 (2010).

13. Tsurumura, T., Tsumori, Y., Qiu, H., Oda, M., Sakurai, J., Nagahama, M. & Tsuge, H. Arginine ADP-ribosylation mechanism based on structural snapshots of iota-toxin and actin complex. *Proc. Natl. Acad. Sci*. **110**, 4267-4272 (2013).
14. Zhen, Y. & Yu, Y. Proteomic Analysis of the Downstream Signaling Network of PARP1. *Biochemistry* **57**, 429–440 (2018).
15. Langelier, M. F., Planck, J. L., Roy, S. & Pascal, J. M. Structural basis for DNA damage-dependent poly(ADP-ribosyl)ation by human PARP-1. *Science*. **336**, 728-732 (2012).
16. Strickfaden, H., McDonald, D., Kruhlak, M. J., Haince, J. F., Th'ng, J. P. H., Rouleau, M., Ishibashi, T., Corry, G. N., Ausio, J., Underhill, D. A., Poirier, G. G. & Hendzel, M. J. Poly(ADP-ribosyl)ation-dependent Transient Chromatin Decondensation and Histone Displacement following Laser Microirradiation. *J. Biol. Chem*. **291**, 1789-1802 (2016).
17. Liu, C., Vyas, A., Kassab, M. A., Singh, A. K. & Yu, X. The role of poly ADP-ribosylation in the first wave of DNA damage response. *Nucleic Acids Res.* **45**, 8129–8141 (2017).
18. Pascal, J. M. The comings and goings of PARP-1 in response to DNA damage. *DNA Repair*. **71**, 177-182 (2018).
19. Bell, N. A. W., Haynes, P. J., Brunner, K., de Oliveira, T. M., Flocco, M. M., Hoogenboom, B. W. & Molloy, J. E. Single-molecule measurements reveal that PARP1 condenses DNA by loop stabilization. *Sci. Adv*. **7**, eabf3641 (2021).
20. Bian, C., Zhang, C., Luo, T., Vyas, A., Chen, S. H., Liu, C., Kassab, M. A., Yang, Y., Kong, M. & Yu, X. $NADP^+$ is an endogenous PARP inhibitor in DNA damage response and tumor suppression. *Nat. Commun*. **10**, 693 (2019).
21. Sun, F. H., Zhao, P., Zhang, N., Kong, L. L., Wong, C. C. L. & Yun, C. H. HPF1 remodels the active site of PARP1 to enable the serine ADP-ribosylation of histones. *Nat. Commun*. **12**, 1028 (2021).
22. Gibbs-Seymour, I., Fontana, P., Rack, J. G. M. & Ahel, I. HPF1/C4orf27 Is a PARP-1-Interacting Protein that Regulates PARP-1 ADP-Ribosylation Activity. *Mol. Cell*. **62**, 432-442 (2016).
23. Rashid, I., Hammel, M., Sverzhinsky, A., Tsai, M. S., Pascal, J. M., Tainer, J. A. & Tomkinson, A. E. Direct interaction of DNA repair protein tyrosyl DNA phosphodiesterase 1 and the DNA ligase III catalytic domain is regulated by phosphorylation of its flexible N-terminus. *J. Biol. Chem*. **297**, 100921 (2021).
24. David, K. K., Andrabi, S. A., Dawson, T. M. & Dawson, V. L. Parthanatos, a messenger of death. *Front Biosci. (Landmark Ed).* **14**, 1116-1128 (2009).

25. Koehler, R. C., Dawson, V. L. & Dawson, T. M. Targeting Parthanatos in Ischemic Stroke. *Front Neurol*. **12**, 662034 (2021).
26. Andrabi, S. A., Kim, N. S., Yu, S. W., Wang, H., Koh, D. W., Sasaki, M., Klaus, J. A., Otsuka, T., Zhang Z, Koehler RC, Hurn, P. D., Poirier, G. G., Dawson, V. L. & Dawson, T. M. Poly(ADP-ribose) (PAR) polymer is a death signal. *Proc. Natl. Acad. Sci*. **103**, 18308-18313 (2006).
27. Ossovskaya, V., Koo, I. C., Kaldjian, E. P., Alvares, C. & Sherman, B. M. Upregulation of Poly (ADP-Ribose) Polymerase-1 (PARP1) in Triple-Negative Breast Cancer and Other Primary Human Tumor Types. *Genes Cancer*. **1**, 812-821 (2010).
28. Wang, L., Liang, C., Li, F., Guan, D., Wu, X., Fu, X., Lu, A. & Zhang, G. PARP1 in Carcinomas and PARP1 Inhibitors as Antineoplastic Drugs. *Int. J. Mol. Sci*. **18**, 2111 (2017).
29. Pulliam, N., Tang, J., Wang, W., Fang, F., Sood, R., O'Hagan, H. M., Miller, K. D., Clarke, R. & Nephew, K. P. Poly-ADP-Ribosylation of Estrogen Receptor-Alpha by PARP1 Mediates Antiestrogen Resistance in Human Breast Cancer Cells. *Cancers*. **11**, 43 (2019).
30. Ronson, G. E., Piberger, A. L., Higgs, M. R., Olsen, A. L., Stewart, G. S., McHugh, P. J., Petermann, E. & Lakin, N. D. PARP1 and PARP2 stabilise replication forks at base excision repair intermediates through Fbh1-dependent Rad51 regulation. *Nat. Commun*. **9**,746, (2018).
31. Obaji, E., Maksimainen, M. M., Galera-Prat, A. & Lehtiö, L. Activation of PARP2/ARTD2 by DNA damage induces conformational changes relieving enzyme autoinhibition. *Nat. Commun*. **12**, 3479 (2021).
32. Ali, S. O., Khan, F. A., Galindo-Campos, M. A. & Yélamos, J. Understanding specific functions of PARP-2: new lessons for cancer therapy. *Am. J. Cancer. Res*. **6**, 1842-1863 (2016).
33. Dantzer, F., Giraud-Panis, M. J., Jaco, I., Amé, J. C., Schultz, I., Blasco, M., Koering, C. E., Gilson, E., Ménissier-de Murcia, J., de Murcia, G. & Schreiber, V. Functional interaction between poly(ADP-Ribose) polymerase 2 (PARP-2) and TRF2: PARP activity negatively regulates TRF2. *Mol. Cell. Biol*. **24**, 1595-1607 (2004).
34. Dantzer, F., Schreiber, V., Villunger, A., Fernández-Capetillo, O. & Yélamos, J. PARP-2 sustains erythropoiesis in mice by limiting replicative stress in erythroid progenitors. *Cell Death Differ*. **22**, 1144-1157 (2015).

35. Kutuzov, M. M., Belousova, E. A., Kurgina, T. A., Ukraintsev, A. A., Vasil'eva, I. A., Khodyreva, S. N. & Lavrik, O. I. The contribution of PARP1, PARP2 and poly(ADP-ribosyl)ation to base excision repair in the nucleosomal context. *Sci. Rep*. **11**, 4849 (2021).
36. Masutani, M., Nozaki, T., Nakamoto, K., Nakagama, H., Suzuki, H., Kusuoka, O., Tsutsumi, M. & Sugimura, T. The response of Parp knockout mice against DNA damaging agents. *Mutat. Res*. **462**, 159-166 (2000).
37. Ménissier de Murcia, J., Ricoul, M., Tartier, L., Niedergang, C., Huber, A., Dantzer, F., Schreiber, V., Amé, J. C., Dierich, A., LeMeur, M., Sabatier, L., Chambon, P. & de Murcia, G. Functional interaction between PARP-1 and PARP-2 in chromosome stability and embryonic development in mouse. *EMBO J*. **22**, 2255-2263 (2003).
38. Dahl, M., Maturi, V., Lönn, P., Papoutsoglou, P., Zieba, A., Vanlandewijck, M., van der Heide, L. P., Watanabe, Y., Söderberg, O., Hottiger, M. O., Heldin, C. H. & Moustakas, A. Fine-tuning of Smad protein function by poly(ADP-ribose) polymerases and poly(ADP-ribose) glycohydrolase during transforming growth factor β signaling. *PLoS One*. **9**,e103651 (2014).
39. Bhardwaj, A., Yang, Y., Ueberheide, B. & Smith, S. Whole proteome analysis of human tankyrase knockout cells reveals targets of tankyrase-mediated degradation. *Nat. Commun*. **8**, 2214 (2017).
40. Smith, S. & de Lange, T. Tankyrase promotes telomere elongation in human cells. *Curr. Biol*. **10**, 1299-1302 (2000).
41. Mariotti, L., Pollock, K. & Guettler, S. Regulation of Wnt/β-catenin signalling by tankyrase-dependent poly(ADP-ribosyl)ation and scaffolding. *Br. J. Pharmacol*. **174**, 4611-4636 (2017).
42. Wang, H., Kuusela, S., Rinnankoski-Tuikka, R., Dumont, V., Bouslama, R., Ramadan, U. A., Waaler, J., Linden, A. M., Chi, N. W., Krauss, S., Pirinen, E. & Lehtonen, S. Tankyrase inhibition ameliorates lipid disorder via suppression of PGC-1α PARylation in db/db mice. *Int. J. Obes*. **44**, 1691-1702 (2020).
43. McGurk, L., Rifai, O. M. & Bonini, N. M. TDP-43, a protein central to amyotrophic lateral sclerosis, is destabilized by tankyrase-1 and -2. *J. Cell. Sci*. **133**, jcs245811 (2020).
44. Yang, H. Y., Shen, J. X., Wang, Y., Liu, Y., Shen, D. Y. & Quan, S. Tankyrase Promotes Aerobic Glycolysis and Proliferation of Ovarian Cancer through Activation of Wnt/*β*-Catenin Signaling. Biomed. Res. Int. **2019**, 2686340 (2019).

45. Schatoff, E. M., Goswami, S., Zafra, M. P., Foronda, M., Shusterman, M., Leach, B. I., Katti, A., Diaz, B. J. & Dow, L. E. Distinct Colorectal Cancer-Associated APC Mutations Dictate Response to Tankyrase Inhibition. *Cancer Discov.* **9**, 1358-1371 (2019).
46. Jang, M. K., Mashima, T. & Seimiya, H. Tankyrase Inhibitors Target Colorectal Cancer Stem Cells via AXIN-Dependent Downregulation of c-KIT Tyrosine Kinase. *Mol. Cancer Ther*. **19**, 765-776 (2020).
47. Tang, B., Wang, J., Fang, J., Jiang, B., Zhang, M., Wang, Y. & Yang, Z. Expression of TNKS1 is correlated with pathologic grade and Wnt/β-catenin pathway in human astrocytomas. *J. Clin. Neurosci*. **19**, 139-143 (2012).
48. Gelmini, S., Poggesi, M., Distante, V., Bianchi, S., Simi, L., Luconi, M., Raggi, C. C., Cataliotti, L., Pazzagli, M. & Orlando, C. Tankyrase, a positive regulator of telomere elongation, is over expressed in human breast cancer. Cancer Lett. **216**, 81-87 (2004).
49. Boehler, C., Gauthier, L. R., Mortusewicz, O., Biard, D. S., Saliou, J. M., Bresson, A., Sanglier-Cianferani, S., Smith, S., Schreiber, V., Boussin, F. & Dantzer, F. Poly(ADP-ribose) polymerase 3 (PARP3), a newcomer in cellular response to DNA damage and mitotic progression. *Proc. Natl. Acad. Sci*. **108**, 2783-2788 (2011).
50. Grundy, G. J., Polo, L. M., Zeng, Z., Rulten, S. L., Hoch, N. C., Paomephan, P., Xu, Y., Sweet, S. M., Thorne, A. W., Oliver, A. W., Matthews, S. J., Pearl, L. H. & Caldecott, K. W. PARP3 is a sensor of nicked nucleosomes and monoribosylates histone H2B(Glu2). *Nat. Commun*. **7**, 12404 (2016).
51. Xing, J., Zhang, A., Du, Y., Fang, M., Minze, L. J., Liu, Y. J., Li, X. C. & Zhang, Z. Identification of poly(ADP-ribose) polymerase 9 (PARP9) as a noncanonical sensor for RNA virus in dendritic cells. *Nat. Commun*. **12**, 2681 (2021).
52. Guo, T., Zuo, Y., Qian, L., Liu, J., Yuan, Y., Xu, K., Miao, Y., Feng, Q., Chen, X., Jin, L., Zhang, L., Dong, C., Xiong, S. & Zheng, H. ADP-ribosyltransferase PARP11 modulates the interferon antiviral response by mono-ADP-ribosylating the ubiquitin E3 ligase β-TrCP. *Nat. Microbiol*. **4**, 1872-1884 (2019).
53. Li, L., Zhao, H., Liu, P., Li, C., Quanquin, N., Ji, X., Sun, N., Du, P., Qin, C. F., Lu, N. & Cheng, G. *PARP12* suppresses Zika virus infection through PARP-dependent degradation of NS1 and NS3 viral proteins. *Sci. Signal*. **11**, eaas9332 (2018).
54. Todorova, T., Bock, F. J. & Chang, P. PARP13 regulates cellular mRNA post-transcriptionally and functions as a pro-apoptotic factor by destabilizing TRAILR4 transcript. *Nat. Commun*. **5**, 5362 (2014).

55. Grunewald, M. E., Chen, Y., Kuny, C., Maejima, T., Lease, R., Ferraris, D., Aikawa, M., Sullivan, C. S., Perlman, S. & Fehr, A. R. The coronavirus macrodomain is required to prevent PARP-mediated inhibition of virus replication and enhancement of IFN expression. *PLoS Pathog*. **15**, e1007756 (2019).
56. Zhu, H., Tang, Y. D., Zhan, G., Su, C. & Zheng, C. The Critical Role of PARPs in Regulating Innate Immune Responses. *Front. Immunol*. **12**, 712556 (2021).
57. Verheugd, P., Forst, A. H., Milke, L., Herzog, N., Feijs, K. L., Kremmer, E., Kleine, H. & Lüscher, B. Regulation of NF-κB signalling by the mono-ADP-ribosyltransferase ARTD10. Nat Commun. **4**, 1683 (2013).
58. Jwa, M. & Chang, P. PARP16 is a tail-anchored endoplasmic reticulum protein required for the PERK- and IRE1α-mediated unfolded protein response. *Nat. Cell. Biol*. **14**, 1223-1230 (2012).
59. Vermehren-Schmaedick, A., Huang, J. Y., Levinson, M., Pomaville, M. B., Reed, S., Bellus, G. A., Gilbert, F., Keren, B., Heron, D., Haye, D., Janello, C., Makowski, C., Danhauser, K., Fedorov, L. M., Haack, T. B., Wright, K. M. & Cohen, M. S. Characterization of PARP6 Function in Knockout Mice and Patients with Developmental Delay. *Cells*. **10**, 1289 (2021).
60. Daugherty, M. D., Young, J. M., Kerns, J. A. & Malik, H. S. Rapid evolution of PARP genes suggests a broad role for ADP-ribosylation in host-virus conflicts. *PLoS Genet*. **10**, e1004403 (2014).
61. Bock, F. J., Todorova, T. T. & Chang, P. RNA Regulation by Poly(ADP-Ribose) Polymerases. *Mol. Cell*. **58**, 959-969 (2015).
62. Yao, N., Chen, Q., Shi, W., Tang, L. & Fu, Y. PARP14 promotes the proliferation and gemcitabine chemoresistance of pancreatic cancer cells through activation of NF-κB pathway. *Mol. Carcinog*. **58**, 1291-1302 (2019).
63. Iansante, V., Choy, P.M., Fung, S. W., Liu, Y., Chai, J. G., Dyson, J., Del Rio, A., D'Santos, C., Williams, R., Chokshi, S., Anders, R. A., Bubici, C. & Papa, S. PARP14 promotes the Warburg effect in hepatocellular carcinoma by inhibiting JNK1-dependent PKM2 phosphorylation and activation. *Nat. Commun*. **6**, 7882 (2015).
64. Schleicher, E. M., Galvan, A. M., Imamura-Kawasawa, Y., Moldovan, G. L. & Nicolae, C. M. PARP10 promotes cellular proliferation and tumorigenesis by alleviating replication stress. *Nucleic Acids Res*. **46**, 8908-8916 (2018).
65. Beck, C., Rodriguez-Vargas, J. M., Boehler, C., Robert, I., Heyer, V., Hanini, N., Gauthier, L. R., Tissier, A., Schreiber, V., Elofsson, M., Reina San Martin, B. & Dantzer,

F. PARP3, a new therapeutic target to alter Rictor/mTORC2 signaling and tumor progression in BRCA1-associated cancers. *Cell Death Differ*. **26**, 1615-1630 (2019).

66. Gunderson, C. C. & Moore, K. N. Olaparib: an oral PARP-1 and PARP-2 inhibitor with promising activity in ovarian cancer. *Futur. Oncol.* **11**, 747–757 (2015).
67. Patel, M., Nowsheen, S., Maraboyina, S. & Xia, F. The role of poly(ADP-ribose) polymerase inhibitors in the treatment of cancer and methods to overcome resistance: a review. *Cell Biosci.* **10**, 35 (2020).
68. Antolin, A. A., Ameratunga, M., Banerji, U., Clarke, P. A., Workman, P. & Al-Lazikani, B. The kinase polypharmacology landscape of clinical PARP inhibitors. Sci. Rep. **10**, 2585 (2020).
69. Yi, M., Dong, B., Qin, S., Chu, Q., Wu, K. & Luo, S. Advances and perspectives of PARP inhibitors. *Exp. Hematol. Oncol*. **8**, 29 (2019).
70. Visochek, L., Atias, D., Spektor, I., Castiel, A., Golan, T. & Cohen-Armon, M. The phenanthrene derivative PJ34 exclusively eradicates human pancreatic cancer cells in xenografts. *Oncotarget*. **10**, 6269-6282 (2019).
71. Lindgren, A. E., Karlberg, T., Thorsell, A. G., Hesse, M., Spjut, S., Ekblad, T., Andersson, C. D., Pinto, A. F., Weigelt, J., Hottiger, M. O., Linusson, A., Elofsson, M. & Schüler, H. PARP inhibitor with selectivity toward ADP-ribosyltransferase ARTD3/PARP3. *ACS Chem. Biol*. **8**, 1698-1703 (2013).
72. Menon, M., Elliott, R., Bowers, L., Balan, N., Rafiq, R., Costa-Cabral, S., Munkonge, F., Trinidade, I., Porter, R., Campbell, A. D., Johnson, E. R., Esdar, C., Buchstaller, H. P., Leuthner, B., Rohdich, F., Schneider, R., Sansom, O., Wienke, D., Ashworth, A. & Lord, C. J. A novel tankyrase inhibitor, MSC2504877, enhances the effects of clinical CDK4/6 inhibitors. Sci. Rep. **9**, 201 (2019).
73. Verma, A., Kumar, A., Chugh, A., Kumar, S. & Kumar, P. Tankyrase inhibitors: emerging and promising therapeutics for cancer treatment. *Med. Chem. Res*. **30**, 50-73 (2021).
74. Murthy, S., Desantis, J., Verheugd, P., Maksimainen, M. M., Venkannagari, H., Massari, S., Ashok, Y., Obaji, E., Nkizinkinko, Y., Lüscher, B., Tabarrini, O. & Lehtiö, L. 4-(Phenoxy) and 4-(benzyloxy)benzamides as potent and selective inhibitors of mono-ADP-ribosyltransferase PARP10/ARTD10. *Eur. J. Med. Chem*. **156**, 93-102 (2018).
75. Kirby, I. T., Kojic, A., Arnold, M. R., Thorsell, A. G., Karlberg, T., Vermehren-Schmaedick, A., Sreenivasan, R., Schultz, C., Schüler, H. & Cohen, M. S. A Potent and

Selective PARP11 Inhibitor Suggests Coupling between Cellular Localization and Catalytic Activity. *Cell Chem. Biol*. **25**, 1547-1553 (2018).

76. Schenkel, L. B., Molina, J. R., Swinger, K. K., Abo, R., Blackwell, D. J., Lu, A. Z., Cheung, A. E., Church, W. D., Kunii, K., Kuplast-Barr, K. G., Majer, C. R., Minissale, E., Mo, J. R., Niepel, M., Reik, C., Ren, Y., Vasbinder, M. M., Wigle, T. J., Richon, V. M., Keilhack, H. & Kuntz, K. W. A potent and selective PARP14 inhibitor decreases protumor macrophage gene expression and elicits inflammatory responses in tumor explants. *Cell Chem. Biol*. **28**, 1158-1168 (2021).
77. Laing, S., Koch-Nolte, F., Haag, F. & Buck, F. Strategies for the identification of arginine ADP-ribosylation sites. *J. Proteomics*. **75**, 169-176 (2011).
78. Ino, Y., Kinoshita, E., Kinoshita-Kikuta, E., Akiyama, T., Nakai, Y., Nishino, K., Osada, M., Ryo, A., Hirano, H., Koike, T. & Kimura, Y. Evaluation of four phosphopeptide enrichment strategies for mass spectrometry-based proteomic analysis. *Proteomics*. **22**, e2100216 (2022).
79. Paulo, J. A., Navarrete-Perea, J., Erickson, A. R., Knott, J. & Gygi, S. P. An Internal Standard for Assessing Phosphopeptide Recovery from Metal Ion/Oxide Enrichment Strategies. J Am Soc Mass Spectrom. **29**, 1505-1511 (2018).
80. Zhang, Y., Wang, J., Ding, M. & Yu, Y. Site-specific characterization of the Asp- and Glu-ADP-ribosylated proteome. *Nat. Methods*. **10**, 981-984 (2013).
81. Müller, K. H., Hayward, R., Rajan, R., Whitehead, M., Cobb, A. M., Ahmad, S., Sun, M., Goldberga, I., Li, R., Bashtanova, U., Puszkarska, A. M., Reid, D. G., Brooks, R. A., Skepper, J. N., Bordoloi, J., Chow, W. Y., Oschkinat, H., Groombridge, A., Scherman, O. A., Harrison, J. A., Verhulst, A., D'Haese, P. C., Neven, E., Needham, L. M., Lee, S. F., Shanahan, C. M. & Duer, M. J. Poly(ADP-Ribose) Links the DNA Damage Response and Biomineralization. *Cell Rep*. **27**, 3124-3138 (2019).
82. Gulen, B., Rosselin, M., Fauser, J., Albers, M. F., Pett, C., Krisp, C., Pogenberg, V., Schlüter, H., Hedberg, C. & Itzen, A. Identification of targets of AMPylating Fic enzymes by co-substrate-mediated covalent capture. *Nat. Chem*. **12**, 732-739 (2020).
83. Ardito, F., Giuliani, M., Perrone, D., Troiano, G. & Lo Muzio, L. The crucial role of protein phosphorylation in cell signaling and its use as targeted therapy (Review). *Int. J. Mol. Med*. **40**, 271-280 (2017).
84. Kawamitsu, H., Hoshino, H., Okada, H., Miwa, M., Momoi, H. & Sugimura, T. Monoclonal antibodies to poly(adenosine diphosphate ribose) recognize different structures. *Biochemistry*. **23**, 3771-3777 (1984).

85. Gagné, J. P., Isabelle, M., Lo, K. S., Bourassa, S., Hendzel, M. J., Dawson, V. L., Dawson, T. M. & Poirier, G. G. Proteome-wide identification of poly(ADP-ribose) binding proteins and poly(ADP-ribose)-associated protein complexes. *Nucleic Acids Res*. **36**, 6959-6976 (2008).
86. Chen, Q., Bian, C., Wang, X., Liu, X., Ahmad Kassab, M., Yu, Y. & Yu, X. ADP-ribosylation of histone variant H2AX promotes base excision repair. *EMBO J.* **40**, e104542 (2021).
87. Lu, A. Z., Abo, R., Ren, Y., Gui, B., Mo, J. R., Blackwell, D., Wigle, T., Keilhack, H. & Niepel, M. Enabling drug discovery for the PARP protein family through the detection of mono-ADP-ribosylation. *Biochem. Pharmacol*. **167**, 97-106 (2019).
88. Bonfiglio, J. J., Leidecker, O., Dauben, H., Longarini, E. J., Colby, T., San Segundo-Acosta, P., Perez, K. A. & Matic, I. An HPF1/PARP1-Based Chemical Biology Strategy for Exploring ADP-Ribosylation. *Cell*. **183**, 1086-1102 (2020).
89. Forst, A. H., Karlberg, T., Herzog, N., Thorsell, A. G., Gross, A., Feijs, K. L., Verheugd, P., Kursula, P., Nijmeijer, B., Kremmer, E., Kleine, H., Ladurner, A. G., Schüler, H. & Lüscher, B. Recognition of mono-ADP-ribosylated ARTD10 substrates by ARTD8 macrodomains. *Structure*. **21**, 462-475 (2013).
90. Gibson, B. A., Conrad, L. B., Huang, D. & Kraus, W. L. Generation and Characterization of Recombinant Antibody-like ADP-Ribose Binding Proteins. *Biochemistry*. **56**, 6305-6316 (2017).
91. Zhang, Y., Liu, S., Mickanin, C., Feng, Y., Charlat, O., Michaud, G. A., Schirle, M., Shi, X., Hild, M., Bauer, A., Myer, V. E., Finan, P. M., Porter, J. A., Huang, S. M. & Cong, F. RNF146 is a poly(ADP-ribose)-directed E3 ligase that regulates axin degradation and Wnt signalling. *Nat. Cell. Biol*. *13*, 623-629 (2011).
92. Wang, Z., Michaud, G. A., Cheng, Z., Zhang, Y., Hinds, T. R., Fan, E., Cong, F. & Xu, W. Recognition of the iso-ADP-ribose moiety in poly(ADP-ribose) by WWE domains suggests a general mechanism for poly(ADP-ribosyl)ation-dependent ubiquitination. *Genes Dev*. **26**, 235-240 (2012).
93. Allen, M. D., Buckle, A. M., Cordell, S. C., Löwe, J. & Bycroft, M. The crystal structure of AF1521 a protein from Archaeoglobus fulgidus with homology to the non-histone domain of macroH2A. *J. Mol. Biol*. **330**, 503-511 (2003).
94. Karras, G. I., Kustatscher, G., Buhecha, H. R., Allen, M. D., Pugieux, C., Sait, F., Bycroft, M. & Ladurner, A. G. The macro domain is an ADP-ribose binding module. *EMBO J*. **24**, 1911-1920 (2005).

95. Buch-Larsen, S. C., Rebak, A. K. L. F. S., Hendriks, I. A. & Nielsen, M. L. Temporal and Site-Specific ADP-Ribosylation Dynamics upon Different Genotoxic Stresses. *Cells*. **10**, 2927 (2021).
96. Nowak, K., Rosenthal, F., Karlberg, T., Bütepage, M., Thorsell, A. G., Dreier, B., Grossmann, J., Sobek, J., Imhof, R., Lüscher, B., Schüler, H., Plückthun, A., Leslie Pedrioli, D. M. & Hottiger, M. O. Engineering Af1521 improves ADP-ribose binding and identification of ADP-ribosylated proteins. *Nat. Commun*. **11**, 5199 (2020).
97. Larsen, S. C., Hendriks, I. A., Lyon, D., Jensen, L. J. & Nielsen, M. L. Systems-wide Analysis of Serine ADP-Ribosylation Reveals Widespread Occurrence and Site-Specific Overlap with Phosphorylation. *Cell Rep*. **24**, 2493-2505 (2018).
98. Hendriks, I. A., Larsen, S. C. & Nielsen, M. L. An Advanced Strategy for Comprehensive Profiling of ADP-ribosylation Sites Using Mass Spectrometry-based Proteomics. *Mol. Cell. Proteomics*. **18**, 1010-1026 (2019).
99. Buch-Larsen, S. C., Hendriks, I. A., Lodge, J. M., Rykær, M., Furtwängler, B., Shishkova, E., Westphall, M. S., Coon, J. J. & Nielsen, M. L. Mapping Physiological ADP-Ribosylation Using Activated Ion Electron Transfer Dissociation. *Cell Rep*. **32**, 10817 (2020).
100. Hendriks, I. A., Buch-Larsen, S. C., Prokhorova, E., Elsborg, J. D., Rebak, A. K. L. F. S., Zhu, K., Ahel, D., Lukas, C., Ahel, I. & Nielsen, M. L. The regulatory landscape of the human HPF1- and ARH3-dependent ADP-ribosylome. Nat. Commun. **12**, 5893 (2021).
101. Gill, D. M. & Woolkalis, M. J. Cholera toxin-catalyzed [32P]ADP-ribosylation of proteins. *Methods Enzymol*. **195**, 267-280 (1991).
102. Panzeter, P. L., Realini, C. A., Althaus, F. R. Noncovalent interactions of poly(adenosine diphosphate ribose) with histones. Biochemistry. **31**, 1379-1385 (1992).
103. Chen, Q., Kassab, M. A., Dantzer, F. & Yu, X. PARP2 mediates branched poly ADP-ribosylation in response to DNA damage. *Nat. Commun*. **9**, 3233 (2018).
104. Zhang, J. & Snyder, S. H. Purification of a nitric oxide-stimulated ADP-ribosylated protein using biotinylated beta-nicotinamide adenine dinucleotide. *Biochemistry*. **32**, 2228-2233 (1993).
105. Du, J., Jiang, H. & Lin, H. Investigating the ADP-ribosyltransferase activity of sirtuins with NAD analogues and 32P-NAD. *Biochemistry.* **48**, 2878-2890 (2009).

106. Jiang, H., Kim, J. H., Frizzell, K. M., Kraus, W. L. & Lin, H. Clickable NAD analogues for labeling substrate proteins of poly(ADP-ribose) polymerases. *J. Am. Chem. Soc*. **132**, 9363-9372 (2010).
107. Buntz, A., Wallrodt, S., Gwosch, E., Schmalz, M., Beneke, S., Ferrando-May, E., Marx, A. & Zumbusch, A. Real-Time Cellular Imaging of Protein Poly(ADP-ribos)ylation. *Angew. Chem. Int. Ed*. **55**, 11256-11260 (2016).
108. Wallrodt, S., Simpson, E. L. & Marx, A. Investigation of the action of poly(ADP-ribose)-synthesising enzymes on NAD^+ analogues. *Beilstein J. Org. Chem*. **13**, 495-501 (2017).
109. Lehner, M., Rieth, S., Höllmüller, E., Spliesgar, D., Mertes, B., Stengel, F. & Marx, A. Profiling of the ADP-Ribosylome in Living Cells. *Angew. Chem. Int. Ed*. **61**, e202200977 (2022).
110. Wallrodt, S., Buntz, A., Wang, Y., Zumbusch, A. & Marx, A. Bioorthogonally Functionalized NAD(+) Analogues for In-Cell Visualization of Poly(ADP-Ribose) Formation. *Angew. Chem. Int. Ed*. **55**, 7660-7664 (2016).
111. Langelier, M. F., Zandarashvili, L., Aguiar, P. M., Black, B. E. & Pascal, J. M. NAD^+ analog reveals PARP-1 substrate-blocking mechanism and allosteric communication from catalytic center to DNA-binding domains. *Nat. Commun*. **9**, 844 (2018).
112. Wang, Y., Rösner, D., Grzywa, M. & Marx, A. Chain-terminating and clickable NAD^+ analogues for labeling the target proteins of ADP-ribosyltransferases. *Angew. Chem. Int. Ed*. **53**, 8159-8162 (2014).
113. Zhang, X. N., Cheng, Q., Chen, J., Lam, A. T., Lu, Y., Dai, Z., Pei, H., Evdokimov, N. M., Louie, S. G. & Zhang, Y. A ribose-functionalized NAD^+ with unexpected high activity and selectivity for protein poly-ADP-ribosylation. *Nat. Commun*. **10**, 4196 (2019).
114. Carter-O'Connell, I., Jin, H., Morgan, R. K., David, L. L. & Cohen, M. S. Engineering the substrate specificity of ADP-ribosyltransferases for identifying direct protein targets. *J. Am. Chem. Soc*. **136**, 5201-5204 (2014).
115. Carter-O'Connell, I., Jin, H., Morgan, R. K., Zaja, R., David, L. L., Ahel, I. & Cohen, M. S. Identifying Family-Member-Specific Targets of Mono-ARTDs by Using a Chemical Genetics Approach. *Cell Rep*. **14**, 621-631 (2016).
116. Carter-O'Connell, I., Vermehren-Schmaedick, A., Jin, H., Morgan, R. K., David, L. L. & Cohen, M. S. Combining Chemical Genetics with Proximity-Dependent Labeling Reveals Cellular Targets of Poly(ADP-ribose) Polymerase 14 (PARP14). *ACS Chem. Biol*. **13**, 2841-2848 (2018).

117. Rodriguez, K. M., Buch-Larsen, S. C., Kirby, I. T., Siordia, I. R., Hutin, D., Rasmussen, M., Grant, D. M., David, L. L., Matthews, J., Nielsen, M. L. & Cohen, M. S. Chemical genetics and proteome-wide site mapping reveal cysteine MARylation by PARP-7 on immune-relevant protein targets. *Elife*. **10**, e60480 (2021).
118. Gibson, B. A., Zhang, Y., Jiang, H., Hussey, K. M., Shrimp, J. H., Lin, H., Schwede, F., Yu, Y. & Kraus, W. L. Chemical genetic discovery of PARP targets reveals a role for PARP-1 in transcription elongation. *Science*. **353**, 45-50 (2016).
119. Palavalli Parsons, L. H., Challa, S., Gibson, B. A., Nandu, T., Stokes, M. S., Huang, D., Lea, J. S. & Kraus, W. L. Identification of PARP-7 substrates reveals a role for MARylation in microtubule control in ovarian cancer cells. Elife. **10**, e60481 (2021).
120. Lam, A. T., Zhang, X. N., Courouble, V. V., Strutzenberg, T. S., Pei, H., Stiles, B. L., Louie, S. G., Griffin, P. R. & Zhang, Y. A Bifunctional NAD^+ for Profiling Poly-ADP-Ribosylation-Dependent Interacting Proteins. ACS Chem. Biol. **16**, 389-396 (2021).
121. Šileikytė, J., Sundalam, S., David, L. L. & Cohen, M. S. Chemical Proteomics Approach for Profiling the NAD Interactome. *J. Am. Chem. Soc*. **143**, 6787-6791 (2021).
122. Abele, F., Höfer, K., Bernhard, P., Grawenhoff, J., Seidel, M., Krause, A., Kopf, S., Schröter, M. & Jäschke, A. A Novel NAD-RNA Decapping Pathway Discovered by Synthetic Light-Up NAD-RNAs. *Biomolecules*. **10**, 513 (2020).
123. Hertz, N. T., Wang, B. T., Allen, J. J., Zhang, C., Dar, A. C., Burlingame, A. L. & Shokat, K. M. Chemical genetic approach for kinase-substrate mapping by covalent capture of thiophosphopeptides and analysis by mass spectrometry. *Curr. Protoc. Chem. Biol*. **2**, 15-36 (2010).
124. Islam, K., Bothwell, I., Chen, Y., Sengelaub, C., Wang, R., Deng, H. & Luo, M. Bioorthogonal profiling of protein methylation using azido derivative of S-adenosyl-L-methionine. *J. Am. Chem. Soc*. **134**, 5909-5915 (2012).
125. Yang, C., Mi, J., Feng, Y., Ngo, L., Gao, T., Yan, L. & Zheng, Y. G. Labeling lysine acetyltransferase substrates with engineered enzymes and functionalized cofactor surrogates. *J. Am. Chem. Soc*. **135**, 7791-7794 (2013).
126. Kim, I. K., Stegeman, R. A., Brosey, C. A. & Ellenberger, T. A quantitative assay reveals ligand specificity of the DNA scaffold repair protein XRCC1 and efficient disassembly of complexes of XRCC1 and the poly(ADP-ribose) polymerase 1 by poly(ADP-ribose) glycohydrolase. *J. Biol. Chem*. **290**, 3775-3783 (2015).
127. Min, W., Bruhn, C., Grigaravicius, P., Zhou, Z. W., Li, F., Krüger, A., Siddeek, B., Greulich, K. O., Popp, O., Meisezahl, C., Calkhoven, C. F., Bürkle, A., Xu, X. & Wang,

Z. Q. Poly(ADP-ribose) binding to Chk1 at stalled replication forks is required for S-phase checkpoint activation. *Nat. Commun*. **4**, 2993 (2013).

128. Gagné, J. P., Isabelle, M., Lo, K. S., Bourassa, S., Hendzel, M. J., Dawson, V. L., Dawson, T. M. & Poirier, G. G. Proteome-wide identification of poly(ADP-ribose) binding proteins and poly(ADP-ribose)-associated protein complexes. *Nucleic Acids Res*. **36**, 6959-6976 (2008).
129. Dasovich, M., Beckett, M. Q., Bailey, S., Ong, S. E., Greenberg, M. M. & Leung, A. K. L. Identifying Poly(ADP-ribose)-Binding Proteins with Photoaffinity-Based Proteomics. *J. Am. Chem. Soc*. **143**, 3037-3042 (2021).
130. Kliza, K. W., Liu, Q., Roosenboom, L. W. M., Jansen, P. W. T. C., Filippov, D. V. & Vermeulen, M. Reading ADP-ribosylation signaling using chemical biology and interaction proteomics. *Mol. Cell*. **81**, 4552-4567 (2021).
131. Chen, Y. G., Kowtoniuk, W. E., Agarwal, I., Shen, Y. & Liu, D. R. LC/MS analysis of cellular RNA reveals NAD-linked RNA. *Nat. Chem. Biol*. **5**, 879-881 (2009).
132. Kiledjian, M. Eukaryotic RNA 5'-End NAD^+ Capping and DeNADding. Trends Cell Biol. **28**, 454-464 (2018).
133. Parker, C. G., Pratt, M. R. Click Chemistry in Proteomic Investigations. *Cell*. **180**, 605-632 (2020).
134. Fantoni, N. Z., El-Sagheer, A. H. & Brown, T. A Hitchhiker's Guide to Click-Chemistry with Nucleic Acids. *Chem. Rev*. **121**, 7122-7154 (2021).
135. Horisawa, K. Specific and quantitative labeling of biomolecules using click chemistry. *Front. Physiol.* **5**, 457 (2014).
136. Duan, X., Li, Y., Rajan, N. K., Routenberg, D. A., Modis, Y. & Reed, M. A. Quantification of the affinities and kinetics of protein interactions using silicon nanowire biosensors. *Nat. Nanotechnol*. **7**, 401-407 (2012).
137. Li, P., Zhen, Y. & Yu, Y. Site-specific analysis of the Asp- and Glu-ADP-ribosylated proteome by quantitative mass spectrometry. *Methods Enzymol*. **626**, 301-321 (2019).
138. Jiang, X., Hao, X., Jing, L., Wu, G., Kang, D., Liu, X. & Zhan, P. Recent applications of click chemistry in drug discovery. *Expert Opin. Drug Discov*. **14**, 779-789 (2019).
139. Li, L. & Zhang, Z. Development and Applications of the Copper-Catalyzed Azide-Alkyne Cycloaddition (CuAAC) as a Bioorthogonal Reaction. *Molecules*. **21**, 139 (2016).

140. Agard, N. J, Prescher, J. A. & Bertozzi C. R. A Strain-Promoted [3 + 2] Azide-Alkyne Cycloaddition for Covalent Modification of Biomolecules in Living Systems. *J. Am. Chem. Soc*. **126**, 15046-15047 (2004).
141. Macias-Contreras, M., He, H., Little, K. N., Lee, J. P., Campbell, R. P., Royzen, M. & Zhu, L. SNAP/CLIP-Tags and Strain-Promoted Azide-Alkyne Cycloaddition (SPAAC)/Inverse Electron Demand Diels-Alder (IEDDA) for Intracellular Orthogonal/Bioorthogonal Labeling. *Bioconjug. Chem*. **31**, 1370-1381 (2020).
142. Oliveira, B. L., Guo, Z. & Bernardes, G. J. L. Inverse electron demand Diels-Alder reactions in chemical biology. *Chem. Soc. Rev.* **46**, 4895-4950 (2017).
143. Edem, P. E., Sinnes, J. P., Pektor, S., Bausbacher, N., Rossin, R., Yazdani, A., Miederer, M., Kjær, A., Valliant, J. F., Robillard, M. S., Rösch, F. & Herth, M. M. Evaluation of the inverse electron demand Diels-Alder reaction in rats using a scandium-44-labelled tetrazine for pretargeted PET imaging. *EJNMMI Res*. **9**, 49 (2019).
144. Yang, B., Kwon, K., Jana, S., Kim, S., Avila-Crump, S., Tae, G., Mehl, R. A. & Kwon, I. Temporal Control of Efficient *In Vivo* Bioconjugation Using a Genetically Encoded Tetrazine-Mediated Inverse-Electron-Demand Diels-Alder Reaction. *Bioconjug. Chem*. **31**, 2456-2464 (2020).
145. Saxon, E. & Bertozzi, C. R. Cell surface engineering by a modified Staudinger reaction. *Science*. **287**, 2007-2010 (2000).
146. Ovaa, H., van Swieten, P. F., Kessler, B. M., Leeuwenburgh, M. A., Fiebiger, E., van den Nieuwendijk, A. M., Galardy, P. J., van der Marel, G. A., Ploegh, H. L. & Overkleeft, H. S. Chemistry in living cells: detection of active proteasomes by a two-step labeling strategy. *Angew. Chem. Int. Ed*. **42**, 3626-3629 (2003).
147. Köhn, M. & Breinbauer, R. The Staudinger Ligation—A Gift to Chemical Biology. *Angew. Chemie Int. Ed.* **43**, 3106–3116 (2004).
148. Lang, K. & Chin, J. W. Bioorthogonal reactions for labeling proteins. *ACS Chem. Biol*. **9**, 16-20 (2014).
149. Wallace, S. R., Chihab, L. Y., Yamasaki, M., Yoshinaga, B. T., Torres, Y. M., Rideaux, D., Javed, Z., Turumella, S., Zhang, M., Lawton, D. R., Fuller, A. A. & Carter-O'Connell, I. Rapid Analysis of ADP-Ribosylation Dynamics and Site-Specificity Using TLC-MALDI. *ACS Chem. Biol*. **16**, 2137-2143 (2021).
150. Rosenthal, F., Nanni, P., Barkow-Oesterreicher, S. & Hottiger, M. O. Optimization of LTQ-Orbitrap Mass Spectrometer Parameters for the Identification of ADP-Ribosylation Sites. *J. Proteome Res*. **14**, 4072-4079 (2015).

151. Pourfarjam, Y., Kasson S., Tran. L., Ho, C., Lim, S. & Kim, I. K. PARG has a robust endo-glycohydrolase activity that releases protein-free poly(ADP-ribose) chains. *Biochem. Biophys. Res. Commun*. **527**, 818-823 (2020).
152. Fontana, P., Bonfiglio, J. J., Palazzo, L., Bartlett, E., Matic, I. & Ahel, I. Serine ADP-ribosylation reversal by the hydrolase ARH3. *Elife*. **6**, e28533 (2017).
153. Mueller-Dieckmann, C., Kernstock, S., Lisurek, M., von Kries, J. P., Haag, F., Weiss, M. S. & Koch-Nolte, F. The structure of human ADP-ribosylhydrolase 3 (ARH3) provides insights into the reversibility of protein ADP-ribosylation. Proc. Natl. Acad. Sci. **103**, 15026-15031 (2006).
154. Wielckens, K., Bredehorst, R., Adamietz, P. & Hilz, H. Protein-bound polymeric and monomeric ADP-ribose residues in hepatic tissues. Comparative analyses using a new procedure for the quantification of poly(ADP-ribose). *Eur. J. Biochem*. **117**, 69-74 (1981).
155. Moss, J., Yost, D. A. & Stanley, S. J. Amino acid-specific ADP-ribosylation. J Biol Chem. 1983 May 25; **258**, 6466-6470 (1983).
156. Palazzo, L., Leidecker, O., Prokhorova, E., Dauben, H., Matic, I. & Ahel, I. Serine is the major residue for ADP-ribosylation upon DNA damage. *Elife*. **7**, e34334 (2018).
157. Zhen, Y., Zhang, Y. & Yu, Y. A Cell-Line-Specific Atlas of PARP-Mediated Protein Asp/Glu-ADP-Ribosylation in Breast Cancer. *Cell Rep*. **21**, 2326-2337 (2017).
158. Gagné, J. P., Langelier, M. F., Pascal, J. M. & Poirier, G. G. Hydrofluoric Acid-Based Derivatization Strategy To Profile PARP-1 ADP-Ribosylation by LC-MS/MS. *J. Proteome Res*. **17**, 2542-2551 (2018).
159. Chapman, J. D., Gagné, J. P., Poirier, G. G. & Goodlett, D. R. Mapping PARP-1 auto-ADP-ribosylation sites by liquid chromatography-tandem mass spectrometry. *J. Proteome Res*. **12**, 1868-1880 (2013).
160. Daniels, C. M., Ong, S. E. & Leung, A. K. Phosphoproteomic approach to characterize protein mono- and poly(ADP-ribosyl)ation sites from cells. *J. Proteome Res*. **13**, 3510-3522 (2014).
161. Palazzo, L., Thomas, B., Jemth, A. S., Colby, T., Leidecker, O., Feijs, K. L., Zaja, R., Loseva, O., Puigvert, J. C., Matic, I., Helleday, T. & Ahel, I. Processing of protein ADP-ribosylation by Nudix hydrolases. *Biochem. J*. **468**, 293-301 (2015).
162. Daniels, C. M., Thirawatananond, P., Ong, S. E., Gabelli, S. B. & Leung, A. K. Nudix hydrolases degrade protein-conjugated ADP-ribose. Sci. Rep. **5**, 18271 (2015).

163. Daniels, C. M., Ong, S. E. & Leung, A. K. L. ADP-Ribosylated Peptide Enrichment and Site Identification: The Phosphodiesterase-Based Method. *Methods Mol. Biol*. **1608**, 79-93 (2017).
164. Westcott, N. P., Fernandez, J. P., Molina, H. & Hang, H. C. Chemical proteomics reveals ADP-ribosylation of small GTPases during oxidative stress. *Nat. Chem. Biol*. **13**, 302-308 (2017).
165. Matic, I., Ahel, I. & Hay, R. T. Reanalysis of phosphoproteomics data uncovers ADP-ribosylation sites. *Nat. Methods*. **9**, 771-772 (2012).
166. Olsen, J. V., Macek, B., Lange, O., Makarov, A., Horning, S. & Mann, M. Higher-energy C-trap dissociation for peptide modification analysis. *Nat. Methods*. **4**, 709-712 (2007).
167. Johnson, A. R. & Carlson, E. E. Collision-Induced Dissociation Mass Spectrometry: A Powerful Tool for Natural Product Structure Elucidation. *Anal. Chem*. **87**, 10668-10678 (2015).
168. Martin, D. B., Eng, J. K., Nesvizhskii, A. I., Gemmill, A. & Aebersold, R. Investigation of neutral loss during collision-induced dissociation of peptide ions. *Anal. Chem*. **7**, 4870-4882 (2005).
169. Brown, R., Stuart, S. A., Houel, S., Ahn, N. G. & Old, W. M. Large-Scale Examination of Factors Influencing Phosphopeptide Neutral Loss during Collision Induced Dissociation. *J. Am. Soc. Mass Spectrom*. **26**, 1128-1142 (2015).
170. Zhurov, K. O., Fornelli, L., Wodrich, M. D., Laskay, Ü. A. & Tsybin, Y. O. Principles of electron capture and transfer dissociation mass spectrometry applied to peptide and protein structure analysis. *Chem. Soc. Rev*. **42**, 5014-5030 (2013).
171. Han, H., Xia, Y. & McLuckey, S. A. Ion trap collisional activation of c and z* ions formed via gas-phase ion/ion electron-transfer dissociation. *J. Proteome Res*. **6**, 3062-3069 (2007).
172. Lermyte, F., Verschueren, T., Brown, J. M., Williams, J. P., Valkenborg, D. & Sobott, F. Characterization of top-down ETD in a travelling-wave ion guide. *Methods*. **89**, 22-29 (2015).
173. Frese, C. K., Altelaar, A. F., van den Toorn, H., Nolting, D., Griep-Raming, J., Heck, A. J. & Mohammed, S. Toward full peptide sequence coverage by dual fragmentation combining electron-transfer and higher-energy collision dissociation tandem mass spectrometry. *Anal. Chem*. **84**, 9668-9673 (2012).
174. Penkert, M., Hauser, A., Harmel, R., Fiedler, D., Hackenberger, C. P. R, & Krause, E. Electron Transfer/Higher Energy Collisional Dissociation of Doubly Charged Peptide

Ions: Identification of Labile Protein Phosphorylations. *J. Am. Soc. Mass Spectrom*. **30**, 1578-1585 (2019).

175. Bilan, V., Leutert, M., Nanni, P., Panse, C. & Hottiger, M. O. Combining Higher-Energy Collision Dissociation and Electron-Transfer/Higher-Energy Collision Dissociation Fragmentation in a Product-Dependent Manner Confidently Assigns Proteomewide ADP-Ribose Acceptor Sites. Anal. Chem. **89**, 1523-1530 (2017).
176. Yu, Q., Wang, B., Chen, Z., Urabe, G., Glover, M. S., Shi, X., Guo, L. W., Kent, K. C. & Li, L. Electron-Transfer/Higher-Energy Collision Dissociation (EThcD)-Enabled Intact Glycopeptide/Glycoproteome Characterization. *J. Am. Soc. Mass Spectrom*. **28**, 1751-1764 (2017).
177. Frese. C. K., Zhou, H., Taus, T., Altelaar, A. F., Mechtler, K., Heck, A. J. & Mohammed, S. Unambiguous phosphosite localization using electron-transfer/higher-energy collision dissociation (EThcD). *J. Proteome Res*. **12**, 1520-1525 (2013).
178. Ledvina, A. R., McAlister, G. C., Gardner, M. W., Smith, S. I., Madsen, J. A., Schwartz, J. C., Stafford, G. C. Jr., Syka, J. E., Brodbelt, J. S. & Coon, J. J. Infrared photoactivation reduces peptide folding and hydrogen-atom migration following ETD tandem mass spectrometry. *Angew. Chem. Int. Ed*. **48**, 8526-8528 (2009).
179. Ledvina, A. R., Beauchene, N. A., McAlister, G. C., Syka, J. E., Schwartz, J. C., Griep-Raming, J., Westphall, M. S. & Coon, J. J. Activated-ion electron transfer dissociation improves the ability of electron transfer dissociation to identify peptides in a complex mixture. *Anal. Chem*. **82**, 10068-10074 (2010).
180. Riley, N. M., Westphall, M. S. & Coon, J. J. Activated Ion-Electron Transfer Dissociation Enables Comprehensive Top-Down Protein Fragmentation. *J. Proteome Res*. **16**, 2653-2659 (2017).
181. Fouda, A. E. & Pflum, M. K. A Cell-Permeable ATP Analogue for Kinase-Catalyzed Biotinylation. *Angew. Chem. Int. Ed*. **54**, 9618-9621 (2015).
182. Morgan, R. K. & Cohen, M. S. A Clickable Aminooxy Probe for Monitoring Cellular ADP-Ribosylation. *ACS Chem. Biol*. **10**, 1778-1784 (2015).
183. Okabe, K., Yaku, K., Tobe, K. & Nakagawa, T. Implications of altered NAD metabolism in metabolic disorders. *J. Biomed. Sci*. **26**, 34 (2019).
184. Xie, N., Zhang, L., Gao, W., Huang, C., Huber, P. E., Zhou, X., Li, C., Shen, G. & Zou, B. NAD^+ metabolism: pathophysiologic mechanisms and therapeutic potential. *Signal Transduct. Target Ther*. **5**, 227 (2020).

185. Kalesh, K., Lukauskas, S., Borg, A. J., Snijders, A. P., Ayyappan, V., Leung, A. K. L., Haskard, D. O. & DiMaggio, P. A. An Integrated Chemical Proteomics Approach for Quantitative Profiling of Intracellular ADP-Ribosylation. *Sci. Rep*. **9**, 6655 (2019).
186. Boswell-Casteel, R. C. & Hays, F. A. Equilibrative nucleoside transporters-A review. *Nucleosides Nucleotides Nucleic Acids*. **36**, 7-30 (2017).
187. Poddar, S. K., Sifat, A. E., Haque, S., Nahid, N. A., Chowdhury, S. & Mehedi, I. Nicotinamide Mononucleotide: Exploration of Diverse Therapeutic Applications of a Potential Molecule. *Biomolecules*. **9**, 34 (2019).
188. Kulikova, V., Shabalin, K., Nerinovski, K., Yakimov, A., Svetlova, M., Solovjeva, L., Kropotov, A., Khodorkovskiy, M., Migaud, M. E., Ziegler, M. & Nikiforov, A. Degradation of Extracellular NAD^+ Intermediates in Cultures of Human HEK293 Cells. *Metabolites*. **9**, 293 (2019).
189. Kropotov, A., Kulikova, V., Nerinovski, K., Yakimov, A., Svetlova, M., Solovjeva, L., Sudnitsyna, J., Migaud, M. E., Khodorkovskiy, M., Ziegler, M. & Nikiforov, A. Equilibrative Nucleoside Transporters Mediate the Import of Nicotinamide Riboside and Nicotinic Acid Riboside into Human Cells. Int *J. Mol. Sci*. **22**, 1391 (2021).
190. Ratajczak, J., Joffraud, M., Trammell, S. A., Ras, R., Canela, N., Boutant, M., Kulkarni, S. S., Rodrigues, M., Redpath, P., Migaud, M. E., Auwerx, J., Yanes, O., Brenner, C. & Cantó, C. NRK1 controls nicotinamide mononucleotide and nicotinamide riboside metabolism in mammalian cells. *Nat. Commun*. **7**, 13103 (2016).
191. Boison, D. Adenosine kinase: exploitation for therapeutic gain. *Pharmacol. Rev*. **65**, 906-943 (2013).
192. Panayiotou, C., Solaroli, N. & Karlsson, A. The many isoforms of human adenylate kinases. *Int. J. Biochem. Cell Biol*. **49**, 75-83 (2014).
193. Jonckheere, A. I., Smeitink, J. A. & Rodenburg, R. J. Mitochondrial ATP synthase: architecture, function and pathology. *J. Inherit. Metab. Dis*. **35**, 211-225 (2012).
194. Ryu, K. W., Nandu, T., Kim, J., Challa, S., DeBerardinis, R. J. & Kraus, W. L. Metabolic regulation of transcription through compartmentalized NAD^+ biosynthesis. *Science*. **360**, eaan5780 (2018).
195. Mayer, P. R., Huang, N., Dewey, C. M., Dries, D. R., Zhang, H. & Yu, G. Expression, localization, and biochemical characterization of nicotinamide mononucleotide adenylyltransferase 2. *J. Biol. Chem*. **285**, 40387-40396 (2010).
196. Martínez-Reyes, I. & Chandel, N. S. Mitochondrial TCA cycle metabolites control physiology and disease. Nat Commun. **11**, 102 (2020).

197. Peterson, L. W. & McKenna, C. E. Prodrug approaches to improving the oral absorption of antiviral nucleotide analogues. *Expert Opin. Drug Deliv*. **6**, 405-420 (2009).
198. Pradere, U., Garnier-Amblard, E. C., Coats, S. J., Amblard, F. & Schinazi, R. F. Synthesis of nucleoside phosphate and phosphonate prodrugs. *Chem. Rev*. **114**, 9154-9218 (2014).
199. Derudas,, M., Carta, D., Brancale, A., Vanpouille, C., Lisco, A., Margolis, L., Balzarini, J. & McGuigan, C. The application of phosphoramidate protide technology to acyclovir confers anti-HIV inhibition. J. Med. Chem. **52**, 5520-5530 (2009).
200. Furuta, Y., Gowen, B. B., Takahashi, K., Shiraki, K., Smee, D. F. & Barnard, D. L. Favipiravir (T-705), a novel viral RNA polymerase inhibitor. *Antiviral Res*. **100**, 446-454 (2013).
201. Slusarczyk, M., Serpi, M. & Pertusati, F. Phosphoramidates and phosphonamidates (ProTides) with antiviral activity. *Antivir. Chem. Chemother*. **26**, 2040206618775243 (2018).
202. McGuigan, C., Murziani, P., Slusarczyk, M., Gonczy, B., Vande Voorde, J., Liekens, S. & Balzarini, J. Phosphoramidate ProTides of the anticancer agent FUDR successfully deliver the preformed bioactive monophosphate in cells and confer advantage over the parent nucleoside. *J. Med. Chem*. **54**, 7247-7258 (2011).
203. Mehellou, Y., Rattan, H. S. & Balzarini, J. The ProTide Prodrug Technology: From the Concept to the Clinic. *J. Med. Chem*. **61**,2211-2226 (2018).
204. Saboulard, D., Naesens, L., Cahard, D., Salgado, A., Pathirana, R., Velazquez, S., McGuigan, C., De Clercq, E. & Balzarini, J. Characterization of the activation pathway of phosphoramidate triester prodrugs of stavudine and zidovudine. *Mol. Pharmacol*. **56**, 693-704 (1999).
205. Yang, Y., Mohammed, F. S., Zhang, N. & Sauve, A. A. Dihydronicotinamide riboside is a potent NAD^+ concentration enhancer *in vitro* and *in vivo*. *J. Biol. Chem*. **294**, 9295-9307 (2019).
206. Giroud-Gerbetant, J., Joffraud, M., Giner, M. P., Cercillieux, A., Bartova, S., Makarov, M. V., Zapata-Pérez, R., Sánchez-García, J. L., Houtkooper, R. H., Migaud, M. E., Moco, S. & Canto, C. A reduced form of nicotinamide riboside defines a new path for NAD^+ biosynthesis and acts as an orally bioavailable NAD^+ precursor. *Mol. Metab*. **30**, 192-202 (2019).
207. Yang, Y., Zhang, N., Zhang, G. & Sauve, A. A. NRH salvage and conversion to NAD^+ requires NRH kinase activity by adenosine kinase. *Nat. Metab*. **2**, 364-379 (2020).

208. Gong, B., Pan, Y., Vempati, P., Zhao, W., Knable, L., Ho, L., Wang, J., Sastre, M., Ono, K., Sauve, A. A. & Pasinetti, G. M. Nicotinamide riboside restores cognition through an upregulation of proliferator-activated receptor-γ coactivator 1α regulated β-secretase 1 degradation and mitochondrial gene expression in Alzheimer's mouse models. *Neurobiol. Aging*. **34**, 1581-1588 (2013).
209. Grozio, A., Mills, K. F., Yoshino, J., Bruzzone, S., Sociali, G., Tokizane, K., Lei, H. C., Cunningham, R., Sasaki, Y., Migaud, M. E. & Imai, S. I. Slc12a8 is a nicotinamide mononucleotide transporter. *Nat. Metab*. **1**, 47-57 (2019).
210. Meng, X. Y., Zhang, H. X., Mezei, M. & Cui, M. Molecular docking: a powerful approach for structure-based drug discovery. *Curr. Comput. Aided Drug Des*. **7**, 146-157 (2011).
211. Pagadala, N. S., Syed, K. & Tuszynski, J. Software for molecular docking: a review. *Biophys. Rev*. **9**, 91-102 (2017).
212. Yan, Y., Zhang, D., Zhou, P., Li, B. & Huang, S. Y. HDOCK: a web server for protein-protein and protein-DNA/RNA docking based on a hybrid strategy. Nucleic. Acids. Res. **45**, W365-W373 (2017).
213. Corbeil, C. R., Williams, C. I. & Labute, P. Variability in docking success rates due to dataset preparation. *J. Comput. Aided Mol. Des*. **26**, 775-786 (2012).
214. Muhammed, M. T. & Aki-Yalcin, E. Homology modeling in drug discovery: Overview, current applications, and future perspectives. *Chem. Biol. Drug Des*. **93**, 12-20 (2019).
215. Hameduh, T., Haddad, Y., Adam, V. & Heger, Z. Homology modeling in the time of collective and artificial intelligence. *Comput. Struct. Biotechnol. J*. **18**, 3494-3506 (2020).
216. Rost, B. & Sander, C. Bridging the protein sequence-structure gap by structure predictions. *Annu. Rev. Biophys. Biomol. Struct*. **25**, 113-136 (1996).
217. Otto, H., Reche, P. A., Bazan, F., Dittmar, K., Haag, F. & Koch-Nolte, F. In silico characterization of the family of PARP-like poly(ADP-ribosyl)transferases (pARTs). *BMC Genomics*. **6**, 139 (2005).
218. Pires, D. E., Chen, J., Blundell, T. L. & Ascher, D. B. In silico functional dissection of saturation mutagenesis: Interpreting the relationship between phenotypes and changes in protein stability, interactions and activity. *Sci Rep*. **6**, 19848 (2016).
219. Chen, J. & Shen, B. Computational Analysis of Amino Acid Mutation: A Proteome Wide Perspective. *Curr. Proteom*. **6**, 228-234 (2009).

220. Voet, A. & Zhang, K. Y. Pharmacophore modelling as a virtual screening tool for the discovery of small molecule protein-protein interaction inhibitors. *Curr. Pharm. Des*. **18**, 4586-4598 (2012).
221. Imrie, F., Hadfield, T. E., Bradley, A. R. & Deane, C. M. Deep generative design with 3D pharmacophoric constraints. *Chem. Sci*. **12**, 14577-14589 (2021).
222. Acharya, K. R. & Lloyd, M. D. The advantages and limitations of protein crystal structures. *Trends Pharmacol. Sci*. **26**, 10-14 (2005).
223. Kielkowski, P., Buchsbaum, I. Y., Kirsch, V. C., Bach, N. C., Drukker, M., Cappello, S. & Sieber, S. A. FICD activity and AMPylation remodelling modulate human neurogenesis. *Nat. Commun*. **11**, 517 (2020).
224. Mathews, I. I., Erion, M. D. & Ealick, S E. Structure of human adenosine kinase at 1.5 A resolution. *Biochemistry*. **37**, 15607-15620 (1998).
225. Müller, C. W. & Schulz, G. E. Structure of the complex between adenylate kinase from Escherichia coli and the inhibitor Ap5A refined at 1.9 A resolution. A model for a catalytic transition state. *J. Mol. Biol*. **224**, 159-177 (1992).
226. Berry, M. B., Meador, B., Bilderback, T., Liang, P., Glaser, M. & Phillips, G. N. Jr. The closed conformation of a highly flexible protein: the structure of E. coli adenylate kinase with bound AMP and AMPPNP. *Proteins*. **19**, 183-198 (1994).
227. Schlauderer, G. J., Proba, K. & Schulz, G. E. Structure of a mutant adenylate kinase ligated with an ATP-analogue showing domain closure over ATP. *J. Mol. Biol*. **256**, 223-227 (1996).
228. Filippakopoulos, P., Bunkoczi, G., Jansson, A., Schreurs, A., Knapp, S., Edwards, A., von Delft, F. & Sundstrom, M. Crystal structure of human AK1A in complex with AP5A. *Structural Genomics Consortium (SGC)*. (2005). doi: 10.2210/pdb1z83/pdb
229. Menz, R. I., Walker, J. E. & Leslie, A. G. Structure of bovine mitochondrial F(1)-ATPase with nucleotide bound to all three catalytic sites: implications for the mechanism of rotary catalysis. *Cell*. **106**, 331-341 (2001).
230. Kabaleeswaran, V., Puri, N., Walker, J. E., Leslie, A. G. & Mueller, D. M. Novel features of the rotary catalytic mechanism revealed in the structure of yeast F1 ATPase. *EMBO J*. **25**, 5433-5442 (2006).
231. Zhou, T., Kurnasov, O., Tomchick, D. R., Binns, D. D., Grishin, N. V., Marquez, V. E., Osterman, A. L. & Zhang, H. Structure of human nicotinamide/nicotinic acid mononucleotide adenylyltransferase. Basis for the dual substrate specificity and activation of the oncolytic agent tiazofurin. *J. Biol. Chem*. **277**, 13148-13154 (2002).

232. Kielkowski, P., Buchsbaum, I. Y., Becker, T., Bach, K., Cappello, S. & Sieber, S. A. A Pronucleotide Probe for Live-Cell Imaging of Protein AMPylation. *Chembiochem*. **21**, 1285-1287 (2020).
233. Butora, G., Schmitt, C., Levorse, D. A., Streckfuss, E., Doss, G. A., & MacCoss, M. The elusive 8-fluoroadenosine: a simple non-enzymatic synthesis and characterization. *Tetrahedron*. **63**, 3782-3789 (2007).
234. Ikehara, M. & Yamada, S. Studies of Nucleosides and Nucleotides. XLIX. Synthesis of 8-Fluoroadenosine. *Chem. Pharm. Bull*. **19**, 104-109 (1971).
235. Benneche, T. & Undheim, K. Synthesis and Isomerization Studies of 2-Alkenylthiopyrimidines and 2-Alkynylthiopyrimidines and Their S-Oxides. *Acta Chemica Scandinavica*. **37**, 115-119 (1983).
236. Ting, R., Lermer, L. & Perrin, D. M. Triggering DNAzymes with light: a photoactive C8 thioether-linked adenosine. *J. Am. Chem. Soc*. **126**, 12720-12721 (2004).
237. Abad, J. L., Gaffney, B. L. & Jones, R. A. 15N-Multilabeled Adenine and Guanine Nucleosides. Syntheses of [1,3,NH(2)-(15)N(3)]- and [2-(13)C-1,3,NH(2)-(15)N(3)]-Labeled Adenosine, Guanosine, 2'-Deoxyadenosine, and 2'-Deoxyguanosine. *J. Org. Chem*. **64**, 6575-6582 (1999).
238. Quintiliani, M., Persoons, L., Solaroli, N., Karlsson, A., Andrei, G., Snoeck, R., Balzarini, J. & McGuigan, C. Design, synthesis and biological evaluation of 2'-deoxy-2',2'-difluoro-5-halouridine phosphoramidate ProTides. *Bioorg. Med. Chem*. **19**, 4338-4345 (2011).
239. Kawaguchi, M., Sekimoto, E., Ohta, Y., Ieda, N., Murakami, T. & Nakagawa, H. Synthesis of Fluorescent Probes Targeting Tumor-Suppressor Protein FHIT and Identification of Apoptosis-Inducing FHIT Inhibitors. *J. Med. Chem*. **64**, 9567-9576 (2021).
240. Grammel, M., Luong, P., Orth, K. & Hang, H. C. A chemical reporter for protein AMPylation. *J. Am. Chem. Soc*. **133**, 17103-17105 (2011).
241. Lecka, J., Gillerman, I., Fausther, M., Salem, M., Munkonda, M. N., Brosseau, J. P., Cadot, C., Martín-Satué, M., d'Orléans-Juste, P., Rousseau, E., Poirier, D., Künzli, B., Fischer, B. & Sévigny, J. 8-BuS-ATP derivatives as specific NTPDase1 inhibitors. *Br. J. Pharmacol*. **169**, 179-196 (2013).
242. Yang, T., Chan, N. Y. & Sauve, A. A. Syntheses of nicotinamide riboside and derivatives: effective agents for increasing nicotinamide adenine dinucleotide concentrations in mammalian cells. J. Med. Chem. **50**, 6458-6461 (2007).

243. Hayat, F. & Migaud, M E. Nicotinamide riboside-amino acid conjugates that are stable to purine nucleoside phosphorylase. *Org. Biomol. Chem*. **18**, 2877-2885 (2020).
244. Henderson, D. J. P., Miranda, J. L. & Emerson, B. M. The β-NAD^+ salvage pathway and PKC-mediated signaling influence localized PARP-1 activity and CTCF Poly(ADP)ribosylation. *Oncotarget*. **8**, 64698-64713 (2017).
245. Li, Z., Liu, W., Fu, J., Cheng, S., Xu, Y., Wang, Z., Liu, X., Shi, X., Liu, Y., Qi, X., Liu, X., Ding, J. & Shao, F. Shigella evades pyroptosis by arginine ADP-riboxanation of caspase-11. *Nature*. **599**, 290-295 (2021).
246. Mashimo, M., Onishi, M., Uno, A., Tanimichi, A., Nobeyama, A., Mori, M., Yamada, S., Negi, S., Bu, X., Kato, J., Moss, J., Sanada, N., Kizu, R. & Fujii, T. The 89-kDa PARP1 cleavage fragment serves as a cytoplasmic PAR carrier to induce AIF-mediated apoptosis. *J. Biol. Chem*. **296**, 100046 (2021).
247. Skrypina, N. A., Timofeeva, A. V., Khaspekov, G. L., Savochkina, L. P. & Beabealashvilli, R. Sh. Total RNA suitable for molecular biology analysis. *J. Biotechnol*. **105**, 1-9 (2003).
248. Cajka, T. & Fiehn, O. Toward Merging Untargeted and Targeted Methods in Mass Spectrometry-Based Metabolomics and Lipidomics. *Anal. Chem*. **88**, 524-545 (2016).
249. Yang, Q., Zhang, A. H., Miao, J. H., Sun, H., Han, Y., Yan, G. L., Wu, F. F. & Wang, X. J. Metabolomics biotechnology, applications, and future trends: a systematic review. RSC Adv. **9**, 37245-37257 (2019).
250. Gertsman, I. & Barshop, B. A. Promises and pitfalls of untargeted metabolomics. *J. Inherit. Metab. Dis*. **41**, 355-366 (2018).
251. Roberts, L. D., Souza, A. L., Gerszten, R. E. & Clish, C. B. Targeted metabolomics. *Curr Protoc Mol Biol*. **30**, Unit 30.2.1-24 (2012).
252. Hasmann, M. & Schemainda, I. FK866, a highly specific noncompetitive inhibitor of nicotinamide phosphoribosyltransferase, represents a novel mechanism for induction of tumor cell apoptosis. *Cancer Res*. **63**, 7436-7442 (2003)
253. Billington, R. A., Genazzani, A. A., Travelli, C. & Condorelli, F. NAD depletion by FK866 induces autophagy. *Autophagy*. **4**, 385-387 (2008).
254. Aslam, B., Basit, M., Nisar, M. A., Khurshid, M. & Rasool, M. H. Proteomics: Technologies and Their Applications. *J. Chromatogr*. Sci. **55**, 182-196 (2017).
255. Meissner, F., Geddes-McAlister, J., Mann, M. & Bantscheff, M. The emerging role of mass spectrometry-based proteomics in drug discovery. *Nat. Rev. Drug. Discov*. s41573-022-00409-3 (2022). doi: 10.1038/s41573-022-00409-3

256. Kwon, Y. W., Jo, H. S., Bae, S., Seo, Y., Song, P., Song, M. & Yoon, J. H. Application of Proteomics in Cancer: Recent Trends and Approaches for Biomarkers Discovery. *Front. Med*. **8**, 747333 (2021).
257. Wright, M. H., Paape, D., Storck, E. M., Serwa, R. A., Smith, D. F. & Tate, E. W. Global analysis of protein N-myristoylation and exploration of N-myristoyltransferase as a drug target in the neglected human pathogen Leishmania donovani. *Chem. Biol*. **22**, 342-354 (2015).
258. Kallemeijn, W. W., Lanyon-Hogg, T., Panyain, N., Goya Grocin, A., Ciepla, P., Morales-Sanfrutos, J. & Tate, E. W. Proteome-wide analysis of protein lipidation using chemical probes: in-gel fluorescence visualization, identification and quantification of N-myristoylation, N- and S-acylation, O-cholesterylation, S-farnesylation and S-geranylgeranylation. *Nat. Protoc*. **16**, 5083-5122 (2021).
259. Pappireddi, N., Martin, L. & Wühr, M. A Review on Quantitative Multiplexed Proteomics. *Chembiochem*. **20**, 1210-1224 (2019).
260. Li, J., Van, Vranken, J. G., Pontano Vaites, L., Schweppe, D. K., Huttlin, E. L., Etienne, C., Nandhikonda, P., Viner, R., Robitaille, A. M., Thompson, A. H., Kuhn, K., Pike, I., Bomgarden, R. D., Rogers, J. C., Gygi, S. P. & Paulo, J. A. TMTpro reagents: a set of isobaric labeling mass tags enables simultaneous proteome-wide measurements across 16 samples. *Nat. Methods*. **17**, 399-404 (2020).
261. Bai, B., Tan, H., Pagala, V. R., High, A. A., Ichhaporia, V. P., Hendershot, L. & Peng, J. Deep Profiling of Proteome and Phosphoproteome by Isobaric Labeling, Extensive Liquid Chromatography, and Mass Spectrometry. *Methods Enzymol*. **585**, 377-395 (2017).
262. Jungmichel, S., Rosenthal, F., Altmeyer, M., Lukas, J., Hottiger, M. O. & Nielsen, M. L. Proteome-wide identification of poly(ADP-Ribosyl)ation targets in different genotoxic stress responses. Mol Cell. **52**, 272-285 (2013).
263. Martello, R., Leutert, M., Jungmichel, S., Bilan, V., Larsen, S. C., Young, C., Hottiger, M. O. & Nielsen, M. L. Proteome-wide identification of the endogenous ADP-ribosylome of mammalian cells and tissue. *Nat. Commun*. **7**, 12917 (2016).
264. Sieber, S. A., Cappello, S. & Kielkowski, P. From Young to Old: AMPylation Hits the Brain. *Cell Chem. Biol*. **27**, 773-779 (2020).
265. Houl, J. H., Ye, Z., Brosey, C. A., Balapiti-Modarage, L. P. F., Namjoshi, S., Bacolla, A., Laverty, D., Walker, B. L., Pourfarjam, Y., Warden, L. S., Babu Chinnam, N., Moiani, D., Stegeman, R. A., Chen, M. K., Hung, M. C., Nagel, Z. D., Ellenberger, T.,

Kim, I. K., Jones, D. E., Ahmed, Z. & Tainer, J. A. Selective small molecule PARG inhibitor causes replication fork stalling and cancer cell death. *Nat. Commun*. **10**, 5654 (2019).

266. Tararov, V. I., Tijsma, A., Kolyachkina, S. V., Oslovsky, V. E., Neyts, J., Drenichev, M. S., Leyssen, P. & Mikhailov, S. N. Chemical modification of the plant isoprenoid cytokinin N(6)-isopentenyladenosine yields a selective inhibitor of human enterovirus 71 replication. *Eur. J. Med. Chem*. **90**, 406-413 (2015).

Appendix A

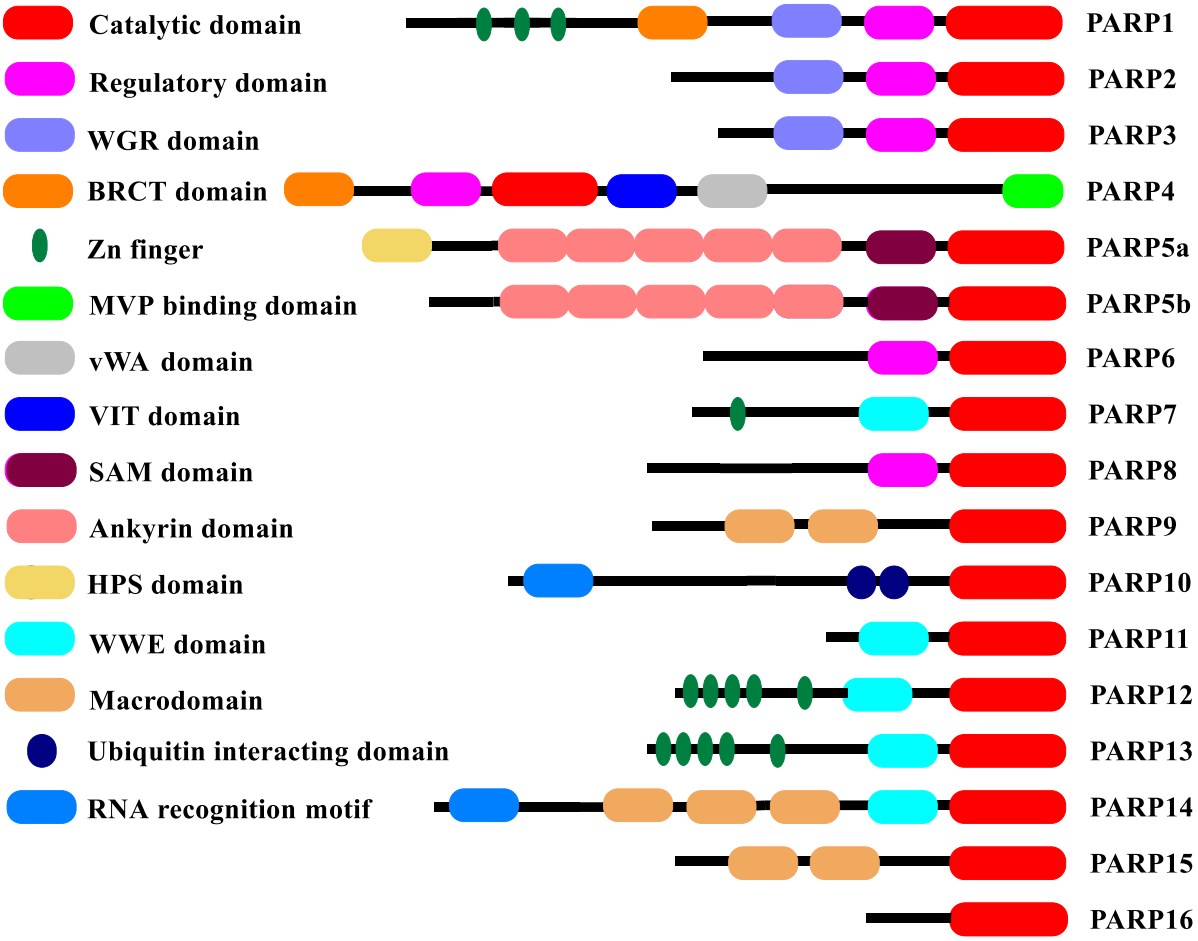


Figure A.1. Domain structures of PARPs. The relative size of PARP domains and overall PARP size is illustrated but not strictly to scale.

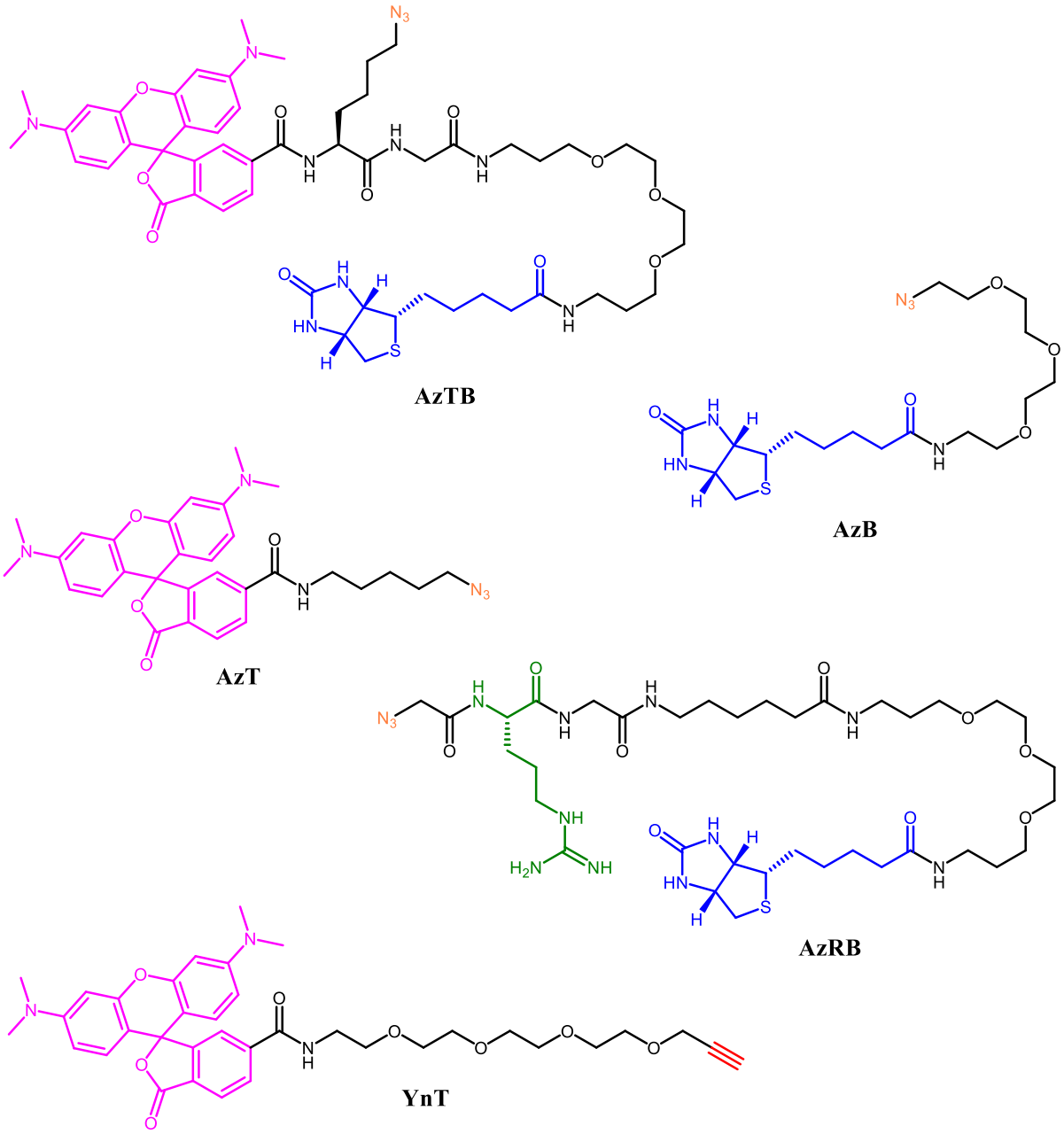


Figure A.2. Structures of all click chemistry capture reagents employed in this work. TAMRA fluorophore (pink), biotin (blue), azide (orange) and alkyne (red) moieties are highlighted.

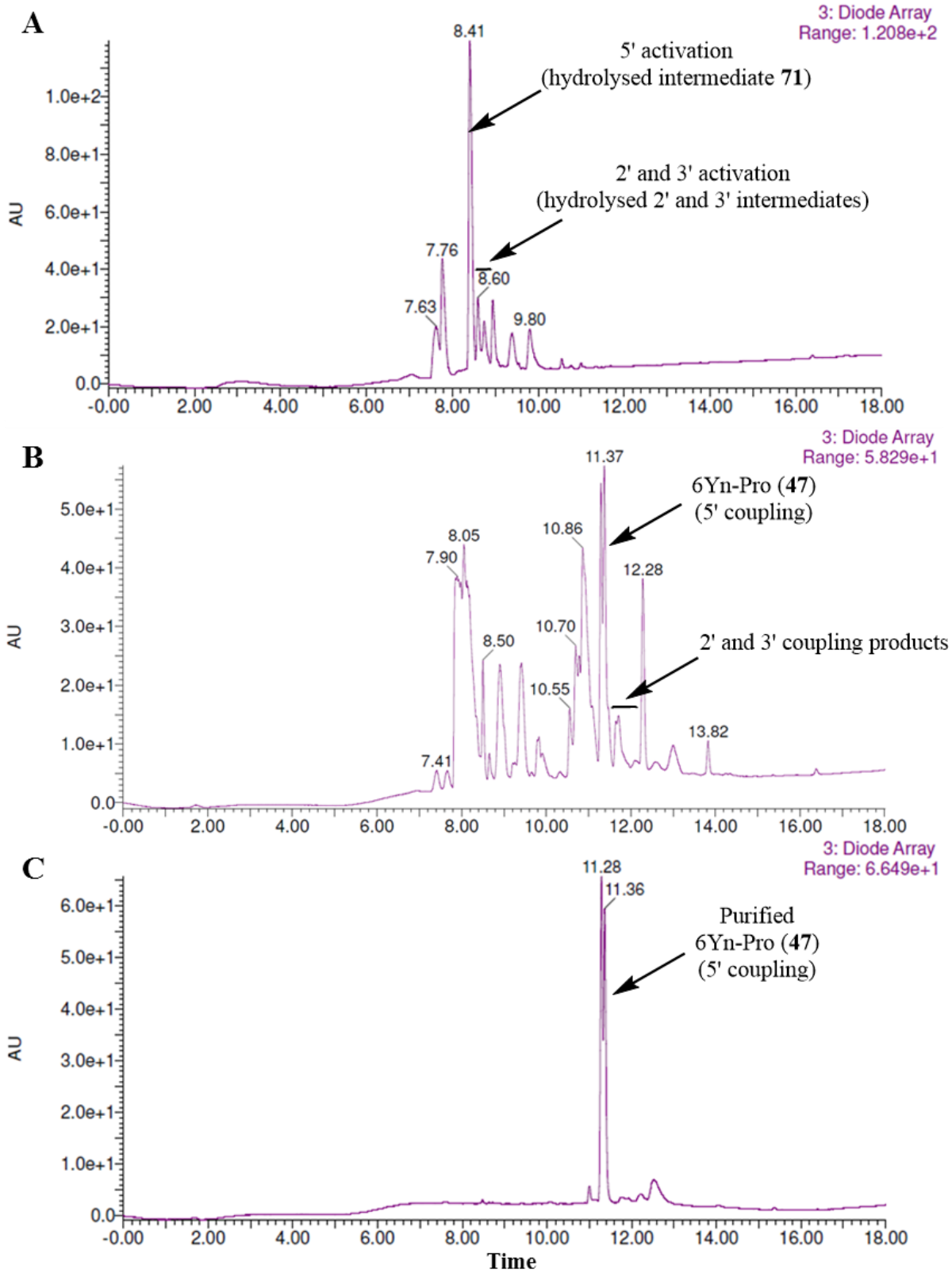


Figure A.3. Analytical LC-MS traces for 6Yn-Pro (**47**) synthesis reactions. **A**. generation of (hydrolysed) intermediate **71** *via* 5' OH activation (R_t = 8.41 mins, major product). 2' and 3' OH activation is also shown (minor products). **B**. Coupling reaction between **71** and **66** to produce 6Yn-Pro (**47**) as the major product (R_t = 11.30-

11.37 mins, major product (stereoisomers)). 2' and 3' OH coupling products are also shown. **C**. Purified 6Yn-Pro (**47**) (R_t = 11.28-11.36 (stereoisomers)).

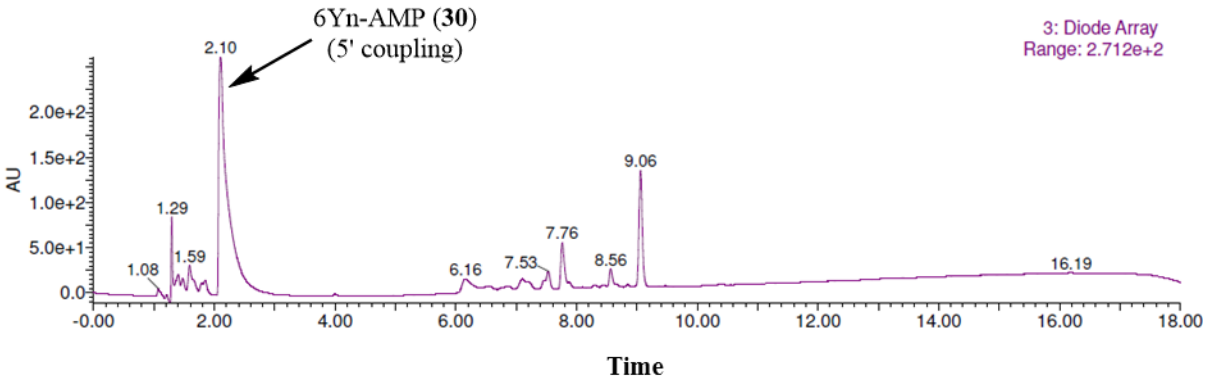


Figure A.4. Analytical LC-MS trace for 6Yn-AMP (**30**) synthesis reaction. 5' phosphorylation (6Yn-AMP (**30**)) is shown as the major product of the reaction (R_t = 2.10 mins). Peaks for 2' and 3' OH phosphorylation were not observed.

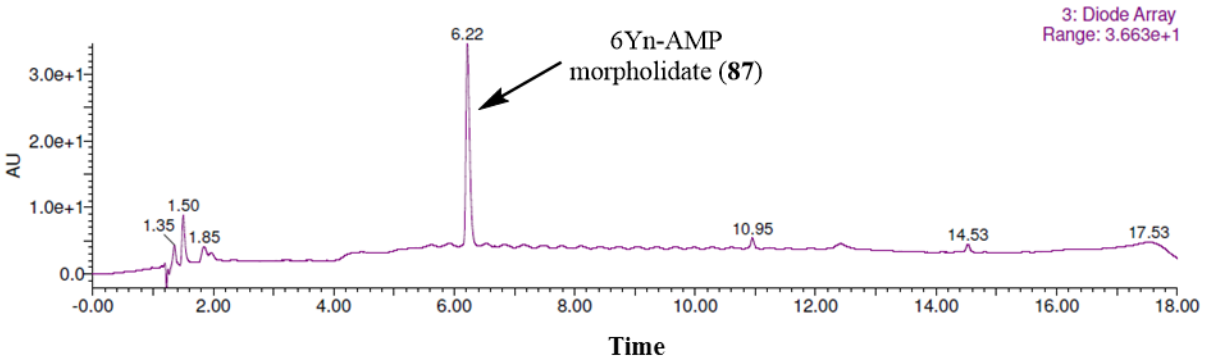


Figure A.5. Analytical LC-MS trace for 6Yn-AMP morpholidate (**87**) after precipitation in MeCN.

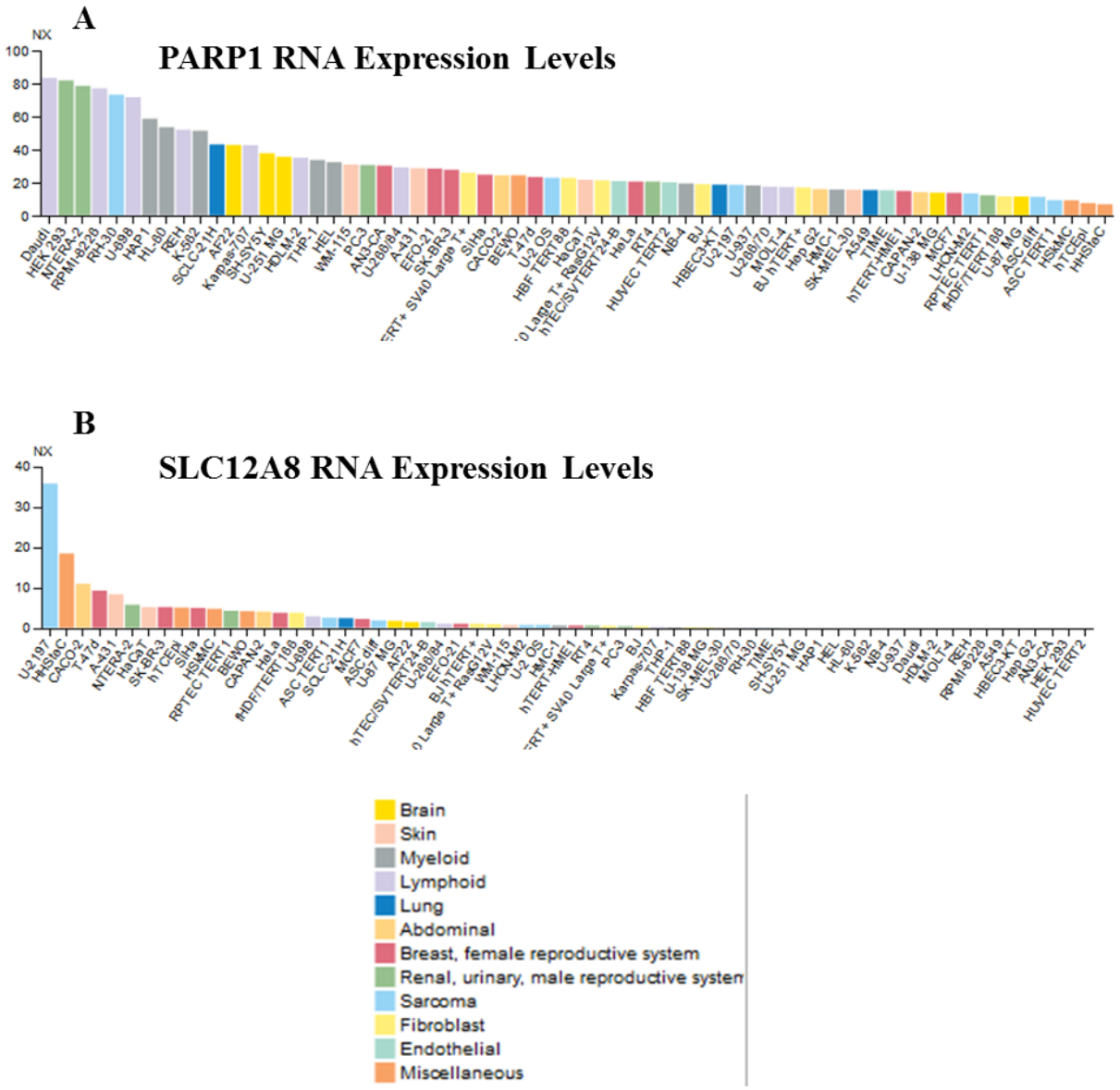
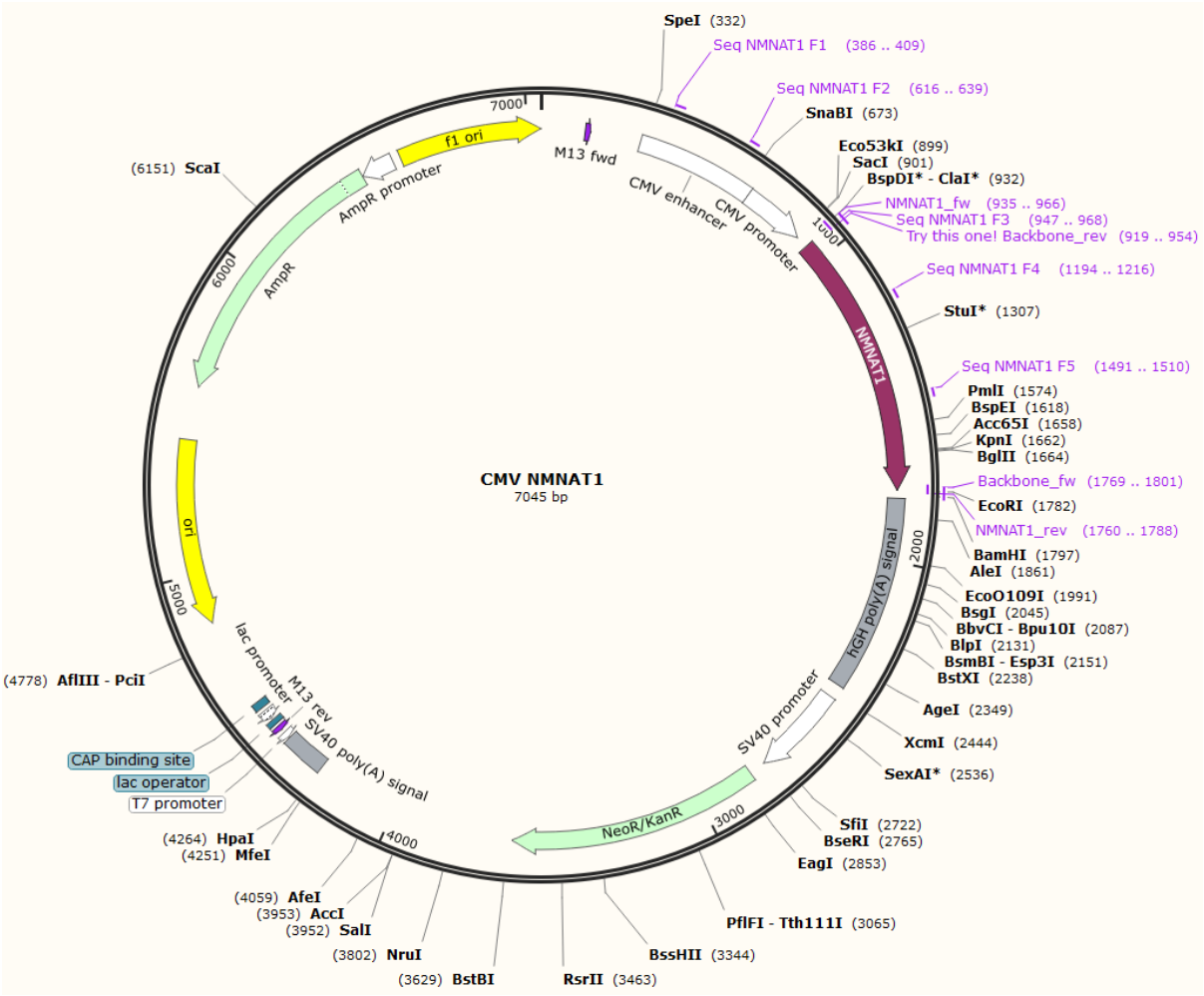


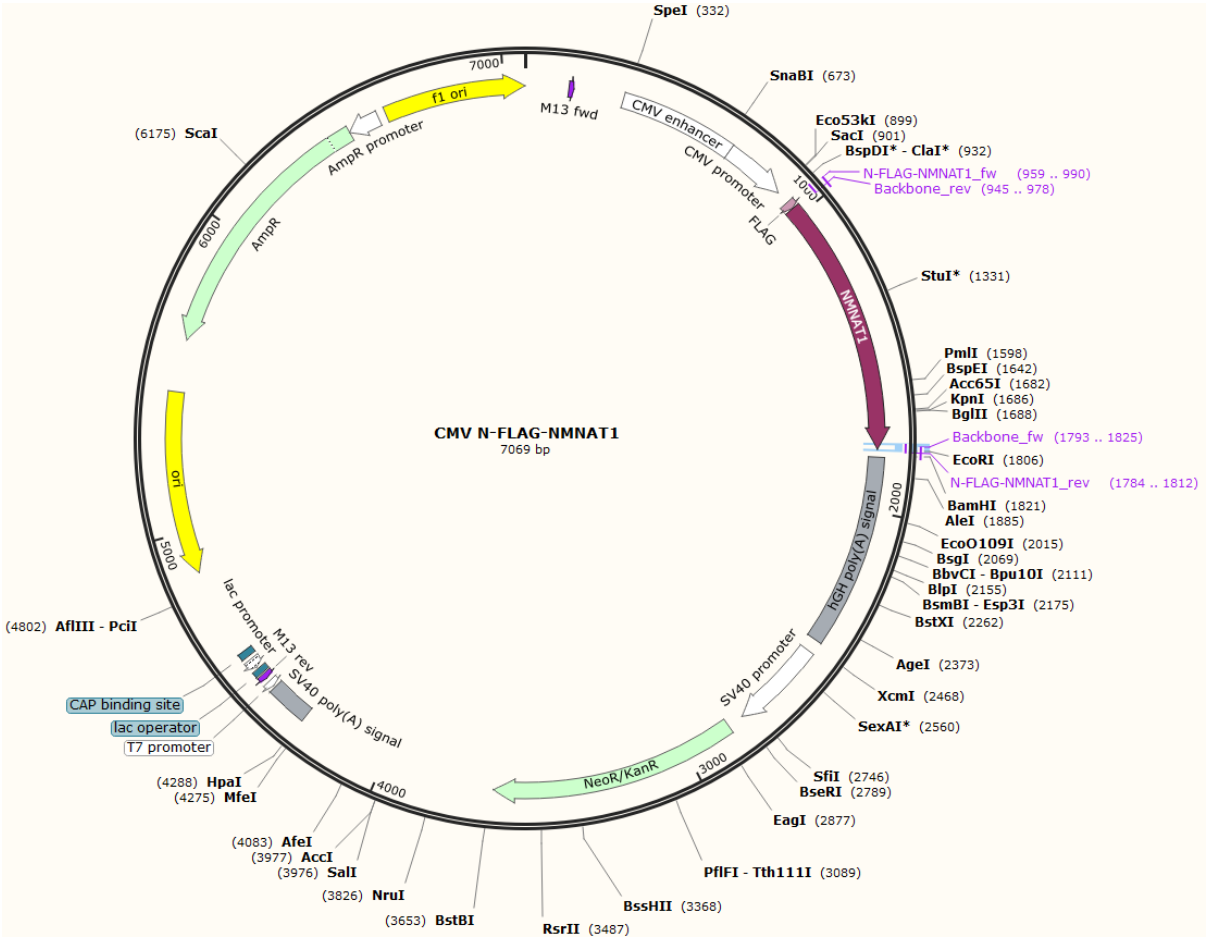
Figure A.6. RNA expression levels of (**A**) SLC12A8 and (**B**) PARP1 in different cell lines. The figures were obtained from The Human Protein Atlas database (available at https://www.proteinatlas.org/).



ATGGAAAATTCCGAGAAGACTGAAGTGGTTCTCCTTGCTTGTGGTTCATTCAATCCCATC
ACCAACATGCACCTCAGGTTGTTTGAGCTGGCCAAGGACTACATGAATGGAACAGGAAG
GTACACAGTTGTCAAAGGCATCATCTCTCCTGTTGGTGATGCCTACAAGAAGAAAGGACT
CATTCCTGCCTATCACCGGGTCATCATGGCAGAACTTGCTACCAAGAACTCTAAATGGGT
GGAAGTTGATACATGGGAAAGTCTTCAGAAGGAGTGGAAAGAGACTCTGAAGGTGCTAA
GACACCATCAAGAGAAATTGGAGGCTAGTGACTGTGATCACCAGCAGAACTCACCTACT
CTAGAAAGGCCTGGAAGGAAGAGGAAGTGGACTGAAACACAAGATTCTAGTCAAAAGA
AATCCCTAGAGCCAAAAACAAAAGCTGTGCCAAAGGTCAAGCTGCTGTGTGGGGCAGAT
TTATTGGAGTCCTTTGCTGTTCCCAATTTGTGGAAGAGTGAAGACATCACCCAAATCGTG
GCCAACTATGGGCTCATATGTGTTACTCGGGCTGGAAATGATGCTCAGAAGTTTATCTAT
GAATCGGATGTGCTGTGGAAACACCGGAGCAACATTCACGTGGTGAATGAATGGATCGC
TAATGACATCTCATCCACAAAAATCCGGAGAGCCCTCAGAAGGGGCCAGAGCATTCGCT
ACTTGGTACCAGATCTTGTCCAAGAATACATTGAAAAGCATAATTTGTACAGCTCTGAGA

GTGAAGACAGGAATGCTGGGGTCATCCTGGCCCCTTTGCAGAGAAACACTGCAGAAGCT
AAGACATGA

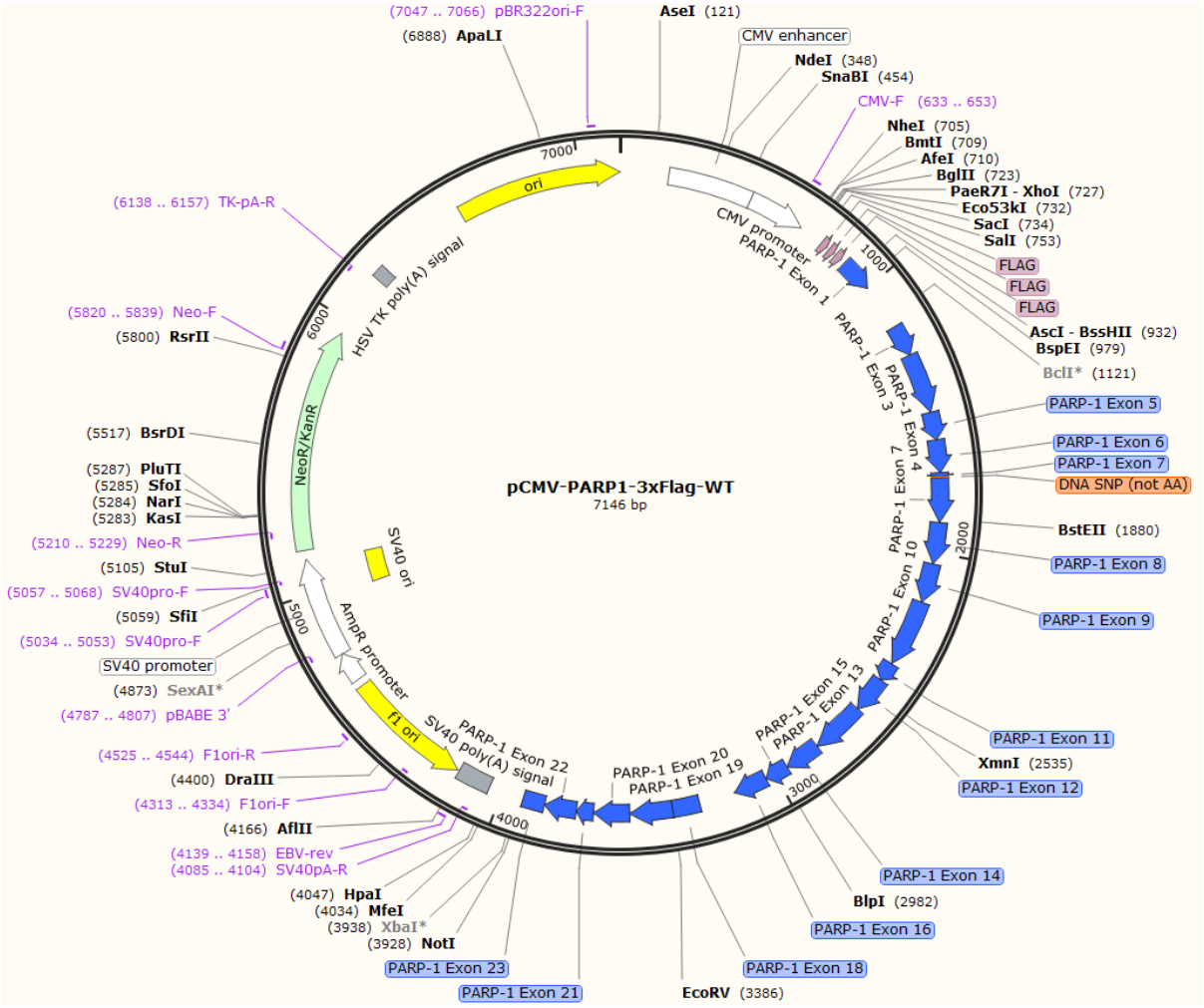
Figure A.7. Plasmid map for CMV NMNAT1 plasmid. NMNAT1 sequence is shown.



ATGGACTACAAAGACGATGACGACAAGGAAAATTCCGAGAAGACTGAAGTGGTTCTCCT
TGCTTGTGGTTCATTCAATCCCATCACCAACATGCACCTCAGGTTGTTTGAGCTGGCCAA
GGACTACATGAATGGAACAGGAAGGTACACAGTTGTCAAAGGCATCATCTCTCCTGTTG
GTGATGCCTACAAGAAGAAAGGACTCATTCCTGCCTATCACCGGGTCATCATGGCAGAA
CTTGCTACCAAGAACTCTAAATGGGTGGAAGTTGATACATGGGAAAGTCTTCAGAAGGA
GTGGAAAGAGACTCTGAAGGTGCTAAGACACCATCAAGAGAAATTGGAGGCTAGTGACT
GTGATCACCAGCAGAACTCACCTACTCTAGAAAGGCCTGGAAGGAAGAGGAAGTGGACT
GAAACACAAGATTCTAGTCAAAAGAAATCCCTAGAGCCAAAAACAAAAGCTGTGCCAAA
GGTCAAGCTGCTGTGTGGGGCAGATTTATTGGAGTCCTTTGCTGTTCCCAATTTGTGGAA
GAGTGAAGACATCACCCAAATCGTGGCCAACTATGGGCTCATATGTGTTACTCGGGCTGG
AAATGATGCTCAGAAGTTTATCTATGAATCGGATGTGCTGTGGAAACACCGGAGCAACA

TTCACGTGGTGAATGAATGGATCGCTAATGACATCTCATCCACAAAAATCCGGAGAGCC
CTCAGAAGGGGCCAGAGCATTCGCTACTTGGTACCAGATCTTGTCCAAGAATACATTGAA
AAGCATAATTTGTACAGCTCTGAGAGTGAAGACAGGAATGCTGGGGTCATCCTGGCCCC
TTTGCAGAGAAACACTGCAGAAGCTAAGACATGA

Figure A.8. Plasmid map for CMV N-FLAG-NMNAT1 plasmid. N-FLAG-NMNAT1 sequence is shown.



ATGGGTTCAGACTATAAAGATGATGATGATAAAGGTGGCTCCGACTACAAGGATGACGA
TGACAAGGGAGGTAGTGACTACAAAGACGATGACGACAAGGGCGGATCTGGCGGATCT
ATGGCGGAGTCTTCGGATAAGCTCTATCGAGTCGAGTACGCCAAGAGCGGGCGCGCCTC
TTGCAAGAAATGCAGCGAGAGCATCCCCAAGGACTCGCTCCGGATGGCCATCATGGTGC
AGTCGCCCATGTTTGATGGAAAAGTCCCACACTGGTACCACTTCTCCTGCTTCTGGAAGG
TGGGCCACTCCATCCGGCACCCTGACGTTGAGGTGGATGGGTTCTCTGAGCTTCGGTGGG
ATGATCAGCAGAAAGTCAAGAAGACAGCGGAAGCTGGAGGAGTGACAGGCAAAGGCCA
GGATGGAATTGGTAGCAAGGCAGAGAAGACTCTGGGTGACTTTGCAGCAGAGTATGCCA
AGTCCAACAGAAGTACGTGCAAGGGGTGTATGGAGAAGATAGAAAAGGGCCAGGTGCG
CCTGTCCAAGAAGATGGTGGACCCGGAGAAGCCACAGCTAGGCATGATTGACCGCTGGT

ACCATCCAGGCTGCTTTGTCAAGAACAGGGAGGAGCTGGGTTTCCGGCCCGAGTACAGT
GCGAGTCAGCTCAAGGGCTTCAGCCTCCTTGCTACAGAGGATAAAGAAGCCCTGAAGAA
GCAGCTCCCAGGAGTCAAGAGTGAAGGAAAGAGAAAAGGCGATGAGGTGGATGGAGTG
GATGAAGTGGCGAAGAAGAAATCTAAAAAAGAAAAAGACAAGGATAGTAAGCTTGAAA
AAGCCCTAAAGGCTCAGAACGACCTGATCTGGAACATCAAGGACGAGCTAAAGAAAGTG
TGTTCAACTAATGACCTGAAGGAGCTACTCATCTTCAACAAGCAGCAAGTGCCTTCTGGG
GAGTCGGCGATCTTGGACCGAGTAGCCGATGGCATGGTGTTCGGTGCCCTCCTTCCCTGC
GAGGAATGCTCGGGTCAGCTGGTCTTCAAGAGCGATGCCTATTACTGCACTGGGGACGTC
ACTGCCTGGACCAAGTGTATGGTCAAGACACAGACACCCAACCGGAAGGAGTGGGTAAC
CCCAAAGGAATTCCGAGAAATCTCTTACCTCAAGAAATTGAAGGTTAAAAAACAGGACC
GTATATTCCCCCCAGAAACCAGCGCCTCCGTGGCGGCCACGCCTCCGCCCTCCACAGCCT
CGGCTCCTGCTGCTGTGAACTCCTCTGCTTCAGCAGATAAGCCATTATCCAACATGAAGA
TCCTGACTCTCGGGAAGCTGTCCCGGAACAAGGATGAAGTGAAGGCCATGATTGAGAAA
CTCGGGGGGAAGTTGACGGGGACGGCCAACAAGGCTTCCCTGTGCATCAGCACCAAAAA
GGAGGTGGAAAAGATGAATAAGAAGATGGAGGAAGTAAAGGAAGCCAACATCCGAGTT
GTGTCTGAGGACTTCCTCCAGGACGTCTCCGCCTCCACCAAGAGCCTTCAGGAGTTGTTC
TTAGCGCACATCTTGTCCCCTTGGGGGGCAGAGGTGAAGGCAGAGCCTGTTGAAGTTGTG
GCCCCAAGAGGGAAGTCAGGGGCTGCGCTCTCCAAAAAAAGCAAGGGCCAGGTCAAGG
AGGAAGGTATCAACAAATCTGAAAAGAGAATGAAATTAACTCTTAAAGGAGGAGCAGCT
GTGGATCCTGATTCTGGACTGGAACACTCTGCGCATGTCCTGGAGAAAGGTGGGAAGGT
CTTCAGTGCCACCCTTGGCCTGGTGGACATCGTTAAAGGAACCAACTCCTACTACAAGCT
GCAGCTTCTGGAGGACGACAAGGAAAACAGGTATTGGATATTCAGGTCCTGGGGCCGTG
TGGGTACGGTGATCGGTAGCAACAAACTGGAACAGATGCCGTCCAAGGAGGATGCCATT
GAGCACTTCATGAAATTATATGAAGAAAAAACCGGGAACGCTTGGCACTCCAAAAATTT
CACGAAGTATCCCAAAAAGTTCTACCCCCTGGAGATTGACTATGGCCAGGATGAAGAGG
CAGTGAAGAAGCTGACAGTAAATCCTGGCACCAAGTCCAAGCTCCCCAAGCCAGTTCAG
GACCTCATCAAGATGATCTTTGATGTGGAAAGTATGAAGAAAGCCATGGTGGAGTATGA
GATCGACCTTCAGAAGATGCCCTTGGGGAAGCTGAGCAAAAGGCAGATCCAGGCCGCAT
ACTCCATCCTCAGTGAGGTCCAGCAGGCGGTGTCTCAGGGCAGCAGCGACTCTCAGATCC
TGGATCTCTCAAATCGCTTTTACACCCTGATCCCCCACGACTTTGGGATGAAGAAGCCTC
CGCTCCTGAACAATGCAGACAGTGTGCAGGCCAAGGCGGAAATGCTTGACAACCTGCTG
GACATCGAGGTGGCCTACAGTCTGCTCAGGGGAGGGTCTGATGATAGCAGCAAGGATCC
CATCGATGTCAACTATGAGAAGCTCAAAACTGACATTAAGGTGGTTGACAGAGATTCTG
AAGAAGCCGAGATCATCAGGAAGTATGTTAAGAACACTCATGCAACCACACACAATGCG
TATGACTTGGAAGTCATCGATATCTTTAAGATAGAGCGTGAAGGCGAATGCCAGCGTTAC
AAGCCCTTTAAGCAGCTTCATAACCGAAGATTGCTGTGGCACGGGTCCAGGACCACCAA
CTTTGCTGGGATCCTGTCCCAGGGTCTTCGGATAGCCCCGCCTGAAGCGCCCGTGACAGG
CTACATGTTTGGTAAAGGGATCTATTTCGCTGACATGGTCTCCAAGAGTGCCAACTACTG
CCATACGTCTCAGGGAGACCCAATAGGCTTAATCCTGTTGGGAGAAGTTGCCCTTGGAAA
CATGTATGAACTGAAGCACGCTTCACATATCAGCAAGTTACCCAAGGGCAAGCACAGTG
TCAAAGGTTTGGGCAAAACTACCCCTGATCCTTCAGCTAACATTAGTCTGGATGGTGTAG
ACGTTCCTCTTGGGACCGGGATTTCATCTGGTGTGAATGACACCTCTCTACTATATAACG
AGTACATTGTCTATGATATTGCTCAGGTAAATCTGAAGTATCTGCTGAAACTGAAATTCA
ATTTTAAGACCTCCCTGTGGTGA

Figure A.9. Plasmid map for CMV 3x N-FLAG-PARP1 plasmid. 3x N-FLAG-PARP1 sequence is shown.

Table A.1. Metabolomics samples treated with isotopically labelled ^{15}N-Pro

Cell line	Sample treatment (24 h)				
HEK293T	0.1% (v/v) DMSO	^{15}N-Pro	^{15}N-Pro + NR	^{15}N-Pro + NRH	^{15}N-Pro + β-NMN
T47D	0.1% (v/v) DMSO	^{15}N-Pro	^{15}N-Pro + NR	^{15}N-Pro + NRH	^{15}N-Pro + β-NMN
MDA-MB-435	0.1% (v/v) DMSO	^{15}N-Pro	^{15}N-Pro + NR	^{15}N-Pro + NRH	^{15}N-Pro + β-NMN

Table A.2. Proteins in **Figures 4.31A** and **4.31C** (**6Yn-Pro+NM1 vs DMSO+NM1**) that were also identified in **Figures 4.31B** and **4.31D** (**6Yn-Pro+NM1+O vs DMSO+NM1**). These proteins are highlighted in green in the corresponding **Figures**. Proteins have been arranged in descending order for Log_2 Fold change. The same list of proteins is shown in **Table A.3**.

Protein	Log_2 Fold change	$-Log_{10}$(p-value)
PARP1	3.846672	1.652674
SMAP	3.336305	0
PRPF40A	2.948371	0
HIST1H1E	2.815618	0
CDKN2A	2.294599	0
PAK2;PAK1;PAK3	2.12165	0.42355
RRS1	1.889938	0
MYL6	1.850293	1.270927
MIF	1.713501	1.233575
HNRNPD	1.709938	0.748445
PPIB	1.660015	0
PA2G4	1.297882	0
CSE1L	1.289517	1.329131
SMARCA5	1.253673	0
APEX1	1.129928	0
PGAM1;PGAM2;PGAM4	1.124841	0.576642
EIF4A1;EIF4A2	1.087206	0.956283
HMGB1	1.048254	0
ANXA2	1.019864	0.571956
DDX5	0.985273	0
RPL29	0.955983	0
PDIA3	0.767563	1.325805
RPL22	0.755857	0.672817
RCC2	0.722015	0.385906
HIST1H1C;HIST1H1D;HIST1H1A;HIST1H1T	0.716428	0.998411
LRRC59	0.713186	0.407246
SUPT5H	0.700761	0.588136
HNRNPA1;HNRNPA1L2	0.667481	0
HSPA9	0.625729	0.58102
MAPRE1	0.617895	0.29806
ILF2	0.598951	0
TOMM20	0.56606	0.269199
SRSF7	0.541213	0.580246
SYNCRIP	0.524401	0
HNRNPH1	0.51946	0.650085

Table A.3. Proteins in **Figures 4.31B** and **4.31D** (**6Yn-Pro+NM1+O vs DMSO+NM1**) that were also identified in **Figures 4.31A** and **4.31C** (**6Yn-Pro+NM1 vs DMSO+NM1**). These proteins are highlighted in green in the corresponding **Figures**. Proteins have been arranged in descending order for Log_2 Fold change. The same list of proteins is shown in **Table A.2**.

Protein	Log_2 Fold change	$-Log_{10}$(p-value)
HIST1H1E	3.361576	0
SMAP	2.375124	0
HNRNPD	2.039172	0.804908
CDKN2A	1.965822	0
PAK2;PAK1;PAK3	1.920835	0.384067
PARP1	1.782814	0.884897
HMGB1	1.302978	0
MYL6	1.245547	0.924293
PGAM1;PGAM2;PGAM4	1.236715	0.618458
HNRNPA1;HNRNPA1L2	1.082097	0
PRPF40A	1.062767	0
MIF	1.044482	0.743345
APEX1	1.018676	0
ILF2	0.975575	0
RCC2	0.965912	0.603751
EIF4A1;EIF4A2	0.963561	0.839643
RPL29	0.922414	0
ANXA2	0.829039	0.612121
CSE1L	0.755544	0.686429
PDIA3	0.737563	1.286092
RPL22	0.496201	0.447573
LRRC59	0.459902	0.197241
HSPA9	0.452761	0.506025
SUPT5H	0.383439	0.305565
HIST1H1C;HIST1H1D;HIST1H1A;HIST1H1T	0.363612	0.466111
PPIB	0.27061	0
DDX5	0.174137	0
MAPRE1	0.15147	0.095668
HNRNPH1	0.086115	0.145777
RRS1	-0.00419	0
SRSF7	-0.15511	0.249834
PA2G4	-0.33419	0
SYNCRIP	-0.3781	0
SMARCA5	-0.83118	0
TOMM20	-0.84178	0.646476

Table A.4. Proteins in **Figures 4.31B** and **4.31D** (**6Yn-Pro+NM1+O vs DMSO+NM1**) that were **not** identified in **Figures 4.31A** and **4.31C** (**6Yn-Pro+NM1 vs DMSO+NM1**). These proteins are highlighted in red in the corresponding **Figures 4.31B** and **4.31D**. Proteins have been arranged in descending order for Log_2 Fold change.

Protein	Log2 Fold change	-Log10(p-value)
DDX21	1.377987	0
EIF4H	0.894744	0
HIST1H3A;H3F3A;HIST2H3A; HIST3H3;H3F3C;HIST2H3PS2	0.885436	0.624118
KHDRBS1	0.883663	0
AHCY	0.841321	0.673293
PCNA	0.652875	0.787144
SFPQ	0.621244	0.732005
VIM	0.607681	1.059016
RTCB	0.58841	0
SNRPB;SNRPN	0.574039	0.600261
PPIA	0.570948	0.668813
CCT4	0.564102	0.528808
H2AFY2	0.50214	0.909467

Table A.5. Proteins in **Figures 4.32A** and **4.33A** (**6Yn-Pro+NM1 vs DMSO+NM1, +H_2O_2**) that were also identified in **Figures 4.32B** and **4.33B** (**6Yn-Pro+NM1 vs DMSO+NM1 (PD1), no H_2O_2**). These proteins are highlighted in green in the corresponding **Figures**. Proteins have been arranged in descending order for Log_2 Fold change. The same list of proteins is shown in **Table A.6**.

Protein	Log2 Fold change	-Log10(p-value)
PARP1	3.846672	1.652674
HIST1H1E	2.815618	0
MIF	1.713501	1.233575
HNRNPD	1.709938	0.748445
PPIB	1.660015	0
PA2G4	1.297882	0
PGAM1	1.124841	0.576642
EIF4A1	1.087206	0.956283
HMGB1	1.048254	0
ANXA2	1.019864	0.571956
DDX5	0.985273	0
RPL29	0.955983	0
PDIA3	0.767563	1.325805
RPL22	0.755857	0.672817
HIST1H1C	0.716428	0.998411
LRRC59	0.713186	0.407246
HNRNPA1	0.667481	0

HSPA9	0.625729	0.58102
MAPRE1	0.617895	0.29806
SYNCRIP	0.524401	0
HNRNPH1	0.51946	0.650085

Table A.6. Proteins in **Figures 4.32B** and **4.33B** (**6Yn-Pro+NM1 vs DMSO+NM1 (PD1), no H_2O_2**) that were also identified in **Figures 4.32A** and **4.33A** (**6Yn-Pro+NM1 vs DMSO+NM1, +H_2O_2**). These proteins are highlighted in green in the corresponding **Figures**. Proteins have been arranged in descending order for Log_2 Fold change. The same list of proteins is shown in **Table A.5**.

Protein	Log2 Fold change	-Log10(p-value)
MIF	0.932961	0.501271
PPIB	0.510748	0.880577
HIST1H1E;HIST1H1D	0.415435	0.740221
HIST1H1C	0.378419	0.212134
HNRNPD	0.211852	0.573071
RPL22	0.073099	1.67071
RPL29	0.065112	0.068278
HNRNPH1	0.053975	0.376998
LRRC59	-0.00626	0.006765
PARP1	-0.04657	0.311125
SYNCRIP	-0.01943	0.080263
HSPA9	-0.02136	0.084425
MAPRE1	-0.05238	0.060811
PDIA3	-0.07126	0.15963
PGAM1;PGAM2;PGAM4	-0.11119	1.644959
HNRNPA1;HNRNPA1L2	-0.1526	0.251962
PA2G4	-0.32071	0.267906
DDX5	-0.37503	0.402074
EIF4A1;EIF4A2	-0.58233	0.398695
ANXA2	-0.63286	0.460383
HMGB1;HMGB1P1	-0.76225	0.516123

Table A.7. Proteins in **Figures 4.32A** and **4.33A** (**6Yn-Pro+NM1 vs DMSO+NM1, +H_2O_2**) that were **not** identified in **Figures 4.32B** and **4.33B** (**6Yn-Pro+NM1 vs DMSO+NM1 (PD1), no H_2O_2**). These proteins are highlighted in red in the corresponding **Figures 4.32A** and **4.33A**. Proteins have been arranged in descending order for Log_2 Fold change.

Protein	Log2 Fold change	-Log10(p-value)
SMAP	3.336305	0
PRPF40A	2.948371	0
CDKN2A	2.294599	0
PAK2;PAK1;PAK3	2.12165	0.42355
RRS1	1.889938	0
MYL6	1.850293	1.270927
CSE1L	1.289517	1.329131
SMARCA5	1.253673	0
APEX1	1.129928	0
RCC2	0.722015	0.385906
SUPT5H	0.700761	0.588136
ILF2	0.598951	0
TOMM20	0.56606	0.269199
SRSF7	0.541213	0.580246

Table A.8. Proteins in **Figures 4.32B** and **4.33B** (**6Yn-Pro+NM1 vs DMSO+NM1 (PD1), no H_2O_2**) that were **not** identified in **Figures 4.32A** and **4.33A** (**6Yn-Pro+NM1 vs DMSO+NM1, +H_2O_2**). These proteins are highlighted in red in the corresponding **Figures 4.32B** and **4.33B**. Proteins have been arranged in descending order for Log_2 Fold change.

Protein	Log2 Fold change	-Log10(p-value)
ARHGDIA	1.17246	0.546882
VIM	0.622622	2.706018
SERBP1	0.547956	0.628423
NME2;NME1;NME2P1	0.528581	0.4484
STIP1	0.504067	0.358553

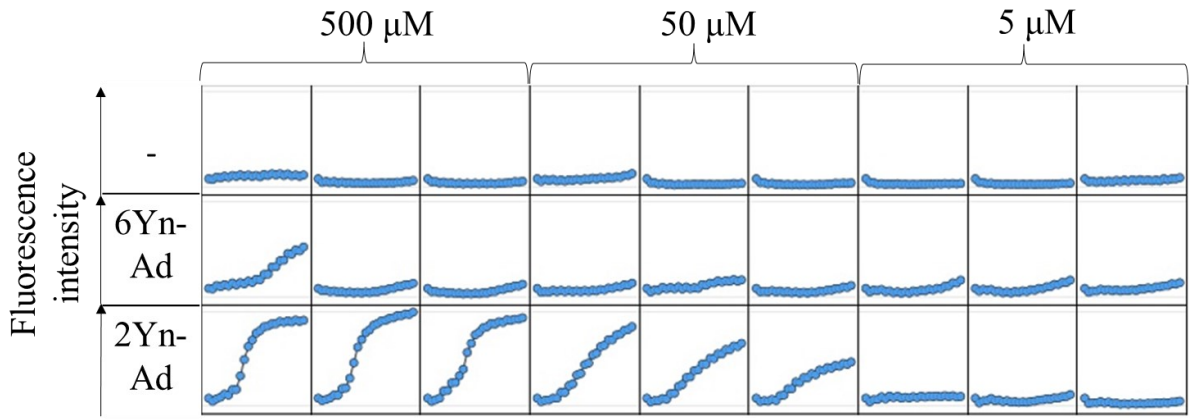


Figure A.10. Cytotoxicity data (IncuCyte assays) for MDA-MB-231 cells following treatment with 6Yn-Ad (**25**) or 2Yn-Ad (**26**). Treatment was done in triplicates at the probe concentrations indicated. Cells were co-treated with Sytox green (fluorescent dye, 250 nm final concentration). Upon cell death, Sytox green permeates into cells and reacts with DNA to produce a fluorescent signal. Increase in fluorescence corresponds to increased cell death due to increased cytotoxicity by a probe. Fluorescent intensity was measured every 1 h (each plotted point = 1 h) for the duration of the probe treatment (24 h).